Universität Bremen

Fachbereich 2: Biologie/Chemie

Dissertation

to obtain the academic degree

Doctor rerum naturalium (Dr. rer. nat.)

# Fundamental Bonding Concepts of Inorganic Chemistry Revisited

*submitted by*

Malte Fugel

July 2019

# Contents

# List of Figures

# List of Tables

# Part I

# Introduction

Chemical bonding is, without a doubt, one of the most significant and fundamental concepts in chemistry, because it describes the interaction that binds atoms together to form molecules. Understanding the nature of chemical bonds is essential for every chemist, because it provides the skills to predict and comprehend molecular properties. However, it needs to be stressed that chemical bonds are only a concept, and not a physical observable for which a unifying theory exists. Therefore, a great variety of different bonding models, which attempt to uncover the theoretical foundations of this concept, have emerged over the past 100 years. A comprehensive review of these concept was recently published by Frenking et al.[1]

The origin of those bonding models dates back to 1916, when G. N. Lewis introduced the notion of *electron pair bonding*,[2] which is also known as covalent bonding.[3] The idea is that a covalent bond corresponds to a pair of electrons shared between two atoms. A solid line connecting these two atoms (e.g. H–H) is used to indicate a covalent bond. This type of representation – the Lewis structure – is still commonly used to portray bonds (Figure 1 shows two examples of Lewis structures). However, Lewis' *electron pair bond* was purely based on empirical findings, and, at that time, it was lacking a physical foundation.[1] Soon after the introduction of *electron pair bonding*, it was postulated that quantum mechanics is necessary for a physically sound description of chemical bonding.[4] The year 1927, when Heitler and London published their quantum mechanical description of the $H_2$ molecule, can be regarded as the advent of quantum chemistry.[5] In that work, they uncovered that the introduction of ionic resonance forms (i.e. $H^+$ $H^-$ and $H^-$ $H^+$) results in an energetic stabilization of the wavefunction of the $H_2$ molecule. Pauling's work to unify Lewis' empirical findings and the new insights provided by quantum chemistry can be regarded as the reason for the continuing success of Lewis structures.[6] Even today, solid lines are used to represent bonds; however, the question arises if every solid line is, in fact, an electron pair shared between two atoms.

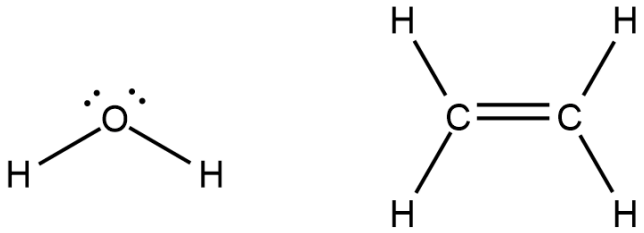


**Figure 1:** Two molecules represented by Lewis structures: Water ($H_2O$, left) and ethene ($C_2H_4$, right). Each bond between two atoms is represented by a line connecting the two atoms. In the water molecule, there are two non-bonded electron pairs at the oxygen, which are referred to as lone pairs. In the ethene molecule, there are two lines representing a C–C double bond, i.e. there are two electron pairs shared between the two carbon atoms.

Besides the *rule of two*, which describes Lewis' observation of electron pair bonding, Lewis also established the *rule of eight*,[4] which is better known as the *octet rule* (this term was later

introduced by Langmuir).[7–9] This rule describes Lewis' finding that most atoms in molecules tend to have a noble gas configuration.[4] Accordingly, for elements of the second period and beyond, eight electrons, corresponding to four electron pairs, are usually found inside the valence shell of the atom, while for hydrogen atoms a noble gas configuration corresponds to the electron configuration of helium, which has two valence electrons. The octet rule is fulfilled for all molecules in Figure 1: The oxygen atom of $H_2O$, for example, has two lone pairs (accounting for four valence electrons) and two O−H bonds, which add another four electrons to its valence electron count, giving a total of eight valence electrons.

In many cases, a bonding description based on Lewis' concepts works remarkably well, however, in other cases, alternative procedures and modifications to the original concept must be applied. One shortcoming of Lewis structures is the assumption that bonds are shared between two atoms (*rule of two*). While this is a good approximation for a great number of bonds, there are many exceptions of molecules containing bonds which are delocalized over the whole molecule.[6] One prominent example for a highly delocalized bonding situation is

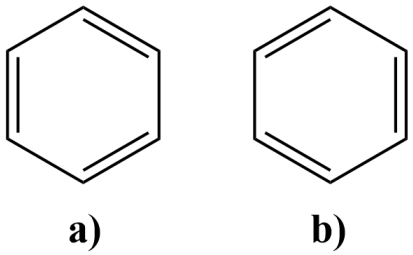


**Figure 2:** Two resonance structures of benzene, which are equally significant for its bonding description.

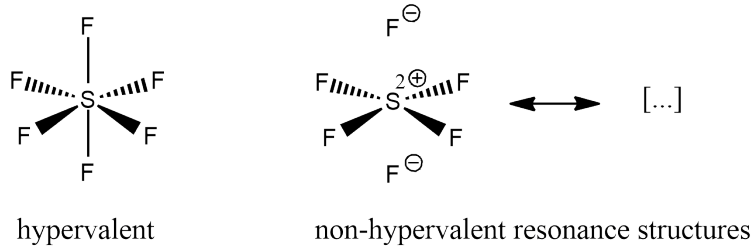


**Figure 3:** Sulfurhexafluoride, $SF_6$, is a molecule, which is often represented by a hypervalent Lewis structure (left, the sulfur atom has 10 valence electrons). However, the bonding can also be described by non-hypervalent resonance structures (right).

the benzene molecule.[10–12] Lewis structure **a)** in Figure 2 has three double bonds, but the arrangement of the three double bonds in Lewis structure **b)** is just as valid. Accordingly, none of the arrangements is favored over the other, and both Lewis structures are equally significant. Ultimately, the "real" bonding situation is described by an average of these two representations. This effect is known as resonance, and the Lewis structures, which are required to account for the "real" bonding situation, are called resonance structures.

Lewis' original model also fails for molecules containing atoms, which, at first glance, violate the octet rule.[7,13,14] Such atoms are termed hypervalent.[14] Lewis took note of the fact that some atoms violate the octet rule, however, he stated that it holds for the vast majority of compounds.[2] If the bonding situation in these molecules is only represented by *electron pair bonds* between two atoms (two-center two electron bonds), d-orbitals must contribute to the bonding (only four bonds can be obtained from s- and p-orbitals alone). However, it has

been shown that d-orbitals play no role in bonds involving elements from the second and third period,[15–17] which has also been shown by Stalke *et al.* experimentally.[18]

Alternative bonding models which go beyond Lewis' theory, such as multi-center multi-electron bonding, have been proposed.[19–23] It is also possible to represent the bonding situation in supposedly hypervalent molecules with the introduction of non-hypervalent resonance structures. In Figure 3, such resonance structures are given for $SF_6$, for which hypervalent Lewis structures are conceivable.[24] Furthermore, traditional Lewis structures do not convey bond polarity, which results in attractive electrostatic interactions between two bonded atoms due to the higher tendency of the more electronegative atom to attract the bonding electrons.[4,25] This is the origin of many molecular properties and is, therefore, an integral part of chemical bonding. Bond polarity also restricts the *rule of two*, because the electron pair is not shared equally between two atoms – the electrons will be more localized at the more electronegative atom. In his seminal paper from 1916, Lewis already distinguished between polar and non-polar bonds,[2] but no solution was presented to quantify bond polarity. Empirically, differences in tabulated electronegativities give an impression on how polarized a bond is,[25–27] but in order to quantify bond polarity, more sophisticated approaches outside the scope of the Lewis picture must be consulted. For example, a method to compute tailor-made electronegativities based on quantum chemical methods was presented by Rahm & Hoffmann.[28]

Although modifications to Lewis' original concepts, such as the introduction of resonance structures, can remedy some of its shortcomings, a quantum chemical treatment of chemical bonding is inevitable, because it provides the theoretical foundation of that concept. In his paper from 1939, Pauling attempted to unify Lewis' *electron pair bonding* and quantum chemistry, which is why he can be regarded as the first mediator between these two concepts.[6] In most contemporary studies on chemical bonding, quantum chemical methods are complemented by a description based on Lewis structures.[29] Every aspect of chemical bonding, which goes beyond Lewis' original concept, is considered to be an effect (e.g. resonance). Hence, the question arises if an effect is only an artefact arsing from the shortcomings of Lewis structures or if it has a direct influence on a molecular property.

As such, the concept of chemical bonding is neither inherent to a molecular wavefunction nor to an electron density. No "bonding operator" exists, which can be applied on a molecular wavefunction to yield chemical bonds. The quantum chemical *valence bond (VB)* theory gives orbitals, which can be readily related to features of Lewis structures,[30,31] however, the *molecular orbital (MO)* theory and *density functional theory (DFT)*, which are much more popular in contemporary quantum chemistry, give orbitals which are mostly delocalized over the whole molecule.[32–34] Therefore, it is often impossible to link MOs to Lewis structures. Consequently, the development of bond analysis methods is necessary to extract information on chemical bonding in terms of the Lewis picture from a wavefunction or an electron density.[35] It is possible to

differentiate between three types of bond analysis methods: Orbital space methods, real space methods and energy space methods.[36] Orbital space methods, such as the *natural bond orbital* approach, give localized orbitals, which can be linked to features of Lewis structures like bonds and lone pairs.[37] For real space methods, on the other hand, the notion of an orbital does not exist.[38–40] Instead, a real space function, such as the electron density,[38] is analyzed topologically. A partitioning of the electron density defines atoms inside a molecule and topological criteria can be applied to identify bonds.[41] Examples for real space bond analysis methods are the *Quantum Theory of Atoms in Molecules (QTAIM)*, which analyzes the electron density,[38,41] and the *electron localization function (ELF)*,[39] which analyzes a function measuring the localization of electrons. Energy space methods analyze chemical bonding in terms of energy contributions. For example, in an *energy decomposition analysis (EDA)*, the interaction energy between two atoms is decomposed into physically meaningful terms, such as orbital and electrostatic interactions and repulsion between electron pairs.[35,42] The mere fact that a large variety of bond analysis methods exists emphasizes that chemical bonds are, in fact, only a concept.

The main focus of the present thesis is the analysis of chemical bonds in light of a complementary bonding analysis. The systems which are regarded are well known to every chemist, however, in some of the systems, the bonding situation is ambiguous, because a description based on a single Lewis structure is not feasible. The intention of the present thesis is to shed light on the bonding situation in these systems, and to resolve misconceptions concerning outdated Lewis representations. Moreover, this thesis aims to provide a better understanding of chemical bonding in these systems, and to give an impression on the information value provided by a complementary bonding analysis. The topics of the present thesis can be assigned into three categories:

1. **A complementary bonding analysis and the Lewis picture** – Can a complementary bonding analysis confirm the Lewis description of some well known inorganic systems, or do we need to rethink about how bonding situations are represented by Lewis structures?

2. **The transformation of chemical bonds** – Can a complementary bonding analysis reveal how the nature of chemical bonds changes in the course of a reaction?

3. **From structure correlation to bonding correlation** – Can the bonding situation in a carefully chosen array of crystal structures represent a chemical reaction, or rather, is there a way to experimentally monitor a chemical reaction using X-ray diffraction in combination with the tools provided by a complementary bonding analysis?

This thesis is comprised of published papers, submitted manuscripts and full research reports. There are four published papers in the first category (**a complementary bonding analysis**

**and the Lewis picture**), two submitted manuscripts in the second category (**The transformation of chemical bonds**), and one submitted manuscript and a full research report in the third category (**From structure correlation to bonding correlation**). In the following paragraphs, the contents of these works is briefly outlined to show what is to come in the present thesis.

## A complementary bonding analysis and the Lewis picture

The systems which are examined in this part have been chosen, so that a broad spectrum of fundamental bonding concepts is covered. Ionic and covalent interactions will be classified, and ambiguous bonding situations involving resonance and hypervalency will be tackled. This part will not only provide a deep understanding of the bonding situation in these systems, but the complex bonding situations, which are investigated, will put a *complementary bonding analysis* to the test.

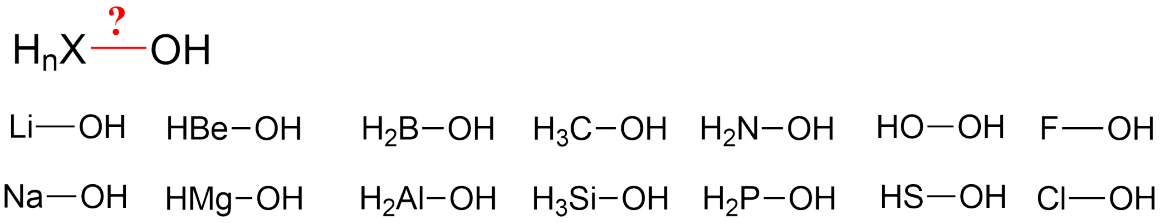


**Figure 4:** The $H_nXOH$ model compounds, for which the X−O bond was analyzed by a complementary bonding analysis.

The first of these papers entitled *"A Variety of Bond Analysis Methods, One Answer? An Investigation of the Element – Oxygen Bond of Hydroxides $H_nXOH$"*[36] gives a good first impression on the information value provided by a complementary bonding analysis in that a systematic array of element-oxygen bonds (the element is from the second or third period) of hydroxide model compounds, which are depicted in Figure 4, is analyzed. This study provides a deep insight into the nature of element-oxygen bonds and it is shown how different bond analysis methods complement each other. Ultimately, the complementary bonding analysis performed in this study allows for a classification of the element-oxygen bonds into different categories: Ionic, highly polarized, polarized covalent, and charge shift bonds can be identified. The latter refers to a bonding type, which cannot be represented by a single Lewis structure.[43,44] Instead, it is required to describe charge-shift bonds using covalent and ionic resonance structures. The most prominent example for a charge shift bond is the F−F bond of the $F_2$ molecule, so even some supposedly simple bonding situations cannot be described by a single Lewis structure.[43,44] This paper is the first of its kind, because properties from a variety of bond analysis methods are compared to each other in a systematic way. This reveals how they can complement each

other to give an unambiguous picture of the bonding situation of the element-oxygen bond.

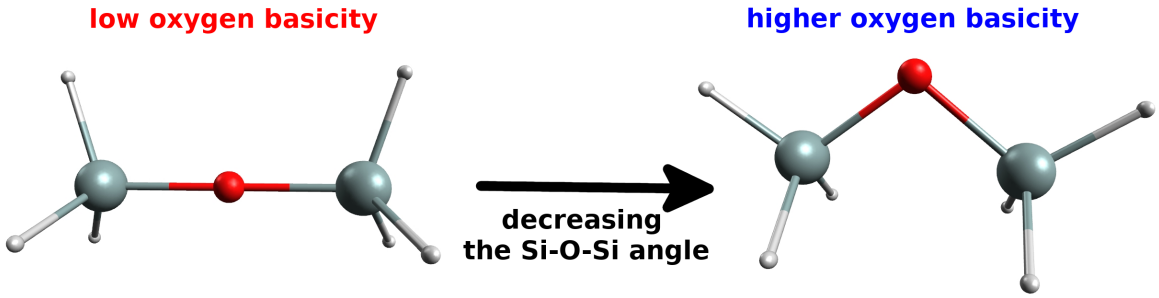


**Figure 5:** Two disiloxane molecules ($H_3SiOSiH_3$) at different Si−O−Si angles.

After gaining an understanding of the information value provided by a complementary bonding analysis, this knowledge can be transferred to comprehend molecular properties. In the second paper attached to this thesis – *"Covalency and Ionicity Do Not Oppose Each Other – Relationship Between Si-O Bond Character and Basicity of Siloxanes"*[45] – the basicity of siloxanes is inspected in relation to the Si−O bond character. The oxygen atom bridging the two silicon atoms of a siloxane unit is known to only act as a weak base, which results in the formation of weak hydrogen bond complexes.[46–50] However, it was found that the basicity of the oxygen atom can be increased if the Si−O−Si angle is decreased (see Figure 5). In this study, the Si−O bond character was investigated for $H_3Si-O-SiH_3$ model compounds at different Si−O−Si angles using a complementary bonding analysis. The aim of this study is to identify the factors responsible for the increased basicity of the oxygen atom at low Si−O−Si angles. Furthermore, cyclic siloxane systems with inherently low Si−O−Si bond angles, which pose interesting systems due to the increased basicity, are investigated.

The next two papers deal with systems, where it is not straightforward to find appropriate Lewis structures. The paper *"Investigating the Resonance in Nitric Acid and the Nitrate Anion Based on a Modern Bonding Analysis"*[51] deals with the bonding in a very common anion found in inorganic chemistry – the nitrate anion ($NO_3^-$). A variety of resonance structures must be considered to adequately describe its bonding situation (see Figure 6). The resonance in the nitrate anion and related compounds ($HNO_3$ and $FNO_3$) is investigated using a complementary bonding analysis. Additionally, a wavefunction of potassium nitrate ($KNO_3$) obtained from an X-ray wavefunction refinement (XWR) is investigated. An XWR provides a way to determine a wavefunction from X-ray diffraction data,[52,53] and, thus, allows for an experimental investigation of the bonding situation.

In the paper *"Revisiting a historic concept using quantum crystallography: Are phosphate, sulfate and perchlorate anions hypervalent?"*[54] the concept of hypervalency is tackled. Phosphate, sulfate and perchlorate anions are often represented by Lewis structures with hypervalent phosphorus, sulfur and chlorine atoms (see Figure 3).[18,55] In this study, a complementary bond-

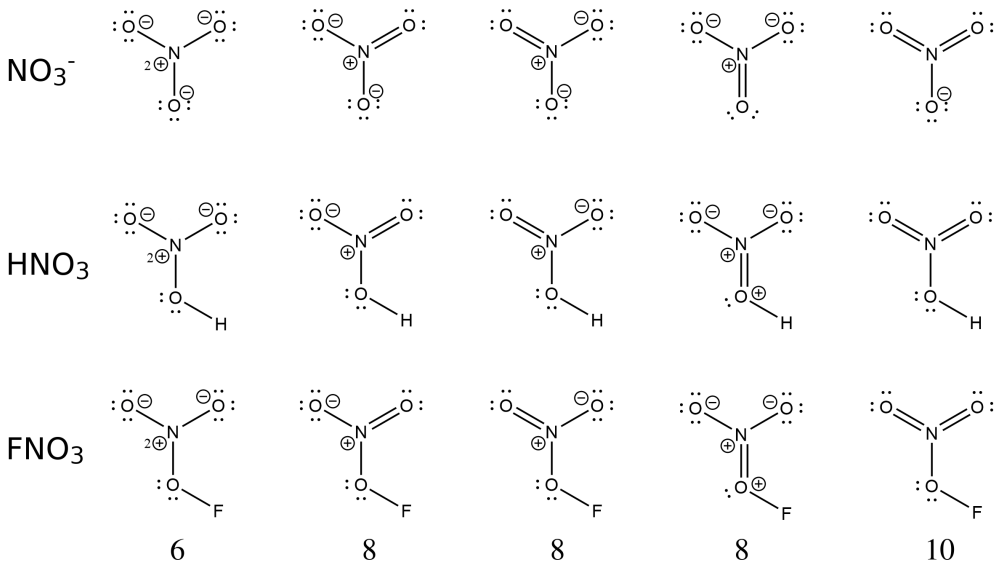


**Figure 6:** A variety of resonance structures of $NO_3^-$, $HNO_3$ and $FNO_3$. The numbers at the bottom of each column signify the valence electron count of the nitrogen atom. The nitrogen atom in the resonance structures of the last column have more than eight valence electrons, which rules out these bonding representations.

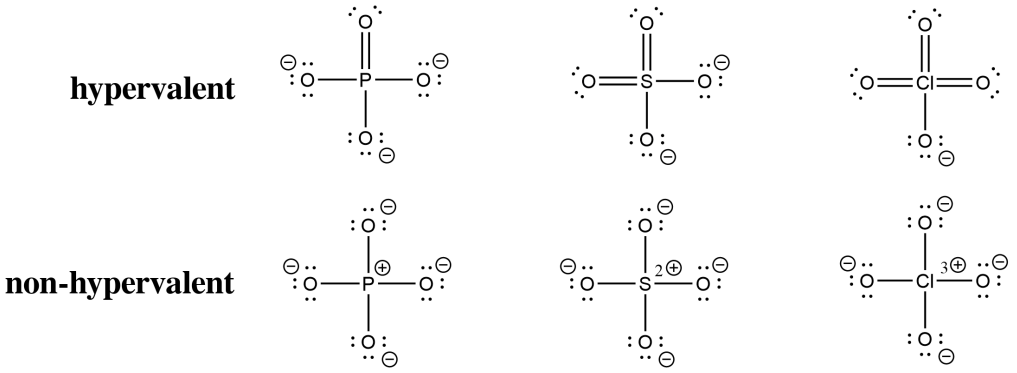


**Figure 7:** Hypervalent and non-hypervalent bonding representations of phosphate ($PO_4^{3-}$), sulfate ($SO_4^{2-}$) and perchlorate ($ClO_4^-$) anions.

ing analysis was employed to determine if hypervalent representations are in fact significant, or if alternative bonding models need to be considered. In addition to theoretical calculations performed on the isolated anions, an X-ray wavefunction refinement was conducted for struvite ($MgNH_4PO_4 \cdot 6\,H_2O$), lithium sulfate ($Li_2SO_4 \cdot H_2O$) and potassium perchlorate ($KClO_4$) crystals.

## The transformation of chemical bonds

In the course of a chemical reaction, chemical bonds are formed, while others are cleaved. The formation of a chemical bond is a continuous process, which can be monitored by properties obtained from a *complementary bonding analysis*. If these properties are related to the potential energy surface along the reaction coordinate, a deeper understanding of the chemical reaction is obtained. In this part, nucleophilic substitution reactions of second order ($S_N2$) are analyzed. This reaction type has been studied extensively,[56–61] but, using a *complementary bonding analysis* an even deeper understanding of $S_N2$ reactions is provided.

Two submitted manuscripts are attached to this thesis which investigate a nucleophilic substitution reaction of second order ($S_N2$) at silicon centers. In the first manuscript, the role of hydrogen bonding in gas-phase $S_N2$ reactions at silicon centers is uncovered. The reaction pathway is modeled for a variety of systems, which are depicted in Figure 8. With the help

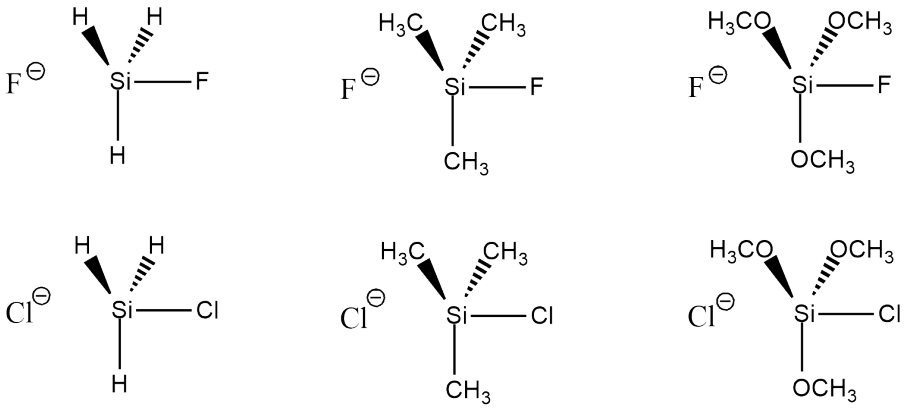


**Figure 8:** Depiction of the silicon systems $XSiR_3X$, which were used to investigate the influence of hydrogen bonding on $S_N2$ reactions at silicon centers.

of an *energy decomposition analysis*,[35,42] it is revealed that weak hydrogen bonds between the methyl or methoxy groups and the nucleophile ($Cl^-$ or $F^-$) lead to an energetic stabilization along the reaction pathway. In some cases, this even results in the formation of stable reaction complexes.[57] In the second paper, the reaction pathway of an $S_N2$ reaction at a silicon center ($Cl^- + H_3Si{-}Cl \longrightarrow ClSiH_3 + Cl^-$) is compared to the corresponding reaction at a carbon center ($Cl^- + H_3C{-}Cl \longrightarrow ClCH_3 + Cl^-$). The purpose of this study is to uncover the difference between the stable transition complex separating the reactants from the products (minimum in the potential energy surface) in the silicon system,[57] and the unstable transition state, which is obtained for the carbon system (saddle point in the potential energy surface).[62] Figure 9 shows a schematic representation of the potential energy surface along the reaction pathway for the carbon and silicon systems.

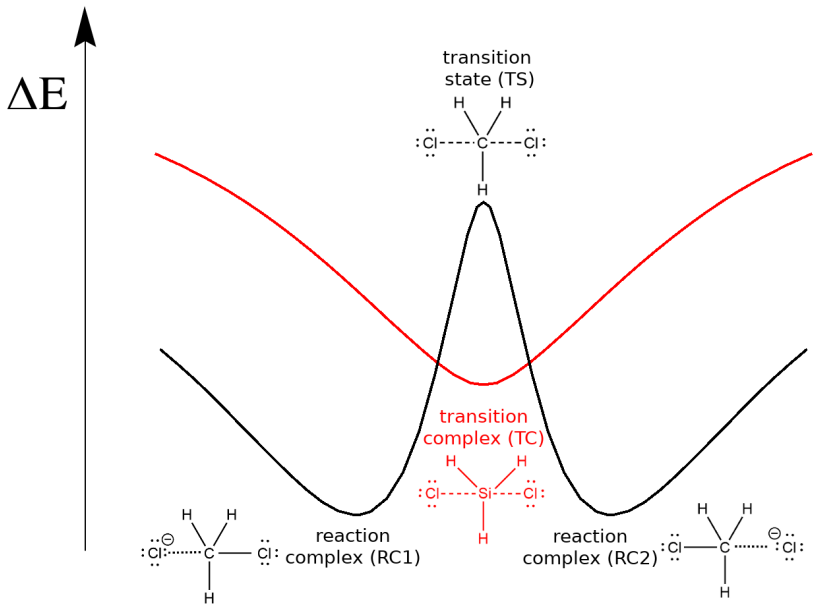


**Figure 9:** Schematic representation of the potential energy surface along the reaction pathway of $S_N2$ reactions at silicon ($Cl^- + H_3Si-Cl \longrightarrow ClSiH_3 + Cl^-$) and carbon centers ($Cl^- + H_3C-Cl \longrightarrow ClCH_3 + Cl^-$).

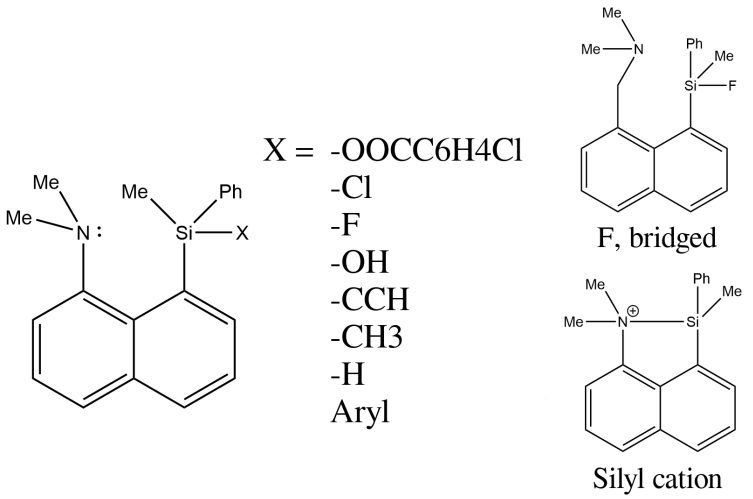


**Figure 10:** Pentacoordinated silicon systems which are used to study a nucleophilic addition of the nitrogen atom to the silicon atom using *structure* and *bonding correlations*.

## From *structure correlation* to *bonding correlation*

The studies of the $S_N2$ reactions, which were just outlined, are purely of theoretical nature. Determining an experimental reaction pathway is an ambitious task, and usually most experimental information is obtained from indirect measurements complemented by theoretical calculations. To get access to a 'molecular movie' through femtosecond electron diffraction or

the use of X-ray free electron lasers, an enormous experimental and financial effort is required. Bürgi's and Dunitz's *structure correlation* approach offers an indirect way to get experimental access to a reaction pathway based on a static crystal structure analysis.[63–67] In that approach, a dynamic process of a particular molecular fragment (this can correspond to a reaction) can be simulated by regarding a variety of crystal structures containing that fragment. Due to the influence of the crystal environment, the fragment will be deformed and polarized in each of the crystal structures, and is "frozen" by its environment. By bringing the crystal structures into a reasonable chronological sequence, the dynamic process can be simulated indirectly. Correlations of structural parameters can be uncovered, and interpreted in a chemical way. In a full research report attached to this thesis, the *structure correlation* approach is extended to a *bonding correlation* approach in that correlations with bond properties obtained from a *complementary bonding analysis* are considered instead of purely geometrical parameters. The formation of a pentacoordinated silicon atom following a nucleophilic attack is modeled by a variety of crystal structures containing the organosilicon fragment depicted in Figure 10. The substituent X is varied in all crystal structures to tune the strength of the N···Si interaction. By choosing substituents which result in weak, medium and strong N···Si interactions, a nucleophilic approach of the nitrogen atom towards the electrophilic silicon atom can be simulated. Both *structure* and *bonding correlations* are found, and analyzed in a chemical way.

All studies attached to the present thesis investigate a complicated bonding situation in an inorganic system. In every study, modern bond analysis methods are applied to study the bonding situation, but the original Lewis picture will not be disregarded. Some studies may show the limits of Lewis' bonding model, but its usefulness will be demonstrated throughout the entire thesis. Before turning to these studies in detail, a brief overview of the evolution of bonding models and theoretical foundations of the methods applied in this study are provided.

# Part II

# Theoretical foundations

# Chapter 1

# The Evolution of Chemical Bonding Concepts

## 1.1 Chemical bonding as an empirical concept

In Lewis' groundbreaking paper *The Atom and the Molecule*, which was published in 1916,[2] he summarized his lectures on *electron pair bonding* which he held from the year 1902. Lewis realized that his concept violates classical physics, in that two negatively charged electrons would repel each other and not form pairs. He stated that, *"electric forces between particles which are very close together do not obey the simple law of inverse squares which holds at greater distances"*.[2] He assumed that valence electrons arrange at the corners of a cube (cubic atoms). Ideally, there is an electron located at each of the eight corners of the cube (this corresponds to

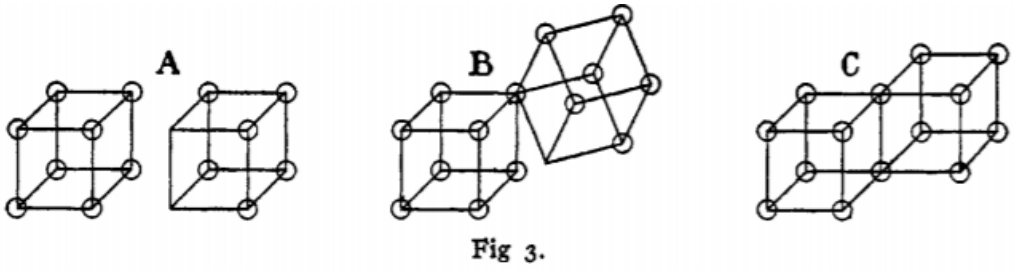


**Figure 1.1:** Representation of Lewis' cubic atoms. **A:** Two separate halogen atoms with seven valence electrons; **B** and **C:** The two halogen atoms connect its vertices to form an $X_2$ molecule, with both atoms acquiring a valence electron count of eight. Reprinted with permission from G. N. Lewis, *J. Am. Chem. Soc.* **1916** 38(4), 762-785. ©Copyright 1916 American Chemical Society.

a noble gas configuration). A fully occupied cube can be obtained by the formation of *electron pair bonds*. For example, a fluorine atom has seven valence electrons, and, thus, it is missing one electron to have all corners of its cube occupied by an electron. If the vertices of two fluorine

"cubes" with only one electron connect, two electrons are shared between the two cubes, and an *electron pair bond* is formed (see Figure 1.1). This model also works for double bonds (where the faces of two cubes are connected), but fails for triple bonds. This is why Lewis introduced the concept of tetrahedral atoms, which also accounts for the formation of triple bonds.[2]

Although the name Lewis is commonly associated with the *electron pair bond*, Langmuir contributed significantly in the further development of the concept. In papers published between 1919 and 1920, he introduced the term covalence and defined the octet rule.[3,7,13] In 1923, Lewis published his book *Valence and the Structure of Atoms and Molecules*, where he first took note of the emerging quantum theory.[4] While he acknowledged that this theory provides the physical foundations of chemical bonding, he also expressed his dislike towards the emerging field of quantum mechanics. In his book, Lewis introduced highly important concepts, such as bond polarity, electronegativity and partial charges of atoms. Furthermore, he introduced his definition of acids and bases: A base is a compound, which acts as an electron pair donor, and an acid is an electron pair acceptor.[4] He also differentiated between shared-electron bonds and dative bonds, which are two variants of covalent bonding.[4] In contrast to a shared-electron bond, where each of the bonded atoms provides one electron for a chemical bond, a dative bond is formed between a lone pair donor (Lewis base) and a lone pair acceptor (Lewis acid) (e.g. $NH_3 + BH_3 \longrightarrow H_3N{-}BH_3$). In one chapter of his book, he noted that there is a series of compounds containing atoms which violate the *rule of eight*.[4] Nowadays, these fundamental concepts are still being taught in undergraduate chemistry lectures.

## 1.2 Chemical bonding as a quantum mechanical concept

In 1926, Schrödinger introduced his famous *Schrödinger equation*, which was employed to comprehend the electronic structure of atoms.[68] Its time-independent version is given in Equation 1.1, where $\hat{H}$ denotes the Hamilton operator, $E$ the energy and $\psi$ the wavefunction of the system.[68]

$$\hat{H}\psi = E\psi \tag{1.1}$$

A wavefunction, which is obtained from the solution of this eigenwert problem, describes a quantum mechanical system in its entirety. According to Born's interpretation of the wavefunction, the probability of finding an electron in the volume element $d\tau$ at the point $r$ is proportional to $|\psi(r)|^2 d\tau$, which entails that the electron density of a molecule can be calculated from its molecular wavefunction.[69] For a hydrogen-like system (one nucleus and one electron) the Hamilton operator can be written as follows (Equation 1.2).[70]

$$\hat{H} = \hat{T} + \hat{V} = -\frac{\hbar}{2m_e}\nabla^2 - \frac{Ze^2}{4\pi\epsilon_0 r} \tag{1.2}$$

The Hamilton operator of hydrogen-like atoms is the sum of the kinetic energy operator $\hat{T} = -\frac{\hbar}{2m_e}\nabla^2$ (where $\hbar$ is the reduced Planck constant ($\hbar = \frac{h}{2\pi}$), $m_e$ the mass of an electron and $\nabla^2$ the Laplace operator) and the potential energy operator $\hat{V} = -\frac{Ze^2}{4\pi\epsilon_0 r}$ (where $Z$ is the charge of the atomic number, $e$ the elementary charge of an electron, $\epsilon_0$ the vacuum permittivity and $r$ the electron-nucleus distance).[70] An analytical solution of the Schrödinger equation is only feasible for hydrogen-like atoms. For systems with more than one electron, on the other hand, the application of numerical procedures and approximations is required.

In 1927, Heitler and London applied the newly introduced Schrödinger equation to comprehend the bonding in the $H_2$ molecule.[5] In their work, they were able to show that two neutral hydrogen atoms attract each other due to quantum mechanical interference between the two one-electron wavefunctions of the hydrogen atoms. A wavefunction can either have a negative or positive sign, and, thus, both constructive and destructive interference, giving rise to attractive (bonding) and repulsive (anti-bonding) configurations, is obtained. In the ground-state $H_2$ molecule, two electrons are located inside the bonding orbital, which corresponds to a singlet state.[70] The Pauli exclusion principle states that a maximum of two electrons with opposite spin can occupy a spatial orbital.[71] This establishes the connection between quantum chemistry and Lewis' empirical bonding model, although it was shown that the cause of chemical bonding is quantum mechanical interference, and not the pairing of electrons.

In Lewis' paper *The Chemical bond* from 1933, he addresses the problem that quantum theory cannot satisfy "qualitative chemical demands".[72] Pauling, on the other hand, supported both quantum theory and Lewis' bonding model. In his paper *The Nature of the Chemical Bond* from 1939, Pauling attempted to relate Lewis' *electron pair bond* to quantum theory.[6] In fact, the continuing success of Lewis' electron pair model can be attributed to Pauling's work. Pauling was a defender of the valence bond theory, which was the quantum chemical concept derived from Heitler's and London's treatment of the $H_2$ molecule.[1] The orbitals which constitute the wavefunction obtained form the valence bond approach can be readily related to features of Lewis structures, because they are usually located at a single atom (core orbitals or lone pairs), or between two atoms (bonds).[31] The introduction of an adequate number of resonance structures remedies the shortcomings of localized Lewis structures outlined in the Introduction. There is an obvious link between the valence bond approach and Lewis structures, and thus, it is often more intuitive to analyze *valence bond* calculations. Although *valence bond theory* started off as the standard procedure to calculate molecular wavefunctions, it is only of minor importance in contemporary quantum chemistry. The greatest shortcoming of this approach is the fact that valence bond calculations are computationally expensive and they converge very slowly, which makes them unfeasible in most chemical systems.[31] Nowadays, the great majority of molecular wavefunctions are computed from *molecular orbital (MO) theory* and *density functional theory (DFT)*, which are much less computationally expensive, and, therefore, they are

suitable for more complex chemical systems. However, the resulting molecular orbitals are rarely localized between two atoms,[37] which makes it harder to link them to Lewis structures, but the resulting MOs have a predictive power of their own. The frontier MO theory, for example, can reliably predict the reactivity of two reactants by analyzing the interaction between the highest occupied molecular orbital (HOMO) of one molecule and the lowest unoccupied molecular orbital (LUMO) of the other molecule.[73] Nevertheless, if one wishes to analyze bonding in terms of the Lewis picture and valence bond calculations are no option, bond analysis methods must be applied to extract bonding information from a molecular wavefunction. In the following, MO, DFT and VB approaches are briefly outlined as methods to calculate wavefunctions.

# Chapter 2

# Foundations of quantum chemistry

## 2.1 The molecular orbital approach

As stated in the preceding chapter, the Schrödinger equation (Equation 1.1) poses the fundamental eigenwert problem, which determines the electronic properties of quantum mechanical systems, such as atoms and molecules.[68] For hydrogen-like atoms, the Hamilton operator only consists of two terms: The kinetic energy operator of one electron and the potential energy operator, which corresponds to the electron-nucleus attraction.[70] For a molecule with $N$ atoms and $n$ electrons, the Hamilton operator is written as follows:[70]

$$\hat{H} = -\frac{\hbar^2}{2m_e}\sum_{i=1}^{n}\nabla_i^2 - \frac{\hbar^2}{2}\sum_{K=1}^{N}\frac{1}{M_K}\nabla_K^2 + \sum_{K=1}^{N}\sum_{L>K}^{N}\frac{Z_K Z_L e^2}{4\pi\epsilon_0 R_{KL}} + \sum_{i=1}^{n}\sum_{i>j}^{n}\frac{e^2}{4\pi\epsilon_0 r_{ij}} - \sum_{K=1}^{N}\sum_{i=1}^{n}\frac{Z_K e^2}{4\pi\epsilon_0 r_{Ki}} \quad (2.1)$$

The first two terms correspond to the kinetic energy operator of $n$ electrons and $N$ nuclei. The third and fourth terms account for the nuclei-nuclei and electron-electron repulsion. Finally, the last term gives the electron-nucleus attraction.

For many-body systems, the Schrödinger equation cannot be solved analytically, and thus, approximations and numerical procedures must be applied.[70] According to the **Born-Oppenheimer** approximation, the molecular Hamilton operator $\hat{H}$ can be split into an electronic Hamilton operator $\hat{H}_e$ and a nuclear Hamilton operator $\hat{H}_n$, which only contains the terms that concern the nucleus (kinetic energy of the nuclei and nucleus-nucleus repulsion).[74] After application of this approximation, the electronic and nuclear Hamilton operator can be dealt with separately. According to the **orbital approximation**, a molecular wavefunction can be built up from one-electron wavefunctions – the molecular orbitals, $\Phi$.[75] Within this approximation, electron-electron interactions are neglected. The exact solution of the Schrödinger equation for hydrogen-like atoms gives atomic orbitals, and thus, it is assumed that a linear combination of

atomic orbitals yields molecular orbitals. This corresponds to the **LCAO-MO approximation** (LCAO = linear combination of atomic orbitals), which forms the basis of MO theory.[76] Equation 2.2 gives the linear combination, which generates the i$^{\text{th}}$ molecular orbital $\phi_i$ from atomic basis functions $\chi_r$ of atom $r$ (a basis function is used to describe an atomic orbital).[70]

$$\phi_i = \sum_r c_{ri}\chi_r \tag{2.2}$$

A multiplication of a spatial molecular orbital with a spin coordinate ($\alpha$ or $\beta$) yields two spin orbitals. According to the Pauli principle each electron must have a unique set of quantum numbers, and thus, only a single electron can occupy such a spin orbital.[77] Consequently, two electrons with opposite spin can occupy a spatial molecular orbital. From the Pauli principle, it also follows that an electronic wavefunction is antisymmetric under particle interchange, or in other words, the wavefunction must change its sign if two electrons indices are exchanged. This criterion is satisfied if a Slater determinant containing all spin orbitals is applied to represent the molecular wavefunction.[78]

The Hartree-Fock approach is a procedure to numerically solve the Schrödinger equation under consideration of the approximations and principles outlined in the preceding paragraph.[78–83] In this approach, the electron-electron repulsion is accounted for by the central field approximation, according to which an electron moves in the average field exerted by all other electrons.[70] For each of the $n$ molecular orbitals, a Hartree-Fock equation is formulated:

$$\begin{aligned}
\hat{F}\Phi_1(1) &= \epsilon_1\Phi_1(1) \\
\hat{F}\Phi_2(1) &= \epsilon_2\Phi_2(1) \\
\hat{F}\Phi_3(1) &= \epsilon_3\Phi_3(1) \\
&\vdots \\
\hat{F}\Phi_n(1) &= \epsilon_n\Phi_n(1)
\end{aligned} \tag{2.3}$$

The Fock operator $\hat{F}$ is defined as follows (Equation 2.4).

$$\hat{F} = \hat{h} + \sum_{i=1}^{n}(2\hat{J}_i - \hat{K}_i) \tag{2.4}$$

The one-electron Hamilton operator $\hat{h}$ corresponds to the Hamilton operator if electron-electron repulsion is completely neglected. The Coulomb operator $\hat{J}$ introduces the electron-electron re-

pulsion by application of the central field approximation, and the exchange operator $\hat{K}$ accounts for the energy contribution originating from the exchange of electrons in the same spin state. Because the Coulomb and exchange operators already contain molecular orbitals, it follows that the Hartree-Fock equations can only be solved iteratively under application of the variation principle, which states that the energy of an approximate wavefunction is always higher than the energy of the true wavefunction.[70] Consequently, the final wavefunction is obtained by minimizing the total energy. Because molecular orbitals are required for the first step of the Hartree-Fock approach, an initial MO guess (e.g. from a Hückel calculation[84]) is required.

One shortcoming associated with wavefunctions obtained from the Hartree-Fock approach directly follows from the application of the central field approximation, which ignores electron correlation.[70] In the central field approximation, the electron-electron repulsion is overestimated, because electrons cannot avoid each other in an average field of electrons. In reality, the motion of electrons is correlated, so that the electron-electron repulsion is minimized (dynamic correlation).[70] Another shortcoming of the Hartree-Fock approach is the fact that only a single Slater determinant corresponding to one possible electron configuration is considered (static correlation). The total energy of a wavefunction is lower if more than one configuration is considered.[70] Post-Hartree-Fock methods, such as the configuration interaction,[85] perturbation theory[86] and coupled cluster calculations,[87] attempt to remedy these shortcomings. In coupled cluster calculations, for example, the molecular wavefunction is expressed as a weighted linear combination of the ground-state Slater determinant and others corresponding to exited states.[70]

## 2.2 Density Functional Theory

Post-Hartree Fock methods are computationally expensive, which often makes the computation of large systems unfeasible. For these systems, the density functional theory (DFT) is sometimes the only practical alternative, since its computational effort is less demanding.[88] As opposed to the wavefunction-based Hartree-Fock approach, DFT is based on the electron density $\rho$.[89,90] According to the Hohenberg-Kohn existence theorem, the ground-state energy of a molecule can be expressed as a function of its ground-state electron density (E[$\rho$]), which is itself a function of the position.[89] A function of a function is called a functional – hence the name "density functional theory". Equation 2.5 shows the ground-state energy of a molecule as a functional of its ground-state electron density.[70]

$$E[\rho] = T[\rho] + V_{ee}[\rho] + \int \rho(r)v(r)dr \tag{2.5}$$

$T[\rho]$ and $V_{ee}[\rho]$ are the kinetic energy and electron-electron repulsion functional, respectively. The last term, where $v(r)$ is the external potential exerted by the nuclei, corresponds the

electron-nuclei attraction.

The Hohenberg-Kohn variational theorem, which is analogous to the variation principle for wavefunctions, states that it is not possible for the energy functional of a trial electron density $E[\rho']$ to be lower than the true ground-state energy of the molecule.[90] To derive the ground-state electron density, Kohn and Sham introduced a reference system with $n$ non-interacting electrons in an external potential $v_{ref}(r)$, which is chosen so that the electron density of the reference system is identical to the true homogeneous electron density.[90] Equation 2.6 gives the Hamilton operator for such a reference system, $h_{ref}$, which is expressed as the sum of one-electron Hamilton operators of the $n$ electrons, $h_i^{KS}$.[70]

$$h_{ref} = \sum_{i=1}^{n} h_i^{KS}, \qquad h_i^{KS} = -\frac{\hbar^2}{2m_e}\nabla_i^2 + v_{ref}(r_i) \tag{2.6}$$

The one-electron Kohn-Sham orbitals $\Phi_m^{KS}$ are eigenfunctions to the one-electron Kohn-Sham Hamilton operator (Equation 2.7).[70]

$$h_i^{KS}\Phi_m^{KS}(i) = \epsilon_m^{KS}\Phi_m^{KS}(i) \tag{2.7}$$

After solving these equations iteratively and self-consistently using an equivalent procedure to the one applied in the Hartree-Fock method, the electron density can be calculated from the one-electron Kohn-Sham orbitals according to Equation 2.8.[70]

$$\rho = \sum_{i=1}^{m} |\Phi_m^{KS}|^2 \tag{2.8}$$

While the true homogeneous electron density can be determined from the reference system, the functionals $T[\rho]$ and $V_{ee}[\rho]$ in Equation 2.5 remain unknown. The total energy functional can be expressed as the sum of contributions from the non-interacting reference system and correction terms which introduce the effects neglected in a non-interacting system – $\Delta T[\rho]$ and $\Delta V_{ee}[\rho]$. If the two correction terms are summed up and termed the exchange-correlation energy functional, $E_{xc}[\rho]$, the total energy functional can be expressed as follows:[70]

$$E[\rho] = T_{ref}[\rho] + \frac{1}{2}\int\int \frac{\rho(\vec{r}_1)\rho(\vec{r}_2)}{r_{12}} d\vec{r}_1 d\vec{r}_2 + \int \rho(r)v(r)dr + E_{xc}[\rho] \tag{2.9}$$

The main challenge of the DFT approach is to find approximations to the exchange-correlation energy functional, because it is unknown. Many different approaches, such as the local density approximation (LDA)[91,92] or the local spin density approximation (LSDA)[93] which rely on expressions for a uniform electron gas, have been developed. The so called hybrid functionals, such as B3LYP,[94,95] which are applied in the present thesis, make use of exchange and correlation

contributions derived from a variety of different methods, such as Hartree-Fock, with empirical scale factors.

## 2.3 The valence bond approach

Nowadays, most molecular wavefunctions are computed by MO theory, however, modern valence bond methods are still being developed up to this day.[30,96] Especially in the field of bonding analysis, valence bond methods enjoy great popularity, because they offer a direct link to the Lewis picture of chemical bonding.[96] In the following, the theoretical foundations of valence bond theory are briefly outlined.

In valence bond theory, the molecular wavefunction is represented by a combination of functions $\Phi_K$, which can be related to explicit covalent and ionic Lewis structures (equation 2.10).[30]

$$\psi = \sum_K C_K \Phi_K \tag{2.10}$$

Each of the valence bond structures $\Phi_K$ can be represented by atomic orbitals or hybridized atomic orbitals. They are spin eigenfunctions which are antisymmetric with respect to the permutation of two electron indices.[96] For a molecule A–B, one covalent structure (A–B) and the two ionic structures ($A^+$ $B^-$ and $A^-$ $B^+$) must be considered, and by application of Equation 2.10, the wavefunction of A–B can be expressed as follows:[96]

$$\psi_{AB} = C_{\mathrm{A-B}}\Phi_{\mathrm{A-B}} + C_{\mathrm{A^+B^-}}\Phi_{\mathrm{A^+B^-}} + C_{\mathrm{A^-B^+}}\Phi_{\mathrm{A^-B^+}} \tag{2.11}$$

The energetic stabilization of the covalent valence bond structure stems from the resonance of

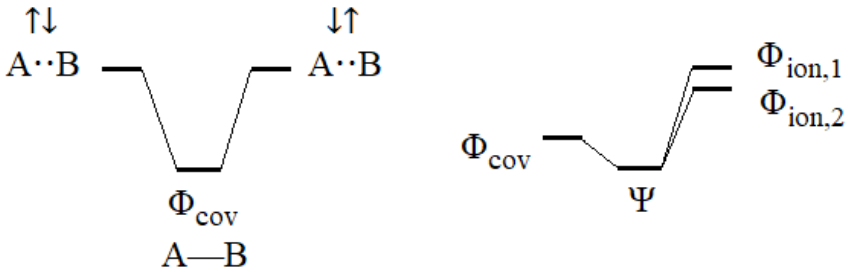


**Figure 2.1:** Left: Resonance between two covalent forms with opposite spin (↑↓ and ↓↑) leads to an energetic stabilization of the covalent valence bond structure $\Phi_{cov}$, right: Resonance between the covalent and ionic resonance structures leads to an energetically stabilized molecular wavefunction

the two covalent forms with opposite spins (A↑↓B and A↑↓B).[96] Figure 2.1 shows a schematic representation of this stabilization. If the bond is primarily covalent, the covalent structure $\Phi_{cov}$

will be lower in energy than the ionic structures $\phi_{ion,1}$ and $\phi_{ion,2}$. For a primarily ionic bond, on the other hand, it is the other way around. The mixing of ionic and covalent valence bond structures will lower the energy of the molecular wavefunction with respect to the energy of the individual covalent and ionic valence bond structures (see Figure 2.1).[96] The stabilization energy is termed the charge-shift resonance energy $RE_{CS}$.[43,44] Even in homopolar bonds A–A, the introduction of ionic forms ($A^+$ $A^-$ and $A^-$ $A^+$) lowers the energy of the molecular wavefunction. For example, the wavefunction of the hydrogen molecule $H_2$ is expressed in terms of the three resonance forms H–H, $H^+$ $H^-$ and $H^-$ $H^+$.[31] In fact, there are bonds which would not be stable if charge shift resonance was neglected (e.g. F–F). Shaik *et al* termed them as charge shift bonds which they proposed as a whole new family of bonds.[43,44]

In practice, an active shell, which contains all electrons that contribute to the bonds of interest, is defined. In order to generate all possible valence bond structures, the active electrons are assigned to valence atomic orbitals or to hybridized atomic orbitals.[96] For example, for an $S_N2$ reaction ($A^- + B–C \longrightarrow A–B + C^-$) valence bond structures with four active electrons, which can be assigned to three active orbitals located at A, B and C, must be generated. Four of these structures are: $A^-$ B–C, A–B $C^-$, $A^-$ $B^+$ $C^-$ and $A^\bullet$ $B^-$ $C^\bullet$, each of which constitutes a term in Equation 2.10.

In the valence bond self-consistent field (VBSCF) method, the structure coefficients $C_K$ and orbitals which make up the valence bond structures $\Phi_K$ are simultaneously optimized to minimize the energy of the molecular wavefunction.[97] The breathing orbital valence bond (BOVB) method is an extension to the VBSCF method, which enhances the accuracy of the calculated energies.[98] In this method, the orbitals are allowed to be different in each of the individual valence bond structures.[98] Figure 2.2 shows the three resonance structures of $H_2$. In

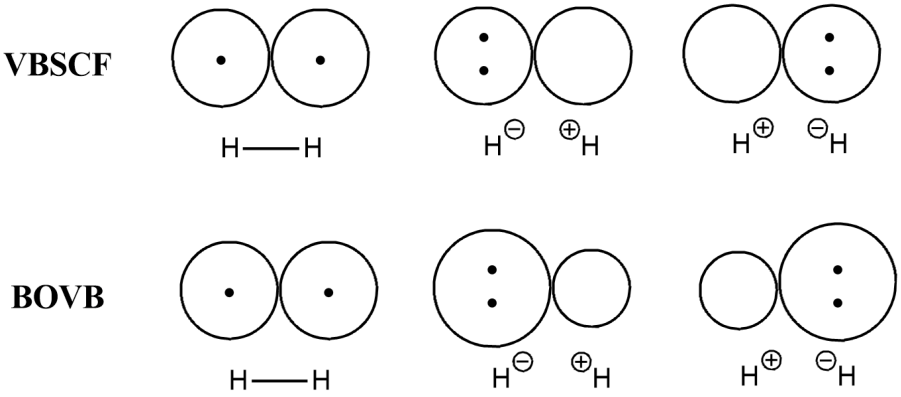


**Figure 2.2:** Representations of the valence bond structures of the $H_2$ molecule in terms of the VBSCF and BOVB methods.

the VBSCF method, each of the orbitals are the same in the three valence bond structures – the orbitals making up the covalent H–H bond are equivalent to the hydrogen lone pair orbital

in either of the ionic structures. However, the lone pair orbital contains two electrons, and thus, it is somewhat "inflated", while the empty orbital "shrinks". This orbital deformation is taken into account in the BOVB method.[98]

## 2.4 Basis sets

A basis set refers to a set of one-electron functions which are used to build up molecular orbitals, Kohn-Sham orbitals or valence bond structures.[70,99] These functions are referred to as basis functions, which (in most cases) represent atomic orbitals. For example, a linear combination of basis functions is used to generate molecular orbitals in the LCAO-MO approach (see Equation 2.2).[70,99] Any arbitrary function can be used as a basis function, but Gaussian functions have proven to work particularly well for this purpose.[99]

$$g_{ijk} = Nx^i y^j z^k e^{-\alpha r^2} \tag{2.12}$$

Equation 2.12 gives the general expression for a Gaussian basis function, where $N$ corresponds to a normalization constant.[99] The coefficients $i$, $j$ and $k$ are either 0, 1 or 2, and determine the type of basis function. If $i + j + k = 0$ (one possible combination), an s-type basis function is obtained; if $i + j + k = 1$, the basis function is of p-type (three possible combinations); and if $i + j + k = 2$, a d-orbital basis function is obtained (six possible combinations). The expression in Equation 2.12 corresponds to a primitive Gaussian, which does not account for the characteristic cusp close to the nucleus. This can be remedied by application of contracted Gaussian functions, which correspond to a linear combination of primitive Gaussian functions, see equation 2.13.[99]

$$\chi_o = \sum_n d_{on} g_n \tag{2.13}$$

Many different basis sets are available, which differ in terms of the parameter $\alpha$ in Equation 2.12, the number of primitive Gaussian functions, and the contraction coefficients $d_{on}$. *STO-3G* is a minimal basis set, where each atomic orbital is described by a single primitive Gaussian function.[100] Such a basis set is computationally inexpensive, but the calculated energies are of poor quality. $N$-$\zeta$ basis sets, where each atomic orbital is represented by $N$ basis functions, are computationally more expensive, but energies obtained form such basis sets are more accurate.[99] For split valence basis sets, the atomic core orbitals are represented by a single basis function, which reduces the computational cost. For example, in the basis set *6-311G*, which was introduced by Pople, the atomic core orbital is build up from a single basis function which is comprised of six primitive Gaussian functions, while each atomic valence orbital is made up of one basis function built up from three primitive Gaussian functions and another two basis func-

tions each corresponding to a single primitive Gaussian function.[101] In basis set *6-311+G(p)*, the + refers to an additional diffuse function and *(p)* signifies that a p-type basis function is used as a polarization function.[101] As the name implies, diffuse functions make the basis functions more diffuse, which is required when dealing with anions. The p-type polarization function can polarize s-orbital type basis functions, and enhances the flexibility of the basis set. Accordingly, p-orbitals can be polarized by d-type basis functions, such as in the basis set *6-311+G(p,d)*.[101] There is a great variety of basis sets available, which are parameterized for a certain range of elements. Dunning's correlation consistent basis sets (such as *cc-pVDZ*, *cc-pVTZ*, referring to double and triple $\zeta$ basis sets, respectively), are optimized for post-Hartree-Fock methods, and contain polarization functions by definition.[102] The prefix *aug-* (e.g. *aug-cc-pVTZ*) refers to the augmented version of Dunning's correlation consistent basis sets, which contain additional diffuse functions.[103] The triple valence def2-TZVP basis set was used on several occasions in this thesis, because it is parameterized for a great variety of elements. The variety of different basis sets is huge, and it is an important task to find a an appropriate basis set for the calculation.

# Chapter 3

# Foundations of quantum crystallography

In the previous Chapter, it was shown how wavefunctions can be derived from quantum chemical methods. No experimental input (apart from empirical density functionals within the DFT approach and dispersion corrections) is required to perform such calculations. A geometry optimization based on quantum chemical methods can determine the global minimum of the potential energy surface, however, if one wishes to obtain an experimental structure other approaches must be followed. In the present chapter, it is shown how X-ray diffraction experiments can provide experimental crystal structures, and how the emerging field of quantum crystallography[104–106] offers a way to get improved structures (*Hirshfeld Atom refinement (HAR)*)[107,108] and wavefunctions fitted to an experimental diffraction pattern (*X-ray constrained wavefunction fitting (XCW)*).[53] In the present thesis, the combined approach of *HAR* and *XCW* – an *X-ray wavefunction refinement (XWR)* – is applied to get an "experimental" wavefunction, which can be analyzed in terms of chemical bonding.[52,109] Before the theoretical foundations of these quantum crystallographic procedures are presented, a brief survey of standard X-ray diffraction studies is presented.

## 3.1 Basics of crystallography and diffraction

The structure of a crystal is characterized by periodically repeating structural motifs, such as atoms, molecules or ions. A space lattice is a three-dimensional array of points corresponding to the locations of these structural motifs. A unit cell, which can reconstruct the entire structure of the crystal by translational displacements (like bricks in a wall), is an imaginary parallelepiped that contains one unit of the space lattice.[110] A unit cell can be formed by connecting neighboring lattice points by a straight line, and it can be described by the unit cell parameters

**Table 3.1:** The seven crystal systems and their rotational symmetry.

| System | Axial lengths | Angles | Rotational symmetry |
|---|---|---|---|
| Cubic | a = b = c | $\alpha = \beta = \gamma = 90°$ | four $C_3$ axes |
| Tetragonal | a = b ≠ c | $\alpha = \beta = \gamma = 90°$ | one $C_4$ axis |
| Orthorhombic | a ≠ b ≠ c | $\alpha = \beta = \gamma = 90°$ | three $C_2$ axes |
| Trigonal | a = b = c | $\alpha = \beta = \gamma \neq 90°$ | one $C_3$ axis |
| Hexagonal | a = b ≠ c | $\alpha = \beta = 90°$ $\gamma = 120°$ | one $C_6$ axis |
| Monoclinic | a = b ≠ c | $\alpha = \gamma = 90°$ $\beta \neq 90°$ | one $C_2$ axis |
| Trinclinic | a ≠ b ≠ c | $\alpha \neq \beta \neq \gamma \neq 90°$ | none |

$a$, $b$ and $c$, which are the lengths of the unit cell axes, and $\alpha$, $\beta$ and $\gamma$, which are the angles between them.[110] The crystal system classifies a unit cell in terms of its rotational symmetry. All seven crystal systems, and the corresponding rotational symmetry are listed in Table 3.1.[110] The symmetry of a crystal can be described by one of the 230 space groups.[110] The unit cell is the smallest unit which contains the entire symmetry of the space group.

The crystal structure can be determined by single-crystal X-ray diffraction experiments. The wavelength of X-rays is in the region of $10^{-10}$ m, and thus, it is comparable to the separation of lattice planes, which can be defined by the Miller indices $h$, $k$ and $l$ (the lattice plane intersects the unit cell at $a/h$, $b/k$ and $c/l$, where $h$, $k$ and $l$ are positive or negative integers).[111] Therefore, it was (correctly) postulated that X-rays scatter when they pass through a crystal.[112–115] The lattice planes can be regarded as semi-transparent mirrors, which reflect the X-ray. According to Bragg's law, constructive interference occurs if the condition $n\lambda = 2d\sin(\Theta)$ is fulfilled.[113] Accordingly, a reflection can be observed if the X-rays hit the lattice plane at a certain angle $\Theta$, which depends on the wavelength $\lambda$ and the separation of lattice planes $d$ (if $n > 1$, the reflection is of second order; in most cases it is absorbed by $d$). The scattering of X-rays is caused by the interaction between the photons and the electron density of the unit cell.[110] The scattering power of a single atom depends on its electron density distribution $\rho(r)$, and is given by its scattering factor $f$ (equation 3.1).[110]

$$f = 4\pi \int_0^\infty \rho(r) \frac{\sin(kr)}{kr} r^2 dr \quad \text{with} \quad k = \frac{4\pi}{\lambda}\sin(\Theta) \tag{3.1}$$

The amplitude of a wave diffracted by the lattice plane $hkl$ is given by Equation 3.2, where $F_{hkl}$ is the structure factor.

$$F_{hkl} = \sum_j f_j \cdot e^{i\phi_{hkl}(j)} \quad \text{with} \quad \phi_{hkl}(j) = 2\pi(hx_j + ky_j + lz_j) \tag{3.2}$$

Accordingly, the structure factor for the reflection $hkl$ depends on the scattering factor of all atoms $j$ inside the unit cell and their coordinates $x_j$, $y_j$ and $z_j$. The intensity of a reflection $I_{hkl}$,

which can be measured at the detector, is proportional to the square modulus of the structure factor $F_{hkl}$, that is, $I_{hkl} = F^*_{hkl}F_{hkl}$.[110] If all structure factors are known, the electron density of the crystal can be calculated with Equation 3.3, which is known as the Fourier synthesis of the electron density.[110]

$$\rho(r) = \frac{1}{V}\sum_{hkl} F_{hkl}e^{-2\pi i(hx+ky+lz)} \tag{3.3}$$

So, in principle, the electron density of the unit cell can be determined from the intensity measured at the detector. However, one cannot simply take the square root of the intensity, because the phase of the structure factor remains unknown. A variety of methods has been developed to overcome this obstacle, which is known as the phase problem.[116] Nowadays, direct methods are the most widely used approaches to overcome the phase problem.[117,118] Ultimately, it is possible to solve the structure, but the coordinates and thermal parameters, which are obtained from this first model, need to be refined. In the structure refinement step, these parameters are adjusted to give the best fit between observed intensities and those calculated from the model of the structure.[110]

## 3.2 Structure refinement

After the structure solution step, initial positions of non-hydrogen atoms are determined. However, not all elements may be correctly assigned, hydrogen atoms are missing, the initial positions are not very accurately determined, and displacement parameters are unresolved. In the structure refinement step, all elements are assigned to their correct positions, hydrogen atoms are added to the structure, and the positions are refined until the calculated intensities give the best fit to the observed ones.[119] This is achieved by application of a least-squares refinement procedure. From the present atomic model, structure factors are calculated from Equation 3.2, and then the calculated intensities $F_c^2$ are compared to the experimental (observed) ones $F_o^2$.[119] By variation of the atomic parameters, the function shown in Equation 3.4 is minimized.[119]

$$M = \sum w(F_o^2 - F_c^2)^2 \tag{3.4}$$

After each refinement step, the atomic positions are more accurately determined, and a more reliable electron density map is obtained. Therefore, hydrogen atoms can be added to the structure, and the non-hydrogen atoms can be described by ellipsoids, which result from the anisotropic atomic displacements.[119]

The quality of a structure model can be judged by a variety of residual factors, such as the R-value (Equation 3.5), the weighted R-value (Equation 3.6) and the goodness of fit (Equation

3.7).[119]

$$R = \frac{\sum ||F_o| - |F_c||}{\sum |F_o|} \tag{3.5}$$

$$wR = \left[\frac{\sum w(F_o^2 - F_c^2)^2}{\sum wF_o^2}\right]^{1/2} \tag{3.6}$$

$$S = \left[\frac{\sum w(F_o^2 - F_c^2)^2}{(N_R - N_p)}\right]^{1/2} \tag{3.7}$$

In the course of the refinement, the R-value and its weighted variant must converge to smaller values (ideally, the R-value should be below 0.05), and the goodness of fit should be $S \approx 1$.[119]

For the calculation of structure factors, atomic scattering factors must be known (see Equation 3.2). However, the electron density of an atom is required for the calculation of atomic scattering factors (see Equation 3.1), and thus, different approaches to obtain scattering factors from theoretical calculations exist, because there are different approaches to model and calculate the electron density of an atom. The simplest approach is the *independent atom model (IAM)*, which is based on spherical atomic electron densities, which are obtained from Hartree-Fock calculations performed on isolated atoms.[110] This model disregards aspherical atomic features, which are caused by the formation of bonds and lone pairs. Despite that approximation, an *IAM* is sufficient to accurately predict the positions of non-hydrogen atoms, because the majority of the electron density is centered at the nucleus, and is not greatly affected by the aspherical shape of the valence shell. However, if one wishes to acquire accurate electron-density distributions and element-hydrogen bond distances, an *IAM* is not applicable, because the determined X–H bond distances are too short. This is caused by the fact that hydrogen atoms, which are bonded to other atoms, do not have core electrons, because their single electron is located in the valence shell.[120] This is remedied in a *Hirshfeld atom refinement (HAR)*, where aspherical atomic electron densities are calculated from quantum chemical calculations.[53,108,120,121] In a *multipole refinement*, aspherical atomic features are modeled by application of the Hansen-Coppens-formalism.[122] In the present thesis, this type of refinement will not be applied, so only the theoretical foundations of *HAR*, as part of an *X-ray wavefunction refinement (XWR)*, will be discussed in the following section.

## 3.3 X-ray wavefunction refinements

The *X-ray wavefunction refinement (XWR)*[52,109] is a two step procedure consisting of a *Hirshfeld atom refinement (HAR)*[53,108] followed by an *X-ray constrained wavefunction fitting (XCW).*[?,123] In the *HAR* step, a crystal structure refinement with aspherical atomic scattering factors is performed. This approach results in an improved structure compared to the *IAM*.[108,120,121]

In the *XCW* step, a wavefunction is fitted to the experimental diffraction data based on the structure obtained from *HAR*.

### Hirshfeld atom refinement

As mentioned before, describing the atomic electron density in terms of spherical atoms, which corresponds to the *IAM*, is a valid approach if structural parameters of non-hydrogen atoms are of interest. However, aspherical features, which are caused by bonds and lone pairs, are disregarded in this model. The *Hirshfeld atom refinement*, which is based on scattering factors derived from the aspherical *Hirshfeld atoms*, remedies this shortcoming.[108] Before starting the least-squares refinement step, tailor-made *Hirshfeld atoms* are calculated from an electron density obtained from a quantum chemical calculation (such as Hartree-Fock or DFT) on the formula unit of the crystal structure.[53] The electron density is partitioned into atomic electron densities by application of Hirshfeld's stockholder partitioning scheme.[124] Equation 3.8 gives the formalism to calculate the electron density of atom $A$ inside any molecule.[124]

$$\rho_A(r) = w_A(r) \cdot \rho_{molecule} \tag{3.8}$$

The weight function $w_A$ is calculated from the ratio of the promolecular atomic electron density of atom $A$ centered at its origin ($\rho_A^0(r-r_A)$) and the promolecular density of the whole molecule, which is the sum of all promolecular atomic densities centered at their origin inside the molecule (see Equation 3.9).[108]

$$w_A(r) = \frac{\rho_A^0(r - r_A)}{\sum_B \rho_B^0(r - r_B)} \tag{3.9}$$

Atoms in crystals are not stationary due to thermal atomic motion, and thus, the thermally smeared *Hirshfeld atoms* must be considered.[108] They are calculated by linking the static *Hirshfeld atom* $\rho_A$ to the thermally smeared *Hirshfeld atom* $< \rho_A >$ with the probability distribution of atom $A$ $P_A$ *via* a convolution (Equation 3.10).[108]

$$< \rho_A >= \rho_A \star P_A \tag{3.10}$$

The atomic scattering factor $f_A$ is ultimately obtained from the Fourier transform of the thermally smeared *Hirshfeld atom* $\rho_A$.[108] Then, a least-squares refinement is performed and a refined crystal structure is obtained. From that refined structure, new *Hirshfeld atoms* are computed and another least-squares refinement is performed. This procedure is repeated until convergence of the structural parameters.[108]

It has been shown that the *anisotropic displacement parameters (ADPs)*, which describe the thermal motion of atoms, and the hydrogen-element bond lengths are more accurate and precise

than the parameters obtained from the *IAM*.[108,120,121] In contrast to the *IAM*, it is also possible to refine *ADPs* for hydrogen atoms.[108,121,125] Because aspherical features of the electron density are taken into account, the residual factors generally indicate a model with a superior quality with respect to the *IAM*.[108,120,121]

### X-ray constrained wavefunction fitting

In the preceding section, it was shown how a wavefunction can be computed by quantum chemical methods. Of course, it is possible to perform a wavefunction calculation based on the experimental geometry obtained from *HAR*. However, effects of the crystal environment, such as intramolecular interactions and the electric field exerted by the surrounding molecules (the crystal field), are neglected. In principle, the information of these crystal effects is contained in the experimental diffraction data. In addition, electron correlation can be extracted from the experimental structure factors.[126] The *X-ray constrained wavefunction fitting (XCW)* is an approach to fit a wavefunction to the structure factors from an X-ray diffraction experiment, thus taking the mentioned effects and other experimental effects into account.[107]

The variation principle of quantum chemistry states that an approximate wavefunction cannot be lower in energy than the true wavefunction, which is why the best possible wavefunction within the Hartree-Fock approach is found by minimization of the energy. Within the XCW approach, the Lagrangian $L$, which is the sum of the wavefunction energy and an experimental penalty, is minimized with respect to the wavefunction coefficients $c$ (see Equation 3.11).[53]

$$L = E_{QM}[\psi(c)] + \lambda\chi^2 \tag{3.11}$$

The first term in Equation 3.11 corresponds to the energy of a single-point calculation (e.g. Hartree-Fock). The second term can be regarded as a penalty to the Lagrangian – if the deviation between the observed and calculated structure factors is high, the penalty to the Lagrangian will be high.[107] Equation 3.12 gives the definition of the parameter $\chi^2$, which is a measure of the deviation between observed and calculated structure factors.[107]

$$\chi^2 = \frac{1}{N_r - N_p} \sum_{n}^{N_r} \frac{|F_{calc}(n) - F_{obs}(n)|^2}{\sigma^2(n)} \tag{3.12}$$

Therefore, an optimum between two criteria – a minimal energy and a smallest possible deviation from the observed structure factors – must be found. In the first step of the *XCW*, the parameter $\lambda$ is set to zero. Consequently, the first iteration of *XCW* corresponds to a purely quantum chemical single-point calculation, because the term introducing the experimental penalty disappears. The parameter $\lambda$ is then slowly increased in a stepwise manner, thus introducing more and more experimental data to the fitted wavefunction.[107] At some point,

the wavefunction fit can no longer meet the requested convergence criteria and comes to an end. The fitted wavefunction includes experimental effects, and can therefore be regarded as an "experimental" wavefunction. It has been shown, that the XCW does not only account for crystal effects, but also other phenomena, which are not accounted for by the quantum chemical methods, such as correlation and relativistic effects.[126] Generally, the residual factors indicate a higher quality of the model with respect to the HAR.[52]

## 3.4 X-ray diffraction experiments in practice

After giving an overview of the models applied to extract a structure from an X-ray diffraction pattern, this section will deal with the experiment itself. First of all, a crystal is required to perform such an experiment. However, there are some strict requirements to the crystal, especially if an *XWR* is performed based on the diffraction data obtained from that crystal. The quality of the crystal is of particular importance. Ideally, it should have well defined faces, it should not be split, and twinning should not be an issue.[110] Furthermore, the size of the crystal should not be larger than the diameter of the X-ray beam, which is usually around 150 $\mu$m. If the crystal is too large, X-ray absorption effects can become an issue. Especially, if the crystal structure contains heavy elements, absorption effects need to be accounted for in the data reduction step.[110] The crystallization of crystals can be a tedious process, but the many crystallization techniques will not be discussed in this thesis.

Once a suitable crystal is found, an X-ray diffraction experiment can be performed. The crystal structures, which are discussed in the present thesis, were either measured at a home diffractometer or at a diffractometer inside a large research facility utilizing synchrotron radiation. The home diffractometer corresponds to a Bruker D8 Venture equipped with a I$\mu$S microfocus Mo$\kappa_\alpha$ radiation source and a Photon 100 detector in shutterless mode. The reason why X-ray diffraction experiments were also performed at large synchrotron facilities is the higher intensity of the X-rays provided by the radiation source, and the high quality of the detector.[127] For that purpose, regular trips to the synchrotron SPring-8 in Japan were conducted. Figure 3.1 shows the experimental set-up of the diffractometer at SPring-8, which will be explained in the following.

The goniometer head (part **1** in Figure 3.1) carries a small needle to which the crystal is mounted. The needle is made from materials, such as cactus needles, glass or plastics, that do not greatly contribute to the background profile measured at the detector. The goniometer head is fixed to the goniometer, which can orient the crystal in a desired position relative to the X-ray beam. The goniometer can move along three axes, which correspond to parts **2**, **3** and **4**. The rotation axis around the angle $\phi$ (part **2**) moves the crystal around its own axis. The angle $\chi$ orients the crystal along the circular segment defined by part **3**. The third rotation axis

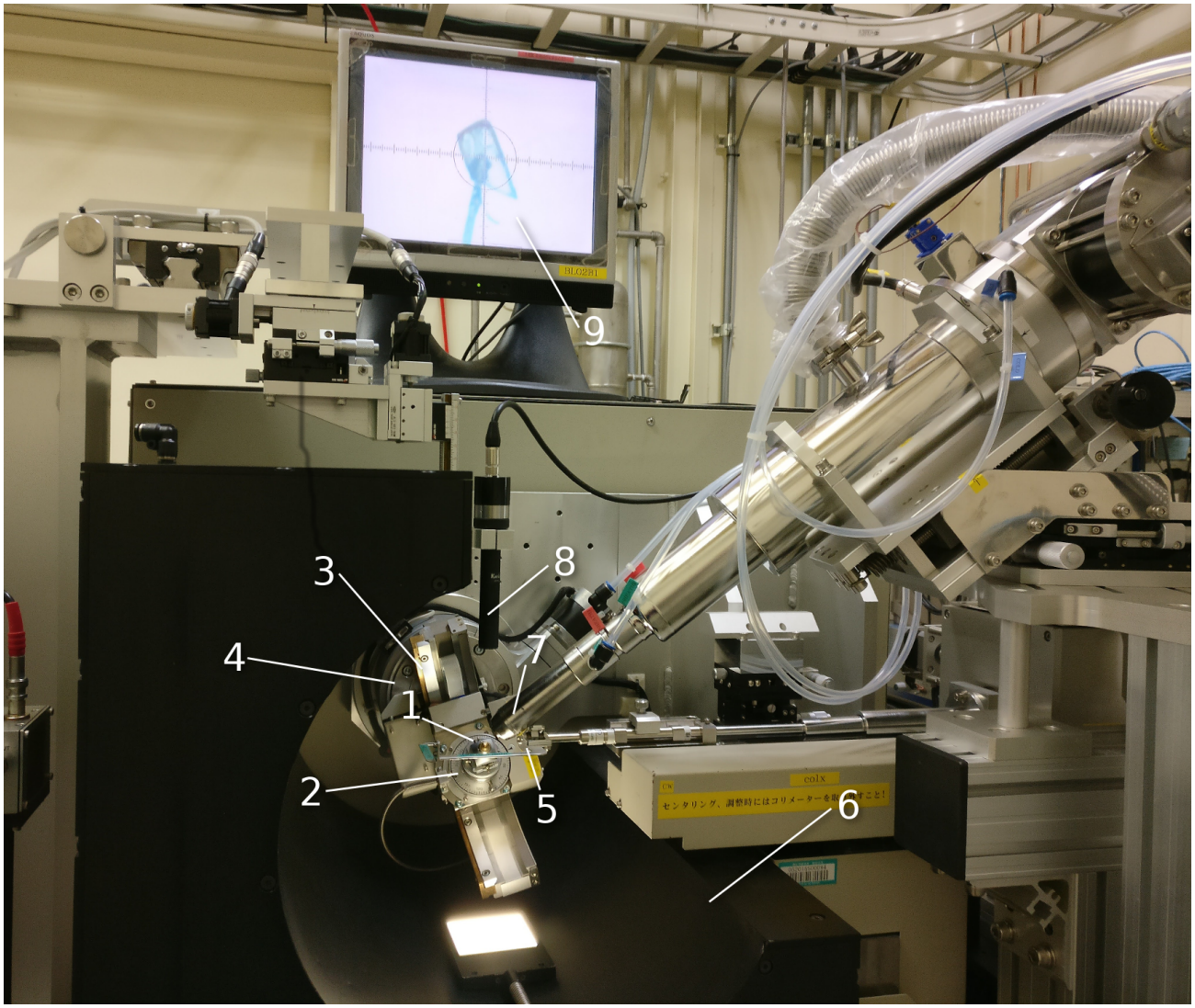


**Figure 3.1:** The diffractometer at SPring-8 beamline BL02B1 in Japan, Hyogo. The components 1 - 9 are explained in the main text.

(part **4**) rotates the whole goniometer around the angle $\omega$. A high degree of freedom is required to measure a complete data set, which is achieved by driving the crystal to all orientations, where the crystal faces are oriented to the X-ray beam so that constructive interference can occur. Part **5** is the collimator, which directs the X-ray beam from the synchrotron source in a parallel orientation through the crystal. The positions and intensities of the reflections are measured by the detector, which corresponds to part **6**. At beam line BL02B1, the detector is a curved image plate with a large area, which enables the simultaneous detection of a large number of reflections. The advantage of this kind of detector is the high dynamic range, which allows for the simultaneous detection of strong and weak reflections. Another reason for the superiority of SPring-8 data sets is the low temperature (around 20 K) at which the data sets can be measured. This is achieved by part **7**, which corresponds to the cryogenic system based on a helium cooling mechanism. Part number **8** is a camera, which is directed towards the crystal. The video recorded by the camera is transmitted to a monitor (part **9**). Before a measurement can be started, the position of the crystal must be oriented in the middle of the crosshair displayed on the screen using the screws at the goniometer head. This makes sure that the X-rays hit the center of the crystal.

A measurement strategy, which determines the drive range or position of the rotation axes $\phi$, $\omega$ and $\chi$, must be specified. Using the diffractometer set up at SPring-8, a measurement takes a couple of hours. The time includes exposure times and the readout time of the detector. Measurements with other detectors, such as pixel detectors, only take a small fraction of that time (in some cases, only a couple of minutes).[128] After the measurement is completed, the images recorded by the detector must be analyzed. This is done in the data reduction step, which includes the unit cell determination from the position of the reflections (indexing step), the integration of the intensities of the reflections (integration step), and the scaling of reflections from different detector images (scaling step).[110] The scaling step also includes an absorption correction and other corrections, where the loss of intensity caused by the absorption of X-ray beams through the crystal is corrected. Ultimately, a file containing the *hkl*-indices of the reflections, and their intensities is obtained (hkl-file). Using that file and the unit cell parameters, the space group can be determined, and finally, the structure can be solved and refined following the procedure outlined in the previous sections.[119]

# Chapter 4

# Bond analysis methods

In the preceding two chapters, it was shown how wavefunctions can be derived from quantum chemical and quantum crystallographic approaches. The main focus of the present study is the analysis of chemical bonds. While valence bond calculations give localized orbitals, which can be easily related to features of Lewis structures,[30,31] the MO theory gives molecular orbitals, for which bond analysis methods must be applied to extract orbitals or properties that make an analysis based on the Lewis picture feasible. The bond analysis methods, which are used in the current thesis are: The *Quantum Theory of Atoms in Molecules (QTAIM)*,[38] the *Natural bond orbital (NBO)* approach,[37] the *electron localizability indicator (ELI)*,[40] and *energy decomposition analyses (EDA)* based on the *Ziegler-Rauk* scheme.[129] In this Chapter, only these bond analysis methods are briefly introduced. Of course, more methods exist, however, due to the high number they cannot all be introduced in this chapter. Further methods which are applied in this study are the Roby bond index,[130] for which a detailed description is given in Chapter 6, and the *Q-analysis*,[28] which will be introduced in Chapter 5.

## 4.1 Quantum Theory of Atoms in Molecules

The *Quantum Theory of Atoms in Molecules (QTAIM)* is based on a topological analysis of the electron density.[38,131] The electron density $\rho$ can be obtained from the molecular orbitals by application of Equation 4.1.[131]

$$\rho = \sum_{i=1}^{N_e} |\phi_i|^2 \tag{4.1}$$

The electron density only depends on the three spatial coordinates $x$, $y$ and $z$, so that it can be analyzed like any other mathematical scalar function. In the first step of the *QTAIM* analysis, a search for *critical points*, where the gradient of the electron density disappears ($\nabla\rho = 0$), is conducted.[131] A *critical point* can be classified according to its three cartesian components of

the curvature ($\lambda_1$, $\lambda_2$ and $\lambda_3$), which are obtained from the diagonalized Hessian matrix of the electron density, see Equation 4.2.[131]

$$D(\vec{r}) = \begin{pmatrix} \frac{\partial^2\rho}{\partial x^2} & 0 & 0 \\ 0 & \frac{\partial^2\rho}{\partial y^2} & 0 \\ 0 & 0 & \frac{\partial^2\rho}{\partial z^2} \end{pmatrix} = \begin{pmatrix} \lambda_1 & 0 & 0 \\ 0 & \lambda_2 & 0 \\ 0 & 0 & \lambda_3 \end{pmatrix} \tag{4.2}$$

There are four types of *critical points*, which are classified by the sign of $\lambda_1$, $\lambda_2$ and $\lambda_3$. Table 4.1 lists all types of *critical points* with the corresponding sign of $\lambda_1$, $\lambda_2$ and $\lambda_3$.[131] A *nuclear attractor* is a local maximum of the electron density. Its position corresponds to the center of an atomic core.[131] Therefore, a *nuclear attractor* is obtained for each of the atoms in the system. A *bond critical point* is a saddle point of the electron density, which can be linked to a bonded interaction between two *nuclear attractors*.[131] There is one minimum along the bond axis, and two maxima perpendicular to it. *Ring critical points* can be found in ring planes. There is one maxima perpendicular to the ring plane, and two minima are located within the ring plane.[131] A *cage critical point*, which is a local minimum of the electron density, can be found inside cages defined by the positions of nuclear attractors.[131] *Bond paths* are paths of maximum electron density, which link the *nuclear attractors* to the *bond critical points*.[41,132] Therefore, they are an indication of bonded interactions. Figure 4.1 shows an example molecule, for which a *critical*

**Table 4.1:** The four types of *critical points* of the electron density, and the corresponding signs of $\lambda_1$, $\lambda_2$ and $\lambda_3$. $\omega$ gives the number of non-zero elements of the Hesse matrix and $\sigma$ the sum of signs.

| | $\lambda_1$ | $\lambda_2$ | $\lambda_3$ | [$\omega$,$\sigma$] |
|---|---|---|---|---|
| Nuclear attractor | - | - | - | [3,-3] |
| Bond critical point | + | - | - | [3,-1] |
| Ring critical point | + | + | - | [3,+1] |
| Cage critical point | + | + | + | [3,+3] |

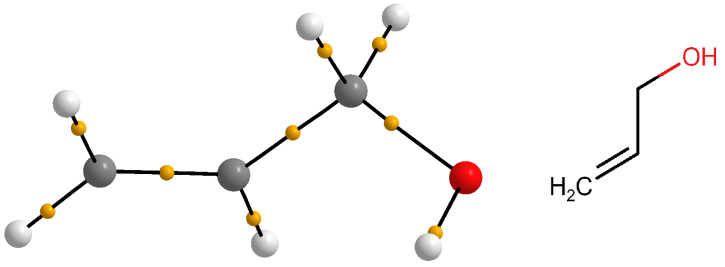


**Figure 4.1:** *Nuclear attractors*, *bond critical points* and *bond paths* of the example molecule (see Lewis structure on the right hand side), which was analyzed to provide a better understanding for the concepts described in this chapter.

*point* search was performed. The *nuclear attractors* are located at the atomic positions, and the orange balls give the positions of the *bond critical points*. For each of the bonds a single *bond critical point* is obtained, and they are always located closer to the more electropositive element. Consequently, their position can be related to the bond polarization. The black lines connecting the *bond critical points* and *nuclear attractors* are the *bond paths*.

The trace of the Hesse matrix ($\nabla^2\rho(\vec{r}) = \lambda_1 + \lambda_2 + \lambda_3$) corresponds to the Laplacian, which is a measure of charge accumulation. Regions of negative Laplacian values correspond to *valence shell charge concentrations (VSCC)*, while positive regions of the Laplacian are *valence shell charge depletions (VSCDs)*.[131,133] Figure 4.2 shows different representations of the Laplacian. Representation **1)** shows a contour plot of the Laplacian, which reveals the distribution of

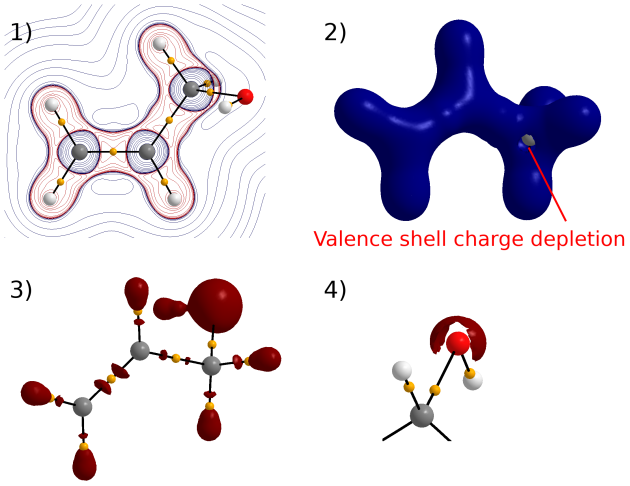


**Figure 4.2: 1)** Contour map of the Laplacian (red regions: negative Laplacian; blue regions: positive Laplacian), **2)** Iso-surface of the Laplacian at an iso-value of 0, **3)** Iso-surface of the Laplacian at a negative iso-value, **4)** Iso-surface of the Laplacian at an even more negative iso-value.

*VSCCs* and *VSCDs* inside the example molecule. The regions around the *bond critical points* of covalent bonds correspond to *VSCCs*, because in covalent bonds electron density is always accumulated in the bonding region.[131] The electron density originates from the region around the atomic cores, which therefore correspond to *VSCDs*.[131] Representation **2)** shows the iso-surface of the Laplacian at an iso-value of 0.[131] Holes in that iso-surface correspond to *VSCDs*, which can be related to nucleophilic regions of the molecule.[131] Representation **3)** and **4)** show iso-surfaces of the Laplacian at negative iso-values. In representation **3)**, the iso-value was chosen, so that the *VSCCs* corresponding to bonded interactions are revealed. In representation **4)**, an even higher iso-value is plotted, which reveals a *VSCC* around the oxygen atom, which can be associated to oxygen's lone pairs.

For the characterization of the bonded interactions, a variety of properties at the *bond critical points* can be regarded. The value of the Laplacian at the bond critical point reveals whether

covalent or ionic interactions prevail. If the value of the Laplacian is negative, electrons are accumulated in the bonding region, and the bonded interaction is covalent.[131] If the Laplacian at the *bond critical point* is positive, on the other hand, ionic interactions to the bonded interaction are more significant.[131] The value of the electron density at the bond critical point often correlates with the strength of the bonded interaction. Another property, which is usually inspected at the *bond critical point*, is the ellipticity $\epsilon$, which is defined in Equation 4.3.[131]

$$\epsilon = \frac{\lambda_1}{\lambda_2} - 1 \tag{4.3}$$

For bonds with a cylindrical symmetry along the bond axis (single and triple bonds), $\epsilon \approx 0$. For elliptical bonds, such as double bonds, $\epsilon > 0$, and for weak interactions, the ellipticity has usually even higher values.[131]

The *QTAIM* analysis also provides access to atomic properties, such as atomic charges.[131] In that approach, the boundary of an atomic basin is defined by a so called *zero-flux surface*, where the scalar product of the gradient of the electron density and the normal vector ($\vec{n}$) disappears, see Equation 4.4.[131]

$$\nabla\rho(\vec{r}) \cdot \vec{n} = 0 \tag{4.4}$$

The gradient of the electron density starts off at a nuclear attractor, but never passes through the zero-flux surface. At the bond critical point, the *zero-flux surface* intersects with the *bond path*. From the definition of an atom, it is straightforward to calculate a charge associated to an atomic basin by taking the difference between the charge of the nucleus ($Z$) and the number of electrons inside the atomic basin. The latter can be calculated by integration of the electron density within the limits of the *zero-flux surface* of the atomic basin $\Omega$, see Equation 4.5.[131]

$$q(\Omega) = Z - \int_{\Omega} \rho(\vec{r}) d\vec{r} \tag{4.5}$$

The *delocalization index* $\delta(A, B)$ gives the number of electron pairs shared between the atomic basins of $A$ and $B$.[134] It can therefore be analyzed as a bond index. The delocalization index can be calculated from Equation 4.6.

$$\delta(A, B) = 2|F^{\alpha}(A, B)| + 2|F^{\beta}(A, B)| \tag{4.6}$$

$F^{\sigma}(A, B)$ denotes the Fermi correlation between the atomic basins $A$ and $B$, see Equation 4.7.

$$F^{\sigma}(A, B) = -\sum_{i}\sum_{j} S_{ij}(A) S_{ji}(B) \tag{4.7}$$

$S_{ij}(A)$ and $S_{ji}(B)$ are the overlap integrals of the two spin orbitals $\phi_i$ and $\phi_j$ of spin $\sigma$ integrated

over the atomic basins $A$ and $B$.[134]

## 4.2 Natural bond orbitals

*Molecular orbitals* are often delocalized over the whole molecule, which makes an analysis based on the Lewis picture unfeasible. *Natural bond orbitals*, on the other hand, can be readily linked to features of Lewis structures, because they are either localized between two atoms (bond orbitals) or at a single atom (lone pair or core orbitals).[37,135–137] *Molecular orbitals* and *natural bond orbitals* are part of a series ranging from completely localized *atomic orbitals (AOs)* to the delocalized *molecular orbitals (MOs)*.[37] The sequence from most localized to least localized orbital type is: *atomic orbitals*, *natural atomic orbitals*, *natural hybrid orbitals*, *natural bond orbitals*, *natural localized molecular orbitals*, and *molecular orbitals*.[37]

*Natural atomic orbitals (NAO)*, which can be regarded as *atomic orbitals* that are optimized with respect to the molecular environment, are derived from *atomic orbitals* under consideration of two criteria: They must ideally have an electron population of $N \approx 2$, and they must enable a quick convergence to the electron density of the molecule.[37,138] The *NAO* of an isolated atom is, therefore, identical to the respective *AO*. Based on the *NAOs*, a *natural population analysis (NPA)* can be carried out.[138] This enables the computation of atomic populations by summing up the populations of all *NAOs* centered at the atom. The charge of atom A can be computed from the difference of the nuclear charge and the electron population of atom A, see equation 4.8.[138]

$$q_A = Z_A - \sum_i N_i \tag{4.8}$$

*Natural hybrid orbitals (NHOs)* are built up from a linear combination of *NAOs* centered at a single atom.[139] In the *NBO* picture, lone pairs correspond to a single *NHO*, while *natural bond orbitals* are formed by a linear combination of two *NHOs*.[37] The *NBO* of a bond between atoms A and B is derived from *NHOs* centered at these two atoms. The linear combinations of these *NHOs* gives one bonding and one anti-bonding *NBO* ($BD$(A–B) and $BD^*$(A–B)), see Equation 4.2.[37]

$$\begin{aligned} BD(\text{A–B}) &= c_A h_A + c_B h_B \\ BD^*(\text{A–B}) &= c_B h_A - c_A h_B \end{aligned} \tag{4.9}$$

The weights $c_A$ and $c_B$ are denoted as the polarization coefficients, because they can be related to the polarization of the A–B bond.[37] Generally, the bonding *NBOs*, which can be associated with bonds in the Lewis picture, have an electron population of $\approx 2$. The anti-bonding *NBOs*, on the other hand, do not exit in the traditional Lewis picture. The Lewis-type donor orbitals, such as lone pair or bond orbitals, can interact with the anti-bonding acceptor orbitals. This

interaction, which is known as (negative) hyperconjugation, diminishes the electron population of the donor orbitals, so that their electron population is slightly below two.[37] At the same time, the electron population of the anti-bonding orbitals is greater than zero. These interactions reveal the significance of resonance structures.[37] Figure 4.3 gives an overview of different types of orbitals which are obtained from an *NBO* analysis.

The *natural localized molecular orbitals* follow the *NBO* in the series outlined above. They are obtained by mixing *NBOs* with their delocalized part.[140] The *NLMO/NPA* bond orders are obtained by combining the results of the *NLMO* analysis and *NPA*.[37]

In the *natural resonance theory*, which is a part of the *NBO* framework, the wavefunction of a molecule is approximated by a linear combination of density matrices, which each correspond to the localized part of an *NBO* structure. From the optimized coefficients, weights of the *NBO* structures can be calculated, and, thus, a quantitative analysis of resonance is possible.[141,142]

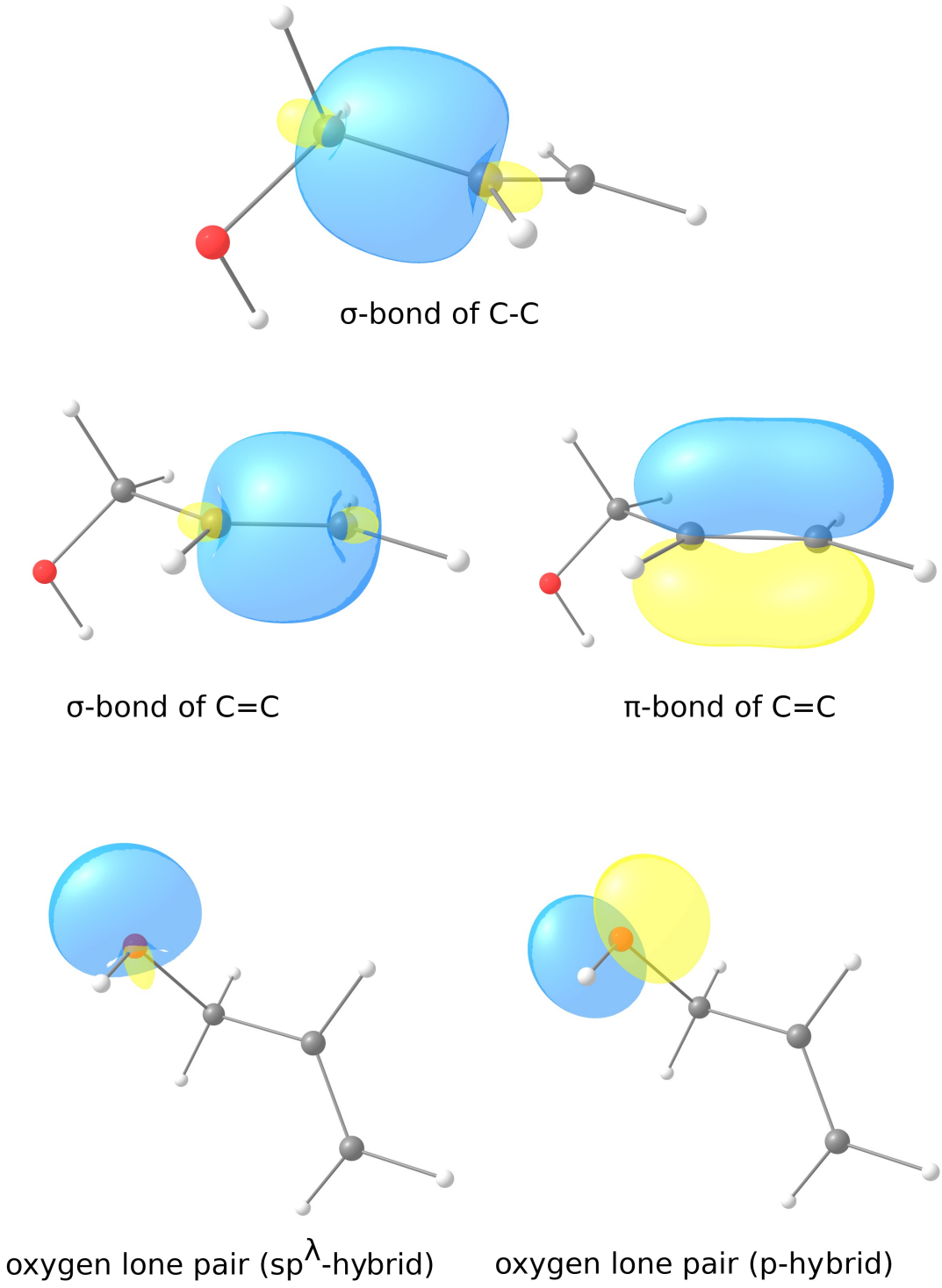


**Figure 4.3:** *Top row:* A *natural bond orbital* which is formed by two *natural hybridized orbitals* centered at the carbon atoms of the C−C bond, *middle row:* $\sigma$- and $\pi$-type *natural bond orbitals* of a C−C double bond, *bottom row:* Two *natural hybridized orbitals*, which can be attributed to the two lone pairs of the oxygen atom. The Lewis structure of the molecule is depicted in Figure 4.1

.

## 4.3 Electron localizability indicator

Just like the electron density, the *electron localizability indicator (ELI-D)*, is a scalar field, which can be analyzed topologically. The *ELI-D* measures the localization of electrons: High values of the *ELI-D* are found in regions of high electron localization.[40] The method is based on the *electron localization function (ELF)* which was introduced by Silvi.[39] In the following, the idea behind this approach is briefly outlined.

In the *ELI-D* approach, the space is partitioned into micro-cells with a variable volume $V_i$, which is chosen, so that each of the micro-cells contains the same number of same spin electron pairs $D^{\sigma\sigma}$.[40] This volume can be calculated from Equation 4.10, where $g(a_i)$ denotes the Fermi hole curvature at the center of a micro-cell $a_i$.[40]

$$V_i \approx \left(\frac{12D^{\sigma\sigma}}{g(a_i)}\right)^{3/8} \tag{4.10}$$

The charge of each micro-cell $Q_i^\sigma$ can be approximately determined by multiplying the volume $V_i$ with the same spin electron density $\rho_\sigma$ at $a_i$, see Equation 4.11.[40]

$$Q_i^\sigma \approx \rho_\sigma(a_i)V_i \tag{4.11}$$

The *ELI-D* $\gamma_D^\sigma$ can now be calculated from Equation 4.12.[40]

$$\gamma_D^\sigma(a_i) = \frac{Q_i^\sigma}{(D^{\sigma\sigma})^{3/8}} \approx \rho_\sigma(a_i)\frac{V_i}{(D^{\sigma\sigma})^{3/8}} = \rho_\sigma(a_i)\tilde{V}_D(a_i) \tag{4.12}$$

In regions, where the number of same spin electron pairs $D^{\sigma\sigma}$ is low, electrons are highly localized. Consequently, the volume $V_i$ is required to be large in these regions, because each micro-cell must contain the same number of same spin electron pairs, and thus, a high *ELI-D* value is obtained. For infinitesimal small values of $D^{\sigma\sigma}$, the *ELI-D* can be regarded as continuous, see Equation 4.13.[40]

$$\gamma_D^\sigma(r) = \rho(r)\tilde{V}_D(r) = \rho(r)\left(\frac{12}{g(r)}\right)^{3/8} \tag{4.13}$$

Just like the electron density utilized in the *QTAIM* approach, a topological analysis of the *ELI-D* yields zero-flux surfaces, which define basins.[40] In contrast to the electron density, these *ELI-D* basins can be related to bonds, lone pairs and atomic shells.[40] The A–B bond basin is in contact with the core basins of atoms A and B (disynapticity). Lone pair basins, one the other hand, are only in contact with the core basin of a single atom (monosynapticity). An integration of the electron density inside these basins corresponds to an electron population, which can be

analyzed in a chemical way.[40] For example, bond basins with a high bond polarization give low electron populations, while bond basins of highly covalent single bonds contain approximately two electrons.[36]

## 4.4 Energy decomposition analysis

In an *energy decomposition analysis (EDA)*, the interaction energy $\Delta E_{int}$ between two fragments A and B is decomposed into three terms: The electrostatic interaction $\Delta E_{elstat}$, the Pauli repulsion $\Delta E_{Pauli}$, and the orbital interaction $\Delta E_{orb}$.[35,42,129] In the first step of an *EDA*, two molecular fragments need to be defined. For example, if the bond between the two hydrogen atoms of $H_2$ is analyzed, these fragments correspond to two hydrogen atoms. The wavefunctions ($\psi_A$ and $\psi_B$) and energies ($E_A$ and $E_B$) of these two fragments are calculated, and then the interaction energy $\Delta E_{int}$ is calculated from the difference between the total energy of the molecule, $E_{AB}$, and the sum of the energies of the two fragments (Equation 4.14).[42]

$$\Delta E_{int} = E_{AB} - (E_A + E_B) \tag{4.14}$$

The electrostatic interaction energy $\Delta E_{elstat}$ can be obtained from the interaction between the frozen charge densities of the two fragments at the equilibrium geometry of the molecule.[42] This quasiclassical Coulomb interaction, which is (almost) always an attractive component to $\Delta E_{int}$, is calculated from Equation 4.15.[42]

$$\Delta E_{elstat} = \sum_{\alpha \epsilon A} \sum_{\beta \epsilon B} \frac{Z_\alpha Z_\beta}{R_\alpha \beta} + \int dr V_B(r) \rho_A(r) + \int dr V_A(r) \rho_B(r) + \int \int dr_1 dr_2 \frac{\rho_A(r_1)\rho_B(r_2)}{r_{12}} \tag{4.15}$$

In the next step of the *EDA*, the product wavefunction $\psi_A \psi_B$ and the corresponding energy $E^0_{AB}$ is calculated.[42] This wavefunction, which violates the Pauli principle, is antisymmetrized and renormalized to give the wavefunction $\Psi^0$ with the energy $E^0$. The Pauli repulsion can be calculated from the difference between $E^0_{AB}$ and $E^0$ (Equation 4.16).[42]

$$\Delta E_{Pauli} = E^0_{AB} - E^0 \tag{4.16}$$

The Pauli repulsion is always repulsive, because additional constrains are introduced to the wavefunction following the antisymmetrization of the wavefunction.[42]

The wavefunction $\psi^0$ is then relaxed to give the final wavefunction of the molecule $\psi_{AB}$.[42] The energy difference between the final energy of the molecule $E_{AB}$ and the energy of the

pre-relaxed molecule $E^0_{AB}$ gives the orbital interaction (Equation 4.17).[42]

$$\Delta E_{orb} = E_{AB} - E^0_{AB} \tag{4.17}$$

The orbital interaction is always attractive, because it is obtained from a wavefunction optimization, which introduces the mixing of orbitals.[42] If an empirical dispersion correction is applied, the dispersion energy $E_{disp}$ constitutes another term to $E_{int}$.

So far, the *EDA* is not yet implemented for post-Hartree Fock methods, so only Hartree-Fock and DFT calculations can be analyzed.[42]

# Part III

# A complementary bonding analysis and the Lewis picture

# Chapter 5

# A variety of Bond Analysis Methods, One Answer?

In the paper "*A variety of Bond Analysis Methods, One Answer? An Investigation of the Element-Oxygen Bond of Hydroxides $H_nXOH$*, the X−O bond of $H_nXOH$ model compounds is investigated using a *complementary bonding analysis*, which is comprised of a *natural bond orbital* analysis, a *QTAIM* analysis, an analysis of the *ELI-D*, *valence bond calculations*, and two types of *EDAs*. This study will give an impression on the information value provided by each of the bond analysis methods, and the the nature of the X−O bond is uncovered. The study was published in *Chemistry – A European Journal* in 2018.

A part of the analysis of this paper (about 50%) was performed during my master's thesis at the AG Grabowsky. The following list contains all aspects, which I have performed as part of my doctoral thesis:

- I wrote about 90% of the text
- I am responsible for all figures
  - I created Figures 1, 4, 10, 11 as part of my doctoral thesis
  - All other figures were redone based on figures from my master's thesis
- I am responsible for all tables
  - I created Tables 1, 3 and 4 as part of my doctoral thesis
  - Table 2 was redone based on a table from my master's thesis
- I performed and analyzed the *valence bond calculations*
- I performed and analyzed the *energy decomposition analysis*

- I calculated the parameter $Q$ and analyzed it
- I performed the analysis of the total energy density at the bond critical point
- All other analyses were performed as part of my master's thesis

ChemPubSoc Europe

DOI: 10.1002/chem.201800453

CHEMISTRY
A European Journal
Full Paper

Bond Analysis

# A Variety of Bond Analysis Methods, One Answer? An Investigation of the Element–Oxygen Bond of Hydroxides $H_nXOH$

Malte Fugel,[a] Jens Beckmann,[a] Dylan Jayatilaka,[b] Gerald V. Gibbs,[c] and Simon Grabowsky*[a]

**Abstract:** There is a great variety of bond analysis tools that aim to extract information on the bonding situation from the molecular wavefunction. Because none of these can fully describe bonding in all of its complexity, it is necessary to regard a balanced selection of complementary analysis methods to obtain a reliable chemical conclusion. This is, however, not a feasible approach in most studies because it is a time-consuming procedure. Therefore, we provide the first comprehensive comparison of modern bonding analysis methods to reveal their informative value. The element–oxygen bond of neutral $H_nXOH$ model compounds (X = Li, Be, B, C, N, O, F, Na, Mg, Al, Si, P, S, Cl) is investigated with a selection of different bond analysis tools, which may be assigned into three different categories: i) real space bonding indicators (quantum theory of atoms in molecules (QTAIM), the electron localizability indicator (ELI-D), and the Raub–Jansen index), ii) orbital-based descriptors (natural bond orbitals (NBO), natural resonance theory (NRT), and valence bond (VB) calculations), and iii) energy analysis methods (energy decomposition analysis (EDA) and the Q-analysis). Besides gaining a deep insight into the nature of the element–oxygen bond across the periodic table, this systematic investigation allows us to get an impression on how well these tools complement each other. Ionic, highly polarized, polarized covalent, and charge-shift bonds are discerned from each other.

## 1. Introduction

Extracting information about chemical bonding from a molecular wavefunction is an ambiguous task because the notion of a chemical bond is itself a fuzzy concept that is not measurable and can therefore not be defined rigidly.[1–7] However, no chemist would deny that the chemical bond is a useful concept! Therefore, it comes as no surprise that numerous ways of depicting and quantifying bonded interactions, such as Bader's bond paths,[8] have emerged.[9–16] However, Bader pointed out that bonded interactions are not to be confused with chemical bonds.[17] In this paper, we will depict and quantify bonded interactions by using various methods, but for brevity we will refer to these bonded interactions as chemical bonds, although we are aware of the imprecision. All methods used to analyze chemical bonds come with their limitations—the nature of a bond will never be captured completely by any of these descriptors and sometimes conflicting results are obtained. It can be regarded as a dilemma that the very same wavefunction if analyzed by different methods might give opposing results on the existence and character of a bond.[18,19] However, there are hardly any studies that attempt to compare the results from a large variety of tools on a single set of compounds without focusing on a specific tool or favoring one. We will provide such a comparison for the first time, and give recommendations on the complementary use of the diverse methods.

[a] M. Fugel, Prof. Dr. J. Beckmann, Prof. Dr. S. Grabowsky
University of Bremen, Department 2: Biology/Chemistry
Institute of Inorganic Chemistry and Crystallography
Leobener Str. 3 and 7, Bremen (Germany)
E-mail: simon.grabowsky@uni-bremen.de

[b] Prof. D. Jayatilaka
University of Western Australia, School of Molecular Sciences
35 Stirling Highway, Perth WA 6009 (Australia)

[c] Prof. G. V. Gibbs
Virginia Polytechnic Institute and State University
Departments of Geoscience, Material Science and Engineering and Mathematics
Blacksburg, Virginia 24061 (USA)

Supporting information (containing additional information on the analysis of the Laplacian of the electron density, the electron localizability indicator, and the natural bond orbitals; all properties presented inside plots are listed in tables and atomic coordinates of the $H_nXOH$ model compounds are given) and the ORCID identification number(s) for the author(s) of this article can be found under https://doi.org/10.1002/chem.201800453.

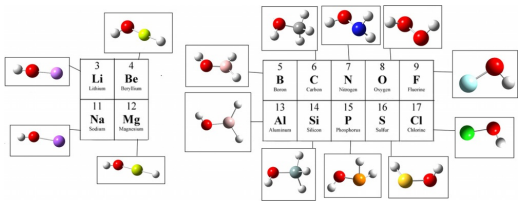

**Figure 1.** Optimized structures of the $H_nX$–OH (X = Li, Be, B, C, N, O, F, Na, Mg, Al, Si, P, S, Cl) model compounds. The number of hydrogen atoms bonded to X is chosen according to the valency of X so that neutral $H_nX$–OH species are obtained.

ChemPubSoc Europe

CHEMISTRY A European Journal Full Paper

In this paper, we study the element–oxygen bond in $H_nXOH$ model compounds, with X being an element of the second or third period, which are depicted in Figure 1. We have focused on these bonds because oxygen is the most abundant element on earth and almost all elements form stable bonds containing oxygen. With an electronegativity of 3.4 on the Pauling scale,[20] it is the second most electronegative element and as a result the nature of the element–oxygen bond exhibits a great diversity. One of the objectives of the paper is to end up with a classification of these X–OH bonds into different categories across all analysis tools. We expect polar covalent and ionic bond types to emerge clearly. Another objective is to see to what extend the recently proposed charge-shift bonds are detected with these tools.[21]

Because of the many tools available, examining all of them would be impossible in all studies. Therefore, a judicious choice needs to be made. Bonding analysis descriptors can be roughly divided into three different categories: There are i) descriptors in the real or position space, ii) orbital-based descriptors, and iii) descriptors in the energy space. We do not consider any momentum space descriptors here, because they are related to dynamic properties of electrons, such as occurring in conductors. Both ii) and iii) are Hilbert space methods, however, orbital methods involve one-particle spaces, whereas energy methods involve *n*-electron determinant spaces. The real space methods i) are somewhat special in that we can look at critical points or integrate properties for domains, which are defined topologically.[22]

In this paper, techniques that follow substantially different approaches are applied for the analysis of the X–OH bonds. They are listed in Table 1 where they are assigned into the three categories outlined above. Both the quantum theory of atoms in molecules (QTAIM)[23] and the analysis of the electron localizability indicator (ELI-D), may be assigned to i), because in both cases a real space function corresponding to the electron density and the electron localizability, respectively, is analyzed topologically. The Raub–Jansen index (RJI), which is a measure of the bond polarization, is a combination of both methods and may therefore also be assigned to i). A clear separation of ii) and iii) is not always possible. Natural bond orbitals (NBO) and valence bond (VB) calculations clearly belong to the realm of ii), but energetic aspects may be analyzed nonetheless. It might appear to be the obvious choice to assign energy decomposition analyses to iii), however, orbital contributions to the bond energy may be retrieved. In a Q-analysis only energetic contributions are considered, so an assignment to iii) is more unambiguous. In the following paragraphs, these tools are briefly reviewed. A detailed description of these methods is available in the literature.[9–16]

### 1.1 An overview of bond analysis methods

In the quantum theory of atoms in molecules (QTAIM), the topology of the electron density is analyzed. The values of the electron density and its second derivative, the Laplacian $\nabla^2\rho(\vec{r})$, at saddle points of the electron density, the bond critical points, are properties that are often inspected when discussing the nature of bonds in a QTAIM analysis. The former often correlates with the bond strength, whereas the latter can be linked to the covalency or, alternatively, to the ionicity of the bond.[24] The Laplacian of the electron density, $\nabla^2\rho(\vec{r})$, is often regarded as a magnifying glass because many features hidden in the electron density, which is dominated by large atomic maxima, are revealed. Negative regions of the Laplacian are valence-shell charge concentrations (VSCCs) and positive regions are valence-shell charge depletions (VSCDs).[25,26] Negative Laplacian values at the bond critical point are therefore associated with shared interactions, that is, covalent bonds, and positive Laplacian values are an indication of closed shell interactions, that is, ionic bonds. However, this classification is too short sighted. The kinetic and potential energy densities at the bond critical point (bcp), $G_{bcp}$ and $V_{bcp}$, respectively, are further indicators that allow the differentiation between shared and closed shell interactions: The sum of the two, the total energy density $H_{bcp}$, is negative if shared interactions are present and positive if the bonding is almost exclusively determined by electrostatic interactions;[27] $H_{bcp}$ may be negative although the Laplacian is positive.[28] Hence, "the employment of a positive value of the Laplacian alone in distinguishing between closed shell and polar covalent interactions is unsatisfactory when $2G(r_c) > |V(r_c)| > G(r_c)$".[29] For example, chemists would not classify the C–O bond in carbon monoxide as purely closed shell because of its large positive Laplacian value.[30] In this paper, we show the behavior of the Laplacian in X–O bonds, its connection to the total energy density, and many complementary bonding descriptors.

**Table 1.** Overview of the bond analysis tools applied in this study, that is, the quantum theory of atoms in molecules (QTAIM) including the source function, the electron localizability indicator (ELI-D), the Raub–Jansen index, the natural bond orbital analysis (NBO), the natural resonance theory (NRT), valence bond calculations (VB), the Ziegler–Rauk energy decomposition analysis (EDA), and the Q-analysis in i) the real space, ii) the orbital space, and iii) the energy space.

| | i) | ii) | iii) | Key advantages |
|---|---|---|---|---|
| QTAIM, source function | ● | | | No reference state required; applicable for experimental electron density studies |
| ELI-D | ● | | | Lone pair and bond populations can be analyzed; shell structure is obtained |
| Raub–Jansen index | ● | | | Measure of the bond polarity |
| NBO, NRT | | ● | ● | Widely available; clear link to Lewis structure; clear link to Coulson |
| VB | | ● | ● | Quantum mechanical rigorous Lewis structures and energies |
| EDA | | | ● | Physically meaningful contributions to bond interaction energy |
| Q-analysis | | | ● | New EDA-type; can be obtained from experiment |

ChemPubSoc Europe

CHEMISTRY A European Journal Full Paper

Each nuclear attractor (i.e., maximum of the electron density) is associated with an atomic basin that is confined by a zero-flux surface, where $\vec{n}\nabla\rho(\vec{r}) = 0$ ($\vec{n}$ = normal vector of the surface). An integration of the electron density in these basins yields atomic charges (Bader charges).[24] The delocalization index $\delta$(A,B) gives the number of electron pairs exchanged between the atomic basins A and B—it can therefore be analyzed as a bond order.[31] The source function is also based on the QTAIM approach and gives information on the electron communication complementary to the Laplacian.[32–34]

The electron localizability indicator (ELI-D), which is calculated from properties of the molecular wavefunction, is a scalar field that describes the distribution of electrons: Electrons are localized in regions of large ELI-D values.[11,35] We only regard the ELI-D and not the electron localization function (ELF), which largely behaves in the same way unless highly correlated calculations are carried out.[36] As opposed to the basins of the electron density, there are different types of ELI-D basins: There are core basins as well as valence basins whose synapticities are characterized by the number of core basins they are in contact with.[37] Monosynaptic valence basins are in contact with one core basin and can be attributed to lone pairs, whereas disynaptic valence basins, which may be associated to bonds, are in contact with two core basins. An integration of the electron density inside these basins yields their electron population. The isosurfaces of high ELI-D values correspond to localization domains that can be related to the corresponding basins. Similar features are obtained from isosurfaces of high-negative Laplacian values (VSCCs), which give domains of electron accumulation.[38]

A combination of the QTAIM and the ELI-D analyses is the Raub–Jansen index (RJI), which is a quantitative measure of bond polarity.[39] The ELI-D bonding basin of an A–B bond overlaps with the atomic QTAIM basins of atoms A and B, which yields two overlap regions, A∩bond(AB) and B∩bond(AB), respectively. The Raub–Jansen index of atom A is defined in Equation (1) in terms of population %, where $N$(A∩bond(AB)) and $N$(B∩bond(AB)) refer to the populations of the overlap regions.

$$\mathrm{RJI} = \frac{N(\mathrm{A}\cap\mathrm{bond(AB)})}{N(\mathrm{A}\cap\mathrm{bond(AB)}) + N(\mathrm{B}\cap\mathrm{bond(AB)})}100\% \qquad (1)$$

Natural bond orbitals (NBOs) are localized orbitals of Lewis and non-Lewis type.[40,41] The former may be related to features of classical Lewis structures, for example, bonds and lone pairs, whereas the latter are nonexistent in the classical Lewis picture. They are, for instance, valence antibonds or Rydberg orbitals. If the bonding situation in a molecule is localized, that is, there is no significant resonance occurring in the system, the exact wavefunction may be sufficiently approximated by the Lewis-type NBOs alone. In case of a completely localized bonding situation, the population of Lewis-type NBOs is $N = 2$ and the non-Lewis NBOs are unoccupied. However, non-Lewis-type NBOs may serve as acceptor orbitals in hyperconjugative interactions, which lead to an energetic stabilization of the molecule. As a result, they are slightly occupied, whereas the population of the corresponding donor orbitals, that is, the Lewis-type NBOs, is slightly diminished. The NBO analysis characterizes hyperconjugative interactions qualitatively and quantitatively, for example, through the electron populations of donor and acceptor orbitals and through delocalization energies. The NBO framework also yields natural atomic charges and NLMO/NPA (natural localized molecular orbital/ natural population analysis) bond orders. Measures of the bond polarization are the polarization coefficients $c$(A) and $c$(B), which correspond to the weights of the natural hybrid orbitals of atoms A and B, respectively, that make up an A–B bond.

An extension of the NBO analysis is the natural resonance theory (NRT), which attempts to recreate the full density matrix from resonance-weighted localized density matrices. Because they represent a specific Lewis structure, the NRT analysis enables an investigation of the molecular resonance based on the weights of the resonating structures.[42]

The analysis of valence bond (VB) calculations is another valuable tool to inspect the nature of chemical bonds.[43] The VB wavefunction is a linear combination of wavefunctions, each of which can be attributed to a specific Lewis formula. The complete VB wavefunction is usually a linear combination of more than one wavefunction, although it is possible to compute purely covalent or ionic wavefunctions, which enable a calculation of covalent or ionic resonance energies when compared to the energy of the complete wavefunction. With this procedure, information on the covalency of bonds may be retrieved. Shaik et al. used this approach to calculate the charge-shift resonance energies to characterize charge-shift bonds.[21]

In an energy decomposition analysis (EDA) the interaction energy of a bond is decomposed into a number of physically meaningful terms. In this study, the Ziegler–Rauk energy decomposition scheme is applied.[44–46] This scheme requires the choice of two molecular fragments that constitute the bond. A bond can be either fragmented homolytically (i.e., $AB \rightarrow A^{\bullet} + B^{\bullet}$) or heterolytically (i.e., $AB \rightarrow A^{+} + B^{-}$). The best fragmentation is indicated by a low Pauli repulsion suggesting that the fragments are prepared for bonding. The interaction energy ($\Delta E_{\mathrm{int}}$) of the bond is the energy difference between the molecule and its fragments. This does not correspond to the bond dissociation energy, because the fragment geometry is unchanged compared to its geometry in the molecule. The interaction energy may be decomposed according to Equation (2).

$$\Delta E_{\mathrm{int}} = \Delta V_{\mathrm{elast}} + \Delta E_{\mathrm{Pauli}} + \Delta E_{\mathrm{orb}} \qquad (2)$$

$\Delta V_{\mathrm{elast}}$ is the electrostatic attraction energy, which is computed in a classical way; $\Delta E_{\mathrm{Pauli}}$ and $\Delta E_{\mathrm{orb}}$ are the Pauli repulsion and the orbital interaction, respectively.

In a very recent method, here referred to as the Q-analysis, developed by Rahm and Hoffmann, energetic contributions to bonding are evaluated in a different way.[47] According to this approach, the energy change per electron upon bonding, $\frac{\Delta E}{n}$, may be expressed as $\Delta\bar{\chi} + \Delta(V_{\mathrm{NN}} + \omega)/n$, where $\Delta\bar{\chi}$ is the change in the average binding energy, $\Delta V_{\mathrm{NN}}$ is the change in the nuclear repulsion, and $\Delta\omega$ is the change in multielectron interactions (such as the electron repulsion and exchange-cor-

ChemPubSoc Europe

CHEMISTRY A European Journal Full Paper

relation energies) referring to a homolytic bond formation ($A^{\bullet}+B^{\bullet} \rightarrow AB$). $\Delta\bar{\chi}$ and $\Delta(V_{NN}+\omega)/n$ scaled to $\Delta E/n$ can be linked to the covalency and multielectron contributions, respectively. The difference between these two terms is the parameter $Q$, which allows a differentiation between a great variety of bonding types when plotted against the bond dissociation energy. Equation (3) gives the definition of the parameter $Q$ in its most convenient form for the following analysis.

$$Q = \frac{\Delta\bar{\chi}}{\Delta E/n} - \frac{(V_{nn}+\omega)/n}{\Delta E/n} \quad (3)$$

Here, $\Delta\bar{\chi}$ is the change in the average binding energy of an electron, $\Delta V_{nn}$ is the change in the nuclear repulsion, $\Delta\omega$ is the change in the multielectron interactions, and $\Delta E$ is the change in energy in a homolytic bond formation; $n$ is the total number of electrons.

#### 1.2 The element–oxygen bond—a great diversity

Many theoretical and experimental studies have been performed on different types of element–oxygen bonds, although systematic studies as performed here are sparse. Alabugin et al. performed an NBO analysis on the same $H_nXOH$ model compounds (X = B, C, N, O, F, Al, Si, P, S, Cl; however, no alkaline and alkaline-earth metals) with the intention to reveal hybridization trends for the X–O bonds of these compounds.[48] They found that the polarization of the X–O bond linearly decreases with increasing electronegativity of the element X as indicated by the polarization coefficient $c$(O) and that the hybridization across the PSE obtained from an NBO analysis is in agreement with Bent's rule.[49] In a study by Martín-Fernández et al., the increase in proton affinity of the OH group in $H_nXOH$ model compounds through non-covalent interactions with Lewis bases was studied.[50] Gillespie and Johnson carried out a systematic study on $H_nX$-O-$XH_n$ model compounds, where they regarded the X-O-X bond angles and a topological analysis of the electron density.[51]

Studies have been performed on the $H_2BOH$ model compound with the intention to verify the $\pi$ character of the B–O bond, which emerges from the strong Lewis acid character of boron arising from its electron deficiency and the ability of oxygen to act as a Lewis base.[48,52–54] Similar studies were performed for $H_2AlOH$. The Al–O bond also shows a $\pi$ character, which is, however, not as pronounced as in the B–O bond.[54,55] The C–O single bond in $H_3COH$ (or other alcohols) is regarded as a textbook example for polar covalent bonds.[56,57]

The homopolar O–O bond in HOOH (hydrogen peroxide) was identified as a charge-shift bond by Shaik et al.[21] In the valence bond theory, charge-shift bonds are characterized by a large resonance energy arising from the mixing of covalent and ionic Lewis formulas. Consequently, for HOOH, the resonance comprises one covalent Lewis formula, that is, HO–OH, as well as two ionic Lewis formulas, namely, $HO^{+}{}^{-}OH$ and $HO^{-}{}^{+}OH$. This resonance leads to an energetic stabilization—the covalent Lewis formula alone is not stable. Another prominent example for a charge-shift bond is the F–F bond in the difluorine molecule.[21] Valence bond calculations show that the covalent formula F–F does not lead to an energetic stabilization due to the repulsion of the fluorine lone pairs and the bonding electrons (lone pair bond weakening effect[58]). Thus, charge-shift bonds can be expected when electronegative and lone-pair-rich atoms are involved in the bonding. The F–O bond is therefore another potential candidate for a charge-shift bond.

The Si–O bond is referred to as a highly ionic bond by some authors,[59–62] whereas others state that it exhibits a "substantial covalent character".[63,64] Gibbs et al. regard the Si–O bond as a mixture of both—they call it the "elusive" bond.[65] The Si–O bond in siloxane systems (i.e., R-Si-O-Si-R') was investigated in terms of the experimental and theoretical electron density by Grabowsky et al.,[66] who confirmed the ionic nature of the Si–O bond. A complementary NBO analysis performed by Weinhold and West[67] found significant hyperconjugative interactions of the type LP(O)→σ*(Si–R) (LP = lone pair) to be of great significance. An increase in covalency was achieved by a decrease of the Si-O-Si angle.[66]

The remaining X–O single bonds are referred to as "semipolar X–O bonds" by Wallmeier and Kutzelnigg.[68] In their study, where the corresponding X–O model compounds were investigated theoretically, geometrical and energetic aspects as well as simple population analyses were performed. A QTAIM and ELF analysis of the P–O bond in the $H_2POH$ model compound was performed by Chestnut, who has identified it as a highly polarized covalent bond.[69] According to Wallmeier and Kutzelnigg, the N–O and Cl–O bonds show many similarities, which can be made plausible by the fact that N and Cl have similar electronegativities.[68]

Considering the results obtained from the bond analyses, it emerges to be meaningful to assign the X–O bonds into four different categories: ionic bonds, highly polarized covalent bonds, polarized covalent bonds, and charge-shift bonds. Of course, doing so poses an oversimplification, but nevertheless an attempt is made in this study. We will try to justify our decisions by regarding all bond analysis tools performed in this study.

## 2. Results and Discussion

In many cases, valuable information on chemical bonding may already be retrieved from the analysis of bond lengths. The beauty in this approach is the fact that they may be obtained easily and accurately from a variety of experimental approaches. It is, however, always necessary to compare to values from reference systems or to regard a systematically chosen set of compounds in order to draw meaningful conclusions. Moreover, bond lengths are affected by the coordination numbers of the bonded atoms. The $H_nXOH$ model compounds have different coordination numbers ranging from one to four, but we cannot isolate the effect that the change in the coordination number might have.

Figure 2 shows the X–O bond lengths of the $H_nX$-OH model compounds plotted against the atomic number of X. It is conspicuous that the model compounds of the third period have

ChemPubSoc Europe

CHEMISTRY A European Journal Full Paper

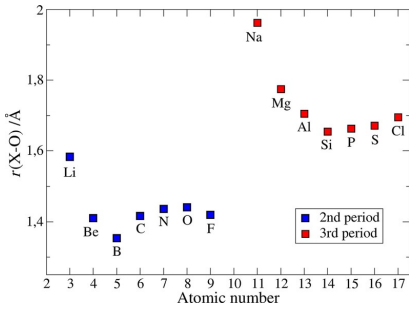


**Figure 2.** X–O bond lengths of the optimized structures (calculated at a CCSD/cc-pVTZ level of theory) plotted against the atomic number of X.

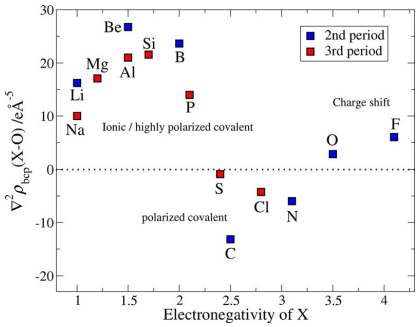


**Figure 3.** The Laplacian of the electron density at the X–O bond critical point, $\nabla^2\rho_{bcp}$, plotted against the electronegativity of X.

substantially longer bond lengths than the model compounds of the second period, which is caused by the larger atomic radii of the third period elements. The two most electropositive elements in the third period—Na and Mg—are involved in the longest X–O bonds. These bonds are dominated by electrostatic interactions and thus, an orbital overlap, which is maximized at small X–O bond lengths, only plays a minor role. The Si–O bond is the shortest bond of the third period model compounds. Starting from X=P, the X–O bond lengths increase slightly. From that point on, the element X has lone pairs, which interact repulsively with the bonding electrons thus, resulting in longer bonds to minimize the repulsion. This is known as the lone pair bond weakening effect.[58] In the second period, lithium is the most electropositive element, so it is of no surprise that the Li–O bond is the longest of the second period model compounds. However, the Be–O bond is comparatively short, although beryllium is the second most electropositive element of the second period. This suggests that the Be–O bond has a substantial covalent character. The B–O bond is the shortest of all model compounds. This may be related to its dative double-bond character stemming from the capability of boron to act as a Lewis acid. The N–O and O–O bonds are slightly longer than the C–O bond, which may be attributed to the lone pair bond weakening effect. Curiously, the F–O bond is slightly shorter than the proceeding bonds, which does not agree with the predicted trend.

First conclusions have been drawn from the analysis of bond lengths in the previous paragraph, although many of these conclusions are highly speculative and need to be correlated by the bond analysis tools applied in the following sections.

### 2.1 Quantum theory of atoms in molecules (QTAIM)

The QTAIM analysis gives bond paths for all X–O bonds regardless of their nature. The Laplacian of the electron density is a descriptor within the QTAIM framework to draw conclusions on the nature of the X–O bond. Figure 3 shows the Laplacian of the electron density at the X–O bond critical point, $\nabla^2\rho_{bcp}$, plotted against the electronegativity of the element X.

The plot shows that the X–O bonds are located in three separate regions characterized by the electronegativity of X and the sign of the Laplacian. The first region is located at low electronegativities of X and high Laplacian values. This is the region that can be associated with bonds where ionic interactions dominate (ionic bonds and highly polarized covalent bonds), because the Laplacian values are positive, that is, suggesting a high degree of closed-shell interactions. The second region is located at medium electronegativities of X and negative Laplacian values. Therefore, covalent interactions are dominant in the X–O bonds associated with this region. The bonds are still polarized towards the oxygen, but ionic interactions play a minor role. Therefore, these bonds can be termed polarized covalent. Finally, there is a region containing the O–O and F–O bonds at high electronegativities of X and positive Laplacian values. At first glance, this seems contradictory because a homopolar bond (O–O) and a slightly polarized bond (F–O) are not expected to have a positive Laplacian. This result hints at the fact that the O–O and F–O bonds are charge-shift bonds, which concurrently exhibit a covalent and ionic character.

As discussed in the introduction, the Laplacian alone does not allow for the differentiation between ionic and highly polarized covalent bonds, because its value may be positive de-

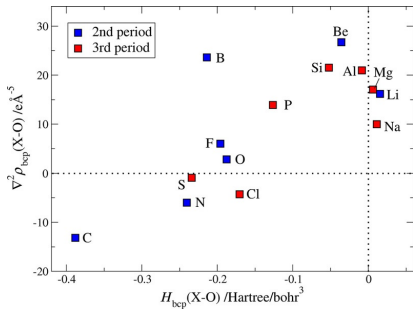


**Figure 4.** The Laplacian of the electron density at the X–O bond critical point $\nabla^2\rho_{bcp}$(X–O) plotted against the energy density at the X–O bond critical point $H_{bcp}$(X–O).

ChemPubSoc Europe

CHEMISTRY A European Journal Full Paper

spite the presence of significant shared interactions. The total energy density at the X–O bond critical point, $H_{bcp}$(X–O), which is the sum of the kinetic energy density $G_{bcp}$(X–O) and the potential energy density $V_{bcp}$(X–O), gives further insight into the X–O interactions. Negative values of $H_{bcp}$(X–O) indicate that covalent interactions are of great importance, whereas positive values are an indication of closed-shell interactions. Figure 4 shows the Laplacian plotted against $H_{bcp}$(X–O). This allows us not only to differentiate between ionic and highly polarized covalent bonds, but other aspects of the X–O bonds become apparent as well.

For the Li–O, Na–O, and Mg–O bonds both the Laplacian and the $\nabla^2\rho_{bcp}$(X–O) values are positive, so these bonds may be characterized as ionic bonds. The Be–O, B–O, Al–O, Si–O, and P–O bonds have positive Laplacian values but negative values of $H_{bcp}$(X–O)—these bonds may therefore be characterized as highly polarized covalent bonds. From the local expression of the viral theorem $[(\hbar^2/4m)\nabla^2\rho = 2G(r) + V(r))$, it follows that $H_{bcp}$(X–O) must be negative if the Laplacian is negative, which is the case for the polarized covalent bonds C–O, N–O, S–O, and Cl–O. Interestingly, the B–O bond is associated with a relatively high negative value of $H_{bcp}$(X–O) located in a region where the polarized covalent bonds are located. This may be attributed to the additional orbital overlap arising from the B–O $\pi$ bond. Also, the O–O and F–O bonds are located in the same region of high negative values of $H_{bcp}$(X–O), which shows the ambivalent character of the charge-shift bonds.

Further insight is gained when the Laplacian is plotted along the X–O bond path. In Figure 5, a selection of X–O Laplacian plots is depicted (the remaining plots are provided in the Supporting Information). It is conspicuous how the position of the bcp along the bond path varies and hence, determines the sign of the Laplacian, which explains the ambiguous character of the Laplacian at the bcp. An analysis of the VSCCs and VSCDs along the bond is more meaningful. The Laplacian plot of the model compound $H_3SiOH$ (Figure 5a) shows features that are inherent in ionic and highly polarized covalent bonds. There is a pronounced VSCC close to the oxygen atom and a plateau of positive Laplacian values at the element X (though the plateau is shifted towards more positive values if the bond is more ionic).

For $H_3COH$ (Figure 5c), the plot shows two VSCCs, which is an indication of the covalent character of the C–O bond. One VSCC is located close the oxygen and the other one is close to the carbon atom. The former is more pronounced than the latter because the bond is polarized towards the oxygen atom. The presence of two VSCCs is characteristic for all polarized covalent bonds (i.e., X = C, N, Cl, S). Despite the fact that the Laplacian at the P–O bond critical point is positive, that is, suggesting ionic interactions to dominate, the Laplacian plot of the model compound $H_2POH$ shows two VSCCs, which is more reminiscent of a polarized covalent bond.

Finally, the Laplacian plot of the model compound HOOH shows features that are characteristic for both ionic and covalent bonds, which coincides with its charge-shift character: There are two pronounced VSCCs close to both oxygen atoms and a VSCD at the center of the O–O bond. The former is characteristic for covalent bonds, whereas the latter shows the ionic character of the bond. A similar plot is obtained for the F–O bond, which also hints at its charge-shift character (see the Supporting Information).

As an alternative to the Laplacian plots, it is also possible to analyze plots of the local source function, which allows a similar analysis (Figure 5e–h). With the bcp chosen as a reference point for the calculation of the source function, the behavior at this position is most relevant. A positive spike can be interpreted as a predominance of covalent interactions in the bonding region (C–O), whereas a negative spike indicates the predominance of ionic contributions (Si–O). For the O–O bond, this behavior highlights the charge-shift character. For the P–O bond, it must be noted that the direction of the spike

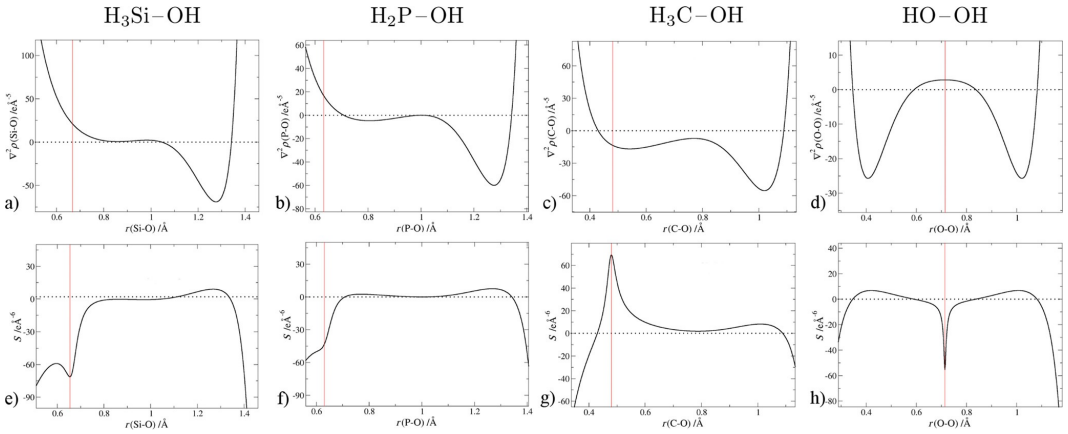


**Figure 5.** Plots along the bond path between the atoms X and O for a selection of $H_nXOH$ model compounds (X = Si, P, C, and O). a–d) Laplacian of the electron density, $\nabla^2\rho$ and e–f) the source function *S*. The red line indicates the position of the bcp. The oxygen is always located at the right hand side.

ChemPubSoc Europe

CHEMISTRY A European Journal Full Paper

would be opposite if a different reference point would have been chosen, for example, inside the small VSCC of Figure 5b).

Another alternative is the investigation of bonded radii defined in the QTAIM framework.[24] Gibbs et al. have shown for X–O-bonded radii averaged over many oxide crystals that these radii follow periodic trends useful for the characterization of the nature of bonding in oxides.[70]

At this stage, it is already possible to differentiate between four categories of X–O bonds based on the analysis of the Laplacian, the energy densities, and the local source function: 1) ionic bonds (X = Li, Na, and Mg), 2) covalent bonds where closed-shell interactions dominate (highly polarized covalent bonds) (X = Be, B, Al, Si, and (P)), 3) bonds where covalent interactions dominate (polarized covalent bonds) (X = C, N, (P), S, and Cl), and 4) charge-shift bonds (X = O and F).

### 2.2 Analysis of the electron localizability indicator (ELI-D)

The ELI-D has basins that may be related to chemical features, such as atomic shells, bonds (disynaptic basins) and lone pairs (monosynaptic basins). Table 2 lists the number of monosynaptic X and O basins and disynaptic X–O basins as well as their electron population.

**Table 2.** Results of the analysis of the ELI-D. $N_{DSB}$(X–O) corresponds to the number of disynaptic X–O basins and $N_{MSB}$(O) and $N_{MSB}$(X) correspond to the number of monosynaptic basins on O and X, respectively. The total electron population is given for these basins (in [e]).

| X | $N_{DSB}$(X–O) | Population | $N_{MSB}$(O) | Population | $N_{MSB}$(X) | Population |
|---|---|---|---|---|---|---|
| Li | 0 | – | 1 | 6.04 | 0 | – |
| Be | 1 | 2.58 | 1 | 3.52 | 0 | – |
| B | 1 | 2.24 | 1 | 3.74 | 0 | – |
| C | 1 | 1.35 | 2 | 4.64 | 0 | – |
| N | 1 | 1.03 | 2 | 4.73 | 1 | 2.45 |
| O | 1 | 0.72 | 2 | 4.76 | 2 | 4.76 |
| F | 1 | 0.49 | 2 | 4.70 | 1 | 6.77 |
| Na | 0 | – | 1 | 6.09 | 0 | – |
| Mg | 0 | – | 1 | 6.11 | 0 | – |
| Al | 2 | 2.42 | 1 | 3.71 | 0 | – |
| Si | 1 | 1.69 | 2 | 4.42 | 0 | – |
| P | 1 | 1.40 | 2 | 4.64 | 1 | 1.96 |
| S | 1 | 1.13 | 2 | 4.77 | 2 | 4.14 |
| Cl | 1 | 0.90 | 2 | 4.82 | 1 | 6.26 |

The absence of a disynaptic X–O basin indicates that the bond is ionic because there is no localization domain, which can be associated to a covalent bond. This is the case for the Li–O, Na–O, and Mg–O bonds. They may therefore be identified as ionic bonds, which has also been suggested by the total energy density at the X–O bond critical point. There is one monosynaptic basin on the oxygen atom, which integrates to approximately six electrons and may therefore be related to three oxygen lone pairs, which is in agreement with an ionic description of the X–O bond.

The analyses of the Laplacian and the total energy density at the X–O bond critical point have already suggested that the X–O bonds with X = Be, B, Al, Si, and P are highly polarized covalent bonds. Accordingly, it comes as no surprise that disynaptic X–O basins are obtained for these bonds. The oxygen atom in the Si–O and P–O bonds exhibits two monosynaptic basins, which may be related to two oxygen lone pairs. The dative double-bond character of the B–O bond is only slightly evident from the analysis of the ELI-D: There is only one disynaptic B–O basin, which does, however, have an electron population greater than two, and a single monosynaptic basin on O with an electron population, which is lower than four. For the Al–O bond, the dative double-bond character is more evident. The analysis yields two disynaptic Al–O basins and a single monosynaptic basin on the oxygen atom. The results for the Be–O bond are somewhat curious. The electron population of the disynaptic X–O basin is substantially higher than two and the monosynaptic oxygen basin has a population substantially lower than four. This observation will be discussed at a later point when we regard the isosurfaces of the ELI-D.

The remaining X–O bonds (X = C, N, O, F, S, and Cl) each have one disynaptic X–O basin and two monosynaptic oxygen basins. The electron population of the disynaptic X–O basins decreases with an increasing atomic number in both periods—the population deviates increasingly from a value of two. The monosynaptic basins on the oxygen and the element X absorb the remaining electron density. Therefore, if lone-pair-rich elements are bonded, the population of the disynaptic X–O basins is low (for X = O, F, and Cl the population is even below one). This could possibly coincide with the charge shift character of these bonds as stated by Shaik et al.[21] for the bonding populations of the ELF. However, it could also be an artifact of the nature of the electron localization methods.

The basins can be represented visually by plotting the isosurfaces of appropriate ELI-D isovalues. These plots are depicted in Figure 6 for a selection of $H_nXOH$ model compounds (the remaining plots are shown in the Supporting Information).

The isosurface of the model compound NaOH is exemplary of the ionic compounds regarded in this study: There is a ring-shaped localization domain at the oxygen atom and there is no isovalue at which a disynaptic X–O basin is detected. For the model compound HBeOH, there is one monosynaptic

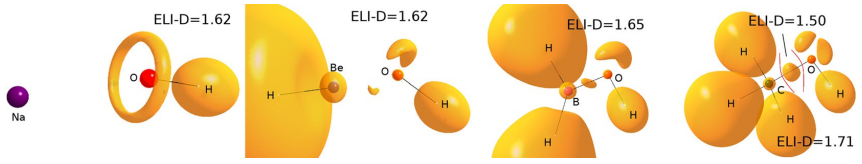


**Figure 6.** Isosurfaces of the ELI-D for a selection of $H_nXOH$ model compounds (NaOH, HBeOH, $H_2BOH$, and $H_3COH$). The corresponding isovalues are given in the plots. Regions of different isovalues are separated by red lines.

ChemPubSoc Europe

CHEMISTRY A European Journal Full Paper

basin at the oxygen and a disynaptic Be–O basin. These basins are represented by a "banana"-like domain and are directed towards each other like a disjoint ring. If a lower ELI-D isovalue is chosen, these two isosurfaces combine to form a ring, which is tilted towards the Be atom. This picture is more reminiscent of an ionic bond. Therefore, the Be–O bond can be regarded as a transition from an ionic to a highly polarized covalent bond when considering the analysis of the ELI-D. The B–O double-bond character is only slightly evident when regarding the populations of the ELI-D basins, but it becomes more visible when inspecting the isosurface of the disynaptic B–O basin: Its elliptical shape can be related to the presence of a B–O $\pi$ orbital. For the model compound $H_2AlOH$ a similar isosurface is obtained (see the Supporting Information). The ELI-D isosurface of the model compound $H_3COH$ is characteristic for all (highly) polarized covalent and charge-shift $H_nXOH$ model compounds that have X–O single bonds. There are two separate domains at the oxygen, which can be attributed to two oxygen lone pairs, and a spherically shaped X–O domain.

The ELI-D particularly provides valuable information on the differentiation between ionic and highly polarized covalent bonds. The former is present if a disynaptic X–O basin is absent and a ring-shaped monosynaptic basin is obtained at the oxygen atom. The analysis of the ELI-D also reveals the dative double-bond character of the B–O and Al–O bonds and an ambivalent Be–O bond, which presents itself to be a highly polarized covalent bond on the edge of becoming an ionic bond. Similar isosurface plots are obtained from the Laplacian (see the Supporting Information), but considering the corresponding Laplacian basin populations is not meaningful.

### 2.3 Measures of bond polarization: atomic charges and the Raub–Jansen index

To get an impression of the polarization of the X–O bonds, the Bader and NPA group charges, $q_{Bader}$ and $q_{NPA}$, respectively, of the OH fragments are regarded alongside the Raub–Jansen index of the oxygen atoms (population %). Figure 7 shows the $q_{Bader}$ and $q_{NPA}$ values plotted against the electronegativity of the element X.

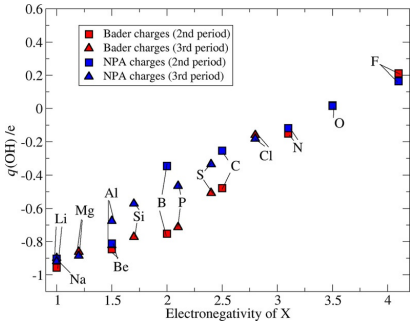


**Figure 7.** NPA and Bader OH group charges, $q_{NPA}$ and $q_{Bader}$, respectively, of the $H_nX$–OH model compounds plotted against the electronegativity of the element X.

Both $q_{Bader}$ and $q_{NPA}$ increase linearly with increasing electronegativity of X. If $q \neq 0$, the bond is polarized, whereas for $q = 0$ there is no polarization, which is only the case for the homopolar O–O bond. The only positive OH charge is obtained for the FOH model compound because the F–O bond is polarized towards the more electronegative fluorine atom. Both $q_{Bader}$ and $q_{NPA}$ show similar values for the elements with the smallest and highest electronegativities. For the mid-region, relatively high deviations are obtained—especially, $q_{Bader}$ and $q_{NPA}$ for the model compound $H_2BOH$ deviate by approximately 0.4 e.

The Raub–Jansen index of the oxygen atom (population %), RIJ, which is, as outlined in the Introduction, a quantitative measure of the bond polarization, is plotted against the electronegativity of X in Figure 8. If RIJ > 50%, the bond is polarized towards the oxygen atom; if RJI = 50%, it indicates a homopolar bond and if RJI < 50% the bond is polarized towards the element X. As already indicated by the OH group charges, the bond polarization decreases approximately linearly with increasing electronegativity of X until it disappears for the O–O bond (RJI = 50%). Finally, the F–O bond is polarized towards the fluorine atom.

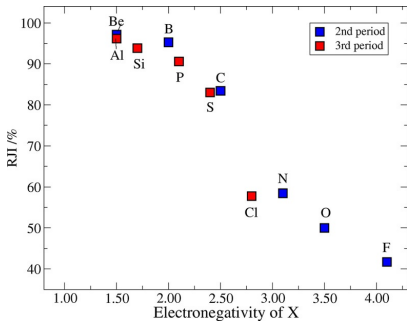


**Figure 8.** Raub–Jansen indices (RJIs) of the X–O bonds (X = Be, B, C, N, O, F, Al, Si, P, S, Cl) plotted against the electronegativity of X.

Both the OH group charges and the Raub–Jansen indices give a consistent trend of the X–O bond polarization. However, regarding the Raub–Jansen index in other studies may be more meaningful than analyzing atomic charges (or groups of atomic charges) because for the RJI no reference system is required.

### 2.4 Natural bond orbitals (NBO)

The Lewis-type NBOs may be related to features of Lewis structures, such as core orbitals, bonds, and lone pairs. Therefore, Lewis formulas are directly obtained from the NBO output. However, the Lewis-type NBOs are only a good approximation of the bonding if their electron population is close to two. Figure 9 shows a schematic representation of the Lewis structures suggested by the Lewis-type NBOs. The composition of the X–O and lone-pair NBOs is given in the Supporting Information.

ChemPubSoc Europe

CHEMISTRY A European Journal Full Paper

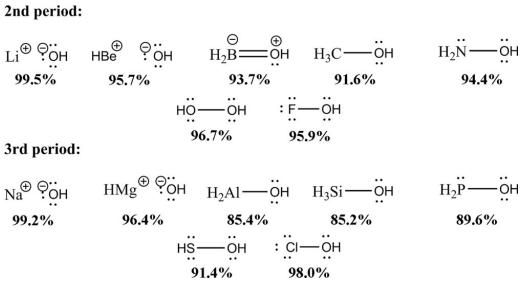


**Figure 9.** Schematic representation of the localized Lewis formulas of the $H_nXOH$ model compounds as suggested by the NBO analysis. The percentages refer to the weight of the shown Lewis formulas according to the NRT.

According to the NBO analysis, the Li–O, Na–O, and Mg–O bonds are ionic, which is in agreement with the previous analyses (there is no NBO associated with an X–O bond and there are three oxygen lone-pair NBOs). However, the Be–O bond is also identified as ionic in the context of the NBO analysis. A B–O π-bond is suggested for the model compound $H_2BOH$, whereas none is found for the Al–O bond. For the remaining X–O bonds, an X–O NBO and two oxygen lone-pair NBOs are obtained. Starting from X = N in the second period and from X = P in the third period, the element X has NBOs corresponding to lone pairs. As shown by Alabugin et al.,[48] the polarization coefficient *c*(O), which is the weight of the natural hybrid orbital of oxygen in an X–O NBO, decreases linearly with increasing electronegativity of X—it can therefore be utilized as another tool to inspect the bond polarization (see the Supporting Information for the corresponding plot).

The Lewis structures depicted in Figure 9 only give a localized picture of the bonding because the Lewis-type NBOs are regarded exclusively. However, there are delocalizations that emerge from the interaction of donor and acceptor orbitals, corresponding to Lewis-type and non-Lewis-type orbitals, respectively. Non-Lewis-type NBOs are Rydberg orbitals, valence antibonds, or lone valencies. All ionic compounds (i.e., X = Li, Be, Na, and Mg) have significant interactions between the oxygen lone pairs (donor orbitals) and lone valencies, Rydberg orbitals at X or X–H antibonds, which result in the lowering of the oxygen lone-pair populations. Thus, it is possible to judge the strength of these interactions by inspecting the oxygen lone-pair populations (see the Supporting Information). These interactions may be regarded as minor shared, that is, covalent, interactions. They are particularly prominent in the HBeOH model compound (low oxygen lone-pair populations) where other analysis tools have previously suggested a highly polarized covalent bond. In the model compound $H_2AlOH$, there is a significant interaction that may be related to an Al–O π bond: An oxygen lone-pair NBO with p character acts as a donor orbital and a lone valency with p character at Al acts as an acceptor orbital. However, the NBO analysis does not give any indication on the charge-shift character of the O–O and F–O bonds—they present themselves as ordinary covalent bonds.

The natural resonance theory (NRT) is an extension to the NBO analysis, which provides information on the resonance in a system. The weights of the main Lewis structure are given in Figure 9. In addition, (negative) hyperconjugation involving the oxygen lone pairs and X–H antibonds plays a role in most X–O model compounds. The NBO analysis has shown that minor shared interactions are suggested for the ionic systems, so the NRT yields covalent resonance structures also for the ionic model compounds, which are, however, associated with a low weight. Also, there are resonance forms for $H_2BOH$ and $H_2AlOH$ that have X–O single and double bonds.

### 2.5 Valence bond (VB) calculations

Valence bond (VB) calculations allow the computation of wavefunctions containing purely ionic ($H_nX^{+-}OH$) or covalent ($H_nX$–OH) bonds. The energies of the ionic and covalent wavefunctions, $E_{ion}$ and $E_{cov}$, respectively, may be compared to the energy of the complete VB wavefunction $E_{tot}$. Here, the difference between $E_{tot}$ and $E_{ion}$ or $E_{cov}$ are termed the ionic or covalent resonance energy, $RE_{ion}$ or $RE_{cov}$, respectively. In Figure 10, $RE_{ion}$ is plotted against the electronegativity of X if $E_{ion}$ is lower in energy than $E_{cov}$, that is, closer to $E_{tot}$, and $RE_{cov}$ is plotted if the opposite is true.

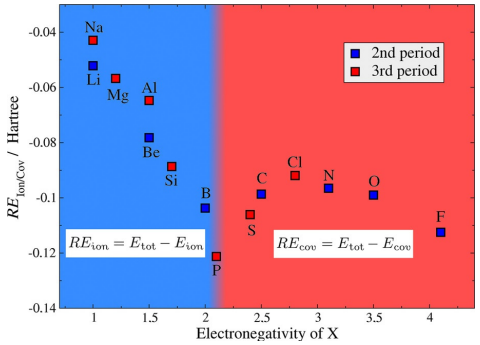


**Figure 10.** Ionic or covalent resonance energy, $RE_{ionic}$ or $RE_{covalent}$, respectively, of the $H_nXOH$ model compounds plotted against the electronegativity of X.

In the first region $RE_{ion} < 0$, which suggests that covalent interactions contribute to an energetic stabilization of the complete VB wavefunction, but the ionic bonding character outweighs the covalent one. With increasing electronegativity, $RE_{ion}$ becomes more negative in a linear fashion—thus, the covalent character of the X–O bond increasingly gains in significance, because $E_{ion}$ departs more and more from $E_{tot}$. For X = P, $E_{ion}$ and $E_{cov}$ are approximately the same—the ionic and covalent interactions are therefore of equal significance in the P–O bond.

The second region (where $E_{cov}$ is lower than $E_{ion}$) starts from X = S. The initial increase of $RE_{cov}$ can be attributed to an increase in the covalency of the X–O bond. However, the increase comes to an end at X = N and $RE_{cov}$ decreases from that

ChemPubSoc Europe

CHEMISTRY A European Journal Full Paper

point on. This decrease, which implies that ionic contributions to the bonding regain in significance, is made plausible by an increase in the charge-shift character of these bonds. In the analysis of the Laplacian, a charge-shift character could only be attributed to the O–O and F–O bonds, but not to the N–O bond. However, the N–O bond contains electronegative atoms carrying lone pairs. Therefore, a certain charge-shift character is to be expected.

Interestingly, the X–O bonds, which lie in the first region (where $E_{ion}$ is closer to $E_{tot}$ than $E_{cov}$) are also the ones that show positive Laplacian values at their bond critical points. So, both the analysis of the Laplacian and the valence bond calculations suggest that ionic interactions are dominant in these X–O bonds.

### 2.6 Energy decomposition analysis (EDA)

The bond interaction energy ($E_{int}$) may be decomposed into physically meaningful terms by using a scheme introduced by Ziegler and Rauk.[44] For the $H_nXOH$ model compounds, the X–O bond is fragmented homolytically and heterolytically. The corresponding fragments are the doublet species $H_nX^{\bullet}$ and $^{\bullet}OH$ for the former and the closed-shell species $H_nX^{+}$ and $^{-}OH$ for the latter. Usually, it is advisable to fragment a bond so that it is prepared for bonding, so covalent bonds should be fragmented homolytically, whereas for ionic bonds a heterolytical bond fragmentation is the judicious choice. In this study, we chose both approaches, because valuable information may be retrieved from either fragmentation scheme (Table 3). The most suitable fragmentation is revealed by the lowest Pauli repulsion term ($\Delta E_{Pauli}$). Based on this criterion, a heterolytical fragmentation is best suited for the Li–O, Be–O, B–O, C–O, Na–O, Mg–O, Al–O, Si–O, and P–O bonds, whereas lower $\Delta E_{Pauli}$ values are obtained for a homolytical bond fragmentation of the N–O, F–O, S–O, and Cl–O bonds. It has been shown previously that the relative importance of the two attractive terms $E_{orb}$ and $V_{elest}$ reflects the bond character.[45] Interestingly, the percentage of the orbital interactions does not vary much in a homolytical bond fragmentation. At first glance, it is peculiar that the percentage of orbital interactions is even greater in highly ionic bonds (e.g., Li–O and Na–O) compared to the bonds that have been shown to be highly covalent (e.g., C–O and S–O). However, for ionic bonds, two neutral fragments are a bad approximation of the actual bonding, because one electron must be transferred from the more electropositive fragment to the more electronegative one. This charge transfer affects $\Delta E_{orb}$ and thus, makes it more stabilizing. The electrostatic interaction between two neutral fragments is very low at high distances. Consequently, it is no surprise that the orbital interaction is the most stabilizing term even for ionic bonds if a homolytical bond fragmentation is chosen. It is also conspicuous that electrostatic interactions are of significance for covalent bonds. This has already been shown by the valence bond calculations where ionic resonance forms always contribute to the bonding even for perfectly homopolar bonds. From a homolytical fragmentation, it is not possible to directly relate to the polarization of the bond. However, the percentages of the orbital and electrostatic interactions give a straightforward correlation to the X–O bond polarization. An assignment into ionic, highly polarized covalent, polarized covalent, and charge-shift bonds is not possible. For brevity, we have only scratched the surface of an EDA. For example, it is also possible to decompose the orbital energy into terms stemming from orbitals of different symmetry in order to determine the significance of σ and π bonding based on energy.

### 2.7 Analysis of the parameter *Q*

Finally, a very recent approach to analyze the bonding character introduced by Rahm and Hoffmann[47] is regarded, which exclusively considers energetic contributions to bonding.

The parameter *Q* of the X–O bonds is plotted against the homolytic X–O bond dissociation energy $D_E$ in Figure 11—this leads to a separation of the X–O bonds. Accordingly, they can be divided into different regions related to a distinct bonding character.

**Table 3.** Results from the Ziegler–Rauk energy decomposition analysis of a homolytical and heterolytical X–O bond fragmentation (the lowest Pauli repulsion is given in bold); the energy terms are given in [kcal mol$^{-1}$].

| | $H_nX^{\bullet}$ $^{\bullet}OH$ | | | | $H_nX^{+}$ $^{-}OH$ | | | |
|---|---|---|---|---|---|---|---|---|
| | $\Delta E_{int}$ | $E_{orb}$ | $\Delta V_{elast}$ | $\Delta E_{Pauli}$ | $\Delta E_{int}$ | $E_{orb}$ | $\Delta V_{elast}$ | $\Delta E_{Pauli}$ |
| LiOH | −105.01 | −132.16 (74.5%) | −45.23 (25.5%) | 72.38 | −198.70 | −32.94 (13.9%) | −203.68 (73.3%) | **37.92** |
| HBeOH | −151.84 | −309.68 (65.2%) | −165.61 (34.8%) | 323.65 | −310.63 | −101.61 (26.7%) | −278.62 (73.3%) | **69.59** |
| $H_2BOH$ | −156.62 | −405.59 (63.8%) | −230.21 (36.2%) | 479.18 | −337.58 | −193.87 (36.7%) | −334.28 (63.3%) | **190.56** |
| $H_3COH$ | −105.02 | −338.61 (64.7%) | −184.62 (35.2%) | 418.20 | −318.95 | −228.22 (42.7%) | −306.00 (57.3%) | **215.27** |
| $H_2NOH$ | −68.81 | −251.65 (64.0%) | −141.86 (36.0%) | **324.70** | −326.21 | −333.94 (50.6%) | −326.24 (49.4%) | 333.51 |
| HOOH | −53.61 | −273.41 (65.9%) | −141.75 (34.1%) | **361.55** | −419.95 | −518.65 (61.0%) | −331.12 (39.0%) | 429.82 |
| FOH | −51.35 | −177.32 (71.0%) | −72.53 (29.0%) | **198.49** | −537.31 | −595.58 (65.4%) | −315.36 (34.6%) | 373.63 |
| NaOH | −75.44 | −93.19 (73.3%) | −33.89 (26.7%) | 51.64 | −156.02 | −15.30 (8.2%) | −170.84 (91.8%) | **30.13** |
| HMgOH | −110.98 | −173.61 (63.3%) | −92.33 (34.7%) | 154.96 | −237.68 | −49.70 (16.4%) | −253.64 (83.6%) | **65.66** |
| $H_2AlOH$ | −131.51 | −248.55 (61.7%) | −154.14 (38.3%) | 271.19 | −273.95 | −91.34 (23.0%) | −304.95 (77.0%) | **122.34** |
| $H_3SiOH$ | −123.45 | −276.01 (62.2%) | −167.56 (37.8%) | 321.12 | −295.30 | −136.75 (29.5%) | −327.59 (70.5%) | **169.04** |
| $H_2POH$ | −86.67 | −246.54 (61.5%) | −154.55 (38.5%) | 314.41 | −269.15 | −202.58 (40.0%) | −303.79 (60.0%) | **237.22** |
| HSOH | −70.70 | −272.19 (63.8%) | −154.41 (36.2%) | **355.91** | −328.89 | −429.53 (54.4%) | −360.54 (45.6%) | 461.18 |
| ClOH | −55.78 | −240.47 (62.8%) | −142.44 (37.2%) | **327.13** | −384.66 | −448.42 (56.3%) | −348.38 (43.7%) | 421.15 |

ChemPubSoc Europe

CHEMISTRY A European Journal Full Paper

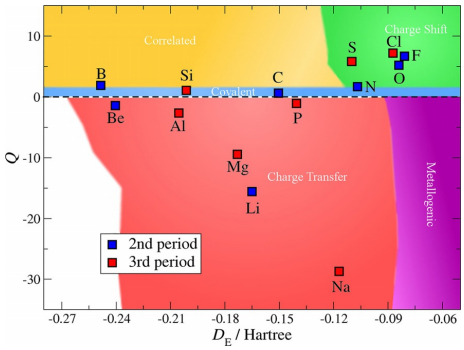


**Figure 11.** The parameter $Q$ plotted against the homolytic bond dissociation energy $D_E$.

Negative values of $Q$ and relatively high values of $D_E$ may be linked to the X–O bonds, which exhibit a high degree of charge transfer. Here, the bond formation is favored by multielectron interactions ($\Delta\omega$), that is, the charge transfer. The Na–O, Li–O, Mg–O, Be–O, Al–O, and P–O bonds are located in this region—the previous analyses also attributed a high ionic character to these bonds, although an equally high covalency was suggested for the P–O bond.

If $Q=1$, the bonding is favored exclusively by $\Delta\bar{\chi}$, which may be related to an orbital stabilization—thus, the bonds around $Q=1$ are covalent. This is the case for the B–O, Si–O, C–O, and N–O bonds. Whereas the previous analyses performed in this study assigned a high covalent character to the C–O and N–O bonds, the B–O and Si–O bonds were identified to be highly polarized covalent. However, when regarding energetic contributions to the bonding these bonds are favored by an orbital stabilization. As mentioned in the Introduction, the Si–O bond was termed the "elusive" bond by Gibbs et al.[65]—this is also reflected in this study.

The third region in which the X–O bonds of this study are located in, is associated with values of $Q>1$ and low bond dissociation energies—this is the region, which contains the charge-shift bonds. The charge-shift bonds are also characterized by negative values of $\Delta\bar{\chi}$, but the term $\Delta(\omega+V_{nn})$ is positive and thus, resists the bonding—the multielectron interactions are opposing the bond formation. Besides the O–O and F–O bonds, whose charge-shift character is most prominent in the previous analyses of this study, the S–O and Cl–O bonds are also located in this region. This is their first manifestation as charge-shift bonds.

## 3. Comparisons and Conclusions

A selection of bond analysis tools has been applied to the X–O bond of $H_nXOH$ model compounds (X = Li, Be, B, C, N, O, F, Na, Mg, Al, Si, P, S, Cl) with the intention to gain an insight into the nature of the X–O bonds and to uncover how well these different tools work together. The nature of the analysis methods is very distinct, so it is of particular interest to find out how these tools complement each other. An attempt is made to assign the X–O bonds into four different categories: 1) ionic bonds, 2) highly polarized covalent bonds, 3) polarized covalent bonds, and 4) charge-shift bonds. This assignment, which will be justified by regarding the previously discussed result in the next few paragraphs, is summarized in Table 4.

**Table 4.** Assignment of the X–O bonds into four categories: 1) ionic, 2) highly polarized covalent, 3) polarized covalent, and 4) charge-shift bonds. ● signifies the main category, while ○ signifies a category that partially applies to the X–O bond.

| Second period | Li | Be | B | C | N | O | F |
|---|---|---|---|---|---|---|---|
| Ionic | ● | ○ | | | | | |
| Highly polarized covalent | | ○ | ● | | | | |
| Polarized covalent | | | ○ | ● | ● | | |
| Charge shift | | | | | ○ | ● | ● |
| **Third period** | **Na** | **Mg** | **Al** | **Si** | **P** | **S** | **Cl** |
| Ionic | ● | ● | | | | | |
| Highly polarized covalent | | | ● | ● | ○ | | |
| Polarized covalent | | | | ○ | ○ | ● | ● |
| Charge shift | | | | | | ○ | ○ |

Ionic and highly polarized covalent bonds are dominated by closed-shell interactions. Hence, other terms for highly polarized covalent bonds could be "mainly ionic" or "covalent ionic", however, the term chosen denominates them as covalent bonds in which closed-shell interactions dominate. Covalent interactions are also present in ionic bonds, but play a minor role and electrostatic interactions almost exclusively constitute the bonding. The fact that ionic interactions dominate the bonding in both ionic and highly polarized bonds is revealed by regarding the Laplacian values at the X–O bond critical points, $\nabla^2\rho_{bcp}$, and the plots of the Laplacian, $\nabla^2\rho$, along the bond path between X and O: $\nabla^2\rho_{bcp}$ is positive and the plots of $\nabla^2\rho$ show a pronounced VSCC located at the oxygen atom and a plateau of positive Laplacian values at the element X. The VB calculations confirm that ionic interactions outweigh the covalent interactions in ionic and highly polarized covalent bonds: The wavefunction for the ionic structure is lower in energy than the wavefunction of the covalent one and therefore, closer to the energy of the wavefunction for the complete state. The total energy density at the X–O bond critical point, $H_{bcp}$(X–O), enables a differentiation between ionic and highly polarized covalent bonds, because for the latter negative values of $H_{bcp}$(X–O) have been obtained, suggesting the presence of significant shared interactions. In an energy decomposition analysis, ionic and highly polarized covalent bonds are best described by a heterolytical fragmentation, as suggested by a lower Pauli repulsion. Isosurfaces of the ELI-D also show a clear distinction between ionic and highly polarized covalent bonds. For the ionic bonds, there is a ring-shaped monosynaptic oxygen basin, which integrates to approximately six electrons, which may be linked to the presence of three oxygen lone pairs. For the highly polarized covalent bonds, there are disynaptic X–O basins corresponding to covalent X–O bonds (the same features are obtained from isosurfaces of the Laplacian). All analyses confirm that the Li–O, Na–O,

ChemPubSoc Europe

CHEMISTRY A European Journal Full Paper

and Mg–O bonds are ionic—in addition to the analysis of the Laplacian and the ELI-D, the analysis of the parameter *Q* attributes a high degree of charge transfer to these bonds and the NBO analysis yields three oxygen lone pairs and no X–O NBO.

The Be–O bond may be regarded as a transition from an ionic to a highly polarized covalent bond, because a disynaptic Be–O basin is obtained in the ELI-D. However, the shape of the isosurfaces of the monosynaptic oxygen basin and the disynaptic Be–O basin are more reminiscent of the ring-shaped monosynaptic oxygen basin of the ionic bonds (though separated into two basins and tilted towards Be) and, moreover, the NBO analysis suggests an ionic bond. The B–O, Al–O, and Si–O bonds are revealed to be highly polarized covalent bonds when regarding the analysis of the Laplacian and the ELI-D. However, the Si–O and B–O bonds have been found to be covalent in the analysis of the parameter *Q*. Therefore, if purely energetic aspects are regarded, these bonds present themselves as covalent bonds, whereas all other analyses suggest them to be highly polarized covalent bonds. Both the B–O and Al–O bonds are dative double bonds as suggested by the analysis of the ELI-D and the NBOs. The P–O bond is a special case where ionic and covalent interactions are present approximately to an equal extent. This is revealed by the VB analysis where the energy of the covalent and ionic wavefunctions have approximately the same energy. Also, $\nabla^2\rho_{bcp} > 0$ suggests a bond where ionic interactions dominate, whereas the plot of the Laplacian between P and O shows two VSCCs, which is characteristic for covalent bonds.

The analysis of the Laplacian suggests that covalent interactions are dominant in the polarized covalent bonds (i.e., C–O, N–O, S–O, and Cl–O): $\nabla^2\rho_{bcp}$ is negative and there are two VSCCs—one is located close to the oxygen atom and the other one close to the element X. The VB calculations confirm this: The energy of the wavefunction for the covalent structure is lower than the one of the ionic structure and thus, closer to the energy of the wavefunction for the complete state. Like the highly polarized covalent bonds, the polarized covalent bonds are associated with disynaptic X–O basins in the analysis of the ELI-D and the NBO analysis yields X–O NBOs. With the exception of the C–O bond, the energy decomposition analysis implies that a homolytical bond fragmentation is best suited for the covalent bonds.

The O–O and F–O bonds could be most unambiguously characterized as charge-shift bonds. For these two bonds the Laplacian clearly indicates a charge-shift character: $\nabla^2\rho_{bcp}$ is positive and the plot of the Laplacian between X and O shows features that are inherent to ionic (VSCD around the bond critical point) and covalent bonds (VSCCs at X and O). However, some of the other tools attribute a charge-shift character to further X–O bonds. The VB calculations suggest that ionic interactions regain significance starting from the Cl–O bond, thus, suggesting the Cl–O, N–O, O–O, and F–O bonds to have certain charge-shift character. The analysis of the parameter *Q* shows that the S–O, Cl–O, O–O, and F–O bonds fall into the region associated to charge-shift bonds. Accordingly, the extraction of the charge-shift character of the X–O bonds poses a particularly difficult task because the tools, which are employed do not always agree. For example, the NBO analysis does not give any indication on the charge-shift character of the O–O and F–O bonds, which is, however, detected when performing an analysis of the Laplacian or VB calculations.

The X–O bond polarization decreases linearly with increasing electronegativity of X (as indicated by the OH group charges and the Raub–Jansen index). This result implies that the electronegativity difference (an empirical concept) is already a good measure of the bond polarization. However, the bond polarization alone does not allow us to draw any conclusions on the nature of the bond. Of course, ionic bonds can be expected if the difference in electronegativities is high, but there is no characteristic threshold value, which indicates the presence of covalent bonds.

Only in few cases, all of the tools employed in this study lead to an unambiguous assignment of an X–O bond into one of the four categories suggested above. However, it would be irrational to attribute this to the failing of one or the other of the bond analysis methods. For example, the analysis of the Laplacian shows that the Cl–O bond is a polarized covalent bond, whereas the analysis of the parameter *Q* suggests it to be a charge-shift bond. Rather than saying that these two tools give conflicting information on the bonding, one can argue that both properties are inherent to the Cl–O bond. Similarly, one can say that the Be–O bond is an ionic bond with substantial shared interactions, which lead to a high distortion of the monosynaptic oxygen basin. In other words, in almost all cases, more than one indication is needed to reveal the full bond character.

The combination of many different bond analysis tools proved to be a very powerful procedure for the analysis of the X–O bonds (complementary bonding analysis). Although many features can already be detected from a single-bond analysis tool, others may remain hidden. Ultimately, the solitary use of one analysis method gives a biased view on the bonding. Applying a selection of different bond analysis tools can remedy this bias, although which ones to apply should depend on the question to be answered. As shown in this study, the character of the element–oxygen bond is diverse and all of the applied tools contributed to the final conclusion—either as a confirmation of previous conclusions or they revealed features, which have not been detected previously.

## 4. Computational Section

Geometry optimizations were performed for the $H_yX$-OH model compounds (X = Li, Be, B, C, N, O, F, Na, Mg, Al, Si, P, S, Cl) on a CCSD/cc-pVTZ level of theory by using the Gaussian 09 software package[71] (see Figure 1 for the optimized structures). A frequency analysis was carried out to check if the resulting geometries coincide with a minimum on the potential energy surface. All consecutive analyses were performed on these geometries.

The QTAIM analysis was performed with AIM2000.[72] Dgrid-4.6[73] was employed for the analysis of the ELI-D, for the calculation of the Raub–Jansen indices (population %), and to create three-dimensional grids of the ELI-D as well as of the Laplacian. Isosurface plots were generated with Moliso.[74] The valence bond calculations were performed with the XMVB software package[75] on the BOVB/

ChemPubSoc Europe

CHEMISTRY A European Journal Full Paper

6-31G* level of theory. The use of the 6-31G* basis set was necessary, because convergence problems occurred with the higher cc-pVTZ basis set, which was employed for the geometry optimization. The NBO analysis was executed with NBO 6.0.[76] When performing ab initio calculations with CCSD chosen as a method, the NBO 6.0 software package cannot provide interaction energies from the second order perturbation theory. Thus, an additional NBO analysis was performed on the B3LYP/cc-pVTZ level of theory. For the calculation of the parameter *Q*, a script, which may be obtained from https://github.com/martinrahm/X-analysis, was applied to compute $\Delta\bar{\chi}$ and $\Delta(V_{nn}+\omega)$ (this analysis was performed on the B3LYP/cc-pVTZ level of theory). The Ziegler–Rauk energy decomposition analysis was carried out with ADF.[77]

## *Acknowledgements*

S.G. thanks the German Research Foundation (Deutsche Forschungsgemeinschaft, DFG) for funding within the Emmy Noether project GR 4451/1-1. We also thank Jonas Warneke for discussion.

## Conflict of interest

The authors declare no conflict of interest.

**Keywords:** bond theory · element–oxygen bonds · hydroxides · Lewis structures · quantum chemistry

[1] R. P. Feynman, *Phys. Rev.* **1939**, *56*, 340.
[2] C. A. Coulson, *J. Chem. Soc.* **1955**, 2069 – 2084.
[3] S. Alvarez, R. Hoffmann, C. Mealli, *Chem. Eur. J.* **2009**, *15*, 8358 – 8373.
[4] G. V. Gibbs, A. F. Wallace, D. F. Cox, R. Downs, N. L. Ross, K. M. Rosso, *Am. Mineral.* **2009**, *94*, 1085 – 1102.
[5] L. Pauling, *J. Chem. Educ.* **1992**, *69*, 519.
[6] S. Shaik, H. S. Rzepa, R. Hoffmann, *Angew. Chem. Int. Ed.* **2013**, *52*, 3020 – 3033; *Angew. Chem.* **2013**, *125*, 3094 – 3109.
[7] G. Frenking, A. Krapp, *J. Comput. Chem.* **2007**, *28*, 15 – 24.
[8] R. F. W. Bader, *J. Phys. Chem. A* **1998**, *102*, 7314 – 7323.
[9] G. Frenking, S. Shaik, *The Chemical Bond: Fundamental Aspects of Chemical Bonding, Vol. 1*, Wiley, New York, **2014**.
[10] S. Mebs, R. Kalinowski, S. Grabowsky, D. Förster, R. Kickbusch, E. Justus, W. Morgenroth, C. Paulmann, P. Luger, D. Gabel, D. Lentz, *Inorg. Chem.* **2011**, *50*, 90 – 103.
[11] M. Kohout, *Faraday Discuss.* **2007**, *135*, 43 – 54.
[12] P. Macchi, A. Sironi, *Coord. Chem. Rev.* **2003**, *238*, 383 – 412.
[13] C. Gatti, *Z. Kristallogr.* **2005**, *220*, 399 – 457.
[14] F. Weinhold, *J. Comput. Chem.* **2012**, *33*, 2363 – 2379.
[15] P. L. Popelier in *Intermolecular Forces and Clusters I* (Ed.: D. J. Wales), Springer, Heidelberg, **2005**, pp. 1 – 56.
[16] S. Mebs, M. A. Chilleck, *Chem. Phys. Lett.* **2014**, *591*, 1 – 4.
[17] R. F. W. Bader, *J. Phys. Chem. A* **2009**, *113*, 10391 – 10396.
[18] J. Henn, D. Leusser, D. Stalke, *J. Comput. Chem.* **2007**, *28*, 2317 – 2324.
[19] H. Jacobsen, *J. Comput. Chem.* **2009**, *30*, 1093 – 1102.
[20] L. Pauling, *J. Am. Chem. Soc.* **1932**, *54*, 3570 – 3582.
[21] S. Shaik, D. Danovich, W. Wu, P. C. Hiberty, *Nat. Chem.* **2009**, *1*, 443 – 449.
[22] P. L. Ayers, R. J. Boyd, P. Bultinck, M. Caffarel, R. Carbó-Dorca, M. Causá, J. Cioslowski, J. Contreras-Garcia, D. L. Cooper, P. Coppens, C. Gatti, S. Grabowsky, P. Lazzeretti, P. Macchi, Á. M. Pendás, P. L. Popelier, K. Ruedenberg, H. Rzepa, A. Savin, A. Sax, W. E. Schwarz, S. Shahbazian, B. Silvi, M. Solá, V. Tsirelson, *Comput. Theor. Chem.* **2015**, *1053*, 2 – 16.
[23] R. F. W. Bader, *Chem. Rev.* **1991**, *91*, 893 – 928.
[24] R. F. W. Bader, *Atoms in Molecules: A Quantum Theory*, Clarendon Press, Oxford, **1994**.
[25] W.-T. Chan, I. Hamilton, *J. Chem. Phys.* **1998**, *108*, 2473 – 2485.
[26] P. Popelier, *Coord. Chem. Rev.* **2000**, *197*, 169 – 189.
[27] G. V. Gibbs, M. Spackman, D. Jayatilaka, K. M. Rosso, D. F. Cox, *J. Phys. Chem. A* **2006**, *110*, 12259 – 12266.
[28] G. V. Gibbs, R. T. Downs, D. F. Cox, N. L. Ross, C. T. Prewitt, K. M. Rosso, T. Lippmann, A. Kirfel, *Z. Kristallogr.* **2008**, *223*, 01 – 40.
[29] G. V. Gibbs, D. Wang, C. Hin, N. L. Ross, D. F. Cox, T. D. Crawford, M. A. Spackman, R. J. Angel, *J. Chem. Phys.* **2012**, *137*, 164313.
[30] D. Himmel, N. Trapp, I. Krossing, S. Altmannshofer, V. Herz, G. Eickerling, W. Scherer, *Angew. Chem. Int. Ed.* **2008**, *47*, 7798 – 7801; *Angew. Chem.* **2008**, *120*, 7914 – 7917.
[31] R. F. W. Bader, M. E. Stephens, *J. Am. Chem. Soc.* **1975**, *97*, 7391 – 7399.
[32] R. F. W. Bader, C. Gatti, *Chem. Phys. Lett.* **1998**, *287*, 233 – 238.
[33] C. Gatti, F. Cargnoni, L. Bertini, *J. Comput. Chem.* **2003**, *24*, 422 – 436.
[34] C. Gatti, L. Bertini, *Acta Crystallogr. Sect. A* **2004**, *60*, 438 – 449.
[35] M. Kohout, *Int. J. Quantum Chem.* **2004**, *97*, 651 – 658.
[36] S. Berski, Z. Latajka, A. J. Gordon, *J. Comput. Chem.* **2011**, *32*, 1528 – 1540.
[37] B. Silvi, *J. Mol. Struct.* **2002**, *614*, 3 – 10.
[38] R. F. W. Bader, S. Johnson, T.-H. Tang, P. Popelier, *J. Phys. Chem.* **1996**, *100*, 15398 – 15415.
[39] S. Raub, G. Jansen, *Theor. Chem. Acc.* **2001**, *106*, 223 – 232.
[40] F. Weinhold, C. R. Landis, *Chem. Educ. Res. Pract.* **2001**, *2*, 91 – 104.
[41] F. Weinhold, C. R. Landis, *Valency and Bonding: A Natural Bond Orbital Donor – Acceptor Perspective*, Cambridge University Press, New York, **2005**.
[42] E. D. Glendening, F. Weinhold, *J. Comput. Chem.* **1998**, *19*, 593 – 609.
[43] W. Wu, P. Su, S. Shaik, P. C. Hiberty, *Chem. Rev.* **2011**, *111*, 7557 – 7593.
[44] T. Ziegler, A. Rauk, *Inorg. Chem.* **1979**, *18*, 1755 – 1759.
[45] F. M. Bickelhaupt, *J. Comput. Chem.* **1999**, *20*, 114 – 128.
[46] F. M. Bickelhaupt, T. Ziegler, *Organometallics* **1995**, *14*, 2288 – 2296.
[47] M. Rahm, R. Hoffmann, *J. Am. Chem. Soc.* **2016**, *138*, 3731 – 3744.
[48] I. V. Alabugin, S. Bresch, M. Manoharan, *J. Phys. Chem. A* **2014**, *118*, 3663 – 3677.
[49] H. A. Bent, *Chem. Rev.* **1961**, *61*, 275 – 311.
[50] C. Martín-Fernández, M. M. Montero-Campillo, I. Alkorta, M. Yáñez, O. Mó, J. Elguero, *Chem. Eur. J.* **2018**, *24*, 1971 – 1977.
[51] R. J. Gillespie, S. A. Johnson, *Inorg. Chem.* **1997**, *36*, 3031 – 3039.
[52] N. Z. Rao, J. D. Larkin, C. W. Bock, *Struct. Chem.* **2016**, *27*, 1081.
[53] O. Gropen, R. Johansen, *J. Mol. Struct.* **1975**, *25*, 161 – 167.
[54] W. H. Fink, P. P. Power, T. L. Allen, *Inorg. Chem.* **1997**, *36*, 1431 – 1436.
[55] M. A. Petrie, M. M. Olmstead, P. P. Power, *J. Am. Chem. Soc.* **1991**, *113*, 8704 – 8708.
[56] J. McMurry, *Fundamentals of Organic Chemistry*, Cengage Learning, Boston, **2007**.
[57] F. A. Bettelheim, W. H. Brown, M. K. Campbell, S. O. Farrell, O. J. Torres, *Introduction to Organic and Biochemistry*, Cengage Learning, Boston, **2010**.
[58] R. Sanderson, *Polar Covalence*, Elsevier, Amsterdam, **2012**.
[59] T. Kudo, S. Nagase, *J. Am. Chem. Soc.* **1985**, *107*, 2589 – 2595.
[60] G. V. Gibbs, K. Rosso, D. Teter, M. Boisen, M. Bukowinski, *J. Mol. Struct.* **1999**, *485*, 13 – 25.
[61] M. S. Gordon, T. J. Packwood, M. T. Carroll, J. A. Boatz, *J. Phys. Chem.* **1991**, *95*, 4332 – 4337.
[62] G. V. Gibbs, M. B. Boisen, F. C. Hill, O. Tamada, R. T. Downs, *Phys. Chem. Miner.* **1998**, *25*, 574 – 584.
[63] V. G. Tsirelson, O. A. Evdokimova, E. L. Belokoneva, V. S. Urusov, *Phys. Chem. Miner.* **1990**, *17*, 275 – 292.
[64] P. Coppens, *X-ray Charge Densities and Chemical Bonding, Vol. 4*, International Union of Crystallography, Chester, **1997**.
[65] G. V. Gibbs, J. W. Downs, M. B. Boisen, *Rev. Min. Geochem.* **1994**, *29*, 331 – 368.
[66] S. Grabowsky, M. F. Hesse, C. Paulmann, P. Luger, J. Beckmann, *Inorg. Chem.* **2009**, *48*, 4384 – 4393.
[67] F. Weinhold, R. West, *Organometallics* **2011**, *30*, 5815 – 5824.
[68] H. Wallmeier, W. Kutzelnigg, *J. Am. Chem. Soc.* **1979**, *101*, 2804 – 2814.
[69] D. B. Chesnut, *J. Phys. Chem. A* **2003**, *107*, 4307 – 4313.
[70] G. V. Gibbs, N. L. Ross, D. F. Cox, K. M. Rosso, B. B. Iversen, M. A. Spackman, *J. Phys. Chem. A* **2013**, *117*, 1632 – 1640.
[71] Gaussian 09, Revision D, 01, M. J. Frisch, G. W. Trucks, H. B. Schlegel, G. E. Scuseria, M. A. Robb, J. R. Cheeseman, G. Scalmani, V. Barone, G. A.

 

ChemPubSoc Europe

CHEMISTRY
A European Journal
Full Paper

Petersson, H. Nakatsuji, X. Li, M. Caricato, A. V. Marenich, J. Bloino, B. G. Janesko, R. Gomperts, B. Mennucci, H. P. Hratchian, J. V. Ortiz, A. F. Izmaylov, J. L. Sonnenberg, D. Williams-Young, F. Ding, F. Lipparini, F. Egidi, J. Goings, B. Peng, A. Petrone, T. Henderson, D. Ranasinghe, V. G. Zakrzewski, J. Gao, N. Rega, G. Zheng, W. Liang, M. Hada, M. Ehara, K. Toyota, R. Fukuda, J. Hasegawa, M. Ishida, T. Nakajima, Y. Honda, O. Kitao, H. Nakai, T. Vreven, K. Throssell, J. A. Montgomery, Jr., J. E. Peralta, F. Ogliaro, M. J. Bearpark, J. J. Heyd, E. N. Brothers, K. N. Kudin, V. N. Staroverov, T. A. Keith, R. Kobayashi, J. Normand, K. Raghavachari, A. P. Rendell, J. C. Burant, S. S. Iyengar, J. Tomasi, M. Cossi, J. M. Millam, M. Klene, C. Adamo, R. Cammi, J. W. Ochterski, R. L. Martin, K. Morokuma, O. Farkas, J. B. Foresman, D. J. Fox, Gaussian Inc., Wallingford CT, 2009.

[72] F. Biegler-König, J. Schönbohm, D. Bayles, *J. Comput. Chem.* **2001**, *22*, 545 – 559.

[73] M. Kohout, Radebeul, Germany **2011**.

[74] C. B. Hübschle, P. Luger, *J. Appl. Crystallogr.* **2006**, *39*, 901 – 904.

[75] L. Song, Y. Mo, Q. Zhang, W. Wu, *J. Comput. Chem.* **2005**, *26*, 514 – 521.

[76] E. D. Glendening, J. K. Badenhoop, A. E. Reed, J. E. Carpenter, J. A. Bohmann, C. M. Morales, C. R. Landis, F. Weinhold, Theoretical Chemistry Institute, University of Wisconsin, Madison **2013**.

[77] G. te Velde, F. M. Bickelhaupt, E. J. Baerends, C. Fonseca Guerra, S. J. van Gisbergen, J. G. Snijders, T. Ziegler, *J. Comput. Chem.* **2001**, *22*, 931 – 967.

Manuscript received: January 29, 2018
Accepted manuscript online: February 21, 2018
Version of record online: April 4, 2018

# Chapter 6

# Covalency and Ionicity Do Not Oppose Each Other – Relationship Between Si–O Bond Character and Basicity of Siloxanes

In this study, a *complementary bonding analysis* is applied to understand the increase in basicity of the oxygen atom of the siloxane group as the Si–O–Si angle decreases. Covalent and ionic interactions to the Si–O bonds is investigated extensively. The study was published in *Chemistry – A European Journal* in 2018. The following list provides an overview of all aspects, which I performed as part of my doctoral thesis:

- I wrote about 90% of the text with the exception of section 4.4.
- I am responsible for all figures
- I performed and analyzed the *NBO* analysis
- I analyzed the *ELI-D*
- I analyzed the *QTAIM*
- I analyzed the hydrogen-bond energies

ChemPubSoc Europe

DOI: 10.1002/chem.201802197

CHEMISTRY A European Journal Full Paper

Bonding Models

# Covalency and Ionicity Do Not Oppose Each Other—Relationship Between Si–O Bond Character and Basicity of Siloxanes

Malte Fugel,[a] Maxie F. Hesse,[a] Rumpa Pal,[a] Jens Beckmann,[a] Dylan Jayatilaka,[b] Michael J. Turner,[b] Amir Karton,[b] Patrick Bultinck,[c] Graham S. Chandler,[b] and Simon Grabowsky*[a]

*Dedicated to Professor Gerald V. Gibbs on the occasion of his 90th birthday*

**Abstract:** Covalency and ionicity are orthogonal rather than antipodal concepts. We demonstrate for the case of siloxane systems $[R_3Si–(O–SiR_2)_n–O–SiR_3]$ that both covalency and ionicity of the Si–O bonds impact on the basicity of the Si-O-Si linkage. The relationship between the siloxane basicity and the Si–O bond character has been under debate since previous studies have presented conflicting explanations. It has been shown with natural bond orbital methods that increased hyperconjugative interactions of LP(O)→σ*(Si-R) type, that is, increased orbital overlap and hence covalency, are responsible for the low siloxane basicity at large Si-O-Si angles. On the other hand, increased ionicity towards larger Si-O-Si angles has been revealed with real-space bonding indicators. To resolve this ostensible contradiction, we perform a complementary bonding analysis, which combines orbital-space, real-space, and bond-index considerations. We analyze the isolated disiloxane molecule $H_3SiOSiH_3$ with varying Si-O-Si angles, and *n*-membered cyclic siloxane systems $Si_2H_4O(CH_2)_{n-3}$. All methods from quite different realms show that both covalent and ionic interactions increase simultaneously towards larger Si-O-Si angles. In addition, we present highly accurate absolute hydrogen-bond interaction energies of the investigated siloxane molecules with water and silanol as donors. It is found that intermolecular hydrogen bonding is significant at small Si-O-Si angles and weakens as the Si-O-Si angle increases until no stable hydrogen-bond complexes are obtained beyond $\phi_{SiOSi} = 168^\circ$, angles typically displayed by minerals or polymers. The maximum hydrogen-bond interaction energy, which is obtained at an angle of 105°, is 11.05 kJ mol$^{-1}$ for the siloxane–water complex and 18.40 kJ mol$^{-1}$ for the siloxane–silanol complex.

## 1. Introduction

The siloxane linkage Si-O-Si is the most common functional group in the earth's crust, where Si and O are the two most abundant elements.[1,2] Polysiloxanes (silicones $[R_3Si–(O–SiR_2)_n–O–SiR_3]$) are indispensable in a wide variety of products used in industry and our everyday lives, for example, supports for heterogeneous catalysts, cosmetics, and coating materials.[3] The oxygen atom linking the siloxane units exhibits low Lewis basicity, which results in hydrophobic material properties, whereas the analogous oxygen atom in organic ethers ($R_3C$-O-$CR_3$) is considerably more basic.[4] The Si-O-Si angle in most siloxane compounds is between 140° and 180°,[5–7] which is far higher than the tetrahedral angle of about 110° adopted by ethers.[8] In previous studies, it has been shown that decreasing the Si-O-Si angle leads to a significant increase in the basicity of siloxanes.[4,9–12] The Si-O-Si angle shows a high dynamic flexibility stemming from a low Si-O-Si bending potential.[13] Therefore, much smaller Si-O-Si angles can be imposed in strained cyclic siloxane systems. As suggested by the angle–basicity correlation, their basicity will be substantially higher in comparison to the basicity of siloxane units incorporated into chains and consequently they have different material properties.[9,14–18] Hence, the coordination chemistry of cyclic siloxanes has been the focus of much recent research.[19–23]

What is the cause of the low siloxane basicity and why does it depend on the Si-O-Si angle? The answer to this question and also to the nature of the Si–O bond, which are two inherently related aspects, are still under debate. The question has

[a] M. Fugel, Dr. M. F. Hesse, Dr. R. Pal, Prof. Dr. J. Beckmann, Prof. Dr. S. Grabowsky
University of Bremen
Department 2—Chemistry/Biology
Institute of Inorganic Chemistry and Crystallography
Leobener Str. 3 and 7, 28359 Bremen (Germany)
E-mail: simon.grabowsky@uni-bremen.de

[b] Prof. D. Jayatilaka, Dr. M. J. Turner, Prof. A. Karton, Prof. G. S. Chandler
University of Western Australia, School of Molecular Sciences
35 Stirling Highway, Perth WA 6009 (Australia)

[c] Prof. Dr. P. Bultinck
Ghent University, Department of Chemistry
Krijgslaan 281 (S3), 9000 Gent (Belgium)

Supporting information and the ORCID identification number(s) for the author(s) of this article can be found under: https://doi.org/10.1002/chem.201802197. The Supporting Information contains computational details, precise values of all plotted properties, ELI plots of the n-membered ring systems, an NBO analysis of the disiloxane-water complexes, and coordinates of the optimized geometries.

ChemPubSoc Europe

CHEMISTRY
A European Journal
Full Paper

been addressed by West and Gibbs and their respective co-workers from 1960 on.[4,24,25] The case was reopened in 2009 with an experimental electron density study of a siloxanol molecule,[9] which triggered recent theoretical investigations.[11,12,26–30] Still, diverging viewpoints are present and unreconciled:[31] although some authors ascribe a highly ionic character to the Si–O bond,[9,32] others state that it has a "substantial covalent character".[11,12,33] Gibbs et al. regard it as the "elusive bond".[34]

Figure 1 depicts four different Lewis structures for disiloxane $H_3Si\text{-}O\text{-}SiH_3$, which is the simplest member of the siloxane family[35,36] and therefore a popular model system. Historically, it has been argued that the hypervalent Lewis structure (**b**) is

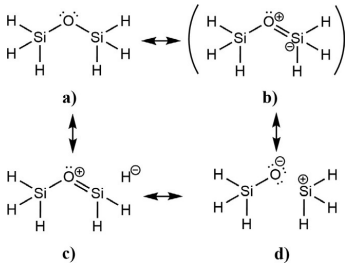


**Figure 1.** Possible resonance structures of disiloxane. a) Classic Lewis formula, b) obsolete hypervalent Lewis formula, c) Lewis formula resulting from hyperconjugative interactions, and d) ionic Lewis formula (equivalent formulas are not depicted).

responsible for the low basicity of siloxane systems, because the electron population of the oxygen lone pairs (LPs) is diminished as a consequence of n(O)→d(Si) back-bonding.[37] However, this Lewis structure is considered obsolete, because d orbitals at the silicon atom only serve as polarization functions.[32,38] Instead, Weinhold and West attribute the low siloxane basicity to n(O)→σ*(Si-R) negative hyperconjugative interactions. Lewis structure **c** is a schematic representation of this bonding model, which may be regarded as a three-center four-electron bond.[11,12] Within this viewpoint, the siloxane basicity decreases at linear Si-O-Si angles owing to the increase in intramolecular hyperconjugative interactions of LP(O)→σ*(Si-R) type, which competes with the hydrogen bonding (which is an intermolecular negative hyperconjugation of LP(O)→σ*(H-O) type).[39] Although this bonding model supports a covalent Si–O bond (high degree of electron sharing) that becomes more covalent with increasing Si-O-Si angle, Lewis formula **d** suggests an ionic Si–O bond, which is supported by studies based on various real-space bonding indicators (quantum theory of atoms in molecules, electron localization functions) carried out by Grabowsky and co-workers and Gillespie and Johnson.[9,10,32] These indicators unambiguously suggest that the Si–O bond is highly ionic and becomes more ionic as the Si-O-Si angle increases. The present contributes towards finally resolving this ostensible contradiction. First, reliable absolute hydrogen-bond interaction energies (computed from the high level, ab initio W1-F12 thermochemical protocol)[40] between the disiloxane molecule and HOX species (X = H and $SiH_3$) were calculated at a range of Si-O-Si angles. In addition, a variety of bonding indicators were applied to examine the bonding situation in the isolated disiloxane molecule with the Si-O-Si angle fixed between values of $\phi_{SiOSi} = 105^\circ$ and $\phi_{SiOSi} = 180^\circ$. The optimized geometry of the isolated disiloxane molecule is depicted in Figure 2a. In cyclic siloxane systems, smaller Si-O-Si angles and therefore a higher basicity may be imposed. Thus, the same analyses are carried out for *n*-membered cyclic siloxanes $(Si_2H_4O(CH_2)_{n-3}$ with $n = 3, 4, 5)$, see Figure 2b–d.

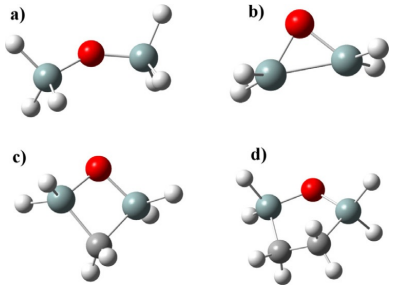


**Figure 2.** The structures regarded in this study with the angles from full geometry optimization: a) disiloxane (155.8°), b) three-membered (80.8°), c) four-membered (96.2°), and d) five-membered (116.1°) siloxane rings.

As chemical bonds are not uniquely defined in quantum mechanics, there are many different bonding descriptors that attempt to extract bonding information from a molecular wavefunction.[41–43] Previous studies have shown that it is crucial to regard a variety of those bonding indicators simultaneously, because the properties obtained from them might complement and/or contradict each other, so that a reliable picture of bonding can only be obtained if all aspects are considered.[44] In this study, real-space indicators, natural bond orbital (NBO) indicators, and a selection of bond indices are applied. The quantum theory of atoms in molecules (QTAIM)[45] and the analysis of the electron localizibility indicator (ELI-D),[46] both of which are applied in this study, may be classified as real-space indicators, because a real-space function, which corresponds to either the electron density (in the QTAIM approach) or the ELI-D, is analyzed topologically. One can look at critical points, where the gradient of the real-space function disappears ($\nabla f(\vec{r}) = 0$), and integrate properties for basins that are defined topologically by the zero-flux surface, where $\nabla f(\vec{r})\cdot\vec{r} = 0$. In QTAIM, these basins may be related to atoms and their integration yields atomic charges (Bader charges). In the ELI-D, basins are related to the shell structure, bonds, and lone pairs and, through integration of the electron density inside them, their electron populations are obtained. The source function is an extension of the QTAIM where the contribution of atomic basins to the electron density at a reference point (mostly a bond critical point) may be revealed.[47] Natural bond orbitals (NBOs) may be associated with features of Lewis structures

ChemPubSoc Europe

CHEMISTRY A European Journal Full Paper

such as bonds and lone pairs.[39,48] There are also non-Lewis NBOs such as valence anti-bonds or extravalent Rydberg-type NBOs, which normally have a low electron population. In this study, it is of particular interest to investigate the interaction between donor (Lewis-type) and acceptor (non-Lewis-type) NBOs in the context of negative hyperconjugation in the siloxane systems (LP(O)→σ*(Si-R)). We will also analyze the results from natural resonance theory (NRT), which attempts to approximate the true density matrix with the sum of weighted localized density matrices.[49–51] This method yields the natural bond order, which is analyzed alongside another four bond indices: The NLMO/NPA bond order (from the NBO analysis),[39] the delocalization index (from the QTAIM analysis),[52] the Hirshfeld-I shared electron density index (SEDI),[53] and the Roby–Gould bond index.[54] In Section 4, the procedure of the complementary bonding analysis is described and a theoretical background is provided for different definitions of atoms in molecules and bond indices.

## 2. Results and Discussion

### 2.1. Hydrogen-bond energies of siloxane···HOX complexes

Figure 3 shows the interaction energies of the two hydrogen-bond complexes plotted against the Si-O-Si angle. The energies were obtained according to Equation (1), where *E*(siloxane) refers to the molecular energy of the fully optimized cyclic siloxane or partially optimized disiloxane molecule (with frozen Si-O-Si angle), *E*(HOX) refers to the energy of a fully optimized water molecule or $HOSiH_3$ silanol molecule, and *E*(siloxane···HOX) refers to the fully optimized cyclic siloxane···$H_2O$ complex or partially optimized disiloxane···HOX complex.

$$E_{int} = E(\text{siloxane}) + E(\text{HOX}) - E(\text{siloxane}\cdots\text{HOX}) \quad (1)$$

The interaction energies of both complexes decrease continuously up to an Si-O-Si angle of $\phi_{SiOSi} = 168^\circ$, above which no convergence for the complex geometries was achieved. Consequently, hydrogen bonding becomes unfeasible for angles higher than $\phi_{SiOSi} = 168^\circ$, which is similar to previous findings.[9,10] In contrast to previous results,[4,9–11,55] the absolute values of the hydrogen-bond energy are reliable and can be used as thermochemical reference properties because of the substantially higher level of theory used. It is also evident that $H_3SiOH$ is a significantly better hydrogen-bond donor than water, because the corresponding interaction energies are higher.[56] The maximum hydrogen-bond interaction energy, which is obtained at an angle of 105°, is 11.05 kJ mol$^{-1}$ for the siloxane–water complex and 18.40 kJ mol$^{-1}$ for the siloxane–silanol complex. At $\phi_{SiOSi} = 156^\circ$, which is the calculated point closest to the fully relaxed geometry of free disiloxane $H_3SiOSiH_3$ (155.8°, see Figure 2), the values drop to 5.75 kJ mol$^{-1}$ for the siloxane–water complex and 11.17 kJ mol$^{-1}$ for the siloxane–silanol complex, before they become insignificant at Si-O-Si angles larger than 168°.

Figure 3 also shows the hydrogen-bond interaction energies of the *n*-membered (*n* = 3, 4, 5) cyclic siloxane···HOH complexes. As expected from the angle–basicity correlation, the interaction energies decrease with increasing Si-O-Si angle: the highest interaction energy is obtained for the three-membered ring (15.80 kJ mol$^{-1}$), an intermediate energy for the four-membered ring (15.01 kJ mol$^{-1}$), whereas the five-membered ring shows the lowest interaction energy (12.78 kJ mol$^{-1}$). Overall, the trend of the cyclic siloxane systems is shifted towards higher interaction energies in relation to the disiloxane···HOH complexes, that is, hydrogen bonding is more favorable in the cyclic systems. The Si-O-Si angle is not the only factor determining the basicity of siloxanes, because the substitution on the silicon also plays an important role, especially if hyperconjugative interactions of LP(O)→σ*(Si-R) type are regarded as the main cause of the low siloxane basicity.

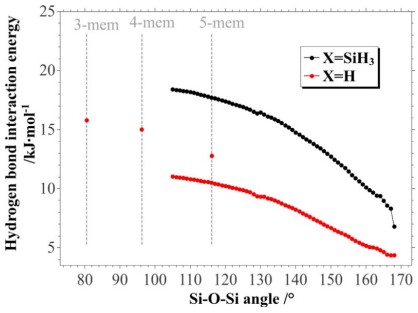


**Figure 3.** The hydrogen-bond energies (zero-point vibrational energy corrected) of disiloxane···HOX (X = H and $SiH_3$) and *n*-membered cyclic siloxane···HOH (*n* = 3, 4, 5) complexes at the W1-F12/A′VTZ level of theory.

### 2.2. Bonding analysis of the siloxane systems

#### 2.2.1. NBO analysis

The NBO analysis enables us to look at the interaction between Lewis-type and non-Lewis-type NBOs, and, thus, it may reveal the negative hyperconjugation of n(O)→σ*(Si-R) type in a straightforward way (Figure 4) as it has previously been done by Weinhold and West for permethylated siloxanes.[11,12] In the following, the NBOs that are involved in this interaction are inspected in detail.

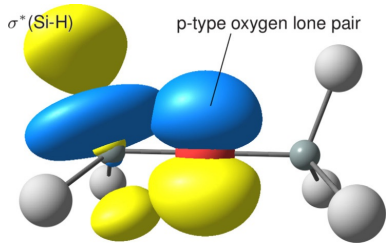


**Figure 4.** Hyperconjugative interaction at the linear Si-O-Si angle of the disiloxane model compound visualized as overlap of an oxygen lone pair NBO (LP(O)) and the Si–H anti-bonding NBO. At the linear geometry, both oxygen LP(O) NBOs are identical, see Figure 5.

ChemPubSoc Europe

CHEMISTRY A European Journal Full Paper

The NBO analysis yields two different types of oxygen lone pair NBOs. One is completely of p character for the whole range of Si-O-Si angles, whereas the hybridization of the other changes from approximately $sp^{1.4}$ to completely p character as the Si-O-Si angle becomes larger (Figure 5, green and blue).

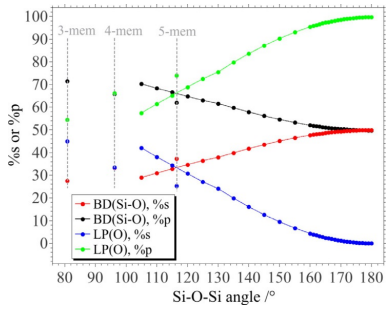


**Figure 5.** The hybridization in terms of percentage s and p character of the $sp^{\lambda}$-type oxygen lone pair NBO ($\lambda = \%p/\%s$) and the oxygen atomic hybrid orbital that is involved in the Si–O bonding NBO BD(Si-O) plotted against the Si-O-Si angle. The second LP(O) is of pure p character and therefore not shown here.

Consequently, the oxygen hybrid orbital that forms the Si–O bond must also undergo rehybridization (Figure 5, black and red). As the oxygen lone pair gains in p character, the p character of the oxygen bonding hybrid orbital decreases. At $\phi_{SiOSi} = 105^{\circ}$, the oxygen bonding hybrid is approximately $sp^{2.4}$, which changes smoothly to sp character as the Si-O-Si angle opens, which is in agreement with Coulson's orthogonality theorem.[57] As the hybridization of the two oxygen lone pairs differs, particularly at bent Si-O-Si angles, their contribution to the negative hyperconjugation is different. This may be revealed by inspecting the oxygen lone pair populations N(LP(O)), previously considered by Weinhold and West,[11] and delocalization energies related to the LP(O)→σ*(Si-H) interactions (Figure 6). If N(LP(O)) is low, it follows that the negative hyperconjugation is strong, as electron density is shifted from the oxygen lone pairs to the σ*(Si-H) NBOs.

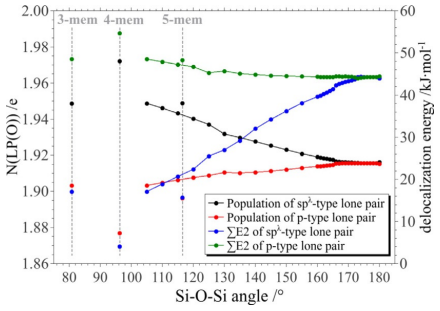


**Figure 6.** The oxygen lone pair populations, N(LP(O)), and the summed delocalization energies, Σ*E*2, which can be attributed to the LP(O)→σ*(Si-H) interactions of the siloxane systems plotted against the Si-O-Si angle.

Figure 6 shows that N(LP(O)) of the $sp^{\lambda}$-type oxygen lone pair decreases with increasing Si-O-Si angle, that is, its involvement in the negative hyperconjugation becomes more significant as it gains in p character. For the p-type lone pair, the opposite trend is observed: Its electron population increases slightly. This is in agreement with the LP(O) delocalization energies. For the $sp^{\lambda}$-type lone pair, the delocalization energy increases, which causes a higher stabilization of the molecule resulting from this interaction, whereas the delocalization energy of the p-type oxygen lone pair decreases slightly. At nearly linear Si-O-Si angles, the two lone pairs become indistinguishable in terms of their hybridization, their electron populations, and delocalization energies. A natural bond orbital analysis of the disiloxane–water complexes shows that the hydrogen bonding is related to the hyperconjugative interaction involving the $sp^{\lambda}$-type oxygen lone pair (donor orbital) and one antibonding O–H orbital of $H_2O$ (acceptor orbital). Consequently, the rehybridization of the $sp^{\lambda}$-type lone pair to completely p character is responsible for the weakening of hydrogen bonding at higher Si-O-Si angles. In the Supporting Information, the interacting orbitals are depicted alongside the respective *E*2 values, which are a measure of the strength of the interaction.

The results for the *n*-membered cyclic siloxane systems support the conclusion of the previous paragraph. For these ring systems, Figure 5 shows that the $sp^{\lambda}$-type oxygen lone pair has a higher p character and the oxygen bonding hybrids have, in turn, higher s character than suggested by the angular trend in the disiloxane molecule. For the disiloxane molecule, an increase in p character is indicative of stronger intramolecular hyperconjugation and thus lower basicity. However, in the ring systems, the jump in p character compared with the open siloxane molecule is associated with a decrease in hyperconjugation as evident from the increased $sp^{\lambda}$ electron populations of the ring systems shown in Figure 6 and the lower delocalization energies from the LP(O)→σ*(Si-R) delocalization, also shown in Figure 6. This decrease in hyperconjugation correlated with the increased basicity shown by the higher hydrogen-bond energies of the ring system, illustrated in Figure 3, reinforces the conclusion that from the point of view of NBO analysis LP(O)→σ*(Si-R) negative hyperconjugation is the driver of the basicity. Although there is a σ*(Si-C) acceptor bond in the four- and five-membered rings, there is a σ*(Si-Si) acceptor bond in the three-membered ring. Therefore, one should not expect the three-membered ring values to align with the four- and five-membered rings.

The NBO analysis showed that there is an overall increase in hyperconjugative interactions and hence covalent contributions with increasing angle. This is in line with decreased basicity. However, the very same NBO analysis also reveals a different trend, namely an increase in ionicity with increasing Si-O-Si angle (Figure 7). Weinhold and co-workers defined the bond ionicity in terms of the polarization coefficients of the silicon and oxygen hybrid atomic orbitals, which form the Si–O NBO and already applied it to the disiloxane molecules at varying Si-O-Si angle,[11,39] shown in Figure 7 for our calculations.

ChemPubSoc Europe
CHEMISTRY A European Journal Full Paper

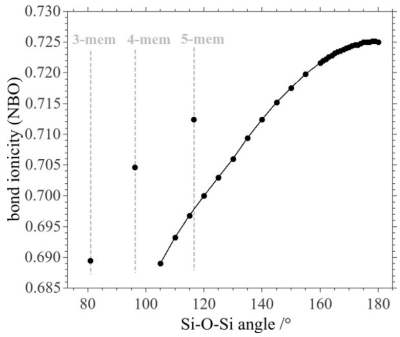


**Figure 7.** NBO bond ionicity parameter.

### 2.2.2. Bond critical point properties

The electron density at the Si–O bond critical points ($\rho_{bcp}$(Si-O)) and the Si–O bond length $r$(Si-O) are plotted against the Si-O-Si angle in Figure 8.

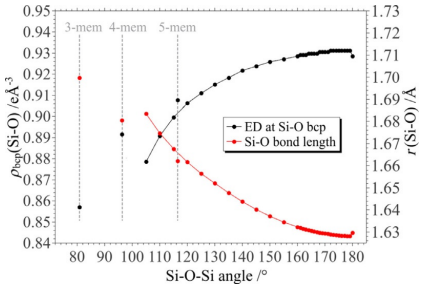


**Figure 8.** The electron density at the Si–O bond critical point, $\rho_{bcp}$(Si-O), and the silicon–oxygen bond length, $r$(Si-O), of the disiloxane and $n$-membered cyclic siloxane systems plotted against the Si-O-Si angle.

The increase in $\rho_{bcp}$(Si-O) and the simultaneous decrease in $r$(Si-O) in the disiloxane molecules may be related to an increase in the partial Si–O double bond character, as shown in Lewis structure **c** in Figure 1, which is a representation of the negative hyperconjugative interactions. For the ring system, the same trend is observed for $\rho_{bcp}$(Si-O), although shifted to higher values, which implies an even higher partial Si–O double bond character, and, thus, overall stronger hyperconjugative interactions. At first glance, this is contradictory to the higher hydrogen-bond energies of the ring systems because stronger hyperconjugative interactions should lead to a lower siloxane basicity. However, in the preceding section, it was shown that the low siloxane basicity is caused by intramolecular hyperconjugation that the $sp^2$-type oxygen lone pair is involved in, but when regarding $\rho_{bcp}$(Si-O) we see the effect from both the $sp^3$- and p-type lone pairs.

Figure 9 shows the Laplacian (the second derivative of the electron density) at the Si–O bond critical point $\nabla^2\rho_{bcp}$(Si-O) plotted against the Si-O-Si angle. The Laplacian is highly positive for all Si-O-Si angles, which is an indication for a highly polarized Si–O bond.[44,45] The increase in $\nabla^2\rho_{bcp}$(Si-O) indicates that the Si–O bond becomes even more polarized as the Si-O-Si angle becomes more linear. Interestingly, two properties at the bond critical point of the electron density give two opposing characterizations of the Si–O bond. Although $\rho_{bcp}$(Si-O) suggests an increase in covalency, $\nabla^2\rho_{bcp}$(Si-O) implies an increase in ionicity. In the Supporting Information, we show the total energy density at the Si–O bond critical point plotted against the Si-O-Si angle. This plot also implies that the Si–O bond becomes increasingly ionic.

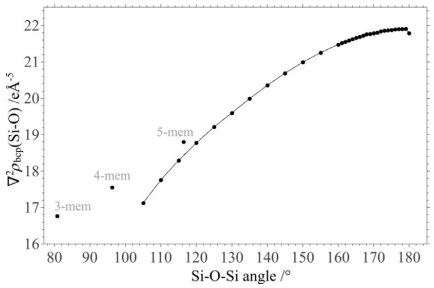


**Figure 9.** The Laplacian of the electron density at the Si–O bond critical point, $\nabla^2\rho_{bcp}$(Si-O), of the disiloxane and $n$-membered cyclic siloxane systems plotted against the Si-O-Si angle.

### 2.2.3. Analysis of the source function

The source function is analyzed with respect to the contribution of the QTAIM oxygen basin to the electron density at the Si–H bond critical points. This is of particular interest because this contribution may be related to the hyperconjugative interactions of LP(O)→σ*(Si-H) type. Figure 10 depicts the sum of the percentage contributions of the oxygen basin to the electron density at the bond critical points of all Si–H bonds of a $SiH_3$ group plotted against the Si-O-Si angle.

The contribution of the oxygen basin to the electron density at the Si–H bond critical points is exceptionally high for the whole range of Si-O-Si angles,[47] which is a measure of negative hyperconjugation. The remaining contributions come almost exclusively from the neighboring silicon and hydrogen atoms. After no clear trend is recognizable for the first three data points, the contribution of the oxygen atom increases steadily with increase in the Si-O-Si angle, which correlates with an increase in negative hyperconjugation.

### 2.2.4. Analysis of the ELI-D

The electron localizibility indicator ELI-D is a measure of electron localization—electrons are less perturbed in regions

ChemPubSoc Europe

CHEMISTRY A European Journal Full Paper

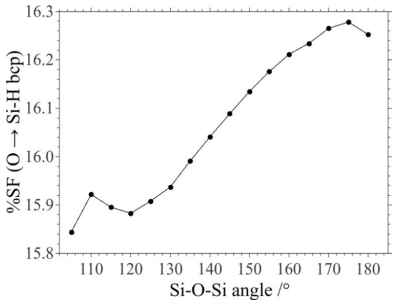


**Figure 10.** Source function given as the sum of the percentage contributions of the oxygen basin to the electron density at the bond critical points of all Si–H bonds of a $SiH_3$ group.

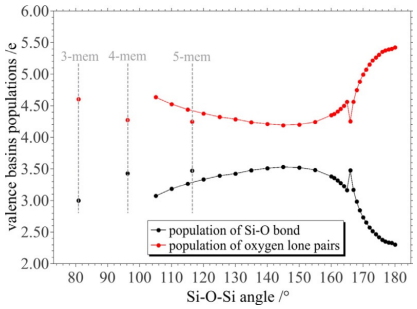


**Figure 11.** The ELI-D oxygen lone pair and Si–O bond populations of the disiloxane and *n*-membered cyclic siloxane systems plotted against the Si-O-Si angle.

where values of the ELI-D are high. The analysis yields different types of basins that are defined by the topology of the ELI-D: there are core basins, monosynaptic basins (in contact with one core basin), which may be related to lone pairs, and disynaptic basins (in contact with two core basins), which may be related to bonds. These ELI-D basins are different to those from QTAIM associated with the electron density, and they also have no direct relation to the bonds and lone pairs from the NBO analysis, which correspond to the localized orbital picture rather than to the real-space picture. This is because of the completely different techniques used for dividing space.

Figure 11 shows the electron populations of the valence basins, that is, the oxygen lone pair and Si–O bond basins, plotted against the Si-O-Si angle. The total number of electrons inside the valence basins of the disiloxane molecules is approximately the same for all Si-O-Si angles. Starting from $\phi_{SiOSi}=105^\circ$ up to $\phi_{SiOSi}=145^\circ$, the lone pair population decreases while the bond population increases. The initial trend is then reversed until a sudden jump appears at $\phi_{SiOSi}=166^\circ$, which is in close proximity to the angle after which hydrogen bonding becomes unfeasible. After that jump, the lone pair population increases steeply. This is accompanied by a steep decrease in the Si–O bond population. The total number of electrons inside the oxygen lone pairs is lowest in the region where hydrogen bonding is feasible. This shows that the total charge around the oxygen atom is not decisive for its basicity, but that this charge must both be concentrated and localized in a suitable way to allow the oxygen atom to act as a base.

The isosurfaces of the ELI-D may be visually analyzed to understand the way charge is localized around the oxygen atom. In Figure 12, three isosurfaces at different Si-O-Si angles are depicted. At $\phi_{SiOSi}=105^\circ$ (Figure 12a), there is a cashew-shaped lone pair domain located at the oxygen atom. The shape remains that way throughout all the angles that allow stable hydrogen-bond complexes. Here, electrons are localized in a region where a proton would approach in an electrophilic attack. Starting from $\phi_{SiOSi}=166^\circ$, which is the angle where the ELI-D valence population shows a jump and close to the angle where hydrogen bonding ceases, an additional attractor located underneath the oxygen atom opposite to the cashew-like lone pair appears (Figure 12b). The localization of electrons at this position may be related to the $sp^2$-type lone pair NBO, which is almost of complete p character at this angle (see Figure 5). The s character of this lone pair NBO is higher at lower Si-O-Si angles, which explains why the appearance of this attractor occurs only at high angles when the p character far outweighs the s character. As the angle opens even further, the three oxygen lone pair domains become increasingly indistinguishable until they are identical at $\phi_{SiOSi}=180^\circ$. Figure 12c shows that the three equivalent lone pair domains form a ring

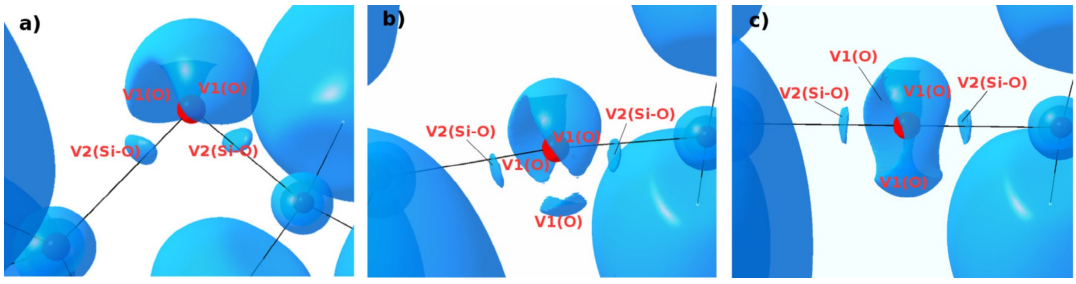


**Figure 12.** ELI-D isosurfaces showing the oxygen lone pair (V1(O)) and Si–O bond (V2(Si-O)) localization domains of the disiloxane molecules at Si-O-Si angles of a) $\phi_{SiOSi}=105^\circ$ ($ELI\text{-}D_{iso}=1.53$), b) $\phi_{SiOSi}=170^\circ$ ($ELI\text{-}D_{iso}=1.52$), and c) $\phi_{SiOSi}=180^\circ$ ($ELI\text{-}D_{iso}=1.52$).

ChemPubSoc Europe
CHEMISTRY A European Journal Full Paper

at this angle. The formation of a ring at angles $\phi_{SiOSi} \geq 168^{\circ}$ and a high electron population of $N \gg 4$ is characteristic for an oxygen atom that is involved in an ionic bond,[44] here corresponding to resonance form **d** in Figure 1.

For the cyclic siloxane systems, the lone pair populations are lower and Si–O bond populations higher compared with the trend of the disiloxane molecules. Here, we cannot make the same argument we made in the NBO analysis: a lower ELI-D lone pair basin population does not result in a lower basicity.

#### 2.2.5. Atomic charges

As there are many different approaches to define an atom inside a molecule as discussed in the Theoretical Background part, there is no unambiguous definition for an atomic charge. The QTAIM and NBO analysis yield the Bader and NPA charges, respectively. Another approach to obtain atomic charges are the Hirshfeld-I charges, which are retrieved by iteratively applying Hirshfeld's stockholder partitioning scheme.[58] It is always beneficial to regard a variety of different approaches, because the magnitude of these charges is conflicting, for example, the Bader charges are known to suggest a substantially more ionic picture compared with the other charges.[59]

Figure 13 shows the Bader, NPA, and Hirshfeld-I charges plotted against the Si-O-Si angle. The Si charges of the *n*-membered rings are not shown here as the Si atoms have different bonding partners. Despite the different methods used in obtaining these charges, they show the same trend as the angle increases. The charge of the silicon atom becomes more positive while the charge of the oxygen becomes more negative.

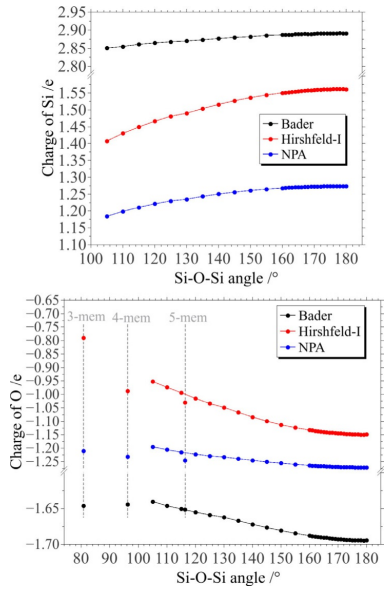


**Figure 13.** The Bader, Hirshfeld-I, and NPA charges of the silicon (top) and oxygen (bottom) atoms plotted against the Si-O-Si angle.

Thus, the charge separation between the silicon and oxygen atom increases—the Si–O bond becomes more ionic, which is confirmed by the Laplacian values at the Si–O bond critical point. This would suggest that Lewis formula **d** in Figure 1 becomes more significant at increasing Si-O-Si angle, which, at first glance, is contradictory to an increase in hyperconjugative interactions. If the increase in ionicity is related to increased electronegativity of the oxygen atom, then electrons should also be withdrawn from the hydrogen atoms of the $SiH_3$ group. But in contrast, Figure 14 shows that the total charge of the hydrogens becomes more negative with increasing Si-O-Si angle. This increase can be related to the increase in hyperconjugative interactions because they result in a shift in electron density into the σ*(Si-H) bonds, thus increasing the charge of the hydrogen atoms and corresponding to the resonance form **c** in Figure 1.

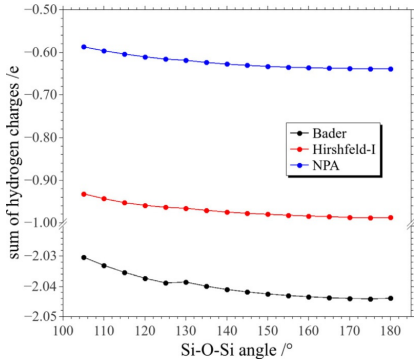


**Figure 14.** The sum of the Bader, Hirshfeld-I, and NPA charges of the three hydrogen atoms of one $SiH_3$ group plotted against the Si-O-Si angle.

#### 2.2.6. Bond indices

In the following, five different types of bond indices—the Hirshfeld-I SEDI, the Roby–Gould bond index, Bader's delocalization index (DI), the NLMO/NPA bond order, and the natural bond order based on a natural resonance theory (NRT) analysis—will be analyzed. Figure 15 shows these bond indices plotted against the Si-O-Si bond angle. All values of the Hirshfeld-I SEDI are above a value of one, whereas the DI, which is also a SEDI, is substantially lower than one. The difference between the Hirshfeld-I SEDI and the DI is the definition of the atom applied in each of these approaches. The charges of the respective atoms (the Hirshfeld-I and Bader charges) have been discussed in the preceding section, where the Bader charges have been found to imply a substantial charge separation between the silicon and oxygen atoms, that is, highly ionic Si–O bonds. The DI shows substantially lower values compared with the Hirshfeld-I SEDI, which directly follows from the different nature of Bader and Hirshfeld-I charges. A highly positive Bader charge of the silicon atom comes with a small atomic volume, and, thus, the number of electron pairs exchanged be-

ChemPubSoc Europe

CHEMISTRY
A European Journal
Full Paper

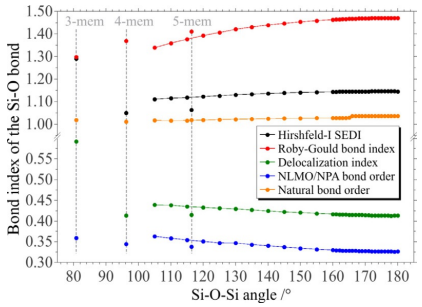


**Figure 15.** Five different bond indices (Hirshfeld-I SEDI, Roby–Gould bond index, delocalization index, NLMO/NPA bond order, and natural bond order) of the disiloxane and *n*-membered cyclic siloxane systems plotted against the Si-O-Si angle.

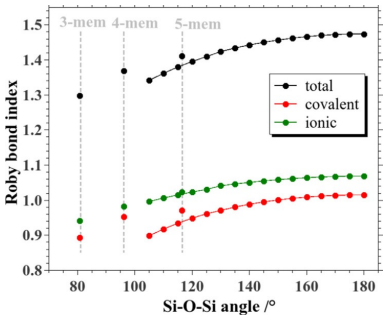


**Figure 16.** Covalent, ionic, and total Roby–Gould bond indices.

tween the silicon and oxygen atom is lower, because they are contained in the larger oxygen atom. The Hirshfeld-I silicon atom is larger and the oxygen atom is smaller compared with the corresponding Bader atoms. Consequently, more electron pairs are exchanged between these atoms, which results in larger bond indices.

The NLMO/NPA bond order is defined as the overlap of natural localized molecular orbitals (NLMO) and atomic populations obtained from the natural population analysis (NPA); therefore, it is derived in a substantially different way compared with the other bond indices. Its values are even lower than the DI, and, thus, suggest an even more ionic Si–O bond. On the other hand, the natural bond order is similar to the Hirshfeld-I SEDI, whereas the Roby–Gould index is higher.

The Roby–Gould bond index, Hirshfeld-I SEDI, and the natural bond order increase with increasing Si-O-Si angle, suggesting the partial Si–O double bond character gains in significance. The DI, on the other hand, decreases with increasing Si-O-Si angle, which may be attributed to the fact that the Si–O bond becomes even more ionic with increasing Si-O-Si angle, thus reducing the number of exchanged electron pairs. Just as the DI, the NLMO/NPA bond order decreases with increasing Si-O-Si angle. It is interesting that out of the five bond orders considered in this study, three support an increase in partial Si–O double bond character with increasing Si-O-Si angle, whereas the other two support a highly ionic Si–O bond description. Consequently, the definition of the atom greatly influences the picture of the bonding situation provided to us and makes meaningful chemical interpretation very difficult.

The Roby–Gould bond index has a total, a covalent, and an ionic part as derived in the Theoretical Background part. This allows comparison of the behavior of covalent and ionic contributions to the bonding within the same definition of an atom, avoiding the problems discussed in the previous paragraph. Figure 16 clearly shows that ionic and covalent contributions have about the same importance for the overall description of the Si–O bond character, and that both increase simultaneously with increasing angle. Hence, covalency and ionicity support and complement each other in increasing the bond order, and consequently bond strength, of the Si–O bond.

The cyclic siloxane systems agree well with the trend of the Roby–Gould bond index. The Hirshfeld-I SEDI, however, implies that the nature of the Si–O bond is different in the ring systems (Figure 15). For the three-membered ring, the Hirshfeld-I SEDI is substantially higher, whereas it is slightly lower for the four- and five-membered rings, which may be related to the weaker intramolecular hyperconjugative interactions. The trend of the NLMO/NPA bond order shifts to lower values than suggested by the disiloxane molecules. Although this shift is also true for the five- and four-membered rings in the delocalization index, the three-membered ring shows an anomalously high delocalization index. These shifts may be attributed to the higher ionic nature of the Si–O bond in the cyclic siloxane systems. This does, however, not apply to the delocalization index of the three-membered ring.

## 3. Conclusion

In contrast to all previous studies on siloxanes, a wide range of bonding indicators has been used in the present study in the sense of a complementary bonding analysis to understand the nature of the Si–O bond and the reason for the strong dependence of the siloxane basicity on the Si-O-Si angle. Various bond indicators present different pictures of bonding and relating these to each other is not simple. Especially, when significantly different definitions of an atom are used, charges and bond indices differ so significantly in terms of absolute values and in terms of trends in dependence of the Si-O-Si angle that chemical interpretation becomes a gamble. If one relies on a single one of these bonding descriptors or methods for chemical interpretation, as we and others have done in the past in the field of siloxanes, incomplete and insufficient pictures arise.

We have found in this study that in four different methods, a simultaneous covalent and ionic description of the Si–O bond and a simultaneous increase in both covalency and ionicity with increasing Si-O-Si angle are present. As this is inherent to the same method, all inconsistencies of definitions discussed in the previous paragraph are irrelevant. i) In NBO, increased negative hyperconjugation with increasing Si-O-Si angle is accompanied by an increase in the bond ionicity,

ChemPubSoc Europe

CHEMISTRY A European Journal Full Paper

which is defined through the same weighting coefficients that determine the NBOs, which are engaged in the negative hyperconjugative interactions. ii) In QTAIM, electron density accumulates in the Si–O bond with increasing Si-O-Si angle, and the Laplacian indicates increased closed-shell interactions simultaneously. iii) The Si–O charge separation increases with increasing Si-O-Si angle revealing an increase in ionicity, whereas the hydrogen atoms become more negative, which represents increased negative hyperconjugation. These trends are the same in QTAIM, NPA, and Hirshfeld-I charges. iv) The total Roby–Gould bond index is made up of a covalent and an ionic bond index, both of which increase simultaneously with increasing Si-O-Si angle. Their absolute values are also very similar, indicating that ionicity and covalency have about the same importance for the Si–O bond. All of the findings summarized in this paragraph clearly show that covalency and ionicity do not oppose each other, but are two complementing properties of the Si–O bond.

This study is an example of the fact that a single Lewis formula can never fully reflect the bonding situation in a molecule especially when lone pair or bond delocalizations are of great significance. For the siloxane molecules, Lewis formula **c** in Figure 1 indicates negative hyperconjugation, that is, covalency, whereas Lewis formula **d** represents an ionic Si–O bond. Both resonance forms have about the same importance for the bonding situation, and both gain in importance simultaneously when the Si-O-Si angle increases.

We plan to synthesize a systematic array of molecular compounds with different Si-O-Si angles to study the tuning of material properties based on the findings of this study. Design of materials with hydrophilic properties might be possible if a desired Si-O-Si angle can be manifested in a template ring structure. This could have implications for heterogeneous catalysis where siloxanes are used as supports. Certainly, further insights into the properties of minerals can be gained this way as Gibbs has argued for many years that "molecules [are] models for bonding in silicates".[25]

We believe that also in chemical systems other than the siloxanes, more insights into bonding situations can be obtained when the textbook notion of covalency and ionicity as antipodes is dropped.

## 4. Methodology and Theoretical Background

### 4.1. Geometry optimizations

Geometry optimizations of the disiloxane molecule and the *n*-membered cyclic siloxane systems $Si_2H_4O(CH_2)_{n-3}$ were carried out at the B3LYP/A′VTZ level of theory,[60,61] by using the Gaussian 09 program suite.[62] The resulting structures were confirmed to be equilibrium structures by harmonic vibrational calculations (i.e., they have all real frequencies). In addition, a relaxed potential energy surface (PES) scan was carried out for the disiloxane molecule between Si-O-Si angles of $\phi_{SiOSi}=105^\circ$ and 160° in 5° intervals and $\phi_{SiOSi}=160^\circ$ and 180° in 1° intervals.

### 4.2. Bonding analysis

NBO analyses were carried out with NBO6.0.[63] The program suite AIMAll was applied for the QTAIM analysis and the calculation of the source function.[64] The computation of the ELI-D and its topological analysis were performed with DGrid-4.6.[65] Related ELI-D isosurfaces were plotted with the program Moliso.[66] The Roby–Gould bond index was calculated by using the Tonto software package.[67] Hirshfeld-I charges and SEDIs were calculated with self-written software.

### 4.3. Hydrogen-bond interaction energies

To obtain reliable absolute hydrogen-bond interaction energies between the siloxane and HOX species (X = H and $SiH_3$), calculations were carried out by using the high-level ab-initio W1-F12 thermochemical protocol with the Molpro 2012.1 program suite.[68] The W1-F12 thermochemical protocol[69] and its earlier version W1[40] are widely used for the calculation of thermochemical and kinetic properties.[70,71]

The calculations were performed with the B3LYP/A′VTZ geometries of the fully optimized cyclic siloxanes, water, and silanol molecules as well as of the partially optimized disiloxane molecules and their HOX (X = H or $SiH_3$) complexes from PES scans with Si-O-Si angles constrained to $\phi_{SiOSi}=105^\circ$ to 180° in 1° intervals. Energy differences according to Equation (1) at the W1-F12 level were calculated with and without zero-point vibrational energy (ZPVE) correction.

### 4.4. Theoretical background

One of the main problems in analyzing chemical bonding is that many of the ideas and concepts that are so central to chemistry, for instance, identifying atoms in molecules or chemical bonds, do not emanate so simply from quantum mechanics.[72] In fact, quantum mechanics does not give a unique recipe to distinguish atoms in molecules[73] or chemical bonding and the best one can do, if one values these concepts, is to propose models or algorithms that rely on sane arguments such as variational principles or projection operators to extract atoms and bonds from the wavefunction. Still, this will not lead to a unique description. As one of the main purposes of the present study is the comparison of methods, we now introduce these methods to the level of detail required here. The NBO method is well known and has been described in detail elsewhere,[39,48] therefore, it is not discussed further.

A key role will be played by the density operator and matrix. Denoting the wavefunction as $\Psi$, the density operator is given by Equation (2):

$$\hat{D} = |\Psi\rangle\langle\Psi| \quad (2)$$

Stepwise integration over all electronic coordinates except one or two electronic position coordinates, leads to the first- and second-order reduced density operators, which may be expressed in the basis of the natural orbitals (NOs) as Equation (3)

ChemPubSoc Europe

CHEMISTRY A European Journal Full Paper

$$\hat{\gamma} = \sum_i |i\rangle \eta_i \langle i| \tag{3}$$

and Equation (4)

$$\hat{\Gamma} = \sum_{ijkl} |ij\rangle \Gamma_{ijkl} \langle kl| \tag{4}$$

where $\eta_i$ are the natural orbital occupation numbers, and $\Gamma_{ijkl}$ are the second-order density matrices expressed in terms of the NOs. At the Hartree–Fock level of theory, $\eta_i$ equal 2 or 0 for a restricted closed-shell calculation. In density functional theory (DFT), no density matrix is defined, although we pragmatically use the same expressions as at the Hartree–Fock level, but with Kohn–Sham orbitals, as experience has shown that this also gives chemically useful results.[74] At both these levels of theory, the second-order reduced density matrix can be easily expressed in terms of the first-order reduced density matrix (1RDM), which will help deriving bond indices. Atoms in molecules (AIMs) can be obtained in many different ways from Equation (3). Most generally, for the atomic electronic population on atom A, denoted $N_A$, one takes the expectation value of an operator $\hat{\mathrm{P}}_\mathrm{A}$

$$N_\mathrm{A} = \langle \hat{\mathrm{P}}_\mathrm{A} \rangle = Tr\left(\hat{\mathrm{P}}_\mathrm{A} \hat{\gamma}\right). \tag{5}$$

One can think of this equation loosely as "projecting" out an atom A from a density operator. The reason why many different AIMs exist is that different authors introduced different forms of $\hat{\mathrm{P}}_\mathrm{A}$, for example,

1. Mulliken:[75,76]

$$\hat{\mathrm{P}}_\mathrm{A} = \sum_{\sigma \epsilon \mathrm{A}} \sum_{\lambda} |\sigma\rangle (\mathbf{S}^{-1})_{\sigma\lambda} \langle\lambda| \tag{6}$$

where $\mathbf{S}^{-1}$ is the inverse overlap matrix and Greek letters signify non-orthogonal (often Gaussian) basis functions.

2. Roby:[77]

$$\hat{\mathrm{P}}_\mathrm{A} = \sum_{i_\mathrm{A} \epsilon \mathrm{A}} |i_\mathrm{A}\rangle \langle i_\mathrm{A}|. \tag{7}$$

where the functions $|i_\mathrm{A}\rangle$ are occupied natural orbitals for atom A, that is, those eigenstates obtained from a spherically averaged unrestricted Hartree–Fock or DFT calculation on atom A with eigenvalue $\eta_\mathrm{i}^\mathrm{A}$ greater than 0.05.

Note the difference in these two Hilbert space operators for the atom A. For the Mulliken case, one summation is over all non-orthogonal basis functions centered on a specific atom and the second summation over all basis functions. The Mulliken formulation is not applicable for basis functions that do not have a natural center such as plane wave basis functions. Also, the summation over $\lambda$ is over the entire basis set, which may become arbitrarily large. The Roby operator on the other hand always makes use of a limited number of orthogonal atomic functions. Both the Mulliken operator [Eq. (6)] and the Roby projection operator [Eq. (7)] are projection operators in the mathematical sense, that is, that $\hat{P}_A$ is idempotent, $\hat{P}_A^2 = \hat{P}_A$. Note, however, that whereas the sum of the atomic populations $N_\mathrm{A}$ equals the number of electrons $N$ in the Mulliken case, this electron population conservation does not hold true of the Roby populations.

Besides these Hilbert-space methods, one also has real-space methods the population operators of which can be written in the form

$$\hat{\mathrm{P}}_\mathrm{A} = \int \mathrm{d}\mathbf{r} |\mathbf{r}\rangle \omega_\mathrm{A}(\mathbf{r}) \langle \mathbf{r}| \tag{8}$$

Substituting the population operator from Equation (8) into Equation (5) gives

$$N_\mathrm{A} = \sum_i \eta_i \int \mathrm{d}\mathbf{r} \langle i|\mathbf{r}\rangle \omega_\mathrm{A}(\mathbf{r}) \langle \mathbf{r}|i\rangle \tag{9}$$

where, for example, $\langle i|\mathbf{r}\rangle = \psi_i^*(\mathbf{r})$. Different methods that work directly in coordinate space exist. In the present paper, both the QTAIM method[45,78] is used where $\omega_\mathrm{A}(\mathbf{r})$ is binary, that is, either 1 or 0, and the Hirshfeld-I method[58,79,80] that uses a model of overlapping AIM and hence has $0 \leq \omega_\mathrm{A}(\mathbf{r}) \leq 1$. In both cases, real space is exhaustively partitioned, that is, $\forall \mathbf{r} : \sum_\mathrm{A} \omega_\mathrm{A}(\mathbf{r}) = 1$ and electron population is conserved.

Turning to bonding indices, we use two types of methods in the present study. These can be distinguished by the type of density matrices used. The first type relies on the 1RDM only, and uses the Roby populations.[54,77] First, a two-atom (mathematical) projection operator for atoms A and B is introduced as

$$\hat{\mathrm{P}}_\mathrm{AB} = \sum_{k \epsilon (\mathrm{A,B})} \sum_{l \epsilon (\mathrm{A,B})} |k\rangle (\mathbf{S}_\mathrm{AB}^{-1})_{kl} \langle l| \tag{10}$$

where $\mathbf{S}_\mathrm{AB}^{-1}$ is the inverse of the overlap matrix formed from the occupied natural orbitals on atoms A and B. Then, the Roby–Gould bond index is defined as[54]

$$\tau_\mathrm{AB} = \sqrt{c_\mathrm{AB}^2 + i_\mathrm{AB}^2} \tag{11}$$

where

$$c_\mathrm{AB}^2 = \left\{ \frac{\hat{\mathrm{P}}_\mathrm{A} + \hat{\mathrm{P}}_\mathrm{B} - \hat{\mathrm{P}}_\mathrm{AB}}{2\left|\hat{\mathrm{P}}_\mathrm{A} + \hat{\mathrm{P}}_\mathrm{B} - \hat{\mathrm{P}}_\mathrm{AB}\right|} \right\} \tag{12}$$

and

$$i_\mathrm{AB}^2 = \left\{ \frac{\hat{\mathrm{P}}_\mathrm{A} - \hat{\mathrm{P}}_\mathrm{B}}{2\left|\hat{\mathrm{P}}_\mathrm{A} - \hat{\mathrm{P}}_\mathrm{B}\right|} \right\} \tag{13}$$

are the covalent and ionic bond indices. The Roby–Gould bond index is best thought of as a two-dimensional quantity. The above equations involve functions of operators; such operator functions are fully characterized as having the same ei-

ChemPubSoc Europe

CHEMISTRY A European Journal Full Paper

genstates as the original operator, except with eigenvalues, which are the same function of the original operators' eigenvalues. In the present case, zero and unit eigenvalues are ignored in all equations as they would lead to infinities in one or the other denominator. As explained more fully elsewhere,[54,81] these formulae arise naturally from the algebra of projection operators, and they generalize the notion of a chemical bond order as "the number of electrons in bonding orbitals minus the number of electrons in antibonding orbitals, divided by two". In practice, for simple organic or ionic compounds, they produce numerical results that are very compatible with those obtained by drawing standard Lewis structures.[54,81]

In contrast, Wiberg, Giambiagi, Mayer, Bader, and co-workers[52,82–85] introduced several indices that can all be gathered under the same umbrella[86] in the sense that they are integrals over diatomic condensed exchange-correlation density matrices (XCD). The XCD is defined as

$$\rho^{\mathrm{xcd}}(\mathbf{r}_1,\mathbf{r}_1';\mathbf{r}_2,\mathbf{r}_2') = \rho(\mathbf{r}_1,\mathbf{r}_1')\rho(\mathbf{r}_2,\mathbf{r}_2') - 2\sum_{ijkl}\Gamma_{ijkl}\psi_i^*(\mathbf{r}_1)\psi_k(\mathbf{r}_1')\psi_j^*(\mathbf{r}_2)\psi_l(\mathbf{r}_2') \quad (14)$$

All these bond indices can be called shared electron density indices (SEDI)[53] and essentially come down to different ways of projecting out the two atoms. In the present work, only position-space operators are considered, notably the QTAIM operator and the Hirshfeld-I operator. At the closed-shell single determinant level of theory (Hartree–Fock and pragmatically also Kohn–Sham DFT), the bond indices are given as:

$$\delta_{AB} = 4\sum_{i,j}^{N/2}\langle i|\omega_A|j\rangle\langle j|\omega_B|i\rangle \quad (15)$$

where the QTAIM and Hirshfeld-I data differ owing to the difference in $\omega$.

## Acknowledgments

Simon Grabowsky thanks the German Research Foundation (Deutsche Forschungsgemeinschaft, DFG) for funding within the Emmy Noether project GR 4451/1-1. The authors also thank Professor E. D. Jemmis (Indian Institute of Science, Bangalore, India) for providing access to a cluster used for computation of natural bond orbitals.

## Conflict of interest

The authors declare no conflict of interest.

**Keywords:** basicity · bonding analysis · covalency · ionicity · quantum chemistry · siloxanes

[1] G. V. Gibbs, R. T. Downs, D. F. Cox, N. L. Ross, C. T. Prewitt, K. M. Rosso, T. Lippmann, A. Kirfel, *Z. Kristallogr.* **2008**, *223*, 1 – 40.
[2] G. V. Gibbs, A. F. Wallace, D. F. Cox, R. T. Downs, N. L. Ross, K. M. Rosso, *Am. Mineral.* **2009**, *94*, 1085 – 1102.
[3] R. K. Iler, *The Chemistry of Silica: Solubility, Polymerization, Colloid and Surface Properties, and Biochemistry*, Wiley Interscience, New York, **1979**.
[4] R. West, L. S. Wilson, D. L. Powell, *J. Organomet. Chem.* **1979**, *178*, 5 – 9.
[5] V. Shklover, H.-B. Bürgi, A. Raselli, T. Armbruster, W. Hummel, *Acta Crystallogr. Sect. B* **1991**, *47*, 544 – 548.
[6] I. L. Karle, J. M. Karle, C. J. Nielsen, *Acta Crystallogr. Sect. C* **1986**, *42*, 64 – 67.
[7] J. Tossell, G. V. Gibbs, *Acta Crystallogr. Sect. A* **1978**, *34*, 463 – 472.
[8] J. E. Mark, *Acc. Chem. Res.* **2004**, *37*, 946 – 953.
[9] S. Grabowsky, M. F. Hesse, C. Paulmann, P. Luger, J. Beckmann, *Inorg. Chem.* **2009**, *48*, 4384 – 4393.
[10] S. Grabowsky, J. Beckmann, P. Luger, *Aust. J. Chem.* **2012**, *65*, 785 – 795.
[11] F. Weinhold, R. West, *Organometallics* **2011**, *30*, 5815 – 5824.
[12] F. Weinhold, R. West, *J. Am. Chem. Soc.* **2013**, *135*, 5762 – 5767.
[13] J. B. Nicholas, R. E. Winans, R. J. Harrison, L. E. Iton, L. A. Curtiss, A. J. Hopfinger, *J. Phys. Chem.* **1992**, *96*, 7958 – 7965.
[14] C. Eaborn, P. B. Hitchcock, P. Lickiss, *J. Organomet. Chem.* **1984**, *264*, 119 – 126.
[15] A. I. Gusev, A. G. Los, Y. M. Varazhkin, M. M. Morgunova, D. Y. Zhinkin, *J. Struct. Chem.* **1976**, *17*, 329 – 331.
[16] A. Spielberger, P. Gspaltl, H. Siegl, E. Hengge, K. Gruber, *J. Organomet. Chem.* **1995**, *499*, 241 – 246.
[17] C. Clobes, P. Jerabek, I. Nußbruch, G. Frenking, C. von Hänisch, *Eur. J. Inorg. Chem.* **2015**, 3264 – 3273.
[18] C. von Hänisch, O. Hampe, F. Weigend, S. Stahl, *Angew. Chem. Int. Ed.* **2007**, *46*, 4775 – 4779; *Angew. Chem.* **2007**, *119*, 4859 – 4863.
[19] T. S. Cameron, A. Decken, I. Krossing, J. Passmore, J. M. Rautiainen, X. Wang, X. Zeng, *Inorg. Chem.* **2013**, *52*, 3113 – 3126.
[20] Y. Yokouchi, S. Ishida, T. Onodera, H. Oikawa, T. Iwamoto, *Chem. Commun.* **2018**, *54*, 268 – 270.
[21] K. Reuter, G. Thiele, T. Hafner, F. Uhlig, C. von Hänisch, *Chem. Commun.* **2016**, *52*, 13265 – 13268.
[22] F. Dankert, K. Reuter, C. Donsbach, C. von Hänisch, *Inorganics* **2018**, *6*, 15.
[23] F. Dankert, C. Donsbach, C.-N. Mais, K. Reuter, C. von Hänisch, *Inorg. Chem.* **2018**, *57*, 351 – 359.
[24] R. West, L. S. Whatley, K. J. Lake, *J. Am. Chem. Soc.* **1961**, *83*, 761 – 764.
[25] G. V. Gibbs, *Am. Mineral.* **1982**, *67*, 421 – 450.
[26] J. Passmore, J. M. Rautiainen, *Eur. J. Inorg. Chem.* **2012**, 6002 – 6010.
[27] A. Vegas, R. Notario, E. Chamorro, P. Pérez, J. F. Liebman, *Acta Crystallogr. Sect. B* **2013**, *69*, 163 – 175.
[28] C. Martín-Fernández, M. M. Montero-Campillo, I. Alkorta, J. Elguero, *J. Phys. Chem. A* **2017**, *121*, 7424 – 7431.
[29] C. Martín-Fernández, M. M. Montero-Campillo, I. Alkorta, J. Elguero, *Mol. Phys.* **2018**, *116*, 1539 – 1550.
[30] I.-T. Moraru, P. M. Petrar, G. Nemes, *J. Phys. Chem. A* **2017**, *121*, 2515 – 2522.
[31] G. V. Gibbs, K. M. Rosso, D. M. Teter, M. B. Boisen, Jr., M. S. T. Bukowinski, *J. Mol. Struct.* **1999**, *485*, 13 – 25.
[32] R. J. Gillespie, S. A. Johnson, *Inorg. Chem.* **1997**, *36*, 3031 – 3039.
[33] V. G. Tsirelson, O. A. Evdokimova, E. L. Belokoneva, V. S. Urusov, *Phys. Chem. Miner.* **1990**, *17*, 275 – 292.
[34] G. V. Gibbs, J. W. Downs, M. B. Boisen, *Rev. Mineral. Geochem.* **1994**, *29*, 331 – 368.
[35] A. Almenningen, O. Bastiansen, V. Ewing, K. Hedberg, M. Traetteberg, *Acta Chem. Scand.* **1963**, *17*, 2455 – 2460.
[36] M. J. Barrow, E. A. V. Ebsworth, M. M. Harding, *Acta Crystallogr. Sect. B* **1979**, *35*, 2093 – 2099.
[37] F. Stone, D. Seyferth, *J. Inorg. Nucl. Chem.* **1955**, *1*, 112 – 118.
[38] H. Oberhammer, J. E. Boggs, *J. Am. Chem. Soc.* **1980**, *102*, 7241 – 7244.
[39] F. Weinhold, C. R. Landis, *Valency and Bonding: A Natural Bond Orbital Donor – Acceptor Perspective*, Cambridge University Press, Cambridge, **2005**.
[40] J. M. L. Martin, G. de Oliveira, *J. Chem. Phys.* **1999**, *111*, 1843 – 1856.
[41] G. Frenking, S. Shaik, *The Chemical Bond: Fundamental Aspects of Chemical Bonding*, Wiley-VCH, Weinheim, **2014**.
[42] C. Gatti, *Z. Kristallogr.* **2005**, *220*, 399 – 457.
[43] J. Henn, D. Leusser, D. Stalke, *J. Comput. Chem.* **2007**, *28*, 2317 – 2324.
[44] M. Fugel, J. Beckmann, D. Jayatilaka, G. V. Gibbs, S. Grabowsky, *Chem. Eur. J.* **2018**, *24*, 6248 – 6261.

ChemPubSoc Europe

CHEMISTRY
A European Journal
Full Paper

[45] R. F. W. Bader, *Atoms in Molecules, A Quantum Theory*, Oxford Science Publications, Oxford, **1990**.
[46] M. Kohout, *Int. J. Quantum Chem.* **2004**, *97*, 651 – 658.
[47] C. Gatti, F. Cargnoni, L. Bertini, *J. Comput. Chem.* **2003**, *24*, 422 – 436.
[48] E. Glendening, C. Landis, F. Weinhold, *WIREs Comput. Mol. Sci.* **2012**, *2*, 1 – 42.
[49] E. D. Glendening, F. Weinhold, *J. Comput. Chem.* **1998**, *19*, 593 – 609.
[50] E. D. Glendening, F. Weinhold, *J. Comput. Chem.* **1998**, *19*, 610 – 627.
[51] E. D. Glendening, J. Badenhoop, F. Weinhold, *J. Comput. Chem.* **1998**, *19*, 628 – 646.
[52] X. Fradera, M. A. Austen, R. F. W. Bader, *J. Phys. Chem. A* **1999**, *103*, 304 – 314.
[53] R. Ponec, D. L. Cooper, *J. Mol. Struct.* **2005**, *727*, 133 – 138.
[54] M. D. Gould, C. Taylor, S. K. Wolff, G. S. Chandler, D. Jayatilaka, *Theor. Chem. Acc.* **2008**, *119*, 275 – 290.
[55] Y. L. Frolov, M. Voronkov, N. Strashnikova, N. Shergina, *J. Mol. Struct.* **1992**, *270*, 205 – 215.
[56] J. Beckmann, S. Grabowsky, *J. Phys. Chem. A* **2007**, *111*, 2011 – 2019.
[57] R. McWeeny, *Coulson's Valence*, Oxford University Press, New York, **1979**.
[58] P. Bultinck, P. W. Ayers, S. Fias, K. Tiels, C. Van Alsenoy, *Chem. Phys. Lett.* **2007**, *444*, 205 – 208.
[59] K. B. Wiberg, P. R. Rablen, *J. Comput. Chem.* **1993**, *14*, 1504 – 1518.
[60] P. J. Stephens, F. J. Devlin, C. F. Chabalowski, M. J. Frisch, *J. Phys. Chem.* **1994**, *98*, 11623 – 11627.
[61] S. Grimme, S. Ehrlich, L. Goerigk, *J. Comput. Chem.* **2011**, *32*, 1456 – 1465.
[62] Gaussian 09 (Revision D.01), M. J. Frisch, G. W. Trucks, H. B. Schlegel, G. E. Scuseria, M. A. Robb, J. R. Cheeseman, G. Scalmani, V. Barone, G. A. Petersson, H. Nakatsuji, X. Li, M. Caricato, A. V. Marenich, J. Bloino, B. G. Janesko, R. Gomperts, B. Mennucci, H. P. Hratchian, J. V. Ortiz, A. F. Izmaylov, J. L. Sonnenberg, D. Williams-Young, F. Ding, F. Lipparini, F. Egidi, J. Goings, B. Peng, A. Petrone, T. Henderson, D. Ranasinghe, V. G. Zakrzewski, J. Gao, N. Rega, G. Zheng, W. Liang, M. Hada, M. Ehara, K. Toyota, R. Fukuda, J. Hasegawa, M. Ishida, T. Nakajima, Y. Honda, O. Kitao, H. Nakai, T. Vreven, K. Throssell, J. A. Montgomery, Jr., J. E. Peralta, F. Ogliaro, M. J. Bearpark, J. J. Heyd, E. N. Brothers, K. N. Kudin, V. N. Staroverov, T. A. Keith, R. Kobayashi, J. Normand, K. Raghavachari, A. P. Rendell, J. C. Burant, S. S. Iyengar, J. Tomasi, M. Cossi, J. M. Millam, M. Klene, C. Adamo, R. Cammi, J. W. Ochterski, R. L. Martin, K. Morokuma, O. Farkas, J. B. Foresman, D. J. Fox, Gaussian, Inc. Wallingford CT, **2009**.
[63] E. D. Glendening, C. R. Landis, F. Weinhold, *J. Comput. Chem.* **2013**, *34*, 1429 – 1437.
[64] T. A. Keith, AIMAll, version 13.05.06, TK Gristmill Software, Overland Park, KS, USA, **2013**.
[65] M. Kohout, DGrid, version 4.6, Dresden, Germany, **2011**.
[66] C. B. Hübschle, P. Luger, *J. Appl. Crystallogr.* **2006**, *39*, 901 – 904.
[67] D. Jayatilaka, D. J. Grimwood, in *International Conference on Computational Science*, Springer, Berlin, pp. 142 – 151.
[68] H.-J. Werner, P. J. Knowles, G. Knizia, F. R. Manby, M. Schütz, *Wiley Interdiscip. Rev.: Comput. Mol. Sci.* **2012**, *2*, 242 – 253.
[69] A. Karton, J. M. L. Martin, *J. Chem. Phys.* **2012**, *136*, 124114.
[70] K. A. Peterson, D. Feller, D. A. Dixon, *Theor. Chem. Acc.* **2012**, *131*, 1079.
[71] T. Helgaker, W. Klopper, D. P. Tew, *Mol. Phys.* **2008**, *106*, 2107 – 2143.
[72] P. Bultinck, P. Popelier, *Atoms in Molecules and Population Analysis*, Taylor and Francis, London, **2009**, pp. 215 – 227.
[73] R. G. Parr, P. W. Ayers, R. F. Nalewajski, *J. Phys. Chem. A* **2005**, *109*, 3957 – 3959.
[74] J. Poater, M. Duran, M. Sola, B. Silvi, *Chem. Rev.* **2005**, *105*, 3911 – 3947.
[75] R. S. Mulliken, *J. Chem. Phys.* **1955**, *23*, 1833 – 1840.
[76] R. S. Mulliken, *J. Chem. Phys.* **1955**, *23*, 1841 – 1846.
[77] K. R. Roby, *Mol. Phys.* **1974**, *27*, 81 – 104.
[78] R. F. W. Bader, *Chem. Rev.* **1991**, *91*, 893 – 928.
[79] P. Bultinck, C. Van Alsenoy, P. W. Ayers, R. Carbo-Dorca, *J. Chem. Phys.* **2007**, *126*, 144111.
[80] P. Bultinck, D. L. Cooper, D. Van Neck, *Phys. Chem. Chem. Phys.* **2009**, *11*, 3424 – 3429.
[81] K. Alhameedi, B. Bohman, A. Karton, D. Jayatilaka, *Int. J. Quantum Chem.* **2018**, e25603.
[82] K. Wiberg, *Tetrahedron* **1968**, *24*, 1083 – 1096.
[83] M. Giambiagi, M. Giambiagi, D. R. Grempel, C. D. Heymann, *J. Chim. Phys.* **1975**, *72*, 15 – 22.
[84] R. F. W. Bader, M. E. Stephens, *Chem. Phys. Lett.* **1974**, *26*, 445 – 449.
[85] R. F. W. Bader, A. Streitwieser, A. Neuhaus, K. E. Laidig, P. Speers, *J. Am. Chem. Soc.* **1996**, *118*, 4959 – 4965.
[86] P. Bultinck, D. L. Cooper, R. Ponec, *J. Phys. Chem. A* **2010**, *114*, 8754 – 8763.

Manuscript received: May 2, 2018
Revised manuscript received: July 11, 2018
Accepted manuscript online: July 12, 2018
Version of record online: September 21, 2018

 

# Chapter 7

# Investigating the Resonance in Nitric Acid and the Nitrate Anion Based on a Modern Bonding Analysis

In this study, a *complementary bonding analysis* is performed to analyze the concept of resonance in a well known inorganic system – the nitrate anion $NO_3^-$. The study is also performed for the related species $HNO_3$ and $FNO_3$. The paper is part of the Graham S. Chandler special issue on the occasion of his 80th birthday and was published in the *Australian Journal of Chemistry* in 2018. In the following my contributions to this work are listed:

- I wrote 90% of the text
- I am responsible for Figures 1, 2, 3, 5, 6 and 7
- I am responsible for Tables 2, 3, 4, 5 and 6
- I performed the geometry optimizations
- I performed all analyses based on the geometry optimized structures and on the *XWR*
- I partly contributed to the X-ray diffraction measurement of the nitrate crystal (≈20%)

RESEARCH FRONT

CSIRO PUBLISHING

*Aust. J. Chem.* **2018**, *71*, 227–237
https://doi.org/10.1071/CH17583

Full Paper

# Investigating the Resonance in Nitric Acid and the Nitrate Anion Based on a Modern Bonding Analysis*

*Malte Fugel,*[A] *Florian Kleemiss,*[A] *Lorraine A. Malaspina,*[A] *Rumpa Pal,*[A] *Peter R. Spackman,*[B] *Dylan Jayatilaka,*[B] *and Simon Grabowsky*[A,C]

[A]University of Bremen, Department 2 – Biology/Chemistry, Institute of Inorganic Chemistry and Crystallography, Leobener Str. 3, 28359 Bremen, Germany.
[B]University of Western Australia, School of Molecular Sciences, 35 Stirling Highway, Perth, WA 6009, Australia.
[C]Corresponding author. Email: simon.grabowsky@uni-bremen.de

The nitrate anion, $NO_3^-$, is often regarded as a textbook example for the very fundamental concept of resonance. Usually, three equivalent resonance structures with one N–O double bond and two N–O single bonds are considered. Consequently, each of the three N–O bonds should have a partial double bond character. In this study, we analyse the resonance in $NO_3^-$ in comparison with the related species $HNO_3$ and $FNO_3$ by applying a combination of the Quantum Theory of Atoms in Molecules (QTAIM), a natural bond orbital (NBO) analysis, the electron localizability indicator (ELI), and valence bond (VB) calculations. Despite the fundamental importance of nitrate salts and nitric acid for the environment, chemistry, and industry, a bonding analysis is absent from the literature so far. The classical resonance structures are clearly reflected by the bond analysis tools, but are not the only contributions to the bonding situation. The resonance in $HNO_3$ and $FNO_3$ is greatly perturbed by the hydrogen and fluorine atoms. In addition to theoretical calculations, experimental electron density and wave function refinements were carried out on a $KNO_3$ crystal.

Manuscript received: 10 November 2017.
Manuscript accepted: 22 December 2017.
Published online: 19 February 2018.

## Introduction

A single Lewis structure is only a good representation of the true bonding situation of a molecule if electron pairs are localized between two atoms or at a single atom corresponding to two-centre two-electron bonds or lone pairs, respectively.[1] However, there are countless systems where electron pairs are highly delocalized and thus several resonance structures are required to give an adequate representation of the bonding situation.[2,3] Ultimately, within the Lewis model, the bonding properties of a molecule or ion are best reflected by a weighted average of all resonance structures. A common example for such a system is the nitrate anion, $NO_3^-$. Its bonding is usually described by the resonance structures **2a–c** depicted in Fig. 1. Consequently, all N–O bonds have a partial double bond character and because none of these structures is favoured over the others, all N–O bonds are equivalent. A subvalent resonance structure (**1**) with three N–O single bonds may also be considered (see Fig. 1). However, it has been shown in numerous examples that well-defined non-Lewis bonding contributions can be significant in inorganic chemistry, e.g. (negative) hyperconjugation,[4] or that the Lewis picture is too limited to capture the bonding in full.[5] A combination of more sophisticated modern bonding indicators from the realms of real space, orbital space, and energy space might be necessary.[6,7]

Here, we investigate how a simple and fundamental textbook example ($NO_3^-$) is represented within and beyond the Lewis notion of bonding with modern bond analysis methods. The nitrate anion has a great impact on biological and environmental factors, and thus an understanding of the underlying bonding model based on experimental and theoretical analyses is long overdue.[8] To the best of our knowledge, such an analysis is missing in the literature; however, there are spectroscopic studies of the nitrate anion from which information about the bonding can be inferred.[9] In the present study, the bonding situation of the nitrate anion is investigated with the basis of the resonance system depicted in Fig. 1. The same analysis is performed on two related species – $HNO_3$ and $FNO_3$. Whereas nitric acid ($HNO_3$) is a stable species and one of the most common chemicals in the laboratory, fluorine nitrate ($FNO_3$) is unstable and is produced in situ when used in a reaction.[10] For both species, resonance structures similar to those of the nitrate anion may be formulated; see Fig. 1. However, the resonance is expected to be greatly perturbed by the introduction of a hydrogen or fluorine atom, respectively. The analysis is performed on theoretically obtained wave functions of $NO_3^-$, $HNO_3$, and $FNO_3$. The optimized geometries are shown in Fig. 2.

In addition, an experimental charge density dataset was obtained for a potassium nitrate ($KNO_3$) crystal via high-resolution

*This paper is part of the Graham S. Chandler special issue on the occasion of his 80th birthday.

 

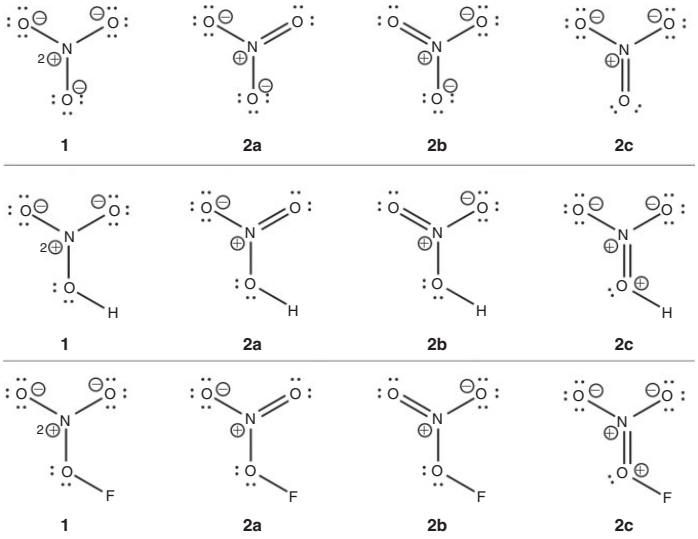


**Fig. 1.** Possible resonance structures (type **1** and type **2**) of $NO_3^-$, $HNO_3$, and $FNO_3$.

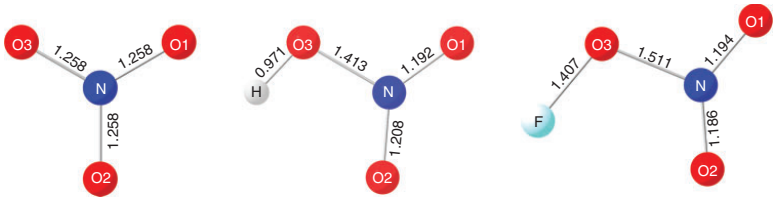


**Fig. 2.** Geometry-optimized structures of $NO_3^-$, $HNO_3$, and $FNO_3$; the numbers correspond to bond lengths in Å.

low-temperature X-ray diffraction. Multipole modelling (MM)[11] and X-ray wavefunction refinement (XWR)[12] of this $KNO_3$ dataset were carried out. In both MM and XWR methods, anharmonic atomic displacement parameters were refined to model the residual electron density features that were obviously caused by anharmonic motion, captured in the high-quality, high-resolution dataset.[13] This presents the first application of anharmonic XWR. Methodological details will be presented in a forthcoming study.[14] Moreover, the B3LYP functional was used in XWR for the first time to be able to use the same level of theory in the crystallographic refinement as in the theoretical calculations to ensure maximum comparability of the experimental and theoretical results.

A multipole model guarantees the most direct link of the modelled electron density to the experimental structure factors; however, chemical analysis cannot go beyond the electron density. In XWR, the molecular orbital coefficients are fitted to the experimental structure factors so that, in principle, the same bonding descriptors are available from XWR as from a purely theoretical calculation. In this study, we use geometrical, Quantum Theory of Atoms in Molecules (QTAIM), bond index, natural bond orbital (NBO), electron localizability indicator (ELI), and valence bond (VB) parameters. This has previously been shown to be a meaningful combination of bond analysis tools for a series of hydroxide compounds.[6] Geometrical and QTAIM parameters are easily obtainable from MM and XWR. ELI parameters were made available from XWR previously,[15] whereas NBO analysis from an experimentally derived wave function was applied in this paper for the first time. VB calculations are at present not linked to the output from XWR. In the list below, the bonding analysis methods are only outlined briefly – a detailed description may be found elsewhere in the literature.[16–20]

- The most straightforward way to draw first conclusions on the bonding situation is to consider bond lengths, which are easily and accurately attainable from experiment and theory alike.
- A topological analysis of the electron density (QTAIM) may be applied to gain a deep insight into the bonding situation based on a theoretically or experimentally obtained electron density.[18,19] In the current paper, we regard a variety of properties at bond critical points (bcps), which are saddle points of the electron density indicating bonded interactions.[21] In addition, the delocalization index is used, which is a bond index that could be considered a measure of bond order.[22]
- NBOs offer a way to analyse bonding based on localized orbitals that may be related to features of Lewis formulae (Lewis-type NBOs) as well as non-Lewis type NBOs such as

Rydberg orbitals, lone valencies or valence antibonds.[23] In the NBO framework, natural localized molecular orbital–natural population analysis (NLMO/NPA) bond indices are defined.

- The Roby bond index is based on Roby's projection operators, and maps ionic as well as covalent contributions to bonding.[24]
- The electron localizibility indicator (ELI-D) is a measure of electron localization.[25] A topological analysis of the ELI-D yields basins that may be related to atomic shells, lone pairs, and bonds. Iso-surfaces of the ELI-D show localization domains that may be attributed to the ELI-D basins.
- VB calculations are based on a VB wave function of the system constructed from a linear combination of wave functions that may each be associated with one of the resonance structures.[26]

## Computational and Experimental Details

### *Geometry Optimizations and Bonding Analysis*

The geometry optimizations were carried out at a B3LYP/aug-cc-pVTZ level of theory using the *Gaussian09* software suite.[27] Frequency analyses were performed on the final geometries (depicted in Fig. 2) to ensure that they corresponded to a minimum on the potential energy surface. The QTAIM analysis was performed with *AIMall*[28] and the NBO analysis with *NBO 6.0*.[29] The valence bond calculations were carried out with *XMVB* at a BOVB/cc-pVDZ level of theory.[30] For the calculation of the ELI-D, the program *DGrid-5.0* was employed.[31]

### *Crystallographic Information*

$KNO_3$ crystals were obtained from a supersaturated solution of 1.264 g $KNO_3$ in 2 mL water, which was added to 2 mL of a 0.4 % agarose gel. This mixture cooled under laboratory conditions and yielded crystals. The crystallographic data were measured at 100 K on a Bruker D8 Venture single-crystal diffractometer fitted with a IμS microfocus radiation source using $MoK_\alpha$ radiation and a Photon-100 CMOS detector. Data integration and reduction were carried out using the *APEX3* software package.[32] Additional information on measurement and refinement is given in Table 1. The structure was solved using *SHELXT*[33] and refined with full-matrix least-squares using the program *SHELXL*[33] within an independent atom model (IAM).

Subsequently, the structure was further refined employing two separate methods, starting from the same geometry (obtained from the IAM). The first model was derived from the multipole formalism in the software *XD2006*.[34] The refinement was carried out on $F^2$ up to a resolution of 0.39 Å. Initially, the scale factor was refined, and then a refinement of the positions of all atoms and their anisotropic displacement parameters (ADPs) was performed, taking into account constraints arising from special positions. At the next stage, multipole parameters were chosen according to the special positions and local site symmetries of the atoms. They were refined by progressively releasing higher terms of the multipole expansion up to hexadecapoles for all atoms. Afterwards, the Gram–Charlier expansion for third-order ADPs was used for all atoms and additional fourth-order terms for potassium.[35] Henceforth, all positions, ADPs, and multipoles were refined together. Iterative refinement of nitrogen and oxygen expansion–contraction parameters and positions, ADPs, and multipoles was carried out until no significant change in parameters was observed. A representation of the structure obtained can be seen in the supplementary material of this paper together with plots of the probability density function (PDF).

**Table 1. Crystallographic information and refinement statistics using MM and XWR**

| | | |
|---|---|---|
| Space group, Z, Z′ | *Pnma*, 4, 0.5 | |
| Crystal system | Orthorhombic | |
| $a$ [Å] | 6.2703(2) | |
| $b$ [Å] | 5.3935(2) | |
| $c$ [Å] | 9.1366(3) | |
| α [°] | 90 | |
| $\beta$ [°] | 90 | |
| $\gamma$ [°] | 90 | |
| $V$ [Å$^3$] | 308.989(13) | |
| $T$ [K] | 100(2) | |
| Radiation | MoKα | |
| Crystal size [mm$^3$] | $0.25 \times 0.19 \times 0.10$ | |
| Max. resolution [Å] | 0.39 | |
| $R_{int}$ | 0.0314 | |
| Redundancy | 14.45 | |
| Completeness | 1.00 | |
| No. of reflns measured | 41524 | |
| No. of unique reflns | 2874 | |
| No. of observed reflns ($I > 2\sigma$) | 2602 | |
| CSD refcode | 433754 | |
| Model | MM | XWR |
| Weighting scheme | $w = 1/\sigma^2(F_o^2)$ | $w = 1/\sigma(F_o)$ |
| No. of parameters refined | 123 | 65 |
| $R1$ | 0.012 | 0.013 |
| $wR2$(MM), $wR1$(XWR) | 0.024 | 0.017 |
| Max. residual density [e Å$^{-3}$] | 0.599 | 0.270 |
| Min. residual density [e Å$^{-3}$] | −0.213 | −0.203 |

The second model was obtained using XWR within the software *Tonto*.[36] XWR is the subsequent execution of Hirshfeld atom refinement (HAR)[37] and X-ray constrained wavefunction (XCW) fitting.[38] A B3LYP/def2-TZVP/aug-cc-pVTZ level of theory was used during the HAR, and a RHF/def2-TZVP/aug-cc-pVTZ level of theory during the XCW fitting. The combination of two basis sets was necessary because potassium is not defined for the aug-cc-pVTZ basis set. A cluster of point charges and dipoles was not applied. Additionally, potassium was refined in HAR using fourth-order Gram–Charlier ADPs. Nitrogen and oxygen atoms were described by aug-cc-pVTZ, using third-order Gram–Charlier ADPs. The corresponding PDF plots are shown in the Supplementary Material. It has to be noted that both HAR refinement and XCW fitting rely on the calculation of a molecular wave function, so that the asymmetric unit, which only contains half of the formula unit ($Z' = 0.5$), had to be completed to a full $KNO_3$ formula unit. This corresponds to the asymmetric unit and its mirrored counterpart (see the Supplementary Material for a representation showing the mirror plane used to generate the formula unit). A final value for the Lagrangian multiplier $\lambda$ of 0.32 was reached, after which the XCW fitting did not converge, corresponding to a $\chi^2$ value of 2.85. The resulting structure of one nitrate anion with all potassium short contacts is shown in Fig. 3. The final IAM, MM, and HAR models together with the structure factor files are deposited with the Inorganic Crystal Structure Database under deposition number 433754.

MM and XWR give similar *R*-value statistics for the electron density and structure refinement (Table 1), but significantly different maximum residual density. The highest positive residual density in the multipole model of 0.6 e Å$^{-3}$ is located close to the potassium cation and represents insufficient treatment of the electron density distribution of heavier elements due to insufficient flexibility of the radial functions used.[12] In XWR, with a much higher basis set used in the electron density modelling, this residual density peak at potassium has nearly disappeared to the level of the negative residual density. Fig. 4 shows the same significant reduction of residual density in XWR in the nitrate plane in comparison with the MM residual density plot, but both methods produce very reasonable static deformation density maps that show the same features.

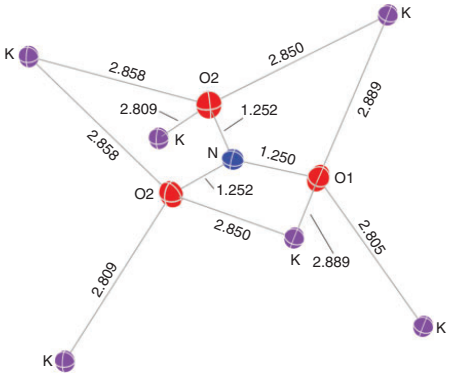


**Fig. 3.** Crystallographic structure of $KNO_3$ from Hirshfeld Atom Refinement. Bond lengths are given in Å. The standard uncertainties in the bond lengths are in the range 0.0003–0.0006 Å. The displacement parameters are visualized at 50 % probability.

## Results and Discussion

### *Geometry*

Fig. 2 contains all bond lengths of the optimized structures of $NO_3^-$, $HNO_3$, and $FNO_3$. The N–O bond lengths in $NO_3^-$ lie between typical values of N–O single (1.40 Å) and double bonds (1.21 Å).[39] This directly follows from the partial N–O double-bond character indicated by the resonance structures in Fig. 1. Although O1 and O2 in $KNO_3$ (Fig. 3) have different interactions with neighbouring cations, the N–O bond lengths are very similar to each other and only slightly shorter compared with the ones in the isolated $NO_3^-$ anion, suggesting that the geometry of the $NO_3^-$ unit in $KNO_3$ is sufficiently unaffected by crystal effects – this ensures that the comparison with the bonding properties of the isolated $NO_3^-$ anion is meaningful. An

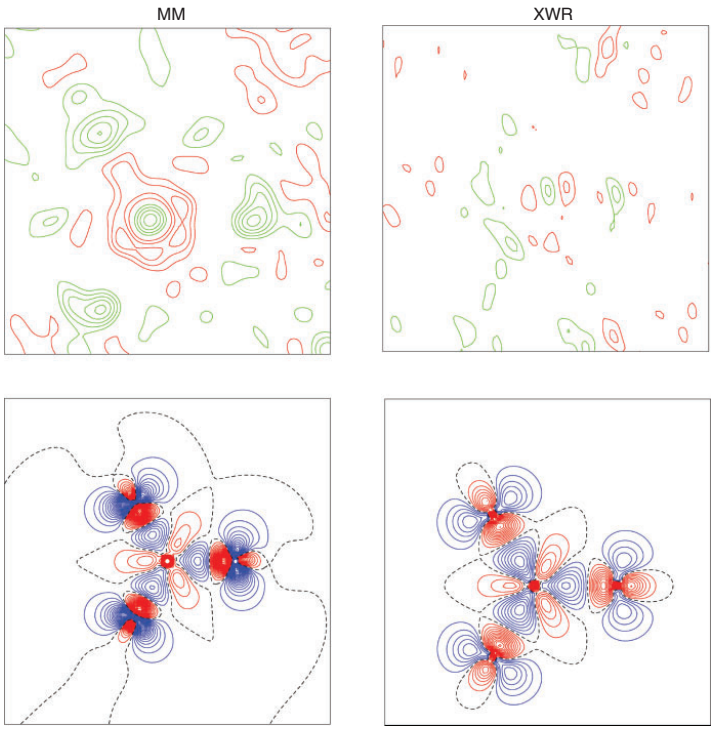


**Fig. 4.** Maps of the residual (top), and deformation density (bottom) in the nitrate plane after MM (left) and XWR (right). Positive residual density is coloured in green, negative in red, positive deformation density in blue and negative in red. The zero isoline is a black dashed line. Residual density is plotted with a step size of 0.05 e Å$^{-3}$ and deformation density with a step size of 0.1 e Å$^{-3}$.

Inorganic Crystal Structure Database survey results in 147 crystal structures of nitrates, which decreases to only 19 different compounds with trustworthy N–O distances (e.g. all ADPs positive, no strong disorder). The N–O bonds range from 1.20 to 1.29 Å. However, most N–O bonds lie between 1.23 and 1.26 Å (with an average of 1.25 Å), indicating that the $NO_3^-$ unit is fairly rigid. The terminal N–O bonds (N–O1 and N–O2) in $HNO_3$ and $FNO_3$ are significantly shorter compared with the N–O bonds in both $NO_3^-$ and $KNO_3$, indicating that their double-bond character is more pronounced. In contrast, the N–O3(X) bonds (X = H or F) are highly elongated, which suggests a much smaller double-bond character and thus a less significant contribution of resonance structures **2c**.

Whereas the three N–O bonds in $NO_3^-$ are required to be equivalent based on symmetry, the introduction of an H or F atom is followed by a loss of the 3-fold symmetry, and thus the three N–O bonds are dissimilar. This also affects the two terminal N–O bonds: N–O1 in $HNO_3$ is somewhat shorter than N–O2, whereas it is the other way around in $FNO_3$. In both cases, the N–O2 bond is oriented to the same side as the O–X bond. In $KNO_3$, the crystallographic mirror plane intersecting atoms O1, N, and K generates two equivalent oxygen atoms (O2 and O2′) and thus two equivalent N–O bonds (N–O2 and N–O2′).

### *Quantum Theory of Atoms in Molecules*

In the QTAIM approach, the topology of the electron density is analysed to derive information on the bonding situation. Conventionally, properties at bcps are considered. In the present study, we employ the electron density ($\rho_{bcp}$), the Laplacian of the electron density (the second derivative of the electron density, $\nabla^2\rho_{bcp}$), and the bond ellipticity ($\varepsilon_{bcp}$) at the N–O bcps. The values are listed in Table 2.

In most cases, a large value of $\rho_{bcp}$ may be attributed to a high orbital overlap of the bonded atoms. The values of $\rho_{bcp}$ conform to the conclusions drawn from the X–O bond lengths: generally, they show that a short X–O bond length is associated with a large value of $\rho_{bcp}$, confirming that N–O1 and N–O2 in $HNO_3$ and $FNO_3$ have a more pronounced double-bond character compared with the N–O bonds in $NO_3^-$ and $KNO_3$. In turn, the decreased double-bond character of N–O3 in $HNO_3$ and $FNO_3$ is reflected by a significantly lower value of $\rho_{bcp}$. Both XWR and MM give slightly larger values of $\rho_{bcp}$ for the N–O bonds in $KNO_3$, compared with the isolated ion.

The negative values of $\nabla^2\rho_{bcp}$ are an indication of dominant covalent contributions to the N–O bonds. This comes as no surprise, because the electronegativity differences of N and O atoms are quite small. However, $\nabla^2\rho_{bcp}$ of the N–O3 bond in $HNO_3$ and $FNO_3$ is substantially less negative compared with the other N–O bonds, indicating that a significantly smaller amount of electron density is accumulated in the bonds involving the oxygen atom to which the hydrogen or fluorine atom is bonded. Although $\nabla^2\rho_{bcp}$ of the N–O bonds in $KNO_3$ from XWR agrees well with the theoretical values of $NO_3^-$, there are greater discrepancies for the MM, which is common especially for polarized bonds.[12] However, a small shift of the position of the bcp may result in considerable differences in $\nabla^2\rho_{bcp}$ if the bcp is located in a steep region of $\nabla^2\rho$.[40]

In the QTAIM approach, the notion of an orbital is nonexistent, and so far, the double-bond character has only been quantified indirectly, but in some cases, the bond ellipticity at the bcp ($\varepsilon_{bcp}$) may be consulted to directly spot π interactions. For single bonds, only cylindrically symmetric σ interactions contribute to the bonding (hence, $\varepsilon = 0$), whereas for double bonds, additional dumbbell-like π interactions are present (hence, $\varepsilon > 0$). It can be seen that even for the N–O3 bonds in $HNO_3$ and $FNO_3$, $\varepsilon > 0$ (see Table 2). In fact, the value of $\varepsilon$ for these bonds is larger than the one of the other N–O bonds for which a substantially higher double-bond character has been proposed by the previously regarded descriptors. This apparent discrepancy will be resolved at a later stage of this paper. Whereas the XWR of $KNO_3$ yields identical values of $\varepsilon_{bcp}$ compared with $NO_3^-$, the N–O2 bond of the MM gives a considerably lower value of $\varepsilon_{bcp}$.

All QTAIM properties reveal that the double-bond character of the N–O1 and N–O2 bonds in $HNO_3$ and $FNO_3$ is somewhat different. For $HNO_3$, N–O2 has less double-bond character, whereas it is the other way around for $FNO_3$. The N–O2 bond corresponds to the bond oriented to the same side as the O–X bond, while the N–O1 bond and O–X (X = H, F) bond have an antiperiplanar orientation (see Fig. 2). The most straightforward explanation for the different N–O double-bond characters is the distinct nature of the hydrogen and fluorine atoms. Whereas the hydrogen has a positive partial charge, the partial charge of the fluorine is negative (see Supplementary Material Tables S2 and S3). Thus, there is an attractive interaction between the negatively charged O2 and the positively charged hydrogen atom. However, there is a repulsive interaction between O2 and the fluorine atom, because both atoms have a negative atomic charge. The introduction of a negative formal charge at O2 promotes the attractive interaction between O2 and H in $HNO_3$, but it also promotes the repulsive interaction between O2 and F in $FNO_3$. Hence, the double-bond character of the N–O2 bond is greater in $FNO_3$ compared with $HNO_3$.

**Table 2. Bond distances *r* (Å), electron density ($\rho_{bcp}$ in e Å$^{-3}$), Laplacian ($\nabla^2\rho_{bcp}$ in e Å$^{-5}$), and bond ellipticity ($\varepsilon_{bcp}$) at the N–O bond critical points of $NO_3^-$, $HNO_3$, $FNO_3$, and the experimentally obtained values for $KNO_3$**

| | $NO_3^-$ | $HNO_3$ | | | $FNO_3$ | | | $KNO_3$ (XWR) | | $KNO_3$ (MM) | |
|---|---|---|---|---|---|---|---|---|---|---|---|
| | N–O | N–O1 | N–O2 | N–O3 | N–O1 | N–O2 | N–O3 | N–O1 | N–O2 | N–O1 | N–O2 |
| $r_{X-O}$ | 1.258 | 1.192 | 1.208 | 1.413 | 1.194 | 1.186 | 1.511 | 1.252(1) | 1.250(1) | 1.255(1) | 1.252(1) |
| $\rho_{bcp}$ | 3.14 | 3.71 | 3.56 | 2.15 | 3.60 | 3.66 | 1.71 | 3.22[A] | 3.23[A] | 3.23(2) | 3.29(2) |
| $\nabla^2\rho_{bcp}$ | −20.2 | −33.5 | −29.3 | −4.3 | −27.3 | −28.1 | −1.5 | −24.5 | −22.6 | −11.4(1) | −18.9(1) |
| $\varepsilon_{bcp}$ | 0.12 | 0.11 | 0.11 | 0.17 | 0.09 | 0.08 | 0.19 | 0.12 | 0.12 | 0.11 | 0.04 |

[A]For the multipole model, it is a standard procedure to determine the standard uncertainties of the electron density parameters at the bcps, whereas it is not for XWR.[41]

### Bond Indices

The partial N–O double-bond character suggested by the previous analyses may also be quantified by the analysis of bond orders. Here, we examine three different definitions of bond orders – the NLMO/NPA bond order (from NBO), the DI (from QTAIM), and the Roby bond index. The NLMO/NPA bond order is a covalent bond order. The DI accounts for the electron pairs exchanged between two atomic basins within QTAIM, so it also includes ionic contributions. The Roby bond index has an explicitly defined ionic part. The N–O bonds are only slightly polarized and, thus, the three bond orders do not differ significantly (Table 3); however, the covalent NLMO/NPA bond order always shows the lowest values.

All bond indices are in agreement with the previously regarded QTAIM and geometry descriptors, but they may be linked more directly to the N–O double bond character, because they correspond to several electron pairs exchanged between two atoms. All three types of bond orders of the N–O1 and N–O2 bonds in $HNO_3$ and $FNO_3$ and the N–O bonds in $NO_3^-$ and $KNO_3$ are well above a value of one, and thus these bonds may be treated as partial double bonds (for ideal homopolar double bonds, bond order = 2). However, the DI and the Roby bond index of the N–O3 bond in $HNO_3$ only slightly exceed a value of one, while the corresponding NLMO/NPA bond order even falls below a value of one. For the N–O3 bond in $FNO_3$, all bond orders suggest a value below one. It has been shown above that the π interactions are less pronounced in these bonds and hence the partial double-bond character should be lowest in these two bonds.

### Natural Bond Orbitals

A routine NBO analysis may only be performed for molecules where a single Lewis formula has a major weight. The bonding situation in $NO_3^-$, $HNO_3$, and $FNO_3$, however, is highly delocalized. Hence, a standard NBO analysis is not feasible, because more than one resonance structure needs to be considered. In order to obtain sensible results for $NO_3^-$, $HNO_3$, and $FNO_3$, special treatment is necessary. NBO structures corresponding to resonance structures **1** (see Fig. 1) were predefined in the input for $NO_3^-$, $HNO_3$, and $FNO_3$ (using the CHOOSE keylist). Of course, the resulting Lewis-type NBOs alone are only a poor representation of the true bonding situation, but significant delocalizations emerge, which remedy the absence of the remaining resonance structures. In the next paragraph, we show that these delocalizations may be related to the remaining resonance structures (**2a–c**) depicted in Fig. 1. An NBO analysis was also carried out for $KNO_3$ using the fitted wave function obtained from XWR.

Table 4 shows the populations and hybridizations of the oxygen lone pairs. For $NO_3^-$, three oxygen lone pairs have been forced onto each of the three oxygen atoms. One is of $sp^{\lambda}$-type (where $\lambda$ is the hybridization coefficient), while the other two are of complete p-character. The $sp^{\lambda}$-type lone pair has a population of $N \approx 2$, so it may be regarded as highly localized. The populations of the p-type lone pairs, however, deviate more significantly from $N = 2$, indicating that they are highly delocalized. The delocalization is caused by major intramolecular donor–acceptor interactions where the p-type lone pairs serve as donor orbitals. There are two different types of major interactions, which will be discussed in the following.

The more significant interaction involves a p-type oxygen lone pair (LP3(O)) as a donor orbital and a lone valency located at the nitrogen (LV(N)) as an acceptor orbital. The latter is a non-Lewis-type orbital and is also of complete p-character (see Table 4). Both interacting orbitals, which are depicted in the top row of Fig. 5, are oriented perpendicular to the molecular plane. By visually inspecting the interacting orbitals, this type of interaction may be clearly linked to the π interactions that introduce the double-bond character to the N–O bonds. As a result, LV(N) is highly populated ($N \approx 1.15$). This is an unacceptably high value for a standard NBO routine that attempts to minimize the number of electrons in non-Lewis orbitals. Similar results are obtained from the XWR of $KNO_3$. Similar π interactions are also present in $HNO_3$ and $FNO_3$. From geometrical considerations and the QTAIM analysis, it has become clear that N–O1 and N–O2 have a greater double-bond character than the N–O bonds in $NO_3^-$ and $KNO_3$. Consequently, LP3(O1) and LP3(O2) have significantly lower populations compared with LP3(O) of $NO_3^-$ and $KNO_3$.

**Table 3. NLMO/NPA bond order, delocalization index (DI), and Roby bond index of the N–O bonds in $NO_3^-$, $HNO_3$, $FNO_3$, and $KNO_3$**

| | $NO_3^-$ | $HNO_3$ | | | $FNO_3$ | | | $KNO_3$ (XWR) | |
|---|---|---|---|---|---|---|---|---|---|
| | N–O | N–O1 | N–O2 | N–O3 | N–O1 | N–O2 | N–O3 | N–O1 | N–O2 |
| NLMO/NPA | 1.335 | 1.602 | 1.343 | 0.880 | 1.371 | 1.620 | 0.753 | 1.47 | 1.20 |
| DI | 1.491 | 1.708 | 1.654 | 1.054 | 1.707 | 1.745 | 0.868 | 1.44 | 1.57 |
| Roby | 1.485 | 1.702 | 1.657 | 1.071 | 1.734 | 1.771 | 0.857 | 1.54 | 1.45 |

**Table 4. Populations (*N* in e) and hybridization (%s and %p) of the oxygen lone pairs and the lone valency at the nitrogen of $NO_3^-$, $HNO_3$, and $FNO_3$**

| | $NO_3^-$ | | | $HNO_3$ | | | $FNO_3$ | | | $KNO_3$ (XWR) | | |
|---|---|---|---|---|---|---|---|---|---|---|---|---|
| | *N* | %s | %p | *N* | %s | %p | *N* | %s | %p | *N* | %s | %p |
| LP1(O1) | 1.982 | 78.7 | 21.3 | 1.979 | 75.3 | 24.6 | 1.978 | 74.9 | 25.1 | 1.981 | 79.5 | 20.5 |
| LP2(O1) | 1.919 | 0.0 | 99.9 | 1.838 | 0.2 | 99.5 | 1.780 | 0.4 | 99.3 | 1.908 | 0.0 | 99.9 |
| LP3(O1) | 1.610 | 0.0 | 99.8 | 1.451 | 0.0 | 99.7 | 1.473 | 0.0 | 99.6 | 1.521 | 0.0 | 99.8 |
| LP1(O2) | 1.982 | 78.7 | 21.3 | 1.979 | 76.5 | 23.5 | 1.978 | 74.0 | 26.0 | 1.980 | 78.3 | 21.7 |
| LP2(O2) | 1.919 | 0.0 | 99.9 | 1.851 | 0.3 | 99.5 | 1.775 | 0.5 | 99.2 | 1.919 | 0.1 | 99.8 |
| LP3(O2) | 1.610 | 0.0 | 99.8 | 1.495 | 0.0 | 99.7 | 1.454 | 0.0 | 99.6 | 1.654 | 0.0 | 99.8 |
| LP1(O3) | 1.982 | 78.7 | 21.3 | 1.987 | 61.1 | 38.9 | 1.992 | 81.2 | 18.8 | – | – | – |
| LP2(O3) | 1.919 | 0.0 | 99.9 | – | – | – | – | – | – | – | – | – |
| LP3(O3) | 1.610 | 0.0 | 99.8 | 1.881 | 0.0 | 99.7 | 1.913 | 0.0 | 99.9 | – | – | – |
| LV(N) | 1.154 | 0.0 | 100.0 | 1.159 | 0.0 | 100.0 | 1.151 | 0.0 | 100.0 | 1.153 | 0.0 | 100.0 |

The somewhat different double-bond character of the N–O1 and N–O2 bonds in $HNO_3$ and $FNO_3$ relative to each other is also reflected by the NBO analysis. For the N–O3 bonds in $HNO_3$ and $FNO_3$, a significantly lower double-bond character has been proposed by the previously regarded descriptors. The NBO analysis shows the same type of π interaction for these bonds (see top row of Fig. 5); however, the populations of LP3 (O3) are substantially higher than the populations of LP3(O1) and LP3(O2). This is in agreement with the weak π interactions suggested by the previous analyses. Consequently, LP3(O3) has a high lone-pair character, because the resulting π interaction is highly polarized towards the oxygen atom, suggesting that resonance structure **2c** has only a low weight. Interestingly, the population of LV(N) is similar in all systems – in $HNO_3$ and $FNO_3$, the low double-bond character of the N–O3 bond is compensated by an increased double-bond character of the N–O1 and N–O2 bonds.

The second major interaction involves the p-type lone pair, which is oriented parallel to the molecular plane, as a donor orbital and an N–O antibond (BD*(N–O)) as an acceptor orbital. The two interacting NBOs are depicted in the bottom row of Fig. 5. This interaction increases the orbital overlap between the nitrogen and the oxygen atom at which the donor lone pair is located, but, at the same time, the population of the N–O antibond leads to a weakening of the corresponding N–O bond. Judging from the lone pair populations, this interaction is a lot less significant when compared with the π interactions, but it is still very meaningful. In fact, the lower double-bond character of the N–O3 bond in $HNO_3$ and $FNO_3$ may be attributed to this interaction as will be shown in the following.

In $HNO_3$ and $FNO_3$, O3 has only two lone pairs in total – the p-type lone pair parallel to the molecular plane is absent, because an oxygen hybrid orbital is required for the O–H and O–F bonds, respectively. Consequently, there is no LP(O) → BD*(N–O) type interaction involving a lone pair at O3 as a donor orbital. Table 5 lists the populations of the N–O antibonds, which may be interpreted as a measure of the strength of these interactions.

For $NO_3^-$, all antibonds are populated to the same extent, because the population of each antibond results from two identical interactions. The XWR of $KNO_3$ gives slightly lower antibond populations, which conforms to the slightly shorter N–O bonds and larger values of $\rho_{bcp}$. For $HNO_3$ and $FNO_3$, the populations of the N–O1 and N–O2 antibonds are only approximately half as large as for $NO_3^-$, because there is only one interaction contributing to their population. The populations of the N–O3 antibonds of $HNO_3$ and $FNO_3$ are very high in comparison with the other N–O antibonds, indicating that they are particularly suited as acceptor orbitals. Because there is no appropriate donor orbital at O3, the N–O3 antibond may only serve as an acceptor orbital, which results in a significant weakening and accompanied elongation of the N–O3 bond. The bond ellipticity discussed in the preceding section has given larger values for the N–O3 bond in $HNO_3$ and $FNO_3$. When considering the orientation of the interacting orbitals of the two major interactions (see Fig. 5), it becomes clear that the N–O bonds have a more cylindrical symmetry along the bond whenever there is a p-type lone pair that is involved in an LP(O) → BD*(N–O)-type interaction. This leads to a lower ellipticity of the N–O1 and N–O2 bonds, although their π interactions are stronger. For the N–O3 bond, there is only the π interaction between the p-type lone pair at the oxygen and the lone valency at the nitrogen, and thus its bond ellipticity is not diminished by the LP(O) → BD*(N–O)-type interaction.

### *Electron Localizibility Indicator*

The ELI-D is a measure of electron localization. Whereas a topological analysis of the electron density yields atomic basins,

**Table 5. Populations of the N–O antibonds (N(BD*(N–O)) in e)**

| | N–O1 | N–O2 | N–O3 |
|---|---|---|---|
| $NO_3^-$ | 0.114 | 0.114 | 0.114 |
| $HNO_3$ | 0.053 | 0.063 | 0.223 |
| $FNO_3$ | 0.053 | 0.053 | 0.362 |
| $KNO_3$ (XWR) | 0.089 | 0.078 | – |

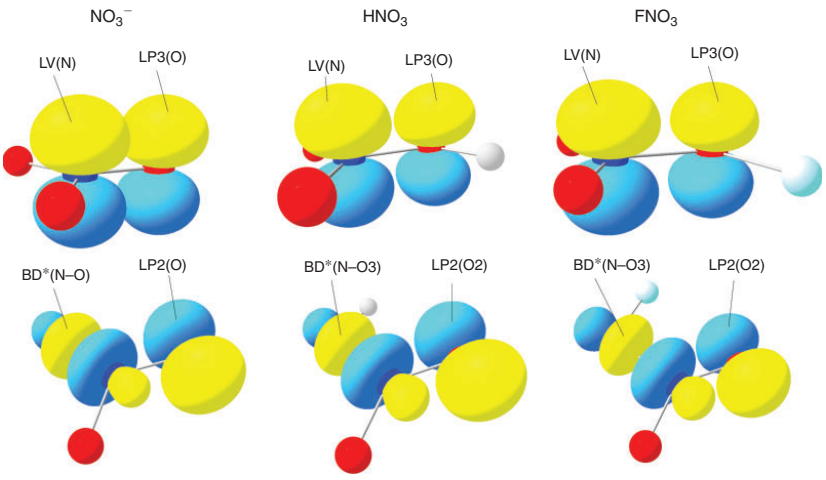


**Fig. 5.** Acceptor and donor NBOs for some of the most significant interactions.

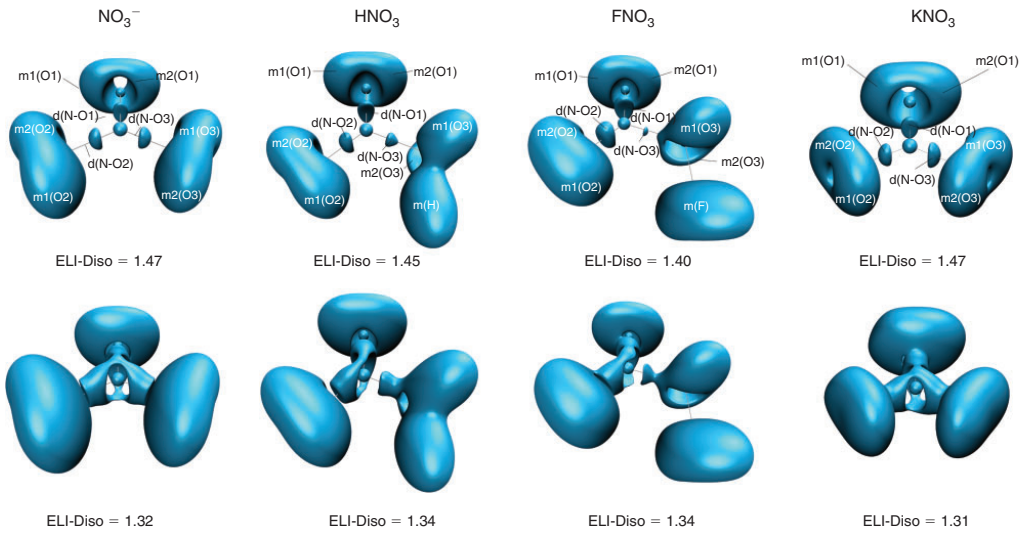


**Fig. 6.** Iso-surfaces of the electron localizibility indicator (ELI-D).

an analogous analysis of the ELI-D yields basins that may be related to regions of high electron localization. Such regions are atomic shells, bonds, and lone pairs. The ELI-D basins may be categorized according to their synapticity, which is defined as the number of core basins they are in contact with. Monosynaptic basins (connected to one core basin) and disynaptic basins (connected to two core basins) may be related to lone pairs and bonds, respectively.

For $NO_3^-$, there are three disynaptic N–O basins (d(N–O)) and two monosynaptic oxygen basins located at each of the three oxygen atoms (m(O)). The former may be related to the three N–O bonds and the latter may be linked to the oxygen lone pairs. The top row of Fig. 6 shows iso-surfaces of the ELI-D, revealing localization domains that may be attributed to d(N–O), m(O), and the core basins of N and O. The localization domains of d(N–O) have an elliptical shape, which may be related to the π character of the N–O bonds. The localization domains of m(O) can also be described as elliptical, but in contrast to the localization domains of d(N–O), the longer axis is aligned parallel to the molecular plane. This is reminiscent of the p-type lone pair NBOs that have an equivalent orientation (LP2(O), see bottom row of Fig. 5). The localization domains of d(N–O1), d(N–O2), m(O1), and m(O2) of $HNO_3$ and $FNO_3$ resemble those of $NO_3^-$. However, different types of localization domains are obtained for d(N–O3) and m(O3). The localization domain of d(N–O3) has also an elliptical shape; however, its volume is substantially smaller compared with the localization domains of d(N–O1) and d(N–O2), suggesting a weaker bond and less significant π interactions. This is particularly true for $FNO_3$. The localization domain of m(O3) has also an elliptical shape, but as opposed to the localization domains of m(O1) and m(O2), its longer axis is oriented perpendicular to the molecular plane. Again, this may be accounted for by the results of the NBO analysis in a straightforward way: LP2(O3) is absent owing to the existence of the O–X bond and thus only LP3(O3), which corresponds to a p-type lone pair NBO oriented perpendicular to the molecular plane, and the spherical $sp^2$-type lone pair are responsible for the shape of m(O3).

**Table 6. Electron populations (in e) of the monosynaptic (m(O) and m(N)) and disynaptic (d(N–O)) ELI-D basins**

| | d(N–O1) | d(N–O2) | d(N–O3) | m(O1) | m(O2) | m(O3) | m(N) |
|---|---|---|---|---|---|---|---|
| $NO_3^-$ | 1.76 | 1.78 | 1.79 | 5.90 | 5.90 | 5.90 | 0.31 |
| $HNO_3$ | 2.36 | 2.07 | 1.75 | 5.56 | 5.65 | 4.72 | – |
| $FNO_3$ | 1.90 | 1.90 | 0.99 | 5.48 | 5.44 | 5.61 | 0.80 |
| $KNO_3$ (XWR) | 2.08 | 1.71 | 1.70 | 5.73 | 5.91 | 5.91 | 0.17 |

Table 6 gives the electron populations of the valence basins. For $NO_3^-$, the populations of d(N–O) differ slightly, although the bonding properties are expected to be equivalent based on the 3-fold symmetry. This discrepancy may be attributed to errors of the numerical approach applied for the calculation of the basins. The populations of d(N–O) are well below two electrons, which is even less than one electron pair. The monosynaptic oxygen basins have a population of approximately six electrons at each of the three oxygen atoms, corresponding to approximately three electron pairs. At first glance, the populations of the valence basins of $NO_3^-$ suggest resonance structure **1** in Fig. 1 to be of greatest significance. However, it needs to be stated that monosynaptic basins are known to absorb a great part of the electron density of disynaptic basins whenever they are located directly next to each other.[42]

Interestingly, there are two additional monosynaptic basins located at the nitrogen atom (m(N)), which may be related to the p-orbital at the nitrogen that is involved in the π interactions. The bottom row of Fig. 6 shows iso-surfaces of the ELI-D at an iso-value that reveals the localization domains of m(N). This iso-surface nicely reflects the resonance, because the disynaptic N–O bond basins and the monosynaptic nitrogen basin are

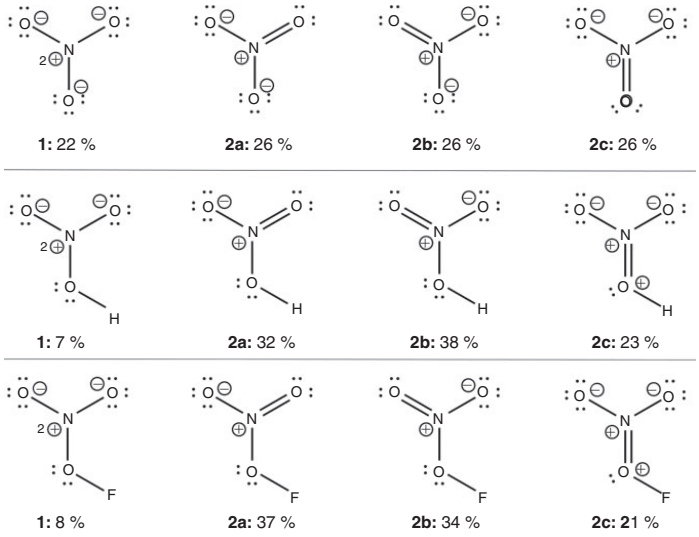


**Fig. 7.** Valence bond structures of $NO_3^-$, $HNO_3$, and $FNO_3$ and their weights.

perfectly connected at that specific iso-value, while they are disjointed from all other localization domains.

The greater double-bond character of the N–O1 and N–O2 bonds in $HNO_3$ is reflected by higher populations of d(N–O1) and d(N–O2) and lower populations of m(O1) and m(O2) compared with $NO_3^-$. There is no monosynaptic nitrogen basin obtained for $HNO_3$, but an iso-surface revealing regions of electron localization at the nitrogen atom are obtained nonetheless (see bottom row of Fig. 6). As for $NO_3^-$, this iso-surface gives a representation of the resonance system that, however, only involves the N–O1 and N–O2 bonds at that specific iso-value. Of course, at a lower iso-value, d(N–O3) will also be connected to d(N–O1) and d(N–O2), but the fact that the localization domains are disjointed at that specific iso-value suggests that the contribution of the N–O3 bond to the resonance system is less meaningful. This is also supported by a lower population of d(N–O3).

In contrast to $HNO_3$, a monosynaptic nitrogen basin with a significant electron population is obtained for $FNO_3$. Again, the iso-surface of $FNO_3$ depicted in the bottom row of Fig. 6 implies that only N–O1 and N–O2 significantly contribute to the resonance system. The electron populations of d(N–O1) and d(N–O2) are equivalent and below a value of two. They are lower compared with the populations of $HNO_3$; however, no monosynaptic nitrogen basin is obtained for $HNO_3$, so the electrons are only located inside d(N–O), whereas they are located inside d(N–O) and m(N) for $FNO_3$. The population of d(N–O3) is particularly small, confirming that the contribution of the N–O3 bond to the resonance system of $FNO_3$ is less significant.

### *Valence Bond Calculations*

VB calculations were performed only on $NO_3^-$, $HNO_3$, and $FNO_3$ from the theoretical wave functions. Only the four p-orbitals that constitute the π system were defined as active (there is one at the nitrogen atom and one at each of the three oxygen atoms), because they are the only ones required to account for the resonance structures depicted in Fig. 7. The VB wave function is calculated from a linear combination of the four localized wave functions corresponding to the four resonance structures of $NO_3^-$, $HNO_3$, and $FNO_3$ shown in Fig. 7. Ultimately, the VB calculation yields weights for each of the four resonance structures based on their energetic contributions to the total wave function, which are discussed in the following.

For $NO_3^-$, all four resonance structures are highly significant. Structures **2a–c** each make up 26 % of the resonance, accounting for a total contribution of 78 %. Structure **1** is also quite significant for $NO_3^-$ (22 % contribution), whereas it is less meaningful for the resonance in both $HNO_3$ (7 % contribution) and $FNO_3$ (8 % contribution). The major resonance structures for $HNO_3$ and $FNO_3$ are **2a** and **2b** with a combined contribution of 70 and 71 %, respectively. Again, it is shown that resonance structure **2b** has a higher weight than structure **2a** for $HNO_3$, whereas resonance structure **2a** has a higher weight than structure **2b** for $FNO_3$. Structure **2c** has a slightly lower but significant contribution to the resonance of $HNO_3$ and $FNO_3$, suggesting that there is a significant N–O3 double-bond character, although it has been more cumbersome to spot by other descriptors.

The VB calculations further confirm the results obtained from the previously investigated descriptors and relate them even more closely to the resonance structures considered throughout the study. Moreover, it has been shown that the resonance structures depicted in Figs 1 and 7 are sufficient to derive the complete wave function of $NO_3^-$, $HNO_3$, and $FNO_3$.

## Conclusions

We investigated the bonding situation in $NO_3^-$, $HNO_3$, $FNO_3$, and $KNO_3$ using a variety of bond analysis tools from theoretical and experimental data. From the simple Lewis model, the resonance structures in Fig. 1 appear to be the most significant ones. In fact, a combination of sophisticated bond analysis tools can quantify the significance of these structures relative to each

other. To the best of our knowledge, there has not been any other study attempting to investigate the bonding in $NO_3^-$ quantitatively, although it is often used as an example for the very fundamental concept of resonance.

All analysis tools have demonstrated that there is a significant double-bond character for the three equivalent N–O bonds in $NO_3^-$. The valence bond calculations have shown that it is possible to derive a wave function of $NO_3^-$ by defining one active orbital at the nitrogen and one at each of the three oxygen atoms. These orbitals, which are sufficient to account for the resonance outlined in Fig. 1, are almost exclusively constructed by p-orbitals perpendicular to the molecular plane. An equivalent picture is provided by the NBO analysis where significant interactions involving p-type lone pairs and a lone valency of p-type at the nitrogen atom are revealed. This is in close resemblance to the π system in aromatic species, such as in benzene. The Hückel rule (6π electrons delocalized in a perfectly planar system through p orbitals perpendicular to the plane) is fulfilled. In fact, a simple Hückel calculation, which treats the π system completely separately from the rest of the molecule, yields reasonable stabilization energies confirming that this approach is feasible.

Besides the existence of the π interactions, the NBO analysis also suggests another significant interaction: the oxygen lone pair of p-type (donor orbital), which is oriented parallel to the molecular plane, interacts with the N–O antibonds (acceptor orbitals). This interaction leads to the strengthening of the N–O bond, where the donor lone pair is located, and the weakening of the other N–O bonds. For the highly symmetric $NO_3^-$, these effects approximately compensate each other. This may, however, not be expected for $HNO_3$ and $FNO_3$: the NBO analysis shows that the N–O3 antibond is the most populated one as a result of the LP(O) → σ*(X–O) type interactions. The N–O3 antibond may only serve as an acceptor orbital owing to the lack of an appropriate donor lone pair at O3, and thus the N–O3 bond is significantly weakened.

Throughout this study, all descriptors have shown that the two terminal N–O bonds (N–O1 and N–O2) in $HNO_3$ and $FNO_3$ have a substantially higher double-bond character compared with the N–O bonds in $NO_3^-$. In contrast to that, the double-bond character of the N–O bond (N–O3) whose oxygen atom is bonded to H or F is significantly lower. In fact, this situation could not be unambiguously determined by some descriptors. Interestingly, the resonance in $HNO_3$ and $FNO_3$ is only slightly influenced by the very distinct nature of fluorine and hydrogen. A negative formal charge at the oxygen oriented to the same side as the O–F bond promotes the repulsion between both negatively charged atoms. Thus, structure **2a** is favoured over **2b**. For $HNO_3$, it is the other way around: in contrast to the fluorine, the hydrogen has a positive charge and thus a negative formal charge at the oxygen promotes the attraction between both oppositely charged atoms. Consequently, structure **2b** is favoured over **2a**. However, this perturbation of the resonance is quite small and cannot account for the high stability of $HNO_3$ compared with the instable $FNO_3$. Rather, the instability of $FNO_3$ may be associated with the F–O bond, which is known to be highly reactive.

It has also been shown that an XWR of crystalline $KNO_3$ gives bonding properties that are in good agreement with the ones obtained from theory alone. The $NO_3^-$ unit in $KNO_3$ is only slightly influenced by crystal effects because it is surrounded quite evenly by interacting potassium cations. It has clearly been demonstrated that XWR is superior to MM in terms of modelling electron density from the experiment when the residual density is considered. In addition, it offers a much wider range of analysis possibilities based on the fitted wave function. In the present study, for example, we introduced NBO analysis based on the fitted wave function and applied it for the first time.

Although $NO_3^-$, $HNO_3$, and $FNO_3$ are, at first glance, three simple compounds, details of their bonding situation are rather complex. Only a rationally chosen variety of complementary bonding analysis methods can reveal the bonding situation in full. This confirms the usefulness of simple models such as those of Lewis and Hückel, but highlights where departures from these models are significant and important to consider.

## Supplementary Material

Additional crystallographic information (bond lengths from IAM, MM, and HAR as well as plots of the probability density function), Bader and NPA charges for all atoms, additional results from the NBO analysis, atomic coordinates from the geometry optimizations, and the corresponding observed and calculated structure factors of the high-resolution $KNO_3$ dataset are available on the Journal's website. The crystallographic information files (CIFs) for all three models IAM, MM, HAR are deposited with the Inorganic Crystal Structure Database (CSD no. 433754).

## Conflicts of Interest

The authors declare no conflicts of interest.

## Acknowledgements

We thank Professor Graham S. Chandler for suggesting a study of $FNO_3$, which triggered all the other considerations that have culminated in this paper. We also salute him for his outstanding career. We thank Dr Enno Lork and Mrs Sarah Matz for their constant help and support regarding the diffractometer use at the University of Bremen. S. Grabowsky thanks the German Research Foundation (Deutsche Forschungsgemeinschaft, DFG) for funding within the Emmy Noether project GR 4451/1–1.

## References

[1] (a) G. N. Lewis, *J. Am. Chem. Soc.* **1916**, *38*, 762. doi:10.1021/JA02261A002
(b) G. N. Lewis, *Valence and the Structure of Atoms and Molecules* **1923** (American Chemical Society: New York, NY).
(c) G. H. Purser, *J. Chem. Educ.* **1999**, *76*, 1013. doi:10.1021/ED076P1013

[2] Y. Mo, P. von Ragué Schleyer, *Chem. – Eur. J.* **2006**, *12*, 2009. doi:10.1002/CHEM.200500376

[3] M. K. Cyranski, T. M. Krygowski, A. R. Katritzky, P. von Ragué Schleyer, *J. Org. Chem.* **2002**, *67*, 1333. doi:10.1021/JO016255S

[4] (a) F. Weinhold, C. R. Landis, *Valency and Bonding* **2005 (**Cambridge University Press: Cambridge, UK).
(b) C. L. Deasy, *Chem. Rev.* **1945**, *36*, 145. doi:10.1021/CR60114A001
(c) A. E. Reed, P. von Ragué Schleyer, *J. Am. Chem. Soc.* **1990**, *112*, 1434. doi:10.1021/JA00160A022

[5] (a) X. Fradera, M. A. Austen, R. F. W. Bader, *J. Phys. Chem. A* **1999**, *103*, 304. doi:10.1021/JP983362Q
(b) L. Zhao, M. Hermann, N. Holzmann, G. Frenking, *Coord. Chem. Rev.* **2017**, *344*, 163. doi:10.1016/J.CCR.2017.03.026

[6] M. Fugel, J. Beckmann, D. Jayatilaka, G. V. Gibbs, S. Grabowsky, under review in *Chem. – Eur. J.*

[7] E. Hupf, M. Olaru, C. I. Rat, M. Fugel, C. B. Hübschle, E. Lork, S. Grabowsky, S. Mebs, J. Beckmann, *Chem. – Eur. J.* **2017**, *23*, 10699. doi:10.1002/CHEM.201702201

[8] (a) J. O. Lundberg, M. T. Gladwin, A. Ahluwalia, N. Benjamin, N. S. Bryan, A. Butler, P. Cabrales, A. Fago, M. Feelisch, P. C. Ford, B. A. Freeman, M. Frenneaux, J. Friedman, M. Kelm, C. G. Kevil, D. B.

Kim-Shapiro, A. V. Kozlov, J. R. Lancaster, Jr, D. J. Lefer, K. McColl, K. McCurry, R. P. Patel, J. Petersson, T. Rassaf, V. P. Reutov, G. B. Richter-Addo, A. Schechter, S. Shiva, K. Tsuchiya, E. E. van Faassen, A. J. Webb, B. S. Zuckerbraun, J. L. Zweier, E. Weitzberg, *Nat. Chem. Biol.* **2009**, *5*, 865. doi:10.1038/NCHEMBIO.260
(b) R. F. Spalding, M. E. Exner, *J. Environ. Qual.* **1993**, *22*, 392. doi:10.2134/JEQ1993.00472425002200030002X
(c) A. S. Umar, M. Iqbal, *Agron. Sustain. Dev.* **2007**, *27*, 45. doi:10.1051/AGRO:2006021

[9] (a) M. R. Waterland, D. Stockwell, A. Myers Kelley, *J. Chem. Phys.* **2001**, *114*, 6249. doi:10.1063/1.1355657
(b) M. R. Waterland, A. Myers Kelley, *J. Chem. Phys.* **2000**, *113*, 6760. doi:10.1063/1.1310615
(c) X.-B. Wang, X. Yang, L.-S. Wang, J. B. Nicholas, *J. Chem. Phys.* **2002**, *116*, 561. doi:10.1063/1.1427067

[10] B. Casper, D. A. Dixon, H.-G. Mack, S. E. Ulic, H. Willner, H. Oberhammer, *J. Am. Chem. Soc.* **1994**, *116*, 8317. doi:10.1021/JA00097A044

[11] N. K. Hansen, P. Coppens, *Acta Crystallogr. Sect. A* **1978**, *34*, 909. doi:10.1107/S0567739478001886

[12] M. Woinska, D. Jayatilaka, B. Dittrich, R. Flaig, P. Luger, K. Wozniak, P. M. Dominiak, S. Grabowsky, *ChemPhysChem* **2017**, *18*, 3334. doi:10.1002/CPHC.201700810

[13] R. Herbst-Irmer, J. Henn, J. J. Holstein, C. B. Hübschle, B. Dittrich, D. Stern, D. Kratzert, D. Stalke, *J. Phys. Chem. A* **2013**, *117*, 633. doi:10.1021/JP309985E

[14] J. M. Krzeszczakowska, L. A. Malaspina, H.-B. Bürgi, Y.-S. Chen, C. B. Hübschle, B. Dittrich, M. Woińska, D. Jayatilaka, S. Grabowsky, Manuscript in preparation.

[15] S. Grabowsky, D. Jayatilaka, S. Mebs, P. Luger, *Chem. – Eur. J.* **2010**, *16*, 12818. doi:10.1002/CHEM.201002061

[16] G. Frenking, S. Shaik, *The Chemical Bond: Fundamental Aspects of Chemical Bonding* **2014** (Wiley-VCH: New York, NY).

[17] F. Weinhold, *J. Comput. Chem.* **2012**, *33*, 2363. doi:10.1002/JCC.23060

[18] (a) R. F. W. Bader, *Chem. Rev.* **1991**, *91*, 893. doi:10.1021/CR00005A013
(b) R. F. W. Bader, *Atoms in Molecules – A Quantum Theory* **1995** (Clarendon Press: Oxford).

[19] P. L. A. Popelier, *Intermolecular Forces and Clusters I* **2005** (Springer: Heidelberg).

[20] S. Mebs, R. Kalinowski, S. Grabowsky, D. Förster, R. Kickbusch, E. Justus, W. Morgenroth, C. Paulmann, P. Luger, D. Gabel, D. Lentz, *Inorg. Chem.* **2011**, *50*, 90. doi:10.1021/IC1013158

[21] R. F. Bader, *J. Phys. Chem. A* **1998**, *102*, 7314. doi:10.1021/JP981794V

[22] R. F. Bader, A. Streitwieser, A. Neuhaus, K. E. Laidig, P. Speers, *J. Am. Chem. Soc.* **1996**, *118*, 4959. doi:10.1021/JA953563X

[23] A. E. Reed, L. A. Curtiss, F. Weinhold, *Chem. Rev.* **1988**, *88*, 899. doi:10.1021/CR00088A005

[24] M. D. Gould, C. Taylor, S. K. Wolff, G. S. Chandler, D. Jayatilaka, *Theor. Chem. Acc.* **2008**, *119*, 275. doi:10.1007/S00214-007-0282-X

[25] M. Kohout, *Int. J. Quantum Chem.* **2004**, *97*, 651. doi:10.1002/QUA.10768

[26] W. Wu, P. Su, S. Shaik, P. C. Hiberty, *Chem. Rev.* **2011**, *111*, 7557. doi:10.1021/CR100228R

[27] M. J. Frisch, G. W. Trucks, H. B. Schlegel, G. E. Scuseria, M. A. Robb, J. R. Cheeseman, G. Scalmani, V. Barone, B. Mennucci, G. A. Petersson, H. Nakatsuji, M. Caricato, X. Li, H. P. Hratchian, A. F. Izmaylov, J. Bloino, G. Zheng, J. L. Sonnenberg, M. Hada, M. Ehara, K. Toyota, R. Fukuda, J. Hasegawa, M. Ishida, T. Nakajima, Y. Honda, O. Kitao, H. Nakai, T. Vreven, J. A. Montgomery Jr, J. E. Peralta, F. Ogliaro, M. Bearpark, J. J. Heyd, E. Brothers, K. N. Kudin, V. N. Staroverov, R. Kobayashi, J. Normand, K. Raghavachari, A. Rendell, J. C. Burant, S. S. Iyengar, J. Tomasi, M. Cossi, N. Rega, J. M. Millam, M. Klene, J. E. Knox, J. B. Cross, V. Bakken, C. Adamo, J. Jaramillo, R. Gomperts, R. E. Stratmann, O. Yazyev, A. J. Austin, R. Cammi, C. Pomelli, J. W. Ochterski, R. L. Martin, K. Morokuma, V. G. Zakrzewski, G. A. Voth, P. Salvador, J. J. Dannenberg, S. Dapprich, A. D. Daniels, Ö. Farkas, J. B. Foresman, J. V. Ortiz, J. Cioslowski, D. J. Fox, *Gaussian 09 (Revision D. 01)* **2009** (Gaussian, Inc.: Wallingford, CT).

[28] T. A. Keith, *AIMall (Version 13.05. 06)* **2013** (TK Gristmill Software: Overland Park, KS).

[29] E. D. Glendening, C. R. Landis, F. Weinhold, *J. Comput. Chem.* **2013**, *34*, 1429. doi:10.1002/JCC.23266

[30] L. Song, Y. Mo, Q. Zhang, W. Wu, *J. Comput. Chem.* **2005**, *26*, 514. doi:10.1002/JCC.20187

[31] M. Kohout, *DGrid, Version 5.0* **2017** (Dresden).

[32] Bruker AXS Inc., *APEX3* **2017** (Bruker AXS: Karlsruhe).

[33] G. M. Sheldrick, *Acta Crystallogr. Sect. A* **2015**, *71*, 3. doi:10.1107/S2053273314026370

[34] A. Volkov, P. Macchi, L. J. Farrugia, C. Gatti, P. R. Mallinson, T. Richter, T. Koritsanszky, *XD 2006* (*Version 5.42)* **2006**.

[35] C. K. Johnson, *Acta Crystallogr. A* **1969**, *25*, 187. doi:10.1107/S0567739469000325

[36] D. Jayatilaka, D. J. Grimwood, *Tonto: A Fortran-Based Object-Oriented System for Quantum Chemistry and Crystallography*, in *Computational Science – ICCS 2003*, Part 4 (Eds P. M. A. Sloot, D. Abramson, A. V. Bogdanov, J. J. Dongarra, A. Y. Zomaya, Y. E. Gorbachev) **2003**, pp. 142–151 (Springer Verlag: New York, NY). The program can be obtained free of charge from https://github.com/dylan-jayatilaka/tonto (verified 16 January 2018).

[37] (a) D. Jayatilaka, B. Dittrich, *Acta Crystallogr. A* **2008**, *64*, 383. doi:10.1107/S0108767308005709
(b) S. C. Capelli, H.-B. Bürgi, B. Dittrich, S. Grabowsky, D. Jayatilaka, *IUCrJ* **2014**, *1*, 361. doi:10.1107/S2052252514014845

[38] (a) D. Jayatilaka, *Phys. Rev. Lett.* **1998**, *80*, 798. doi:10.1103/PHYSREVLETT.80.798
(b) D. Jayatilaka, D. J. Grimwood, *Acta Crystallogr. Sect. A* **2001**, *57*, 76. doi:10.1107/S0108767300013155

[39] T. L. Cottrell, *The Strength of Chemical Bonds* **1958** (Butterworth's Publications Ltd: London).

[40] (a) C. Gatti, R. Bianchi, R. Destro, F. Merati, *J. Mol. Struct. THEOCHEM* **1992**, *255*, 409. doi:10.1016/0166-1280(92)85022-D
(b) B. Engels, T. C. Schmidt, C. Gatti, T. Schirmeister, R. F. Fink, in *Electron Density and Chemical Bonding II* (Ed. D. Stalke) **2011**, Structure and Bonding, Vol. 147, pp. 47–97 (Springer: Berlin).

[41] D. J. Grimwood, I. Bytheway, D. Jayatilaka, *J. Comput. Chem.* **2003**, *24*, 470. doi:10.1002/JCC.10238

[42] Although it occurs in many examples (e.g. (a) F. Kraus, N. Korber, *Chem. – Eur. J.* **2005**, *11*, 5945; (b) S. Grabowsky, P. Luger, J. Buschmann, T. Schneider, T. Schirmeister, A. N. Sobolev, D. Jayatilaka, *Angew. Chem. Int. Ed.* **2012**, *51*, 6776), there is no detailed discussion about this phenomenon in the literature. We also refer to private communications with Miroslav Kohout.

# Chapter 8

# Revisiting a Historical Concept by Using Quantum Crystallography: Are Phosphate, Sulfate and Perchlorate Anions Hypervalent?

In this study, the historical concept of hypervalency in phosphate, sulfate and perchlorate anions is tackled by a *complementary bonding analysis*. For this work, we had the chance to create the front cover of *Chemistry – A European Journal*, which is shown before the paper. The paper was published in 2019. In the following, my contributions to this work are listed:

- I wrote 90% of the text
- I carried out the synthesis and crystallization of all compounds
- I partly performed the X-ray diffraction experiments
  - 100% of the home measurements of $MgNH_4PO_4 \cdot 6\,H_2O$ and $Li_2SO_4 \cdot H_2O$
  - ≈30% of the home measurement of the potassium perchlorate crystals
  - The measurments performed at SPring-8 (Japan) were carried out in a team consisting of five people, including myself
- I performed the data reductions and refinements of the crystal structures
- I performed the *complementary bonding analysis*
- I am responsible for all figures and tables
- I designed about 90% of the front cover

# CHEMISTRY
## A European Journal

www.chemeurj.org

A Journal of

ChemPubSoc Europe

2019-25/26


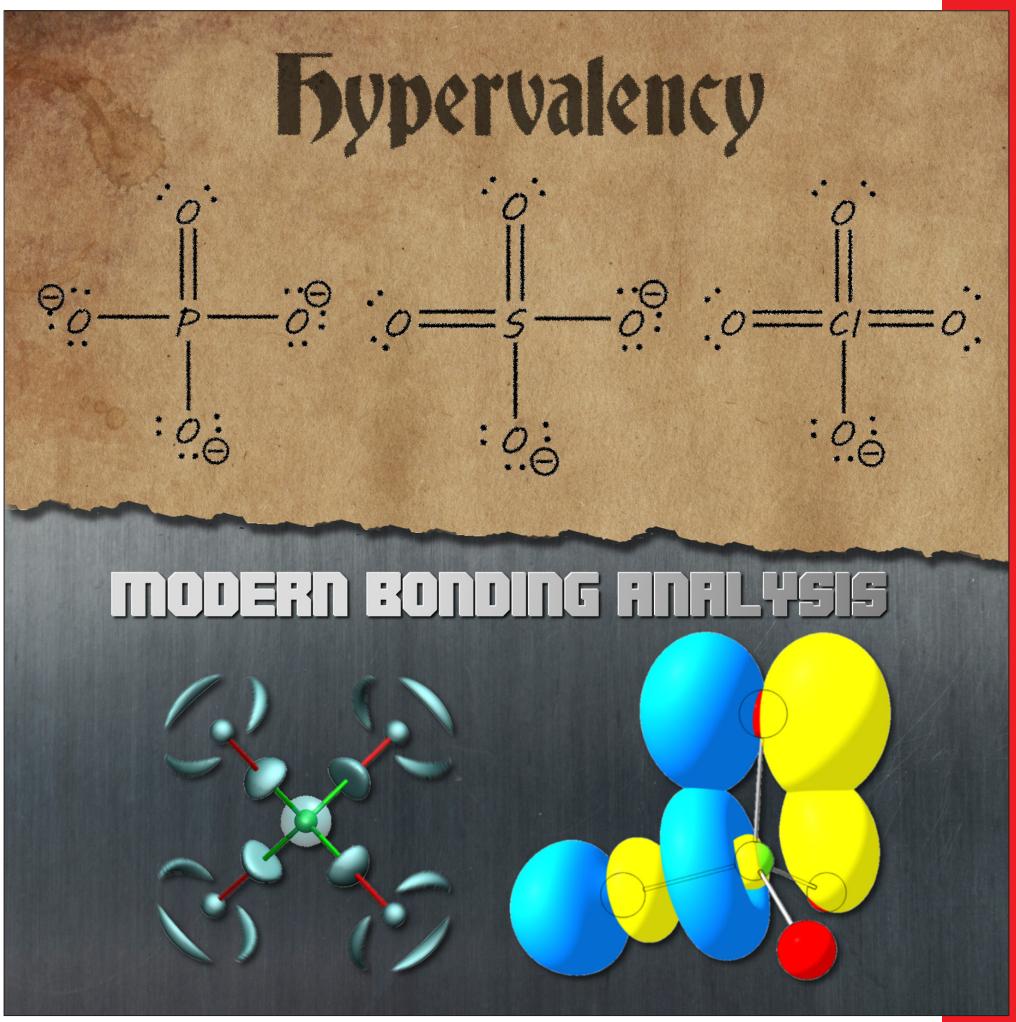


**Front Cover:**
*S. Grabowsky et al.*
Revisiting a Historical Concept by Using Quantum Crystallography: Are Phosphate, Sulfate and Perchlorate Anions Hypervalent?


Supported by

ACES Asian Chemical Editorial Society

WILEY-VCH

ChemPubSoc Europe

DOI: 10.1002/chem.201901182

CHEMISTRY
A European Journal
Cover Profile

# Revisiting a Historical Concept by Using Quantum Crystallography: Are Phosphate, Sulfate and Perchlorate Anions Hypervalent?

*Dedicated to Professor Dietmar Stalke on the occasion of his 60th birthday*


Malte Fugel


Lorraine A. Malaspina


Rumpa Pal


Sajesh P. Thomas


Ming W. Shi


Mark A. Spackman

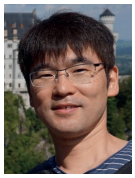
Kunihisa Sugimoto


Simon Grabowsky

Universität Bremen

THE UNIVERSITY OF WESTERN AUSTRALIA

JASRI
公益財団法人 高輝度光科学研究センター
Japan Synchrotron Radiation Research Institute (JASRI)

筑波大学
University of Tsukuba

AARHUS UNIVERSITY

**Invited for the cover of this issue is the group of Simon Grabowsky at the University of Bremen. The image depicts one of the main messages of the present study: Lewis structure representations are not sufficient to understand chemical bonding. Read the full text of the article at 10.1002/chem.201806247.**

***What is your motivation to study chemical bonding?***

Chemical bonding is, undoubtedly, one of the most significant concepts in chemistry. However, some aspects of this concept (such as hypervalency) are debatable and often based on misconceptions. In our work, we use a combination of bonding analysis methods based on theory and experiment and based on different spaces (real, orbital and energy space) to get a fresh perspective on chemical bonding. This helps to clarify the bonding situation in systems in which the Lewis picture of chemical bonding reaches its limits.

***What was the inspiration for this cover design?***

The cover picture shows hypervalent bonding representations of phosphate, sulfate and perchlorate anions, which are printed on an old parchment paper. It reflects the fact that these bonding representations are historic and obsolete. The ripped parchment reveals a modern perspective on hypervalency, which we uncover using a complementary bonding analysis. Hypervalency is indeed a useful concept, but it needs to be seen in a new light.

***How important is collaboration in science?***

The eight collaborators are from six nations (Germany, Brazil, India, China, Australia, and Japan) across four different continents. This international team met in Japan to perform X-ray diffraction experiments at the SPring-8 synchrotron for the compounds analyzed in this study. We believe that, especially in times with increasing intolerance and xenophobia, collaboration in science, which knows no borders but only interesting topics, can help to overcome such unbearable social tendencies. We also want to take this opportunity to remember our team member and good friend Ming, who passed away in a car crash before this work could come to a conclusion, and just before he could receive his Ph.D.

ChemPubSoc Europe

DOI: 10.1002/chem.201806247

CHEMISTRY A European Journal Full Paper

Hypervalency |*Hot Paper*|

# Revisiting a Historical Concept by Using Quantum Crystallography: Are Phosphate, Sulfate and Perchlorate Anions Hypervalent?

Malte Fugel,[a] Lorraine A. Malaspina,[a] Rumpa Pal,[a, d] Sajesh P. Thomas,[b, e] Ming W. Shi†,[b] Mark A. Spackman,[b] Kunihisa Sugimoto,[c] and Simon Grabowsky*[a]

*Dedicated to Professor Dietmar Stalke on the occasion of his 60th birthday*

**Abstract:** There are many examples of atoms in molecules that violate Lewis' octet rule, because they have more than four electron pairs assigned to their valence. These atoms are referred to as hypervalent. However, hypervalency may be regarded as an artifact arising from Lewis' description of molecules, which is based on the assumption that electrons are localized in two-center two-electron bonds and lone pairs. In the present paper, the isoelectronic phosphate ($PO_4^{3-}$), sulfate ($SO_4^{2-}$) and perchlorate ($ClO_4^-$) anions were examined with respect to the concept of hypervalency. Lewis formulas containing a hypervalent central atom exist for all three anions. Based on X-ray wavefunction refinements of high-resolution X-ray diffraction data of representative crystal structures ($MgNH_4PO_4{\cdot}6H_2O$, $Li_2SO_4{\cdot}H_2O$, and $KClO_4$), complementary bonding analyses were performed. In this way, experimental information from the new field of quantum crystallography validate long-known facts, or refute long-standing misunderstandings. It is shown that the P–O and S–O bonds are highly polarized covalent bonds and, thus, the increase in the valence population following three-center four-electron bonding is not sufficient to yield hypervalent phosphorus or sulfur atoms, respectively. However, for the highly covalent Cl–O bond, most bonding indicators imply a hypervalent chlorine atom.

## Introduction

The rule of eight,[1] more commonly known as the octet rule,[2] accounts for Lewis' finding that most atoms in molecules have eight electrons or, rather, four electron pairs in their valence shell.[3,4] However, there are some prominent examples of period 3 elements in molecules that, at first glance, exceed the octet rule, because Lewis structures devoid of formal charges exist that contain atoms with more than eight valence electrons, for example, $SF_6$ and $PCl_5$. Such atoms are referred to as hypervalent.[5] In the past, it was assumed that d orbitals contribute to the bonding of these molecules, however, population analyses have shown that this is not the case for bonds containing period 3 elements.[6–8] For that reason, alternative models have emerged to resolve the bonding in hypervalent molecules (we are aware that only atoms can be regarded as hypervalent; however, for simplicity, we refer to a molecule as hypervalent if it contains a hypervalent atom).

Rundle and Pimentel have introduced explanations based on three-center four-electron (3c–4e) bonding,[9–12] for which Coulson has formulated a valence bond variant.[13] Accordingly, the bonding involving two electron pairs and three atoms A, B and C may be expressed schematically by three resonance structures corresponding to $A–B^+\ ^-C$, $A^-\ ^+B–C$ and $A^-\ B^{2+}\ ^-C$. From a localized orbital perspective, this bonding type is indicated through negative hyperconjugation, that is, the donation of electron density from an occupied n-, p- or π-orbital to a σ*-orbital.[8,14–16] According to the original octet rule, two bonding electrons are assigned to the valence of both bonded atoms regardless of bond polarization.[3,5] However, Lewis discussed already in his seminal paper in 1916[1] that bond polarization influences the valence electron count, which was later termed the modified octet rule.[16–18] It is not rigorously defined, but it includes that, if the bond is polarized towards one

[a] *M. Fugel, L. A. Malaspina, Dr. R. Pal, Prof. Dr. S. Grabowsky*
*Department 2-Chemistry/Biology*
*Institute of Inorganic Chemistry and Crystallography, University of Bremen*
*Leobener Str. 3 and 7, 28359 Bremen (Germany)*
*E-mail: simon.grabowsky@uni-bremen.de*

[b] *Dr. S. P. Thomas, M. W. Shi, Prof. M. A. Spackman*
*School of Molecular Sciences, University of Western Australia*
*35 Stirling Highway, Perth WA 6009 (Australia)*

[c] *Dr. K. Sugimoto*
*SPring-8, Japan Synchrotron Radiation Research Institute*
*1-1-1 Kouto, Sayo-cho, Sayo-gun, Hyogo 679-5198 (Japan)*

[d] *Dr. R. Pal*
*Current address: Division of Physics*
*Faculty of Pure and Applied Sciences, University of Tsukuba*
*1-1-1 Tennodai, Tsukuba, Ibaraki, 305-8571 (Japan)*

[e] *Dr. S. P. Thomas*
*Current address: Interdisciplinary Nanoscience Center - INANO-Kemi*
*Aarhus University, Langelandsgade 140, 8000 Aarhus C (Denmark)*

[†] *Deceased.*

*Supporting information and the ORCID identification number(s) for the author(s) of this article can be found under: https://doi.org/10.1002/chem.201806247.*

ChemPubSoc Europe

CHEMISTRY A European Journal Full Paper

of the atoms, less than two electrons must be assigned to the valence of the other atom, because in polarized bonds the electron pair is not shared equally. Consequently, an atom may follow the modified octet rule, although the original version of the rule is violated.[17,19] Furthermore, there is the theory of recoupled bonding[20,21] and increased-valence structures[22] for hypervalency, as well as a classification by Green and Parkin.[23]

For the most part, the concept of hypervalency has been studied based on theoretical wavefunctions.[24–28] However, quantum crystallographic techniques allow experimental access to wavefunctions and charge densities.[29,30] Stalke and co-workers have pioneered the idea of performing a bonding analysis based on experimentally obtained charge densities for putatively hypervalent molecules.[31–34] Grabowsky et al. have studied the concept of hypervalency in $SO_2$ through X-ray wavefunction refinement.[35] An experimental and theoretical bonding analysis with respect to electron density descriptors was performed on the sulfate anion ($SO_4^{2-}$), which may be regarded as a textbook example for the concept of hypervalency.[36]

The phosphate ($PO_4^{3-}$) and perchlorate anions ($ClO_4^-$) are isoelectronic to the sulfate anion and hypervalent Lewis structures are also obtained for them (see Figure 1).[37] However,

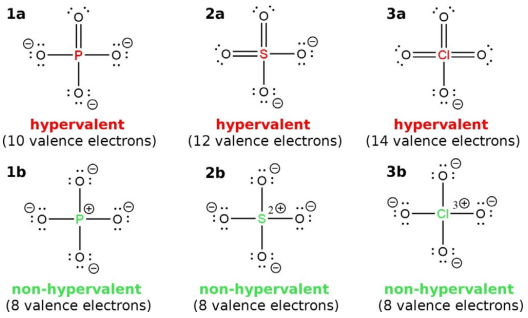


**Figure 1.** Hypervalent and non-hypervalent Lewis structures of the phosphate ($PO_4^{3-}$), sulfate ($SO_4^{2-}$) and perchlorate ($ClO_4^-$) anions (equivalent resonance forms are not depicted).

non-hypervalent Lewis structures, which require the introduction of formal charges at the central atom and at the oxygen atoms, also exist for the phosphate, sulfate, and perchlorate anions (see Figure 1). In fact, the experimental charge density study on the sulfate anion demonstrated that Lewis structure **2b** is most significant and, thus, the central sulfur atom must be regarded as non-hypervalent, because of the strong S–O polarization.[36]

However, the bonding situation in the phosphate, sulfate, and perchlorate anions remains peculiar: the formal charge of the central atom increases in the non-hypervalent Lewis structures from phosphate (+1) to chlorine (+3). Consequently, the charge separation should be the highest between the chlorine and oxygen atoms of the perchlorate and the lowest between the phosphorus and oxygen atoms of the phosphate. However, the electronegativity increases from phosphorus to chlorine, so the Cl–O bond should be the least polarized bond and, thus, the charge separation between Cl and O should be the lowest. Even from that simple assessment, it becomes clear that a single Lewis formula is insufficient to account for the bonding situation of these anions. Negative hyperconjugation can be expected to be highly significant in these anions and since the population of antibonds can potentially lead to more than eight valence electrons, there is a possibility for the phosphate, sulfate and perchlorate anions to be hypervalent.

Naively speaking, it should be an easy task to determine whether an atom is hypervalent, because it "only" requires the counting of valence electrons. However, there are many definitions of an atom (such as Bader's formalism[39] or methods based on natural atomic orbitals[40]) and, thus, an atom may be either hypervalent or non-hypervalent depending on the method used to define the atom. Therefore, it is crucial to perform a complementary bonding analysis that combines different bonding descriptors from real space and orbital space, so that no aspect of bonding is neglected or missed.[41–43]

In the present paper, the bonding situation in the isoelectronic phosphate, sulfate and perchlorate anions is investigated with respect to the concept of hypervalency. Ultimately, we want to answer the question whether it is a good practice to call these anions hypervalent. For that purpose, complementary bonding analyses for the isolated anions from theoretical calculations are compared with the same analyses from experimental quantum crystallographic models in the solid state based on X-ray wavefunction refinements (XWR).[44,45] The crystal structures considered for the experimental studies are struvite ($MgNH_4PO_4{\cdot}H_2O$),[46] lithium sulfate ($Li_2SO_4{\cdot}H_2O$)[47] and potassium perchlorate ($KClO_4$),[48] see Figure 2. They were obtained from low-temperature high-resolution single-crystal X-ray diffraction experiments.

The bond analysis methods applied in the present study may be assigned to two different categories, namely, real-space and orbital-space indicators. Real-space indicators analyze a real space function topologically. In the quantum theory of atoms in molecules (QTAIM), introduced by Bader, this function corresponds to the electron density.[39,49,50] The electron localizability indicator (ELI), a real-space function that measures how localized electrons are, can also be topologically analyzed.[51,52] The notion of an orbital is absent in both of these methods, but the orbital picture cannot be disregarded when investigating hypervalency. Hence, natural bond orbital (NBO) and natural resonance theory (NRT) techniques must be considered to complement the real space picture.[14,40,53] A joint application of these techniques—a complementary bonding analysis—has been proven to be an effective approach for the study of a variety of bonding types.[42,43]

## Results and Discussion

### Geometry and intermolecular interactions

The isolated $PO_4^{3-}$, $SO_4^{2-}$ and $ClO_4^-$ anions have a $T_d$ symmetry, which inflicts four equidistant X–O bond. Henceforth, we will

ChemPubSoc Europe

CHEMISTRY
A European Journal
Full Paper

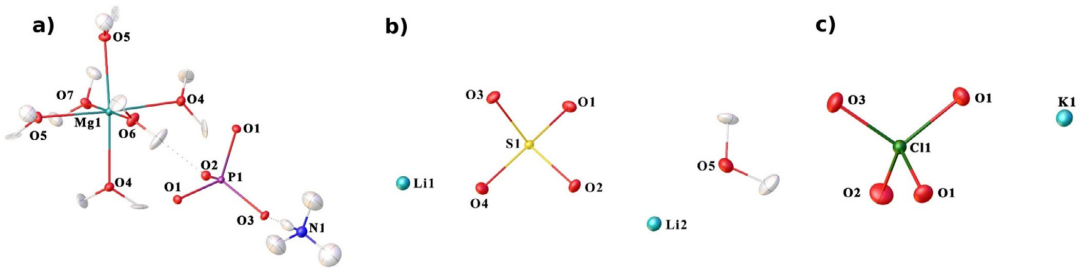


**Figure 2.** Experimental crystal structures (formula units, not asymmetric units) of a) struvite ($MgNH_4PO_4{\cdot}6H_2O$), b) lithium sulfate ($Li_2SO_4{\cdot}H_2O$) and c) potassium perchlorate ($KClO_4$) obtained from Hirshfeld atom refinement; the ellipsoids are given at a 50% probability level; pictures generated with Olex2, see Ref. [38].

only give a single value for the theoretically obtained bonding properties, because they are equivalent for all four X–O bonds. For the experimental structures, the crystal environment leads to a lower symmetry, and, thus, the X–O bond lengths are no longer equivalent. For struvite ($MgNH_4PO_4{\cdot}6H_2O$) and $KClO_4$, a mirror plain intersects the $PO_4^{3-}$ and $ClO_4^-$ units, respectively. Consequently, there are only three independent X–O bonds and, hence, only three bonding properties will be presented for these anions. The $SO_4^{2-}$ unit in $Li_2SO_4{\cdot}H_2O$ is located in the lowest symmetry environment—all four bond lengths are independent. Table 1 gives an overview of all X–O bond lengths obtained from geometry optimizations and Hirshfeld atom refinements (HARs). For more computational and experimental details, see the Experimental Section.

**Table 1.** X–O bond lengths in Å from theory (B3LYP/aug-cc-pVTZ and CCSD/aug-cc-pVTZ level of theory) and Hirshfeld atom refinement.

| Method | Bond | Phosphate | Sulfate | Perchlorate |
|---|---|---|---|---|
| B3LYP | X–O | 1.5940 | 1.5164 | 1.4792 |
| CCSD | X–O | 1.5859 | 1.5034 | 1.4599 |
| HAR | X–O1 | 1.5416(2) | 1.4785(2) | 1.4485(2) |
| HAR | X–O2 | 1.5438(2) | 1.4801(2) | 1.4320(3) |
| HAR | X–O3 | 1.5494(2) | 1.4788(2) | 1.4401(3) |
| HAR | X–O4 | – | 1.4646(1) | – |

The bond lengths obtained at the CCSD/aug-cc-pVTZ level of theory are somewhat shorter than the respective bond lengths calculated at a B3LYP/aug-cc-pVTZ level of theory. The bond lengths obtained from HAR are, in turn, shorter than those theoretically obtained. However, all methods agree that the P–O bonds are the longest and the Cl–O bonds are the shortest. We expect some of the bonding properties to be influenced by the environment, because some of the oxygen atoms are involved in hydrogen bonds or ion-dipole interactions. In struvite, the oxygen atoms of the $PO_4^{3-}$ unit are involved in strong hydrogen bonds involving neighboring water and ammonia molecules (see Figure 2). In $Li_2SO_4{\cdot}H_2O$, the oxygen atoms form hydrogen bonds and strong ion–dipole complexes involving the lithium atoms. In $KClO_4$, there are only weak interactions between the potassium and oxygen atoms. In the Supporting Information, we present Hirshfeld surface fingerprint plots, which give a representation of the strengths of these interactions. However, despite the existence of these interactions of different strengths, the deviation between the symmetry-independent bond lengths in the experimental structures is small. Therefore, the crystal environment only has a minor effect on the bond lengths of the $PO_4^{3-}$, $SO_4^{2-}$ and $ClO_4^-$ units. It is not the purpose of this study to investigate the effect of the crystalline environment on the intramolecular bonding descriptors. Certainly, the results in this study show that the intermolecular interactions do affect the X–O bonds, but not to an extent that would impair the analysis of the nature of the X–O bonding. A detailed analysis of the intermolecular interactions can be found in the Supporting Information.

### Natural bond orbitals

The NBO analysis yields localized orbitals that may either be related to features of conventional Lewis structures or to non-Lewis orbitals, such as extravalent Rydberg orbitals or valence antibonds.[14] Analogous Lewis-type NBOs are obtained for the phosphate, sulfate and perchlorate anions: there is one $\sigma$(X–O) orbital for each of the four X–O bonds and three lone pair orbitals for each of the four oxygen atoms. Two of the oxygen lone pairs are of p type, that is, they are (almost) completely made up of oxygen $2p_x$ and $2p_y$ orbitals, respectively. The remaining lone pair is a $sp^{\lambda}$ hybrid orbital (in which $\lambda$ is the hybridization coefficient) which exhibits a high s character (see the Supporting Information for the composition of all lone pair NBOs).

Accordingly, if only taking the Lewis type NBOs into account, the non-hypervalent Lewis structures **1b**, **2b**, and **3b** are suggested for the phosphate, sulfate and perchlorate anions. However, the Lewis-type NBOs alone are only a good approximation of the actual bonding situation if the bonds and lone pairs are highly localized, that is, if all Lewis type NBOs have a population of $N=2$ and if the non-Lewis type orbitals are unoccupied. However, in the phosphate, sulfate, and perchlorate anions, the orbital populations suggest a highly delocalized bonding situation. Consequently, Lewis structures **1b**, **2b**, and **3b** represent it only poorly.

ChemPubSoc Europe

CHEMISTRY A European Journal Full Paper

The electron populations of the p-type and $sp^2$-type lone pairs, which are listed in Table 2, differ significantly. The $sp^2$-type lone pairs have populations of $N \approx 2$ and may therefore be regarded as localized. In contrast, the p-type lone pairs are delocalized because their populations are substantially lower than $N = 2$. A large amount of electron density is withdrawn from the p-type lone pairs because they are involved in strong hyperconjugative interactions, in which they serve as donor orbitals. The σ*(X–O) antibonds are the corresponding acceptor orbitals involved in this interaction. They are, consequently, slightly occupied. Both the donor and acceptor orbitals are depicted in Figure 3. As mentioned in the Introduction, hyperconjugative interactions may be attributed to 3c–4e bonding. Strong hyperconjugative interactions result in low oxygen lone pair populations and, consequently, in high populations of the σ*(X–O) antibonds. Judging from the parameters obtained from the theoretical NBO, which are listed in Table 2, the hyperconjugative interactions are the strongest in the perchlorate, whereas they are slightly weaker in the phosphate and sulfate anions. According to the NBO from XWR, the oxygen lone pair populations are similar to those of the theoretical NBO, although not all oxygen lone pair populations of the phosphate are higher than those of the sulfate. However, on average, the lone pair populations of the phosphate anion are the highest and those of the perchlorate anion are the lowest. The average lone pair populations from XWR are somewhat larger than those obtained from theory and the average populations of the X-O antibonds are, in turn, somewhat lower compared to theory.

**Table 2.** Properties obtained from the theoretical and experimental NBO analyses: The electron populations *N* (in e) of the $sp^2$- and p-type oxygen lone pairs as well as of the σ*(X–O) antibond. LP = lone pair.

| | | $LP_{sp^2}(O)$ | $LP_p(O)$ | | σ*(X–O) |
|---|---|---|---|---|---|
| | | *N*(LP1) | *N*(LP2) | *N*(LP3) | *N* |
| | | Theory | | | |
| $PO_4^{3-}$ | – | 1.98 | 1.91 | 1.91 | 0.15 |
| $SO_4^{2-}$ | – | 1.98 | 1.88 | 1.88 | 0.20 |
| $ClO_4^-$ | – | 1.99 | 1.84 | 1.84 | 0.25 |
| | | XWR | | | |
| $PO_4^{3-}$ | O1 | 1.98(1) | 1.92(3) | 1.91(3) | 0.13(2) |
| | O2 | 1.98(1) | 1.92(1) | 1.90(2) | 0.12(2) |
| | O3 | 1.97(1) | 1.93(1) | 1.89(1) | 0.12(1) |
| $SO_4^{2-}$ | O1 | 1.98(1) | 1.91(1) | 1.88(2) | 0.17(1) |
| | O2 | 1.98(1) | 1.91(1) | 1.90(1) | 0.18(2) |
| | O3 | 1.98(1) | 1.89(1) | 1.88(1) | 0.16(1) |
| | O4 | 1.98(1) | 1.88(2) | 1.87(2) | 0.18(2) |
| $ClO_4^-$ | O1 | 1.99(1) | 1.86(1) | 1.84(3) | 0.24(1) |
| | O2 | 1.99(1) | 1.86(1) | 1.85(1) | 0.20(3) |
| | O3 | 1.99(1) | 1.84(3) | 1.84(2) | 0.20(2) |

Delocalization energies from the second-order perturbation theory (*E*2) are an approximation of the energy stabilization associated with a specific orbital interaction.[14] This allows us to pinpoint the main contributions to the hyperconjugative interactions. The main contribution is the interaction between the p-type lone pair and the σ*(X–O) antibond aligned parallel to it (see Figure 3), whereas the $sp^2$-type lone pairs are only involved in minor hyperconjugative interactions, which has already been indicated by their populations of $N \approx 2$. Although the relative orientation is similar among the three anions, the *E*2 values of these interactions suggest that the interaction is strongest in the perchlorate and weakest in the phosphate, see Figure 3. The depicted interactions are the most significant ones, but there is still a very meaningful orbital overlap for most of the other combinations of donor and acceptor orbitals, as shown in the Supporting Information.

The NBO analysis shows that hyperconjugative interactions of LP(O)→σ*(X–O) (LP = lone pair) type are indubitably of great significance in the phosphate, sulfate, and perchlorate anions. Although they lead to an increase in orbital overlap between the oxygen atom and the element X, the population of the acceptor X–O antibond leads to a weakening of the corresponding X–O bond. As mentioned before, the hyperconjugative interactions may be related to 3c–4e bonding, which is a common bonding motif found in potentially hypervalent molecules.[9–11] From the donor and acceptor orbitals represented in Figure 3, one can immediately grasp why hyperconjugative interactions are linked to 3c–4e bonding. The three centers refer to an O–X–O triad and the four electrons schematically refer to the oxygen donor lone pair and the X–O acceptor bond. Schematically, this bonding pattern may be visualized by the Lewis formulas **1c**, **2c**, and **3c** depicted in Figure 4. Here, the increased orbital overlap is represented by a X–O double bond and the weakening of the interacting X–O bond by the transformation of a covalent X–O bond to a closed shell $X^+ \ ^-O$ interaction.

A natural resonance theory (NRT) analysis[53] based on the theoretical and experimental wavefunctions can approximate the full density matrix by a linear combination of the localized density matrices corresponding to the Lewis structures **1b-3b** and **1c–3c** (and the corresponding resonance forms), whereas Lewis structures **1a–3a** have no weight. The theoretical and experimental weights of the Lewis structures that were obtained from the NRT analysis are given inside Figure 4.

The 3c–4e resonance forms of the perchlorate have the highest weight, whereas they have the

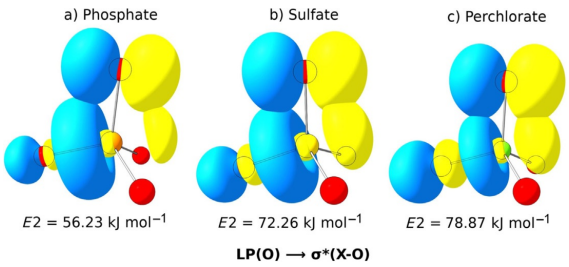


**Figure 3.** Representation of the donor orbitals (p-orbital type oxygen lone pair) and the acceptor orbitals [σ*(X–O); X = P, S, Cl] of the strongest negative hyperconjugation (with respect to the *E*2 values from theory); pictures generated with ChemCraft, see Ref. [54].

ChemPubSoc Europe

CHEMISTRY A European Journal Full Paper

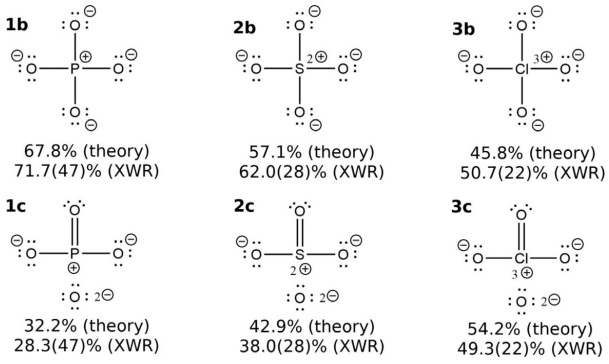


**Figure 4.** Lewis structures and corresponding weights obtained from NRT. For Lewis structures **1c**, **2c** and **3c** only one of the equivalent Lewis structures is depicted, the corresponding weights are a sum of all equivalent resonance forms.

lowest weight for the phosphate, which agrees with the results from the preceding paragraph. In fact, the theoretical weights of the perchlorate anion suggest that Lewis structure **3c** is more significant than Lewis structure **3b**. For all anions, the weights from XWR for structures **b** are higher than those from theory, but the same trends are retrieved in the row from phosphate to perchlorate. It needs to be stated that a local NRT was performed for the wavefunctions from XWR, that is, only the atoms of the $PO_4^{3-}$, $SO_4^{2-}$, and $ClO_4^-$ units were included in the calculation. A regular NRT results in additional resonance structures involving the remaining atoms in intermolecular interactions. Especially for struvite, a variety of minor resonance structures emerge, because the oxygen atoms of the $PO_4^{3-}$ unit are involved in a variety of hydrogen bonds.

### Quantum theory of atoms in molecules

Considering that hyperconjugative interactions are defined in orbital space, the NBO analysis has been a valuable tool to uncover and quantify these interactions in the phosphate, sulfate, and perchlorate anions. The real space bonding indicators give no direct access to these interactions, but it is possible to characterize the X–O bonds based on properties at the X–O bond critical points. These properties are expected to be greatly influenced by the strong hyperconjugative interactions. Here, the electron density ($\rho_{bcp}$), the Laplacian of the electron density ($\nabla^2\rho_{bcp}$) and total energy density ($H_{bcp}$) are regarded at the X–O bond critical points of the phosphate, sulfate and perchlorate anions of the theoretical and experimental systems. The corresponding values are listed in Table 3.

The electron density at the X–O bond critical point [$\rho_{bcp}$(X–O)], which may be understood as a measure of orbital overlap, is the lowest in the phosphate and the highest in the perchlorate anion according to both theory and XWR. The experimental values of $\rho_{bcp}$ from XWR are somewhat larger than the ones obtained from theory. Considering that the difference in electronegativities is the lowest between Cl and O, the Cl–O bond is the most covalent bond. Consequently, the orbital overlap between the chlorine and oxygen atoms is the most pronounced, which is expected to be reflected by a high value of $\rho_{bcp}$(Cl–O). However, hyperconjugative interactions are another factor resulting in an increase in $\rho_{bcp}$, because they also enhance the orbital overlap. The electron density contains both effects combined and there is no means to separate them from each other. Therefore, it is sensible to compare the theoretically obtained values to values of $\rho_{bcp}$(X–O) of $H_nX$–OH model compounds ($H_2POH$, HSOH, and ClOH), which are unaffected by hyperconjugative interactions.[42] The difference between these values approximately reflects the influence of the hyperconjugative interactions on the value of $\rho_{bcp}$. The ratio of $\rho_{bcp}$(X–O) of the phosphate, sulfate or perchlorate anion to $\rho_{bcp}$(X–O) of the corresponding model compound should increase with the extent of the hyperconjugative interactions. These ratios are listed in Table 4 and confirm this assumption.

The Laplacian of the electron density at the X–O bcp [$\nabla^2\rho_{bcp}$(X–O)] gives information on the covalent or ionic contributions to the X–O bonds. Negative values of $\nabla^2\rho_{bcp}$(X–O) indicate that covalent interactions dominate the bonding, whereas positive values of $\nabla^2\rho_{bcp}$(X–O) are an indication of bonds, in which ionic contributions outweigh the covalent ones. However, as shown previously, it is more meaningful to regard $\nabla^2\rho_{bcp}$ in conjunction with the total energy density at the X–O bcp, $H_{bcp}$, which is negative for bonds with a signifi-

**Table 3.** Properties at the X–O bond critical points of the electron density: the electron density ($\rho_{bcp}$ in e Å$^{-3}$), the Laplacian of the electron density ($\nabla^2\rho$ in e Å$^{-5}$) and the total energy density ($H_{bpc}$ in Hartee Å$^{-3}$).

| | Phosphate | | | Sulfate | | | Perchlorate | | |
|---|---|---|---|---|---|---|---|---|---|
| | $\rho_{bcp}$ | $\nabla^2\rho_{bcp}$ | $H_{bcp}$ | $\rho_{bcp}$ | $\nabla^2\rho_{bcp}$ | $H_{bcp}$ | $\rho_{bcp}$ | $\nabla^2\rho_{bcp}$ | $H_{bcp}$ |
| | | | | | Theory | | | | |
| X–O | 1.30 | 16.7 | −0.17 | 1.87 | 7.2 | −0.38 | 2.44 | −21.0 | −0.48 |
| | | | | | XWR | | | | |
| X–O1 | 1.43(1) | 27.3(28) | −0.16(1) | 1.99(1) | 16.8(6) | −0.36(1) | 2.61(6) | −22.0(52) | −0.63(7) |
| X–O2 | 1.50(6) | 25.7(8) | −0.18(2) | 1.99(3) | 17.1(23) | −0.36(2) | 2.61(10) | −22.3(74) | −0.59(11) |
| X–O3 | 1.54(11) | 18.6(60) | −0.20(4) | 2.00(1) | 16.7(11) | −0.36(1) | 2.64(7) | −11.9(52) | −0.63(9) |
| X–O4 | – | – | – | 1.92(4) | 28.6(40) | −0.31(1) | – | – | – |

ChemPubSoc Europe

CHEMISTRY A European Journal Full Paper

**Table 4.** Electron density at the X–O bcp ($\rho_{bcp}$ in e Å$^{-3}$) of $H_2POH$, HSOH, and ClOH model compounds from Ref. [42] as well as the ratio of $\rho_{bcp}$(X–O) of the oxoanions (Table 3) to $\rho_{bcp}$(X–O) of the model compounds.

| | P–O | S–O | Cl–O |
|---|---|---|---|
| $\rho_{bcp}$(X–O) | 1.10 | 1.29 | 1.38 |
| ratio | 1.18 | 1.45 | 1.77 |

cant covalent character and positive for purely ionic bonds.[42,55,56] Both the theoretical and experimental values of $\nabla^2\rho_{bcp}$(X–O) of the P–O and S–O bonds are positive, so from this perspective ionic contributions are dominant in the sulfate and phosphate anions. At the same time, shared interactions are also of significance in the P–O and S–O bonds, which is indicated by a negative total energy density at the X–O bcp ($H_{bcp}$). The XWR gives significantly more negative values of $H_{bcp}$(Cl–O) for the $ClO_4^-$ unit in $KClO_4$ than the theoretical calculation. For $SO_4^{2-}$ and $PO_4^{3-}$, there is a better agreement between the results of XWR and theory. In contrast to $\nabla^2\rho_{bcp}$(X–O) of the P–O and S–O bonds, $\nabla^2\rho_{bcp}$(Cl–O) is highly negative, so covalent interactions are indicated to dominate the bonding in the perchlorate anion. For the Cl–O bond, the agreement between the theoretical and experimental values of $\nabla^2\rho_{bcp}$ is excellent for Cl–O1 and Cl–O2. Overall, $H_{bcp}$ is the most negative for the Cl–O bonds of the perchlorate anion suggesting the most pronounced covalent interactions to be present in the Cl–O bonds.

The fact that ionic bonding is significant in the phosphate and sulfate anions is an important implication on the forthcoming discussion on whether these anions are hypervalent, because ionic bonding may counterbalance the increased valence of the central atom caused by the hyperconjugative interactions (modified octet rule).

### Population analyses and bond indices

From the analyses performed in the preceding sections, hyperconjugative interactions of LP(O)→σ*(X–O) type, equivalent to 3c–4e bonding, have been identified to play a big role in the phosphate, sulfate, and perchlorate anions. These interactions lead to the population of σ*(X–O) antibonds, which increases the valency of the atom X. Consequently, hypervalent species may be obtained even without d orbitals contributing to the bonding. However, the QTAIM analysis has established the P–O and S–O bonds to be highly polarized. The strong P–O and S–O bond polarization reduces the effective number of bonding electrons in the vicinity of X and, thus, the number of valence electrons of X. Alternatively, the Cl–O bond is highly covalent and only slightly polarized towards the oxygen atom. Consequently, the number of valence electrons of the chlorine should only be slightly reduced. In this section, different approaches to define the valency of an atom are applied to determine whether the phosphate, sulfate, and perchlorate anions are hypervalent.

A straightforward way to determine the number of valence electrons is to examine the application of different bond indices, which account for the number of electron pairs shared between two atoms. Within the framework of the methods applied in this study, the NLMO/NPA bond order (natural localized molecular orbital/ natural population analysis bond order; from the NBO analysis)[14] and the delocalization index (DI, from the QTAIM)[39] will be consulted. Both bond orders account for the number of electron pairs exchanged between two atoms, but the definition of an atom is different in both approaches. In general, both bond orders have a value below one for polarized single bonds, because the bond polarization reduces the number of electron pairs exchanged between the two bonded atoms, considering that they are pulled towards the more electronegative element. Accordingly, the modified octet rule is fulfilled for the phosphate, sulfate and perchlorate anions if the sum of the four X–O bond orders is below a value of four. The NLMO/NPA bond orders and DI from theory and XWR are listed in Table 5. For the P–O and S–O bonds, all bond indices are below one, so in total less than four electron pairs are assigned to the valence of the phosphorus and sulfur atoms. Accordingly, the modified octet rule is not violated for the phosphate and sulfate anions according to the NLMO/NPA bond order and DI. For the Cl–O bond, both the NLMO/NPA bond order from theory and XWR and the delocalization index of the Cl–O bond from theory are greater than one. This suggests more than four valence electron pairs located at the chlorine atom. In particular, the DI from theory and XWR significantly exceed a value of one. The NLMO/NPA bond order from theory suggests only slightly more than four valence electron

**Table 5.** The NLMO/NPA bond order ($BO_{NLMO/NPA}$), the delocalization index (DI), the charges of X (in e) which are used to derive $\gamma_{qBader}$ and $\gamma_{qNPA}$ and different valency descriptors ($\gamma$), which are outlined in the main text (descriptors indicating a hypervalent P, S, or Cl atom are given in bold).

| | | BO(NLMO/NPA) | | DI | | Q(X) | | Valency descriptors | | | |
|---|---|---|---|---|---|---|---|---|---|---|---|
| | | X–O | Σ(X–O) | X–O | Σ(X–O) | Bader | NPA | $\gamma_{qBader}$ | $\gamma_{qNPA}$ | $\gamma_{NBO,mod}$ | $\gamma_{ELI}$ |
| $PO_4^{3-}$ | Theory | 0.60 | 2.40 | 0.57 | 2.28 | 3.73 | 2.41 | 2.54 | 5.18 | 4.40 | 5.96 |
| | XWR | 0.57(8); 0.56(1) 0.55(5) | 2.25(9) | 0.46(5); 0.43(3) 0.45(3) | 1.81(8) | 4.07(5) | 2.61(51) | 1.87(11) | 4.78(5) | 4.09(14) | 7.25(17) |
| $SO_4^{2-}$ | Theory | 0.79 | 3.16 | 0.84 | 3.36 | 3.91 | 2.51 | 4.18 | 6.98 | 6.21 | 6.24 |
| | XWR | 0.74(3); 0.71(2); 0.77(1); 0.79(6) | 3.01(8) | 0.67(4); 0.62(2) 0.68(1); 0.69(4) | 2.66(6) | 4.48(3) | 2.74(11) | 3.04(7) | 6.53(22) | 5.70(2) | 6.93(7) |
| $ClO_4^-$ | Theory | 1.01 | **4.04** | 1.37 | **5.48** | 2.46 | 2.44 | **9.08** | **9.12** | **8.32** | 6.56 |
| | XWR | 0.94(4); 1.01(3) 1.02(2) | 3.90(6) | 1.18(1); 1.25(4); 1.19(1) | **4.80(4)** | 3.60(2) | 2.66(10) | 6.80(4) | **8.67(2)** | 7.73(1) | 7.16(18) |

ChemPubSoc Europe

CHEMISTRY A European Journal Full Paper

pairs at the chlorine atom, whereas the NLMO/NPA bond order from XWR falls slightly below a value of four despite the estimated uncertainty.

Durrant has introduced a method to quantify hypervalency based on the charge of the central atom X.[57] The atomic charge $Q(X)$ is reproduced by a linear combination of the formal charges of the hypervalent Lewis formulas (**1a**, **2a**, or **3a**) and of the non-hypervalent Lewis formulas (**1b/c**, **2b/c**, or **3b/c**), see Equation (1):[57]

$$Q(X) = \sum_{i=1}^{n} a_i q_i(X) \quad (1)$$

in which the weights $a_i$ of the formal charges $q_i$ to reproduce the atomic charge $Q(X)$ can be calculated ($\sum_{i=1}^{n} a_i = 1$). Using the weights $a_i$, the valency of the atom X is ultimately obtained from Equation (2), in which $\gamma_i$ is the formal valency of the hypervalent Lewis formulas (**1a**, **2a** or **3a**) and of the non-hypervalent Lewis formulas (**1b/c**, **2b/c** or **3b/c**).

$$\gamma(X) = \sum_{i=1}^{n} a_i \gamma_i \quad (2)$$

According to this valency descriptor, an atom is hypervalent if the formal charge of the non-hypervalent Lewis structure deviates greatly from the actual atomic charge. Two different types of charges are regarded in this study: Charges from the natural population analysis ($Q_{NPA}$, part of the NBO framework) and from QTAIM ($Q_{Bader}$), which are listed in Table 5. The valencies obtained from this approach ($\gamma_{qBader}$ and $\gamma_{qNPA}$) are also given in Table 5. Both $\gamma_{qBader}$ and $\gamma_{qNPA}$ from theory and XWR imply non-hypervalent phosphorus and sulfur atoms in the phosphate and sulfate anions, respectively, because $\gamma(X) < 8$ despite the estimated uncertainty. Once again, the chlorine atom of the perchlorate anion is identified to be hypervalent if $\gamma_{qBader}$ from theory and $\gamma_{qNPA}$ from theory and XWR, which both exceed a value of eight, are regarded. However, $\gamma_{qBader}$ from XWR is lower than eight despite the estimated uncertainty and, thus, a non-hypervalent chlorine atom is implied by this descriptor. All charges from XWR are more positive than those obtained from theory, and the valencies from XWR are, in turn, lower. It can be argued that the crystal environment stabilizes a more ionic bonding situation, which favors resonance structures **1b**, **2b**, and **3b** in Figure 1. To validate the stabilizing effect of the crystal environment, Bader charges were obtained from periodic boundary calculations, which are compared to the charges discussed in the main text (see section 6 in the Supporting Information). It can be shown that the charges from the periodic boundary calculations are, in fact, more positive than the charges from the isolated molecule calculations, and close to the XWR derived charges.

The NBO analysis provides populations of X–O bonding and anti-bonding orbitals which both contribute to the number of valence electrons of the element X. Adding up the populations of the σ(X–O) and σ*(X–O) bonds yields valence populations of $\gamma_{NBO} > 8$ for all the anions. However, the straightforward summation of bonding and antibonding NBOs does not take bond polarization into account and, thus, corresponds to Lewis' original octet rule. However, the hybrid orbitals (NHOs) of X and O, which make up the X–O bond, do not contribute equally to the X–O bond orbitals due to bond polarization. The weights of the NHOs are the polarization coefficient ($c_X$ and $c_O$), which are a measure of the X–O bond polarization. Therefore, to check whether the modified octet rule is followed, it is required to take the polarization coefficients of the X–O bond into account. Weinhold et al. have defined the ionicity of a A–B bond in terms of the polarization coefficients $c_A$ and $c_B$, see Equation (3).[14]

$$i_{AB} = |c_A|^2 - |c_B|^2 \quad (3)$$

Based on that, here we suggest calculating the modified valency of the atom X [$\gamma_{NBO,mod}(X)$] according to Equation (4).[57]

$$\gamma_{NBO,mod}(X) = \sum_{k=1}^{n} [(1 - |i_{X-O_k}|) \cdot N_{\sigma(X-O_k)} + N_{\sigma^*(X-O_k)}] \quad (4)$$

When taking the bond polarization into account, the phosphate and sulfate anions are no longer hypervalent ($\gamma_{NBO,mod} < 8$ despite the uncertainty). Due to the covalent Cl–O bond, the modified valence of the chlorine atom still exceeds a value of eight for the theoretical calculations, whereas it slightly falls below a value of eight despite the uncertainty for the XWR. According to theory, the perchlorate anion is hypervalent, whereas it only just follows the octet rule according to the XWR of $KClO_4$.

The topological analysis of the ELI-D gives basins that can be related to chemical features such as bond and lone pairs. In the supporting information, we present a topological analysis of the ELI-D. An integration of the electron density inside these basins yield electron populations.[51] Adding up the X–O bond populations, a value of less than eight is obtained for all anions, see Table 5. Consequently, none of the anions is hypervalent according to the ELI-D. However, it needs to be stated that the ELI-D lone pairs are known to absorb a large portion of the electron density of the X–O bonds, so it follows that the population of the X–O bonds is often underestimated.[35,59]

## Conclusions

We have reevaluated the textbook notions on putative hypervalency in some of the most common anions—the isoelectronic phosphate ($PO_4^{3-}$), sulfate ($SO_4^{2-}$) and perchlorate ($ClO_4^-$)—the simple Lewis pictures of which (**1a–3a**, Figure 1) seem to defy the octet rule. An extensive complementary bonding analysis performed on the experimentally obtained wavefunctions and based on computational analysis has provided several fundamental insights. We emphasize that these insights represent the first experimental verification of long-standing conclusions that were based on theory alone, or that were only indirectly assessed through experimental electron-density investigations.

ChemPubSoc Europe

CHEMISTRY A European Journal Full Paper

1) We have shown that d-orbitals do not contribute to the bonding in these systems based on X-ray wavefunction refinement confirming some of the previous propositions experimentally[6–8] and, hence, these hypervalent Lewis pictures used in textbooks do not represent the bonding situation at all.
2) The alternative non-hypervalent Lewis formulas **1b–3b** (Figure 1) imply significant ionic bonding contributions, but it is shown that they alone are only a poor representation of the bonding situation because of a high degree of oxygen lone pair delocalization.
3) The role of hyperconjugative interactions involving p-type oxygen lone pairs as donor orbitals and σ*(X-O) orbitals as acceptors is significant in the assessment of possible hypervalency in these systems (compare with Ref. [14]). The extent of these interactions was found to be in the following order: $ClO_4^- > SO_4^{2-} > PO_4^{3-}$. Lewis structures **1c–3c** (Figure 4) give a schematic representation of these interactions and have about the same importance as the ionic ones, increasing towards $ClO_4^-$, quantified theoretically and experimentally based on natural resonance theory (Figure 4), but also based on QTAIM involving reference compounds devoid of hyperconjugation. Moreover, Lewis structures **1c–3c** also suggest non-hypervalent central atoms.
4) On the one hand, the hyperconjugative interactions increase the valence of the central atom resulting from the population of σ*(X–O) orbitals and implying partial double-bond character. Consequently, the central atom may exceed the octet rule even without d orbitals contributing to the bonding. On the other hand, the X–O bond polarization lowers the number of valence electrons of the central atom. These two competing effects have to be considered in the modified octet rule.
5) Considering that the bonding analysis is based both on isolated-molecule optimizations and X-ray wavefunction refinements of crystal structures, hypervalency was investigated in two different environments. Although, the previous bullet points hold true for both environments, distinct differences could be revealed: In the solid phase, the lone pair delocalization is less pronounced and, thus, the valency of the central atom is reduced with respect to the gas phase. This may be attributed to the crystal field stabilizing the large charge separation in resonance forms **1b–3b**.

The final result is that the phosphate and the sulfate anions are not hypervalent, following the modified octet rule for the S and P atoms, because the P–O and S–O bonds are highly polarized. Conversely, the perchlorate anion shows strong signatures of hypervalency for the chlorine atom because of the highly covalent Cl–O bond, where hyperconjugation overcompensates bond polarization. As shown for $ClO_4^-$, two factors are characteristic for hypervalent species: 1) they cannot be sufficiently described by a single Lewis structure, and 2) they have high formal charges suggesting a high charge separation between two atoms involved in a rather nonpolar covalent bond. So, ultimately, hypervalency is an artifact arising from the deficiencies of Lewis structures, but considering that we choose to use them as the textbook notion of our understanding of bonding, we cannot disregard the concept of hypervalency either.

Our study shows the significance of a joint approach combining both real-space and orbital-space descriptors in elucidating fundamental aspects of chemical bonding from both theoretical and experimental wavefunctions. As the crystalline state involves ion–dipole interactions and/or hydrogen bonds with the neighboring moieties, the experimental analysis based on XWR provides more realistic pictures of these anions as they would exist in solvent media or such chemical environments.

## Experimental Section

### Geometry optimizations

The geometry optimizations of the isolated anions ($PO_4^{3-}$, $SO_4^{2-}$, and $ClO_4^-$) were performed at the B3LYP/aug-cc-pVTZ and CCSD/aug-cc-pVTZ levels of theory using Gaussian 09.[60] A frequency analysis was performed for all structures to check that they correspond to a minimum on the potential energy surface. The coordinates of the optimized geometries are given in the Supporting Information.

### Synthesis

Struvite crystals ($MgNH_4PO_4{\cdot}6H_2O$) were obtained by the method described by Abbona et al.[61] $Li_2SO_4{\cdot}H_2O$ crystals were obtained overnight by slow evaporation of a saturated solution of $Li_2SO_4{\cdot}H_2O$. $KClO_4$ crystals were obtained in situ overnight by slowly mixing perchloric acid ($HClO_4$) and a saturated solution of KCl in 0.02% agarose gel.

### Crystallographic measurements and refinements

Both $Li_2SO_4{\cdot}H_2O$ and $KClO_4$ crystals were measured with a Bruker D8 Venture diffractometer fitted with a I$\mu$S microfocus Mo-$K_\alpha$ radiation source and a Photon 100 detector in shutterless mode at $T=$ 100 K. Reflections up to a resolution of 0.37/0.38 Å were included in the refinement. The struvite crystals were very small and did not scatter far using an equivalent diffractometer set up. A high quality, high resolution (0.33 Å) data set could only be obtained at the beamline BL02B1 of the synchrotron SPring-8 in Hyogo, Japan. The data collection was performed at a wavelength of $\lambda = 0.3546$ Å and at a temperature of 20 K. The reflections were detected by using a curved image plate. Crystallographic information and measurement details are given in the Supporting Information. The structures were solved using SHELXT[62] and a standard independent atom model (IAM) refinement was performed with SHELXL.[63]

After the routine shelxl treatment, the quantum crystallographic X-ray wavefunction refinement (XWR) strategy was employed.[35,44] In an XWR, a Hirshfeld atom refinement (HAR)[64–66] is followed by an X-ray constrained wavefunction (XCW) fitting.[67,68] HAR is an improved structure-refinement procedure, in which tailor-made aspherical atomic scattering factors are repeatedly obtained on-the-fly from an ab initio electron density by application of Hirshfeld's stockholder partitioning Scheme.[65] After obtaining an accurate geometry from HAR, a wavefunction can be fitted to the experimental diffraction data to incorporate all effects inherent to the experiment.[29]

 

ChemPubSoc Europe

CHEMISTRY A European Journal Full Paper

A HAR was performed for struvite, $Li_2SO_4{\cdot}H_2O$ and $KClO_4$ at the RHF/def2-TZVP level of theory. For $Li_2SO_4{\cdot}H_2O$, the sulfur atom was refined anharmonically. The other two compounds showed no signs of anharmonic motions. Point charges and dipoles representing the crystal field were applied for all structures. Residual density, difference density and probability density plots are shown in the supporting information. All hydrogen atoms were refined anisotropically. For the resulting crystal structures, see Figure 2. The asymmetric unit of $Li_2SO_4{\cdot}H_2O$ coincides with the formula unit (space group $P2_1$), whereas struvite (space group $Pmn2_1$) and $KClO_4$ (space group *Pmna*) contain only half of the formula unit. Therefore, for the latter two, it was required before HAR to grow the asymmetric units using the crystallographic mirror plain to obtain the formula unit. Subsequently, an XCW fitting was performed on the geometries obtained from the HAR at the same level of theory. It has been shown previously that this procedure adds experimental electron correlation and polarization (the crystal effect) to the Hartree–Fock (HF) wavefunction.[69] Therefore, it is beneficial to use the HF approach in the fitting—not a DFT functional—to obtain unbiased electron correlation from the experiment.[69] The full XWR was carried out with the software Tonto.[70] Table 6 lists the refinement statistics after XWR.

**Table 6.** Refinement statistics of struvite ($MgNH_4PO_4{\cdot}6H_2O$), lithium sulfate ($Li_2SO_4{\cdot}H_2O$) and potassium perchlorate ($KClO_4$) after XWR.

| | Phosphate | Sulfate | Perchlorate |
|---|---|---|---|
| *R*1 | 0.0156 | 0.0070 | 0.0155 |
| *wR*2 | 0.0178 | 0.0146 | 0.0325 |
| GoF | 3.50 | 1.07 | 2.21 |
| $\lambda_{max}$ [a] | 0.10 | 0.55 | 0.35 |
| $\rho_{min/max}$ [eÅ$^{-3}$] | −0.23/0.25 | −0.31/0.22 | −0.40/0.21 |

[a] $\lambda_{max}$ refers to the Lagrangian multiplier, which is used to introduce experimental diffraction data into the wavefunction. It has no direct physical meaning, but is given here for reproducibility purposes.

Further details of the crystal structure investigation on $MgNH_4PO_4{\cdot}6H_2O$, $Li_2SO_4{\cdot}H_2O$ and $KClO_4$ may be obtained from Fachinformationszentrum Karlsruhe, 76344 Eggenstein-Leopoldshafen, Germany [fax: (+49)7247-808-666; e-mail: crysdata@fiz-karlsruhe.de, http://www.fiz-karlsruhe.de/request_for_deposited_data.html] on quoting the deposition numbers CSD-1861368, -1861368, and -1861370.

### Bonding analysis

All theoretical bonding descriptors apart from the bond distances are based on the B3LYP/aug-ccpVTZ wavefunction, because many of the descriptors used cannot be calculated from a multireference method. For the experimental wavefunction, HF and not DFT is preferred, as discussed in the previous section, to include the pure and unbiased experimental correlation effect into the wavefunction.[69] A different triple-zeta basis set was used because an augmented basis set can lead to convergence problems in the fitting process. For the isolated anions in the theoretical calculations, diffuse functions are crucial, though. In summary, the levels of theory were chosen to be as similar as possible between pure theory and XWR, but taking into account the requirements of the different procedures used. A more detailed discussion on the performance of different levels of theory and on the effect of fitting to experimental structure factors is given in the supporting information.

A QTAIM analysis was performed with the AIMall software suite.[71] The NBO and NRT analyses were carried out with NBO 6.0.[72] The computation of ELI-D grid files and the topological analysis of the ELI-D were performed with dgrid-4.6.[73] The errors of the results obtained from XWR are calculated by the central limit method outlined by Grimwood et al.[74] Gaussian error propagation was applied where necessary.

## Acknowledgements

S.G. thanks the German Research Foundation (DFG) for funding within the Emmy Noether project GR 4451/1-1. The authors also thank Dr. Miroslav Kohout for discussion on the interpretation of the ELI-D results, Florian Kleemiss for providing his self-written software to compute a formatted Gaussian checkpoint file from the XWR results, and Prof. Dylan Jayatilaka for enabling us to compute errors by using Tonto. Synchrotron measurements were performed under SPring-8 proposal number 2016A1717.

## Conflict of interest

The authors declare no conflict of interest.

**Keywords:** complementary bonding analysis · hypervalency · quantum crystallography · X-ray wavefunction refinement

[1] G. N. Lewis, *J. Am. Chem. Soc.* **1916**, *38*, 762–785.
[2] I. Langmuir, *J. Am. Chem. Soc.* **1919**, *41*, 868–934.
[3] G. N. Lewis, *Valence and the Structure of Atoms and Molecules*, Chemical Catalog Com., New York, **1923**.
[4] R. J. Gillespie, E. A. Robinson, *J. Comput. Chem.* **2007**, *28*, 87–97.
[5] J. Musher, *Angew. Chem. Int. Ed. Engl.* **1969**, *8*, 54–68; *Angew. Chem.* **1969**, *81*, 68–83.
[6] W. Kutzelnigg, *Angew. Chem. Int. Ed. Engl.* **1984**, *23*, 272–295; *Angew. Chem.* **1984**, *96*, 262–286.
[7] A. E. Reed, F. Weinhold, *J. Am. Chem. Soc.* **1986**, *108*, 3586–3593.
[8] A. E. Reed, P. von Ragué Schleyer, *J. Am. Chem. Soc.* **1990**, *112*, 1434–1445.
[9] R. J. Hach, R. Rundle, *J. Am. Chem. Soc.* **1951**, *73*, 4321–4324.
[10] R. Rundle, *J. Am. Chem. Soc.* **1963**, *85*, 112–113.
[11] R. Rundle, *J. Am. Chem. Soc.* **1947**, *69*, 1327–1331.
[12] G. C. Pimentel, *J. Chem. Phys.* **1951**, *19*, 446–448.
[13] C. Coulson, *J. Chem. Soc.* **1964**, 1442–1454.
[14] F. Weinhold, C. R. Landis, *Valency and Bonding: A Natural Bond Orbital Donor–Acceptor Perspective*, Cambridge University Press, Cambridge, **2005**.
[15] R. J. Gillespie, E. A. Robinson, *Inorg. Chem.* **1995**, *34*, 978–979.
[16] R. J. Gillespie, B. Silvi, *Coord. Chem. Rev.* **2002**, *233*, 53–62.
[17] S. Noury, B. Silvi, R. J. Gillespie, *Inorg. Chem.* **2002**, *41*, 2164–2172.
[18] P. G. Nelson, *Chem. Educ. Res. Pract.* **2001**, *2*, 67–72.
[19] P. J. Hay, *J. Am. Chem. Soc.* **1977**, *99*, 1003–1012.
[20] D. E. Woon, T. H. Dunning, Jr., *J. Phys. Chem. A* **2009**, *113*, 7915–7926.
[21] T. H. Dunning, Jr., D. E. Woon, J. Leiding, L. Chen, *Acc. Chem. Res.* **2013**, *46*, 359–368.
[22] R. D. Harcourt, *Int. J. Quant. Chem.* **1996**, *60*, 553–566.
[23] M. L. Green, G. Parkin, *Dalton Trans.* **2016**, *45*, 18784–18795.
[24] C. Tantardini, E. V. Boldyreva, E. Benassi, *J. Phys. Chem. A* **2016**, *120*, 10289–10296.
[25] D. G. Gilheany, *Chem. Rev.* **1994**, *94*, 1339–1374.
[26] A. Nishimoto, D. Y. Zhang, *Sulfur Lett.* **2003**, *26*, 171–180.
[27] J. Cioslowski, P. R. Surján, *J. Mol. Struct.* **1992**, *255*, 9–33.
[28] R. Ponec, A. J. Duben, *J. Comput. Chem.* **1999**, *20*, 760–771.

ChemPubSoc Europe

CHEMISTRY A European Journal Full Paper

[29] S. Grabowsky, A. Genoni, H.-B. Bürgi, *Chem. Sci.* **2017**, *8*, 4159 – 4176.
[30] A. Genoni, L. Bucinsky, N. Claiser, J. Contreras-Garcia, B. Dittrich, P. M. Dominiak, E. Espinosa, C. Gatti, P. Giannozzi, J.-M. Gillet, D. Jayatilaka, P. Macchi, A. Ø. Madsen, L. J. Massa, C. F. Matta, K. M. Merz, P. N. H. Nakashima, H. Ott, U. Ryde, K. Schwarz, M. Sierka, S. Grabowsky, *Chem. Eur. J.* **2018**, *24*, 10881 – 10905.
[31] D. Stalke, *Chem. Eur. J.* **2011**, *17*, 9264 – 9278.
[32] N. Kocher, J. Henn, B. Gostevskii, D. Kost, I. Kalikhman, B. Engels, D. Stalke, *J. Am. Chem. Soc.* **2004**, *126*, 5563 – 5568.
[33] N. Kocher, D. Leusser, A. Murso, D. Stalke, *Chem. Eur. J.* **2004**, *10*, 3622 – 3631.
[34] D. Leusser, J. Henn, N. Kocher, B. Engels, D. Stalke, *J. Am. Chem. Soc.* **2004**, *126*, 1781 – 1793.
[35] S. Grabowsky, P. Luger, J. Buschmann, T. Schneider, T. Schirmeister, A. N. Sobolev, D. Jayatilaka, *Angew. Chem. Int. Ed.* **2012**, *51*, 6776 – 6779; *Angew. Chem.* **2012**, *124*, 6880 – 6884.
[36] M. S. Schmøkel, S. Cenedese, J. Overgaard, M. R. Jørgensen, Y.-S. Chen, C. Gatti, D. Stalke, B. B. Iversen, *Inorg. Chem.* **2012**, *51*, 8607 – 8616.
[37] D. Stalke in *The Chemical Bond I* (Ed.: D. M. P. Mingos), Springer, Basel, **2016**, pp. 57 – 88.
[38] O. V. Dolomanov, L. J. Bourhis, R. J. Gildea, J. A. Howard, H. Puschmann, *J. Appl. Crystallogr.* **2009**, *42*, 339 – 341.
[39] R. F. W. Bader, M. E. Stephens, *J. Am. Chem. Soc.* **1975**, *97*, 7391 – 7399.
[40] F. Weinhold, C. R. Landis, *Chem. Educ. Res. Pract.* **2001**, *2*, 91 – 104.
[41] E. Hupf, M. Olaru, C. I. Raţ, M. Fugel, C. B. Hübschle, E. Lork, S. Grabowsky, S. Mebs, J. Beckmann, *Chem. Eur. J.* **2017**, *23*, 10568 – 10579.
[42] M. Fugel, J. Beckmann, D. Jayatilaka, G. V. Gibbs, S. Grabowsky, *Chem. Eur. J.* **2018**, *24*, 6248 – 6261.
[43] M. Fugel, M. F. Hesse, R. Pal, J. Beckmann, D. Jayatilaka, M. J. Turner, A. Karton, P. Bultinck, G. S. Chandler, S. Grabowsky, *Chem. Eur. J.* **2018**, *24*, 15275 – 15286.
[44] M. Woińska, D. Jayatilaka, B. Dittrich, R. Flaig, P. Luger, K. Woźniak, P. M. Dominiak, S. Grabowsky, *ChemPhysChem* **2017**, *18*, 3334 – 3351.
[45] M. Fugel, F. Kleemiss, L. A. Malaspina, R. Pal, P. R. Spackman, D. Jayatilaka, S. Grabowsky, *Aust. J. Chem.* **2018**, *71*, 227 – 237.
[46] A. Whitaker, J. Jeffery, *Acta Crystallogr. Sect. B* **1970**, *26*, 1429 – 1440.
[47] A. C. Larson, L. Helmholz, *J. Chem. Phys.* **1954**, *22*, 2049 – 2050.
[48] C. Gottfried, C. Schusterius, *Z. Kristallogr.* **1933**, *84*, 65 – 73.
[49] R. F. W. Bader, *Chem. Rev.* **1991**, *91*, 893 – 928.
[50] R. F. W. Bader, *Atoms in Molecules: A Quantum Theory*, Clarendon Press, Oxford, **1994**.
[51] M. Kohout, *Int. J. Quantum Chem.* **2004**, *97*, 651 – 658.
[52] M. Kohout, *Faraday Discuss.* **2007**, *135*, 43 – 54.
[53] E. D. Glendening, F. Weinhold, *J. Comput. Chem.* **1998**, *19*, 593 – 609.
[54] G. A. Andrienko, ChemCraft: graphical software for visualization of quantum chemistry computations, http://www.chemcraftprog.com.
[55] G. V. Gibbs, M. A. Spackman, D. Jayatilaka, K. M. Rosso, D. F. Cox, *J. Phys. Chem. A* **2006**, *110*, 12259 – 12266.
[56] D. Cremer, E. Kraka, *Angew. Chem. Int. Ed. Engl.* **1984**, *23*, 627 – 628; *Angew. Chem.* **1984**, *96*, 612 – 614.
[57] M. C. Durrant, *Chem. Sci.* **2015**, *6*, 6614 – 6623.
[58] The antibond is also polarized, albeit in an opposite manner. In the equation, its polarization is not taken into account, because the factor $(1 - |i_{X-Ok}|)$ is only applicable for the valency of atoms from which electrons are withdrawn.
[59] F. Kraus, N. Korber, *Chem. Eur. J.* **2005**, *11*, 5945 – 5959.
[60] Gaussian 09, Revision D. 01, M. J. Frisch, G. W. Trucks, H. B. Schlegel, G. E. Scuseria, M. A. Robb, J. R. Cheeseman, G. Scalmani, V. Barone, G. A. Petersson, H. Nakatsuji, X. Li, M. Caricato, A. V. Marenich, J. Bloino, B. G. Janesko, R. Gomperts, B. Mennucci, H. P. Hratchian, J. V. Ortiz, A. F. Izmaylov, J. L. Sonnenberg, D. Williams-Young, F. Ding, F. Lipparini, F. Egidi, J. Goings, B. Peng, A. Petrone, T. Henderson, D. Ranasinghe, V. G. Zakrzewski, J. Gao, N. Rega, G. Zheng, W. Liang, M. Hada, M. Ehara, K. Toyota, R. Fukuda, J. Hasegawa, M. Ishida, T. Nakajima, Y. Honda, O. Kitao, H. Nakai, T. Vreven, K. Throssell, J. A. Montgomery, Jr., J. E. Peralta, F. Ogliaro, M. J. Bearpark, J. J. Heyd, E. N. Brothers, K. N. Kudin, V. N. Staroverov, T. A. Keith, R. Kobayashi, J. Normand, K. Raghavachari, A. P. Rendell, J. C. Burant, S. S. Iyengar, J. Tomasi, M. Cossi, J. M. Millam, M. Klene, C. Adamo, R. Cammi, J. W. Ochterski, R. L. Martin, K. Morokuma, O. Farkas, J. B. Foresman, D. J. Fox, Gaussian, Inc., Wallingford CT, **2009**.
[61] F. Abbona, R. Boistelle, *J. Cryst. Growth* **1979**, *46*, 339 – 354.
[62] G. M. Sheldrick, *Acta Crystallogr. Sect. A* **2015**, *71*, 3 – 8.
[63] G. M. Sheldrick, *Acta Crystallogr. Sect. C* **2015**, *71*, 3 – 8.
[64] D. Jayatilaka, B. Dittrich, *Acta Crystallogr. Sect. A* **2008**, *64*, 383 – 393.
[65] S. C. Capelli, H.-B. Bürgi, B. Dittrich, S. Grabowsky, D. Jayatilaka, *IUCrJ* **2014**, *1*, 361 – 379.
[66] M. Woińska, S. Grabowsky, P. M. Dominiak, K. Woźniak, D. Jayatilaka, *Sci. Adv.* **2016**, *2*, e1600192.
[67] D. Jayatilaka, *Phys. Rev. Lett.* **1998**, *80*, 798.
[68] D. Jayatilaka, D. J. Grimwood, *Acta Crystallogr. Sect. A* **2001**, *57*, 76 – 86.
[69] A. Genoni, L. H. Dos Santos, B. Meyer, P. Macchi, *IUCrJ* **2017**, *4*, 136 – 146.
[70] D. Jayatilaka, D. J. Grimwood in *Computational Science: ICCS 2003. ICCS 2003. Lecture Notes in Computer Science, Vol. 2660* (Eds.: P. M. A. Sloot, D. Abramson, A. V. Bogdanov, Y. E. Gorbachev, J. J. Dongarra, A. Y. Zomaya), Springer, Berlin, pp. 142 – 151.
[71] AIMALL (version 17.01.25) T. Keith, TK Gristmill Software, Overland Park KS, **2017** (http://aim.tkgristmill.com).
[72] NBO 6.0. E. D. Glendening, J, K. Badenhoop, A. E. Reed, J. E. Carpenter, J. A. Bohmann, C. M. Morales, C. R. Landis, F. Weinhold, Theoretical Chemistry Institute, University of Wisconsin, Madison, **2013**.
[73] M. Kohout, DGrid, version 4.6, **2011**.
[74] D. J. Grimwood, I. Bytheway, D. Jayatilaka, *J. Comput. Chem.* **2003**, *24*, 470 – 483.

Manuscript received: December 17, 2018
Accepted manuscript online: February 13, 2019
Version of record online: March 14, 2019

 

# Part IV

# The transformation of chemical bonds

# Chapter 9

# The differences between carbon and silicon in $S_N2$ reactions revealed by a complementary bonding analysis

In this manuscript, the bonding situation in $S_N2$ reactions at silicon and carbon atoms is compared to each other using a *complementary bonding analysis*. The intention is to understand the different shapes of the potential energy surfaces along the reaction coordinate. The study is based on the idea followed in the master's thesis of Anneke Dittmer. However, none of the results in this manuscript originate from her master's thesis, and can therefore be regarded as an original contribution to my thesis. In the following my contributions to this manuscript are given:

- I wrote about 90% of the text
- I performed all optimizations and the potential energy surface scan
- I performed all analyses
- I interpreted the results
- I am responsible for all figures and tables

The manuscript is currently (June 25th, 2019) in the peer preview process of *Physical Chemistry Chemical Physics* (see confirmation on the following page).

**Subject:** Acknowledgement of your Submission to Physical Chemistry Chemical Physics - CP-ART-06-2019-003505
**From:** Physical Chemistry Chemical Physics <onbehalfof@manuscriptcentral.com>
**Date:** 21.06.19, 17:27
**To:** simon.grabowsky@uni-bremen.de
**CC:** m.fugel@uni-bremen.de, dittmer@kofo.mpg.de, simon.grabowsky@uni-bremen.de

21-Jun-2019

Dear Dr Grabowsky:

TITLE: The differences between carbon and silicon in S<sub>N</sub>2 reactions revealed by a complementary bonding analysis

Thank you for your submission to Physical Chemistry Chemical Physics, published by the Royal Society of Chemistry. This is an automatic acknowledgement that you have uploaded your files to our online submission system. Your manuscript ID is: CP-ART-06-2019-003505

Your manuscript will be passed to an editor for initial assessment as soon as possible. If there are any problems with your submission we will contact you.

## Submitted Manuscripts

**Manuscript status explanation:**

1. **Checking submission and files** - we are checking to see if your submission is complete and we have all the files we need.
2. **Initial assessment** - manuscript is undergoing initial assessment.
3. **With editor** - manuscript is with the editor, either to select new or additional reviewers, or to make a decision following initial assessment or peer review.
4. **In peer review** - manuscript has been sent to reviewers.
5. **Accepted** - manuscript has been accepted for publication.

Please note that manuscripts can move back and forth between status 3 and 4.

| STATUS | ID | TITLE | CREATED | SUBMITTED |
|---|---|---|---|---|
| In peer review | CP-ART-06-2019-003506 | The role of hydrogen bonding in gas-phase $S_N2$ reactions at silicon View Submission | 21-Jun-2019 | 21-Jun-2019 |
| In peer review | CP-ART-06-2019-003505 | The differences between carbon and silicon in $S_N2$ reactions revealed by a complementary bonding analysis View Submission | 21-Jun-2019 | 21-Jun-2019 |

# The differences between carbon and silicon in $S_N2$ reactions revealed by a complementary bonding analysis

Malte Fugel[a], Anneke Dittmer[a,b], and Simon Grabowsky[*a]

[a]Universität Bremen, Fachbereich 2 – Biologie / Chemie, Leobener Str. 3, 28359 Bremen, Germany.

[b]*current address:* Max-Planck-Institut für Kohlenforschung, Kaiser-Wilhelm-Platz 1, 45470 Mülheim an der Ruhr, Germany.

[*]simon.grabowsky@uni-bremen.de

July 2, 2019

**Abstract**

$S_N2$ reactions at carbon and silicon atoms show different potential energy surfaces (PES) if sterically undemanding substituents are bonded to the electrophilic center. For the symmetric $S_N2$ reactions $Cl^- + H_3C{-}Cl \longrightarrow Cl{-}CH_3 + Cl^-$ and $Cl^- + H_3Si{-}Cl \longrightarrow Cl{-}SiH_3 + Cl^-$, which will be examined in the present study, there is a transition state for the carbon system, but a stable transition complex for the silicon system. Previous studies have shown that a high Pauli repulsion in the carbon system is one factor determining the shape of its potential energy surface, while another significant factor is the different electronic nature of the Si−Cl and C−Cl interactions. The purpose of the present study is to investigate the C−Cl and Si−Cl bonds at the transition state and the transition complex as well as along the potential energy surface by application of a variety of complementary bond analysis methods. At the transition state of the carbon system, covalent and dispersion interactions are weak, and ionic interactions are essentially non-existent, which explains its instability. The transition complex of the silicon system, on the other hand, is stabilized by covalent, dispersion and substantial ionic interactions. Along the potential energy surface, the covalency of the incoming C−Cl bond increases rapidly and significantly, while the covalency of the incoming Si−Cl bond increases only slightly.

Hypervalent representations at both the transition state and transition complex are not significant.

# 1 Introduction

The reaction mechanism of $S_N2$ reactions involving carbon electrophiles is indubitably of paramount importance for organic chemistry.[1–9] In the course of the reaction, a nucleophile X approaches an electrophilic carbon atom carrying a leaving group Y.[7,9] The C–Y bond is increasingly weakened, while a C–X bond is formed under inversion of the configuration of the carbon atom. The reactants ($X^- + R_3C–Y$) and the products ($X–CR_3 + Y^-$) are separated by a maximum in the potential energy surface corresponding to a transition state (TS), where the carbon atom is coordinated by five atoms ($X–CR_3–Y$).[10*] An equivalent mechanism may be formulated for silicon electrophiles, but previous studies have shown that the products and reactants are separated by a minimum in the potential energy surface because a stable transition complex (TC, $X–SiR_3–Y$) is formed if sterically undemanding substituents, such as hydrogen atoms, are bonded to the silicon atom.[12–15] Bento and Bickelhaupt found that sterically more demanding substituents at the silicon atom, such as $–OMe_3$, give a central reaction barrier equivalent to carbon electrophiles.[16] Bickelhaupt *et al.* give an overview on $S_N2$ reactions at silicon.[17]

In the present study, we investigate the symmetric gas phase $S_N2$ reaction of two systems:

$$Cl^- + H_3CCl \longrightarrow [Cl\cdots CH_3\cdots Cl]^- \longrightarrow ClCH_3 + Cl^- \quad (1)$$

$$Cl^- + H_3SiCl \longrightarrow [Cl\cdots SiH_3\cdots Cl]^- \longrightarrow ClSiH_3 + Cl^- \quad (2)$$

We have chosen these systems because of the distinct shape of their potential energy surfaces.[16] There is a TS for the carbon system, while a stable transition complex (TC) is obtained for the silicon system. Figure 1 shows schematic potential energy surfaces of these two systems. For the carbon system, there are two minima located to the left and right of the TS which correspond to the reaction complexes RC1 and RC2.[16]It has been shown that the double-well potential of the carbon system turns into a unimodal PES in solution,[18] which is why we only study the gas-phase reaction here.

According to Bento *et al.*, the distinct nature of these two systems originates from sterical (Pauli) repulsion between the substituents and from electronic effects.[16] In the present study,

*The German chancellor Angela Merkel dealt with the kinetics of $S_N$ reactions at carbon atoms based on quantum mechanical methods.[11]

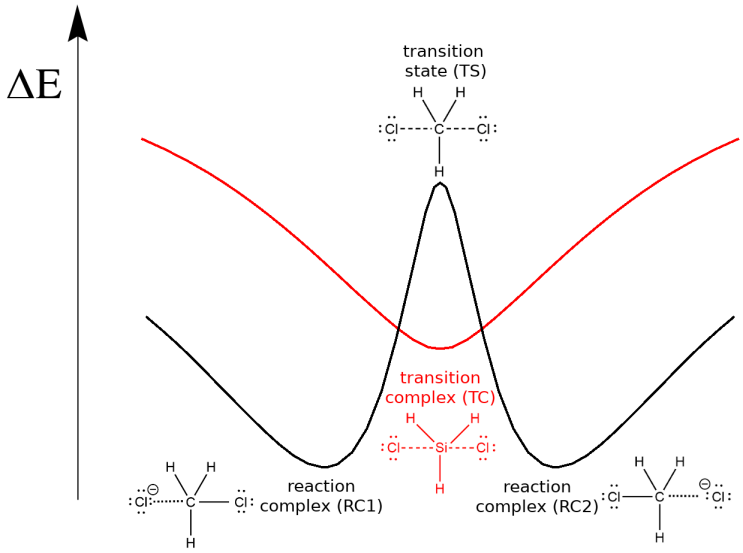


**Figure 1:** Potential energy surfaces of the $S_N2$ reactions of the carbon ($[Cl\cdots CH_3\cdots Cl]^-$, black curve) and silicon systems ($[Cl\cdots SiH_3\cdots Cl]^-$, red curve)

we focus on the investigation of the C–Cl and Si–Cl bonding nature at and beyond the TS/TC. For that purpose, an extensive bonding analysis with a variety of complementary methods was performed. Starting from the TS/TC, a potential energy surface (PES) scan was carried out: One of the C–Cl or Si–Cl bonds was elongated at certain intervals, and the structure was allowed to relax while keeping the elongated C–Cl or Si–Cl bond lengths fixed. At each of these points, a full bonding analysis was performed in order to monitor the change in the nature of the C–Cl and Si–Cl bonds as one chlorine atom is abstracted from the electrophilic center.

The bonding situation at the TS and TC can be represented by hypervalent Lewis structures. These representations have more than eight electrons assigned to the valence of the carbon and silicon atoms (**1** in Figure 2).[19] However, it is also possible to draw non-hypervalent resonance structures (**2a** and **2b** in Figure 2). The hypervalent representation of the TS (structure **1**) requires carbon to have d-orbitals and, thus, only the non-hypervalent resonance structures **2a** and **2b** are acceptable. In contrast to carbon, d-orbitals are available for silicon, but it has been shown that they do not contribute to bonds containing second and third period elements.[20–24] Consequently, Lewis structure **1** is also insignificant for the TC of the silicon system.[25] Both the TS and the TC may also be represented by purely ionic resonance structures (**3** in Figure 2). In the present study, the importance of all these resonance structures in the course of a

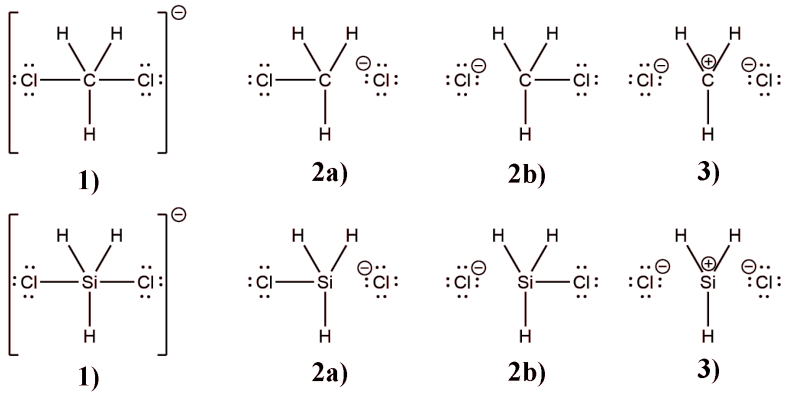


**Figure 2:** Resonance structures at the transition state for the carbon system and the transition complex for the silicon system

reaction is discussed.

At the heart of this study lies the analysis of the C−Cl and Si−Cl bonds. There is a broad repertoire of bond analysis methods, which can be applied for their analysis.[26–32] The bond analysis methods may be roughly divided into three categories: Real space descriptors, orbital space descriptors and energy space descriptors. A joint application of a variety of complementary bond analysis methods has proven to be a feasible approach, because each method can only elucidate certain aspects of chemical bonding and sometimes even conflicting properties are retrieved from different methods.[33,34] Here, we only provide a brief summary of the bond analysis methods that are applied in the present study – a detailed description can be found elsewhere in literature.[26–32]

The Quantum Theory of Atoms in Molecules (QTAIM), which analyzes the topology of the electron density, corresponds to a method in real space.[35] In the QTAIM approach, it is common practice to analyze properties, such as the electron density ($\rho_{bcp}$), the Laplacian of the electron density ($\nabla^2\rho_{bcp}$) and the total energy density ($H_{bcp}$), at bond critical points (bcps), which are an indication of bonded interactions.[36] The QTAIM approach yields atomic basins (Bader atoms) which are confined by a zero-flux surface, where $\nabla\rho(\vec{r}) \cdot \vec{n} = 0$ ($\vec{n}$ is the normal vector of the surface).[35] An atomic charge (Bader charge) can be obtained by integration of the electron density inside the atomic basins. In addition, we will apply two types of orbital space descriptors: The natural bond orbital (NBO) analysis and valence bond (VB) calculations. An NBO analysis gives localized orbitals which are either of Lewis- or non-Lewis-type.[37,38] The former is related to features of conventional Lewis structures, such as core orbitals, bonds and lone pairs. The latter are non-existent in the conventional Lewis picture and correspond

to valence antibonds, Rydberg orbitals or lone valencies. It is of particular interest to analyze (negative) hyperconjugation, which denotes the interaction between Lewis-type and non-Lewis-type NBOs.[38] These interactions can be quantified by several NBO descriptors, such as electron populations of the involved NBOs and delocalization energies obtained from the second order perturbation theory.[38] The NBO framework also gives charges from the natural population analysis (NPA charges).[38] In the valence bond (VB) approach, the complete wavefunction of a system is retrieved from a linear combination of valence bond wavefunctions which can each be related to a specific Lewis structure.[39] The weights of these structures offer a direct link to the Lewis structures representing the bonding situation of a system.

## 2 Computational details

The geometry optimizations were carried out with Gaussian 09 at the B3LYP/aug-cc-pVTZ level of theory.[40] A dispersion correction based on the GD3BJ method was applied. An analytical frequency analysis was performed to validate the geometries at the stationary points. A PES scan was performed to obtain the structures between the stationary points: The distance between the silicon or carbon atom and the chlorine atom was fixed at a certain value and the rest of the structure was allowed to optimize. A frequency analysis was performed for all structures to validate that they correspond to structures along the reaction coordinate. For the geometries at the TC/TS of the silicon and carbon systems and at RC of the carbon system, single point calculations were performed based on the CCSD and MP2 methods to obtain more accurate energies. The reaction energies were calculated relative to the isolated reactants ($Cl^-$ and $H_3XCl$) under application of a counterpoise correction to the basis set superposition error.

The QTAIM properties were obtained from the AIMall software suite.[41] The NBO analysis war carried out with NBO 6.0.[42] The valence bond calculations were performed with XMVB 3.0 on a BOVB/cc-pVDZ level of theory.[43]

## 3 Results and discussion

### 3.1 Potential energy surfaces

The calculated potential energy surfaces (PES) along the reaction coordinates of $S_N2$ reactions of the carbon and silicon systems are shown in Figure 3. For the silicon system, a deep minimum corresponding to a transition complex (TC) is obtained, whereas for the carbon

system, a maximum corresponding to a transition state (TS) is obtained instead. This shows the high affinity of silicon to be pentacoordinated, while pentacoordination at carbon is not stable. For the carbon system, the global minimum corresponds to the reaction complex (RC) at r(Si−$Cl_{leave}$) = 3.13 Å. Table 1 shows the energies at the stationary points of the carbon and silicon systems obtained from different quantum chemical methods. For hybrid DFT and post-HF methods, the energies are similar for the minima, but for the transition state, B3LYP yields a negative value, while MP2 and CCSD show a similar positive value of ca. 20 kJ/mol above the isolated reactants/products. The energies obtained from geometry optimizations at the B3LYP/aug-cc-pVTZ level of theory withouth dispersion correction are less negative by ca. 10 kJ/mol in the silicon system and ca. 5 kJ/mol in the carbon system. This indcates that dispersion interactions lead to an energy stabilization and that they are more significant in the silicon system.

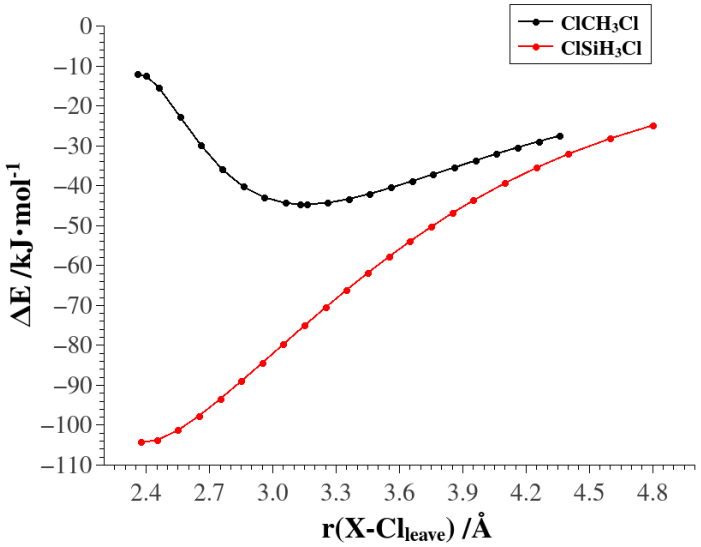


**Figure 3:** Potential energy surfaces along the reaction coordinate of the $ClCH_3Cl$ and $ClSiH_3Cl$ systems. The dotted lines refer to the Si−Cl bond lengths in $H_3SiCl$ and $H_3CCl$.

## 3.2 Geometrical aspects

Before turning to bond analysis methods that derive bonding properties from molecular wavefunctions, the Si−Cl and C−Cl bond lengths at the TC/TS and along the PES are analyzed. At the TC/TS, both the carbon and silicon systems have a $D_{3h}$ symmetry, with two equivalent

**Table 1:** Relative energies ($Cl^- + H_3XCl$) in kJ·mol$^{-1}$ at the stationary points of the $ClCH_3Cl$ and $ClSiH_3Cl$ systems obtained from different methods using the aug-cc-pVTZ basis set. The CCSD and MP2 energies were calculated based on the geometries obtained from the optimizations at the B3LYP/aug-cc-pVTZ basis set with dispersion correction (GD3BJ). ZPVE = zero-point vibrational energy.

| system | ΔE(B3LYP) incl. ZPVE + GD3BJ | ΔE(B3LYP) incl. GD3BJ | ΔE(B3LYP) incl. ZPVE | ΔE(B3LYP) | ΔE(CCSD) | ΔE(MP2) |
|---|---|---|---|---|---|---|
| $ClSiH_3Cl$, TC | -104.3 | -107.0 | -94.7 | -97.3 | -101.8 | -108.7 |
| $ClCH_3Cl$, TS | -12.0 | -10.3 | -5.1 | -3.4 | 22.4 | 20.7 |
| $ClCH_3Cl$, RC | -44.7 | -45.2 | -39.3 | -39.7 | -41.0 | -42.8 |

**Table 2:** $X-Cl_{leave}$ and $X-Cl_{in}$ bond lengths (in Å) obtained from geometry optimizations at the B3LYP/aug-cc-pVTZ level of theory with and without dispersion correction (GD3BJ).

| system | r(Si−$Cl_{leave}$) (incl. GD3BJ) | r(Si−$Cl_{leave}$) | r(Si−$Cl_{in}$) (incl. GD3BJ) | r(Si−$Cl_{in}$) |
|---|---|---|---|---|
| ClSiH3Cl, TC | 2.373 | 2.377 | 2.373 | 2.377 |
| ClCH3Cl, TS | 2.353 | 2.356 | 2.353 | 2.356 |
| ClCH3Cl, RC | 3.129 | 3.186 | 1.854 | 1.851 |

C−Cl or Si−Cl bond lengths. The optimized geometries of the TS and TC are depicted in Figure 4 and the C−Cl and Si−Cl bond lenghts are given in Table 2. Curiously, the C−Cl and Si−Cl bonds lengths are almost identical (2.35 Åvs 2.37 Å). Usually, one would expect C−Cl bonds to be shorter than Si−Cl bonds due to the larger atomic radius of the silicon atom. In fact, the bond lengths of the geometry optimized products of the $S_N2$ reaction, $H_3SiCl$ and $H_3CCl$, show that the C−Cl bond length (1.80 Å) is considerably shorter than the Si−Cl bond length (2.07 Å). This already indicates that the nature of the C−Cl bond in the TS is considerably different to a conventional C−Cl bond. If no dispersion correction is applied the bond lengths are only somewhat increased. At the reaction complex of the carbon system, the application of a dispersion correction has a greater influence on r(Si−$Cl_{leave}$) (3.13 Å with dispersion correction and 3.19 Å without dispersion correction), however, r(Si−$Cl_{in}$) is almost identical. Henceforth, all analyses are based on the geometries obtained with the application of a dispersion correction.

Along the PES, one X−Cl bond (X = C, Si) elongates causing the other X−Cl bond to shorten in response. Henceforth, we will index the properties of the bonds involving the leaving and incoming chlorine atoms with 'leave' and 'in', respectively. Figure 5 shows the C−Cl and Si−Cl bond lengths ($r_{in}$ and $r_{leave}$) plotted against each other. Both Si−Cl and C−Cl bond lengths start off at approximately the same value, however, the subsequent trend differs signifi-

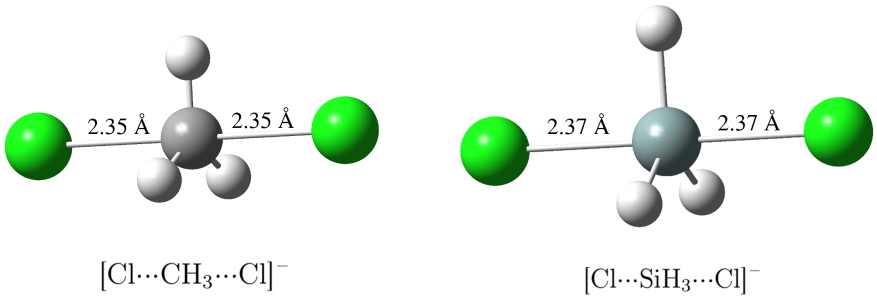


**Figure 4:** Geometry optimized structures at the B3LYP/aug-cc-pVTZ level of theory (incl. GD3BJ) of the transition state ($[Cl\cdots CH_3\cdots Cl]^-$) and the transition complex ($[Cl\cdots SiH_3\cdots Cl]^-$)

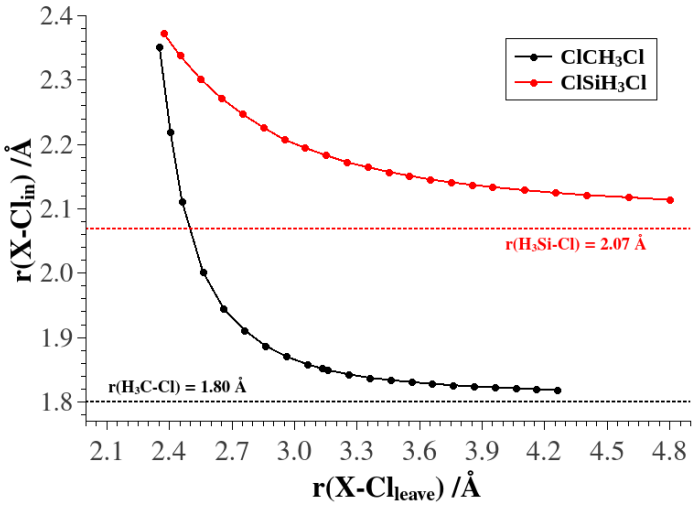


**Figure 5:** X−Cl bond lengths (X = Si, C), r(X−$Cl_{in}$) and r(X−$Cl_{leave}$), plotted against each other (units in Å).

cantly. As C−$Cl_{leave}$ is elongated, C−$Cl_{in}$ immediately responses with a drastic shortening. For the silicon system, the decrease in the Si−$Cl_{in}$ bond length is more moderate, which indicates that the change in the nature of the Si−$Cl_{in}$ bond is more subtle.

## 3.3 QTAIM analysis

The electron density at bond critical points ($\rho_{bcp}$) gives a representation of the strength of covalent interactions. Figure 6 shows $\rho_{bcp}$ plotted against the distance of the X−$Cl_{leave}$ bond. At the TC/TS, the silicon and carbon systems have similar values of $\rho_{bcp}$ (0.349 eÅ$^{-3}$ for C−Cl and

0.375 eÅ$^{-3}$ for Si−Cl). Normally, one would expect much higher values for conventional C−Cl bonds (e.g. 1.185 eÅ$^{-3}$ for $H_3C$−Cl). The unusually low value of $\rho_{bcp}$ and the long C−Cl bond length at the TS are an indication of a weak covalent interaction between C and Cl. Following

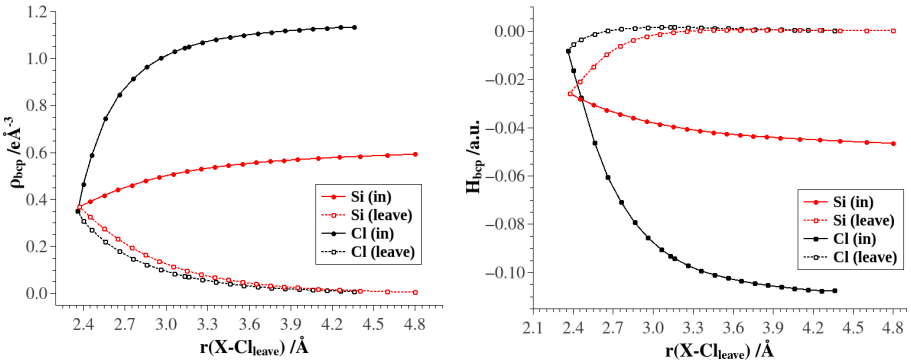


**Figure 6:** Properties at the X−Cl bond critical points plotted against the elongation of the X−Cl bond (X = C, Si): The electron density ($\rho_{bcp}$, left), and the total energy density ($H_{bcp}$, right).

the elongation of C−$Cl_{leave}$, $\rho_{bcp}$ of C−$Cl_{in}$ increases abruptly, which indicates a substantial increase in covalent interactions to C−$Cl_{in}$. Simultaneously, $\rho_{bcp}$ of C−$Cl_{leave}$ approaches a value of zero indicating covalent interactions to disappear completely. Interestingly, $\rho_{bcp}$ of C−$Cl_{leave}$ and Si−$Cl_{leave}$ show an almost identical trend. But the increase in $\rho_{bcp}$ of Si−$Cl_{in}$ is much less pronounced compared to the carbon system, and, thus, the strength of covalent interactions increases only slightly.

The total energy density at the X−Cl bcp ($H_{bcp}$), which is another indicator of covalent interactions, is plotted against the elongation of the X−Cl bond in Figure 6. At the TS, $H_{bcp}$ of C−Cl is only slightly negative, which indicates minor covalent interactions. Along the PES, C−$Cl_{leave}$ quickly approaches $H_{bcp} = 0$, while C−$Cl_{in}$ becomes substantially more negative, which is caused by an increase in covalent interactions. At the TC, $H_{bcp}$ of Si−Cl is more negative than C−Cl, but the subsequent decrease towards more negative values is substantially less pronounced. Also, $H_{bcp}$ of Si−$Cl_{leave}$ approaches zero at a slower rate. Accordingly, covalent interactions in Si−$Cl_{leave}$ remain significant beyond the TC.

## 3.4 Charges

Based on the electronegativity of C, Si and Cl, significant ionic interactions may only be expected for the Si−Cl bond. Figure 7 shows the Bader and NPA charges ($q_{\mathrm{Bader}}$ and $q_{\mathrm{NPA}}$)

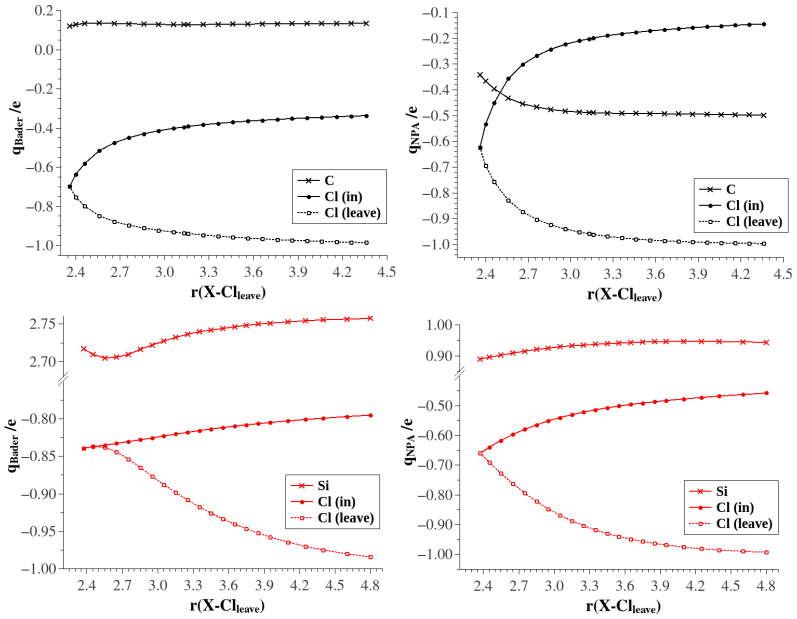


**Figure 7:** Bader and NPA charges of Si, C, $Cl_{in}$ and $Cl_{leave}$ plotted against the elongation of the X−Cl bond (X = C, Si)

of C, Si, $Cl_{in}$ and $Cl_{leave}$ plotted against the elongation of the C−Cl and Si−Cl bonds. Both $q_{Bader}$ and $q_{NPA}$ suggest a large charge separation between Si and Cl at the TC, which is more pronounced in $q_{Bader}$. The charge separation between C and Cl at the TS, on the other hand, can hardly induce attractive Coulomb interactions, because $q_{Bader}$ of the carbon atom is only slightly positive and $q_{NPA}$ even suggests a negative charge of the carbon atom. Along the PES, the C−$Cl_{in}$ charge separation is reduced, because the charge of $Cl_{in}$ decreases towards less negative values and the charge of the carbon atom remains approximately constant. In $q_{NPA}$, the charge of $Cl_{in}$ even crosses the charge of the carbon atom. In the silicon system, the charge of $Cl_{in}$ decreases only slightly and the charge of Si increases towards more positive values to a similar extent. Accordingly, the Si−$Cl_{in}$ charge separation remains approximately constant along the PES, and electrostatic interactions remain the most substantial contribution to the Si−$Cl_{in}$ bond. The charges of $Cl_{leave}$ of the carbon and silicon systems approach a value of $q = -1$, which corresponds to the charge of an isolated chlorine atom.

### 3.5 NBO analysis

For the systems regarded in this study, a special treatment was necessary to obtain reasonable results from an NBO analysis. An NBO structure was predefined in the input, because a default analysis gives NBOs with high d-orbital populations, which is contradictory to the results of the natural population analysis.[44] To avoid a faulty NBO analysis, four lone pairs were predefined at the two chlorine atoms, schematically resulting in the NBO structures $Cl^-\,CH_3{}^+\,Cl^-$ and $Cl^-\,SiH_3{}^+\,Cl^-$. Due to the absence of C−Cl and Si−Cl NBOs, strong interactions between one of the chlorine lone pairs and a lone valency of the Si and C atoms emerge. The interacting NBOs are, for the most part, constructed of p-orbitals which are aligned with the Cl−X−Cl axis.

The change in X−Cl bond character can be analyzed in terms of the electron populations of the chlorine lone pairs and the lone valencies at C and Si. In case of a strong covalent interaction, the Cl lone pair population is low and the population of the lone valency is high. The remaining three chlorine lone pairs have electron populations of $N \approx 2$ and can therefore be regarded as localized. Figure 8 shows the population of the chlorine lone pair (N(LP(Cl)))

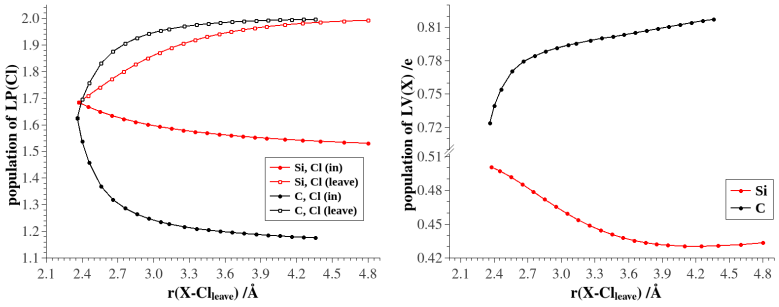


**Figure 8:** Properties from the NBO analysis: The populations of the chlorine lone pairs N(LP(Cl)) and the lone valency (LV(X)) involved in the bonded interaction

and the population of the lone valency (N(LV(X)) plotted against the elongation of the X−Cl bond. Starting from the TC/TS, the lone pair population of $Cl_{in}$ decreases in the carbon and silicon systems, which suggests an increase in covalency to the C−$Cl_{in}$ and Si−$Cl_{in}$ bonds. However, the decrease is considerably more pronounced in the carbon system. The lone pair populations of $Cl_{leave}$, on the other hand, increase in the carbon and silicon systems towards a value of $N = 2$, which corresponds to the population of a localized lone pair which is not involved in a bonded interaction.

The electron population of the lone valency at C and Si is a descriptor which monitors

the electronic changes at the electrophilic center alone. The carbon and silicon systems show an opposite trend: While N(LV(C)) increases, N(LV(Si)) decreases as the X−Cl bond is elongated. The previously regarded descriptors show that the covalency increases in the C−$Cl_{in}$ and Si−$Cl_{in}$ bonds. However, the populations of the lone valency show that the overall covalent interactions increase in the carbon system, while they become less significant in the silicon system. For the carbon system, a maximum of covalency is obtained if the carbon atom is involved in four covalent bonds. In contrast to that, a pentacoordination gives the highest possible extent of covalency in the silicon system. All previously regarded descriptors show that the covalency of the Si−$Cl_{in}$ bond increases, however, this increase cannot counterbalance the decrease of covalent interactions resulting from the loss of the Si−$Cl_{leave}$ bonded interaction.

## 3.6 Analysis of valence bond calculations

Structures **2a)**, **2b)** and **3)** in Figure 2 were considered for the valence bond (VB) calculations of the carbon and silicon systems. Figure 9 shows the corresponding weights of these structures plotted against the elongation of the X−Cl bond. At the TC/TS, the weights of the carbon and silicon systems are similar. The ionic structures (**3)**) are most significant, and the weights of the two covalent structures (**2a)** and **2b)**) are identical due to the symmetric X−Cl bonds.

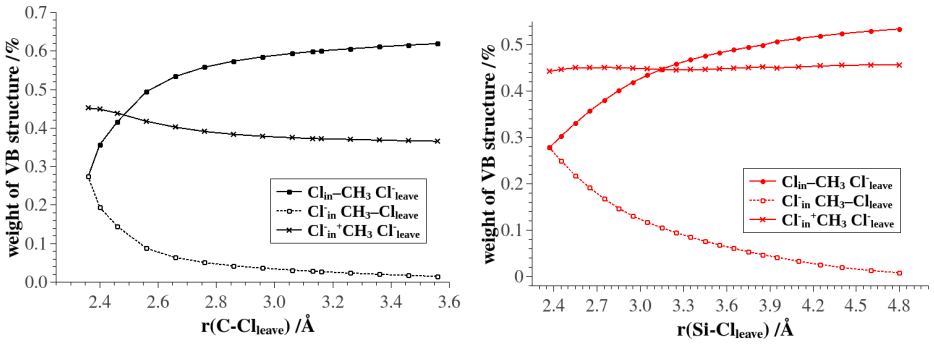


**Figure 9:** Weights of the the valence bond structures of the carbon and silicon systems plotted against the elongation of the X−Cl bond

In the carbon system, the VB structure with a bond between carbon and $Cl^-_{in}$ rapidly gains in significance and quickly becomes more meaningful than the ionic structure (**3)**). At the same time, the weight of the VB structure with C−$Cl_{leave}$ decreases at a similar rate. The VB structure with a bond between silicon and $Cl_{in}$ also gains in significance, however, at a

slower rate compared to the carbon system. The weight of this structure becomes larger than the one of the ionic structure at a much later stage indicating that closed shell interactions are more meaningful in the silicon system. The weight of the ionic structure of the carbon system decreases only slightly, while the ionic structure of the silicon system remains approximately constant. Ultimately, both C−$Cl_{in}$ and Si−$Cl_{in}$ contain covalent and ionic interactions as indicated by the weights of the covalent and ionic structures, but overall the ionic interactions are more meaningful for Si−$Cl_{in}$ than for C−$Cl_{in}$.

According to the valence bond calculations, the bonding situation at the TC/TS can be expressed by three non-hypervalent Lewis structures. In fact, valence bond calculations fail if hypervalent structures are also considered. Because of the significance of the ionic structures, the Si−Cl and C−Cl bonds contain less than two electrons.

# 4 Conclusions

Using a variety of bond analysis methods from the realms of real space and orbital space, we could gain a deep insight into the distinct bonding nature at the transition state of the carbon system and the transition complex of the silicon system. The covalency in the C−Cl and Si−Cl bonds is low and similar to each other. In contrast to the TS, C−Cl bonds of tetracoordinated carbon atoms show a much higher covalency. Also, ionic interactions do not play a role in the C−Cl bonds of the TS, because the charge of the carbon atom is more or less neutral. In the silicon system, Si is very positive and Cl very negative, so ionic interactions play a big role in the stabilization of the transition complex. In contrast, the carbon system is only stabilized by weak covalent interactions at the TS. At the TS and TC of the carbon and silicon systems, the application of a dispersion correction does not greatly influence the X−Cl bond lengths. However, the significance of dispersion interactions is reflected by lower relative energies if a dispersion correction is applied. At the RC of the carbon system, the C−$Cl_{leave}$ distance is somewhat shorter for the dispersion corrected geometry optimization.

All bonding descriptors agree that the covalent interactions of C−$Cl_{in}$ increase rapidly and substantially in the carbon system. They also increase for Si−$Cl_{in}$ in the silicon system, however, less rapidly and to a smaller extent. For the carbon system, the total covalent interactions increase as C−$Cl_{leave}$ is elongated. This is caused by the substantial increase in covalency of C−$Cl_{in}$. At the same time, the covalency of C−$Cl_{leave}$ decreases until there is no significant interaction between C and $Cl_{leave}$, but since the covalent interactions are weak at the transition state, the drastic increase in covalency of C−$Cl_{in}$ more than compensates for the decrease in

covalency of C – $Cl_{leave}$. The opposite is true for the silicon system: At the TC, the total covalent interactions are at a maximum and decrease from there on, because the covalency of Si – $Cl_{in}$ only increases slightly, while the covalency of Si – $Cl_{leave}$ is lost completely.

The valence bond calculations have shown that the bonding situation in the carbon and silicon systems can be sufficiently expressed by three resonance structures corresponding to $Cl^-$ $CH_3$ – Cl, Cl – $CH_3$ $^-$Cl and $Cl^-$ $^+CH_3$ $^-$Cl for the carbon system and $Cl^-$ $SiH_3$ – Cl, Cl – $SiH_3$ $^-$Cl and $Cl^-$ $^+SiH_3$ $^-$Cl for the silicon system. Hypervalent representations, corresponding to $[Cl-CH_3-Cl]^-$ and $[Cl-SiH_3-Cl]^-$, that require d-orbital participation, are of no importance.

At the transition state of the carbon system, neither covalent nor ionic interactions can sufficiently stabilize the C – Cl bonds, which describes the nature of a TS. This is different at the transition complex of the silicon system, which is stablized by major ionic interactions as well as minor covalent interactions. This undelines that pentacoordination is feasible in silicon systems and, thus, a stable transition complex can be obtained.

## Acknowledgements

S.G. thanks the German Research Foundation(Deutsche Forschungsgemeinschaft, DFG) for funding within the Emmy Noether project GR 4451/1-1.

## References

[1] W. Cowdrey, E. Hughes, C. Ingold, S. Masterman and A. Scott, *J. Chem. Soc.*, 1937, 1252–1271.

[2] J. Xie and W. L. Hase, *Science*, 2016, **352**, 32–33.

[3] G. Vayner, K. Houk, W. L. Jorgensen and J. I. Brauman, *J. Am. Chem. Soc.*, 2004, **126**, 9054–9058.

[4] L. Sun, K. Song and W. L. Hase, *Science*, 2002, **296**, 875–878.

[5] W. N. Olmstead and J. I. Brauman, *J. Am. Chem. Soc.*, 1977, **99**, 4219–4228.

[6] P. Manikandan, J. Zhang and W. L. Hase, *J. Phys. Chem. A*, 2012, **116**, 3061–3080.

[7] W. L. Hase, *Science*, 1994, **266**, 998–1002.

[8] S. Gronert, *Acc. Chem. Res.*, 2003, **36**, 848–857.

[9] M. L. Chabinyc, S. L. Craig, C. K. Regan and J. I. Brauman, *Science*, 1998, **279**, 1882–1886.

[10] W. N. Olmstead and J. I. Brauman, *J. Am. Chem. Soc.*, 1977, **99**, 4219–4228.

[11] A. Merkel, Z. Havlas and R. Zahradnik, *J. Am. Chem. Soc.*, 1988, **110**, 8355–8359.

[12] P. Baybutt, *Mol. Phys.*, 1975, **29**, 389–403.

[13] S. Gronert, R. Glaser and A. Streitwieser, *J. Am. Chem. Soc.*, 1989, **111**, 3111–3117.

[14] J. Payzant, K. Tanaka, L. Betowski and D. Bohme, *J. Am. Chem. Soc.*, 1976, **98**, 894–899.

[15] Z. Shi and R. J. Boyd, *J. Phys. Chem.*, 1991, **95**, 4698–4701.

[16] A. P. Bento and F. M. Bickelhaupt, *J. Org. Chem.*, 2007, **72**, 2201–2207.

[17] T. A. Hamlin, M. Swart and F. M. Bickelhaupt, *ChemPhysChem*, 2018, **19**, 1315–1330.

[18] M. A. van Bochove and F. M. Bickelhaupt, *Eur. J. Org. Chem.*, 2008, **2008**, 649–654.

[19] K.-Y. Akiba, M. Yamashita, Y. Yamamoto and S. Nagase, *J. Am. Chem. Soc.*, 1999, **121**, 10644–10645.

[20] W. Kutzelnigg, *Angew. Chem.*, 1984, **96**, 262–286.

[21] A. E. Reed and F. Weinhold, *J. Am. Chem. Soc.*, 1986, **108**, 3586–3593.

[22] A. E. Reed and P. v. R. Schleyer, *J. Am. Chem. Soc.*, 1990, **112**, 1434–1445.

[23] M. Fugel, L. A. Malaspina, R. Pal, S. P. Thomas, M. W. Shi, M. A. Spackman, K. Sugimoto and S. Grabowsky, *Chem. Eur. J.*, 2019, **25**, 6523–6532.

[24] M. S. Schmøkel, S. Cenedese, J. Overgaard, M. R. Jørgensen, Y.-S. Chen, C. Gatti, D. Stalke and B. B. Iversen, *Inorg. Chem.*, 2012, **51**, 8607–8616.

[25] R. J. Gillespie and E. A. Robinson, *Inorg. Chem.*, 1995, **34**, 978–979.

[26] G. Frenking and S. Shaik, *The Chemical Bond: Fundamental Aspects of Chemical Bonding*, Wiley, 2014.

[27] S. Mebs, R. Kalinowski, S. Grabowsky, D. Förster, R. Kickbusch, E. Justus, W. Morgenroth, C. Paulmann, P. Luger, D. Gabel *et al.*, *Inorg. Chem.*, 2010, **50**, 90–103.

[28] M. Kohout, *Faraday Discuss.*, 2007, **135**, 43–54.

[29] P. Macchi and A. Sironi, *Coord. Chem. Rev.*, 2003, **238**, 383–412.

[30] C. Gatti, *Z. Kristallog. Cryst. Mater.*, 2005, **220**, 399–457.

[31] F. Weinhold, *J. Comput. Chem.*, 2012, **33**, 2363–2379.

[32] P. L. Popelier, *Intermolecular forces and clusters I*, Springer, 2005, pp. 1–56.

[33] M. Fugel, J. Beckmann, D. Jayatilaka, G. V. Gibbs and S. Grabowsky, *Chem. Eur. J.*, 2018, **24**, 6248–6261.

[34] M. Fugel, M. F. Hesse, R. Pal, J. Beckmann, D. Jayatilaka, M. J. Turner, A. Karton, P. Bultinck, G. S. Chandler and S. Grabowsky, *Chem. Eur. J.*, 2018, **24**, 15275–15286.

[35] R. F. W. Bader, *Chem. Rev.*, 1991, **91**, 893–928.

[36] R. F. Bader, *J. Phys. Chem. A*, 1998, **102**, 7314–7323.

[37] F. Weinhold and C. R. Landis, *Chem. Educ. Res. Pract.*, 2001, **2**, 91–104.

[38] F. Weinhold and C. R. Landis, *Valency and bonding: a natural bond orbital donor-acceptor perspective*, Cambridge University Press, 2005.

[39] W. Wu, P. Su, S. Shaik and P. C. Hiberty, *Chem. Rev.*, 2011, **111**, 7557–7593.

[40] M. J. Frisch, G. W. Trucks, H. B. Schlegel, G. E. Scuseria, M. A. Robb, J. R. Cheeseman, G. Scalmani, V. Barone, G. A. Petersson, H. Nakatsuji, X. Li, M. Caricato, A. V. Marenich, J. Bloino, B. G. Janesko, R. Gomperts, B. Mennucci, H. P. Hratchian, J. V. Ortiz, A. F. Izmaylov, J. L. Sonnenberg, D. Williams-Young, F. Ding, F. Lipparini, F. Egidi, J. Goings, B. Peng, A. Petrone, T. Henderson, D. Ranasinghe, V. G. Zakrzewski, J. Gao, N. Rega, G. Zheng, W. Liang, M. Hada, M. Ehara, K. Toyota, R. Fukuda, J. Hasegawa, M. Ishida, T. Nakajima, Y. Honda, O. Kitao, H. Nakai, T. Vreven, K. Throssell, J. A. Montgomery, Jr., J. E. Peralta, F. Ogliaro, M. J. Bearpark, J. J. Heyd, E. N. Brothers, K. N. Kudin, V. N. Staroverov, T. A. Keith, R. Kobayashi, J. Normand, K. Raghavachari, A. P. Rendell, J. C. Burant, S. S. Iyengar, J. Tomasi, M. Cossi, J. M. Millam, M. Klene, C. Adamo, R. Cammi, J. W. Ochterski, R. L. Martin, K. Morokuma, O. Farkas, J. B. Foresman and D. J. Fox, *Gaussian 09, revision D. 01*, 2009.

[41] T. A. Keith, *TK Gristmill Software, Overland Park KS, USA*, 2013.

[42] E. D. Glendening, C. R. Landis and F. Weinhold, *J. Comput. Chem.*, 2013, **34**, 1429–1437.

[43] L. Song, Y. Mo, Q. Zhang and W. Wu, *J. Comput. Chem.*, 2005, **26**, 514–521.

[44] M. Fugel, F. Kleemiss, L. A. Malaspina, R. Pal, P. R. Spackman, D. Jayatilaka and S. Grabowsky, *Austr. J. Chem.*, 2018, **71**, 227–237.

# Chapter 10

# The role of hydrogen bonding in gas-phase $S_N2$ reactions at silicon

In this manuscript, the influence of hydrogen bonding on $S_N2$ reactions at silicon atoms is uncovered, and it is shown how they influence the potential energy surfaces of these reactions. Just like the previous manuscript, the study is based on the idea followed in the master's thesis of Anneke Dittmer. Again, none of the results in this manuscripts are from her master's thesis, but can be regarded as an original contribution to my thesis. In the following my contributions to this manuscript are given:

- I wrote $\approx 90\%$ of the text
- I performed all optimizations and the potential energy surface scan
- I performed all analyses
- I interpreted the results
- I am responsible for all figures and tables

The manuscript is currently (June 25th, 2019) in the peer preview process of *Physical Chemistry Chemical Physics* (see confirmation on the following page).

**Subject:** Acknowledgement of your Submission to Physical Chemistry Chemical Physics - CP-ART-06-2019-003506
**From:** Physical Chemistry Chemical Physics <onbehalfof@manuscriptcentral.com>
**Date:** 21.06.19, 17:33
**To:** simon.grabowsky@uni-bremen.de
**CC:** m.fugel@uni-bremen.de, dittmer@kofo.mpg.de, florian.kleemiss@uni-bremen.de, simon.grabowsky@uni-bremen.de

21-Jun-2019

Dear Dr Grabowsky:

TITLE: The role of hydrogen bonding in gas-phase S<sub>N</sub>2 reactions at silicon

Thank you for your submission to Physical Chemistry Chemical Physics, published by the Royal Society of Chemistry. This is an automatic acknowledgement that you have uploaded your files to our online submission system. Your manuscript ID is: CP-ART-06-2019-003506

Your manuscript will be passed to an editor for initial assessment as soon as possible. If there are any problems with your submission we will contact you.

## Submitted Manuscripts

**Manuscript status explanation:**

1. **Checking submission and files** - we are checking to see if your submission is complete and we have all the files we need.
2. **Initial assessment** - manuscript is undergoing initial assessment.
3. **With editor** - manuscript is with the editor, either to select new or additional reviewers, or to make a decision following initial assessment or peer review.
4. **In peer review** - manuscript has been sent to reviewers.
5. **Accepted** - manuscript has been accepted for publication.

Please note that manuscripts can move back and forth between status 3 and 4.

| STATUS | ID | TITLE | CREATED | SUBMITTED |
|---|---|---|---|---|
| In peer review | CP-ART-06-2019-003506 | The role of hydrogen bonding in gas-phase $S_N2$ reactions at silicon View Submission | 21-Jun-2019 | 21-Jun-2019 |
| In peer review | CP-ART-06-2019-003505 | The differences between carbon and silicon in $S_N2$ reactions revealed by a complementary bonding analysis View Submission | 21-Jun-2019 | 21-Jun-2019 |

# The role of hydrogen bonding in gas-phase $S_N2$ reactions at silicon

Malte Fugel[a], Anneke Dittmer[a,b], Florian Kleemiss[a], and Simon Grabowsky[*a]

[a]Universität Bremen, Fachbereich 2 – Biologie / Chemie, Leobener Str. 3, 28359 Bremen, Germany.

[b]*current address:* Max-Planck-Institut für Kohlenforschung, Kaiser-Wilhelm-Platz 1, 45470 Mülheim an der Ruhr, Germany.

[*]simon.grabowsky@uni-bremen.de

July 2, 2019

**Abstract**

The shape of the potential energy surface (PES) of gas-phase $S_N2$ reactions at silicon is determined by the type of nucleophile, leaving group and substituents which remain bonded to the silicon. In this study, we present PES scans along the reaction coordinate of six symmetrical $S_N2$ reactions: $X^- + SiR_3X \longrightarrow XSiR_3 + X^-$, where X = Cl or F, and R = H, Me or OMe. While the fluorine systems and the $ClSiH_3Cl$ system only give single-well PESs, $ClSiMe_3Cl$ and $ClSi(OMe)_3Cl$ give triple and double well PESs with stable pre- and post-reaction complexes. Energy decomposition analyses (EDA) as well as analyses based on the Quantum Theory of Atoms in Molecules (QTAIM) and natural bond orbitals (NBO) reveal that the leaving group ($X^-$) is stabilized by hydrogen bonding in the $XSiMe_3X$ and $XSi(OMe)_3X$ systems. It is shown that this stabilization, along with $\sigma$-hole bonding, is responsible for the shapes of the PESs of $ClSiMe_3Cl$ and $ClSi(OMe)_3Cl$ in the gas phase.

# 1 Introduction

Nucleophilic substitutions following the $S_N2$ mechanism are among the most important and most investigated chemical reactions.[1–9] For $S_N2$ reactions at carbon atoms, reactants and products are separated by a transition state corresponding to a maximum in the potential energy surface (PES).[5] This is caused by the instability of the pentacoordinated species at the transition state ($X\cdots CR_3\cdots Y$). However, complexes with pentacoordinated silicon atoms often show a high stability[10] and, thus, $S_N2$ reactions at silicon atoms can give stable pentacoordinated transition complexes ($X\cdots SiR_3\cdots Y$) separating the reactands and products.[11] Whether an instable transition state (TS) or a stable transition complex (TC) is formed depends on the type of nucleophile, the leaving group and the substituents which remain bonded to the electrophilic center.[11,12] Bento *et al* showed that there are three distinct shapes of the PES for $S_N2$ reactions at silicon atoms,[11] which are depicted in Figure 1:

1. A single-well potential with a stable intermediate transition complex (TC)
2. A double-well potential with a transition state (TS) and a stable reaction complex before and after the central TS (RC1 and RC2)
3. A triple-well potential with a stable intermediate TC and a TS before and after it (TS1 and TS2), as well as a stable reaction complex before TS1 and after TS2 (RC1 and RC2)

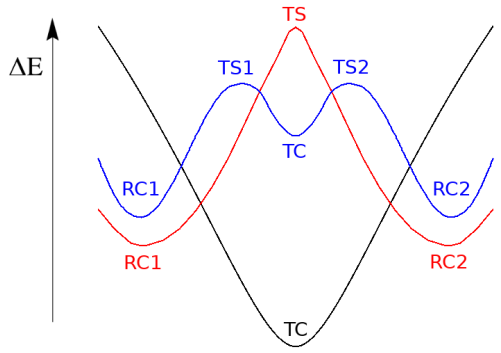


**Figure 1:** Single- (black), double- (red) and triple-well (blue) potential energy surfaces of $S_N2$ reactions at silicon atoms (TS = transition state; TC = transition complex; RC = reaction complex)

It has been shown previously that the shape of the PES is drastically influenced by the presence of a solvent, in that the energy of the central reaction species is raised. Consequently,

the TC of the single-well PES can turn into a TS, and a double-well PES can lose its two minima and turn into a unimodal PES.[13] Therefore, we only consider gas-phase reactions here.

An energy decomposition analysis (EDA) revealed that an interplay of steric (Pauli) repulsion and electronic effects is responsible for the distinct shapes of the PES.[11,12,14] In the present paper, we investigate the PES of $S_N2$ reactions at silicon centers of six model systems (see reactions 1 – 6), which include all three PES shapes.

$$Cl^- + H_3SiCl \longrightarrow [Cl\cdots SiH_3\cdots Cl]^- \longrightarrow ClSiH_3 + Cl^- \quad (1)$$

$$Cl^- + Me_3SiCl \longrightarrow [Cl\cdots SiMe_3\cdots Cl]^- \longrightarrow ClSiMe_3 + Cl^- \quad (2)$$

$$Cl^- + (OMe)_3SiCl \longrightarrow [Cl\cdots Si(OMe)_3\cdots Cl]^- \longrightarrow ClSi(OMe)_3 + Cl^- \quad (3)$$

$$F^- + H_3SiF \longrightarrow [F\cdots SiH_3\cdots F]^- \longrightarrow FSiH_3 + F^- \quad (4)$$

$$F^- + Me_3SiF \longrightarrow [F\cdots SiMe_3\cdots F]^- \longrightarrow FSiMe_3 + F^- \quad (5)$$

$$F^- + (OMe)_3SiF \longrightarrow [F\cdots Si(OMe)_3\cdots F]^- \longrightarrow FSi(OMe)_3 + F^- \quad (6)$$

It was believed so far as textbook knowledge that the reaction complexes are stabilized by $\sigma$-hole bonding between the electrophilic silicon atom and the nucleophilic atom. A $\sigma$-hole is an electropositive region located opposite to a covalent bond (A – B), which can therefore bind a nucleophile (Nu···A – B) in a highly-directional interaction.[15] The concept of $\sigma$-hole bonding can also be expressed in terms of negative hyperconjugation, which can be understood as the interaction between a lone pair of the nucleophile and the $\sigma^*$-orbital of a covalent bond (LP(Nu) $\rightarrow$ $\sigma^*(A-B)$).[16] For carbon chemistry, it was recently shown that hydrogen bonding also plays a major and so far underestimated role.[17] Hydrogen bonding can also be considered as negative hyperconjugation, where the lone pair of a nucleophile acts as a donor, and the $\sigma^*$-orbital of an X – H bond as a lone pair acceptor (LP(Nu) $\rightarrow$ $\sigma^*$(X – H)).

The purpose of the present paper is to investigate how the PES along the reaction coordinate of gas-phase $S_N2$ reactions at silicon atoms are influenced by hydrogen bonding in comparison to $\sigma$-hole bonding. With regard to the six model systems investigated in the present study, hydrogen bonds may be formed between the C – H bonds of the methyl and methoxy systems (reactions 2, 3, 5, 6) and the leaving group $X^-$. C – H···X hydrogen bonding is much weaker than N – H···X and O – H···X hydrogen bonding,[18–20] but nonetheless it plays an important role in mechanisms of biological action[21] and crystal engineering[22]. If a solvent, which can act as a donor for hydrogen bonds, is present, the weak hydrogen bonds formed between $R_3SiX$ and $X^-$ will only play a minor role, and will no longer significantly affect the shape of the PES. For

that reason, the analysis is only performed in the gas phase without taking solvation effects into account.

In the present paper, PES scans were performed for the model systems of reactions 1 – 6. Starting from the TS or TC, the leaving group $X^-$ was pulled away from the silicon atom and the structure was relaxed while keeping the Si–X distance fixed. The calculations were performed on the isolated species with the inclusion of a dispersion correction (GD3BJ).[23] A Ziegler-Rauk EDA[24,25] and a QTAIM analysis[26] were performed for the species along the PES. Additionally, an NBO analysis[27] was performed for a qualitative understanding of the interactions. These bond analysis methods are briefly outlined in the following. A more detailed description can be found elsewhere in literature.[16,28–31]

In an EDA, the interaction energy between two fragments ($\Delta E_{int}$) is decomposed into physically meaningful components according to equation 7.[25]

$$\Delta E_{int} = \Delta E_{orb} + \Delta E_{elect} + \Delta E_{Pauli}(+\Delta E_{disp}) \tag{7}$$

where $\Delta E_{orb}$ is the orbital interaction, $\Delta E_{elect}$ is the electrostatic interaction, $\Delta E_{Pauli}$ is the Pauli repulsion, and $\Delta E_{disp}$ is the dispersion interaction. The results of the EDA depend on the choice of fragmentation.[30] Here, a heterolytical fragementation was applied: One fragment corresponds to the negatively charged leaving group ($X^-$), while the other fragment corresponds to the neutral $R_3SiX$ species.

In an analysis based on the Quantum Theory of Atoms in Molecules (QTAIM), atomic basins are obtained from a topological analysis of the electron density.[29] The delocalization index (DI) measures the number of electron pairs exchanged between two atomic basins. Therefore, it can be regarded as a covalent bond index.[32] Natural bond orbitals are localized orbitals which can be related to features of conventional Lewis formulas (e.g. bonds and lone pairs) and non-Lewis type orbitals (e.g. extra-valenent Rydberg orbitals or antibonds).[16] The interaction between donor and acceptor orbitals can reveal interactions, such as negative hyperconjugation.

## 2 Computational Details

The geometry optimizations were carried out with Gaussian 09 at the B3LYP/aug-cc-pVTZ level of theory, with inclusion of a dispersion correction (GD3BJ).[33] An analytical frequency analysis was performed to validate the geometries at the stationary points. The energies were corrected by the zero point vibrational energy and the basis set superposition error (BSSE) with respect to the reactands ($R_3SiX$ and $X^-$). A PES scan was performed to obtain the structures

along the gas-phase $S_N2$ reaction coordinate. For that purpose, the leaving group was pulled away from the central atom, while keeping the Si−X distance fixed, and optimizing all other atomic positions freely. A frequency analysis was performed for the resulting structures to validate that they lie on the reaction coordinate. Reaction energies were calculated relative to the geometry-optimized reactants/products of the reaction, that is, $R_3SiX$ and $X^-$. CCSD and MP2 calculations with the aug-cc-pVTZ basis set and BSSE correction were performed on the geometry-optimized structures at the stationary points to obtain more accurate energies.

The energy decomposition analysis (EDA) was performed with ADF[34] at a B3LYP/ATZP level of theory and a diserpersion correction (GD3BJ) based on the optimized geometries from Gaussian 09. The QTAIM analysis was carried out with AIMall[35] and NBO6 was applied for the NBO analysis.[36]

# 3 Results and discussion

## 3.1 Potential energy surfaces

The potential energy surfaces of the six model systems (reactions 1 - 6) are depicted in Figure 2. $FSiH_3F$, $FSiMe_3F$, $FSi(OMe)_3F$ and $ClSiH_3Cl$ give single-well potential energy surfaces with a

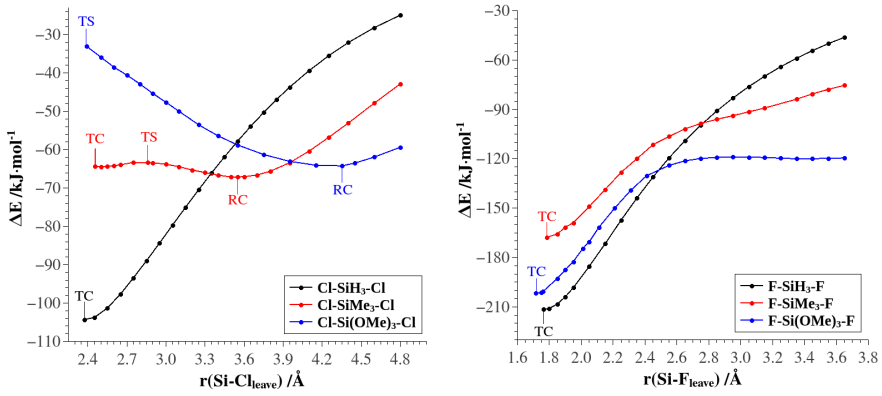


**Figure 2:** Potential energy surfaces of the six model systems along the $S_N2$ reaction reaction coordinate at silicon atoms; The reaction energy $\Delta E$ is measured relative to the reactants/products $H_3SiX$ and $X^-$.

stable transition complex (TC). A TC is also obtained for $ClSiMe_3Cl$, which gives a triple-well PES, while a double-well PES with a transtion state (TS) is obtained for $ClSi(OMe)_3Cl$. Close

to the TC, the fluorine systems are energetically significantly more stable (more negative $\Delta E$ values) than the chlorine systems, which shows the high affinity of fluorine to be bonded to silicon. For $ClSiH_3Cl$ and the fluorine systems, the pentacoordinated species at the central TC corresponds to the global minimum of the PES. For $ClSiMe_3Cl$ and $ClSi(OMe)_3Cl$, on the other hand, the global minima are the reaction complexes (RC, see Figure 2). The central TC of the $ClSiH_3Cl$ system is energetically significantly more stable than the central TC and TS of $ClSiMe_3Cl$ and $ClSi(OMe)_3Cl$, respectively. However, the energy of the $ClSiH_3Cl$ system increases rapidly towards less negative values until the $ClSiMe_3Cl$ and $ClSi(OMe)_3Cl$ systems show a higher stability. Beyond the RC of these systems, the energy starts increasing towards less negative values. At its TC, the $FSiH_3F$ system is the most stable system. However, starting from $r(Si–F_{leave}) \approx 2.5$ Å, the $FSi(OMe)_3F$ system shows the highest stability, while the $FSiH_3F$ system is the least stable one. Consequently, there must be some factor that results in an energetic stabilization of the methyl and methoxy systems at high $Si–X_{leave}$ distances.

The energies at the extrema of the PES were calculated with different methods (see Table 1). For the fluorine systems, CCSD and MP2 energies are generally more negative than the DFT energies. For the chlorine systems, this trend is not confirmed. In general, the differences between the methods are bigger than the ZPVE correction, but confirm that the trends in the DFT energies can safely be discussed in the following chapters; the shapes of the PESs are not altered by using post-HF instead of dispersion corrected DFT methods.

**Table 1:** Relative energies (in kJ/mol) of the silicon systems at the TC, TS and RC obtained with different methods. The calculations were performed at the B3LYP/aug-cc-pVTZ geometries. ZPVE = zero point vibrational energy.

| Method | $ClSiH_3Cl$ | $ClSiMe_3Cl$ | | | $ClSi(OMe_3)_3Cl$ | | $FSiH_3F$ | $FSiMe_3F$ | $FSi(OMe_3)_3F$ |
|---|---|---|---|---|---|---|---|---|---|
| | TC | TC | TS | RC | TS | RC | TC | TC | TC |
| B3LYP-D3 (ZPVE correction) | -104.3 | -64.4 | -63.3 | -67.1 | -33.0 | -64.1 | -211.4 | -167.7 | -201.6 |
| B3LYP-D3 (no ZPVE correction) | -107.0 | -65.8 | -63.9 | -68.2 | -31.4 | -64.6 | -215.7 | -168.7 | -204.2 |
| CCSD(no ZPVE correction) | -101.8 | -62.7 | -60.4 | -64.4 | -25.5 | -58.6 | -223.1 | -183.3 | -221.3 |
| MP2 (no ZPVE correction) | -108.7 | -74.2 | -69.3 | -69.6 | -39.6 | -62.7 | -218.9 | -178.6 | -215.1 |

## 3.2 Energy decomposition analysis

An EDA, based on two fragments corresponding to $R_3SiX$ and $X^-_{leave}$, which describe a heterolytical bond cleavage, can help uncover the interactions which lead to the PESs depicted in Figure 2. Figure 3 shows the bond interaction energy ($\Delta E_{int}$), its individual components ($\Delta E_{orb}$, $\Delta E_{elect}$, and $\Delta E_{Pauli}$) and the percentage of $\Delta E_{orb}$ to the attractive energy components

($\Delta E_{orb}$, $\Delta E_{elect}$ and $\Delta E_{disp}$) plotted against the Si–$X_{leave}$ distance. A dispersion correction (GD3BJ) was performed within the EDA, which shows that dispersion interactions also lead to an energetic stabilization of the PES, but these interactions are only of minor importance in comparison to the other energy components. Details for $\Delta E_{disp}$ are given in the Supporting Information.

For all systems, the highest interaction energy ($\Delta E_{int}$) is obtained at the TS or TC. From that point on, $\Delta E_{int}$ increases towards less negative values, which indicates that the interaction of $X^-_{leave}$ to the $R_3SiX$ fragment decreases with the distance between the two fragments. Close to the TC or TS, $\Delta E_{int}$ shows an almost identical trend for the three chlorine systems. Only at Si–$Cl_{leave}$ distances starting from ≈3 Å, the plots of $\Delta E_{int}$ start to deviate from each other. From that point on, $ClSi(OMe)_3Cl$ shows the highest interaction energy ($\Delta E_{int}$ is the most negative), and, shortly after, the interaction energy of $ClSiMe_3Cl$ is also higher than the one of $ClSiH_3Cl$. The interaction energy of $ClSi(OMe)_3Cl$ remains relatively constant from r(Si–$Cl_{leave}$) ≈ 3.0 Å onwards. In the fluorine systems, $\Delta E_{int}$ already deviates close to the TC: The interaction energy is the highest in $FSi(OMe)_3F$ and the lowest in $FSiMe_3F$. Only starting from r(Si–$F_{leave}$) ≈ 2.7 Å, the interaction energy of $FSiMe_3F$ is higher than the one in $FSiH_3F$. The interaction energy in $FSi(OMe)_3F$ remains the strongest throughout the whole range of the plot.

For the whole range of Si–$X_{leave}$ distances, the strongest electrostatic interactions (most negative values of $\Delta E_{elect}$) are present in the methoxy systems ($ClSi(OMe)_3Cl$ and $FSi(OMe)_3F$), while they are the weakest in the hydrogen systems ($ClSiH_3Cl$ and $FSiH_3F$). This is caused by the fact that the methoxy group is the most electron-withdrawing substituent and, thus, the silicon atoms of $ClSi(OMe)_3Cl$ and $FSi(OMe)_3F$ are the most polarized ones, which, in turn, inflict the strongest electrostatic interactions between $R_3SiX$ and $X^-$. However, the methoxy substituents are also the bulkiest ones, which causes the highest sterical repulsion to be present in $ClSi(OMe)_3Cl$ and $FSi(OMe)_3F$. Close to the central TC or TS, the influence of the type of substituent on the Pauli repulsion energy ($\Delta E_{Pauli}$) is relatively small. Only when $X^-$ starts interacting with the methyl and methoxy substituents, which is only the case at higher Si–$X_{leave}$ distances, significant differences start to show. Overall, the Pauli repulsion decreases for all systems with increasing Si–$X_{leave}$ distance, however, in the methoxy systems, the decrease is the least pronounced, because the flexible methoxy groups can rearrange so that they remain in close proximity to $X^-$. This maximizes the sterical repulsion, however, at the same time, the interaction between the $X^-$ and $Si(OMe)_3X$ fragments is also maximized. This is also true for the methyl systems, however, the Pauli repulsion is lower in comparison to the methoxy

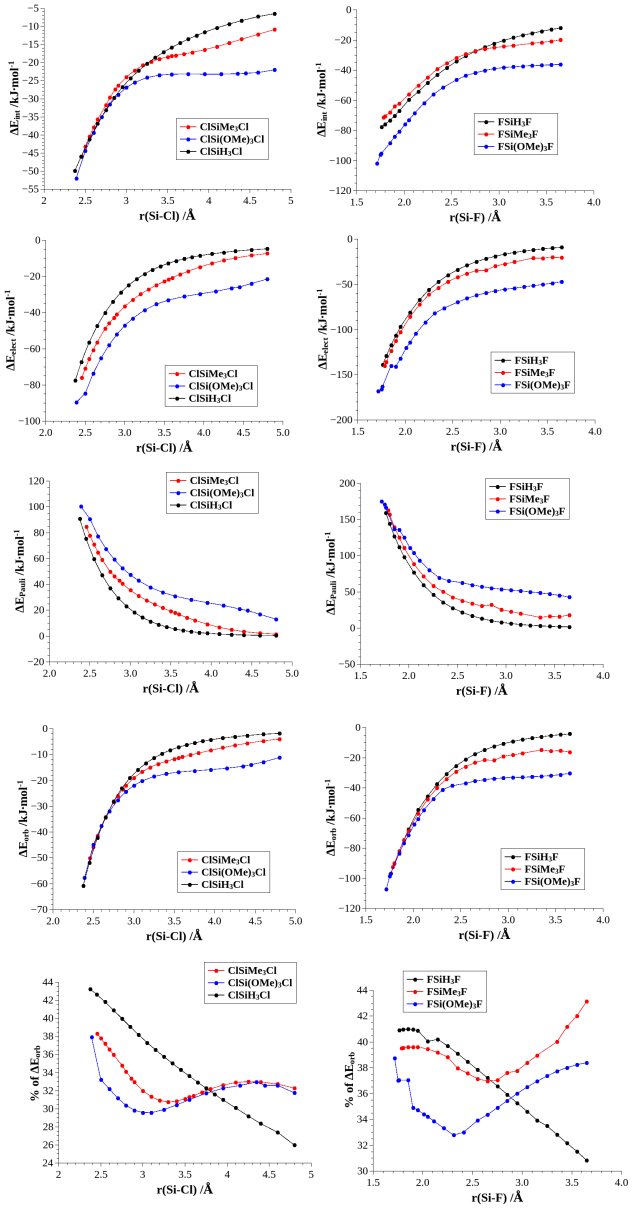


**Figure 3:** Energy decompostion analysis (EDA): Plots of the bond interaction energy ($\Delta E_{int}$), the electrostatic interaction energy ($\Delta E_{elect}$), the Pauli repulsion energy ($\Delta E_{Pauli}$), the orbital interaction energy ($\Delta E_{orb}$), and the ratio of $\Delta E_{orb}$ to the sum of the attractive energy components ($\Delta E_{orb}$, $\Delta E_{elect}$ and $\Delta E_{disp}$) plotted against the Si–$X_{leave}$ distance. Plots of $\Delta E_{disp}$ can be found in the supporting information.

system. Hydrogen is a small and inflexible substituent and, thus, the Pauli repulsion energy is the lowest in the hydrogen systems.

Initially, the orbital interaction energy ($\Delta E_{orb}$) shows an almost identical trend in the chlorine (up to r(Si$-$X$_{\text{leave}}$) = 2.7 Å) and fluorine systems (up to r(Si$-$X$_{\text{leave}}$) = 2.1 Å). This implies that the hydrogen, methyl and methoxy substituents do not greatly affect the orbital interactions at low Si$-$X$_{\text{leave}}$ distances. In this region, $\sigma$-hole bonding prevails (Si$\cdots$X$^-$). However, the plots start to deviate at higher distances between the two fragments. For the fluorine and chlorine systems, $\Delta E_{orb}$ is the most negative for the methoxy systems, and the least negative for the hydrogen systems. Consequently, there must be some factor enhancing the orbital interaction in the methoxy and methyl systems at high Si$-$X$_{\text{leave}}$ distances in addition to the $\sigma$-hole bonding, which becomes weaker with increasing distance. Here, we argue that the orbital stabilization is caused by the introduction of hydrogen bonds. While X$\cdots$H$-$C hydrogen bonding is well-known,[18,19] X$\cdots$H$-$Si hydrogen bonding is not feasible, which is due to the reversed polarization of the hydrogen atoms. Consequently, the XSiH$_3$X systems cannot be stabilized through hydrogen bonding. From a natural bond orbitals point of view, $\sigma$-hole bonding can be understood as negative hyperconjugation between a donor lone pair orbital at X$_{\text{leave}}$ and an Si$-$X acceptor antibond. Hydrogen bonding is indicated by the interaction between a lone pair of X$_{\text{leave}}$ (donor orbital) and a C$-$H antibond (acceptor orbital). Consequently, hydrogen bonding can also be understood as a type of negative hyperconjugation.[16] Figure 4 depicts the interacting orbitals for some representative geometries of the reaction complexes of ClSiMe$_3$Cl and ClSi(OMe)$_3$Cl.

The percentage of the orbital interaction to the sum of the attractive energy components ($\Delta E_{orb}$, $\Delta E_{elect}$ and $\Delta E_{disp}$) of ClSiH$_3$Cl and FSiH$_3$F decreases in a linear fashion (see Figure 3, last row). In other words, both the orbital and electrostatic interactions decrease continuously, however, the long range electrostatic interaction decreases more slowly than the short range orbital interactions. Such a trend is expected if only $\sigma$-hole bonding is significant, because in that event, there is no factor slowing down the decrease in orbital interactions. The systems, in which hydrogen bonding is feasible (the methoxy and methyl systems), on the other hand, show a different behaviour: After an initial decrease, orbital interactions are reinforced in relation to electrostatic interactions, which is when the methoxy or methyl substituents are oriented such that hydrogen bonding becomes feasible. The introduction of hydrogen bonding slows down the decrease of $\Delta E_{orb}$ towards less negative values, which compensates the loss in orbital interactions caused by $\sigma$-hole bonding. Overall, it shows that the strength of hydrogen bonding is at a maximum close to the RCs of ClSiMe$_3$Cl and ClSi(OMe)$_3$Cl. There are no RCs for

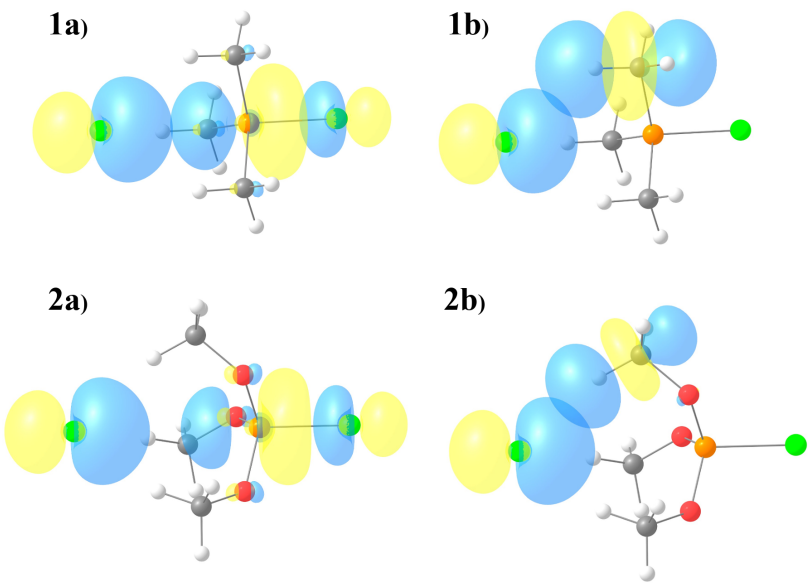


**Figure 4:** Interacting natural bond orbitals in $ClSiMe_3Cl$ and $ClSi(OMe)_3Cl$. **1a)** and **2a)** show negative hyperconjugation between a p-type lone pair at X and an Si−X antibond, which corresponds to $\sigma$-hole bonding. **1b)** and **2b)** show negative hyperconjugation between the same p-type lone pair at X and a C−H antibond, which can be related to hydrogen bonding.

$FSiMe_3F$ and $FSi(OMe)_3F$, because electrostatic and orbital interactions are more significant in the fluorine systems, which results in a very high stability based on $\sigma$-hole bonding alone. This overcompensates the existence of relatively weak hydrogen bonds, and therefore, features caused by hydrogen bonding are hidden in the PES of the fluorine systems. However, the EDA could indeed show that hydrogen bonding is also significant for $FSiMe_3F$ and $FSi(OMe)_3F$.

### 3.3 Quantum Theory of Atoms in Molecules

For a direct analysis of the hydrogen bonding, a QTAIM analysis was performed. Figure 5 shows the sum of the delocalization indices (DIs) between the $X^-$ QTAIM basins and the hydrogen atoms of the methyl and methoxy systems. The DI of both systems increases with increasing $Si-X_{leave}$ distance until a maximum between 3.5 Å and 4.0 Å is reached. This indicates that covalent interactions are increased between the hydrogen atoms of the $Me_3SiX$ or $(OMe)_3SiX$ fragments and $X^-$, which is in line with hydrogen bonding becoming more significant as the distance between the two fragments increases. This compensates the loss in stabilization through Si···X $\sigma$-hole bonding. Therefore, the different trends of $\Delta E_{orb}$ from

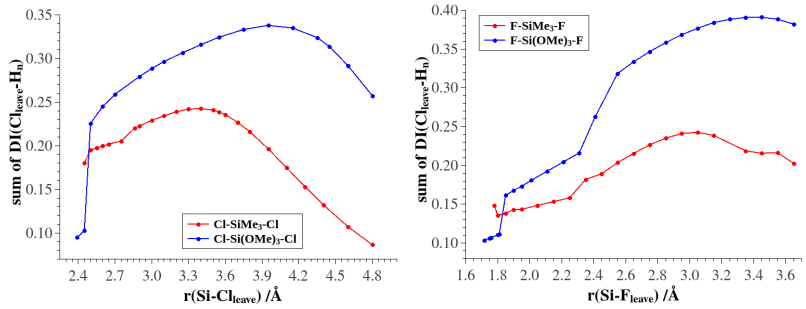


**Figure 5:** Sum of the delocalization indices between $X^-_{leave}$ (X= F or Cl) and the hydrogen atoms of the methyl and methoxy systems

the EDA may be rationalized with the introduction of hydrogen bonding to the methyl and methoxy systems. Both the EDA and the DI imply that hydrogen bonding is more pronounced in the methoxy systems, which is caused by the higher flexibility of the methoxy substituents in comparison to the methyl substituents, because a geometrical arrangement promoting hydrogen bonding can be obtained more readily.

Within the QTAIM approach, bond paths, which indicate bonded interactions, are paths of maximum electron density connecting two atoms. Bond paths are obtained between Si and X for the central TC and TS of all chlorine and fluorine systems (Figure 6 and 7). At the reaction complexes of $ClSiMe_3Cl$ and $ClSi(OMe)_3Cl$, however, Cl−H bond paths are obtained in place of Si−Cl bond paths (Figure 6). These bond paths indicate the significance of hydrogen bonding at the reaction complexes of the chlorine systems. At higher Si−$F_{leave}$ distances, F−H bond paths are also obtained for $FSiMe_3F$ and $FSi(OMe)_3F$ (see Figure 7).

The electron density at the bond critical point, which is associated to a bond path, measures the strength of a bonded interaction. Figure 8 shows the electron density $\rho_{bcp}$ at the Si−X bcps and the sum of $\rho_{bcp}$ at all H−$X_{leave}$ bcps plotted against r(Si−$X_{leave}$). The plots of $\rho_{bcp}$(Si−Cl) and $\rho_{bcp}$(Si−F) for the hydrogen, methyl and methoxy systems show an almost identical trend, which indicates that the strength of the Si−X bonded interaction is almost independent of the type of substituent R. The identical decrease of $\rho_{bcp}$(Si−X) indicates that $\sigma$-hole bonding decreases with increasing Si−$X_{leave}$ distance as the sole factor. Only the hydrogen systems give bond paths for the whole range of the plot. The plots of the methyl and methoxy systems, on the other hand, stop abruptly, because at some point Si−X bond paths are no longer obtained (see Figure 8). At higher Si−$X_{leave}$ distances, bond paths between the hydrogen atoms and $X^-_{leave}$ emerge, which indicates that hydrogen bonding becomes significant. For the $ClSiMe_3Cl$

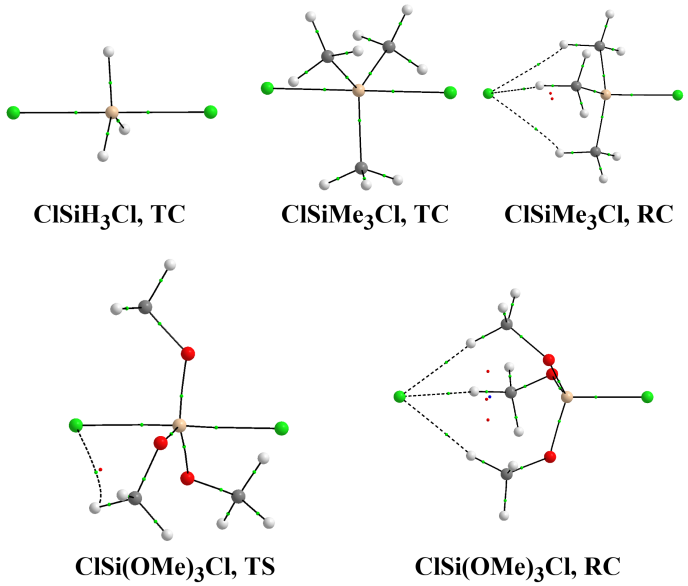


**Figure 6:** Bond paths of the chlorine systems. The small spheres correspond to bond critical (green) and ring critical points (red).

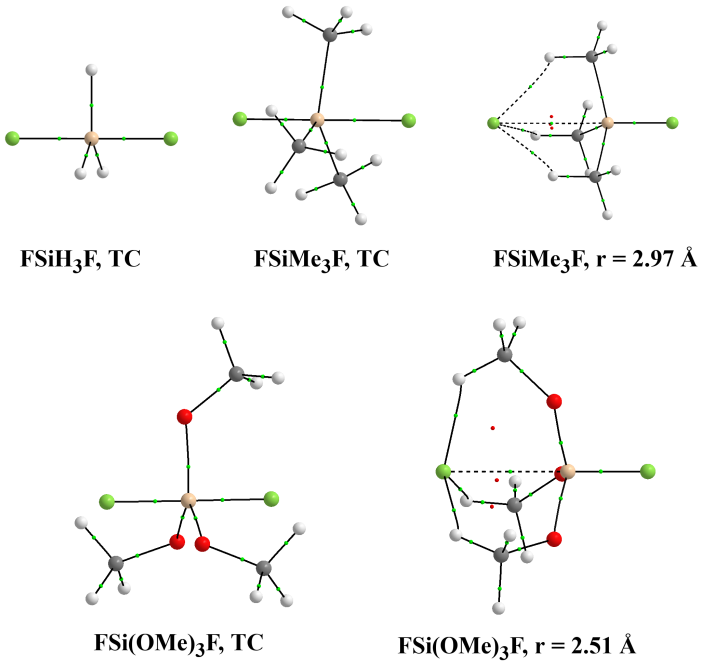


**Figure 7:** Bond paths of the fluorine systems. The small spheres correspond to bond critical (green) and ring critical points (red).

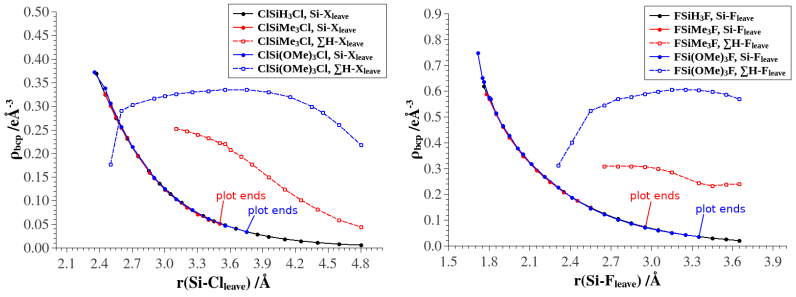


**Figure 8:** The electron density $\rho_{bcp}$ at the Si−X bcps and the sum of $\rho_{bcp}$ at all H−$X_{leave}$ bcps plotted against r(Si−$X_{leave}$)

system, the appearance of H−X bond paths coincides with its TS. The summed up values of $\rho_{bcp}$(H−X) are higher in the methoxy system in comparison to the methyl systems, which shows that stronger hydrogen bonds are obtained between X and the hydrogen atoms of the methoxy group.

# 4 Conclusions

In this study, it was shown that methoxy and methyl substituents can act as hydrogen bond acceptors in the course of $S_N2$ reactions at silicon atoms with $F^-$ and $Cl^-$ leaving groups. In fact, the stabilization due to hydrogen bonding has a significant effect on the shape of the potential energy surfaces (PES). The PES of $ClSiMe_3Cl$ and $ClSi(OMe)_3Cl$ show stable reaction complexes before and after the central transition complex ($ClSiMe_3Cl$) or transition state ($ClSi(OMe)_3Cl$). In this region, hydrogen bonding is most pronounced, and therefore, plays a crucial role in the stabilization of the reaction complexes. Hydrogen bonding has also a stabilizing effect in the fluorine systems ($FSiMe_3F$ and $FSi(OMe)_3F$), however, stable reaction complexes are not obtained. It was shown that fluorine has a higher affinity to be bonded to silicon than chlorine, and thus, pentacoordination is more feasible. The reasons for that are the smaller size of the fluorine atom reducing steric repulsion, and the stronger electrostatic interactions. Accordingly, F···H−C hydrogen bonding only plays a minor role relative to the other interactions, and in contrast to the chlorine systems, hydrogen bonding is not the main influence on the PES. Therefore, single-well PES are obtained for the fluorine systems. Nevertheless, the additional stabilization is clearly seen in EDA and QTAIM.

In previous studies, the influence of hydrogen boning on the PES of $S_N2$ reactions at silicon was neglected, to the best of our knowledge. Instead, only $\sigma$-hole bonding between Si and

the leaving group $X^-$ was considered. In this study, we have shown that $\sigma$-hole bonding is in competition with hydrogen bonding, which can both be understood as a type of negative hyperconjugation from a natural bond orbital perspective. Close to the central transition state or complex, $\sigma$-hole bonding is most significant, but at higher distances between $R_3SiX$ and the leaving group $X^-$, hydrogen bonding plays a more important role.

## Acknowledgements

S.G. thanks the German Research Foundation(Deutsche Forschungsgemeinschaft, DFG) for funding within the Emmy Noether project GR 4451/1-1.

## References

[1] W. Cowdrey, E. Hughes, C. Ingold, S. Masterman and A. Scott, *J. Chem. Soc.*, 1937, 1252–1271.

[2] J. Xie and W. L. Hase, *Science*, 2016, **352**, 32–33.

[3] G. Vayner, K. Houk, W. L. Jorgensen and J. I. Brauman, *J. Am. Chem. Soc.*, 2004, **126**, 9054–9058.

[4] L. Sun, K. Song and W. L. Hase, *Science*, 2002, **296**, 875–878.

[5] W. N. Olmstead and J. I. Brauman, *J. Am. Chem. Soc.*, 1977, **99**, 4219–4228.

[6] P. Manikandan, J. Zhang and W. L. Hase, *J. Phys. Chem. A*, 2012, **116**, 3061–3080.

[7] W. L. Hase, *Science*, 1994, **266**, 998–1002.

[8] S. Gronert, *Acc. Chem. Res.*, 2003, **36**, 848–857.

[9] M. L. Chabinyc, S. L. Craig, C. K. Regan and J. I. Brauman, *Science*, 1998, **279**, 1882–1886.

[10] C. Chuit, R. J. Corriu, C. Reye and J. C. Young, *Chem. Rev.*, 1993, **93**, 1371–1448.

[11] A. P. Bento and F. M. Bickelhaupt, *J. Org. Chem.*, 2007, **72**, 2201–2207.

[12] A. P. Bento, M. Solà and F. M. Bickelhaupt, *J. Comput. Chem.*, 2005, **26**, 1497–1504.

[13] M. A. van Bochove and F. M. Bickelhaupt, *Eur. J. Org. Chem.*, 2008, **2008**, 649–654.

[14] T. A. Hamlin, M. Swart and F. M. Bickelhaupt, *ChemPhysChem*, 2018, **19**, 1315–1330.

[15] P. Politzer, J. S. Murray and P. Lane, *Int. J. Quantum Chem.*, 2007, **107**, 3046–3052.

[16] F. Weinhold and C. R. Landis, *Valency and bonding: a natural bond orbital donor-acceptor perspective*, Cambridge University Press, 2005.

[17] J. Zhang, J. Mikosch, S. Trippel, R. Otto, M. Weidemüller, R. Wester and W. L. Hase, *J. Phys. Chem. Lett.*, 2010, **1**, 2747–2752.

[18] A. Allerhand and P. Von Rague Schleyer, *J. Am. Chem. Soc.*, 1963, **85**, 1715–1723.

[19] U. Koch and P. L. Popelier, *J. Phys. Chem.*, 1995, **99**, 9747–9754.

[20] I. V. Alabugin, M. Manoharan, S. Peabody and F. Weinhold, *J. Am. Chem. Soc.*, 2003, **125**, 5973–5987.

[21] G. A. Jeffrey and W. Saenger, *Hydrogen bonding in biological structures*, Springer Science & Business Media, 2012.

[22] G. R. Desiraju, *Acc. Chem. Res.*, 2002, **35**, 565–573.

[23] S. Grimme, *J. Comput. Chem.*, 2006, **27**, 1787–1799.

[24] T. Ziegler and A. Rauk, *Inorg. Chem.*, 1979, **18**, 1558–1565.

[25] M. P. Mitoraj, A. Michalak and T. Ziegler, *J. Chem. Theory Comput.*, 2009, **5**, 962–975.

[26] R. F. Bader, *Chem. Rev.*, 1991, **91**, 893–928.

[27] F. Weinhold and C. R. Landis, *Chem. Educ. Res. Pract.*, 2001, **2**, 91–104.

[28] G. Frenking and S. Shaik, *The Chemical Bond: Chemical Bonding Across the Periodic Table*, John Wiley & Sons, 2014, vol. 2.

[29] R. F. Bader, *J. Phys. Chem.*, 2009, **113**, 10391–10396.

[30] M. Fugel, J. Beckmann, D. Jayatilaka, G. V. Gibbs and S. Grabowsky, *Chem. Eur. J.*, 2018, **24**, 6248–6261.

[31] M. Fugel, M. F. Hesse, R. Pal, J. Beckmann, D. Jayatilaka, M. J. Turner, A. Karton, P. Bultinck, G. S. Chandler and S. Grabowsky, *Chem. Eur. J.*, 2018, **24**, 15275–15286.

[32] R. F. Bader and M. E. Stephens, *J. Am. Chem. Soc.*, 1975, **97**, 7391–7399.

[33] M. J. Frisch, G. W. Trucks, H. B. Schlegel, G. E. Scuseria, M. A. Robb, J. R. Cheeseman, G. Scalmani, V. Barone, G. A. Petersson, H. Nakatsuji, X. Li, M. Caricato, A. V. Marenich, J. Bloino, B. G. Janesko, R. Gomperts, B. Mennucci, H. P. Hratchian, J. V. Ortiz, A. F. Izmaylov, J. L. Sonnenberg, D. Williams-Young, F. Ding, F. Lipparini, F. Egidi, J. Goings, B. Peng, A. Petrone, T. Henderson, D. Ranasinghe, V. G. Zakrzewski, J. Gao, N. Rega, G. Zheng, W. Liang, M. Hada, M. Ehara, K. Toyota, R. Fukuda, J. Hasegawa, M. Ishida, T. Nakajima, Y. Honda, O. Kitao, H. Nakai, T. Vreven, K. Throssell, J. A. Montgomery, Jr., J. E. Peralta, F. Ogliaro, M. J. Bearpark, J. J. Heyd, E. N. Brothers, K. N. Kudin, V. N. Staroverov, T. A. Keith, R. Kobayashi, J. Normand, K. Raghavachari, A. P. Rendell, J. C. Burant, S. S. Iyengar, J. Tomasi, M. Cossi, J. M. Millam, M. Klene, C. Adamo, R. Cammi, J. W. Ochterski, R. L. Martin, K. Morokuma, O. Farkas, J. B. Foresman and D. J. Fox, *Gaussian 09, revision D. 01*, 2009.

[34] E. J. Baerends, J. Autschbach, A. Bérces, C. Bo, P. M. Boerrigter, L. Cavallo, D. P. Chong, L. Deng, R. M. Dickson, D. E. Ellis *et al.*, *Amsterdam density functional*, 2006.

[35] T. A. Keith, *AIMAll (Version 13.11. 04)*, 2013.

[36] E. D. Glendening, C. R. Landis and F. Weinhold, *J. Comput. Chem.*, 2013, **34**, 1429–1437.

# Part V

# From Structure Correlation to Bonding Correlation – An investigation of the formation of pentacoordinated silicon compounds

# Chapter 11

# Introduction to *bonding* and *structure correlations*

Modeling a reaction pathway experimentally is an ambiguous endeavor, since the time scale of a chemical transformation is in the range of femtoseconds;[143] no routine method is capable of capturing molecular snapshots at such a high time resolution. X-ray (or electron) diffraction experiments only give access to electron densities averaged over a long period of time ranging from a few hours to a couple of days.[110] However, with the advent of free electron lasers and ultra-bright electrons, time resolved snapshots of single molecules undergoing chemical transformations are no longer a vision of the future.[144–147] For example, Miller *et al.* have invested a lot of time and money to capture a "molecular movie" using femtosecond electron diffraction experiments.[148] As of today, this technology is not fully matured, and it is far away from becoming a routine application. Therefore, a direct investigation of reaction pathways at atomic scales is usually based on theoretical methods.

An indirect way to gain access to an experimental reaction pathway is the *structure correlation* approach proposed by Bürgi in 1973.[63–65,67] For the analysis of a molecular fragment undergoing a dynamic process, a set of different crystal structures containing that specific fragment are regarded.[67] Resulting from the forces exerted by the crystal environment, the structure of the molecular fragment will be deformed to some extent. Therefore, each of the deformed molecular fragements inside the different crystal structures can be regarded as a snapshot of a dynamical process.[67] These snapshots can be brought into a reasonable chronological sequence representing the gradual deformation of the fragment.[67] A careful analysis of the sequence of snapshots may provide correlations between structural parameters (such as bond lengths, angles and torsion angles), which can be interpreted in a chemical way.[67] The predictive power of this approach was demonstrated by its accomplishment to uncover that a nucleophile attacks the electrophilic carbon atom of a carbonyl group at an angle of $\approx 107°$ – the Bürgi-Dunitz angle.[64,149] The angle was determined through an analysis of a set of crystal structures con-

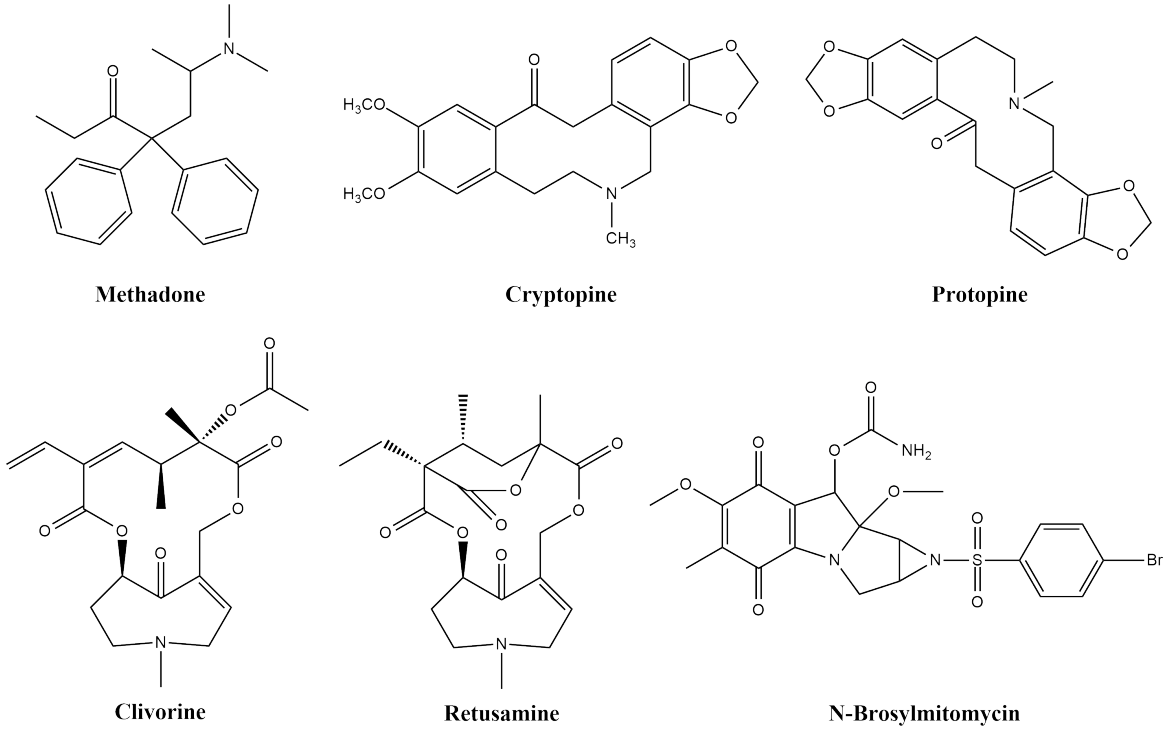


**Figure 11.1:** The six compounds used in the original determination of the Bürgi-Dunitz angle.[64]

taining a nucleophilic nitrogen atom coordinated to a carbonyl group.[64] Figure 11.1 shows six compounds which were used in the analysis.[64] The N···C−O angle is approximately 107° in all cases.[64] Additionally, two structural correlations were detected: i) The C−O distance increases with decreasing N···C distance and ii) the carbon atom of the carbonyl group increasingly deviates from the plane defined by the oxygen atom and the substituents of the carbonyl group R and R' with decreasing N···C distance.[64] Correlation i) is in line with a transformation of a C−O double bond into a single bond, while correlation ii) indicates a rehyridization of the carbon atom from $sp^2$- to $sp^3$-character.

In the preceding chapters, it was shown that bond analysis methods give properties which allow for a more comprehensive study of chemical bonding and reactivity than structural parameters, and it was demonstrated that these properties can be derived from "experimental" wavefunctions of crystal structures obtained from an X-ray Wavefunction Refinement (XWR).[36,45,51,54] Extending the *structure correlation* approach to a *bond property correlation* approach is therefore a logical step. In fact, *bond property correlations* have, in a way, already been presented in the present thesis: In chapter 6, correlations between the Si−O−Si angle and bond properties were presented and analyzed in a chemical way.[45] However, the bond analysis was based on wavefunctions derived from a theoretical potential energy surface scan. The *bond property correlation* approach presented in this part is different, in that the procedure in Bürgi's

*structure correlation* approach, which is based on experimental crystal structures, is followed. In order to see a *bond property correlation* in action, the formation of a pentacoordinated silicon species is investigated through that approach.

Compounds with pentacoordinated silicon atoms have already been encountered in Chapters 9 and 10, where it was shown that electronegative and sterically undemanding substituents promote the formation of stable pentacoordinated species. Hence, the reaction between a tetracoordinated silicon compound and a nucleophile sometimes corresponds to a nucleophilic addition under formation of a pentacoordinated species rather than a nucleophilic substitution under conservation of tetracoordination.[150–152] This shows the ability of tetracoordinated silicon compounds to act as Lewis acids. This behaviour is in contrast to reactions involving nucleophiles and tetracoordinated carbon atoms, where tetracoordination is always conserved.[153] While tetracoordinated silicon compounds still make up the majority of known compounds, numerous stable penta- and hexacoordinated species are found in literature.[150–152] Because the coordination number of four is exceeded, penta- and hexacoordinated silicon compounds are termed hypercoordintated. However, considering the findings in Chapter 8 and numerous other studies, hypercoordinated species of silicon or other third-period elements are not expected to be hypervalent due to the predominance of ionicity in bonds involving silicon.[15–18,154] The approach of a nucleophile towards a tetracoordinated silicon center has been modelled in Chapters 9 and 10 of the present thesis and in other studies, where different shapes of the potential energy surface were uncovered.[56–59] The systems regarded in Chapter 9 and 10 showed single-, double- and triple-well potential energy surfaces. In case of single- and triple-well potential energy surfaces, stable pentacoordinated species are obtained, and the approach of the nucleophile results in a nucleophilic addition to the silicon atom. However, both nucleophilic additions and substitutions start off in the same way, in that a nucleophile approaches an electrophilic silicon center, which results in the formation of a pentacoordinated species.

The nucleophilic addition to a tetracoordinated silicon atom has been subject to numerous *structure correlation* studies, in which crystal structures of pentacoordinated silicon compounds were used as snapshots along the reaction pathway.[155–166] Figure 11.2 shows a selection of compounds used in these studies. In all of these structures, there is an intramolecular interaction between a nucleophilic atom (either N or O) and the silicon atom. The strength of the interaction can be tuned by changing the substituents which influence the electronic nature of the nucleophilic or electrophilic region of the compound. A systematic row of these compounds with different combinations of substituents was synthesized, and then the compounds were brought into a chronological sequence which can be related to the approach of the nucleophile towards the silicon atom. Logically, compounds with a long distance between the nucleophile and the silicon atom mark the beginning of the sequence, while compounds with a short nucleophile-silicon distance correspond to more advanced steps of the nucleophilic addition.[162] The most

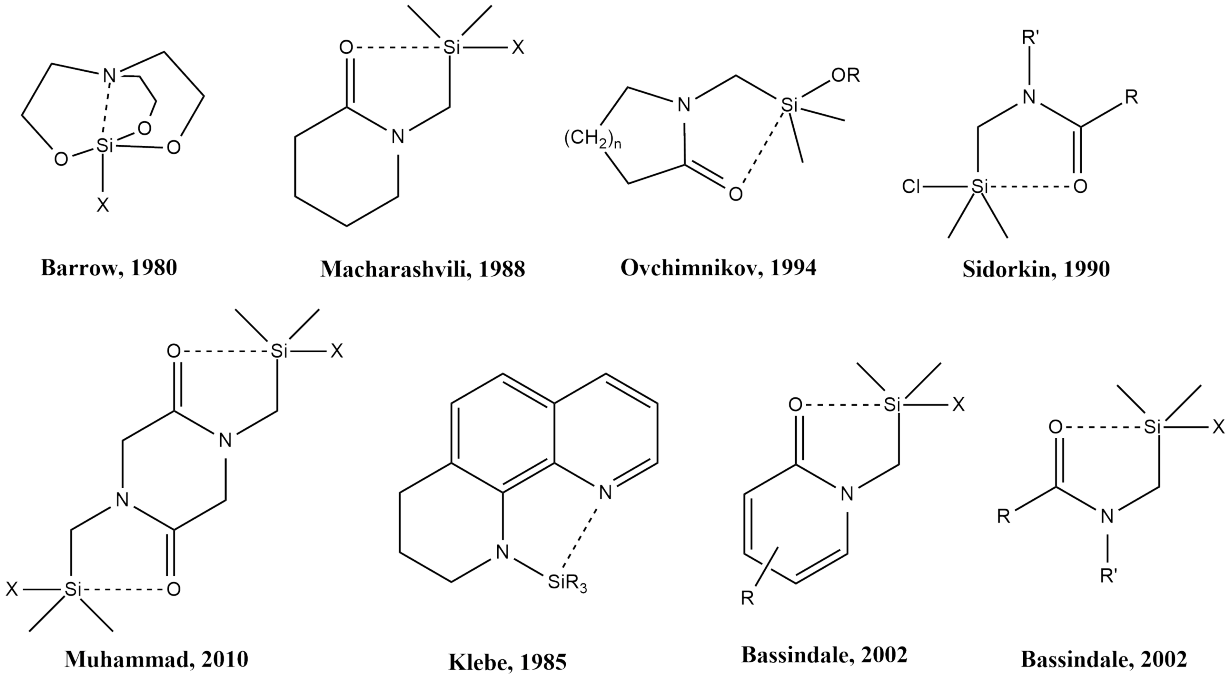


**Figure 11.2:** Pentacoordinated silicon compounds used for an investigation of the nucleophilic attack of the silicon atom based on the *structure correlation* approach. A dashed line is used to indicate the interaction between the nucleophile and the silicon atom.[160–166]

typical structure correlations obtained from these studies are increased Si–X bond lengths and a less distorted bipyramidial arrangement of substituents at the silicon atom with decreasing nucleophile-silicon distance.[162,166] In the present study, a very similar approach is applied using the compounds depicted in Figure 11.3, which were synthesized by Dr. Maksym Ponomarenko. The general structure of these compounds consists of a 8-(dimethylamino)-1-naphthyl framework with a $SiR_3$ group substituted in peri-position to the dimethylamino group.[167] The nitrogen atom has a nucleophilic character and therefore coordinates to the electrophilic silicon atom. Two of the substituents of the silicon atom – a phenyl and a methyl group – are held constant in each of the structures, while the third substituent (X) is varied. The nature of the substituent X drastically influences the electrophilic nature of the silicon atom, and thus a spectrum of compounds with different strengths of the N···Si interaction is obtained. High resolution, low temperature single-crystal X-ray diffraction data sets of these compounds were determined carried out at the synchrotron SPring-8 (Hyogo, Japan) and at a home source.

The aim of this study is to investigate the nucleophilic addition of a nitrogen atom to a silicon atom based on experimental data using a *complementary bonding analysis* in conjunction with *structure* and *bonding correlation* approaches. The N–Si distance can be consulted as a straightforward criterion to determine the chronological sequence of the reaction snapshots obtained from the crystal structures of the compounds in Figure 11.3. In addition to a *bonding correlation* study based on XWRs of the crystal structures, which are of high enough quality,

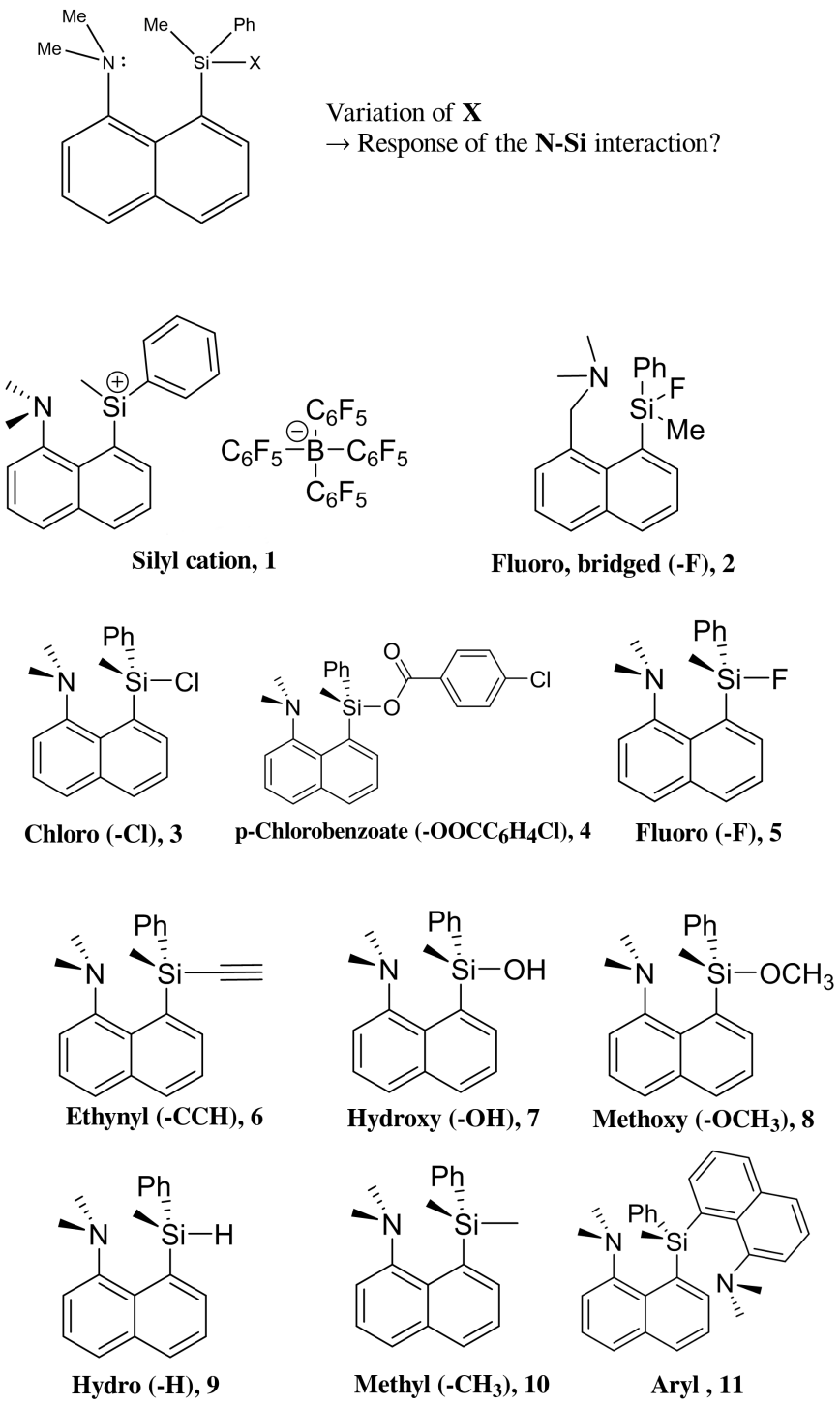


**Figure 11.3:** Pentacoordinated silicon compounds regarded in the analysis of the nucleophilic addition to a silicon atom in this thesis using the *structure* and *bonding correlation* approaches.

the same analysis is also performed for geometry optimized structures. Firstly, more data points are generated through that approach, and secondly, the effects of the crystal environment on

the N···Si interaction can be uncovered. Moreover, a *potential energy surface (PES)* scan is carried out for each of the compounds, where everything except for the N–Si distance, which is fixed to a set of distances at a certain interval ($\Delta d = 0.1$Å from 1.9 Å to 3.1 Å), is optimized. This procedure is applied, in order to compare the correlations obtained from the systematically chosen array of structures to the trends obtained from a PES scan of the respective structures. In this study, properties from natural bond orbitals (NBO),[37] the Quantum Theory of Atoms in Molecules (QTAIM)[131] and the electron localizability indicator (ELI-D)[40] are regarded. The structural and bond property correlations will be interpreted in a chemical way to draw conclusions on the electronic changes occurring in the course of a nucleophilic addition to a silicon atom.

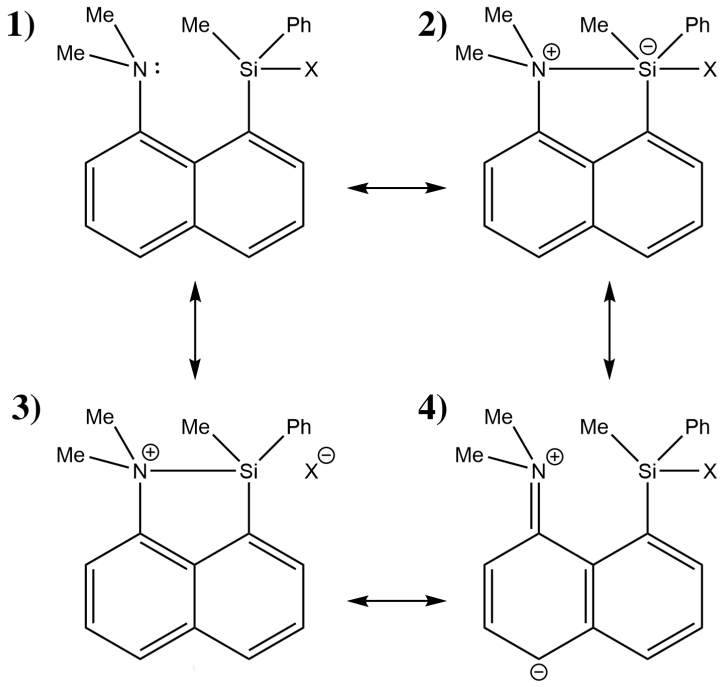


**Figure 11.4:** Resonance structures affecting the N···Si interaction: **1)** The nitrogen lone pair is localized resulting in the absence of an N···Si interaction; **2)** Hypervalent representation; **3)** Bond between the nitrogen and silicon atom, and no bond between the silicon atom and X; **4)** Interaction of the nitrogen lone pair with the aromatic system resulting in a N–C double bond and the absence of a N···Si interaction

For the compounds regarded in this study, a variety of resonance structures, which describe the N···Si interaction, need to be considered. Figure 11.4 depicts four resonance structures with different configurations of the nitrogen lone pair. In resonance structure **1)** the nitrogen lone pair is localized at the nitrogen atom and is not involved in any interaction. Resonance structure **2)** contains a hypervalent silicon atom (10 valence electrons), which requires d-orbitals of the silicon atom to participate in the bonding. Based on previous findings, the significance of this

resonance structure will be negligible.[15–18,154] In resonance structure **3)**, on the other hand, the octet rule is not violated: There is a bond between the nitrogen and silicon atom, while the silicon atom and the substituent X are non-bonded. Finally, resonance structure **4)** presents the possibility for the nitrogen lone pair to interact with the naphthalene system, which introduces a double bond character to the N−C bond. Since the N···Si interaction corresponds to a dative bond (all electrons originate from the nitrogen atom),[72] resonance structure **1)** will always be significant. If the substituent X promotes a strong N···Si interaction, resonance structure **3)** will gain in significance. In case of a weak N···Si interaction, on the other hand, the nitrogen lone pair is more available to interact with the naphthalene system, and thus, resonance structure **4)** will be more significant.

In Chapter 12, the methodology of the experimental and theoretical procedures are outlined. The crystal structures are analyzed thoroughly in terms of their environment in Chapter 13. In Chapters 15 and 16, *structure* and *bonding correlations* are presented and analyzed chemically. Finally, the results are summarized and conclusions are drawn in Chapter 17.

# Chapter 12

# Experimental and computational details

## 12.1 Synthesis and Characterization

Apart from the hydroxy compound (**7**), it was possible to synthesize all compounds depicted in Figure 11.3. The synthesis of all compounds was performed by Dr. Maksym Ponomarenko, and is not part of this thesis. The synthetic procedure is given in the appendix. Most of the synthesized structures showed a low stability when exposed to air, which is why their exposure to air was avoided or kept to a minimum. Apart from the hydro compound (**9**), it was possible to crystallize all synthesized compounds as described in the appendix.

## 12.2 Crystallography

### 12.2.1 Crystal structure determination

X-ray diffraction experiments were performed for all crystal structures using home source and synchrotron radiation (apart from the bridged fluoro compound (**2**), for which no synchrotron data exists). The home measurements were conducted at a temperature of T=100 K. The synchrotron experiments, which were required to obtain high-quality, high-resolution (up to $d = 0.4$ Å), low-temperature (T = 20 K) data-sets, were performed at the beamline BL02B1 of the synchrotron SPring-8 in Hyogo, Japan. The data sets were collected at different beamtimes, which is why different wavelengths were applied. The crystallographic information of the compounds, and measurement details can be found in Table 12.1.

The data reduction of the home data sets was carried out with *SAINT*,[168] where a numerical absorption correction after indexing of the crystal faces was applied. For the synchrotron data sets, the data reduction was performed with the program *RapidAuto* under application of an

empirical absorption correction. The space groups were determined with *Xprep*.[169]

### 12.2.2 Refinements

The structures were solved using the intrinsic phasing mechanism implemented inside *shelxt*.[170] Refinements based on the *Independent Atom Model (IAM)* were performed using *shelxl*[171] linked to *Olex2*.[172] All non-hydrogen atoms were refined anisotropically. The hydrogen atoms were added freely at the corresponding residual density peaks, and were refined without applying any constrains or restrains. After *IAM*, the resulting structures were closely inspected with respect to their quality, which showed that both methyl structures and the structure of the silyl cation (**1**) obtained from the home source are not suitable for *HAR*, because they show a significant degree of twinning. *Hirshfeld Atom Refinements (HARs)*[107] were performed with *tonto*[173] using the *IAM* geometry as the starting point. The *RHF/def2-TZVP* level of theory was applied, and the hydrogen atoms were refined anisotropically. A cluster of charges and dipoles within a radius of 8 Å were applied to mimic the crystal field. The resulting *HAR* (or *IAM* if no *HAR* was performed) geometries are depicted in Figure 12.1. The silyl cation (**1**) and the fluoro compound (**5**) show non-positive definite (NPD) *ADPs*. It has been shown in the literature that the element-hydrogen bond lengths are not negatively impacted if the corresponding hydrogen ADPs are negative.[52,125,174] This is also the case for the silyl cation (**1**) and the fluoro compound (**5**), which show reasonable hydrogen-element bond lengths.

An *X-ray constrained wavefunction fitting (XCW)*[53] was performed at the final *HAR* geometry, and at the same level of theory as employed for the *HAR*. For each structure, an XCW was only performed for the data sets with the highest resolution, which always corresponds to the data set collected at SPring-8 (apart from the bridged fluoro compound (**2**), where only the home data set is available). For the methyl compound (**10**) and the silyl cation (**1**), no *HAR* was performed, and, thus, an XCW could also not be performed, because an even higher data quality is required. Table 12.2 shows the final $\lambda$-values for each *XCW*, as well as the refinement statistics after *IAM*, *HAR* and *XCW*. Figure 12.2 shows fractal dimension plots of the residual density after *HAR* and *XCW*.[175] The plots show that the residual density slightly improves after XCW compared to HAR. According to these plots, untreated effects, such as anharmonic motion, are not significant. Residual and deformation density plots of the crystal structures are found in the appendix.

**Table 12.1:** Crystallographic information and measurement details of crystal structures of the compounds depicted in Figure 11.3 from home and source and synchrotron (SPring-8) experiments.

| | silyl cation (**1**) | | F, bridged (**2**) | Chloro (**3**) | | p-Chlorobenzoate (**4**) | | Fluoro (**5**) | |
|---|---|---|---|---|---|---|---|---|---|
| | home | SPring8 | home | home | SPring8 | home | SPring8 | home | SPring8 |
| Empirical formula | $C_{43}H_{20}BF_{20}NSi$ | | $C_{20}H_{22}FNSi$ | $C_{19}H_{20}ClNSi$ | | $C_{26}H_{24}ClNO_2Si$ | | $C_{19}H_{20}FNSi$ | |
| Space group | P-1 | | P2(1) | P2(1)/c | | P-1 | | P2(1)2(1)2(1) | |
| Crystal system | triclinic | | monoclinic | monoclinic | | triclinic | | orthorhombic | |
| a /Å | 14.179(3) | 14.143(3) | 7.5718(3) | 7.3930(3) | 7.2145(14) | 9.3974(5) | 9.3830(19) | 9.6093(5) | 9.5986(19) |
| b /Å | 15.036(3) | 15.017(3) | 17.2362(6) | 16.6138(6) | 16.325(3) | 9.7435(5) | 9.7360(19) | 11.4746(6) | 11.430(2) |
| c /Å | 19.142(4) | 19.091(4) | 13.0930(5) | 13.8732(5) | 13.674(3) | 13.0658(7) | 13.071(3) | 29.1583(17) | 29.056(6) |
| $\alpha$ /° | 89.057(4) | 88.63(3) | 90 | 90 | 90 | 70.0640(10) | 70.04(3) | 90 | 90 |
| $\beta$ /° | 68.814(4) | 68.79(3) | 95.9760(10) | 97.378(2) | 97.14(3) | 81.3460(10) | 81.54(3) | 90 | 90 |
| $\gamma$ /° | 89.107(4) | 88.66(3) | 90 | 90 | 90 | 81.5390(10) | 81.67(3) | 90 | 90 |
| wavelength /Å | 0.7107 | 0.3546 | 0.7107 | 0.7107 | 0.2472 | 0.7107 | 0.225 | 0.7107 | 0.4133 |
| T /K | 100(2) | 25(2) | 100(2) | 100(2) | 25(2) | 100(2) | 25(2) | 100(2) | 25(2) |
| Crystal dimensions /$\mu m^3$ | not measured | not measured | 137x179x212 | 96x136x164 | 210x150x120 | 85x165x255 | 105x87.5x87.5 | 82x120x181 | 80x60x50 |
| $\sin(\Theta)/\lambda_{max}$ /$Å^{-1}$ | 0.63 | 0.63 | 0.91 | 0.63 | 1.11 | 0.83 | 1.11 | 0.71 | 0.83 |
| $R_{int}$ | 0.0611 | 0.0222 | 0.0439 | 0.0747 | 0.029 | 0.0345 | 0.0535 | 0.0471 | 0.0304 |
| $N_{meas}$, $N_{uniq}$ | 63473, 15501 | 50436, 15385 | 183013, 10700 | 55640, 3462 | 130479, 18278 | 55582, 10650 | 112755, 25237 | 57327, 9747 | 71871, 15418 |
| $N_t extobs$ (F >4$\sigma$) | 11959 | 13392 | 8971 | 2874 | 16125 | 8163 | 19246 | 8742 | 15240 |
| Redundancy | 4.09 | 3.28 | 17.1 | 16.07 | 7.14 | 5.22 | 4.47 | 5.88 | 4.66 |
| Completeness | 1.00 | 1.00 | 1.00 | 1.00 | 1.00 | 0.99 | 1.00 | 0.99 | 1.00 |
| CCDC No. | 1037662 | 1937661 | 1937643 | 1937703 | 1937701 | 1937711 | 1937709 | 1937694 | 1937692 |

**Table 12.1 (continued)**

| | Ethynyl (**6**) | | Methoxy (**8**) | | Methyl (**10**) | | Aryl (**11**) | |
|---|---|---|---|---|---|---|---|---|
| | home | SPring8 | home | SPring8 | home | SPring8 | home | SPring8 |
| Empirical formula | $C_{21}H_{21}NSi$ | | $C_{20}H_{23}NOSi$ | | $C_{20}H_{23}NSi$ | | $C_{31}H_{32}N_2Si$ | |
| Space group | Pbca | | P2(1) | | P2(1)2(1)2(1) | | P-1 | |
| Crystal system | orthorhombic | | monoclinic | | orthorhombic | | triclinic | |
| a /Å | 14.7360(6) | 14.713(3) | 10.9416(4) | 10.901(2) | 29.6547(15) | 29.608(6) | 7.9530(5) | 7.9520(16) |
| b /Å | 14.7087(6) | 14.634(3) | 7.1325(3) | 7.1216(14) | 6.9985(4) | 6.9858(14) | 12.8907(8) | 12.898(3) |
| c /Å | 16.0383(5) | 15.998(3) | 11.2862(4) | 11.272(2) | 16.5166(9) | 16.497(3) | 13.2485(8) | 13.239(3) |
| $\alpha$ /° | 90 | 90 | 90 | 90 | 90 | 90 | 67.9340(10) | 67.90(3) |
| $\beta$ /° | 90 | 90 | 95.7020(10) | 95.69(3) | 90 | 90 | 88.2940(10) | 88.32(3) |
| $\gamma$ /° | 90 | 90 | 90 | 90 | 90 | 90 | 74.5620(10) | 74.54(3) |
| wavelength /Å | 0.7107 | 0.4015 | 0.7107 | 0.4273 | 0.7107 | 0.2472 | 0.7107 | 0.4133 |
| T /K | 100(2) | 25(2) | 100(2) | 25(2) | 100(2) | 25(2) | 100(2) | 25(2) |
| Crystal dimensions /$\mu m^3$ | 92x138x156 | 170x150x150 | 82x200x271 | 122x87.5x105 | 130x146x197 | 210x150x120 | 128x181x216 | 110x110x80 |
| $\sin(\Theta)/\lambda_{max}$ /$Å^{-1}$ | 0.7 | 1.25 | 0.91 | 1.11 | 0.7 | 1 | 0.83 | 1.11 |
| $R_{int}$ | 0.0439 | 0.0414 | 0.0312 | 0.0318 | 0.0405 | 0.0482 | 0.0418 | 0.0325 |
| $N_{meas}$, $N_{uniq}$ | 101793, 5022 | 230254, 28154 | 53687, 10994 | 64123, 19474 | 101548, 9991 | 119433, 27792 | 66474, 11700 | 120716, 26405 |
| $N_t extobs$ (F $>4\sigma$) | 4191 | 22779 | 10035 | 17724 | 9142 | 24239 | 9157 | 21906 |
| Redundancy | 20.27 | 8.18 | 4.88 | 3.29 | 10.16 | 4.3 | 5.68 | 4.57 |
| Completeness | 0.99 | 1.00 | 1.00 | 0.99 | 1.00 | 0.99 | 0.99 | 0.95 |
| CCDC No. | 1937699 | 1937697 | 1937707 | 1937705 | 1937657 | 1937649 | 1937715 | 1937713 |

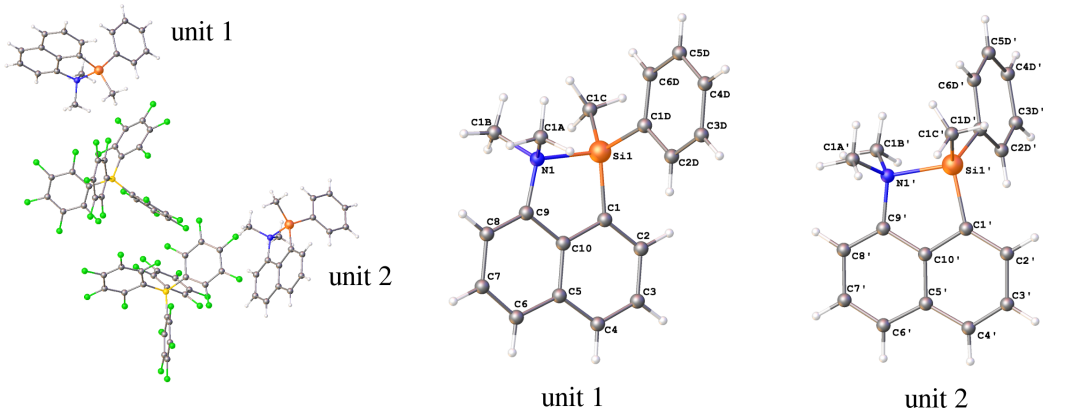


**Silyl cation (1), home source (IAM)**

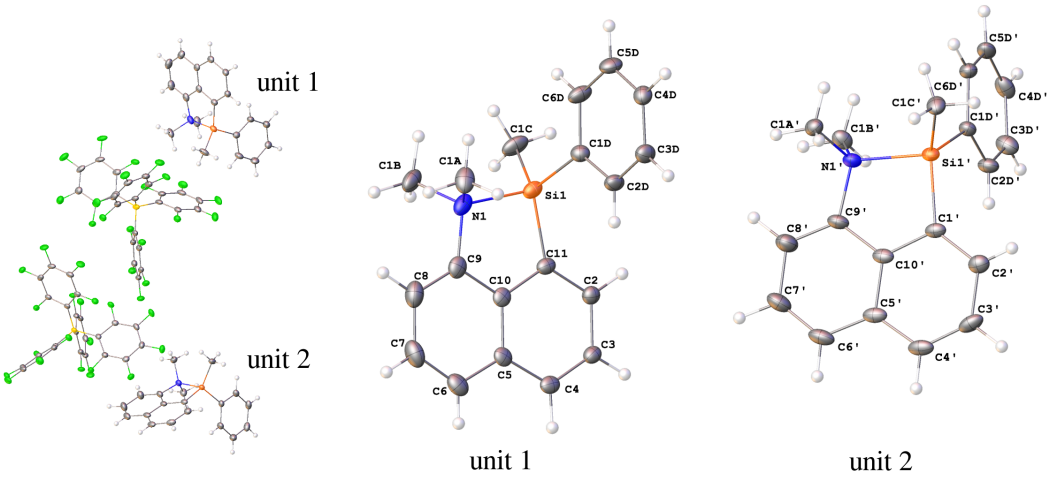


**Silyl cation (1), SPring-8 (IAM)**

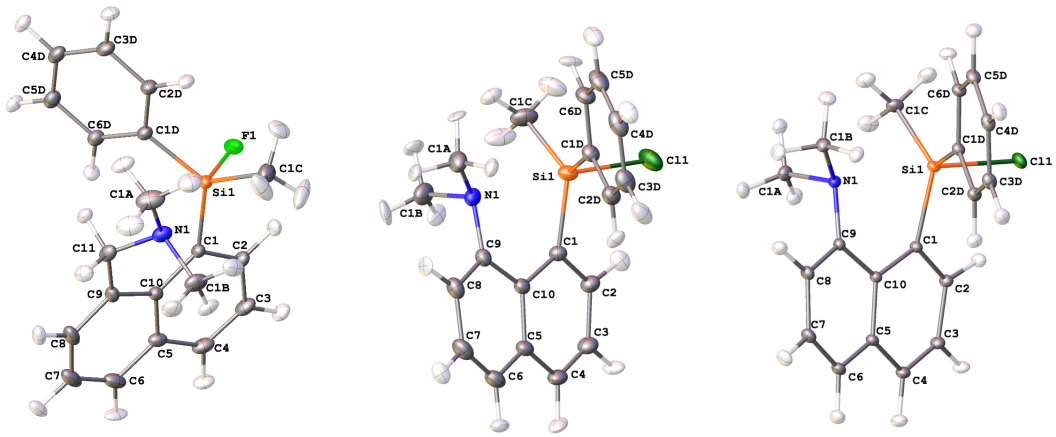

**Fluoro, bridged (2), home source (HAR)**

**Chloro (3), home source (HAR)**

**Chloro (3), Spring-8 (HAR)**

**Figure 12.1:** Crystal structures after HAR (or IAM if no HAR structure is available) from home source and synchrotron measurements. The anisotropic displacement parameters (ADP) correspond to a 50% probability surface.

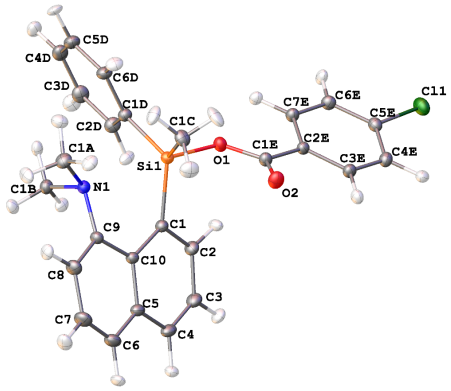


**p-Chlorobenzoate (4), home source (HAR)**

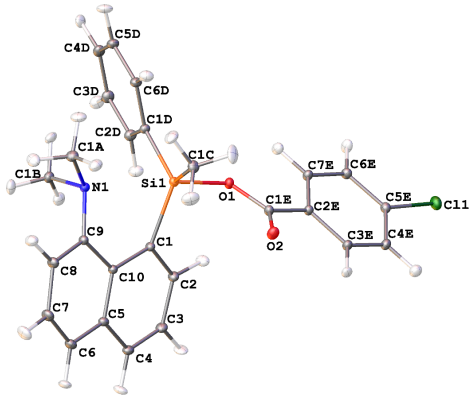


**p-Chlorobenzoate (4), SPring-8 (HAR)**

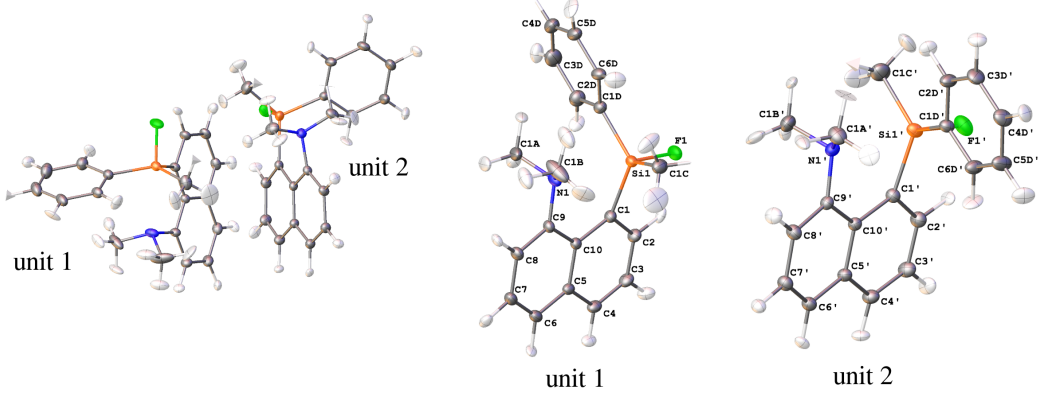


**Fluoro (5), home source (HAR)**

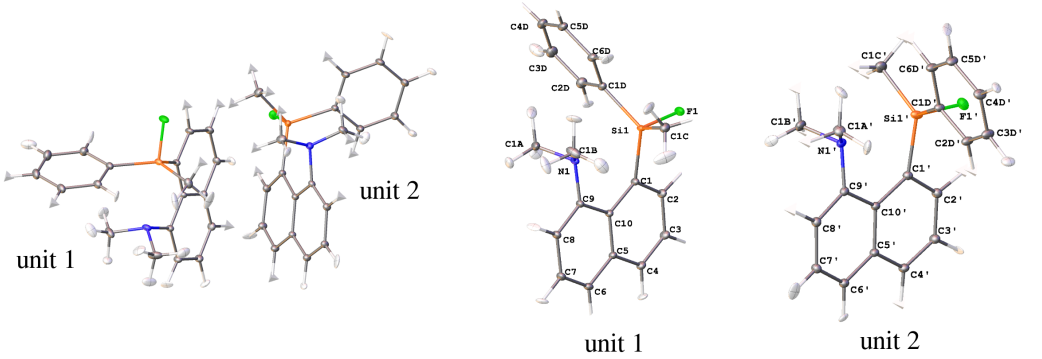


**Fluoro (5), SPring-8 (HAR)**

## 12.1 (continued)

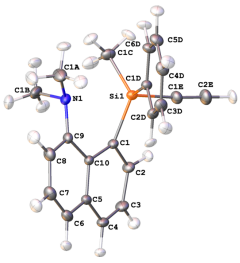

**Ethynyl (6), home source (HAR)**

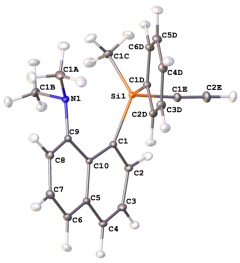

**Ethynyl (6), SPring-8 (HAR)**

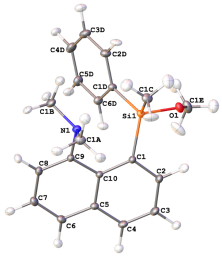

**Methoxy (8), home source (HAR)**

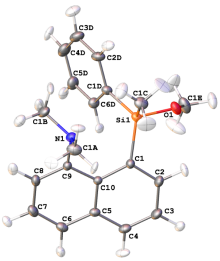

**Methoxy (8), SPring-8 (HAR)**

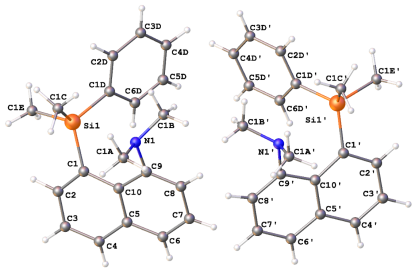

**Methyl (10), home source (HAR)**

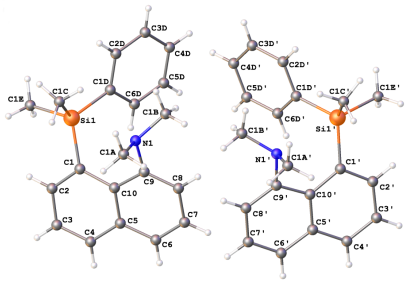

**Methyl (10), SPring-8 (HAR)**

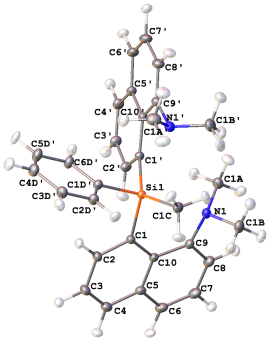

**Aryl (11), home source (HAR)**

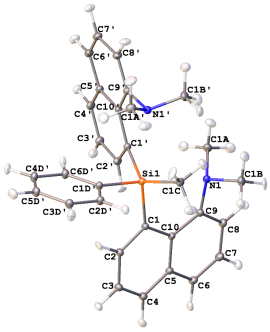

**Aryl (11), SPring-8 (HAR)**

**12.1 (continued)**

**Table 12.2:** Refinement statistics after IAM, HAR and XCW. The minimal and maximal residual density peaks ($\Delta\rho_{min/max}$) are given in e·Å$^{-3}$.

| | silyl cation (**1**) | | F, bridged (**2**) | Chloro (**3**) | | p-Chlorobenzoate (**4**) | | Fluoro (**5**) | |
|---|---|---|---|---|---|---|---|---|---|
| | home | SPring8 | home | home | SPring8 | home | SPring8 | home | SPring8 |
| **after IAM** | | | | | | | | | |
| R1 | 0.1354 | 0.0435 | 0.0354 | 0.0394 | 0.0275 | 0.0413 | 0.0412 | 0.0362 | 0.0344 |
| wR2 | 0.3865 | 0.1101 | 0.1082 | 0.1011 | 0.0899 | 0.1128 | 0.1095 | 0.0876 | 0.0918 |
| $\Delta\rho_{min/max}$ | -0.76/1.42 | -0.50/0.97 | -0.34/0.62 | -0.21/0.45 | -0.51/0.80 | -0.28/0.60 | -0.31/0.83 | -0.24/0.36 | -0.56/0.81 |
| **after HAR** | | | | | | | | | |
| R1 | – | – | 0.0231 | 0.0288 | 0.0189 | 0.0308 | 0.0340 | 0.0243 | 0.0251 |
| wR2 | – | – | 0.0322 | 0.0424 | 0.0263 | 0.0362 | 0.0357 | 0.0305 | 0.0430 |
| $\Delta\rho_{min/max}$ | – | – | -0.22/0.17 | -0.21/0.25 | -0.28/0.34 | -0.27/0.40 | -0.52/0.52 | -0.18/0.22 | -0.28/0.37 |
| **after XCW** | | | | | | | | | |
| $\lambda_{max}$ | – | – | 0.20 | – | 0.30 | – | 1.00 | – | 0.15 |
| R1 | – | – | 0.0169 | – | 0.0165 | – | 0.0328 | – | 0.0244 |
| wR2 | – | – | 0.0266 | – | 0.0211 | – | 0.0326 | – | 0.0398 |
| $\Delta\rho_{min/max}$ | – | – | -0.19/0.16 | – | -0.25/0.29 | – | -0.40/0.45 | – | -0.27/0.33 |

## Table 12.2 (continued)

| | Ethynyl (**6**) | | Methoxy (**8**) | | Methyl (**10**) | | Aryl (**11**) | |
|---|---|---|---|---|---|---|---|---|
| **after IAM** | home | SPring8 | home | SPring8 | home | SPring8 | home | SPring8 |
| R1 | 0.0356 | 0.0316 | 0.033 | 0.0323 | 0.04 | 0.0497 | 0.0414 | 0.0415 |
| wR2 | 0.0978 | 0.0955 | 0.0905 | 0.081 | 0.1042 | 0.1356 | 0.1259 | 0.1233 |
| $\Delta\rho_{min/max}$ | -0.34/0.31 | -0.27/0.98 | -0.19/0.42 | -0.21/1.04 | -0.25/0.79 | -0.76/1.78 | -0.30/0.60 | -0.57/0.89 |
| **after HAR** | | | | | | | | |
| R1 | 0.0213 | 0.0253 | 0.0216 | 0.0235 | – | – | 0.0275 | 0.0331 |
| wR2 | 0.024 | 0.0352 | 0.0355 | 0.0333 | – | – | 0.0355 | 0.0476 |
| $\Delta\rho_{min/max}$ | -0.13/0.11 | -0.15/0.25 | -0.12/0.20 | -0.19/0.49 | – | – | -0.18/0.28 | -0.42/0.52 |
| **after XCW** | | | | | | | | |
| $\lambda_{max}$ | – | 0.4 | – | 0.6 | – | – | – | 0.55 |
| R1 | – | 0.0227 | – | 0.0195 | – | – | – | 0.0307 |
| wR2 | – | 0.0282 | – | 0.0246 | – | – | – | 0.0402 |
| $\Delta\rho_{min/max}$ | – | -0.13/0.21 | – | -0.12/0.46 | – | – | – | -0.38/0.54 |

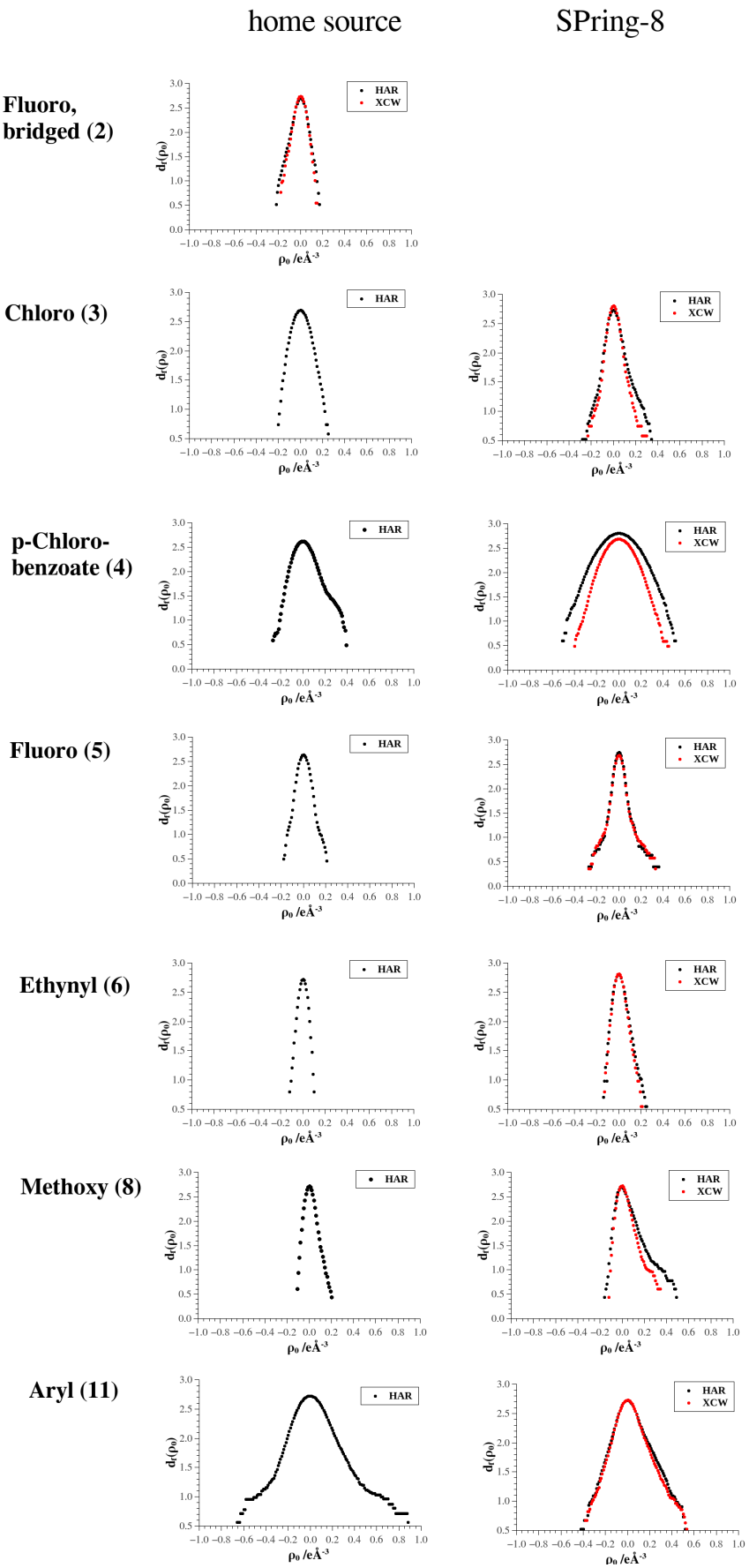


**Figure 12.2:** Fractal dimension plots after *HAR* and *XCW*.

## 12.3 Computational details

### 12.3.1 Geometry optimizations

In addition to X-ray refined wavefunctions, wavefunctions were also obtained from isolated molecule optimizations of all compounds depicted in Figure 11.3 (also for the hydroxy (**7**) and hydro (**9**) compounds, for which no crystal structures were obtained). The geometry optimizations were carried out with *Gaussian 09*[176] on a *B3LYP/def2-TZVP* level of theory. An empirical dispersion correction based on the D3 version of Grimme's approach with Becke-Johnson damping (*GD3BJ*) was applied.[177] A frequency analysis was performed to ensure that the optimized structure corresponds to a minimum in the potential energy surface.

For the chloro (**3**) and ethynyl (**6**) compounds, geometry optimizations were also performed with explicit solvent corrections using the dielectric constants of water and acetonitrile. Additionally, geometry optimizations with periodic boundary conditions using the program *Crystal14*[178] and a cluster of point charges and dipoles (compare to the approach used in *HAR*) were performed. The purpose of these geometry optimizations is to get an impression of the role of the crystal environment on the geometry of the two compounds.

In order to obtain a relaxed potential energy surface scan of all compounds, the N–Si distance was fixed to a range of distances (from 1.9 Å to 3.1 Å at intervals of 0.1 Å), while all other parameters were optimized freely. Figure 12.3 compares the *structure correlation* approach to the *PES* scan.

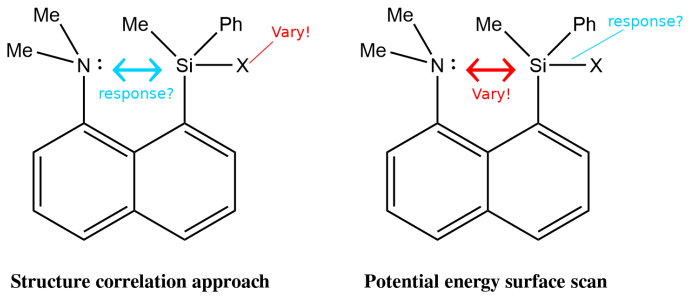


**Figure 12.3:** On the left hand side, the *structure correlation* approach is visualized: Exchanging the substituent X changes the electrophilic character of the silicon atom, which, in turn, leads to a change in the nature of the N–Si interaction. The principle of the *potential energy surface (PES)* scans, is visualized on the right hand side: The N–Si distance is artificially constrained to a certain value, which affects the nature of the Si–X bond.

### 12.3.2 Bond property analysis

Based on the wavefunctions obtained from XWR and from the geometry optimizations, a *complementary bonding analysis* was performed. Properties obtained from a *natural bond orbital (NBO)* analysis,[37] and analyses based on the *electron localizability indicator (ELI-D)*[40] and the *Quantum Theory of Atoms in Molecules (QTAIM)*[131] were computed. The *NBO* analysis was carried out with *NBO 6*[179] linked to *Gaussian 09*,[176] and the *QTAIM* analysis was performed with the *AIMall*[180] software package. *D-grid 5.0*[181] was used to compute the *ELI-D*.

# Chapter 13

# Analysis of the crystal environment

In the forthcoming analysis of *structure* and *bonding correlations*, the N–Si interaction is of particular interest. However, inside a crystal structure, all atoms may be involved in a variety of intermolecular interactions, which influence the intramolecular N–Si interaction. This is particularly the case for interactions involving the nitrogen and silicon atoms. Significant intermolecular interactions are often characterized by close contacts between interacting units. This is the basis of a Hirshfeld surface analysis,[182,183] which will be performed in this Chapter. Also, one can expect that the electric field, in which all molecules in a crystal are embedded, favors a more ionic bonding situation, which has a great effect on the N–Si interaction. Accordingly, the weight of resonance structures **3)** and **4)** in Figure 11.4, corresponding to the bonding representations with an N–Si bond and an N–C double bond, will be increased, because in both cases positive and negative formal charges, which are stabilized by an electric field, are obtained. In the present thesis, it is expected that the main influence on the N–Si interaction originates from the nature of the substituent X, however, influences from the crystal environment will also play a significant role. In the *structure* and *bonding correlation* studies for the *XWR* compounds, these interactions are not expected to result in outliers, because perturbations resulting in structure deformations are the foundation of the *structure correlation approach* introduced by Bürgi & Dunitz. Accordingly, it is expected that the geometrical and bonding properties, which will be regarded in these correlations, are a function of the N–Si distance, which is, in turn, influenced by the crystal environment. The purpose of the present Chapter is to closely inspect all intermolecular interactions in terms of close contacts, and to uncover the influence of the electric field on the N–Si interaction.

## 13.1 Analysis of close contacts

As seen in Figure 12.1, both the nitrogen and silicon atoms are surrounded by bulky substituents, which impair intermolecular interactions involving these atoms. However, all other atoms,

such as those of the substituent X and the naphthalene system, are freely exposed to the environment, and thus, interactions involving these atoms can be expected. In the following, a Hirshfeld surface analysis, which offers an efficient way to get a qualitative impression on intermolecular interactions between molecules inside crystal structures,[182,183] is performed for all crystal structures using *CrystalExplorer*.[184] A Hirshfeld surface is an approach to partition the electron density of a crystal into fragments.[124] In Chapter 3, a definition for a Hirshfeld atom was provided (equation 3.8). In analogy to this approach, a molecular fragment can be obtained from the molecular weight function, see Equation 13.1.

$$w_A(r) = \rho_{\text{promolecule}}(r)/\rho_{\text{procrystal}}(r) \tag{13.1}$$

The Hirshfeld surface of molecule A is defined as the surface corresponding to an iso-value of $w_A = 0.5$.[182] The distances $d_i$ and $d_e$ are measured from the Hirshfeld surface to the nearest nucleus inside (internal) and outside (external) the surface, respectively.[182] A Hirshfeld fingerprint plot shows these distances in a two-dimensional histogram binned in intervals of 0.01 Å.[182] Each bin is colored according to the number of surface points inside it, ranging from blue (few points) through green to red (many points). In the following analysis, its usefulness to uncover intermolecular interactions is demonstrated. Figure 13.1 shows Hirshfeld surfaces and fingerprint plots for the molecules inside the crystal structures regarded in this study. The normalized contact distance $d_{\text{norm}}$, which combines $d_e$ and $d_i$ normalized by the van-der-Waals radius of the atoms involved in the close contact to the surface, is mapped on top of the Hirshfeld surfaces.[182] Red regions are obtained for contacts, which are shorter than the sum of the van-der-Waals radii – they show short contacts, which may be attributed to strong intermolecular interactions. In the following, the compounds are discussed in the order of increasing N–Si distance.

### Silyl cation (1)

There are two independent silyl cations (**1**) and two independent $B(C_6F_5)_4^-$ anions in the asymmetric unit. However, the fingerprint plots of both silyl cations (**1**) are quite similar to each other, which indicates that there are comparable intermolecular interactions in both entities. This results in very similar N–Si distances (there is only a difference of 0.007 Å, which is in the magnitude of the experimental error). For both cations, there are very close F–H contacts between hydrogen atoms located at the cation and fluorine atoms located at the $B(C_6F_5)_4^-$ anion. The sharp tip at $d_i, d_e \approx 1.2, 0.9$, which is found in both fingerprint plots, can be attributed to the closest F–H contact, which involves a hydrogen atom located at one amine methyl group. There are also C–F, C–H and C–C contacts, but none of them indicates a strong interaction. No contacts involving the nitrogen and silicon atoms are obtained.

### Fluoro, bridged (2)

The fingerprint plot of the bridged fluoro compound (**2**) does not show any characteristic sharp tips, but close contacts are obtained nonetheless. Overall, only C−H and F−H contacts are obtained. There are two close F−H contacts, which are indicated by the two symmetrical tips at $d_i, d_e \approx 1.3, 1.1$ and $d_i, d_e \approx 1.1, 1.3$ in the fingerprint plot. Both hydrogen atoms, which are involved in this contact, are part of the naphthalene unit. The two symmetrical tips at $d_i, d_e \approx 1.6, 1.1$ and $d_i, d_e \approx 1.1, 1.6$ can be attributed to the closest C−H contact between a naphthalene hydrogen atom and a phenyl carbon atom.

### Chloro (3)

There is only a single molecule in the asymmetric unit of the crystal structure of the chloro compound (**3**). There are two significant close C−H contacts: One is between a hydrogen atom of the methyl group of the amine and a naphthalene carbon atom, and the other one is between a naphthalene hydrogen atom and a phenyl carbon atom. Both interactions can be attributed to the symmetrical pair of tips at $d_i, d_e \approx 1.5, 1.0$ and $d_i, d_e \approx 1.0, 1.5$ in the fingerprint plot. There are also Cl−H contacts, but none of them can be considered to be a close contact.

### p-Chlorobenzoate (4)

For the p-Chlorobenzoate molecule (**4**), there are close C−H, H−H, O−H, and less significant C−C and Cl−H contacts. The two symmetrical tips at $d_i, d_e \approx 1.4, 1.1$ and $d_i, d_e \approx 1.1, 1.4$ indicate close O−H contacts between the carboxylic oxygen atom and hydrogen atoms from the phenyl ring and the p-chlorobenzoate unit. Again, this close contact can be related to weak hydrogen bonding. All close C−H contacts are between hydrogen and carbon atoms from aromatic sites. The closest H−H contact at $d_i, d_e \approx 1.1, 1.1$ can be attributed to hydrogen atoms of the methyl groups bonded to the nitrogen atom. The fingerprint plot shows many surface points at high distances, which indicate large voids in the crystal structure.

### Fluoro (5)

In the crystal structure of the fluoro compound (**5**) , there are two racemic molecules inside the asymmetric unit. In these molecules, the N−Si distance differs by $\approx 0.05$ Å. The fingerprint plots show quite distinct features, which reveals that the intermolecular interactions are different in both molecules. The asymmetrical appearance of the two fingerprint plots indicates that there are contacts between the two independent molecules. There is one close contact between a hydrogen atom of a methyl group bonded to the nitrogen atom and a naphthalene carbon atom, which is located at the other molecule (with the shorter N−Si distance). In fact, this is the

only significant close C−H contact involving the molecule with the shorter N−Si distance. The molecule with the longer N−Si distance has another close C−H contact between a phenyl group and a naphthalene hydrogen atom (this corresponds to the symmetrical tips at $d_i, d_e \approx 1.6, 1.0$ and $d_i, d_e \approx 1.0, 1.6$). Other than that, both molecules show contacts between the fluorine atom and a hydrogen atom of the methyl group bonded to the nitrogen atom. This can be attributed to weak fluorine hydrogen bonding.

### Ethynyl (6)

For the single molecule inside the asymmetric unit of the crystal structure of the ethynyl compound (**6**), there are only C−H and H−H contacts. The pronounced tip in the fingerprint plot at $d_i, d_e \approx 1.0, 1.0$ can be attributed to the close H−H contact between one phenyl hydrogen atom and one naphthalene hydrogen atom. The other two symmetrical tips at $d_i, d_e \approx 1.6, 1.1$ and $d_i, d_e \approx 1.1, 1.6$ correspond to the closest C−H contact, where the carbon atom is from the naphthalene unit and the hydrogen atom is from the ethynyl group.

### Methoxy (8)

No close contacts involving nitrogen and silicon atoms are obtained for the single molecule inside the asymmetric unit of the crystal structure of the methoxy compound (**8**). In addition to C−H and H−H close contacts, which were also obtained for all other crystal structures so far, there are also close O−H contacts. In the fingerprint plots, they correspond to the two partially hidden symmetrical tips at $d_i, d_e \approx 1.4, 1.1$ and $d_i, d_e \approx 1.4, 1.1$. The hydrogen atom involved in this contact is from the naphthalene unit. The interaction, which causes this close contact, may be regarded as a weak C−H···O hydrogen bond (smaller distances would indicate a stronger hydrogen bond). The pronounced tip at $d_i, d_e \approx 1.1, 1.1$ can be associated with a H−H close contact between one naphthalene and one phenyl hydrogen atom. There are two pairs of symmetrical chicken-wing-like tips, which both correspond to close C−H contacts between two naphthalene hydrogen and carbon atoms, which may be attributed to interactions between a C−H bond and the $\pi$ system of the naphthalene unit.

### Methyl (10)

There are two independent molecules in the asymmetric unit of the crystal structure of the methyl compound (**10**), and therefore, two distinct Hirshfeld surfaces and fingerprint plots are shown in Figure 13.1. The fact that the N−Si distance only differs by about 0.01 Å (2.8538(8) Å vs. 2.8653(8) Å) shows that the environment does not significantly influence the N−Si interaction. In terms of close contacts, only C−H and H−H contacts are uncovered for both molecules in the asymmetric unit. Another common feature is the tip at $d_i, d_e \approx 1.1, 1.1$ in both

fingerprint plots, which corresponds to the closest H−H contact between a hydrogen atom of the methyl group, which is bonded to the silicon atom, and a hydrogen atom of the naphthalene unit. From the shape of the fingerprint plots, it can already be concluded that not all interactions are the same. In the fingerprint plot of the molecule with the shorter N−Si distance, there are two symmetrical tips, which resemble a chicken wing (at $d_i, d_e \approx 1.6, 1.0$ and $d_i, d_e \approx 1.0, 1.6$). The corresponding tips of the other molecule (at $d_i, d_e \approx 1.6, 1.0$ and $d_i, d_e \approx 1.0, 1.6$), are less pronounced and do not have the appearance of a chicken wing. In both cases, the tips can be related to a close C−H contact, where the carbon and hydrogen atoms are part of an aromatic ring system. For the molecule with the shorter N−Si distance, the carbon and hydrogen atoms are part of the naphthalene unit, while they are part of the phenyl ring bonded to the silicon atom in the other molecule. Apart from that, the contacts are largely the same, which is indicated by a similar appearance of both fingerprint plots.

### Aryl (11)

There is one molecule in the asymmetric unit of the crystal structure of the aryl compound (**11**), however, there are two intermolecular N−Si interactions involving two different axial substituents, corresponding to a phenyl group and an N,N-Dimethyl-1-naphthylamine group, respectively. The Hirshfeld fingerprint plot does not reveal any contacts for the silicon and nitrogen atoms, and therefore, intermolecular interactions involving these atoms are not obtained. However, there are many close C−H and H−H contacts. In the fingerprint plot, the tip at $d_i = 1.1$ and $d_e = 1.1$ corresponds to the closest H−H contact between a hydrogen atom of the naphthalene unit and a hydrogen atom of one of the methyl groups bonded to the nitrogen atom. The closest C−H contact is found between a hydrogen and a carbon of the naphthalene system (the tip at $d_i, d_e \approx 1.6, 1.1$ in the fingerprint plot). This interaction my be attributed to an interaction between a C−H bond and the $\pi$-system of the naphthalene unit.
In summary, it can be stated that neither the nitrogen nor the silicon atoms are involved in any close contacts. There are, however, intermolecular interactions involving the substituent X and the naphthalene system. Both aspects can influence the N−Si interaction, because the nucleophilic character of the nitrogen atom or the electrophilic character of the silicon atom are influenced.

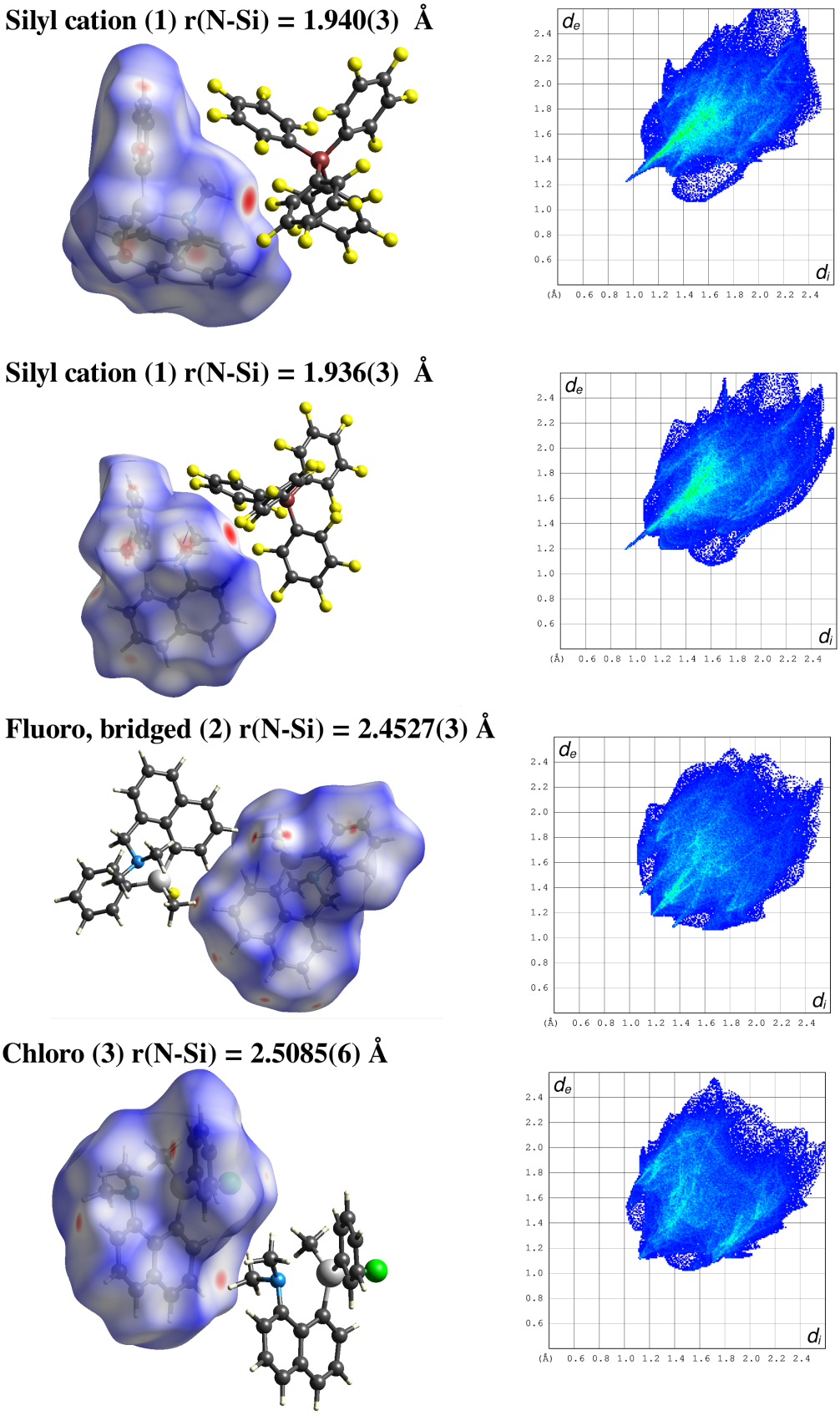


**Figure 13.1:** Left: Hirshfeld-Surfaces mapped with $d_{norm}$ of the *Hirshfeld atom refined* structures; and right: The corresponding Hirshfeld fingerprint plot, where $d_i$ and $d_e$ are the distances from the Hirshfeld surface to the nearest nucleus inside (internal) and outside (external) the surface, respectively.

**p-Chlorobenzoate (4) r(N-Si) = 2.6452(7) Å**

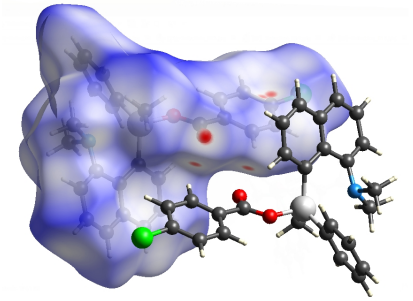

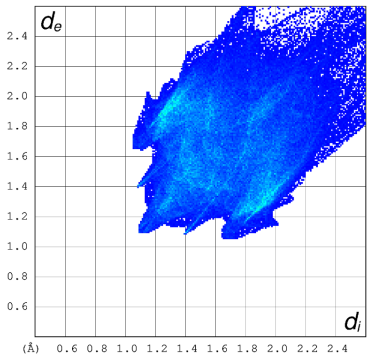


**Fluoro (5) r(N-Si) = 2.703(1) Å**

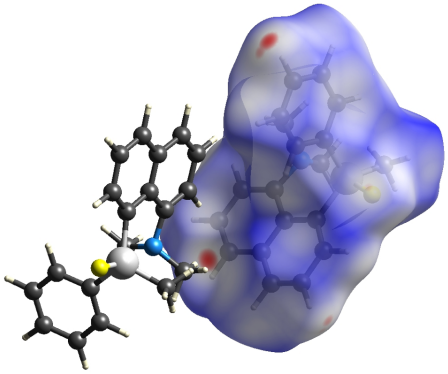

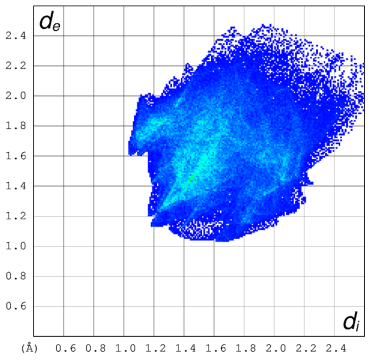


**Fluoro (5) r(N-Si) = 2.659(1) Å**

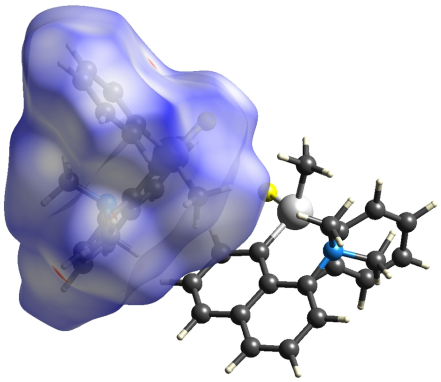

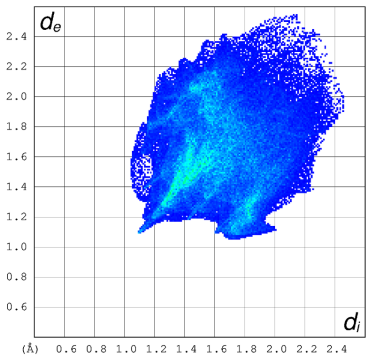


**Ethynyl (6) r(N-Si) = 2.7729(4) Å**

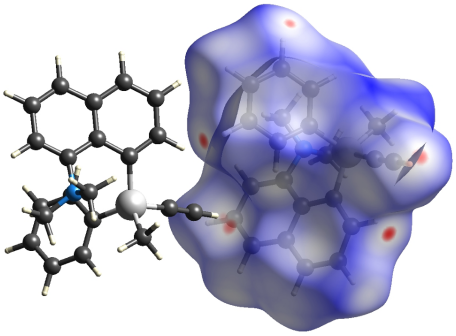

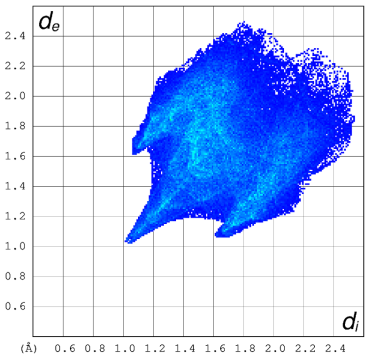


**Figure 13.1 (continued)**

**Methoxy (8) r(N-Si) = 2.8024(8) Å**

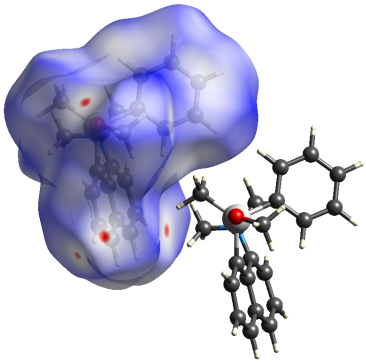

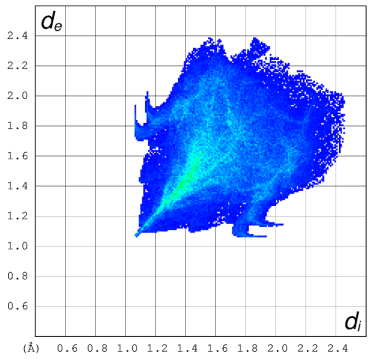


**Methyl (10) r(N-Si) = 2.8538(8) Å**

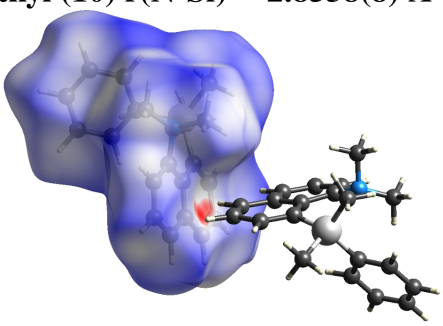

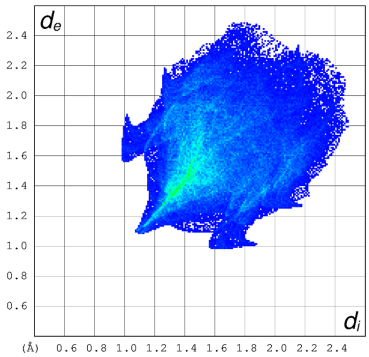


**Methyl (10) r(N-Si) = 2.8653(8) Å**

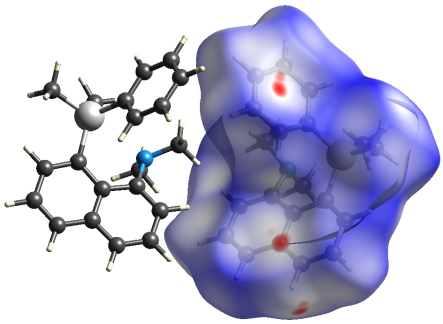

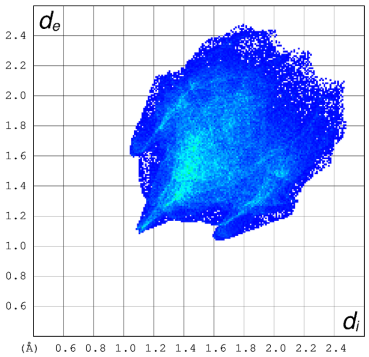


**Aryl (11) r(N-Si) = 2.8978(8) Å, 2.9581(8)**

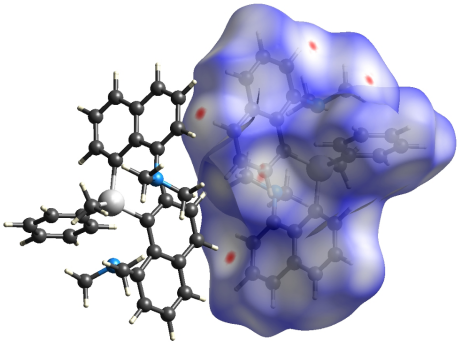

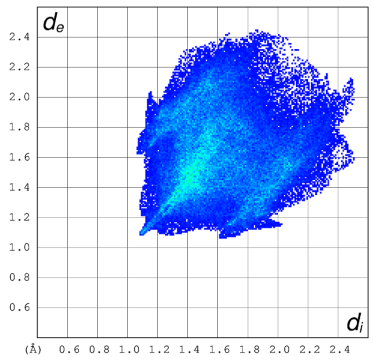


**Figure 13.1 (continued)**

## 13.2 The influence of the electric field

The electric field exerted by the crystal environment promotes ionic bonding representations. Consequently, it is expected that the N–Si interaction is stronger, because a N–Si bond formation would come with a positive formal charge at the nitrogen and a negative formal charge at the substituent X (see Figure 11.4). In the present section, the N–Si distances of the chloro (**3**) and ethynyl (**6**) compounds of geometry optimizations in different environments are compared to the corresponding bond lengths of the crystal structures from *HAR*. These compounds have been chosen, because the N–Si bond distances of the chloro compound (**3**) show a great dependence on the environment (crystal structure vs. geometry optimized structure of the isolated molecule), while the difference between these two bond lengths is relatively small in the ethynyl compound (**6**). Table 13.1 lists N–Si bond lengths in different environments, on which the following discussion is based.

**Table 13.1:** The N–Si and Si–X distances (in Å) of the chloro (**3**) and ethynyl (**6**) compounds obtained from different environments.

| Environment | Chloro (**3**) r(N-Si) | Ethynyl (**6**) r(N-Si) |
|---|---|---|
| HAR, SPring8 | 2.5085(6) | 2.7729(4) |
| Geometry optimization, dispersion | 2.732 | 2.835 |
| Geometry optimization, dispersion, water solvation | 2.542 | 2.789 |
| Geometry optimization, dispersion, acetonitrile solvation | 2.551 | 2.791 |
| Geometry optimization, cluster charges, r = 16 Å | 2.649 | 2.825 |
| Periodic boundary geometry optimization (Crystal14) | 2.507 | – |

A comparison of the structures from *HAR* and from the geometry optimization of the isolated compound reveals that the N–Si bond length is in fact shorter in the crystal environment. The decrease in the chloro compound (**3**) is more significant (≈0.22 Å) compared to the decrease in the ethynyl compound (**6**) (≈0.06 Å). The different bond lengths are either caused by explicit intermolecular interactions, which have been analyzed in the preceding section, or by the electric field exerted by the crystal environment. However, if the geometry optimization is performed with the same parameters (level of theory and dispersion correction), but an implicit water or acetonitrile solvation correction is added, the N–Si bond lengths are decreased to a similar extent. An implicit solvation correction mimics the effect of a solvent based on its dielectric constant ($\epsilon$(water) = 78.4 and $\epsilon$(Acetonitrile) = 36.6), and thus, no explicit intermolecular interactions based on orbital overlap are considered. The fact that the N–Si bond lengths are similar to those obtained from *HAR*, if a solvent correction with a polar solvent is applied, implies that the most significant effect on the shortened bond lengths is the electric field exerted by the crystal. For the chloro compound (**3**), the effect of the electric field is more significant

than for the ethynyl compound (**6**). This is caused by the high stability of the chloride anion if it interacts with positive charges. The $CCH^-$ anion is less stable, and thus, the Si–C bond will keep much of its covalent character, while ionic bonding is only slightly increased. If cluster charges, which are point charges and dipoles representing the crystal environment, are applied, the Si–N bond lengths are also decreased in comparison to the isolated molecules, however, they are not as effective as an implicit solvent correction. For the ethynyl compound (**6**), the N–Si bond length is only somewhat shorter if cluster charges are applied. For the chloro compound (**3**), a geometry optimization with periodic boundaries was performed with Crystal14[178] at the B3LYP/pob-TZVP level of theory. The optimization gives an almost identical N–Si bond length to the one obtained in the crystal structure.

# Chapter 14

# The nature of the N−Si interaction from the perspective of a *complementary bonding analysis*

In the submitted manuscript entitled *"Complementary bonding analysis on the N−Si interaction in pentacoordinated silicon compounds"*, the N−Si interaction of the non-bridged (**5**) and bridged fluoro compounds is analyzed by a *complementary bonding analysis*. These two compounds have been chosen for this study, because they both have a fluorine atom as their substituent X, and therefore, the only difference between them is an additional methylene group bridging the naphthalene unit and the amino group in the bridged fluoro compound (**2**). This study shows that the N−Si interaction can be described by negative hyperconjugation between a lone pair of the nitrogen and an Si−F antibond. The signifiacance of the interaction between the nitrogen lone pair and the aromatic ring system is also revealed. It is shown how the N−Si interaction can be classified by the complementary bond analysis methods. In both compounds the attractive interaction between the nitrogen and silicon is stronger than the repulsion between these two atoms. The compound IDs in this manuscript are different to the ones used in the other chapters of this part.

**My contributions to this manuscript:**

- I wrote 80% - 90% of the text
- I performed the geometry optimizations of the compounds
- I performed the X-ray diffraction experiments for the bridged fluoro compound

- I performed the data reduction and crystallographic refinements (*IAM* and*HAR*)
- I performed the *XCW*
- I performed the NBO, QTAIM and ELI-D analyses
- I analyzed and interpreted all results
- I am responsible for all figures and all tables

The paper was submitted to *Daton Transactions* on July 3rd, 2019 (see confirmation below).

**Subject:** Acknowledgement of your Submission to Dalton Transactions - DT-ART-07-2019-002772
**From:** Dalton Transactions <onbehalfof@manuscriptcentral.com>
**Date:** 03.07.19, 18:23
**To:** simon.grabowsky@uni-bremen.de
**CC:** m.fugel@uni-bremen.de, m.ponomarenko@jacobs-university.de, maxie.hesse@uni-bremen.de, lama@uni-bremen.de, florian.kleemiss@uni-bremen.de, ksugimoto@spring8.or.jp, Alessandro.Genoni@univ-lorraine.fr, g.roeschenthaler@jacobs-university.de, simon.grabowsky@uni-bremen.de

03-Jul-2019

Dear Dr Grabowsky:

TITLE: Complementary bonding analysis of the N – Si interaction in pentacoordinated silicon compounds using quantum crystallography

Thank you for your submission to Dalton Transactions, published by the Royal Society of Chemistry. This is an automatic acknowledgement that you have uploaded your files to our online submission system. Your manuscript ID is: DT-ART-07-2019-002772

Your manuscript will be passed to an editor for initial assessment as soon as possible. If there are any problems with your submission we will contact you.

# Complementary bonding analysis of the N−Si interaction in pentacoordinated silicon compounds using quantum crystallography

Malte Fugel[a], Maksym V. Ponomarenko[b], Maxie F. Hesse[a], Lorraine A. Malaspina[a], Florian Kleemiss[a], Kunihisa Sugimoto[c], Alessandro Genoni[d], Gerd-Volker Röschenthaler[b], and Simon Grabowsky[a*]

[a]University of Bremen, Department 2: Biology/Chemistry, Institute of Inorganic Chemistry and Crystallography, Leobener Str. 3, 28359 Bremen, Germany.
[b]Jacobs University, Life Sciences & Chemistry, Campus Ring 1, 28759 Bremen, Germany.
[c]JASRI / Diffraction & Scattering Division, 1-1-1 Kouto, Sayo-cho, Sayo-gun, Hyogo 679-5198, Japan.
[d]Université de Lorraine, CNRS, Laboratoire LPCT, 1 Boulevard Arago, F-57078 Metz, France.

Electronic supplementary information (ESI) available: characterization of compounds, crystallographic details, coordinates of optimized structures. CCDC: 1937643, 1937692, 1937940.

**Abstract**

The N−Si interaction in two pentacoordinated silicon compounds is investigated based on a *complementary bonding analysis*, which consists of bonding descriptors from real space and orbital space. These are derived from X-ray wavefunction refinements of high-resolution X-ray diffraction data of single crystals and from isolated-molecule theoretical wavefunctions. The compounds can be regarded as snapshots of an intramolecular nucleophilic attack of the nitrogen atom at the electrophilic silicon atom. Therefore, understanding the N−Si interaction gives an insight into the properties playing a role in the course of a nucleophilic addition or substitution of nitrogen to silicon. The two pentacoordinated compounds only differ in one methylene group, so that the amino substituent is more flexible in one of the structures, hence probing the attractive or repulsive character of the N−Si interaction. All studies suggest weak dative interactions, which do, however, greatly influence the character of the Si−F bond: A strong N−Si interaction results in a weakened Si−F bond, which is quantified in this study experimentally and theoretically.

## 1 Introduction

Numerous compounds with pentacoordinated silicon atoms are found in the literature.[1–6] In some cases, a stable pentacoordinated silicon complex is obtained in the course of $S_N2$ reactions involving silicon electrophiles, which is in contrast to $S_N2$ reactions involving carbon electrophiles, where the pentacoordinated

species is always a transition state.[7–9] Accordingly, pentacoordinated silicon compounds in the solid state have proven to be a suitable model system for the experimental simulation of $S_N2$ reactions.[10–16] In the present paper, we analyze the bonding situation in two pentacoordinated silicon compounds (**1** and **2**), which are depicted in Figure 1. In both of these structures, the nitrogen atom is coordinated to the silicon, thus, inflicting a certain degree of pentacoordination. According to the philosophy of Bassindale et al.,[10–16] both structures may be regarded as snapshots of an intramolecular $S_N2$ reaction with the nitrogen and fluorine atoms representing the nucleophile and leaving group, respectively.

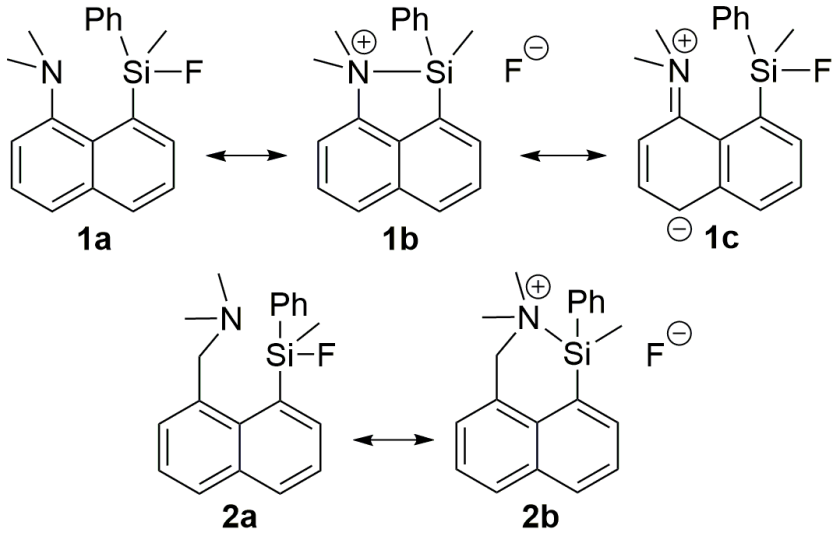


**Figure 1:** Resonance structures involving the nitrogen lone pair of the non-bridged (**1a-c**) and bridged (**2a-b**) compounds

The compounds only differ in that compound **2** has a methylene group bridging the amino group and the naphthalene unit. In compound **1**, the N–Si interaction is a peri-interaction, which is enforced by geometric proximity.[17] Hence, the interaction always has an attractive and a repulsive component, as investigated in detail by Beckmann and Mebs.[18–22] In compound **2**, free rotation around the methylene group allows the N–Si contact to avoid all enforced interactions, and hence it can serve as a measure of the degree of attractive or repulsive interactions. One of the main objectives of the present paper is to uncover the differences of the N–Si interaction resulting from the additional methylene group in the bridged compound. There are three factors differentiating compounds **1** and **2**:

1. The additional methylene group makes the $R_3N$ group rotationally flexible, so a closer approach of the nitrogen atom towards the silicon atom is possible, or, in turn, avoidance of the contact leading to a longer N–Si distance.

2. The additional methylene group in the bridged compound makes one of the substituents bulkier, which causes a higher steric repulsion in the bridged compound **2** compared to the non-bridged

compound **1**.

3. Only in the non-bridged compound **1**, the nitrogen lone pair is involved in a resonance with the aromatic system of the naphthalene unit leading to resonance structure **1c** depicted in Figure 1.

The N−Si interaction itself may be represented by resonance structures **1b** and **2b** for the non-bridged and bridged compound, respectively. These resonance structures have a N−Si bond, while the silicon and fluorine atoms are not covalently bonded to each other. In terms of a localized orbital picture, this interaction can be classified as negative hyperconjugation with the nitrogen lone pair acting as a donor orbital and the Si−F antibond acting as an acceptor orbital.[23] Resonance structures with both N−Si and Si−F bonds are not considered, because these hypervalent bonding representations suggest d-orbital participation, which has been shown to be insignificant for bonds involving atoms from the second and third periods.[24–29]

We have discussed previously that a joint application of bond analysis methods from real space (e.g. Quantum Theory of Atoms in Molecules, QTAIM,[30] and the electron localizability indicator, ELI-D[31]) and orbital space (e.g. natural bond orbitals, NBO[23,32]) enhances the information value due to the complementary of the methods (complementary bonding analysis).[33–35] In the present study, we apply QTAIM, ELI-D, NBO and unconstrained ELMO-VB (extremely localized molecular orbital valence bond)[36,37] analyses to shed light on the N−Si interaction and related bonding properties. The results are produced using X-ray wavefunction refinements (XWR)[38,39] of high-resolution single crystal X-ray diffraction data measured at the synchrotron SPring-8 in Japan. XWR is a novel method from the field of quantum crystallography.[40,41] For a comparison, purely theoretical calculations were performed in addition.

## 2 Experimental and computational details

### 2.1 Synthesis

#### Synthesis of the non-bridged compound (1)

Previously, compound **3** was synthesized by Carré *et al.*[42] However, in this study an alternative route was chosen. 12.52 mL (1 equiv) of n-BuLi (2.5 M, in n-hexane) were added at 0°C to a solution of N,N-dimethylnaphthalen-1-amine (5.36 g, 31.3 mmol) in 35 mL of diethyl ether. The mixture was stirred for 48 h at room temperature. The formed precipitate of the lithiated product was filtered off, and washed with pentane (2 x 20 mL) under argon; then it was dried for 30 min in oil-pump vacuum at room temperature. The solid product was transferred into a 100 mL Schlenk flask, and then 40mL of diethyl ether was added. The mixture was cooled to -60°C, and 4.46 g (23.33 mmol, 1.3 equiv) of $PhSiMeCl_2$ was added through a syringe. The cooling bath was removed after 30 min, and the mixture was stirred for 24 h at room temperature. The formed precipitate was filtered off under argon, and washed with diethyl ether (2 x 5 mL). Diethyl ether was evaporated, and the rest was recrystallized from a saturated hot diethyl ether solution (under argon) giving 1.2 g (20%) of the clean product **3**. The white precipitate, which was

collected after first filtration of the reaction mixture, was mixed with 20 mL of $CH_2Cl_2$, and the mixture was filtered to remove LiCl. The solvent was evaporated giving 3.6 g (61% yield) of **3**.

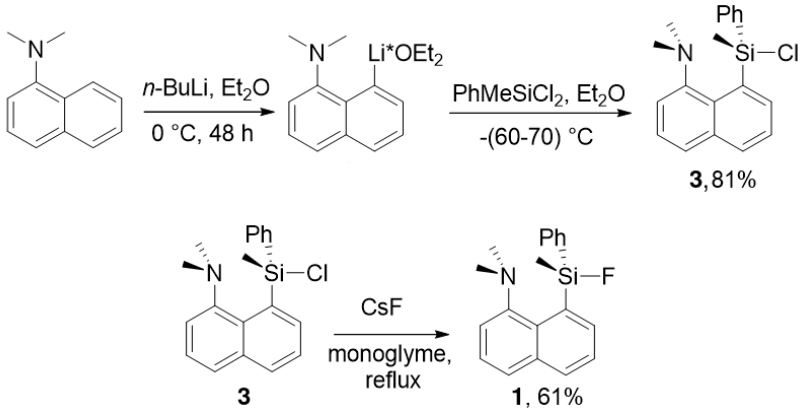


**Scheme 1**

0.55 g (1.69 mmol) of **3** were added to a mixture of dried CsF (2.56 g, 16.9 mmol) in 20 mL of monoglyme. The mixture was refluxed for 12 h, and cooled to ambient temperature. 20 mL of $CH_2Cl_2$ was added, and then the reaction mixture was filtered under inert atmosphere. The solvents were removed in oil-pump vacuum. The residue was recrystallized from an n-hexane/$CH_2Cl_2$ mixture giving 0.318 g (61%) of the fluorinated product **1**. Colorless good quality single crystals of **1** were grown by slow evaporation technique (air) from an n-hexane/$CH_2Cl_2$ ( 80/20 v/v) mixture. The fluorinated product **1** becomes darker after two to three weeks of storage at ambient conditions. However, **1** is stable for a long time under inert atmosphere.

**Synthesis of the bridged compound (2)**

$\beta$-Dimethylaminomethylnaphthalene was prepared according to the literature.[43] 3.1 mL (1 equiv) of n-BuLi (2.5 M, in n-hexane) was added at 0°C to a solution of $\beta$-dimethylaminomethylnaphthalene (1.44 g, 7.77 mmol) in 25 mL of diethyl ether. The mixture was stirred for 24 h at room temperature. The mixture was cooled to 0°C, and left to stay without stirring for a few hours. The dark red supernatant was removed using a syringe, and the solid lithiated amine was dissolved in 50 mL of fresh diethyl ether. The mixture was cooled to -50°C, and 1.98 g (10.86 mmol, 1.4 equiv) of $PhSiMe(OMe)_2$ was added dropwise through a syringe. The cooling bath was removed after 30 min, and the mixture was stirred for 24 h at room temperature. The solvent was evaporated, and the residue was kept for 4 h in oil pump vacuo at 200°C giving 2.24 g (86%) of raw **4**. The product **4** was used in the next step without additional purification. 0.91 g (2.71 mmol) of **4** was diluted in 15 mL of n-hexane. The solution was cooled with an ice bath, and $BF_3$-etherate (0.19 g, 1.34 mmol) was added. The mixture was intensively stirred for 2 h at room temperature. The n-hexane phase was removed into another 50 mL Schlenk flask by a syringe. The solid residue was washed with hot n-hexane (3 x 5mL). All n-hexane fractions were combined in the Schlenk

flask containing the n-hexane phase collected from the reaction mixture. The solvent was removed in oil pump vacuo. The white solid obtained was recrystallized three times from a hot saturated solution in n-hexane in inert atmosphere giving 0.40 g (48%) of **2**.

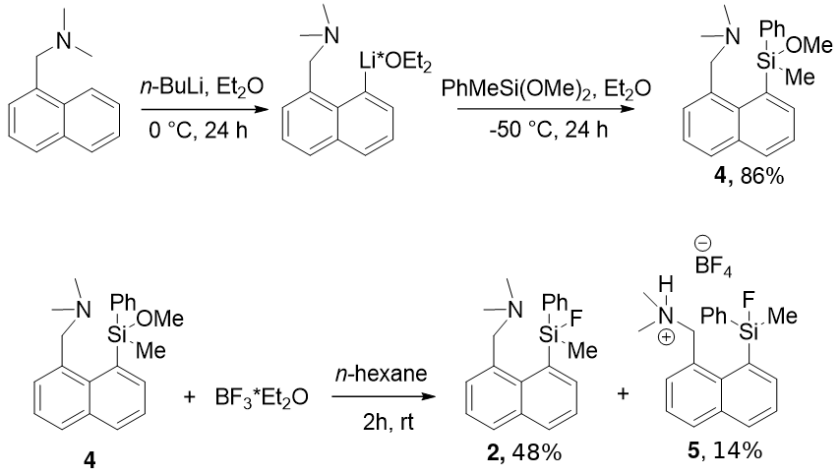


**Scheme 2**

The slightly yellow residue left in the reaction flask after washing with n-hexane was dissolved in a small amount of $CH_2Cl_2$ (ca. 2 mL). 10 mL of n-hexane was carefully layered on top of the $CH_2Cl_2$ solution. During the solvents diffusion at room temperature white crystals of **5** were formed. The solvents were removed using a syringe, and the product **5** was recrystallized twice in the same manner from a fresh $CH_2Cl_2$/n-hexane mixture giving 0.156 g (14%) of **5**.

$^1$H-, $^1$3C-, $^{19}$F-, $^{29}$Si-NMR and high-resolution mass spectrometry data of all synthesized compounds are found in the supporting information.

## 2.2 Quantum crystallography

Single crystals were obtained from these compounds as explained in the preceding section. High-resolution X-ray diffraction experiments were carried out. For the non-bridged compound **1**, the X-ray diffraction experiment was performed at the synchrotron SPring-8 (Hyogo, Japan) at a temperature of 20 K. For the bridged compound **2**, the X-ray diffraction data set was obtained from an in-house measurement with a Bruker D8 Venture at 100 K. Crystallographic information of these structures is given in Table 1. This table also contains the crystallographic information of compound **5**, for which a measurement was performed at SPring8.

After a structure refinement with spherical structure factors (independent atom model), an X-ray wavefunction refinement (XWR) was carried out for compounds **1** and **2**.[38] The first step of an XWR consists of a Hirshfeld atom refinement (HAR) which corresponds to a structure refinement with tailor-made aspherical structure factors obtained from an *ab initio* wavefunction (level of theory: HF/def2-TZVP)

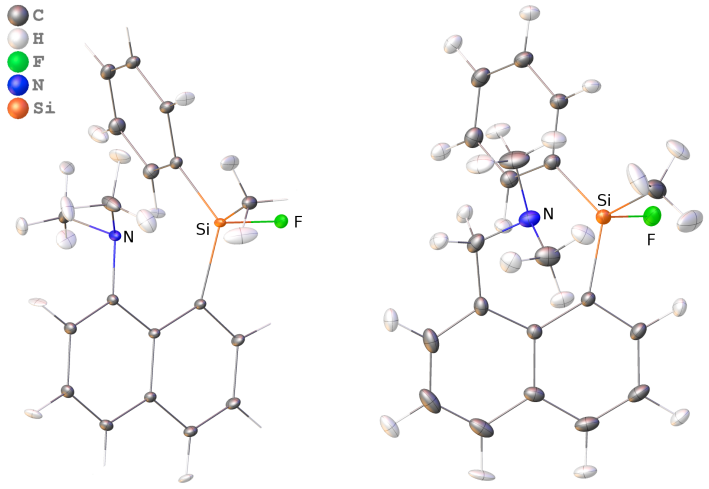


**1** **2**

**Figure 2:** Molecular structures of the non-bridged (left, **1**, only one out of two symmetry-independent molecules is shown) and bridged (right, **2**) compounds after HAR (ellipsoids are shown at a probability of 50%). Free refinement of hydrogen anisotropic displacement parameters sometimes leads to non-positive definite values (here seen for **1**), but the C–H distances are most accurate nontheless. A detailed discussion about this is found in the literature.[38,46,47]

by application of Hirshfeld's stockholder partitioning scheme.[44,45] Cluster point charges and dipoles in a radius of r = 8 Å were used to mimic the crystal environment. The refined crystal structures are shown in Figure 2. There are two molecules in the asymmetric unit of the non-bridged compound. Therefore, properties from both units are given in the following.

In the second step, a wavefunction was fitted to the experimental diffraction data (X-ray constrained wavefunction fitting, XCW).[48] Crystallographic details of the bridged and non-bridged compounds, as well as for compound **5**, can be obtained from the Cambridge Structural Database numbers listed in Table 1.

Geometry optimizations of the two isolated molecules (**1** and **2**) were carried out with Gaussian 09 at the B3LYP/aug-cc-pVTZ level of theory and application of a dispersion correction (GD3BJ). Frequency analyses were performed to make sure that the optimized structures correspond to minima on the potential energy surfaces.

The X-ray constrained wavefunctions as well as wavefunctions obtained from the geometry optimizations were analyzed with a variety of methods to investigate the bonding situation in these compounds. The NBO analysis was performed with NBO 6.0,[49] and for the QTAIM analysis AIMall[50] was applied. The ELI-D analysis was performed with Dgrid 5.0.[51]

**Table 1:** Crystallographic information and refinement statistics.

| | non-bridged, **1** SPring8 | bridged, **2** Home | bridged (protonated), **5** SPring8 |
|---|---|---|---|
| Empirical formula | $C_{19}H_{20}FNSi$ | $C_{20}H_{22}FNSi$ | $C_{20}H_{23}FNSi^{+}\ BF_4{}^{-}$ |
| Space group | P2(1)2(1)2(1) | P2(1)/c | Pn |
| Crystal system | Orthorhombic | Monoclinic | Monoclinic |
| a /Å | 9.5986(19) | 7.5718(3) | 13.131(3) |
| b /Å | 11.430(2) | 17.2362(6) | 7.7980(16) |
| c /Å | 29.056(6) | 13.0930(5) | 21.291(4) |
| $\alpha$ /° | 90 | 90 | 90 |
| $\beta$ /° | 90 | 95.9760(10) | 99.58(3) |
| $\gamma$ /° | 90 | 90 | 90 |
| wavelength /Å | 0.4133 | 0.71073 | 0.4015 |
| T /K | 25(2) | 100(2) | 20(2) |
| Crystal dimensions /$\mu m^3$ | 80x60x50 | 137x179x212 | 250x180x130 |
| $\sin(\theta)/\lambda_{max}$ /Å$^{-1}$ | 0.83 | 0.91 | 1.11 |
| $R_{int}$ | 0.0304 | 0.0439 | 0.0435 |
| $N_{meas}$, $N_{uniq}$ | 71871, 15418 | 183013, 10700 | 134595, 44848 |
| $N_{obs}$ (F >4$\sigma$) | 15240 | 8971 | 34497 |
| Redundancy | 4.66 | 17.1 | 3.0 |
| Completeness | 1.00 | 1.00 | 0.99 |
| CCDC no. | 1937692 | 1937643 | 1937940 |
| After IAM | | | |
| R1 | 0.0344 | 0.0354 | 0.0602 |
| wR2 | 0.0918 | 0.1082 | 0.1818 |
| $\Delta\rho_{min/max}$ /eÅ$^{-3}$ | -0.56/0.81 | -0.34/0.62 | -0.88/1.65 |
| After HAR | | | |
| R1 | 0.0251 | 0.0231 | – |
| wR2 | 0.0430 | 0.0322 | – |
| $\Delta\rho_{min/max}$ /eÅ$^{-3}$ | -0.28/0.37 | -0.22/0.17 | – |
| After XWR | | | |
| $\lambda_{max}$ | 0.15 | 0.20 | – |
| R1 | 0.0244 | 0.016854 | – |
| wR2 | 0.0398 | 0.026609 | – |
| $\Delta\rho_{min/max}$ /eÅ$^{-3}$ | -0.27/0.33 | -0.19/0.16 | – |

## 3 Results and discussion

The analysis of structural parameters provides first hints regarding the bonding situation in the non-bridged and bridged compounds. Table 2 gives a selection of structural parameters of the refined crystal structures and isolated-molecule optimized structures. The N−Si distances in the crystal structures of both the non-bridged and bridged compounds are much shorter than the respective N−Si distances of the gas phase optimized structures. The reason for this is that the electric field of the crystal causes a charge stabilization, which favors a more ionic fluorine atom and, thus, the weights of resonance forms **1b** and **2b** are more significant in the crystal structure compared to the gas phase. Consequently, the N−Si distances are shorter and the Si−F bonds are somewhat elongated. If a geometry optimization is performed with an implicit water solvation without changing any of the other input parameters, the N−Si distances in

the non-bridged **1** and bridged compound **2** are 2.677 Å and 2.415 Å, respectively, which are close to the distances obtained in the crystal structures. This means that both the electric field in the crystal and the water solvation can stabilize an ionic bonding situation, thus enhancing the N–Si interaction.

The N–Si interaction seems to be stronger in the bridged compound, which is implied by a shorter N–Si distance. In turn, the Si–F bond in the bridged compound is slightly elongated. With respect to the simulation of $S_N2$ reactions, the shorter N–Si distance and elongated Si–F bond length in the bridged compound coincide with a more advanced progression of the reaction. Therefore, it is suggested that resonance structure **2b** is more significant than resonance structure **1b**, see discussion below. At the transition complex of an $S_N2$ reaction, the Si–F bond is oriented approximately 90° to the axial substituents.[7] In fact, the average of these angles is closer to a value of 90° in the bridged compound, see Table 2. This is another indication that the bridged compound is closer to a transition complex than the non-bridged compound, but since all R–Si–F angles exceed a value of 90°, a transition complex is not yet achieved. For the bridged compound, the N–Si–F angle is close to 180°. For the non-bridged compound, on the other hand, the N–Si–F angle is below 180°.

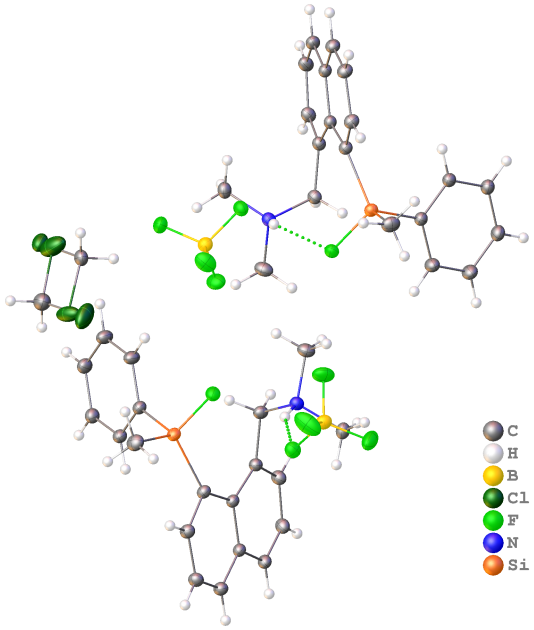


**Figure 3:** Molecular structures of compound **5** with two symmetry-independent $C_{20}H_{23}FNSi^+$ $BF_4^-$ units after *IAM*; disorder in solvent dichloromethane, anisotropic displacement parameters displayed at 50% probability.

Figure 3 shows the crystal structure of compound **5** after a refinement based on the IAM. There are two $C_{20}H_{23}FNSi^+$ $BF_4^-$ units in the asymmetric unit of the crystal structure. The compounds in the structure are the protonated form of the bridged compound **2**. The protonated nitrogen atom can no longer serve as a lone pair donor in the hyperconjugative interaction between the nitrogen lone pair and

the Si−F antibond. Instead, an intramolecular hydrogen bond between the fluorine atom and the N−H bond is obtained for one of the symmetry independent units; for the other unit, there is an intermolecular N−H···F hydrogen bond. Consequently, the nitrogen, silicon and fluorine atoms are no longer located on a straight line, but span an angle of 45.40° and 44.75°. The N−Si distance is r(N−Si) = 3.669 Å and 3.683 Å, which demonstrates the high degree of freedom of the N−Si distance despite the naphthyl scaffold.

**Table 2:** Structural parameters from the geometry optimizations and HAR: The N-Si bond length ($r$(N-Si) in Å), the Si-F bond length ($r$(Si-F) in Å), the N-Si-F angle ($\alpha$(N-Si-F) in Å) and the average R-Si-F angle ($<\alpha$(R-Si-F)$>$ in °). The uncertainty of $<\alpha$(R−Si−F)$>$ was derived from the standard deviation of the three R−Si−F angles.

| | non-bridged, **1** | | | bridged, **2** | |
|---|---|---|---|---|---|
| | opt. | HAR | | opt. | HAR |
| r(N-Si) | 2.7535 | 2.6593(8) | 2.7103(8) | 2.6478 | 2.4527(3) |
| r(Si-F) | 1.6379 | 1.6442(7) | 1.6426(7) | 1.6511 | 1.6662(2) |
| $<\alpha$(R-Si-F)$>$ | 101.7(26) | 100.2(16) | 99.3(8) | 98.0(8) | 95.5(8) |
| $\alpha$(N-Si-F) | 172.79 | 171.62(3) | 173.02(3) | 179.00 | 178.36(1) |

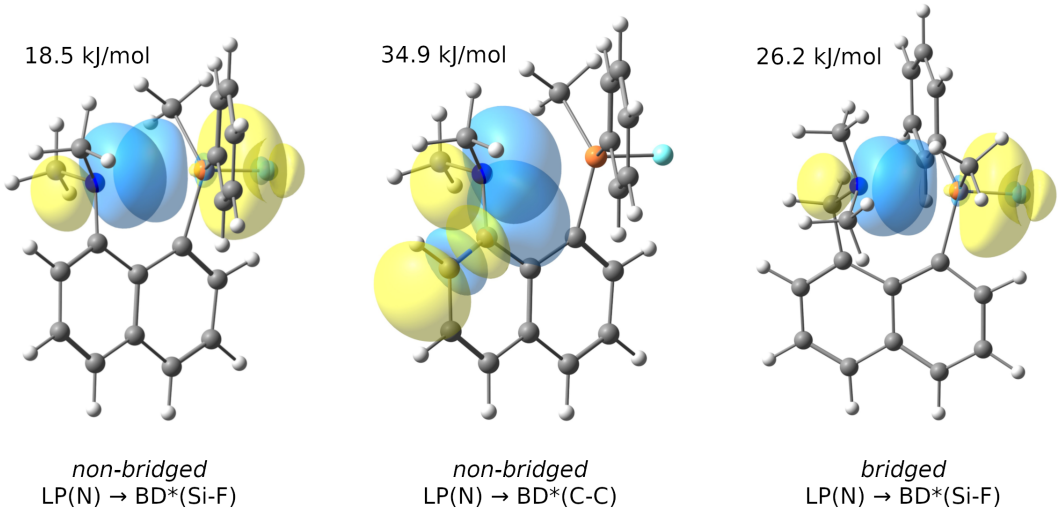


**Figure 4:** Representation of the natural bond orbitals involved in the LP(N)→BD*(Si−F) and LP(N)→BD*(C−C) negative hyperconjugative interactions with the corresponding delocalization energies (E2) from theory based on the optimized geometries.

A natural bond orbital (NBO) analysis can provide both a qualitative and quantitative description of the bonding situation based on a localized orbital point of view. The N−Si interaction can be linked to the interaction of the nitrogen lone pair NBO (donor orbital) and the Si−F antibond (acceptor orbital), that

is, negative hyperconjugation. Figure 4 depicts the interacting orbitals for the non-bridged and bridged compounds. Delocalization energies, which are given inside Figure 4 for the optimized geometries[1], provide a measure of the strength of these interactions based on the second order perturbation theory. These values reveal that the N–Si interaction is more pronounced in the bridged compound by ≈8 kJ/mol. Figure 4 also shows the interaction of the nitrogen lone pair NBO with a C–C antibond of the naphthalene unit in the non-bridged compound, which can be attributed to resonance structure **1c**. Based on the delocalization energy, this interaction is even more significant than the N–Si hyperconjugative interactions.

**Table 3:** Bonding properties from NBO (populations of the nitrogen lone pair and Si–F antibond (n(LP(N)) and n(BD*(Si-F)) in e) and NRT weights of the N-Si$^+$ F$^-$ resonance structure ($w_{\mathrm{NRT}}$) in %)

| | non-bridged, **1** | | | bridged, **2** | |
|---|---|---|---|---|---|
| | opt. | XWR | | opt. | XWR |
| $n$(LP(N)) | 1.821 | 1.863 | 1.867 | 1.818 | 1.817 |
| $n$(BD*(Si-F)) | 0.064 | 0.066 | 0.063 | 0.075 | 0.094 |
| $w_{\mathrm{NRT}}$(N-Si$^+$ F$^-$) | 3.64 | 3.20 | 3.04 | 4.09 | 4.89 |

The population of the Si–F antibonds (see Table 3) is another measure of the strength of the N–Si interaction. The anti-bond population is the highest in the bridged compound indicating stronger hyperconjugative interactions than those in the non-bridged compound. However, the populations are quite small and do not account for all electrons withdrawn from the nitrogen lone pair orbitals, which are involved in a variety of interactions. Therefore, an analysis of the nitrogen lone pair population in terms of the strength of the N–Si interaction is not applicable. A more direct access to the resonance structures depicted in Figure 1 is obtained from a local natural resonance theory (NRT) analysis.[52] Resonance structures involving only the nitrogen, silicon and fluorine atoms are calculated and a weight is assigned to them. Table 3 lists the weights of resonance structures **1b** and **2b**, which once again indicates that resonance structure **2b** is more significant than resonance structure **1b**. However, it is shown that the localized resonance structures **1a** and **2a** are most significant with weights far exceeding 90%. The N–Si interaction may therefore be regarded as a dative bond with nitrogen's electron pair largely maintaining its lone pair character.

Valence bond (VB) calculations based on extremely localized molecular orbitals (ELMOs) also provide an access to structural weights.[36,37,53] The weights of the ELMO-VB structures depicted in Figure 1 are listed in Table 4. Resonance structures **1a** and **1b** are by far the most significant ones as for NRT, but the respective weights are lower by about 10%. The weight of resonance structure **2b** of the bridged compound is higher than the weight of resonance structure **1b** of the non-bridged compound. Here, the ELMO-VB approach shows an even more pronounced difference compared to the weights from NRT. The weight of resonance structure **1c** is ≈4% in the non-bridged compound, which indicates that the N–Si interaction is more significant than the N–C interaction, in contrast to the delocalization energies from NBO.

[1]The calculation of delocalization energies from XWR is not yet applicable

**Table 4:** Weights of the resonance structures (see Figure 1) obtained from the ELMO-VB calculations (using the cc-pVDZ basis set) based on optimized and HAR geometries.

| | non-bridged, **1** | | | bridged, **2** | |
|---|---|---|---|---|---|
| | opt. | HAR | | opt. | HAR |
| $w_{\text{ELMO-VB}}(\mathbf{1a}/\mathbf{2a})$ | 0.87 | 0.85 | 0.86 | 0.88 | 0.82 |
| $w_{\text{ELMO-VB}}(\mathbf{1b}/\mathbf{2b})$ | 0.08 | 0.11 | 0.10 | 0.12 | 0.18 |
| $w_{\text{ELMO-VB}}(\mathbf{1c})$ | 0.04 | 0.04 | 0.04 | – | – |

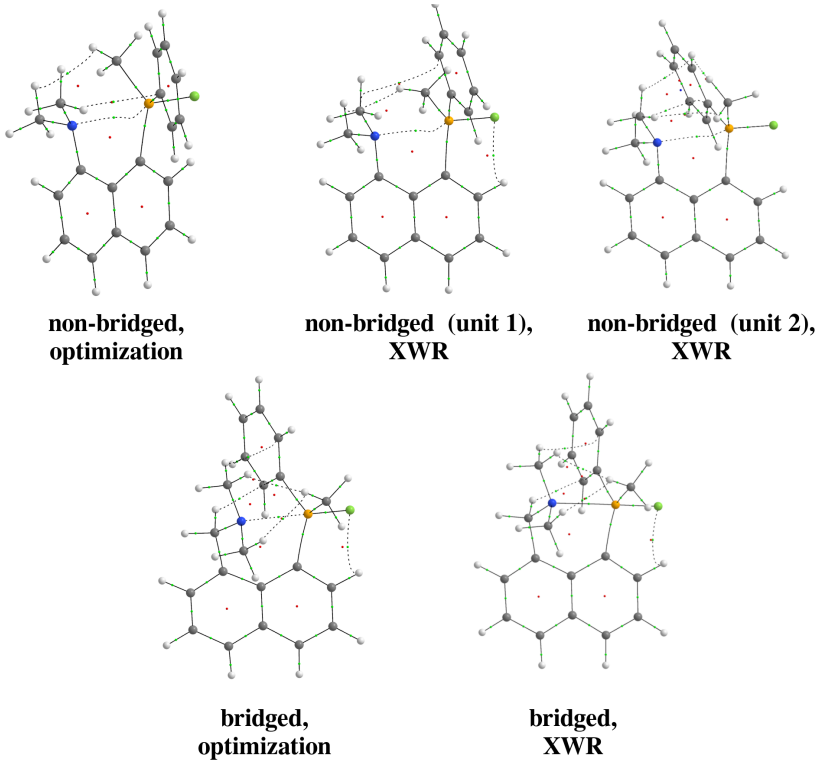


**Figure 5:** QTAIM bond paths obtained from theory and XWR (a dashed line corresponds to a weak interaction as defined in the software AIMAll by the value of the electron density at the bond critical point), red speres = bond critical points, green spheres = ring critical points

An analysis based on the Quantum Theory of Atoms in Molecules (QTAIM) provides further insight into the character of the dative N–Si bond as well as the Si–F bond. Figure 5 shows all bond paths obtained for the non-bridged and bridged compounds from theory and XWR. A bond path corresponds to a path of maximum electron density which indicates a bonded interaction.[54,55] In all cases, the analyses yield an N–Si bond path. However, they differ from bond paths of regular covalent bonds in that they are curved close to the silicon atom (compare to the straight C–C, N–C, Si–C and Si–F bond paths), with

the exception of the bridged compound from XWR, for which a straight N–Si bond path is obtained. A curved bond path is an indication of a weak interaction. Accordingly, the straight bond path obtained for the bridged compound from the XWR hints at a stronger N–Si interaction. The character of the N–Si interactions and Si–F bonds can be quantified by examining properties at the N–Si and Si–F bond critical points (bcps, saddle points of the electron density which are intersected by the bond paths), see Table 5.

**Table 5:** N-Si and Si-F bond critical point properties from QTAIM: Electron density ($\rho_{bcp}$ in e·Å$^{-3}$) and total energy density ($H_{bcp}$ in Hartree·Å$^{-3}$)

| | non-bridged, **1** | | | bridged, **2** | |
|---|---|---|---|---|---|
| | opt. | XWR | | opt. | XWR |
| $\rho_{bcp}$(N-Si) | 0.140 | 0.166 | 0.153 | 0.168 | 0.240 |
| $H_{bcp}$(N-Si) | -0.0014 | -0.0033 | -0.0023 | -0.0038 | -0.0114 |
| $\rho_{bcp}$(Si-F) | 0.847 | 0.844 | 0.849 | 0.821 | 0.769 |
| $H_{bcp}$(Si-F) | -0.0376 | -0.0390 | -0.0395 | -0.0365 | -0.0275 |

The value of the electron density at a bond critical point is indicative of the strength of bonded interactions. Once again, the N–Si interactions in the bridged compound are revealed to be the strongest ones. This is in agreement with the value of the total energy density at the N–Si bond critical points, which is more negative for the bridged compounds suggesting a higher degree of covalency.[56–58] However, the magnitude of these values implies relatively weak interactions in comparison to the respective values at the Si–F bond critical points. The electron density at the Si–F bond critical points of the non-bridged compound is higher than the one of the bridged compound indicating the Si–F bonds to be weaker in the bridged compound. Consequently, a stronger N–Si interaction comes with a weakened Si–F bond. This is in agreement with the previous analyses which found that the Si–F bonds are elongated, and that the Si–F antibonds are more populated in the bridged compound.

A topological analysis of the electron localizability indicator (ELI-D) yields basins which can be linked to features of Lewis structures, such as bonds and lone pairs.[31] Figure 6 depicts ELI-D iso-surfaces revealing bonding and lone pair domains in the non-bridged and bridged compounds. For the non-bridged compounds and the gas phase optimized bridged compound, a nitrogen lone pair basin is obtained. The bridged compound from XWR, on the other hand, gives an N–Si bonding basin instead. Whether a lone pair or bonding basin is obtained depends on the number of neighboring core basins: The nitrogen lone pair is only in contact with a nitrogen core basin (monosynaptic), while the N–Si bond is in contact with the nitrogen and silicon core basins (disynaptic).[31] Both types of basins are located in close proximity to the nitrogen core basin and they have a similar appearance. However, the lone pair basin of the bridged compound already shows a hump directed towards the silicon atom, which indicates that it is very close to forming a disynaptic bond basin (Figure 6).

An integration of the electron density inside these basins yields electron populations of the lone pair

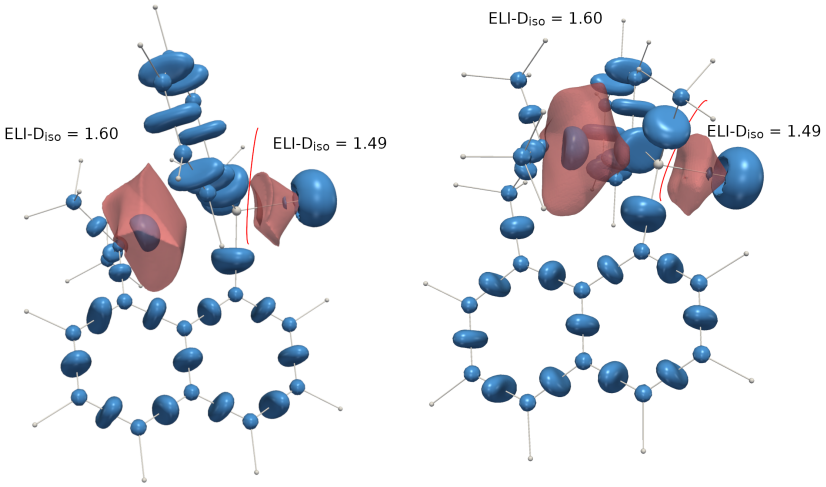


**Figure 6:** Iso-surfaces (blue) of the ELI-D showing bonding and lone pair domains and topological ELI-D basins (red) of the nitrogen lone pair and Si−F bonds from theory. For the bridged compound **2** from XWR, the nitrogen lone pair basin turns into an N−Si bond basin, however, the representation looks virtually indentical (not shown).

**Table 6:** ELI-D electron populations ($n$ in e) of the disynaptic Si-F and N-Si basins and the monosynaptic N basin

| | non-bridged, **1** | | | bridged, **2** | |
|---|---|---|---|---|---|
| | opt. | XWR | | opt. | XWR |
| $n$(Si-F) | 0.936 | 1.4311 | 1.356 | 0.914 | 0.556 |
| $n$(N-Si) | – | – | – | – | 2.148 |
| $n$(LP(N)) | 2.131 | 2.202 | 2.100 | 2.185 | – |
| $n$(LP(F)) | 6.829 | 6.359 | 6.441 | 6.846 | 7.223 |

and bonding basins, which are listed in Table 6 for the nitrogen lone pairs as well as N−Si and Si−F bonding basins. The populations of the Si−F bonds are far below two electrons, according to which the Si−F bonds are not fully single bonds. This is caused by the fact that the lone pair basins of the fluorine atom absorb a large amount of the bonding electron density. This is a common feature of the ELI-D observed for bonds involving electronegative and lone pair rich atoms.[33] The Si−F bonding populations are similar for the geometry optimized non-bridged and bridged compounds, with the population of the bridged compound being only slightly lower. The Si−F population of the bridged compound from XWR, on the other hand, is significantly lower than the one of the non-bridged compound from XWR suggesting

a more ionic fluorine atom. Accordingly, the lone pair population of the bridged compound from XWR are closer to eight electrons. Directly measuring the strength of the N–Si interaction through nitrogen lone pair populations is not feasible. In fact, the population of the N–Si bonding basin of the bridged compound from XWR is similar to those of the nitrogen lone pair basins, which once again indicates a similar character.

Finally, we study two types of bond orders – the NLMO/NPA bond order (from the NBO analysis)[23] and the delocalization index (DI, from the QTAIM)[59] – which measure the number of electron pairs shared between two atoms. For homopolar single bonds, a bond order of approximately one is expected. Bond polarization reduces the number of shared electrons and, thus, bond orders of below one are obtained. The N–Si bond orders are far below one for both the non-bridged and bridged compounds, which is in line with its dative bond character. All NLMO/NPA bond orders are lower than the delocalization indices, but both bond orders give the same trend. The N–Si bond orders of the bridged compound are higher than those of the non-bridged compound, which is caused by a stronger N–Si interaction in the bridged compound. From the aforementioned bonding descriptors, lower Si–F bond orders are expected for the bridged compounds. However, this trend is only observed when comparing the bond orders of the geometry optimized structures among each other. For the bond orders derived from XWR, an opposite trend is retrieved. The fact that all Si–F bond orders are much smaller than one reflects the highly polarized character of the Si–F bonds.

**Table 7:** NLMO/NPA bond orders and delocalization index (DI) of the N–Si and Si–F bonds

| | non-bridged, **1** | | | bridged, **2** | |
|---|---|---|---|---|---|
| | opt. | XWR | | opt. | XWR |
| $BO_{NLMO/NPA}$(N-Si) | 0.038 | 0.044 | 0.043 | 0.050 | 0.092 |
| $BO_{NLMO/NPA}$(Si-F) | 0.292 | 0.260 | 0.272 | 0.278 | 0.255 |
| $DI$(N-Si) | 0.056 | 0.058 | 0.058 | 0.082 | 0.114 |
| $DI$(Si-F) | 0.337 | 0.255 | 0.253 | 0.324 | 0.259 |

## 4 Conclusions

The N–Si peri-interaction was investigated in the two naphthyl-based pentacoordinated silicon compounds depicted in Figure 1. An investigation of structural parameters confirms that the N–Si interaction is the strongest in the bridged compound. This is caused by the higher conformational flexibility of the nitrogen atom due to the insertion of the additional bridging methylene group and the absence of interactions involving the nitrogen lone pair and naphthalene unit. Hence, attractive N–Si interactions are more important than steric repulsion in the peri-contact. At the same time, longer Si–F bond lengths are obtained for the bridged compound which imply weaker Si–F bonds. Although the analysis of structural parameters already allows for these conclusions, the nature of the N–Si interaction remains uncertain. This is

remedied by a *complementary bonding analyis* which comprises NBO, QTAIM, ELI-D and unconstrained ELMO-VB analyses. Apart from confirming the conclusions drawn from the analysis of structural parameters, a *complementary bonding analysis* enables a characterization of the N–Si interaction leading to the following remarks:

1. The NBO analysis attributes the N–Si interaction to a negative hyperconjugation involving the nitrogen lone pair as a donor orbital and the Si–F antibond as an acceptor orbital.
2. The N–Si interaction is weak and can be regarded as a dative bond – the nitrogen lone pair character is largely maintained.
3. The Si–F bond is highly polarized. The degree of Si–F bond polarization increases even further with the strength of the N–Si interaction.

Both compounds can be related to snapshots of a simulated intramolecular $S_N2$ reaction involving a nitrogen nucleophile, an electrophilic silicon center and a fluorine leaving group. The bridged compound is closer to a transition complex than the non-bridged compound, because the N–Si interaction is the strongest and the Si–F bond is the weakest. In this case, the difference in the strength of the N–Si interaction is caused by the additional methylene group, but, alternatively, the N–Si interaction can be tuned by exchanging the fluorine atom with a variety of different substituents. In a forthcoming study, we present such a systematic array of pentacoordinated silicon compounds, in which we go beyond Bürgi's structure correlation attempting to find correlations with properties obtained from a *complementary bonding analysis*.

## Conflicts of interest

The authors declare no conflicts.

## Acknowledgements

S.G. thanks the German Research Foundation (Deutsche Forschungsgemeinschaft, DFG) for funding within the Emmy Noether project GR 4451/1-1.

## References

[1] C. Chuit, R. J. P. Corriu, C. Reye and J. C. Young, *Chem. Rev.*, 1993, **93**, 1371–1448.

[2] C. Breliere, F. Carre, R. J. Corriu, M. Poirier and G. Royo, *Organometallics*, 1986, **5**, 388–390.

[3] J. M. Anglada, C. Bo, J. M. Bofill, R. Crehuet and J. M. Poblet, *Organometallics*, 1999, **18**, 5584–5593.

[4] R. J. Corriu, A. Kpoton, M. Poirier, G. Royo, A. de Saxcé and J. C. Young, *J. Organomet. Chem.*, 1990, **395**, 1–26.

[5] M. S. Gordon, L. P. Davis and L. W. Burggraf, *Chem. Phys. Lett.*, 1989, **163**, 371–374.

[6] R. J. Corriu, A. Kpoton, M. Poirier, G. Royo and J. Y. Corey, *J. Org. Chem.*, 1984, **277**, C25–C30.

[7] A. P. Bento, M. Solà and F. M. Bickelhaupt, *J. Comput. Chem.*, 2005, **26**, 1497–1504.

[8] L. H. Sommer, *Stereochemistry, mechanism and silicon*, McGraw-Hill, 1965.

[9] A. P. Bento and F. M. Bickelhaupt, *J. Org. Chem.*, 2007, **72**, 2201–2207.

[10] A. R. Bassindale, M. Borbaruah, S. J. Glynn, D. J. Parker and P. G. Taylor, *Perkin Trans.*, 1999, 2099–2109.

[11] M. Sohail, R. Panisch, A. Bowden, A. Bassindale, P. Taylor, A. Korlyukov, D. Arkhipov, L. Male, S. Callear, S. Coles *et al.*, *Dalton Trans.*, 2013, **42**, 10971–10981.

[12] A. Macharashvili, V. Shklover, Y. T. Struchkov, G. Oleneva, E. Kramarova, A. Shipov and Y. I. Baukov, *ChemComm*, 1988, 683–685.

[13] A. R. Bassindale, M. Borbaruah, S. J. Glynn, D. J. Parker and P. G. Taylor, *J. Org. Chem.*, 2000, **606**, 125–131.

[14] A. R. Bassindale, S. J. Glynn, P. G. Taylor, N. Auner and B. Herrschaft, *J. Org. Chem.*, 2001, **619**, 132–140.

[15] A. R. Bassindale, D. J. Parker, P. G. Taylor, N. Auner and B. Herrschaft, *J. Org. Chem.*, 2003, **667**, 66–72.

[16] A. R. Bassindale, D. J. Parker, P. G. Taylor and R. Turtle, *Z. Anorg. Allg. Chem.*, 2009, **635**, 1288–1294.

[17] V. Balasubramaniyan, *Chem. Rev.*, 1966, **66**, 567–641.

[18] J. Beckmann, T. G. Do, S. Grabowsky, E. Hupf, E. Lork and S. Mebs, *Z. Anorg. Allg. Chem.*, 2013, **639**, 2233–2249.

[19] J. Beckmann, E. Hupf, E. Lork and S. Mebs, *Inorg. Chem.*, 2013, **52**, 11881–11888.

[20] E. Hupf, E. Lork, S. Mebs, L. Chęcinska and J. Beckmann, *Organometallics*, 2014, **33**, 7247–7259.

[21] E. Hupf, E. Lork, S. Mebs and J. Beckmann, *Organometallics*, 2014, **33**, 2409–2423.

[22] E. Hupf, M. Olaru, C. I. Raţ, M. Fugel, C. B. Hübschle, E. Lork, S. Grabowsky, S. Mebs and J. Beckmann, *Chem. Eur. J.*, 2017, **23**, 10568–10579.

[23] F. Weinhold and C. R. Landis, *Valency and bonding: a natural bond orbital donor-acceptor perspective*, Cambridge University Press, 2005.

[24] W. Kutzelnigg, *Angew. Chem. Int. Ed.*, 1984, **23**, 272–295.

[25] A. E. Reed and F. Weinhold, *J. Am. Chem. Soc.*, 1986, **108**, 3586–3593.

[26] A. E. Reed and P. von Ragué Schleyer, *J. Am. Chem. Soc.*, 1990, **112**, 1434–1445.

[27] M. Fugel, L. A. Malaspina, R. Pal, S. P. Thomas, M. W. Shi, M. A. Spackman, K. Sugimoto and S. Grabowsky, *Chem. Eur. J.*, 2019, **25**, 6523–6532.

[28] M. S. Schmøkel, S. Cenedese, J. Overgaard, M. R. Jørgensen, Y.-S. Chen, C. Gatti, D. Stalke and B. B. Iversen, *Inorg. Chem.*, 2012, **51**, 8607–8616.

[29] D. Stalke, *Chem. Eur. J.*, 2011, **17**, 9264–9278.

[30] R. F. W. Bader, *Chem. Rev.*, 1991, **91**, 893–928.

[31] M. Kohout, *Int. J. Quantum Chem.*, 2004, **97**, 651–658.

[32] F. Weinhold and C. R. Landis, *Chem. Educ. Res. Pract.*, 2001, **2**, 91–104.

[33] M. Fugel, J. Beckmann, D. Jayatilaka, G. V. Gibbs and S. Grabowsky, *Chem. Eur. J.*, 2018, **24**, 6248–6261.

[34] M. Fugel, M. F. Hesse, R. Pal, J. Beckmann, D. Jayatilaka, M. J. Turner, A. Karton, P. Bultinck, G. S. Chandler and S. Grabowsky, *Chem. Eur. J.*, 2018, **24**, 15275–15286.

[35] M. Fugel, F. Kleemiss, L. A. Malaspina, R. Pal, P. R. Spackman, D. Jayatilaka and S. Grabowsky, *Aust. J. Chem.*, 2018, **71**, 227–237.

[36] A. Genoni, *Acta Cryst. A*, 2017, **73**, 312–316.

[37] N. Casati, A. Genoni, B. Meyer, A. Krawczuk and P. Macchi, *Acta Cryst. B*, 2017, **73**, 584–597.

[38] M. Woińska, D. Jayatilaka, B. Dittrich, R. Flaig, P. Luger, K. Woźniak, P. M. Dominiak and S. Grabowsky, *ChemPhysChem*, 2017, **18**, 3334–3351.

[39] S. Grabowsky, P. Luger, J. Buschmann, T. Schneider, T. Schirmeister, A. N. Sobolev and D. Jayatilaka, *Angew. Chem. Int. Ed.*, 2012, **51**, 6776–6779.

[40] S. Grabowsky, A. Genoni and H.-B. Bürgi, *Chem. Sci.*, 2017, **8**, 4159–4176.

[41] A. Genoni, L. Bučinskỳ, N. Claiser, J. Contreras-García, B. Dittrich, P. M. Dominiak, E. Espinosa, C. Gatti, P. Giannozzi, J.-M. Gillet, D. Jayatilaka, P. Macchi, A. Ø. Madsen, L. Massa, C. F. Matta, K. M. Merz, P. N. H. Nakashima, H. Ott, U. Ryde, K. Schwarz, M. Sierka and S. Grabowsky, *Chem. Eur. J.*, 2018, **24**, 10881–10905.

[42] F. Carré, R. J. Corriu, A. Kpoton, M. Poirier, G. Royo, J. C. Young and C. Belin, *J. Organomet. Chem.*, 1994, **470**, 43–57.

[43] R. L. Gay and C. R. Hauser, *J. Am. Chem. Soc.*, 1967, **89**, 2297–2303.

[44] D. Jayatilaka and B. Dittrich, *Acta Cryst. A*, 2008, **64**, 383–393.

[45] S. C. Capelli, H.-B. Bürgi, B. Dittrich, S. Grabowsky and D. Jayatilaka, *IUCrJ*, 2014, **1**, 361–379.

[46] L. A. Malaspina, A. J. Edwards, W. Magdalena, D. Jayatilaka, M. J. Turner, J. R. Price, R. Herbst-Irmer, K. Sugimoto, E. Nishibori and S. Grabowsky, *Cryst. Growth Des.*, 2017, **17**, 3812–3825.

[47] B. Dittrich, J. Lübben, S. Mebs, A. Wagner, P. Luger and R. Flaig, *Chem. Eur. J.*, 2017, **23**, 4605–4614.

[48] D. Jayatilaka and D. J. Grimwood, *Acta Cryst. A*, 2001, **57**, 76–86.

[49] E. D. Glendening, C. R. Landis and F. Weinhold, *J. Comput. Chem.*, 2013, **34**, 1429–1437.

[50] T. A. Keith, *Version 17*, 2013, **11**, 16.

[51] M. Kohout, *DGrid, version 5.0*, 2016.

[52] E. D. Glendening and F. Weinhold, *J. Comput. Chem.*, 1998, **19**, 593–609.

[53] A. Genoni and M. Sironi, *Theor. Chem. Acc.*, 2004, **112**, 254–262.

[54] R. F. W. Bader, *J. Phys. Chem. A*, 1998, **102**, 7314–7323.

[55] R. F. W. Bader, *J. Phys. Chem. A*, 2009, **113**, 10391–10396.

[56] G. V. Gibbs, M. A. Spackman, D. Jayatilaka, K. M. Rosso and D. F. Cox, *J. Phys. Chem. A*, 2006, **110**, 12259–12266.

[57] G. V. Gibbs, R. T. Downs, D. F. Cox, N. L. Ross, C. T. Prewitt, K. M. Rosso, T. Lippmann and A. Kirfel, *Z. Kristallogr. Cryst. Mater.*, 2008, **223**, 01–40.

[58] D. Cremer and E. Kraka, *Angew. Chem. Int. Ed.*, 1984, **23**, 627–628.

[59] R. F. Bader, A. Streitwieser, A. Neuhaus, K. E. Laidig and P. Speers, *J. Am. Chem. Soc.*, 1996, **118**, 4959–4965.

# Chapter 15

# Structure Correlations

Before employing bond analysis methods to find correlations between bond properties and the N–Si distance, traditional *structure correlations*[67] are presented in the present chapter. As mentioned in the introduction to this part, the information value provided by structural parameters alone is not to be underestimated if the properties are carefully analyzed. As seen in Section 12.2.2, not all crystal structures had a high enough quality to make an XWR feasible. However, even structure refinements of low quality data based on the IAM can give accurate structural parameters for non-hydrogen atoms, and thus, these compounds can be included in the present analysis along with the high quality crystal structures. In Figure 15.1, the labeling of the naphthalene system, and the color scheme, which is henceforth used in all Figures, are introduced.


**Figure 15.1:** The labeling of the naphthalene system, and the color code for the substituent X as used throughout all figures.

In all correlations, the N–Si distance is used as the parameter which mirrors the progress of the nucleophilic attack of the nitrogen atom to the silicon atom. Figure 15.2 shows the N–Si distances obtained from the crystal structures and the geometry optimized structures. In Chapter 13, it was shown that the crystal structures have a shorter N–Si distance than the respective geometry optimized structures. This behavior was explained by the fact that the electric field exerted by the crystal environment stabilizes a more ionic bonding situation,

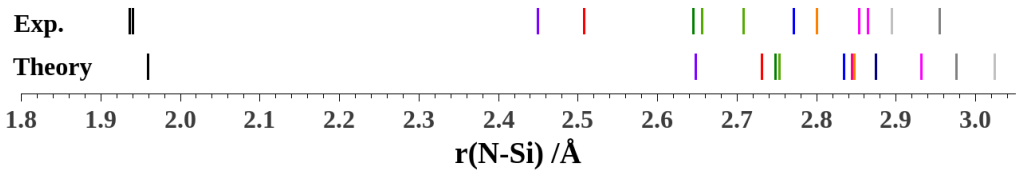


**Figure 15.2:** N–Si distances in the crystal structures (after HAR based on the SPring-8 dataset if available, or after IAM for the methyl compound (**10**) and the silyl cation (**1**)), and the optimized geometries (at the B3LYP/def2-TZVP level of theory), see Figure 15.1 for the color code used for the different compounds. For exact numbers, see Figure 13.1.

thus promoting a heterolytical Si–X bond cleavage. Figure 15.2 confirms that this is true for all compounds, but the same sequence of compounds is obtained in both environments. The sequence of structures from high to low N–Si distances is as follows (for the compounds in brackets, no respective crystal structure exists): Aryl (**11**), methyl (**10**), (hydro (**9**)), methoxy (**8**), (hydroxy (**7**)), ethynyl (**6**), fluoro (**5**), p-chlorobenzoate (**4**), chloro (**3**), bridged fluoro (**2**), and the silyl cation (**1**). Of course, it does not come as a surprise that the silyl cation (**1**) has the shortest N–Si distance – it can be regarded as the product of the intramolecular $S_N2$ reaction involving the compounds analyzed in this study, because the bond between the substituent X and the silicon atom is fully cleaved. There is a vast gap between the N–Si distance of the silyl cation (**1**) and the next structure, which is the bridged fluoro compound (**2**). For all compounds starting from the bridged fluoro compound (**2**), there is a substituent X bonded to the silicon atom. In Chapter 14, it was shown that the N–Si interaction can be related to negative hyperconjugation, and an Si–X antibond corresponds to an inferior acceptor orbital than an unoccupied orbital (lone valency) at the silicon atom. In other words, the silicon atom of the silyl cation (**1**) has a significantly higher electrophilic character, which accounts for the gap between the N–Si distance of the silyl cation (**1**) and the bridged fluoro compound (**2**).

Depending on the nature of the substituent X, the N–Si distance is greatly influenced. For example, the chloro compound (**3**) has an experimental N–Si distance of r(N–Si) = 2.5085(6) Å, while the methyl compound (**10**) has an N–Si distance of r(N–Si) = 2.8653(3) Å. This shows that the N–Si distance in these system is able to respond to the nature of the substituent X. However, the introduction of a $CH_2$ unit bridging the naphthalene system and the amino group increases the flexibility of the nitrogen atom, and thus, the nitrogen and silicon atoms can get much closer to each other (see Chapter 14). From all non-bridged compounds, the chloro compound (**3**) has the lowest N–Si distance, however, the N–Si distance in the bridged fluoro compound (**2**) is even shorter, although the non-bridged fluoro compound (**5**) has a longer N–Si distance than the non-bridged chloro compound (**3**). This shows that the N–Si interaction could potentially be stronger in the non-bridged systems, but the rigid nature of the naphthalene system prevents the N–Si distance to be even shorter.

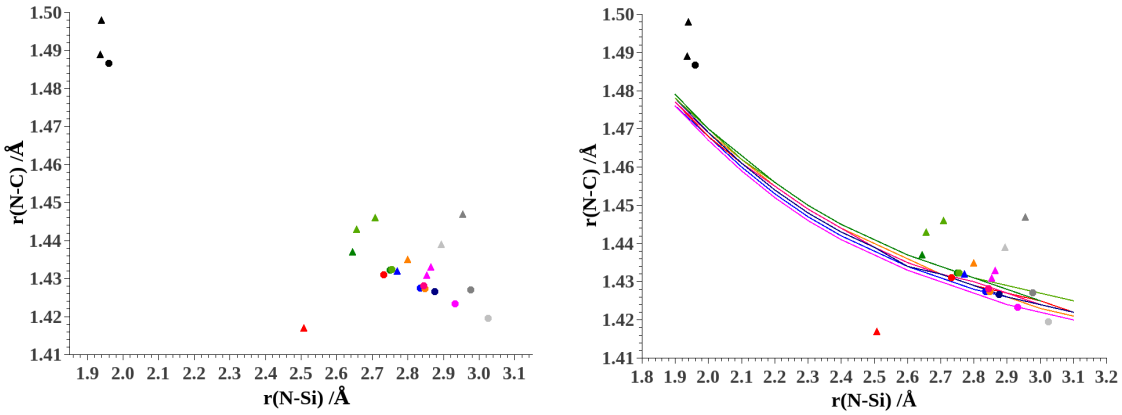


**Figure 15.3:** Correlation between the N−Si and N−C distances (the plot on the right shows the same plot including the results from the PES scan). The bridged fluoro compound (**2**) is not regarded in this correlation. *See Figure 15.1 for the color code used for the different compounds;* ● *= geometry optimized structure,* ▲ *= crystal structure.*

The first structure correlation, which will be discussed in the following, is shown in Figure 15.3. This correlation shows that the N−C9 bond length decreases with increasing N−Si distance. The correlation holds for all compounds except for the crystal structure of the chlorine compound, which can be regarded as an outlier. To understand the chemical interpretation behind this correlation, Figure 11.4, which shows all possible resonance structures involving the nitrogen lone pair, must be consulted. At short N−Si distances, the interaction between the nitrogen and silicon atoms is strong. Accordingly, the weight of resonance structure **3)** is high. At long N−Si distances, on the other hand, the nitrogen lone pair is not strongly involved in the N−Si interaction, and thus, it is free to interact with the naphthalene system. This interaction is represented by resonance structure **4)**, which suggests the N−C bond to have a partial double bond character. In all compounds, there is a competition between resonance structures **3)** and **4)**. If the substituent X promotes a strong N−Si interaction, the interaction between the nitrogen lone pair and the naphthalene system will be weak, and *vice versa*. Since resonance structure **4)** introduces a partial double bond character to the N−C9 bond, the N−C9 distance is shorter at high N−Si distances. At short N−Si distances, however, resonance structure **4)** will be less significant, and the N−C9 double bond character will be lower, which results in a longer N−C9 bond length. The PES scans of all the compounds confirm this correlation. All PES plots nearly overlap with each other, which shows that the N−C9 interaction almost entirely depends on the N−Si distance, and that additional electronic effects exerted by the substituent X only play a minor role. At low N−Si distances around r(N−Si) = 1.9 Å, the PES plots do not quite match the value of the silyl cation (**1**), which shows that the absence of the substituent X has a great effect on the N−C interaction.

Figure 15.4 shows the structure correlation between the average R−Si−X angle, and the

N–Si distance. There is a total of three R–Si–X angles, which are visualized in Figure 15.5.

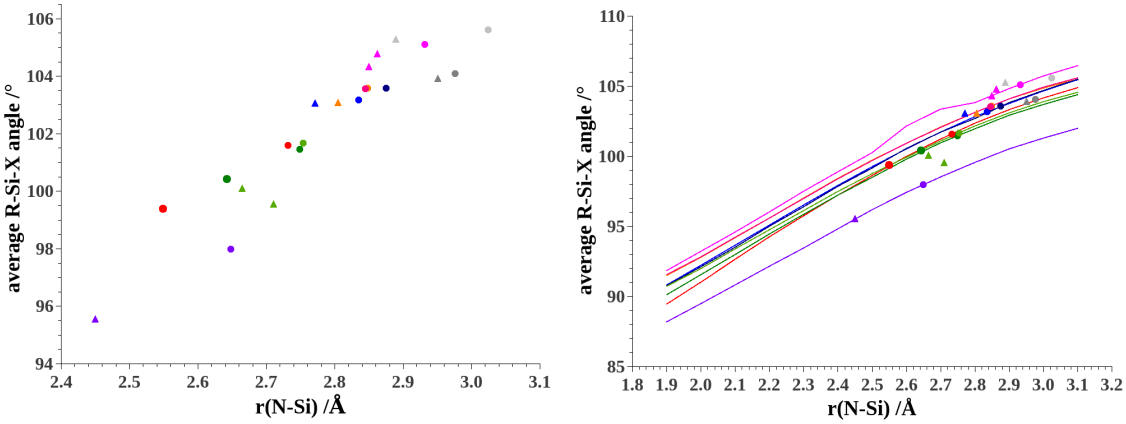


**Figure 15.4:** Correlation between the average R–Si–X angle (R refers to the three axial substitents bonded to the carbon atom), and the N–Si distance (the plot on the right shows the same plot including the results from the PES scan). Since the silyl cation (**1**) has no substituent X, it is not included in this correlation. *See Figure 15.1 for the color code used for the different compounds;* ● *= geometry optimized structure,* ▲ *= crystal structure.*

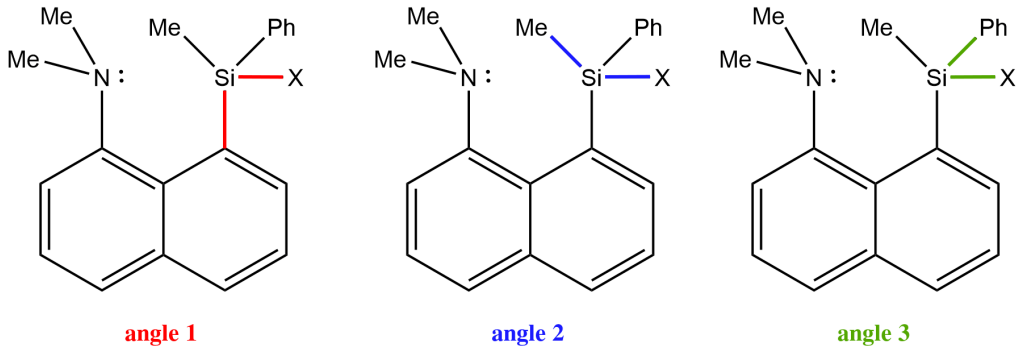


**Figure 15.5:** The three R–Si–X angles used in the correlation depicted in Figure 15.4.

In case of a perfectly tetrahedral arrangement of the four substituents around the silicon atom, one would expect all angles to be ≈109°. However, if there are five substituents bonded to the silicon, a trigonal bipyramidal arrangement of the substituents is obtained instead. In this case, the R–Si–X angles are expected to be ≈90°. Consequently, one can anticipate that the average R–Si–X angle is close to 90° at short N–Si distances, and close to the tetrahedral angle at high N–Si distances. In fact, the correlation in Figure 15.4 shows that the average R–Si–X angle increases with the N–Si distance. The lowest angle is obtained for the experimental bridged fluoro compound (**2**) (95.6°), while the highest angle is obtained for the aryl compound (**11**) from theory (105.6°). This correlation shows that the tetrahedral arrangement of the substituents bonded to the silicon atom continuously transforms into a trigonal bipyramidal arrangement

with decreasing N–Si distance. The PES scan shows that all plots, except for the one of the bridged fluoro compound (**2**), are nearly identical. The plot of the bridged fluoro compound (**2**) is shifted towards lower angles, which can be explainded by the additional sterical repulsion exerted by the $CH_2$ group. Ultimately, the decrease of the R–Si–X angles minimizes the sterical repulsion between the substituents R and the $(Me)_2NCH_2$-group.

A strong N–Si interaction comes with a short N–Si distance, but the question arises as to how the nitrogen and silicon atoms are able to move closer to each other. Both the nitrogen and silicon atoms are (in case of the non-bridged compounds) bonded to the naphthalene system, and thus, their motion is restricted. One mechanism for those atoms to approach each other is the decrease of the N–C9–C10 and C10–C1–Si angles (see Figure 15.1). Conversely, the atoms can move away from each other by an increase of these angles. In a naphthalene system, where two substituents in peri-position do not interact with each other, both of these angles are expected to be 120°. Accordingly, it is possible to define a parameter for each of these angles, which describes the difference between the non-interacting and interacting systems. This parameter, $\Delta\alpha$, is defined in Equation 15.1.

$$\begin{aligned} \Delta\alpha(\text{N–C9–C10}) &= 120^\circ - \alpha(\text{N–C9–C10}) \\ \Delta\alpha(\text{C10–C1–Si}) &= 120^\circ - \alpha(\text{C10–C1–Si}) \end{aligned} \tag{15.1}$$

The sum of these two parameters is a property which reveals some interesting features of the

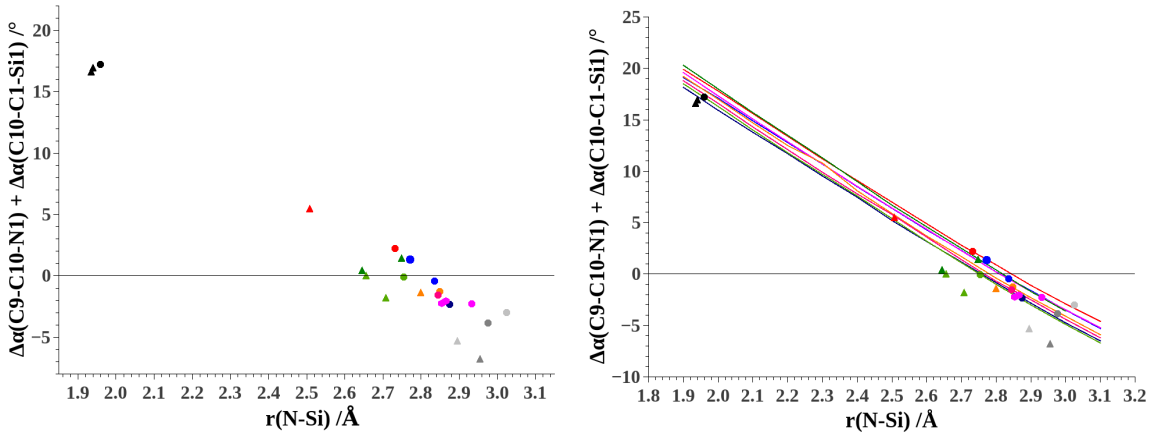


**Figure 15.6:** Correlation between the sum of $\Delta\alpha$(C9-C10-N1) and $\Delta\alpha$(C10-C9-Si1) ($\Delta\alpha = 120^\circ - \alpha$), and the N–Si distance (the plot on the right shows the same plot including the results from the PES scan). *See Figure 15.1 for the color code used for the different compounds;* ● *= geometry optimized structure,* ▲ *= crystal structure.*

system: If the sum is negative, the two substituents have moved away from each other; and if the sum is positive, the two substituents have approached each other. If the interaction is strong, the sum is expected to be positive, while, in the case of weak N–Si interactions, the

sum is expected to be negative. In that case, the repulsion between the two substituents is stronger than the stabilization caused by the N–Si interaction. In Figure 15.6, the sum of these two parameters is correlated against the N–Si distance. It is shown, that the sum decreases towards negative values in a linear fashion with the N–Si distance. Negative values are obtained for the vast majority of compounds. Positive values are only obtained for the silyl cation (**1**), the chloro, and p-chlorobenzoate (**4**) compounds from theory and experiment, as well as for the ethynyl (**6**) and fluoro (**5**) (only the unit with the shorter N–Si distance) compounds from experiment. The PES plots show a perfectly linear trend, which even intersect with the values obtained for the silyl cation (**1**). Once again, the nature of the substituent X does not greatly affect the PES plots.

It was found that the difference between the Si–C1 and N–C9 bond lengths is highly correlated to the N–Si distance, as shown in Figure 15.7. The difference between these bond

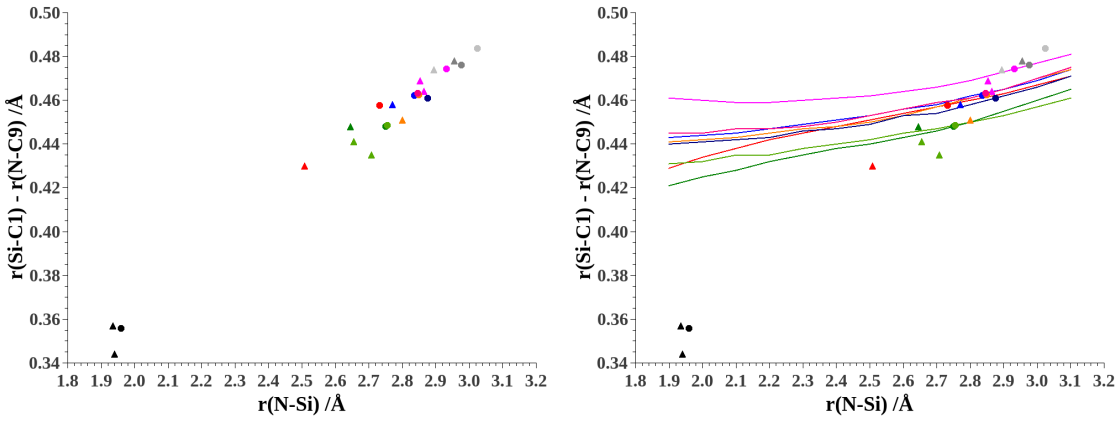


**Figure 15.7:** Correlation between the difference between the Si–C1 and N–C9 distances, and the N–Si distance (the plot on the right shows the same plot including the results from the PES scan).*See Figure 15.1 for the color code used for the different compounds;* ● *= geometry optimized structures,* ▲ *= crystal structures.*

lengths increases with the N–Si distance, which suggests that the N–Si interaction is stronger if they are more similar to each other. In Figure 15.3, it was shown that the N–C9 bond length decreases with the N–Si distance. In the Appendix, the Si–C1 bond length is plotted against the N–Si distance. This plot shows that the Si–C1 bond length increases with the N–Si distance, which explains why the difference between r(Si–C1) and r(N–C9) increases towards high N–Si distances. However, the correlations involving only the Si–$C_1$ and N–C9 bond length are not as clear as the correlation involving the difference of these two bond lengths. No definite explanation can be provided for that behavior. One possible explanation is the fact that this geometrical distortion can maximize the orbital overlap between the silicon and nitrogen atoms. Interestingly, the PES plots do not show the same trend as the values obtained from

the different compounds – they show a much less pronounced increase with the N–Si distance. Therefore, it can be concluded that the substituent X determines the difference between these two bond lenghts. However, it is interesting that a correlation is obtained nonetheless.

# Chapter 16

# Bonding correlations

## 16.1 Bond indices

In the previous studies presented in this thesis, it has been shown that bond indices are a powerful tool for the analysis of chemical bonds. In general, they can be related to the number of electron pairs that are shared between two atoms. Therefore, the bond index for a homopolar single bond is expected to be one, because in that case a single electron pair is shared between two atoms. In this thesis, it has already been shown that the bond index of polarized bonds and dative bonds is below one, because the electron pair is more localized at the more electronegative atom (in case of polarized bonds) or at the electron pair donor (in case of dative bonds). It was shown in Chapter 14 that the N–Si interaction can be regarded as a dative bond, and thus, the N–Si bond order is expected to be below one.

In Figure 16.1, the N–Si *NLMO/NPA bond order* (**a)**) and the *delocalization index* (**b)**) is correlated to the N–Si distance. The behavior of the two bond indices is, on the whole, very similar to each other. The subtle differences are discussed at the end of this paragraph. It does not come as a surprise that the N–Si bond index decreases with the N–Si distance. At long N–Si distances, the bond index approaches a value of zero – the N–Si interaction slowly vanishes completely. Even the bond index of the silyl cation (**1**), which is regarded as the product of an intramolecular $S_N2$ reaction with a completed N–Si bond formation, is significantly below one, which can be attributed to the high N–Si bond polarity caused by the high electronegativity difference between silicon and nitrogen. There is no threshold value of a bond index, which indicates a significant interaction. However, the value obtained for the silyl cation (**1**) can be regarded as the highest possible N–Si bond index, which the non-bridged compounds can approach.

On the whole, the *delocalization index* is shifted towards higher values compared to the *NLMO/NPA bond order*. Normally, one would expect to see a more ionic picture from the

*delocalization index*, but here, the opposite is true. The PES plots are relatively close to each other, but the bond index of the silyl cation (**1**) is not intersected by any of the plots. The *PES* plots from the *NLMO/NPA bond order* deviate more strongly from each other than the *PES* plots of the *delocalization index*. The nature of the Si–X bond will be analyzed at a later stage of this section, but it can already be deduced that more polarized Si–X bonds generally give a plot, which is shifted to higher *NLMO/NPA bond orders* relative to the other plots: The plot of the hydro compound is shifted towards lower bond indices, while the plot of the fluoro compound (**5**) is shifted towards higher bond indices. Consequently, the nature of the substituent X affects the bond index, but overall the same trend is obtained for each *PES* plot regardless of the type of the substituent X.

In the preceding chapter, it was shown that the N–C9 bond length decreases with the N–Si distance, which was attributed to an increased double bond character to the N–C9 bond. Accordingly, this should also be reflected by an increase of the N–C9 bond index with the N–Si distance. In fact, this correlation is confirmed by the plots in Figure 16.1c) and d), which show the N–C9 *NLMO/NPA bond order* and the N–C9 *delocalization index* plotted against the N–Si distance. If only the theoretical values are considered, both bond indices give a clear correlation: The N–C9 bond index increases with the N–Si distance, thus, confirming an increase in N–C9 double bond character. However, only the NLMO/NPA bond order also gives a correlation for the results from *XWR*. In this plot, even the chloro compound (**3**) can be described by this correlation (the chloro compound (**3**) is an outlier in the correlation between the N–C9 bond length and the N–Si distance). The PES plots are relatively close to each other, however, they neither intersect with the bond index of the silyl cation (**1**) nor do they intersect with most of the values obtained from *XWR*. In Chapter 13, it was shown that the naphthalene system is usually involved in a variety of intermolecular interactions with neighboring molecules in the crystal structure, which may have an influence on the N–C9 interaction.

Figure 16.2 shows the Si–X *NLMO/NPA bond order* and *delocalization index* plotted against the N–Si distance. For the Si–X *NLMO/NPA bond order* and for the Si–X *delocalization index* only weak correlations are obtained. From these plots, it can be deduced, that, in most cases, a short N–Si distance comes with a low Si–X bond index, but the correlation is too weak to generalize this statement. Low Si–X bond indices can be related to highly polarized Si–X bonds. Consequently, a high Si–X bond polarization is one factor promoting a strong N–Si interaction. This does not come as a surprise, because in almost all hypercoordinated silicon compounds, the silicon atom is bonded to at least one electronegative substituent. The PES plots show that the Si–X bond index is not greatly influenced by the N–Si distance. It only increases slightly towards higher N–Si distances. The highest Si–X bond index is obtained for the Si–H bond, which can therefore be regarded as the most covalent bond out of the compounds analyzed in this study. Even at very low N–Si distances, the Si–H bond remains

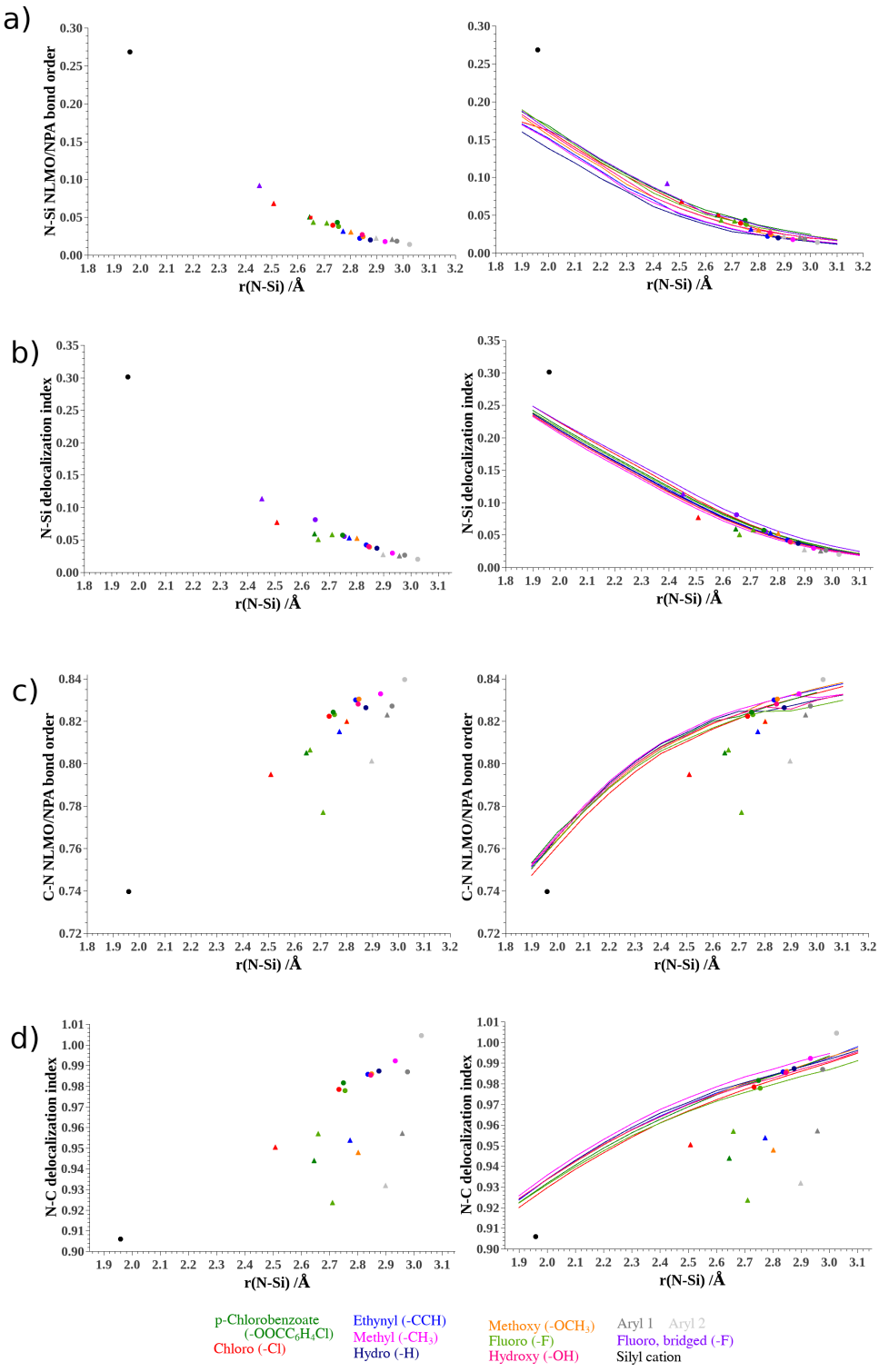


**Figure 16.1:** Bonding correlations between bond indices (NLMO/NPA bond order and delocalization index), and the N−Si distance: a) N−Si NLMO/NPA bond order, b) N−Si delocalization index, c) C−N NLMO/NPA bond order, and d) C−N delocalization index. The plots on the right hand side show properties obtained from various PES scans. ● = *geometry optimized structure*, ▲ = *XWR*.

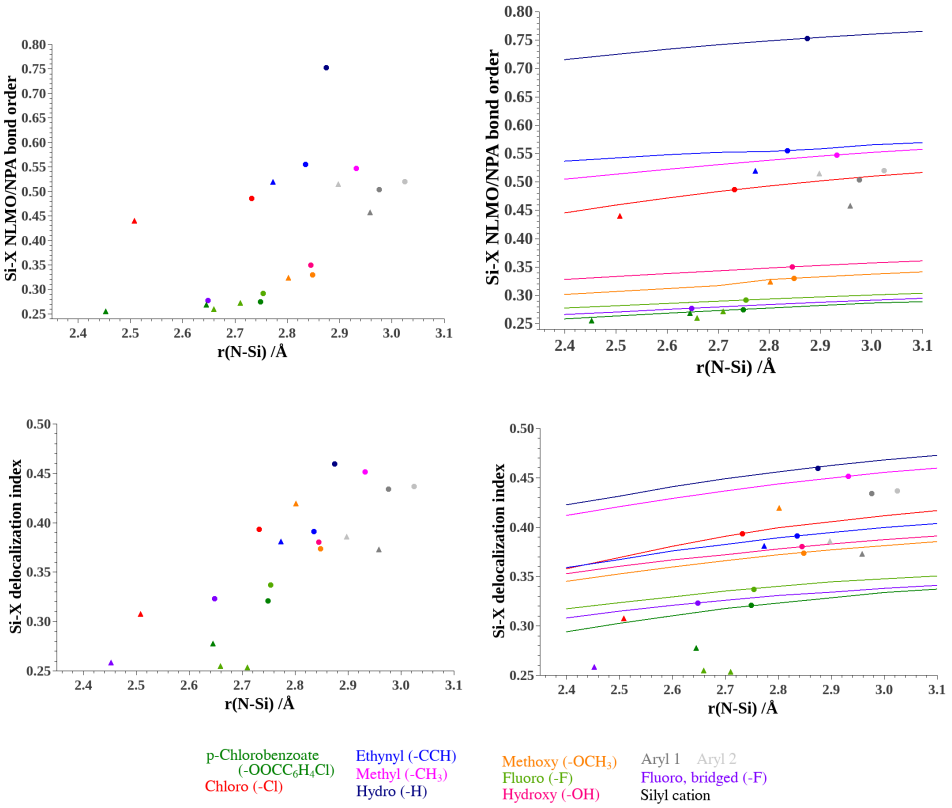


**Figure 16.2:** Bonding correlations between Si−X bond indices (NLMO/NPA bond order and delocalization index), and the N−Si distance: a) Si−X NLMO/NPA bond order, and b) Si−X delocalization index. ● = *geometry optimized structure*, ▲ = *XWR*.

highly covalent. However, its N−Si distance is not the longest. For example, the Si−C bond of the methyl compound (**10**) shows a lower bond index, but its N−Si distance is longer. Consequently, the Si−X bond polarization is not the only factor, which determines the strength of the N−Si interaction. For example, sterical effects of the peri-interaction will always play a decisive role. The higher N−Si distance of the methyl compound (**10**) in comparison to the hydro compound, for instance, can be attributed to the sterically more demanding methyl group. Another interesting case is the chloro compound (**3**): The Si−Cl bond indices are among the highest, but its N−Si distance is among the shortest. Chlorine is the only substituent from the third period, and thus, the size of its valence orbitals is increased,[185] which leads to an enhanced orbital overlap.

## 16.2 Natural bond orbitals

From a *natural bond orbitals (NBO)* point of view, the N−Si interaction corresponds to negative hyperconjugation where nitrogen's lone pair orbital and the Si−X antibond are the donor and

acceptor orbitals, respectively. Figure 16.3 shows this interaction and the interaction between the nitrogen lone pair orbital and a C–C antibond of the naphthalene system, which can be related to resonance structure **4)** in Figure 11.4. Only the *NBO* analysis of the silyl cation (**1**)

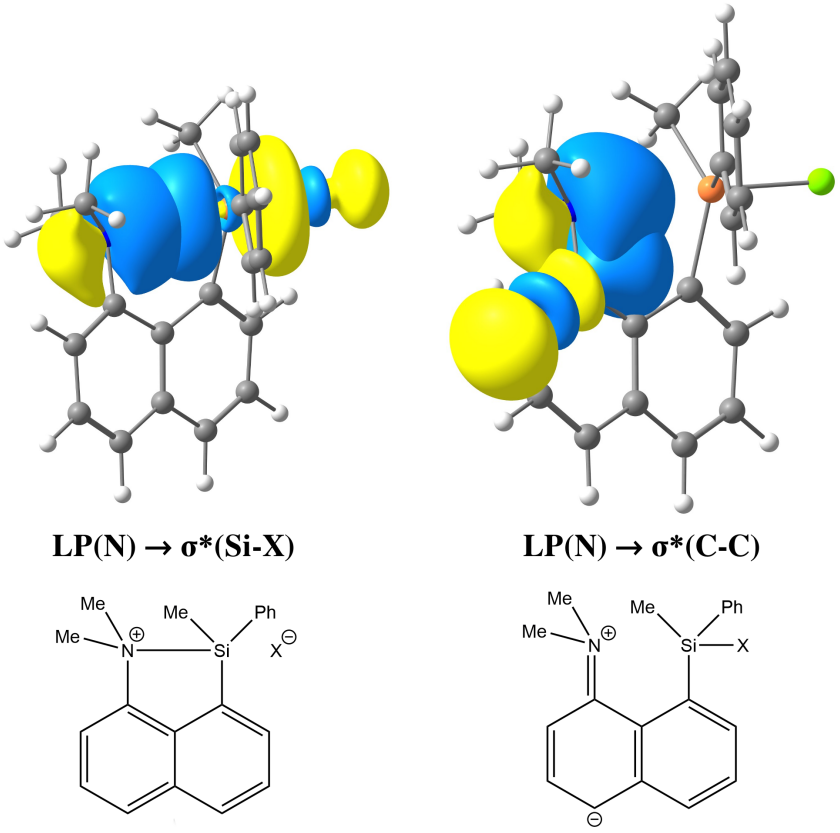


**Figure 16.3:** The interactions of the nitrogen lone pair and the corresponding Lewis structures.

gave an N–Si bond orbital. In the following, properties of these orbitals are correlated against the N–Si distance.

Figure 16.4a) shows the hybridization coefficient $\lambda$ of the nitrogen lone pair orbital plotted against the N–Si distance. The coefficient $\lambda$ corresponds to the ratio between p- and s-character of the nitrogen lone pair orbital (%p/%s = $\lambda$). For example, if the p-character is 75% and the s-character is 25%, $\lambda = 3$, which can be expressed as $sp^3$ hybridization. According to the correlation in Figure 16.4, $\lambda$ increases with the N–Si distance, or in other words, the p-character of the nitrogen lone pair orbital becomes more significant at high N–Si distances. According to Coulson's orthogonality theorem, the hybridization of an atom is related to the arrangement of substituents around it.[186] For the silyl cation (**1**), $\lambda = 3.4$, which is close to $sp^3$ hybridization, which would entail a tetrahedral arrangement of the substituents around it. This is consistent with a tetracoordinated nitrogen atom, which indicates an N–Si bond formation. At higher N–Si distances, the N–C9 interaction, which can be regarded as a dative double bond, gains

in significance. In Chapter 14, it was shown that this interaction can be related to negative hyperconjugation between nitrogen's lone pair orbital and an C–C antibond of the naphthalene system (see Figure 16.3). From Figure 3 in Chapter 14, it becomes clear that the overlap between these two orbitals is maximized if the p-character of the nitrogen lone pair is high – after all, it is a $\pi$-type interaction. Conversely, the N–Si interaction is enhanced if the nitrogen lone pair orbital is close to $sp^3$ hybridization, because in that case orbital lobe of the nitrogen lone pair, which is directed towards the orbital lobe of the Si–X antibond, is enhanced, which improves the overlap between these two orbitals (compare to Figure 3 in Chapter 14). The PES plots, except for those of the chloro (**3**) and bridged fluoro (**2**) compounds, are very similar to each other. The plot of the chloro compound (**3**) shows the same trend than the other non-bridged compounds, but it increasingly deviates from the other plots towards short N–Si distances. Based on the fact that the chlorine is the only substituent from the third period, this behavior may be explained by the different nature of the Si–Cl antibond, but no definite explanation can be given at this point. The PES plot of the bridged fluoro compound (**2**) deviates more significantly from the other plots. It is shifted towards lower values of $\lambda$, and thus, it shows the highest s-character throughout the whole range of the plot. This reveals that the increase in p-character at high N–Si distances of the non-bridged compound is, in fact, caused by the introduction of double bond character to the N–C9 bond. In the bridged fluoro compound (**2**), this interaction does not exist, and thus, the p-character only increases slightly, which is exclusively caused by the decrease of the diminishing N–Si interaction.

The *NBO* analyses of the compounds regarded in this study, give a nitrogen lone pair orbital, and an Si–X bond orbital, but an N–Si bond orbital is not obtained (except for the silyl cation (**1**)). Therefore, no N–Si bond properties can be analyzed. However, it is possible to define an *NBO* structure in the input, for which the specified NBOs are calculated. For example, a structure with an N–Si bond, but without an Si–X bond can be defined (this corresponds to resonance structure **3)** in Figure 11.4). From the N–Si bond orbital, properties can be extracted, which would otherwise remain hidden. One of those properties is the N–Si bond ionicity ($i_{NSi}$), which can be calculated from the polarization coefficients of the nitrogen and silicon hybrids ($c_N$ and $c_{Si}$). The N–Si bond ionicity is defined in Equation 16.1.[37]

$$i_{NSi} = c_N^2 - c_{Si}^2 \tag{16.1}$$

If $i_{NSi} = 1$, the bond can be regarded as fully ionic. In this case the electron pair is not shared between the nitrogen and silicon atoms, but corresponds to a lone pair localized at the nitrogen atom. If $i_{NSi} = 0$, the bond is fully covalent, and if $i_{NSi}$ is between 0 or 1, the N–Si bond is polarized towards the more electronegative nitrogen atom. Figure 16.4b) shows that the N–Si bond ionicity increases with the N–Si distance. Consequently, the electron pair is increasingly

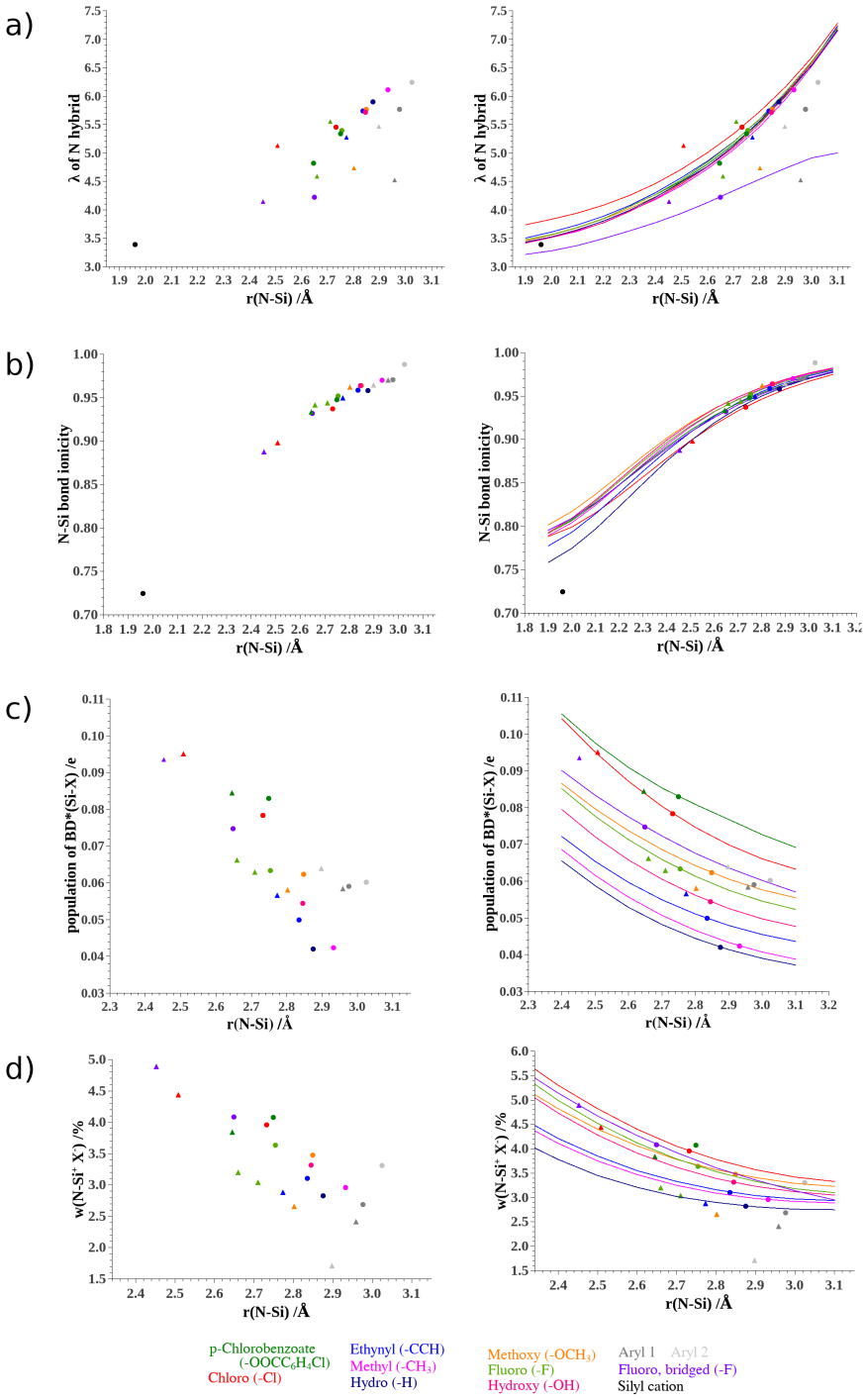


**Figure 16.4:** Bonding correlations between properties from a *natural bond orbital* analysis, and the N−Si distance: a) The hybridisation of the N hybrid orbital $\lambda$ ($sp^{\lambda}$), b) N−Si bond ionicity, c) population of the Si−X antibond, and d) the weight of resonance structure 3) in Figure 11.4 according to the *natural resonance theory*. The plots on the right hand side show properties obtained from a PES scan. ● = *geometry optimized structure*, ▲ = *XWR*.

localized at the nitrogen atom, that is, its lone pair character is enhanced. At high N−Si

distances, the N–Si bond ionicity is close to $i_{NSi} = 1$, which suggests that the nitrogen lone pair is highly localized. Towards shorter N–Si distances, the lone pair character decreases, and the bond character of the electron pair is enhanced. The lowest N–Si bond ionicity is obtained for the silyl cation (**1**), which suggests a polarized N–Si bond. The PES plots show the same trend for all compounds, however, especially at short N–Si distances they start to deviate from each other.

The negative hyperconjugation of LP(N) $\rightarrow \sigma^*$(Si–X) type, which is visualized in Figure 16.3, results in the population of the Si–X antibond. If the interaction is strong, more electrons are shifted to the acceptor orbital, and consequently, its electron population is expected to increase. This is confirmed by the correlation in Figure 16.4c), which shows that the population of the Si–X antibond decreases with the N–Si distance. This uncovers that the nature of the Si–X bond is the main influence on the strength of the N–Si interaction. If the acceptor quality of the Si–X antibond is low, the N–Si interaction will be weak, and *vice versa*. In the analysis of the correlations based on bond indices, it was shown the Si–X bond polarization is one factor which influences the strength of the N–Si interaction. However, the high acceptor quality of the Si–Cl antibond could not be explained by this argument.

The PES plots decrease only slightly with the N–Si distance, and they do not follow the slope of the correlation. While they show the same trend, they do not overlap with each other. Instead, they are stacked on top of each other. The sequence can be related to the acceptor quality of the Si–X bond: The plot of the hydro compound (**9**) is shifted towards the lowest populations, and thus, the Si–H antibond corresponds to the weakest acceptor orbital. The p-chlorobenzoate compound (**4**), on the other hand, is shifted towards the highest populations – its Si–O antibond can be regarded as the best acceptor orbital. According to this argument, the plot of the chloro compound (**3**) suggests that the Si–Cl antibond is the second best acceptor orbital. The fact that the chloro compound (**3**) has a shorter N–Si distance compared to the p-chlorobenzoate compound (**4**) reveals that there must be a higher sterical repulsion in the p-chlorobenzoate compound (**4**), which leads to an increase in the N–Si antibond. If the chlorine compound is not considered, the Si–X bond index correlation gives the same sequence of compounds (only the fluoro (**5**) and methoxy (**8**) compounds are interchanged). Consequently, the Si–X bond polarization can be related to the acceptor quality of the Si–X antibond if the elements to which the silicon is bonded are from the same period. A covalent Si–X bond comes with a low acceptor quality, while a high acceptor quality is obtained for highly polarized Si–X bonds. For some compounds, the N–Si interaction should be stronger, if the quality of the acceptor orbital is regarded as the only criterion that determines the strength of the N–Si interaction. For example, the Si–H antibond has consistently the lowest electron population – simply based on the quality of the acceptor orbital, its N–Si distance should be the longest. However, the methyl (**10**) and aryl (**11**) compounds have longer N–Si distances. This can be

explained by the fact that there is a higher sterical repulsion in these systems, which prevents the nitrogen and silicon atoms to get even closer to each other.

An analysis based on the *natural resonance theory (NRT)* assigns weights to a set of predefined resonance forms.[141,142] In Figure 16.4d), it is shown that the weight of the resonance structure with an N–Si bond (structure **3)** in Figure 11.4) decreases with the N–Si distance. This is in line with a decrease in the N–Si interaction, which indicates a decline of the N–Si bond character. Much like the population of the Si–X antibond, the PES plots of the *NRT* weights reflect the acceptor quality. Only the sequence of the methoxy (**8**) and fluoro (**5**) plots are interchanged at short N–Si distances, which consequently yields the same sequence as obtained from the Si–X bond indices.

## 16.3 Quantum Theory of Atoms in Molecules

Before analyzing correlations involving properties at the *bond critical points*, the N–Si bond paths, which are shown in Figure 16.5, are inspected. The bond paths obtained from theory and *XWR*, are arranged from long to short N–Si distances (from left to right). For the aryl compound (**11**) from theory and *XWR*, no N–Si bond paths are obtained. The same is the case for the hydro, methoxy (**8**) and hydroxy compounds (**7**) from theory. Instead a curved N–C1 bond path is obtained for these three compounds. Only starting from the ethynyl compound (**6**), there are N–Si bond paths for the geometry optimized structures, whereas the *XWR* already yields N–Si bond paths starting from the methoxy compound (**8**). At high N–Si distances, the bond paths are somewhat curved close to the silicon atom, which indicates weak N–Si interactions.

In Figure 16.6a) and b), correlations involving properties at the N–Si *bond critical points* are plotted. The correlation between the electron density at the N–Si *bond critical point* ($\rho_{bcp}$(N–Si)) with the N–Si distance is depicted in Figure 16.6a). The plot shows that $\rho_{bcp}$(N–Si) decreases with the N–Si distance, which can be attributed to a decrease in the N–Si interaction towards high N–Si distances. The corresponding PES plots perfectly overlap each other, and nearly match the value of the silyl cation (**1**). Consequently, $\rho_{bcp}$(N–Si) is a property which is not greatly influenced by the nature of the substituent X. Instead $\rho_{bcp}$(N–Si) only depends on the N–Si distance. The same is true for the correlation between the total energy density at the N–Si *bond critical point* ($H_{bcp}$(N–Si)) and the N–Si distance, which is shown in Figure 16.6b). With an increase in the N–Si distance, $H_{bcp}$(N–Si) approaches a value of zero, which marks the point at which N–Si interactions cease to exist. According to both $\rho_{bcp}$(N–Si) and $H_{bcp}$(N–Si), the strength of the N–Si distance only depends on the N–Si distance.

The total energy density at the *bond critical point* ($H_{bcp}$(Si–X)) can be regarded as an indicator, which reveals the extent of covalency to the Si–X bond. High negative values indicate

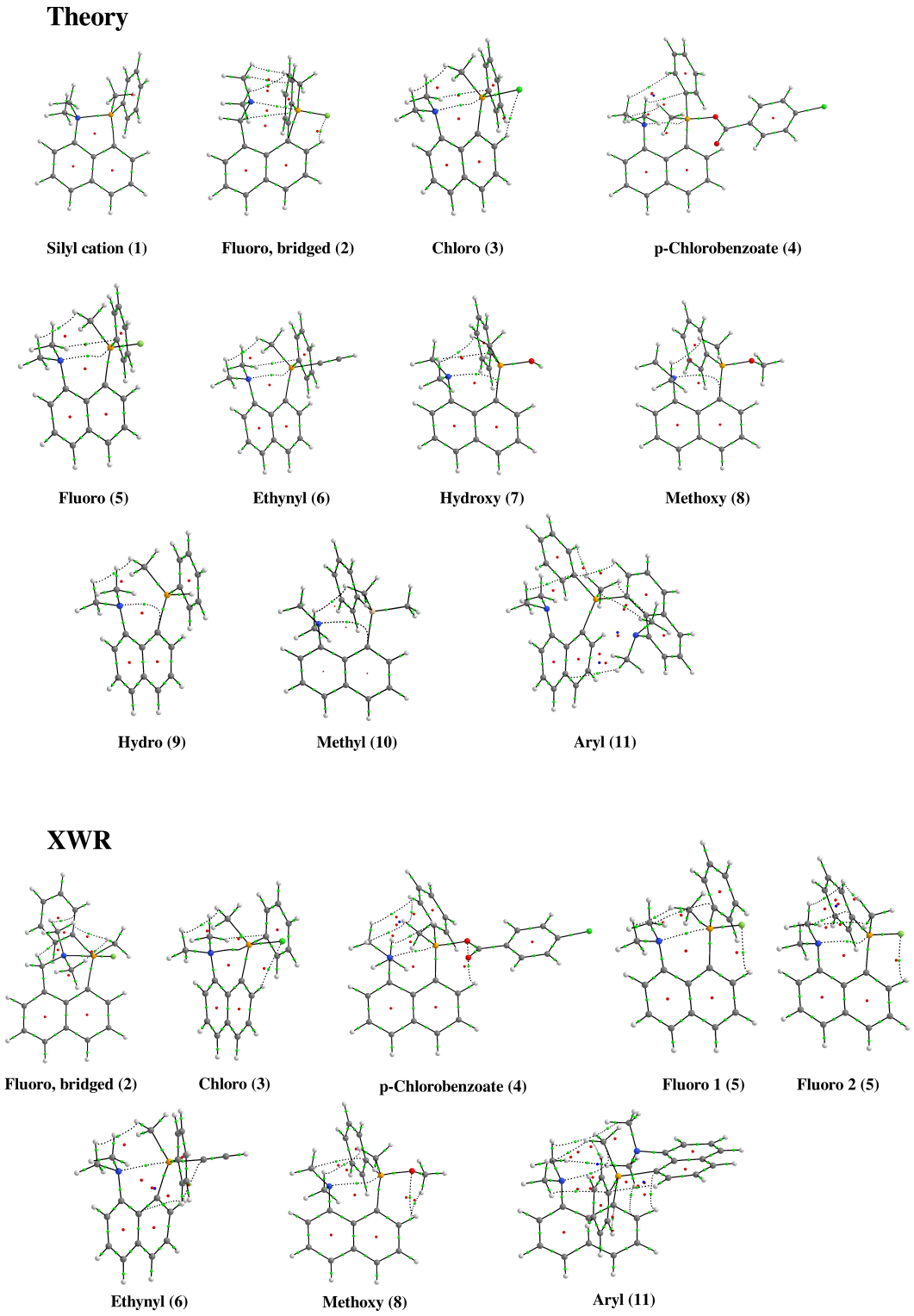


**Figure 16.5:** Bond paths, and the position of bond, ring and cage critical points (green, red and blue balls) obtained from theory and XWR.

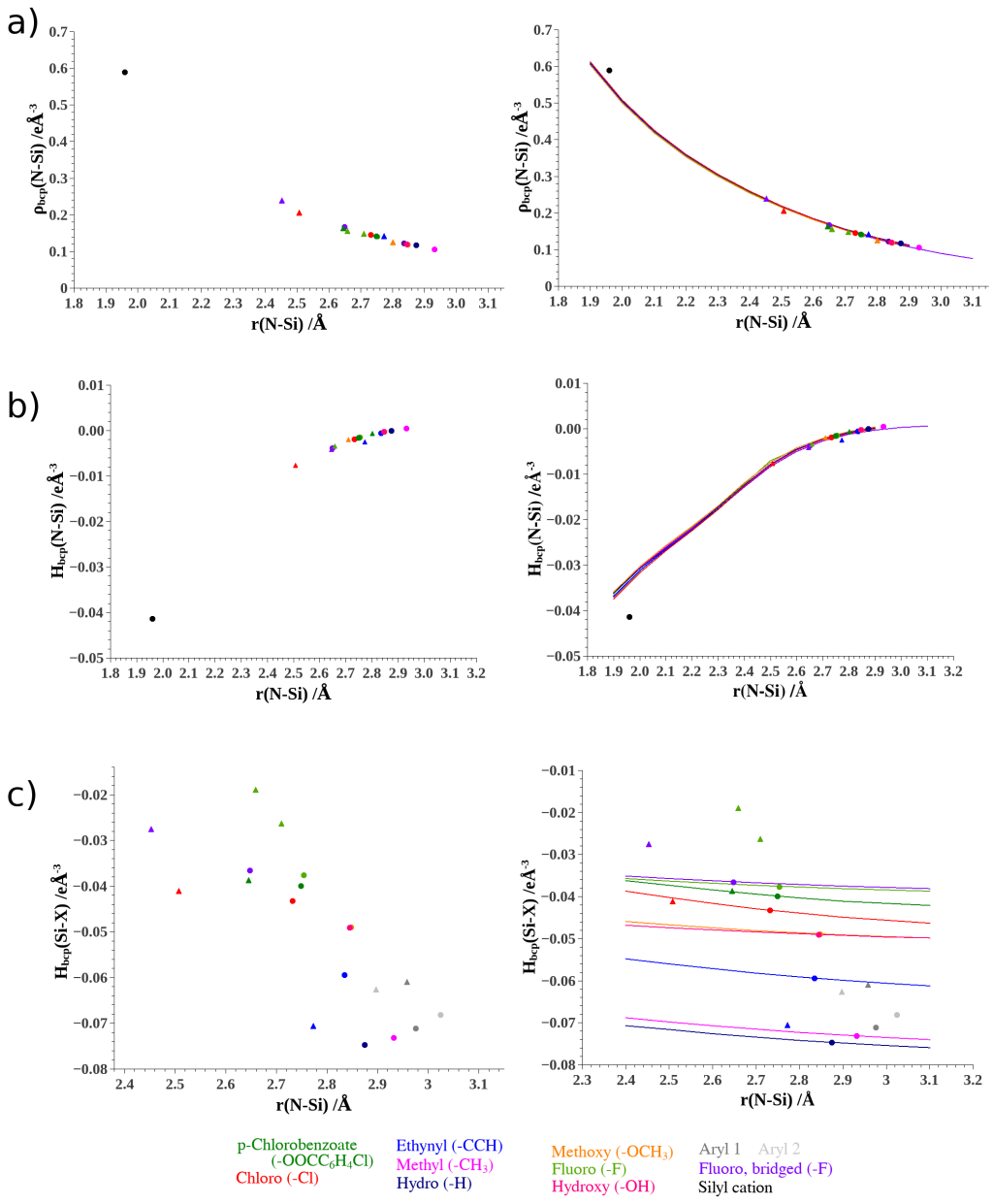


**Figure 16.6:** Bonding correlations between properties from a *QTAIM* analysis, and the N−Si distance: a) The electron density at the N−Si bond critical point ($\rho_{\mathrm{bcp}}$(N−Si)), b) the total energy density at the N−Si bond critical point ($H_{\mathrm{bcp}}$(N−Si)), and c) the total energy density at the Si−X bond critical point ($H_{\mathrm{bcp}}$(Si−X)) The plots on the right hand side show properties obtained the PES scans. ● = *geometry optimized structure*, ▲ = *XWR*.

covalent interactions to be of significance, while values close to zero indicate a high bond polarization. The influence of the Si−X bond polarization on the strength of the N−Si interaction has already been uncovered from the correlations between the Si−X bond indices and the N−Si distance. However, the total energy density at the Si−X *bond critical points* is a complementary method, which provides access to the Si−X bond polarization. The sequences obtained from

PES plots of the Si−X bond indices and $H_{bcp}$(Si−X) are similar, but not identical to the other correlations involving properties of the Si−X bond. The Si−Cl bond of the chloro compound (**3**) and the Si−F bonds of the non-bridged (**5**) and bridged fluoro (**2**) compounds have a higher bond polarization according to $H_{bcp}$(Si−X), which is in line with the tabulated electronegativities. Other than that, the analysis of $H_{bcp}$(Si−X) and the Si−X bond indices give the same conclusions: The Si−X bond polarization is one decisive factor which determines the strength of the N−Si interaction.

## 16.4 Electron localizability indicator

The *electron localizability indicator (ELI-D)* measures the localization of electrons. In Figure 16.7, iso-surfaces of the *ELI-D* are shown and the basins of the nitrogen lone pair and the Si−X bond are plotted for the chloro (**3**) and methyl (**10**) compounds. Accordingly, a plot of the ELI-D along a line connecting the nitrogen and silicon atoms can provide information on the nature of the N−Si interaction. Such a plot is shown in Figure 16.8 for all compounds. The

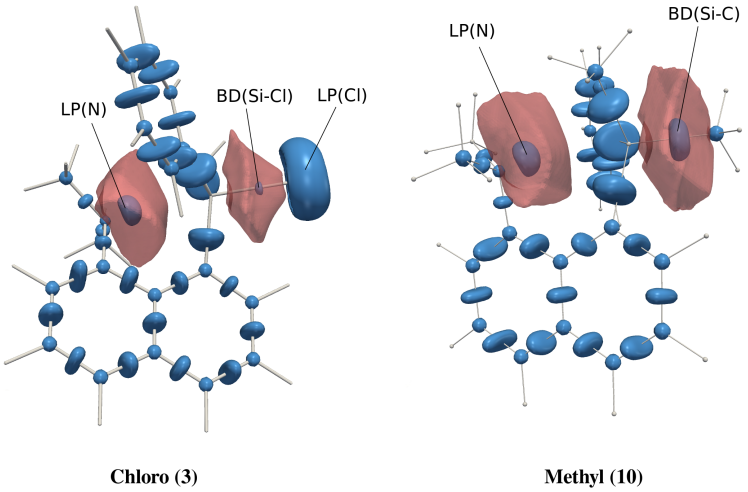


**Figure 16.7:** *ELI-D* iso-surfaces (blue) of the chloro (**3**) (left, iso-value = 1.63) and methyl (**10**) (right, iso-value = 1.54) compounds revealing regions of high electron localization. Bonding, lone pair and core domains are uncovered. The outlines of the nitrogen lone pair and Si−X basins are shown (red).

first maximum on the left hand side of the plot can be related to the lone pair basin of the nitrogen atom. Interestingly, its shape is nearly identical for all compounds. This is even the case for the bridged fluoro compound (**2**) and the silyl cation (**1**) from theory and *XWR*. For these compounds, this maximum corresponds to a bond basin, which is in direct contact to the core basins of the nitrogen and silicon atoms (disynapticity). For the other compounds, this maximum corresponds to a monosynaptic basin, because they are only in contact with

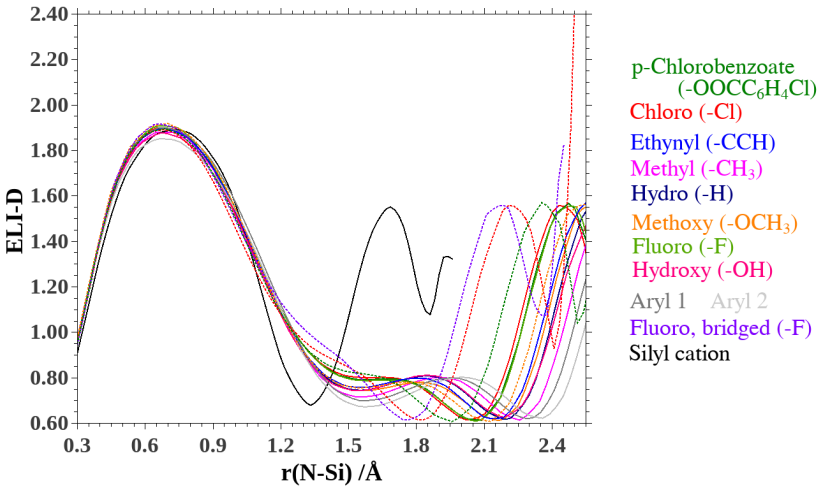


**Figure 16.8:** The *ELI-D* plotted on a line between the nitrogen and silicon atoms (solid lines = theory; dashed lines = *XWR*). The nucleus of the nitrogen atom is located at r(N−Si) = 0 and the nucleus of the silicon atom is located at the N−Si distance of the respective compound.

core basins of the nitrogen atom. For the silyl cation (**1**), the first maximum is more narrow and completely overlaps with the valence basin of the silicon atom, hence causing disynapticity. Consequently, the next maximum corresponds to a core basin of silicon. For the chloro, p-chlorobenzoate (**4**) and bridged fluoro compounds (**2**) from *XWR* the first maximum mostly overlaps with the valence basin of the silicon atom, which suggests that their N−Si interactions are strong. For the other compounds, the valence basin of the silicon atom can be perceived as a separate maximum, but the plots reveal that a significant amount of electrons are localized between the nitrogen and silicon atoms, which can be attributed to the N−Si interaction.

For a covalent bond, one would expect the nitrogen atom, the attractor of the bonding basin and the silicon atom to be on a straight line, that is, the angle defined by these three points should be 180°. With decreasing strength of the N−Si interaction, this angle is expected to increasingly deviate from that value. Figure 16.9a) shows this angle plotted against the N−Si distance, which confirms this assessment. The PES plots show a zigzag trend, but overall they decrease with increasing N−Si distance.

The nitrogen lone pair basins or the N−Si bond basins (for the bridged fluoro compound (**2**) from *XWR* and silyl cation (**1**) from *XWR* and theory) are characterized by their electron population and volume. The electron population does not show a correlation with the N−Si bond length, but remains approximately constant (see Appendix). The volume of the basin, on the other hand, shows an increase with the N−Si bond distance. However, a clearer correlation is obtained if the ratio between the electron population of the basin and its volume is plotted against the N−Si distance. The resulting correlation is depicted in Figure 16.8b) which shows that the ratio decreases with increasing N−Si distance. If a large number of electrons is contained

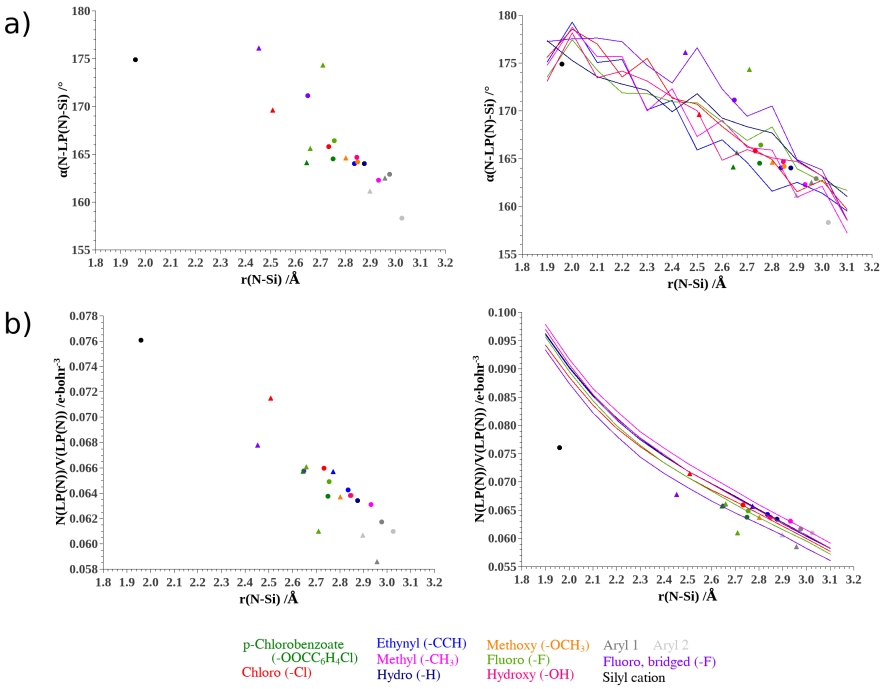


**Figure 16.9:** Bonding correlations between properties from an analysis of the *ELI-D*, and the N−Si distance: a) , and b) . The plots on the right hand side show properties obtained from a PES scan. ● = *geometry optimized structure,* ▲ = *XWR*.

in a small volume, the ratio is large, and a high localization of these electrons is indicated. Generally, it can be expected that the electrons are more localized in a bonded interaction compared to a lone pair, because the former requires a high directionality. Accordingly, a decrease in the N−Si interaction is also suggested by this correlation. The PES plots confirm this correlation, however, the ratio obtained for the silyl cation (**1**) is not matched, because the plots suggest a much higher increase. It can therefore be concluded that the presence of a substituent X comes with a higher directionality of the N−Si interaction.

# Chapter 17

# Conclusions to Part V

In this Part, it was shown that an extension of Bürgi's and Dunitz' *structure correlation* approach to a *bonding correlation* approach is, in fact, feasible. Using that approach, a systematic array of pentacoordinated silicon compounds (see Figure 11.3) could be analyzed in terms of a nucleophilic addition of nitrogen to silicon. Overall, a great variety of *structure* and *bonding correlations* could be uncovered, which enables an analysis of the bonding situation in the course of a simulated chemical reaction.

A wide range of different N–Si distances which can be related to the progress of the nucleophilic attack, was obtained for the different pentacoordinated silicon compounds. The main influence on this distance is the nature of the substituent X that is bonded to the silicon atom, but not its perceived leaving group quality. However, it could also be shown that environmental effects, such as the electric field exerted by a crystal environment, have an influence on the strength of the N–Si interaction. Consequently, a crystal environment favors a more ionic bonding situation in these compounds, which leads to an increase in the strength of the N–Si interaction, and an accompanied shortening of the distance between these atoms. The shortest N–Si distance was obtained for the silyl cation (**1**), which contains a tetracoordinated silicon atom. The silyl cation (**1**) can be regarded as the product of an $S_N2$ reaction with a completed bond formation between the nitrogen and silicon atoms. The bridged fluoro compound (**2**) (from *HAR*) has the shortest N–Si distance out of the pentacoordinated silicon compounds analyzed in this study, with the non-bridged chloro compound (**3**) from *HAR* coming in second. In these compounds the N–Si interaction is strong, however, there is a large gap between the N–Si distance in the pentacoordinated silicon compounds and the one in the silyl cation (**1**). Consequently, the question arises if substituents can be found which give N–Si distances that can fill in this gap. However, it is important to remember that $S_N2$ reactions at silicon atoms sometimes go through a deep minimum in the potential energy surface (PES) where the silicon atom is pentacoordinated.[58] At that point, the reaction comes to a halt, and, therefore, the reaction corresponds to a nucleophilic addition, rather than a nucleophilic substitution. Because

the N–Si distance can be regarded as a weak dative bond, with the Si–X bond showing a much stronger bond character, the pentacoordinated silicon compounds, which were analyzed in this study, can only represent the reaction pathway of a nucleophilic addition, which ultimately gives a fully pentacoordinated silicon species. This situation was clearly reflected by the *structure correlation* between the average R–Si–X angle and the N–Si distance: At long bond distances the average R–Si–X angle suggests a tetrahedral arrangement of four substituents around the silicon atom, while at short N–Si distance a more trigonal bipyramidal arrangement of five substituents around the silicon atom is obtained. Compounds, which would fill in the gap between the bridged fluoro compound (**2**) and the silyl cation (**1**), would be able to represent a full $S_N2$ reaction, that is, the transformation of a pentacoordinated silicon compound towards a tetracoordinated silicon compound under abstraction of the substituent X.

The *structure* and *bonding correlations* could also provide a qualitative and quantitative understanding on how the weight of resonance structures, which represent the bonding situation in the pentacoordinated silicon compounds, changes from high to short N–Si distances. At long N–Si distances, the resonance structure with a N–Si bond only has a low weight (resonance structure **3)** in Figure 11.4). Instead, the resonance structure with a double bond between the nitrogen atom and a carbon atom from the naphthalene system (resonance structure **4)** in Figure 11.4) is more significant. The weight associated with this resonance structure decreases with a shortening of the N–Si distance, and the weight of the resonance structure with a N–Si bond becomes increasingly significant. This was reflected by correlations between the N–C distance and the N–Si distance, and N–C bond indices and the N–Si distance. Also, it could be shown that the hybridization of the nitrogen lone pair changes, so that the N–C double bond character is promoted at long N–Si distances. The weight of the resonance structure with a N–Si bond increases at short N–Si distances, which can be related to an increase in the strength of the N–Si interaction. This could be uncovered by the electron density and the total energy density at the N–Si bond critical point, N–Si bond indices and the N–Si bond ionicity from an *NBO* analysis. All of these properties gave clear correlations with the N–Si distance.

The N–Si interaction can be related to negative hyperconjugation involving the nitrogen lone pair as a donor orbital and the Si–X antibond as an acceptor orbital. This entails that the strength of the N–Si interaction is influenced by the nature of the Si–X bond. The analysis of correlations involving Si–X bond properties revealed that the Si–X bond polarization is one factor that influences the ability of the Si–X antibond to act as an acceptor orbital. A high Si–X bond polarization comes with a high quality of the acceptor orbital. In the compounds with a highly covalent Si–X bond character, on the other hand, the N–Si interaction is weak. This can be attributed to the fact that a stabilization of a negative charge at the substituent X is more feasible if the Si–X bond polarization is high. In case of the p-chlorobenzoate substituent the negative charge can be additionally stabilized due to the presence of aromatic

resonance structures. Also, the chloro compound (**3**) shows a stronger N–Si interaction than expected from the polarization of the Si–Cl bond, which can be related to the high stability of the chloride anion. However, the ability to stabilize a negative charge, is not the only factor, which determines the strength of the N–Si interaction. It could also be concluded that sterical repulsion between the two "arms" of the naphthalene system leads to an elongation of the N–Si distance. Consequently, sterically demanding substituents, such as the p-chlorobenzoate, give longer N–Si distances, although the acceptor quality of the Si–X antibond would allow a stronger N–Si interaction. With respect to the Si–X bond properties, the PES plots did not overlap each other, and the nature of a particular Si–X bond does not change much with the N–Si distance. Even at N–Si bond lengths close to the one of the silyl cation (**1**), the Si–X bond character is largely maintained, which shows the high affinity of silicon to be pentacoordinated.

On the whole, the nature of the substituents X is diverse, and thus, different strengths of the N–Si interaction could be uncovered, which comes with a great variety of different N–Si distances. Therefore, the synthesized and crystallized compounds in Figure 11.3 were a reasonable selection for the analysis of *structure* and *bonding correlation*. Based on the analysis of experimental crystal structures, it is possible to learn about aspects of a chemical transformation, if the properties are carefully analyzed. The *structure correlations*, which were uncovered in this analysis, already provided a good understanding of a nucleophilic addition. However, *bonding correlations* give a more direct access to the bonding situation in these systems, and thus, an even deeper understanding of the chemical changes in the course of a nucleophilic addition of nitrogen to silicon is obtained. The applicability of *bonding correlations* could be clearly shown.

# Part VI

# Conclusions and Outlook

# Conclusions

A great variety of bond analysis methods, which enable an analysis of chemical bonding based on a molecular wavefunction or charge density, have been developed up to this day. In many studies, the analysis of chemical bonding is only based on a single method, which provides a biased view on chemical bonding in that particular system. Due to the fact that the chemical bond is only a concept, there is no ultimate bond analysis method that can provide a full characterization of chemical bonding. In a *complementary bonding analysis*, which was presented in the present study, a variety of bond analysis methods is applied on the same system, which eventually provides a much less biased view, because chemical bonding is elucidated from different sometimes even contradictory, certainly complementing perspectives.

In Chapter 5, the usefulness of a *complementary bonding analysis* was demonstrated by an investigation of the element-oxygen bond of hydroxide model compounds. Ultimately, it was possible to characterize the element-oxygen bonds as ionic, highly polarized, polarized covalent and charge shift bonds. In the chapters following that study, it was shown that a *complementary bonding analysis* is able to provide a clear picture of the bonding situation in a great variety of systems. The approach, which was followed throughout this thesis, was to find a link between Lewis' picture of chemical bonding and the picture obtained from a *complementary bonding analysis*. Lewis structures, which have been used for over a century, were revealed to always be a good starting point when it comes to the analysis of chemical bonding. However, while revisiting some fundamental bonding concepts of inorganic chemistry, it was shown that some rules, which have been established in the past, must be followed in order to find appropriate Lewis structures. For example, it has long been known that Lewis structures containing hypervalent atoms from the third period are not reasonable, because d-orbitals only serve as polarization functions in these molecules. Instead alternative bonding representations must be applied.

Schematically, multi-center multi-electron bonding models can be used to represent the bonding situation in these systems. For example, $[ClSiH_3Cl]^-$, which was studied in Chapters 9 and 10, can be expressed with the two resonance structures $Cl{-}SiH_3 + Cl^-$ and $Cl^- + H_3Si{-}Cl$. The silicon atom follows the octet rule in both resonance structures, and thus, hypervalent bonding representations must not be taken into account, even for transition structures. This type of bonding, which is known as three-center four-electron bonding, can be related to negative hyperconjugation in the localized orbital picture of chemical bonding. A real space method, such as the *QTAIM* approach, where the notion of an orbital does not exist, can only provide an indirect characterization of hyperconjugative interactions. This underlines the importance of looking at a variety of bond analysis methods, because some aspects of chemical bonding remain hidden if only a single bond analysis method is applied.

In the present thesis, the concept of hypervalency was extensively studied in systems contain-

ing phosphate, sulfate and perchlorate anions. This study revealed that only non-hypervalent resonance structures are required to represent the bonding situation in the $PO_4^{3-}$, $SO_4^{2-}$ and $ClO_4^-$ anions. However, population analyses of the chlorine atom of the $ClO_4^-$ anion revealed that an electron population of eight is exceeded, and thus, the chlorine atom is hypervalent, because the octet rule is violated. In this case, the valence electron count is raised by negative hyperconjugation, and not by d-orbital back-bonding. However, in all three anions the same type of interactions play a role. The higher electron population of the chlorine atom can be explained by the stronger hyperconjugative interactions and the more covalent Cl–O bond character. So, in principle, there is nothing special about the perchlorate anion. In fact, there are many definitions of an atom, and it is likely that the chlorine atom has less than eight valence electrons in some of these definitions. Ultimately, it is not important if an atom is hypervalent or not, because the molecular properties do not change abruptly once the limit of eight electrons is exceeded. However, the Cl–O bond polarization and the extent of hyperconjugative interactions directly influence the properties of the perchlorate anion, which can be measured experimentally. It is well-known that bond polarization determines the molecular dipole moment, which affects bulk properties, such as the boiling point of liquids.

In Chapter 6, it was also shown that the extent of hyperconjugative interactions in siloxanes influences the basicity of the oxygen atom. Consequently, the concept of hyperconjugation is not only an artifact arising from the use of a localized orbital picture, but corresponds to a property, which actually has an effect on molecular properties.

In Chapters 7 and 8 as well as in Part V, the wavefunction, which is required to apply bond analysis methods, was also obtained from an *X-ray wavefunction refinement*. Accordingly, the wavefunction contains experimental information, and thus, the bonding situation can be analyzed experimentally. Many aspects of chemical bonding, which have so far only been studied by theoretical methods, can therefore be studied based on experimental X-ray diffraction experiments. The analysis of the molecular geometry based on X-ray refined crystal structures has been performed since the advent of X-ray crystallography, however, bond analysis methods provide a much higher information value compared to the analysis of the molecular geometry alone. This is one of the aspects that inspired the extension of Bürgi's and Dunitz' *structure correlation* approach to a *bonding correlation* approach. In Part V, it was shown that a systematic array of pentacoordinated silicon compounds can be used to investigate a nucleophilic addition of a nitrogen atom to a silicon atom. Information on the reaction pathway of a nucleophilic addition was obtained from both *structure* and *bonding correlation* approaches.

# Outlook

Of course, only a small fraction of inorganic systems could be revisited in the present thesis. There are plenty of fundamental inorganic systems, where the bonding situation is not fully understood. In this thesis, a *complementary bonding analysis* is presented as a powerful approach to extensively study the bonding situation in these systems. In the following two ongoing projects are outlined.

There is a great variety of compounds, for which hypervalent Lewis structures are being used. One prominent example is the $SF_6$ molecule, for which Lewis structures with six S–F bonds are often encountered. A *complementary bonding analysis* of the $SF_6$ molecule will be performed in the future. The S–F bond is highly polarized, and may therefore account for the high stability of the $SF_6$ molecule. The S–H bond in the hypothetical $SH_6$ molecule is, on the other hand, highly covalent. Consequently, it is interesting to compare these two systems based on a *complementary bonding analysis*. In addition, a variety of crystal structures containing a R–$SF_5$ unit were measured, for which *X-ray wavefunction refinements* will be performed to study the concept of hypervalency experimentally.

In Chapter 6, the basicity of the oxygen atom of siloxanes was studied in dependence of the Si–O–Si angle. At low Si–O–Si angles, the basicity of the oxygen atom is enhanced. It was proposed that cyclic siloxane systems, which have low Si–O–Si angles caused by the ring strain, can pose as systems with an enhanced basicity of the oxygen atom. However, this aspect was only studied by theoretical methods. For a future study, high quality, high resolution crystal structures containing cyclic siloxane units were measured, and can be used for *X-ray wavefunction refinements*, in order to study the siloxane basicity experimentally.

These are only two projects, which will be performed in the near future. There are countless of interesting systems, for which a *complementary bonding analysis* can provide a deep insight into the bonding situation. However, despite the academic interest for complicated bonding situations, a *complementary bonding analysis* can also be applied on biologically active systems. The properties obtained from that analysis can be inspected for a variety of modifications of a system to eventually come up with the modification, which shows the highest biological activity.

# Summary

Lewis structures are used to represent the bonding situation in molecules in a simple way. However, the Lewis picture lacks a physical foundation – a quantum chemical approach to chemical bonding is inevitable. Bond analysis methods from the realms of real space, orbital space and energy space attempt to provide a link between schematic Lewis structures, which are easily comprehensible for every chemist, and the molecular wavefunction, which is delocalized and hard to interpret. In the present thesis, some well known bonding concepts of inorganic systems were revisited using a *complementary bonding analysis*. The intention is to get a better understanding of chemical bonding in these systems, and to show how Lewis structures can be used to represent the bonding situation in these systems.

The element-oxygen bond, where the element is from the second or third period, was investigated in Chapter 5. It was shown how the concept of **bond polarity** is reflected by a variety of bond analysis methods. Ultimately, it was possible to assign the element-oxygen bond into four categories: Ionic bonds, highly polarized bonds, polarized covalent bonds and charge shift bonds. The usefulness of the joint application of bond analysis methods – a *complementary bonding analysis* – was demonstrated.

In Chapter 6, the increase in basicity of the oxygen atom of siloxanes ($R_3Si-O-SiR_3$) with a decrease in the Si−O−Si angle was investigated *via* a *complementary bonding analysis*. It was found that both **covalent and ionic interactions** play a role in the Si−O bonds, and that both aspects increase simultaneously with an increase in the Si−O−Si angle. The covalent interactions can be related to negative hyperconjugation involving the oxygen lone pairs and the Si−R antibonds. Accordingly, the higher basicity at low Si−O−Si angles can be related to the fact that the oxygen lone pairs are more localized at low Si−O−Si angles.

In Chapter 7, it was shown how the concept of **resonance** in the nitrate anion and related species is reflected by a *complementary bonding analysis*. All resonance structures that contribute to the bonding situation of the nitrate anion could be uncovered by theoretical calculations and *X-ray wavefunction refinements*. The resonance resembles aromatic systems closely.

The concept of **hypervalency** in phosphate ($PO_4^{3-}$), sulfate ($SO_4^{2-}$) and perchlorate ($ClO_4^-$) anions was tackled in Chapter 8. The analysis was based on isolated molecule optimizations and *X-ray wavefunction refinements*. It was found that negative hyperconjugation

between the oxygen lone pairs and the X–O (X = P, S, Cl) antibonds is significant in all anions. This interaction leads to an increase in the electron population of the central atom. The P–O and S–O bonds are highly polarized and, thus, the electron population of the sulfur and phosphorus atoms is below eight despite the increase in electron population caused by negative hyperconjugation. Consequently, they follow the octet rule and are not hypervalent. The Cl–O bond, on the other hand, shows a high degree of covalency, and according to some bond analysis methods, the chlorine atom is hypervalent. Here, hyperconjugation causes hypervalency, and not d-orbital participation.

In Chapters 9 and 10, the bonding situation in the course of $S_N2$ reactions is investigated based on a *complementary bonding analysis*. $S_N2$ reactions at carbon and silicon atoms are compared to each other to uncover the reason for the different appearance of the potential energy surfaces along the reaction coordinate. While a transition state is obtained for the carbon system ($[Cl\cdots CH_3\cdots Cl]^-$), the silicon system ($[Cl\cdots SiH_3\cdots Cl]^-$) gives a stable transition complex, which is caused by the fact that pentacoordination is feasible at silicon due to a large stabilization through large ionic contributions. In the second study, $S_N2$ reactions of a variety of silicon systems were investigated to uncover the role of hydrogen bonding in the course of the reaction. It was found that the potential energy surface along the reaction coordinate is significantly influenced by the formation of hydrogen bonds at higher distances between the silicon atom and the leaving group. The existence of single-, double- and triple-well potential energy surfaces can be attributed to the formation of hydrogen bonds, which can be formed if substituents are bonded to the silicon atom that can act as hydrogen bond donors, such as methyl or methoxy.

In Part V, Bürgi's and Dunitz' *structure correlation* approach was extended to a *bonding correlation* approach. The crystal structures and theoretically obtained structures of pentacoordinated silicon compounds with a N–Si peri-interaction were brought into a reasonable sequence representing a gradual approach of the nitrogen towards the silicon. This systematic array of structures can be interpreted as a nucleophilic addition of nitrogen to silicon. Correlations between structural parameters as well as bonding properties and the N–Si distance were uncovered, and analyzed with respect to a nucleophilic addition. In that way, the N–Si bond formation could be quantified using a *complementary bonding analysis*. The *bonding correlation* approach was confirmed to be a feasible procedure to study chemical bonding during a dynamical process based on single-crystal X-ray diffraction experiments.

# Zusammenfassung

Lewis-Strukturen werden benutzt, um die Bindungssituation in Molekülen auf eine einfache Art darzustellen. Dem Lewis-Bild fehlt es jedoch an einer physikalischen Grundlage – eine quantenchemische Herangehensweise an chemische Bindungen ist grundsätzlich notwendig. Bindungsanalysemethoden aus den Gebieten des Realraums, Orbitalraums und Energieraums versuchen eine Verbindung zwischen den schematischen Lewistrukturen, die für jeden Chemiker einfach zu verstehen sind, und molekularen Wellenfunktionen, welche delokalisiert und schwer zu interpretieren sind, herzustellen. In der vorliegenden Arbeit werden einige bekannte Bindungskonzepte aus der anorganischen Chemie mittels einer *komplementären Bindungsanalyse* wiederaufgegriffen. Es ist die Absicht, ein besseres Verständnis für chemische Bindungen in diesen Systemen zu bekommen und zu zeigen, wie Lewis-Strukturen trotz allem genutzt werden können, um die Bindungssituation in diesen Systemen darzustellen.

Die Element-Sauerstoff-Bindung, bei der das Element von der zweiten oder dritten Periode stammt, wurde im Kapitel 5 untersucht. Es wurde gezeigt, wie das Konzept der **Bindungspolarität** durch eine Vielzahl von Bindungsanalysemethoden widergespiegelt wird. Letztendlich war es möglich, die Element-Sauerstoff-Bindungen in vier Kategorien einzuteilen: Ionische Bindungen, stark polarisierte Bindungen, polarisierte kovalente Bindungen und *Charge-Shift*-Bindungen. Die Nützlichkeit einer gemeinsamen Anwendung von Bindungsanalysemethoden – einer *komplementären Bindungsanalyse* – wurde demonstriert.

In Kapitel 6 wurde der Anstieg der Basizität des Sauerstoffatoms von Siloxanen ($R_3Si-O-SiR_3$) bei Verringerung des Si – O – Si-Winkels mittels einer *komplementären Bindungsanalyse* untersucht. Es stellte sich heraus, dass sowohl **Kovalenz als auch Ionizität** in der Si – O-Bindung eine Rolle spielen, und dass beide Aspekte gleichzeitig mit einem Anstieg des Si – O – Si-Winkels an Bedeutung gewinnen. Die kovalenten Wechselwirkungen können mit negativer Hyperkonjugation zwischen den freien Elektronenpaaren am Sauerstoff und der Si – R Antibindung in Verbindung gebracht werden. Demnach kann die höhere Basizität bei niedrigen Si – O – Si-Winkeln so begründet werden, dass die freien Elektronenpaare am Sauerstoffatom lokalisierter sind.

In Kapitel 7 wurde gezeigt, wie das Konzept der **Resonanz** im Nitrat-Anion und verwandten Spezies durch eine *komplementäre Bindungsanalyse* widergespiegelt wird. Alle Res-

onanzstrukturen, welche zur Bindungssituation des Nitrat-Anions beitragen, konnten durch theoretische Berechnungen und *Röntgenwellenfunktionsverfeinerungen* enthüllt werden. Die Resonanz ähnelt der Aromatizität.

Das Konzept der **Hypervalenz** in Phosphat- ($PO_4^{3-}$), Sulfat- ($SO_4^{2-}$) und Perchlorat-Anionen ($ClO_4^-$) wurde in Kapitel 8 angegangen. Die Analyse basiert auf Optimierungen von isolierten Molekülen und *Röntgenwellenfunktionsverfeinerungen*. Es hat sich herausgestellt, dass negative Hyperkonjugation zwischen den freien Elektronenpaaren am Sauerstoff und der X – O-Antibindung (X = P, S, Cl) in allen Anionen signifikant ist. Diese Wechselwirkung führt zu einem Anstieg der Elektronenpopulation des zentralen Atoms. Die P – O- und S – O-Bindungen sind stark polarisiert, weswegen die Elektronenpopulationen des Phosphors und Schwefels, trotz des Anstiegs der Elektronenpopulationen durch die negative Hyperkonjugation, unter 8 Elektronen ist. Demzufolge wird die Oktettregel befolgt und beide Anionen sind nicht hypervalent. Die Cl – O-Bindung ist hingegen hochgradig kovalent, weswegen einige Bindungsanalysemethoden eine hypervalente Bindungssituation für das Chlor-Atom zeigen. Hypervalenz kommt in diesem Fall durch Hyperkonjuation zustande, und nicht durch die Beteiligung von d-Orbitalen.

In den Kapiteln 9 und 10, wurde die Bindungssituation im Verlauf von $S_N2$-Reaktionen basierend auf einer *komplementären Bindungsanalyse* untersucht. $S_N2$-Reaktionen an Kohlenstoff- und Silizium-Atomen wurden miteinander verglichen, um den Grund für das unterschiedliche Aussehen der Hyperpotentialfläche entlang der Reaktionskoordinate aufzuklären. Während das Kohlenstoffsystem ($[Cl\cdots CH_3\cdots Cl]^-$) einen Übergangszustand aufweist, gibt das Silizium-System ($[Cl\cdots SiH_3\cdots Cl]^-$) ein stabiles Intermediat, was durch die Begünstigung von Pentakoordination am Silizium durch das hohe Maß an ionischen Bindungsanteilen zu erklären ist. In der zweiten Studie wurde eine Auswahl an $S_N2$-Reaktionen am Silizium untersucht, um die Rolle von Wasserstoffbrückenbindungen im Verlauf der Reaktion zu bestimmen. Es wurde festgestellt, dass die Hyperpotentialfläche entlang der Reaktionskoordinate signifikant durch die Bildung von Wasserstoffbrücken bei großen Abständen zwischen dem Silizium-Atom und der Abgangsgruppe beeinflusst wird. Die Existenz von Hyperpotentialfläche mit einem, zwei oder drei Minima kann mit der Bildung von Wasserstoffbrückenbindungen erklärt werden, wenn Substituenten wie Methyl- and Methoxy-Gruppen am Silizium gebunden sind, welche als Wasserstoffbrücken-Donatoren fungieren können.

In Teil V wurde Bürgis und Dunitz *Strukturkorrelationsansatz* zu einem *Bindungskorrelationsansatz* erweitert. Die Kristallstrukturen und theoretisch bestimmten Strukturen von pentakoordinierten Siliziumverbindungen mit einer N – Si-peri-Wechselwirkung wurde in eine angemessene Reihenfolge, welche die graduelle Annäherung des Stickstoffatoms zum Siliziumatom beschreibt, gebracht. Diese systematische Strukturreihe kann als Simulation einer nukleophilen Addition eines Stickstoffatoms an ein Siliziumatom interpretiert werden. Es wurden sowohl Korrelationen zwischen Struktureigenschaften und dem N – Si-Abstand als auch Kor-

relationen zwischen Bindungseigenschaften und dem N–Si-Abstand gefunden und in Hinblick auf eine nukleophile Addition analysiert. Auf diese Weise konnte die N–Si-Bindungsbildung durch eine *komplementäre Bindungsanalyse* quantifiziert werden. Der *Bindungskorrelationsansatz* wurde als ein realisierbares Verfahren für die Bindungsanalyse während eines dynamischen Prozesses durch Röntgenbeugungsexperimente an Einkristallen bestätigt.

# Bibliography


[1] L. Zhao, W. H. E. Schwarz, G. Frenking, *Nat. Rev. Chem.* **2019**, 1.

[2] G. N. Lewis, *J. Am. Chem. Soc.* **1916**, *38*(4), 762–785.

[3] I. Langmuir, *J. Am. Chem. Soc.* **1919**, *41*(10), 1543–1559.

[4] G. N. Lewis, *Valence and the Structure of Atoms and Molecules*, 14, Chemical Catalog Company, Incorporated, **1923**.

[5] W. Heitler, F. London, *Z. Phys.* **1927**, *44*(6-7), 455–472.

[6] L. Pauling, *The Nature of the Chemical Bond and the Structure of Molecules and Crystals*, Cornell university press Ithaca, NY, **1939**.

[7] I. Langmuir, *J. Am. Chem. Soc.* **1920**, *42*(2), 274–292.

[8] R. E. Kohler, *Hist. Stud. Nat. Sci.* **1974**, *4*, 39–87.

[9] R. E. Kohler, *Hist. Stud. Nat. Sci.* **1975**, *6*, 431–468.

[10] D. L. Cooper, J. Gerratt, M. Raimondi, *Nature* **1986**, *323*(6090), 699.

[11] L. Pauling, *Nature* **1987**, *325*(6103), 396.

[12] R. P. Messmer, P. A. Schultz, *Nature* **1987**, *329*(6139), 492.

[13] I. Langmuir, *J. Am. Chem. Soc.* **1919**, *41*(6), 868–934.

[14] J. I. Musher, *Angew. Chem. Int. Ed.* **1969**, *8*(1), 54–68.

[15] W. Kutzelnigg, *Angew. Chem. Int. Ed.* **1984**, *23*(4), 272–295.

[16] A. E. Reed, F. Weinhold, *J. Am. Chem. Soc.* **1986**, *108*(13), 3586–3593.

[17] A. E. Reed, P. v. R. Schleyer, *J. Am. Chem. Soc.* **1990**, *112*(4), 1434–1445.

[18] M. S. Schmøkel, S. Cenedese, J. Overgaard, M. R. V. Jørgensen, Y.-S. Chen, C. Gatti, D. Stalke, B. B. Iversen, *Inorg. Chem.* **2012**, *51*(15), 8607–8616.

[19] R. J. Hach, R. E. Rundle, *J. Am. Chem. Soc.* **1951**, *73*(9), 4321–4324.

[20] R. E. Rundle, *J. Am. Chem. Soc.* **1947**, *69*(6), 1327–1331.

[21] R. E. Rundle, *J. Am. Chem. Soc.* **1963**, *85*(1), 112–113.

[22] G. C. Pimentel, *J. Chem. Phys.* **1951**, *19*(4), 446–448.

[23] D. E. Woon, T. H. Dunning Jr, *J. Phys. Chem. A* **2009**, *113*(27), 7915–7926.

[24] R. J. Gillespie, B. Silvi, *Coord. Chem. Rev.* **2002**, *233*, 53–62.

[25] L. Pauling, *J. Am. Chem. Soc.* **1932**, *54*(9), 3570–3582.

[26] R. S. Mulliken, *J. Chem. Phys.* **1934**, *2*(11), 782–793.

[27] R. S. Mulliken, *J. Chem. Phys.* **1935**, *3*(9), 573–585.

[28] M. Rahm, R. Hoffmann, *J. Am. Chem. Soc.* **2016**, *138*(11), 3731–3744.

[29] D. Stalke, *Chemistry–A European Journal* **2011**, *17*(34), 9264–9278.

[30] S. Shaik, P. C. Hiberty, *Rev. Com. Ch.* **2004**, *20*, 1.

[31] S. S. Shaik, P. C. Hiberty, *A chemist's guide to valence bond theory*, John Wiley & Sons, **2007**.

[32] C. C. J. Roothaan, *Rev. Mod. Phys.* **1951**, *23*(2), 69.

[33] J. A. Pople, D. L. Beveridge, *McGraw-Hill, New York* **1970**.

[34] W. J. Hehre, *Acc. Chem. Res.* **1976**, *9*(11), 399–406.

[35] G. Frenking, S. Shaik, *The chemical bond: fundamental aspects of chemical bonding*, John Wiley & Sons, **2014**.

[36] M. Fugel, J. Beckmann, D. Jayatilaka, G. V. Gibbs, S. Grabowsky, *Chem. Eur. J.* **2018**, *24*(23), 6248–6261.

[37] F. Weinhold, C. R. Landis, *Valency and bonding: a natural bond orbital donor-acceptor perspective*, Cambridge University Press, **2005**.

[38] R. F. Bader, *Chem. Rev.* **1991**, *91*(5), 893–928.

[39] B. Silvi, A. Savin, *Nature* **1994**, *371*(6499), 683.

[40] M. Kohout, *Int. J. Quantum Chem.* **2004**, *97*(1), 651–658.

[41] R. F. W. Bader, *J. Phys. Chem. A* **1998**, *102*(37), 7314–7323.

[42] M. v. Hopffgarten, G. Frenking, *Wiley Interdiscip. Rev. Comput. Mol.* **2012**, *2*(1), 43–62.

[43] S. Shaik, D. Danovich, W. Wu, P. C. Hiberty, *Nat Chem.* **2009**, *1*(6), 443.

[44] S. Shaik, P. Maitre, G. Sini, P. C. Hiberty, *J. Am. Chem. Soc.* **1992**, *114*(20), 7861–7866.

[45] M. Fugel, M. F. Hesse, R. Pal, J. Beckmann, D. Jayatilaka, M. J. Turner, A. Karton, P. Bultinck, G. S. Chandler, S. Grabowsky, *Chem. Eur. J.* **2018**, *24*(57), 15275–15286.

[46] R. West, L. S. Wilson, D. L. Powell, *J. Organomet. Chem.* **1979**, *178*(1), 5–9.

[47] S. Grabowsky, M. F. Hesse, C. Paulmann, P. Luger, J. Beckmann, *Inorg. Chem.* **2009**, *48*(10), 4384–4393.

[48] S. Grabowsky, J. Beckmann, P. Luger, *Aust. J. Chem.* **2012**, *65*(7), 785–795.

[49] F. Weinhold, R. West, *Organometallics* **2011**, *30*(21), 5815–5824.

[50] F. Weinhold, R. West, *J. Am. Chem. Soc.* **2013**, *135*(15), 5762–5767.

[51] M. Fugel, F. Kleemiss, L. A. Malaspina, R. Pal, P. R. Spackman, D. Jayatilaka, S. Grabowsky, *Aust. J. Chem* **2018**, *71*(4), 227–237.

[52] M. Woińska, D. Jayatilaka, B. Dittrich, R. Flaig, P. Luger, K. Woźniak, P. M. Dominiak, S. Grabowsky, *ChemPhysChem* **2017**, *18*(23), 3334–3351.

[53] D. Jayatilaka, *Phys. Rev. Lett.* **1998**, *80*(4), 798.

[54] M. Fugel, L. A. Malaspina, R. Pal, S. P. Thomas, M. W. Shi, M. A. Spackman, K. Sugimoto, S. Grabowsky, *Chem. Eur. J.* **2019**, *80*, 798.

[55] D. M. P. Mingos, *The Chemical Bond I*, Springer International Publishing Switzerland, **2016**.

[56] A. P. Bento, M. Solà, F. M. Bickelhaupt, *J. Comput. Chem.* **2005**, *26*(14), 1497–1504.

[57] A. P. Bento, F. M. Bickelhaupt, *J. Org. Chem.* **2007**, *72*(6), 2201–2207.

[58] A. P. Bento, F. M. Bickelhaupt, *J. Org. Chem.* **2008**, *73*(18), 7290–7299.

[59] T. A. Hamlin, M. Swart, F. M. Bickelhaupt, *ChemPhysChem* **2018**, *19*(11), 1315–1330.

[60] W. L. Hase, *Science* **1994**, *266*(5187), 998–1002.

[61] J. Xie, W. L. Hase, *Science* **2016**, *352*(6281), 32–33.

[62] W. N. Olmstead, J. I. Brauman, *J. Am. Chem. Soc.* **1977**, *99*(13), 4219–4228.

[63] H. B. Bürgi, *Inorg. Chem.* **1973**, *12*(10), 2321–2325.

[64] H. B. Bürgi, J. D. Dunitz, E. Shefter, *J. Am. Chem. Soc.* **1973**, *95*(15), 5065–5067.

[65] H. B. Bürgi, J. D. Dunitz, *Structure correlation*, John Wiley & Sons, **2008**.

[66] J. D. Dunitz, J. M. Lehn, G. Wipff, *Tetrahedron* **1974**, *30*(12), 1563–1572.

[67] H. B. Buergi, J. D. Dunitz, *Acc. Chem. Res.* **1983**, *16*(5), 153–161.

[68] E. Schrödinger, *Ann. Phys.* **1926**, *385*(13), 437–490.

[69] M. Born, *Z. Phys.* **1926**, *38*(11-12), 803–827.

[70] P. W. Atkins, R. S. Friedman, *Molecular quantum mechanics*, Oxford university press, **2011**.

[71] W. E. F. Pauli, G. Källén **1958**.

[72] G. N. Lewis, *J. Chem. Phys.* **1933**, *1*(1), 17–28.

[73] K. Fukui, T. Yonezawa, H. Shingu, *J. Chem. Phys.* **1952**, *20*(4), 722–725.

[74] M. Born, R. Oppenheimer, *Ann. Phys.* **1927**, *389*(20), 457–484.

[75] R. S. Mulliken, *Spectroscopy, molecular orbitals, and chemical bonding*, Norstedt, **1967**.

[76] J. E. Lennard-Jones, *J. Chem. Soc. Faraday Trans.* **1929**, *25*, 668–686.

[77] W. Pauli, *Z. Phys.* **1925**, *31*(1), 765–783.

[78] J. C. Slater, *Phys. Rev.* **1929**, *34*(10), 1293.

[79] D. R. Hartree **1928**, *24*(1), 89–110.

[80] J. C. Slater, *Phys. Rev.* **1928**, *32*(3), 339.

[81] J. C. Slater, *Phys. Rev.* **1930**, *35*(2), 210.

[82] V. Fock, *Z. Phys.* **1930**, *61*(1-2), 126–148.

[83] D. R. Hartree, W. Hartree, *Proc. Royal Soc. Lond.* **1935**, *150*(869), 9–33.

[84] E. Hückel, *Z. Phys.* **1933**, *83*(9-10), 632–668.

[85] U. Fano, *Phys. Rev.* **1961**, *124*(6), 1866.

[86] C. Møller, M. S. Plesset, *Phys. Rev.* **1934**, *46*(7), 618.

[87] J. Čížek, *J. Chem. Phys.* **1966**, *45*(11), 4256–4266.

[88] R. O. Jones, *Rev. Mod. Phys.* **2015**, *87*(3), 897.

[89] P. Hohenberg, W. Kohn, *Phys. Rev.* **1964**, *136*(3B), B864.

[90] W. Kohn, L. J. Sham, *Phys. Rev.* **1965**, *140*(4A), A1133.

[91] E. Wigner, *Phys. Rev.* **1934**, *46*(11), 1002.

[92] E. Wigner, F. Seitz, *Phys. Rev.* **1933**, *43*(10), 804.

[93] G. S. Painter, F. W. Averill, *Phys. Rev. B* **1982**, *26*(4), 1781.

[94] A. D. Becke, *J. Chem. Phys.* **1993**, *98*(7), 5648–5652.

[95] P. J. Stephens, F. J. Devlin, C. F. N. Chabalowski, M. J. Frisch, *J. Phys. Chem.* **1994**, *98*(45), 11623–11627.

[96] D. L. Cooper, J. Gerratt, M. Raimondi, *Adv. Chem. Phys.* **1987**, *69*, 319–397.

[97] J. H. Van Lenthe, G. G. Balint-Kurti, *J. Chem. Phys.* **1983**, *78*(9), 5699–5713.

[98] P. C. Hiberty, S. Shaik, *Theor. Chem. Acc.* **2002**, *108*(5), 255–272.

[99] F. Jensen, *Wiley Interdiscip. Rev. Comput. Mol.* **2013**, *3*(3), 273–295.

[100] W. J. Hehre, R. F. Stewart, J. A. Pople, *J. Chem. Phys.* **1969**, *51*(6), 2657–2664.

[101] W. J. Hehre, R. Ditchfield, J. A. Pople, *J. Chem. Phys.* **1972**, *56*(5), 2257–2261.

[102] D. E. Woon, T. H. Dunning Jr, *J. Chem. Phys.* **1993**, *98*(2), 1358–1371.

[103] R. A. Kendall, T. H. Dunning Jr, R. J. Harrison, *J. Chem. Phys.* **1992**, *96*(9), 6796–6806.

[104] L. Massa, L. Huang, J. Karle, *Int. J. Quantum Chem.* **1995**, *56*(S29), 371–384.

[105] S. Grabowsky, A. Genoni, H. B. Bürgi, *Chem. Sci.* **2017**, *8*(6), 4159–4176.

[106] A. Genoni, L. Bučinskỳ, N. Claiser, J. Contreras-García, B. Dittrich, P. M. Dominiak, E. Espinosa, C. Gatti, P. Giannozzi, J.-M. Gillet, D. Jayatilaka, P. Macchi, A. Madsen, L. Massa, C. F. Matta, K. M. Merz, P. N. H. Nakashima, H. Ott, U. Ryde, K. Schwarz, M. Sierka, S. Grabowsky, *Chem. Eur. J.* **2018**, *24*(43), 10881–10905.

[107] D. Jayatilaka, B. Dittrich, *Acta Cryst. A* **2008**, *64*(3), 383–393.

[108] S. C. Capelli, H. B. Bürgi, B. Dittrich, S. Grabowsky, D. Jayatilaka, *IUCrJ* **2014**, *1*(5), 361–379.

[109] S. Grabowsky, P. Luger, J. Buschmann, T. Schneider, T. Schirmeister, A. N. Sobolev, D. Jayatilaka, *Angew. Chem. Int. Ed.* **2012**, *51*(27), 6776–6779.

[110] W. Massa, *Crystal structure determination*, Springer Science & Business Media, **2013**.

[111] W. H. Miller, *A treatise on crystallography*, For J. & JJ Deighton, **1839**.

[112] W. L. Bragg, *Nature* **1912**, *90*(2250), 410.

[113] W. H. Bragg, W. L. Bragg, *Proc. Royal Soc. A* **1913**, *88*(605), 428–438.

[114] W. L. Bragg **1929**.

[115] W. Friedrich, P. Knipping, M. Laue, *Ann. Phys.* **1913**, *346*(10), 971–988.

[116] K. Cowtan, *e LS* **2001**.

[117] J. Karle, H. Hauptman, *Acta Cryst.* **1950**, *3*(3), 181–187.

[118] H. A. Hauptman, J. Karle, *Solution of the phase problem*, 3, American Crystallographic Association, **1953**.

[119] R. Herbst-Irmer, A. Spek, T. Schneider, M. Sawaya, *Crystal Structure Refinement: A Crystallographer's Guide to SHELXL*, vol. 8, Oxford University Press, **2006**.

[120] M. Woińska, S. Grabowsky, P. M. Dominiak, K. Woźniak, D. Jayatilaka, *Sci. Adv.* **2016**, *2*(5), e1600192.

[121] M. Fugel, D. Jayatilaka, E. Hupf, J. Overgaard, V. R. Hathwar, P. Macchi, M. J. Turner, J. A. Howard, O. V. Dolomanov, H. Puschmann, B. B. Iversen, H. B. Bürgi, S. Grabowsky, *IUCrJ* **2018**, *5*(1), 32–44.

[122] N. K. Hansen, P. Coppens, *Acta Cryst. A* **1978**, *34*(6), 909–921.

[123] D. J. Grimwood, D. Jayatilaka, *Acta Cryst. A* **2001**, *57*(1), 87–100.

[124] F. L. Hirshfeld, *Isr. J. Chem.* **1977**, *16*(2-3), 198–201.

[125] L. A. Malaspina, A. J. Edwards, W. Magdalena, D. Jayatilaka, M. J. Turner, J. R. Price, R. Herbst-Irmer, K. Sugimoto, E. Nishibori, S. Grabowsky, *Cryst. Growth Des* **2017**, *17*(7), 3812–3825.

[126] A. Genoni, L. H. R. Dos Santos, B. Meyer, P. Macchi, *IUCrJ* **2017**, *4*(2), 136–146.

[127] K. Sugimoto, H. Ohsumi, S. Aoyagi, E. Nishibori, C. Moriyoshi, Y. Kuroiwa, H. Sawa, M. Takata **2010**, *1234*(1), 887–890.

[128] B. Henrich, A. Bergamaschi, C. Broennimann, R. Dinapoli, E. F. Eikenberry, I. Johnson, M. Kobas, P. Kraft, A. Mozzanica, B. Schmitt, *Nucl. Instrum. Methods Phys. Res.* **2009**, *607*(1), 247–249.

[129] T. Ziegler, A. Rauk, *Inorg. Chem.* **1979**, *18*(6), 1558–1565.

[130] M. D. Gould, C. Taylor, S. K. Wolff, G. S. Chandler, D. Jayatilaka, *Theo. Chem. Acc.* **2008**, *119*(1-3), 275–290.

[131] R. F. W. Bader, *Atoms in Molecules: A Quantum Theory*, Clarendon Press, Oxford, **1994**.

[132] R. F. W. Bader, *J. Phys. Chem. A* **2009**, *113*(38), 10391–10396.

[133] R. F. W. Bader, P. J. MacDougall, C. D. H. Lau, *J. Am. Chem. Soc.* **1984**, *106*(6), 1594–1605.

[134] R. F. Bader, A. Streitwieser, A. Neuhaus, K. E. Laidig, P. Speers, *J. Am. Chem. Soc.* **1996**, *118*(21), 4959–4965.

[135] F. Weinhold, C. R. Landis, *Chem. Educ. Res. Pract.* **2001**, *2*(2), 91–104.

[136] A. E. Reed, F. Weinhold, *J. Chem. Phys.* **1983**, *78*(6), 4066–4073.

[137] E. D. Glendening, C. R. Landis, F. Weinhold, *Wiley Interdiscip. Rev.-Comput. Mol. Sci.* **2012**, *2*(1), 1–42.

[138] A. E. Reed, R. B. Weinstock, F. Weinhold, *J. Chem. Phys.* **1985**, *83*(2), 735–746.

[139] J. P. Foster, F. Weinhold, *J. Am. Chem. Soc.* **1980**, *102*(24), 7211–7218.

[140] A. E. Reed, F. Weinhold, *J. Chem. Phys.* **1985**, *83*(4), 1736–1740.

[141] E. D. Glendening, F. Weinhold, *J. Comput. Chem.* **1998**, *19*(6), 593–609.

[142] E. D. Glendening, F. Weinhold, *J. Comput. Chem.* **1998**, *19*(6), 610–627.

[143] A. H. Zewail, *Pure Appl. Chem.* **2000**, *72*(12), 2219–2231.

[144] A. Barty, J. Küpper, H. N. Chapman, *Annu. Rev. Phys. Chem.* **2013**, *64*, 415–435.

[145] R. Neutze, *Philos. Trans. Royal Soc. B* **2014**, *369*(1647), 20130318.

[146] H. N. Chapman, A. Barty, M. J. Bogan, S. Boutet, M. Frank, S. P. Hau-Riege, S. Marchesini, B. W. Woods, S. Bajt, W. H. Benner, R. A. London, E. Pl´onjes, M. Kuhlmann, R. Treusch, S. Düsterer, T. Tschentscher, J. R. Schneider, E. Spiller, T. Möller, C. Bostedt, M. Hoener, D. A. Shapiro, K. O. Hodgson, D. van der Spoel, F. Burmeister, M. Bergh, C. Caleman, G. Huldt, M. M. Seibert, F. R. N. C. Maia, R. W. Lee, A. Szöke, A. N. Timneanu, J. Hajdu, *Nat Phys.* **2006**, *2*(12), 839.

[147] R. D. Miller, *Annu. Rev. Phys. Chem.* **2014**, *65*, 583–604.

[148] J. R. Dwyer, C. T. Hebeisen, R. Ernstorfer, M. Harb, V. B. Deyirmenjian, R. E. Jordan, R. Dwayne Miller, *Philosophical Transactions of the Royal Society A: Mathematical, Physical and Engineering Sciences* **2006**, *364*(1840), 741–778.

[149] H. B. Bürgi, *Angew. Chem. Int. Ed.* **1975**, *14*(7), 460–473.

[150] N. Kano, in *Organosilicon Compounds*, Elsevier, **2017**, 645–716.

[151] C. Chuit, R. J. P. Corriu, C. Reye, J. C. Young, *Chem. Rev.* **1993**, *93*(4), 1371–1448.

[152] G. Cerveau, C. Chuit, R. J. P. Corriu, C. Reye, *J. Organomet. Chem.* **1987**, *328*(3), C17–C20.

[153] J. Clayden, *Organic Chemistry*, Oxford University Press, **2012**.

[154] N. Kocher, J. Henn, B. Gostevskii, D. Kost, I. Kalikhman, B. Engels, D. Stalke, *J. Am. Chem. Soc.* **2004**, *126*(17), 5563–5568.

[155] A. Bassindale, S. Glynn, D. Parker, P. Taylor, *Perkin Trans.* **1999**, *10*, 2099–2109.

[156] A. R. Bassindale, S. J. Glynn, P. G. Taylor, N. Auner, B. Herrschaft, *J. Organomet. Chem.* **2001**, *619*(1-2), 132–140.

[157] A. R. Bassindale, D. J. Parker, P. G. Taylor, *Perkin Trans.* **2000**, *5*, 1059–1066.

[158] A. R. Bassindale, Y. I. Baukov, M. Borbaruah, S. J. Glynn, V. V. Negrebetsky, D. J. Parker, P. G. Taylor, R. Turtle, *J. Organomet. Chem.* **2003**, *669*(1-2), 154–163.

[159] M. Sohail, R. Panisch, A. Bowden, A. R. Bassindale, P. G. Taylor, A. A. Korlyukov, D. E. Arkhipov, L. Male, S. Callear, S. J. Coles, M. B. Hursthouse, R. W. Harrington, W. Clegg, *Dalton Trans.* **2013**, *42*(30), 10971–10981.

[160] A. A. Macharashvili, V. E. Shklover, Y. T. Struchkov, G. I. Oleneva, E. P. Kramarova, A. G. Shipov, Y. I. Baukov, *ChemComm* **1988**, *10*, 683–685.

[161] S. Muhammad, A. R. Bassindale, P. G. Taylor, L. Male, S. J. Coles, M. B. Hursthouse, *Organometallics* **2011**, *30*(3), 564–571.

[162] A. R. Bassindale, D. J. Parker, P. G. Taylor, N. Auner, B. Herrschaft, *J. Organomet. Chem.* **2003**, *667*(1-2), 66–72.

[163] Y. E. Ovchinnikov, Y. T. Struchkov, Y. I. Baukov, A. Shipov, E. Kramarova, S. Y. Bylikin, *Russ. Chem. Bull.* **1994**, *43*(8), 1346–1350.

[164] M. J. Barrow, E. A. V. Ebsworth, M. M. Harding, *Dalton Trans.* **1980**, *10*, 1838–1844.

[165] V. F. Sidorkin, V. V. Vladimirov, M. G. Voronkov, V. A. Pestunovich, *J. Mol. Struct.* **1991**, *228*, 1–9.

[166] G. Klebe, *Acta Cryst. A* **1984**, *40*, C105–C105.

[167] K. Tamao, M. Asahara, T. Saeki, A. Toshimitsu, *J. Organomet. Chem.* **2000**, *600*(1-2), 118–123.

[168] Bruker, SAINT software reference manual, **1998**.

[169] G. M. Sheldrick, *Bruker AXS Inc., Madison, Wisconsin, USA* **2003**.

[170] G. M. Sheldrick, *Acta Cryst. A* **2015**, *71*(1), 3–8.

[171] G. M. Sheldrick, *Acta Cryst. C* **2015**, *71*(1), 3–8.

[172] O. V. Dolomanov, L. J. Bourhis, R. J. Gildea, J. A. Howard, H. Puschmann, *J. Appl. Crystallogr.* **2009**, *42*(2), 339–341.

[173] D. Jayatilaka, D. J. Grimwood, in *International Conference on Computational Science*, Springer, 142–151.

[174] B. Dittrich, J. Lübben, S. Mebs, A. Wagner, P. Luger, R. Flaig, *Chem. Eur. J.* **2017**, *23*(19), 4605–4614.

[175] K. Meindl, J. Henn, *Acta Cryst. A* **2008**, *64*(3), 404–418.

[176] M. J. Frisch, G. W. Trucks, H. B. Schlegel, G. E. Scuseria, M. A. Robb, J. R. Cheeseman, G. Scalmani, V. Barone, G. A. Petersson, H. Nakatsuji, X. Li, M. Caricato, A. V. Marenich, J. Bloino, B. G. Janesko, R. Gomperts, B. Mennucci, H. P. Hratchian, J. V. Ortiz, A. F. Izmaylov, J. L. Sonnenberg, D. Williams-Young, F. Ding, F. Lipparini, F. Egidi, J. Goings, B. Peng, A. Petrone, T. Henderson, D. Ranasinghe, V. G. Zakrzewski, J. Gao, N. Rega, G. Zheng, W. Liang, M. Hada, M. Ehara, K. Toyota, R. Fukuda, J. Hasegawa, M. Ishida, T. Nakajima, Y. Honda, O. Kitao, H. Nakai, T. Vreven, K. Throssell, J. A. Montgomery, Jr., J. E. Peralta, F. Ogliaro, M. J. Bearpark, J. J. Heyd, E. N. Brothers, K. N. Kudin, V. N. Staroverov, T. A. Keith, R. Kobayashi, J. Normand, K. Raghavachari, A. P. Rendell, J. C. Burant, S. S. Iyengar, J. Tomasi, M. Cossi, J. M. Millam, M. Klene, C. Adamo, R. Cammi, J. W. Ochterski, R. L. Martin, K. Morokuma, O. Farkas, J. B. Foresman, D. J. Fox, Gaussian 09, revision D. 01, **2009**.

[177] S. Grimme, *J. Comput. Chem.* **2006**, *27*(15), 1787–1799.

[178] R. Dovesi, R. Orlando, A. Erba, C. M. Zicovich-Wilson, B. Civalleri, S. Casassa, L. Maschio, M. Ferrabone, M. De La Pierre, P. D'Arco, Y. Noël, M. Causà, M. Rérat, *Int. J. Quantum Chem.* **2014**, *114*(19), 1287–1317.

[179] E. D. Glendening, C. R. Landis, F. Weinhold, *J. Comput. Chem.* **2013**, *34*(16), 1429–1437.

[180] T. A. Keith, AIMAll, Version 17, **2013**.

[181] M. Kohout, DGrid, version 5.0, **2016**.

[182] M. A. Spackman, D. Jayatilaka, *CrystEngComm* **2009**, *11*(1), 19–32.

[183] J. J. McKinnon, D. Jayatilaka, M. A. Spackman, *ChemComm* **2007**, (37), 3814–3816.

[184] S. Wolff, D. Grimwood, J. McKinnon, M. Turner, D. Jayatilaka, M. Spackman, Crystal explorer, **2012**.

[185] I. V. Alabugin, S. Bresch, M. Manoharan, *J. Phys. Chem. A* **2014**, *118*(20), 3663–3677.

[186] C. A. Coulson, *Coulson's valence*, Oxford University Press, USA, **1979**.

# Appendix

CHEMISTRY
A European Journal

Supporting Information

# A Variety of Bond Analysis Methods, One Answer? An Investigation of the Element–Oxygen Bond of Hydroxides $H_nXOH$

Malte Fugel,[a] Jens Beckmann,[a] Dylan Jayatilaka,[b] Gerald V. Gibbs,[c] and Simon Grabowsky*[a]

chem_201800453_sm_miscellaneous_information.pdf

## 1 Laplacian of the electron density

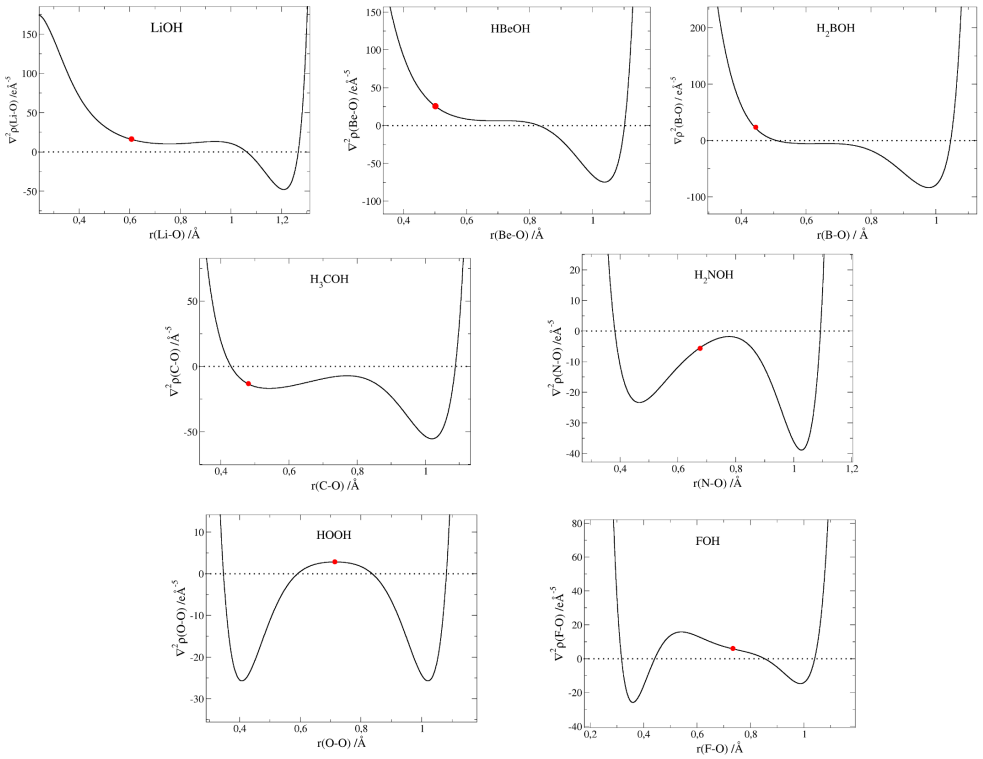


**Figure S1.** The Laplacian of the electron density, $\nabla^2\rho$, plotted along the X – O bond for the 2nd period model compounds.

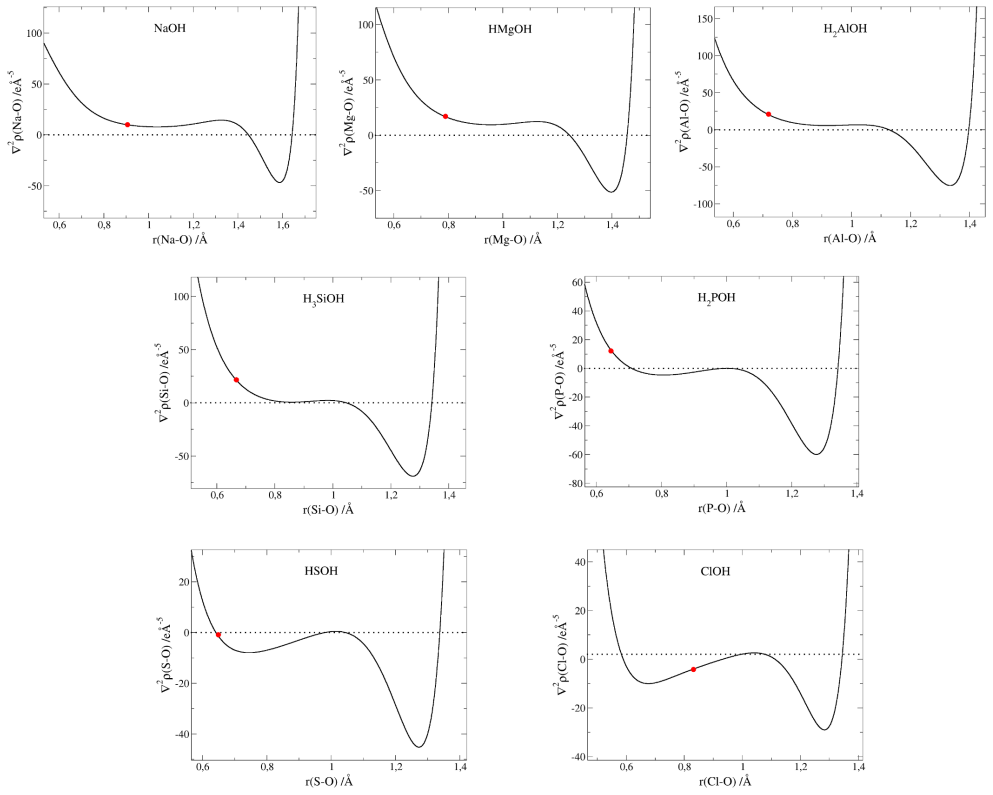


**Figure S2.** The Laplacian of the electron density, $\nabla^2\rho$, plotted along the X – O bond for the 3rd period model compounds.

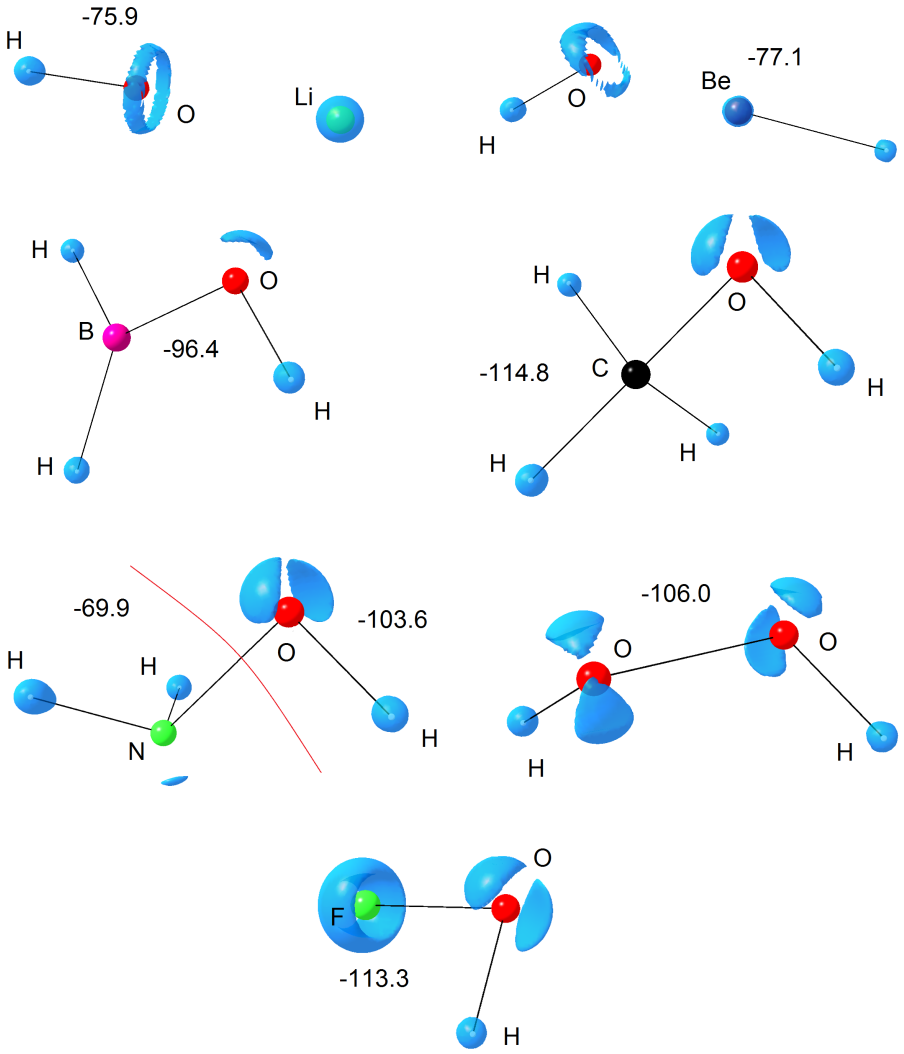


**Figure S3.** Iso-surfaces of the Laplacian of the electron density, $\nabla^2\rho$ (in eÅ$^{-5}$), of the 2nd period model compounds revealing features that may be attributed to atomic shells, lone pairs and bonds; the iso-values are given inside the figures; regions of different iso-values are separated by a red line

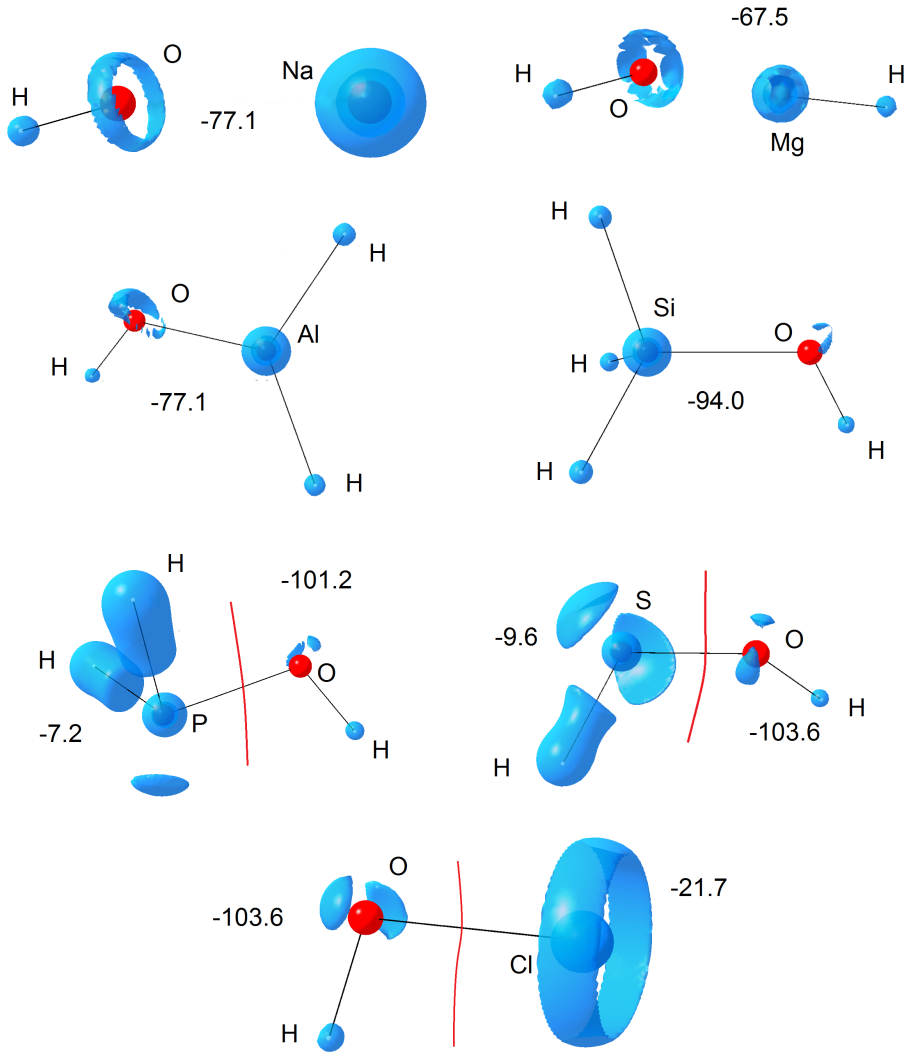


**Figure S4.** Iso-surfaces of the Laplacian of the electron density, $\nabla^2\rho$ (in eÅ$^{-5}$), of the 3rd period model compounds revealing features that may be attributed to atomic shells, lone pairs and bonds; the iso-values are given inside the figures; regions of different iso-values are separated by a red line

## 2 Local source function

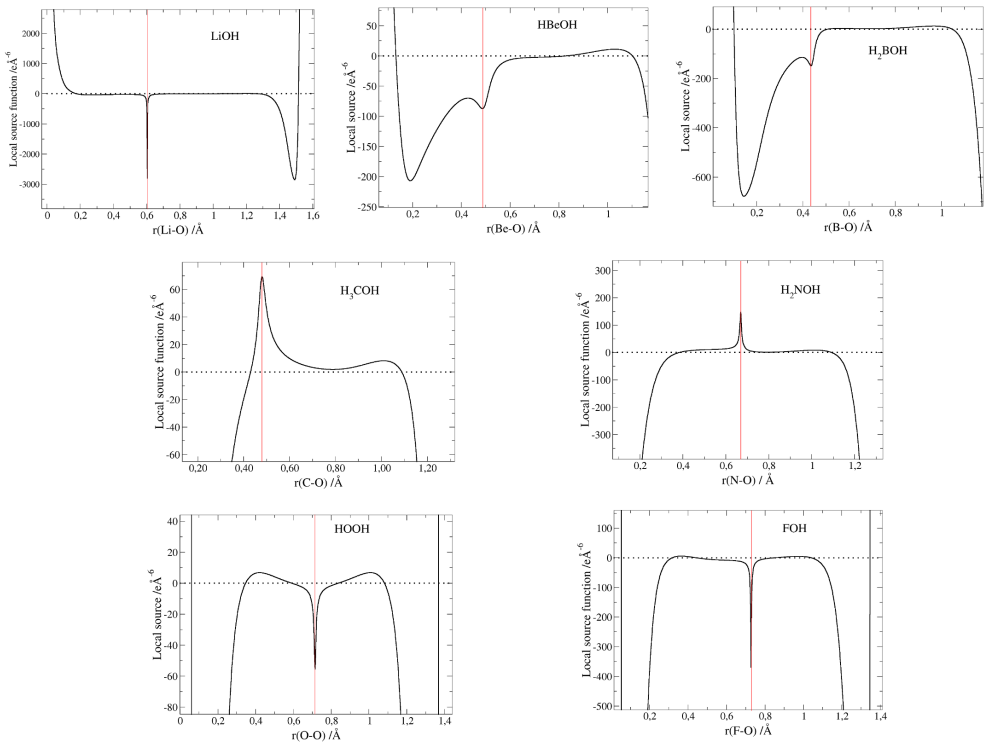


**Figure S5.** The local source function plotted along the X – O bond for the 2nd period model compounds.

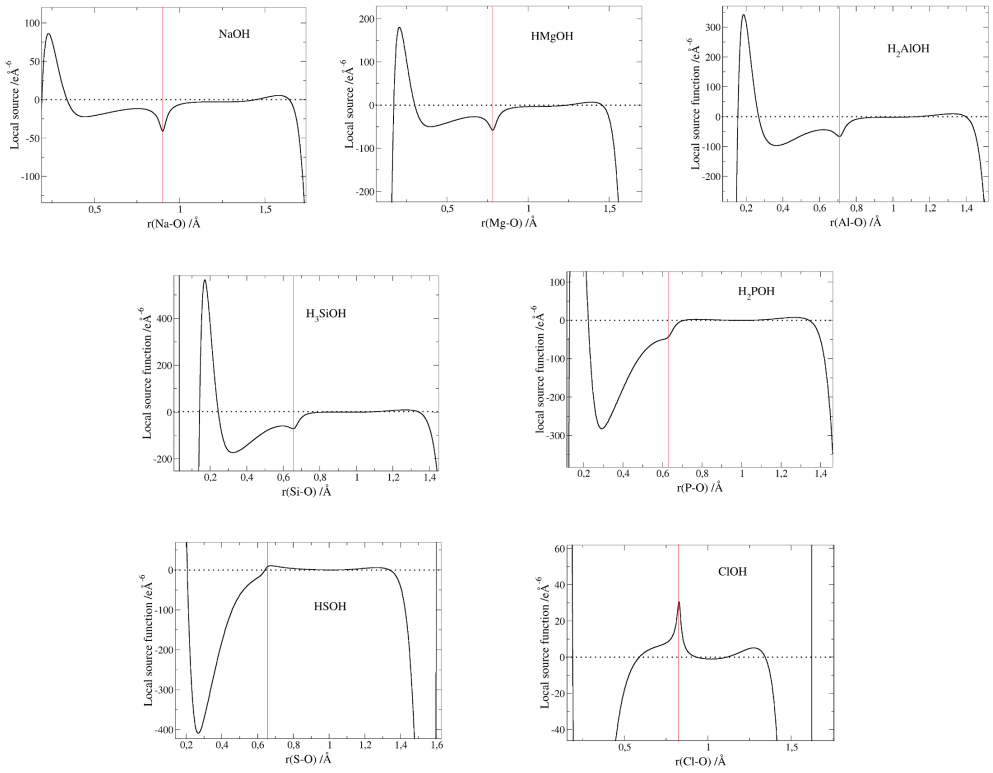


**Figure S6.** The local source function plotted along the X – O bond for the 3rd period model compounds.

### 3 Electron localizability indicator

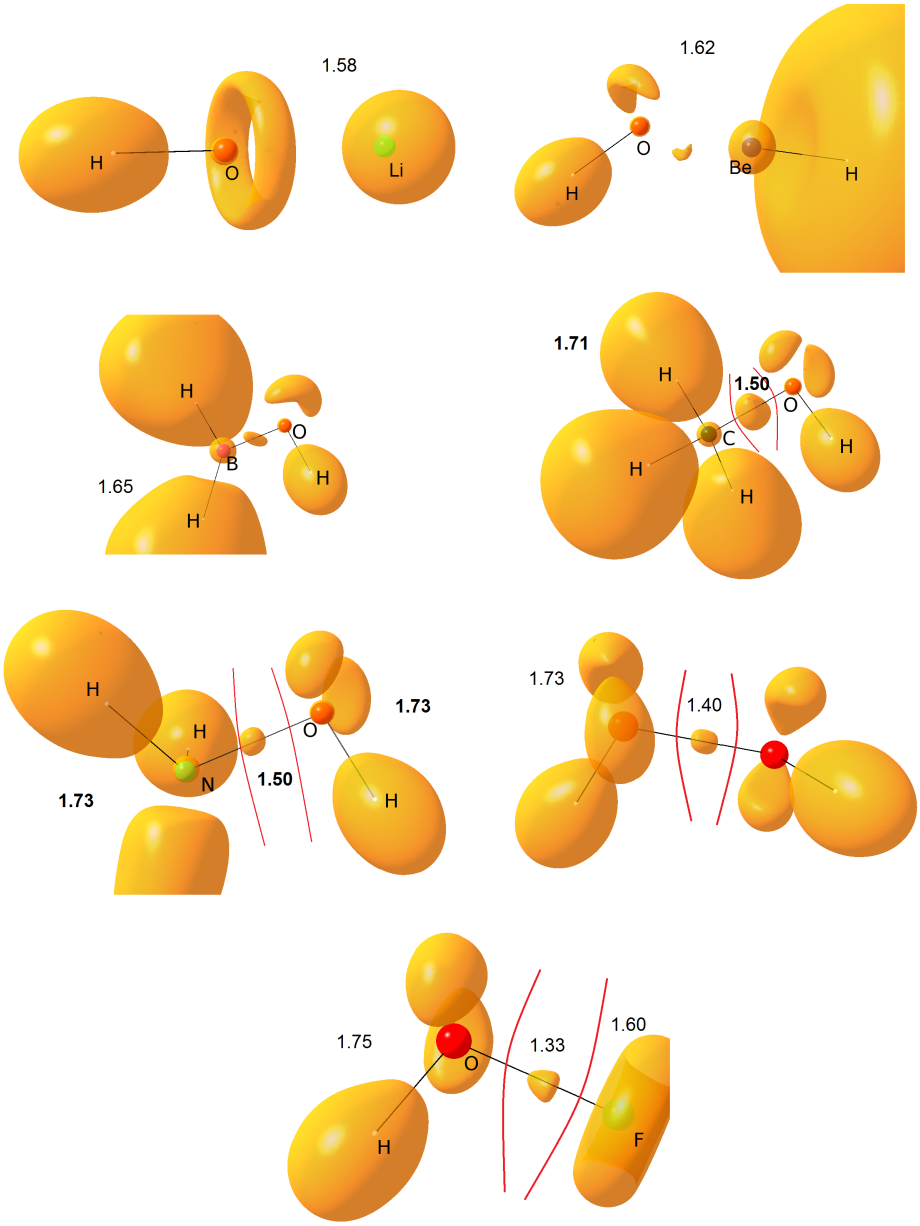


**Figure S7.** Iso-surfaces of the ELI-D of the 2nd period model compounds revealing features that may be attributed to atomic shells, lone pairs and bonds; the iso-values are given inside the figures; regions of different iso-values are separated by a red line

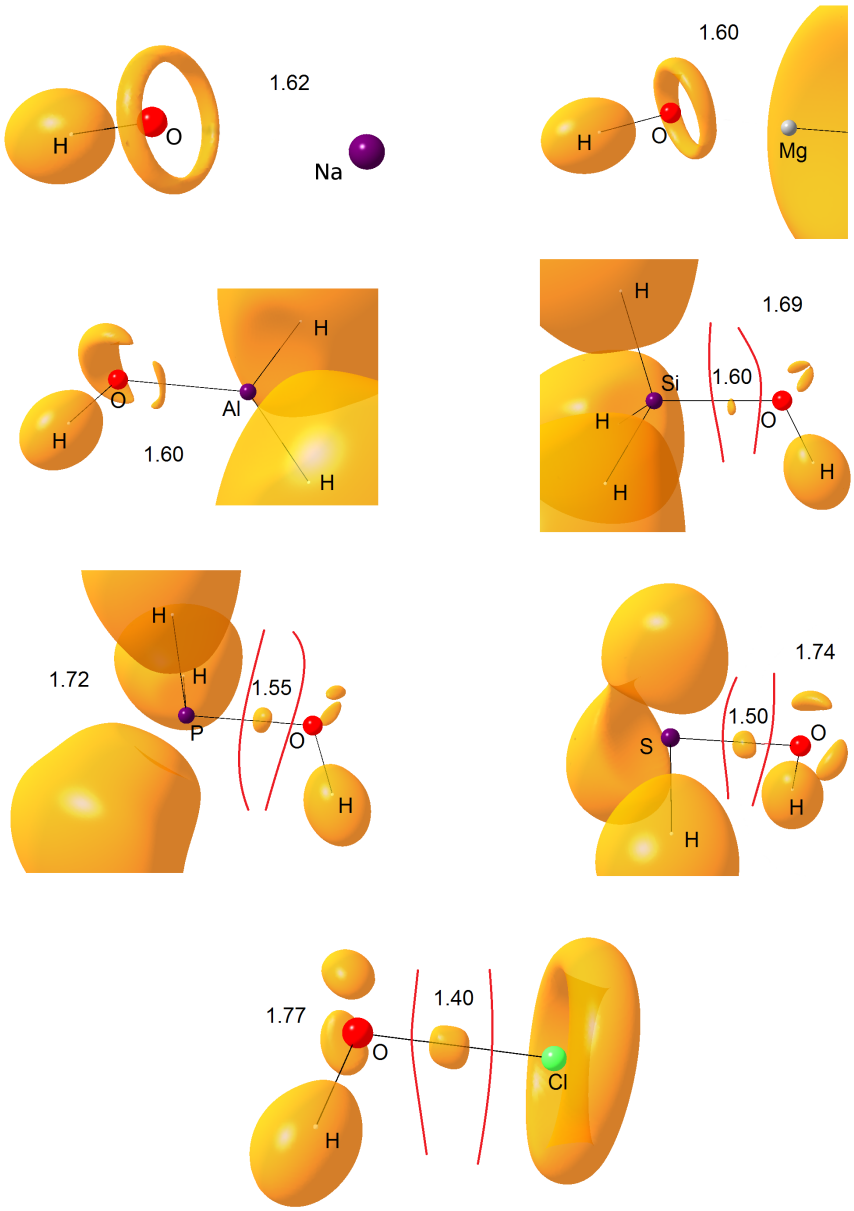


**Figure S8.** Iso-surfaces of the ELI-D of the 3rd period model compounds revealing features that may be attributed to atomic shells, lone pairs and bonds; the iso-values are given inside the figures; regions of different iso-values are separated by a red line

## 4 Natural bond orbitals

**Table S1.** Population (N in e) of the X – O natural bond orbitals, the percentages of the polarization coefficients (%c(O) and %c(X)) and the s- and p-character of the X and O hybrids (%s and %p)

| | N | %c(O) | %s(O) | %p(O) | %c(X) | %s(X) | %p(X) |
|---|---|---|---|---|---|---|---|
| LiOH | – | – | – | – | – | – | – |
| HBeOH | – | – | – | – | – | – | – |
| $H_2BOH$ | 1.96935 | 80.29 | 44.74 | 54.83 | 19.71 | 27.48 | 72.24 |
| | 1.95511 | 90.20 | 0.00 | 99.78 | 9.80 | 0.00 | 99.12 |
| $H_3COH$ | 1.96042 | 66.34 | 24.57 | 75.19 | 33.66 | 24.57 | 75.19 |
| $H_2NOH$ | 1.94713 | 57.80 | 17.80 | 81.89 | 42.20 | 17.70 | 81.95 |
| HOOH | 1.93568 | 50.00 | 11.76 | 87.90 | 50.00 | 11.75 | 87.90 |
| FOH | 1.93036 | 42.05 | 7.87 | 91.63 | 57.95 | 8.37 | 91.42 |
| NaOH | – | – | – | – | – | – | – |
| HMgOH | – | – | – | – | – | – | – |
| $H_2AlOH$ | 1.95788 | 91.05 | 43.81 | 55.96 | 8.98 | 23.74 | 74.52 |
| $H_3SiOH$ | 1.95809 | 84.62 | 38.07 | 61.59 | 15.38 | 19.14 | 78.71 |
| $H_2POH$ | 1.95474 | 78.05 | 26.58 | 72.96 | 21.95 | 12.55 | 85.42 |
| HSOH | 1.99599 | 69.95 | 20.32 | 79.33 | 30.05 | 12.06 | 86.23 |
| ClOH | 1.93884 | 60.55 | 10.79 | 88.74 | 39.45 | 7.82 | 90.61 |

**Table S2.** Population (N in e) and s- and p-character (%s and %p) of the oxygen lone pair NBOs

| | LP1(O) | | | LP2(O) | | | LP3(O) | | |
|---|---|---|---|---|---|---|---|---|---|
| | N | %s | %p | N | %s | %p | N | %s | %p |
| LiOH | 1.98937 | 71.68 | 28.30 | 1.98173 | 0 | 99.98 | 1.98173 | 0.00 | 99.98 |
| HBeOH | 1.97496 | 24.93 | 74.94 | 1.95910 | 0.00 | 99.88 | 1.89276 | 43.48 | 56.36 |
| $H_2BOH$ | 1.95061 | 35.61 | 64.27 | – | – | – | – | – | – |
| $H_3COH$ | 1.95777 | 51.81 | 48.09 | 1.93205 | 0.00 | 99.81 | – | – | – |
| $H_2NOH$ | 1.97044 | 60.97 | 38.98 | 1.94859 | 0.00 | 99.86 | – | – | – |
| HOOH | 1.97155 | 67.27 | 32.69 | 1.96120 | 0.02 | 99.85 | – | – | – |
| FOH | 1.97162 | 71.47 | 28.50 | 1.96516 | 0.00 | 99.87 | – | – | – |
| NaOH | 1.95972 | 73.36 | 26.64 | 1.93587 | 0.00 | 99.98 | 1.93449 | 1.44 | 98.54 |
| HMgOH | 1.94912 | 20.86 | 79.11 | 1.94330 | 0.00 | 99.98 | 1.91381 | 50.38 | 49.59 |
| $H_2AlOH$ | 1.94903 | 33.16 | 66.72 | 1.87981 | 0.00 | 99.85 | – | – | – |
| $H_3SiOH$ | 1.94415 | 40.02 | 59.83 | 1.91185 | 0.00 | 99.81 | – | – | – |
| $H_2POH$ | 1.96321 | 51.21 | 48.66 | 1.91473 | 0.00 | 99.75 | – | – | – |
| HSOH | 1.99555 | 55.70 | 44.22 | 1.97183 | 0.38 | 99.44 | – | – | – |
| ClOH | 1.97010 | 67.33 | 32.60 | 1.95890 | 0.00 | 99.82 | – | – | – |

**Table S3.** Population (N in e) and s- and p-character (%s and %p) of the X lone pair NBOs

| | LP1(X) | | | LP2(X) | | | LP3(X) | | |
|---|---|---|---|---|---|---|---|---|---|
| | N | %s | %p | N | %s | %p | N | %s | %p |
| $H_2NOH$ | 1.95718 | 33.96 | 65.92 | – | – | – | – | – | – |
| HOOH | 1.97155 | 67.27 | 32.69 | 1.96120 | 0.02 | 99.85 | – | – | – |
| FOH | 1.97387 | 91.76 | 8.24 | 1.97151 | 0.07 | 99.90 | 1.97162 | 71.47 | 28.50 |
| $H_2POH$ | 1.93711 | 57.88 | 42.10 | – | – | – | – | – | – |
| HSOH | 1.95327 | 75.60 | 24.26 | 1.93527 | 0.94 | 98.97 | – | – | – |
| ClOH | 1.96757 | 92.44 | 7.53 | 1.95142 | 0.00 | 99.99 | 1.94809 | 0.18 | 99.80 |

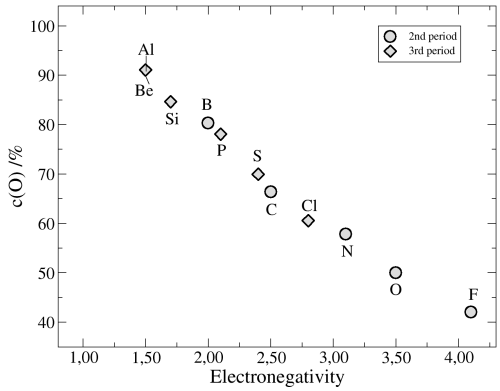


**Figure S9.** Plot of the polarization coefficient c(O) from the NBO analysis against the electronegativity of X

## 5 Tabulated properties

**Table S4.** Values of all plotted properties: Electronegativity (EN), X–O bond lengths ($r$(X–O) in Å), the Laplacian of the electron density at the X–O bcp ($\nabla^2\rho_{bcp}$ in eÅ$^{-5}$), the total energy density at the X–O bcp ($H_{bcp}$ in Hartree/bohr$^3$), the Bader and NPA charges of the OH fragment ($q_{Bader}$ and $q_{NPA}$ in e), the Raub-Jansen index of the oxygen atom ($RJI$(O) in %), the ionic or covalent resonance energy from the valence bond calculations ($RE_{ion/cov}$ in Hartree), the parameter $Q$ and the bond dissociation energy ($D_E$ in Hartree)

| | EN | $r$(X–O) | $\nabla^2\rho_{bcp}$ | $H_{bcp}$ | $q_{Bader}$(OH) | $q_{NPA}$(OH) | $RJI$(O) | $RE_{ion/cov}$ | $Q$ | $D_E$ |
|---|---|---|---|---|---|---|---|---|---|---|
| LiOH | 1.0 | 1.583 | 16.2 | 0.015 | -0.96 | -0.90 | – | -0.052 | -15.56 | -0.165 |
| HBeOH | 1.5 | 1.410 | 26.7 | -0.036 | -0.85 | -0.81 | 97.1 | -0.078 | -1.43 | -0.240 |
| $H_2BOH$ | 2.0 | 1.354 | 23.6 | -0.214 | -0.75 | -0.35 | 95.3 | -0.104 | 1.90 | -0.249 |
| $H_3COH$ | 2.5 | 1.416 | -13.1 | -0.388 | -0.48 | -0.25 | 83.4 | -0.099 | 0.61 | -0.150 |
| $H_2NOH$ | 3.1 | 1.436 | -6.0 | -0.241 | -0.15 | -0.12 | 58.5 | -0.096 | 1.69 | -0.107 |
| HOOH | 3.5 | 1.441 | 2.8 | -0.188 | 0.02 | 0.02 | 50.0 | -0.099 | 5.19 | -0.084 |
| FOH | 4.1 | 1.419 | 6.0 | -0.196 | 0.21 | 0.16 | 41.7 | -0.112 | 6.71 | -0.081 |
| NaOH | 1.0 | 1.962 | 10.0 | 0.011 | -0.90 | -0.92 | – | -0.043 | -28.69 | -0.117 |
| HMgOH | 1.2 | 1.775 | 17.1 | 0.006 | -0.86 | -0.89 | – | -0.057 | -9.43 | -0.173 |
| $H_2AlOH$ | 1.5 | 1.705 | 21.0 | -0.009 | -0.82 | -0.68 | 96.2 | -0.065 | -2.63 | -0.205 |
| $H_3SiOH$ | 1.7 | 1.655 | 21.6 | -0.052 | -0.77 | -0.57 | 93.8 | -0.089 | -1.06 | -0.141 |
| $H_2POH$ | 2.1 | 1.663 | 14.0 | -0.127 | -0.71 | -0.46 | 90.6 | -0.121 | 1.08 | -0.201 |
| HSOH | 2.4 | 1.672 | -0.9 | -0.234 | -0.51 | -0.34 | 83.0 | -0.106 | 5.84 | -0.110 |
| ClOH | 2.8 | 1.696 | -4.2 | -0.171 | -0.16 | -0.18 | 57.8 | -0.092 | 7.18 | -0.087 |

## 6 Coordinates of geometry optimized structures

**Table S5.** Atomic coordinates of the geometry optimized $H_nXOH$ model compounds (in Å)

| | x | y | z |
|---|---|---|---|
| Li | -0.556293 | 0.462423 | -0.006609 |
| O | -2.029643 | 1.020901 | 0.013102 |
| H | -2.917158 | 1.361753 | 0.025130 |

| | x | y | z |
|---|---|---|---|
| Be | 0.041250 | 0.852850 | 0.000000 |
| H | 0.083273 | 2.185075 | 0.000000 |
| O | 0.062345 | -0.557223 | 0.000000 |
| H | -0.602108 | -1.234281 | 0.000000 |

| | x | y | z |
|---|---|---|---|
| B | -1.850381 | -0.104836 | 0.069221 |
| H | -2.284732 | 1.003725 | 0.190678 |
| H | -2.526220 | -1.023006 | -0.276588 |
| O | -0.547251 | -0.367340 | 0.324440 |
| H | -0.059409 | 0.410704 | 0.597182 |

| | x | y | z |
|---|---|---|---|
| C | -1.405722 | 0.767151 | -0.009285 |
| H | -1.033792 | -0.254621 | -0.026462 |
| H | -1.046449 | 1.246934 | 0.904817 |
| H | -2.497998 | 0.733473 | 0.016112 |
| O | -0.917172 | 1.405023 | -1.175767 |
| H | -1.239236 | 2.305959 | -1.172245 |

| | x | y | z |
|---|---|---|---|
| N | -2.554956 | -0.453428 | 0.013820 |
| H | -2.128301 | -1.373132 | -0.004808 |
| H | -2.128292 | 0.022232 | 0.801172 |
| O | -1.991340 | 0.207076 | -1.130055 |
| H | -2.773868 | 0.482056 | -1.607480 |

| | x | y | z |
|---|---|---|---|
| O | -1.488038 | 0.878341 | 0.095750 |
| H | -1.646897 | 1.805227 | -0.102538 |
| O | -0.048045 | 0.851230 | 0.061263 |
| H | 0.094206 | 0.300567 | -0.713453 |

| | x | y | z |
|---|---|---|---|
| F | -2.133458 | -0.450529 | 0.000978 |
| O | -3.551270 | -0.513735 | -0.001229 |
| H | -3.732889 | 0.4330050 | 0.031832 |

| | x | y | z |
|---|---|---|---|
| Na | 0.001750 | -0.933587 | 0.000000 |
| O | 0.030090 | 1.028656 | 0.000000 |
| H | -0.177708 | 1.955062 | 0.000000 |

| | x | y | z |
|---|---|---|---|
| Mg | -0.135331 | 0.236788 | -0.028322 |
| H | -1.821052 | 0.462798 | 0.044629 |
| O | 1.630580 | 0.070101 | -0.082125 |
| H | 2.476203 | -0.332742 | -0.212153 |

| | x | y | z |
|---|---|---|---|
| Al | -1.695415 | -0.501383 | 0.066740 |
| H | -2.540587 | 0.811994 | -0.174426 |
| H | -2.267994 | -1.982421 | 0.005254 |
| O | -0.020760 | -0.230834 | 0.421148 |
| H | 0.591531 | -0.958384 | 0.586217 |

| | x | y | z |
|---|---|---|---|
| Si | -0.827023 | -0.785963 | 0.429001 |
| H | -0.305026 | -2.165667 | 0.369030 |
| H | -0.348794 | -0.119532 | 1.666072 |
| H | -2.310533 | -0.809637 | 0.470856 |
| O | -0.264590 | -0.029238 | -0.931133 |
| H | -0.512901 | 0.885140 | -1.053238 |

| | x | y | z |
|---|---|---|---|
| P | -1.373893 | 0.291627 | -0.000153 |
| H | -0.621650 | 0.916753 | 1.027000 |
| H | -0.622975 | 0.918730 | -1.026716 |
| O | -0.612251 | -1.186772 | -0.004326 |
| H | -1.278705 | -1.873080 | 0.004197 |

| | x | y | z |
|---|---|---|---|
| S | -1.415771 | 1.002485 | 0.190476 |
| H | -0.602972 | 1.099105 | -0.876302 |
| O | -2.007488 | 2.565844 | 0.187160 |
| H | -2.804859 | 2.555977 | -0.346047 |

| | x | y | z |
|---|---|---|---|
| Cl | 0.68935 | 0.127089 | -0.017750 |
| O | -1.00549 | 0.078551 | -0.019445 |
| H | -1.24208 | 1.010430 | 0.013097 |

CHEMISTRY
A European Journal

Supporting Information

# Covalency and Ionicity Do Not Oppose Each Other—Relationship Between Si–O Bond Character and Basicity of Siloxanes

Malte Fugel,[a] Maxie F. Hesse,[a] Rumpa Pal,[a] Jens Beckmann,[a] Dylan Jayatilaka,[b] Michael J. Turner,[b] Amir Karton,[b] Patrick Bultinck,[c] Graham S. Chandler,[b] and Simon Grabowsky*[a]

chem_201802197_sm_miscellaneous_information.pdf

# Supporting Information – Covalency and ionicity do not oppose each other – Relationship between Si-O bond character and basicity of siloxanes

**Malte Fugel[a], Maxie F. Hesse[a], Rumpa Pal[a], Jens Beckmann[a], Dylan Jayatilaka[b], Michael J. Turner[b], Amir Karton[b], Patrick Bultinck[c], Graham S. Chandler[b], and Simon Grabowsky[a,*]**

[a]University of Bremen, Department 2: Biology/Chemistry, Institute of Inorganic Chemistry and Crystallography, Leobener Str. 3 and 7, 28359 Bremen, Germany.
[b]University of Western Australia, School of Molecular Sciences, 35 Stirling Highway, Perth WA 6009, Australia.
[c]Ghent University, Department of Inorganic and Physical Chemistry, Krijgslaan 281, 9000 Gent, Belgium.
[*]simon.grabowsky@uni-bremen.de

## 1 Details on the W1-F12 thermochemical protocol

In order to obtain reliable H-bond interaction energies between the siloxane and the HOX species (X = H and $SiH_3$), calculations have been carried out using the high-level, ab initio W1-F12 thermochemical protocol with the Molpro 2012.1 program suite.[1] The W1-F12 thermochemical protocol[2] (and its earlier version W1[3]) are widely used for the calculation of thermochemical and kinetic properties.[4,5] These theories represent layered extrapolations to the relativistic, all-electron CCSD(T) (coupled cluster with singles, doubles, and quasiperturbative triple excitations) basis-set-limit energy, and can achieve "sub-chemical accuracy" (e.g., W1-F12 theory is associated with a mean absolute deviation of 0.32 kcal/mol from accurate atomization energies of molecules whose wave functions are dominated by dynamical correlation).[2] Nevertheless, it should be pointed out that for H-bond interactions these theories yield even better performance due to a larger degree of systematic error cancelation between reactants and products.[6] W1-F12 theory combines explicitly-correlated F12 methods with extrapolation techniques in order to approximate the CCSD(T) basis-set-limit energy.[6] The computational protocol of the W1-F12 method has been specified and rationalized in detail in 2. In brief, the Hartree-Fock component is extrapolated from the cc-pVDZ-F12 and cc-pVTZ-F12 basis sets, which were specifically developed for explicitly correlated calculations,[7] using the $E(L) = E_{\text{inf}} + A/L\alpha$ two-point extrapolation formula with $\alpha = 5.00$. The valence CCSD-F12 correlation energy is extrapolated from the same basis sets, using the same two-point extrapolation formula but with $\alpha = 3.67$. In all of the explicitly correlated coupled cluster calculations the diagonal, fixed-amplitude 3C(FIX) ansatz[8] and the CCSD-F12b approximation are employed.[9,10] The (T) valence correlation energy is obtained in the same way as in the original W1 theory i.e., extrapolated from the A'VDZ and A'VTZ basis sets using the above two-point extrapolation formula with $\alpha = 3.22$ (where A'VnZ indicates the combination of the standard correlation-consistent cc-pVnZ basis sets on H,[11] the aug-cc-pVnZ basis sets on first-row elements,[12] and the aug-cc-pV(n+d)Z basis sets on second-row elements[13]). The CCSD inner-shell contribution is calculated with the core-valence weighted correlation-consistent aug'-cc-pwCVTZ basis set of Peterson and Dunning, whilst the (T) inner-shell contribution is calculated with the cc-pwCVTZ (no f) basis set (where cc-pwCVTZ (no f) indicates the cc-pwCVTZ basis set without the f functions).[14] The scalar relativistic contribution (in the second-order Douglas-Kroll-Hess approximation)[15,16] is obtained as the difference between non-relativistic CCSD(T)/A'VDZ and relativistic CCSD(T)/A'VDZ-DK calculations.[17] The W1-F12 hydrogen-bond strengths were calculated using two sets of geometries. The first set consists of fully relaxed structures. These structures were confirmed to be equilibrium structures via harmonic vibrational calculations (i.e. they have all real frequencies). The second set of structures consists of partially constrained reference geometries. In these geometry optimizations the $H_3Si-O-SiH_3$ angle was kept fixed at a value of $\alpha$, while all other degrees of freedom were fully relaxed. The $\alpha$ angle was scanned between 103° and 168°. All the geometry optimizations were carried out at the B3LYP/A'VTZ level of theory,[18,19] using the Gaussian 09 program suite.[20]

## 2 Tabulated values

**Table S1.** The hydrogen bond interaction energies ($E_e$ and $E_0$ referring to the energy at the minimum of the potential energy surface and the zero-point corrected energy, respectively) of disiloxane···HOX and n-membered cyclic siloxane···HOX (X = H and $SiH_3$; n = 3, 4, 5) complexes (in $kJ{\cdot}mol^{-1}$) calculated from the W1-F12 thermochemical protocol in dependence of the Si – O – Si angle

| | $E_e$ | | $E_0$ | |
|---|---|---|---|---|
| Si-O-Si angle /° | X = H | X = $SiH_3$ | X = H | X = $SiH_3$ |
| 103 | 17.33 | 23.06 | 11.13 | 18.48 |
| 104 | 17.26 | 23.00 | 11.08 | 18.44 |
| 105 | 17.21 | 22.94 | 11.05 | 18.41 |
| 106 | 17.15 | 22.88 | 11.00 | 18.37 |
| 107 | 17.09 | 22.81 | 10.96 | 18.32 |
| 108 | 17.03 | 22.74 | 10.92 | 18.28 |
| 109 | 16.96 | 22.67 | 10.87 | 18.23 |
| 110 | 16.89 | 22.59 | 10.82 | 18.17 |
| 111 | 16.83 | 22.52 | 10.77 | 18.12 |
| 112 | 16.76 | 22.44 | 10.72 | 18.04 |
| 113 | 16.69 | 22.35 | 10.67 | 17.96 |
| 114 | 16.62 | 22.26 | 10.62 | 17.88 |
| 115 | 16.55 | 22.18 | 10.57 | 17.81 |
| 116 | 16.46 | 22.09 | 10.51 | 17.73 |
| 117 | 16.38 | 21.98 | 10.44 | 17.65 |
| 118 | 16.29 | 21.88 | 10.37 | 17.57 |
| 119 | 16.20 | 21.78 | 10.30 | 17.48 |
| 120 | 16.11 | 21.68 | 10.24 | 17.39 |
| 121 | 16.02 | 21.57 | 10.17 | 17.30 |
| 122 | 15.93 | 21.46 | 10.10 | 17.20 |
| 123 | 15.84 | 21.35 | 10.02 | 17.11 |
| 124 | 15.75 | 21.23 | 9.94 | 17.02 |
| 125 | 15.65 | 21.11 | 9.87 | 16.92 |
| 126 | 15.55 | 20.99 | 9.79 | 16.81 |
| 127 | 15.44 | 20.87 | 9.70 | 16.69 |
| 128 | 15.29 | 20.71 | 9.53 | 16.53 |
| 129 | 15.16 | 20.58 | 9.36 | 16.39 |
| 130 | 15.01 | 20.46 | 9.32 | 16.46 |
| 131 | 14.89 | 20.31 | 9.33 | 16.29 |
| 132 | 14.79 | 20.15 | 9.19 | 16.13 |
| 133 | 14.68 | 20.04 | 9.14 | 16.04 |
| 134 | 14.55 | 19.87 | 9.02 | 15.89 |
| 135 | 14.41 | 19.69 | 8.89 | 15.73 |
| 136 | 14.27 | 19.51 | 8.75 | 15.56 |
| 137 | 14.12 | 19.32 | 8.62 | 15.38 |
| 138 | 13.96 | 19.13 | 8.49 | 15.19 |
| 139 | 13.81 | 18.93 | 8.36 | 14.98 |
| 140 | 13.64 | 18.72 | 8.22 | 14.77 |
| 141 | 13.48 | 18.51 | 8.07 | 14.57 |
| 142 | 13.30 | 18.29 | 7.92 | 14.38 |
| 143 | 13.13 | 18.07 | 7.77 | 14.19 |
| 144 | 12.95 | 17.84 | 7.61 | 14.00 |
| 145 | 12.76 | 17.61 | 7.45 | 13.81 |
| 146 | 12.57 | 17.36 | 7.30 | 13.61 |
| 147 | 12.38 | 17.11 | 7.15 | 13.41 |
| 148 | 12.18 | 16.85 | 6.99 | 13.18 |
| 149 | 11.98 | 16.59 | 6.84 | 12.95 |
| 150 | 11.77 | 16.32 | 6.68 | 12.72 |
| 151 | 11.56 | 16.04 | 6.53 | 12.48 |
| 152 | 11.35 | 15.76 | 6.38 | 12.24 |
| 153 | 11.15 | 15.47 | 6.25 | 12.00 |
| 154 | 10.92 | 15.17 | 6.10 | 11.78 |
| 155 | 10.68 | 14.87 | 5.96 | 11.49 |
| 156 | 10.45 | 14.56 | 5.75 | 11.17 |
| 157 | 10.21 | 14.24 | 5.59 | 10.9 |
| 158 | 9.98 | 13.91 | 5.45 | 10.63 |
| 159 | 9.74 | 13.58 | 5.30 | 10.37 |
| 160 | 9.49 | 13.24 | 5.17 | 10.11 |
| 161 | 9.25 | 12.89 | 5.08 | 9.87 |
| 162 | 9.00 | 12.54 | 5.04 | 9.68 |
| 163 | 8.74 | 12.17 | 4.96 | 9.43 |
| 164 | 8.49 | 11.81 | 4.82 | 9.40 |
| 165 | 8.22 | 11.51 | 4.65 | 8.99 |
| 166 | 7.96 | 11.12 | 4.44 | 8.59 |
| 167 | 7.71 | 10.77 | 4.38 | 8.32 |
| 168 | 7.44 | 8.84 | 4.38 | 6.82 |
| 3-mem (80.5°) | 22.00 | – | 15.80 | – |
| 4-mem (96.2°) | 21.29 | – | 15.01 | – |
| 5-mem (116.1°) | 18.78 | – | 12.78 | – |
| freely optimized disiloxane | 13.63 (141.2°) | 18.90 (138.9°) | 7.85 (141.2°) | 14.59 (138.9°) |

**Table S2.** The hybridization of the oxygen hybrid orbital of the Si−O bond and the $sp^{\lambda}$-type oxygen lone pair NBO, $\lambda = \%p/\%s$, of the disiloxane and n-membered cyclic siloxane systems in dependence of the Si−O−Si angle

| Si-O-Si angle /° | LP(O), %s | LP(O), %p | BD(Si-O), %s | BD(Si-O), %p |
|---|---|---|---|---|
| 105 | 42.08 | 57.46 | 28.97 | 70.27 |
| 110 | 38.10 | 61.44 | 30.96 | 68.34 |
| 115 | 34.38 | 65.17 | 32.83 | 66.54 |
| 120 | 30.73 | 68.84 | 34.66 | 64.77 |
| 125 | 27.12 | 72.48 | 36.48 | 63.01 |
| 130 | 24.10 | 75.52 | 37.90 | 61.62 |
| 135 | 19.90 | 79.76 | 39.87 | 59.71 |
| 140 | 16.09 | 83.60 | 41.74 | 57.88 |
| 145 | 12.60 | 87.11 | 43.49 | 56.16 |
| 150 | 9.47 | 90.26 | 45.07 | 54.60 |
| 155 | 6.71 | 93.03 | 46.47 | 53.22 |
| 160 | 4.34 | 95.41 | 47.67 | 52.03 |
| 161 | 3.92 | 95.83 | 47.88 | 51.82 |
| 162 | 3.52 | 96.23 | 48.08 | 51.62 |
| 163 | 3.13 | 96.61 | 48.27 | 51.43 |
| 164 | 2.77 | 96.98 | 48.46 | 51.24 |
| 165 | 2.42 | 97.32 | 48.63 | 51.07 |
| 166 | 2.30 | 97.44 | 48.78 | 50.93 |
| 167 | 1.98 | 97.75 | 48.94 | 50.77 |
| 168 | 1.69 | 98.04 | 49.08 | 50.62 |
| 169 | 1.42 | 98.31 | 49.22 | 50.49 |
| 170 | 1.18 | 98.56 | 49.34 | 50.37 |
| 171 | 0.95 | 98.78 | 49.45 | 50.26 |
| 172 | 0.75 | 98.99 | 49.55 | 50.15 |
| 173 | 0.57 | 99.16 | 49.64 | 50.07 |
| 174 | 0.42 | 99.31 | 49.72 | 49.99 |
| 175 | 0.29 | 99.44 | 49.78 | 49.93 |
| 176 | 0.19 | 99.55 | 49.83 | 49.87 |
| 177 | 0.10 | 99.63 | 49.87 | 49.83 |
| 178 | 0.05 | 99.69 | 49.90 | 49.80 |
| 179 | 0.01 | 99.73 | 49.92 | 49.79 |
| 180 | 0.00 | 99.73 | 49.93 | 49.78 |
| 3-mem (80.8°) | 44.99 | 54.47 | 27.53 | 71.49 |
| 4-mem (96.2°) | 33.38 | 66.12 | 33.32 | 65.90 |
| 5-mem (116.4°) | 25.29 | 73.99 | 37.25 | 61.99 |

**Table S3.** The oxygen lone pair populations, N(LP(O)) (in e), and the summed delocalization energies $\sum$ E(2) (in kJ·mol$^{-1}$), which can be attributed to the LP(O) $\rightarrow \sigma^*$(Si – H) interactions in dependence of the Si – O – Si angle

| Si-O-Si angle /° | N(LP(O)), sp$^\lambda$ | N(LP(O)), p | $\sum$E(2), sp$^\lambda$ | $\sum$E(2), p |
|---|---|---|---|---|
| 105 | 1.94876 | 1.90334 | 17.11256 | 48.53440 |
| 110 | 1.94613 | 1.90488 | 18.91168 | 47.90680 |
| 115 | 1.94328 | 1.90633 | 20.66896 | 47.27920 |
| 120 | 1.94026 | 1.90764 | 22.38440 | 46.73528 |
| 125 | 1.93710 | 1.90880 | 25.52240 | 45.31272 |
| 130 | 1.93182 | 1.91046 | 26.98680 | 45.73112 |
| 135 | 1.92986 | 1.91024 | 29.20432 | 45.10352 |
| 140 | 1.92762 | 1.91060 | 32.00760 | 44.85248 |
| 145 | 1.92534 | 1.91122 | 34.22512 | 44.64328 |
| 150 | 1.92306 | 1.91208 | 36.23344 | 44.51776 |
| 155 | 1.92092 | 1.91303 | 38.11624 | 44.43408 |
| 160 | 1.91910 | 1.91389 | 39.62248 | 44.35040 |
| 161 | 1.91877 | 1.91406 | 39.91536 | 44.30856 |
| 162 | 1.91843 | 1.91424 | 40.33376 | 44.30856 |
| 163 | 1.91812 | 1.91441 | 40.62664 | 44.30856 |
| 164 | 1.91782 | 1.91457 | 41.00320 | 44.30856 |
| 165 | 1.91753 | 1.91473 | 41.42160 | 44.26672 |
| 166 | 1.91668 | 1.91553 | 42.38392 | 44.43408 |
| 167 | 1.91650 | 1.91559 | 42.67680 | 44.43408 |
| 168 | 1.91635 | 1.91560 | 42.88600 | 44.39224 |
| 169 | 1.91622 | 1.91567 | 43.13704 | 44.43408 |
| 170 | 1.91611 | 1.91570 | 43.34624 | 44.39224 |
| 171 | 1.91602 | 1.91573 | 43.51360 | 44.39224 |
| 172 | 1.91587 | 1.91577 | 43.72280 | 44.18304 |
| 173 | 1.91580 | 1.91578 | 44.30856 | 44.01568 |
| 174 | 1.91579 | 1.91574 | 44.35040 | 44.14120 |
| 175 | 1.91579 | 1.91570 | 44.26672 | 44.22488 |
| 176 | 1.91578 | 1.91566 | 44.26672 | 44.26672 |
| 177 | 1.91577 | 1.91565 | 44.26672 | 44.30856 |
| 178 | 1.91575 | 1.91566 | 44.26672 | 44.30856 |
| 179 | 1.91572 | 1.91562 | 44.26672 | 44.26672 |
| 180 | 1.91631 | 1.91534 | 43.97384 | 44.47592 |
| 3-mem (80.8°) | 1.94876 | 1.90334 | 17.11256 | 48.53440 |
| 4-mem (96.2°) | 1.97220 | 1.87698 | 4.10032 | 54.72672 |
| 5-mem (116.4°) | 1.94892 | 1.89626 | 15.73184 | 48.28336 |

**Table S4.** The electron density at the Si – O bond critical point, $\rho_{bcp}$(Si – O) (in e·Å$^{-3}$), and the silicon-oxygen bond length, r(Si – O), (in Å) of the disiloxane and n-membered cyclic siloxane systems in dependence of the Si – O – Si angle

| Si – O – Si angle /° | $\rho_{bcp}$(Si – O) | r(Si – O) |
|---|---|---|
| 105 | 1.6835 | 0.8786 |
| 110 | 1.6746 | 0.8908 |
| 115 | 1.6676 | 0.8996 |
| 120 | 1.6616 | 0.9063 |
| 125 | 1.6564 | 0.9110 |
| 130 | 1.6520 | 0.9151 |
| 135 | 1.6477 | 0.9184 |
| 140 | 1.6437 | 0.9218 |
| 145 | 1.6402 | 0.9238 |
| 150 | 1.6371 | 0.9259 |
| 155 | 1.6345 | 0.9272 |
| 160 | 1.6323 | 0.9286 |
| 161 | 1.6319 | 0.9292 |
| 162 | 1.6315 | 0.9292 |
| 163 | 1.6312 | 0.9292 |
| 164 | 1.6308 | 0.9299 |
| 165 | 1.6305 | 0.9299 |
| 166 | 1.6302 | 0.9299 |
| 167 | 1.6300 | 0.9299 |
| 168 | 1.6296 | 0.9306 |
| 169 | 1.6295 | 0.9306 |
| 170 | 1.6293 | 0.9306 |
| 171 | 1.6292 | 0.9306 |
| 172 | 1.6288 | 0.9313 |
| 173 | 1.6287 | 0.9313 |
| 174 | 1.6286 | 0.9313 |
| 175 | 1.6285 | 0.9313 |
| 176 | 1.6283 | 0.9313 |
| 177 | 1.6283 | 0.9313 |
| 178 | 1.6282 | 0.9313 |
| 179 | 1.6282 | 0.9313 |
| 180 | 1.6296 | 0.9286 |
| 3-mem (80.8°) | 0.857 | 1.6997 |
| 4-mem (96.2°) | 0.8915 | 1.6805 |
| 5-mem (116.4°) | 0.9077 | 1.6622 |

**Table S5.** The Laplacian of the electron density at the Si – O bond critical point, $\nabla^2\rho_{bcp}$(Si – O) (in e·Å$^{-5}$), of the disiloxane and n-membered cyclic siloxane systems in dependence of the Si – O – Si angle

| Si-O-Si angle /° | $\nabla^2\rho_{bcp}$(Si – O) |
|---|---|
| 105 | 17.1246 |
| 110 | 17.7632 |
| 115 | 18.2958 |
| 120 | 18.7753 |
| 125 | 19.2139 |
| 130 | 19.5995 |
| 135 | 19.9899 |
| 140 | 20.3562 |
| 145 | 20.6912 |
| 150 | 20.9900 |
| 155 | 21.2527 |
| 160 | 21.4768 |
| 161 | 21.5178 |
| 162 | 21.5563 |
| 163 | 21.5925 |
| 164 | 21.6262 |
| 165 | 21.6599 |
| 166 | 21.6889 |
| 167 | 21.7202 |
| 168 | 21.7563 |
| 169 | 21.7684 |
| 170 | 21.7877 |
| 171 | 21.8045 |
| 172 | 21.8383 |
| 173 | 21.8527 |
| 174 | 21.8672 |
| 175 | 21.8792 |
| 176 | 21.8913 |
| 177 | 21.9009 |
| 178 | 21.9058 |
| 179 | 21.9082 |
| 180 | 21.7901 |
| 3-mem (80.8°) | 16.7703 |
| 4-mem (96.2°) | 17.5511 |
| 5-mem (116.4°) | 18.8067 |

**Table S6.** The source function of the oxygen basin to the electron density at the bond critical point of all three Si−H bonds of the $SiH_3$ group in dependence of the Si−O−Si angle

| Si-O-Si angle /° | %SF(O→Si-H bcp) |
|---|---|
| 105 | 15.8442 |
| 110 | 15.9218 |
| 115 | 15.8953 |
| 120 | 15.8827 |
| 125 | 15.9079 |
| 130 | 15.9371 |
| 135 | 15.9908 |
| 140 | 16.0409 |

| Si-O-Si angle /° | %SF(O→Si-H bcp) |
|---|---|
| 145 | 16.0889 |
| 150 | 16.1348 |
| 155 | 16.1757 |
| 160 | 16.2117 |
| 165 | 16.2341 |
| 170 | 16.2654 |
| 175 | 16.2783 |
| 180 | 16.2525 |

**Table S7.** The ELI-D oxygen lone pair and Si−O bond populations (in e) of the disiloxane and n-membered cyclic siloxane systems in dependence of the Si−O−Si angle

| Si-O-Si angle /° | N(LP(O)) | N(Si-O) |
|---|---|---|
| 105 | 4.6359 | 3.0722 |
| 110 | 4.5266 | 3.1841 |
| 115 | 4.4425 | 3.2674 |
| 120 | 4.3795 | 3.3325 |
| 125 | 4.3230 | 3.3910 |
| 130 | 4.2894 | 3.4267 |
| 135 | 4.2411 | 3.4786 |
| 140 | 4.2140 | 3.5102 |
| 145 | 4.1938 | 3.5306 |
| 150 | 4.2035 | 3.5215 |
| 155 | 4.2444 | 3.4847 |
| 160 | 4.3489 | 3.3837 |
| 161 | 4.3742 | 3.3568 |
| 162 | 4.4102 | 3.3205 |
| 163 | 4.4517 | 3.2791 |
| 164 | 4.5007 | 3.2290 |
| 165 | 4.5644 | 3.1665 |
| 166 | 4.2547 | 3.4781 |

| Si-O-Si angle /° | N(LP(O)) | N(Si-O) |
|---|---|---|
| 167 | 4.5647 | 3.1681 |
| 168 | 4.7476 | 2.9825 |
| 169 | 4.8827 | 2.8450 |
| 170 | 4.9942 | 2.7347 |
| 171 | 5.0768 | 2.6556 |
| 172 | 5.1554 | 2.5760 |
| 173 | 5.2181 | 2.5162 |
| 174 | 5.2657 | 2.4656 |
| 175 | 5.3101 | 2.4212 |
| 176 | 5.3540 | 2.3798 |
| 177 | 5.3791 | 2.3530 |
| 178 | 5.3956 | 2.3372 |
| 179 | 5.4032 | 2.3272 |
| 180 | 5.4275 | 2.3010 |
| 3-mem (80.8°) | 2.9978 | 4.6045 |
| 4-mem (96.2°) | 3.4298 | 4.2770 |
| 5-mem (116.4°) | 3.4738 | 4.2477 |

**Table S8.** The Bader ($q_{Bader}$ in e), Hirshfeld-I ($q_{HI}$ in e) and NPA charges ($q_{NPA}$ in e) of the silicon atom of the disiloxane systems in dependence of the Si−O−Si angle.

| Si-O-Si angle /° | $q_{Bader}$ | $q_{HI}$ | $q_{NPA}$ |
|---|---|---|---|
| 105 | 2.8507 | 1.4080 | 1.1842 |
| 110 | 2.8548 | 1.4304 | 1.1989 |
| 115 | 2.8608 | 1.4496 | 1.2109 |
| 120 | 2.8645 | 1.4665 | 1.2213 |
| 125 | 2.8680 | 1.4812 | 1.2300 |
| 130 | 2.8699 | 1.4902 | 1.2350 |
| 135 | 2.8732 | 1.5041 | 1.2434 |
| 140 | 2.8770 | 1.5165 | 1.2503 |
| 145 | 2.8799 | 1.5275 | 1.2561 |
| 150 | 2.8820 | 1.5366 | 1.2609 |
| 155 | 2.8853 | 1.5443 | 1.2650 |
| 160 | 2.8869 | 1.5505 | 1.2683 |
| 161 | 2.8872 | 1.5516 | 1.2689 |
| 162 | 2.8877 | 1.5526 | 1.2694 |
| 163 | 2.8877 | 1.5536 | 1.2699 |
| 164 | 2.8887 | 1.5546 | 1.2704 |

| Si-O-Si angle /° | $q_{Bader}$ | $q_{HI}$ | $q_{NPA}$ |
|---|---|---|---|
| 165 | 2.8889 | 1.5555 | 1.2709 |
| 166 | 2.8889 | 1.5564 | 1.2712 |
| 167 | 2.8900 | 1.5573 | 1.2716 |
| 168 | 2.8892 | 1.5580 | 1.2720 |
| 169 | 2.8895 | 1.5587 | 1.2724 |
| 170 | 2.8902 | 1.5593 | 1.2727 |
| 171 | 2.8909 | 1.5599 | 1.2730 |
| 172 | 2.8912 | 1.5605 | 1.2733 |
| 173 | 2.8913 | 1.5609 | 1.2736 |
| 174 | 2.8913 | 1.5613 | 1.2738 |
| 175 | 2.8911 | 1.5616 | 1.2740 |
| 176 | 2.8912 | 1.5619 | 1.2741 |
| 177 | 2.8912 | 1.5621 | 1.2743 |
| 178 | 2.8917 | 1.5623 | 1.2744 |
| 179 | 2.8913 | 1.5623 | 1.2743 |
| 180 | 2.8908 | 1.5617 | 1.2742 |

**Table S9.** The Bader ($q_{Bader}$ in e), Hirshfeld-I ($q_{HI}$ in e) and NPA charges ($q_{NPA}$ in e) of the oxygen atom of the disiloxane and n-membered cyclic siloxane systems in dependence of the Si – O – Si angle.

| Si-O-Si angle /° | $q_{Bader}$ | $q_{HI}$ | $q_{NPA}$ |
|---|---|---|---|
| 105 | -1.6404 | -0.9518 | -1.1945 |
| 110 | -1.6464 | -0.9735 | -1.2055 |
| 115 | -1.6507 | -0.9934 | -1.2144 |
| 120 | -1.6551 | -1.0145 | -1.2221 |
| 125 | -1.6591 | -1.0341 | -1.2288 |
| 130 | -1.6623 | -1.0484 | -1.2324 |
| 135 | -1.6673 | -1.0663 | -1.2390 |
| 140 | -1.6720 | -1.0837 | -1.2451 |
| 145 | -1.6766 | -1.0996 | -1.2507 |
| 150 | -1.6807 | -1.1130 | -1.2557 |
| 155 | -1.6846 | -1.1237 | -1.2602 |
| 160 | -1.6879 | -1.1322 | -1.2640 |
| 161 | -1.6885 | -1.1337 | -1.2647 |
| 162 | -1.6891 | -1.1351 | -1.2653 |
| 163 | -1.6897 | -1.1365 | -1.2659 |
| 164 | -1.6902 | -1.1379 | -1.2665 |
| 165 | -1.6907 | -1.1392 | -1.2671 |
| 166 | -1.6907 | -1.1403 | -1.2676 |
| 167 | -1.6916 | -1.1414 | -1.2681 |
| 168 | -1.6921 | -1.1424 | -1.2685 |
| 169 | -1.6924 | -1.1434 | -1.2690 |
| 170 | -1.6928 | -1.1443 | -1.2694 |
| 171 | -1.6931 | -1.1451 | -1.2698 |
| 172 | -1.6937 | -1.1459 | -1.2701 |
| 173 | -1.6937 | -1.1466 | -1.2704 |
| 174 | -1.6940 | -1.1472 | -1.2706 |
| 175 | -1.6942 | -1.1478 | -1.2709 |
| 176 | -1.6943 | -1.1482 | -1.2710 |
| 177 | -1.6943 | -1.1486 | -1.2712 |
| 178 | -1.6945 | -1.1489 | -1.2713 |
| 179 | -1.6946 | -1.1492 | -1.2713 |
| 180 | -1.6942 | -1.1488 | -1.2713 |
| 3-mem (80.8°) | -1.6464 | -0.7894 | -1.2101 |
| 4-mem (96.2°) | -1.6443 | -0.9878 | -1.2308 |
| 5-mem (116.4°) | -1.6513 | -1.0305 | -1.2451 |

**Table S10.** The Bader, Hirshfeld-I and NPA charges ($\sum q_{Bader}(H)$, $\sum q_{HI}(H)$ and $\sum q_{NPA}(H)$ in e) of the three hydrogen atoms of one $SiH_3$ group in dependence of the Si – O – Si angle

| Si-O-Si angle /° | $\sum q_{Bader}(H)$ | $\sum q_{HI}(H)$ | $\sum q_{NPA}(H)$ |
|---|---|---|---|
| 105 | -2.0303 | -0.9318 | -0.5872 |
| 110 | -2.0331 | -0.9432 | -0.5964 |
| 115 | -2.0353 | -0.9527 | -0.6041 |
| 120 | -2.0372 | -0.9590 | -0.6106 |
| 125 | -2.0388 | -0.9635 | -0.6160 |
| 130 | -2.0385 | -0.9659 | -0.6188 |
| 135 | -2.0399 | -0.9707 | -0.6239 |
| 140 | -2.0410 | -0.9747 | -0.6277 |
| 145 | -2.0418 | -0.9776 | -0.6307 |
| 150 | -2.0425 | -0.9800 | -0.6331 |
| 155 | -2.0430 | -0.9820 | -0.6349 |
| 160 | -2.0434 | -0.9839 | -0.6363 |
| 165 | -2.0437 | -0.9854 | -0.6373 |
| 170 | -2.0439 | -0.9874 | -0.6380 |
| 175 | -2.0441 | -0.9880 | -0.6386 |
| 180 | -2.0439 | -0.9873 | -0.6385 |

**Table S11.** Different bond indices (Hirshfeld-I SEDI, Roby bond index, Bader's delocalization index, NLMO/NPA bond order and natural bond order) of the Si – O bonds of the disiloxane and n-membered cyclic siloxane systems in dependence of the Si – O – Si angle

| Si-O-Si angle /° | Hirshfeld-I SEDI | Roby bond index | Delocalization index | NLMO/NPA BO | Natural BO |
|---|---|---|---|---|---|
| 105 | 1.1116 | 1.3394 | 0.4392 | 0.3629 | 1.0171 |
| 110 | 1.1153 | 1.3592 | 0.4382 | 0.3584 | 1.0155 |
| 115 | 1.1183 | 1.3770 | 0.4348 | 0.3544 | 1.0167 |
| 120 | 1.1222 | 1.3927 | 0.4330 | 0.3508 | 1.0188 |
| 125 | 1.1264 | 1.4065 | 0.4308 | 0.3473 | 1.0206 |
| 130 | 1.1310 | 1.4207 | 0.4294 | 0.3468 | 1.0220 |
| 135 | 1.1338 | 1.4309 | 0.4269 | 0.3432 | 1.0235 |
| 140 | 1.1365 | 1.4396 | 0.4244 | 0.3404 | 1.0248 |
| 145 | 1.1389 | 1.4471 | 0.4221 | 0.3371 | 1.0259 |
| 150 | 1.1410 | 1.4534 | 0.4204 | 0.3343 | 1.0268 |
| 155 | 1.1427 | 1.4588 | 0.4185 | 0.3319 | 1.0276 |
| 160 | 1.1440 | 1.4632 | 0.4167 | 0.3298 | 1.0282 |
| 161 | 1.1443 | 1.4640 | 0.4164 | 0.3294 | 1.0283 |
| 162 | 1.1445 | 1.4647 | 0.4159 | 0.3291 | 1.0284 |
| 163 | 1.1447 | 1.4654 | 0.4159 | 0.3287 | 1.0285 |
| 164 | 1.1449 | 1.4660 | 0.4155 | 0.3284 | 1.0286 |
| 165 | 1.1451 | 1.4666 | 0.4151 | 0.3281 | 1.0287 |
| 166 | 1.1452 | 1.4673 | 0.4149 | 0.3285 | 1.0361 |
| 167 | 1.1454 | 1.4678 | 0.4149 | 0.3282 | 1.0363 |
| 168 | 1.1456 | 1.4683 | 0.4151 | 0.3276 | 1.0364 |
| 169 | 1.1456 | 1.4687 | 0.4148 | 0.3277 | 1.0368 |
| 170 | 1.1457 | 1.4691 | 0.4145 | 0.3275 | 1.0363 |
| 171 | 1.1457 | 1.4695 | 0.4139 | 0.3273 | 1.0363 |
| 172 | 1.1460 | 1.4698 | 0.4135 | 0.3266 | 1.0367 |
| 173 | 1.1461 | 1.4701 | 0.4134 | 0.3265 | 1.0365 |
| 174 | 1.1462 | 1.4703 | 0.4136 | 0.3268 | 1.0366 |
| 175 | 1.1462 | 1.4705 | 0.4137 | 0.3267 | 1.0366 |
| 176 | 1.1463 | 1.4707 | 0.4136 | 0.3266 | 1.0366 |
| 177 | 1.1464 | 1.4708 | 0.4134 | 0.3265 | 1.0374 |
| 178 | 1.1465 | 1.4709 | 0.4129 | 0.3264 | 1.0366 |
| 179 | 1.1465 | 1.4710 | 0.4135 | 0.3260 | 1.0368 |
| 180 | 1.1453 | 1.4708 | 0.4134 | 0.3264 | 1.0373 |
| 3-mem (80.8°) | 1.2910 | 1.2978 | 0.5926 | 0.3593 | 1.0188 |
| 4-mem (96.2°) | 1.0507 | 1.3692 | 0.4137 | 0.3444 | 1.0109 |
| 5-mem (116.4°) | 1.0631 | 1.4111 | 0.4153 | 0.3382 | 1.0189 |

**Table S12.** NBO bond ionicity of the Si – O bonds of the disiloxane and n-membered cyclic siloxane systems in dependence of the Si – O – Si angle

| Si – O – Si angle /° | Bond ionicity |
|---|---|
| 105 | 0.6890 |
| 110 | 0.6932 |
| 115 | 0.6968 |
| 120 | 0.7000 |
| 125 | 0.7030 |
| 130 | 0.7060 |
| 135 | 0.7094 |
| 140 | 0.7124 |
| 145 | 0.7152 |
| 150 | 0.7175 |
| 155 | 0.7198 |
| 160 | 0.7216 |
| 161 | 0.7220 |
| 162 | 0.7222 |
| 163 | 0.7226 |
| 164 | 0.7228 |
| 165 | 0.7232 |
| 166 | 0.7234 |
| 167 | 0.7236 |
| 168 | 0.7238 |
| 169 | 0.7240 |
| 170 | 0.7242 |
| 171 | 0.7244 |
| 172 | 0.7246 |
| 173 | 0.7246 |
| 174 | 0.7248 |
| 175 | 0.7250 |
| 176 | 0.7250 |
| 177 | 0.7250 |
| 178 | 0.7252 |
| 179 | 0.7252 |
| 180 | 0.7250 |
| 3-mem (80.8°) | 0.6894 |
| 4-mem (96.2°) | 0.7046 |
| 5-mem (116.4°) | 0.7124 |

**Table S13.** The total Roby bond index and the covalent and ionic Roby bond index of the Si – O bond of the disiloxane and n-membered cyclic siloxane systems in dependence of the Si – O – Si angle

| Si-O-Si angle /° | covalent | ionic | total |
|---|---|---|---|
| 105 | 0.9965 | 0.8985 | 1.3418 |
| 110 | 1.0062 | 0.9177 | 1.3618 |
| 115 | 1.0152 | 0.9344 | 1.3797 |
| 120 | 1.0234 | 0.9489 | 1.3956 |
| 125 | 1.0309 | 0.9614 | 1.4096 |
| 130 | 1.0413 | 0.9710 | 1.4238 |
| 135 | 1.0465 | 0.9805 | 1.4341 |
| 140 | 1.0511 | 0.9885 | 1.4429 |
| 145 | 1.0551 | 0.9952 | 1.4504 |
| 150 | 1.0587 | 1.0007 | 1.4568 |
| 155 | 1.0618 | 1.0053 | 1.4622 |
| 160 | 1.0644 | 1.0090 | 1.4666 |
| 165 | 1.0664 | 1.0115 | 1.4701 |
| 170 | 1.0679 | 1.0139 | 1.4725 |
| 175 | 1.0688 | 1.0151 | 1.4740 |
| 180 | 1.0690 | 1.0152 | 1.4742 |
| 3-mem (80.8°) | 0.9413 | 0.8935 | 1.2978 |
| 4-mem (96.2°) | 0.9831 | 0.9530 | 1.3692 |
| 5-mem (116.4°) | 1.0237 | 0.9712 | 1.4111 |

## 3 ELI-D of cyclic siloxanes

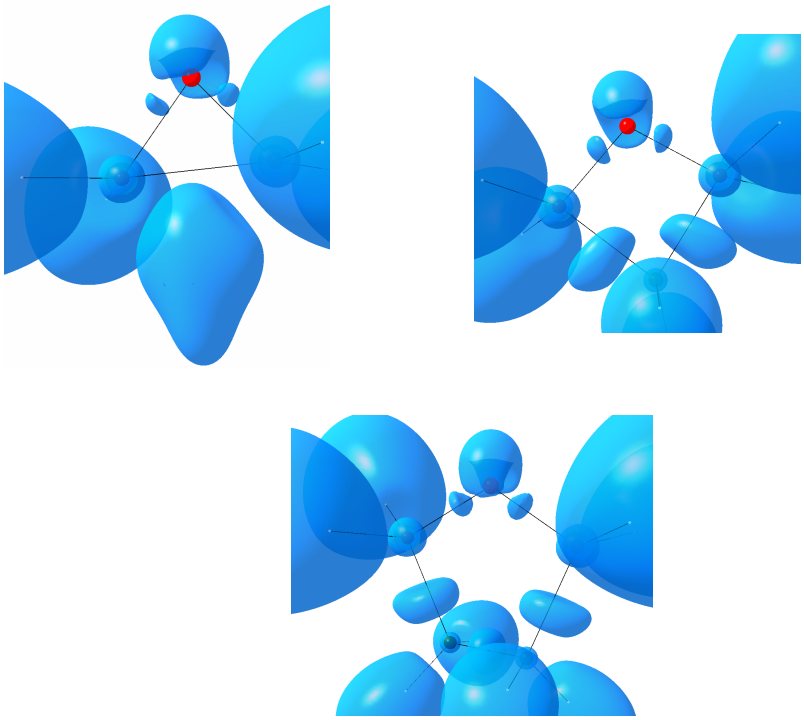

**Figure S1.** ELI-D iso surfaces (iso-value = 1.52) of the 3-, 4- and 5-membered cyclic siloxane systems.

## 4 Natural bond orbital analysis of selected complexes

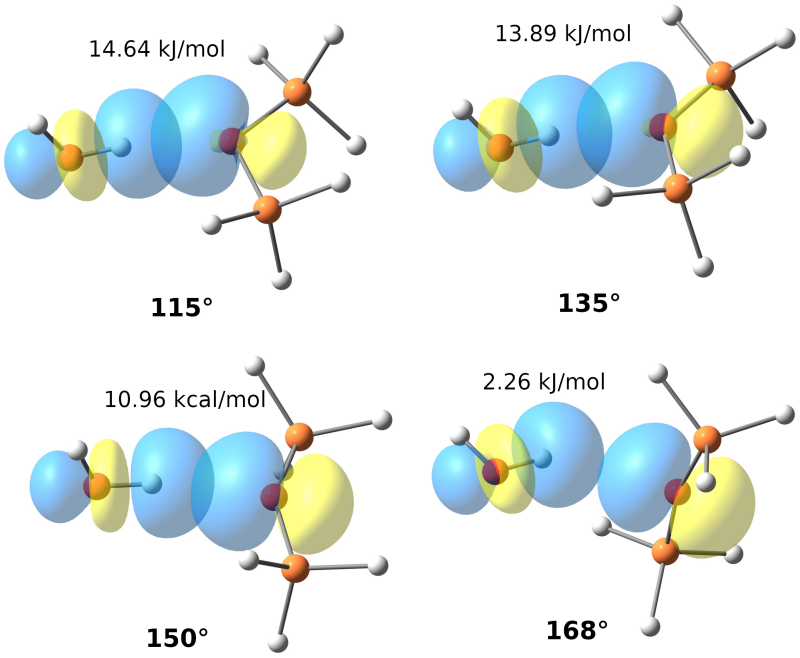


**Figure S2.** Interacting oxygen lone pair NBO of $sp^{\lambda}$-type and O – H anti-bonding NBO ($BD^{*}$(O – H)) which are related to the O···H – O hydrogen bonding. The E2 values given inside the figure show that the hydrogen bond becomes weaker as the Si – O – Si angle opens

## 5 Total energy density at Si – O bcps

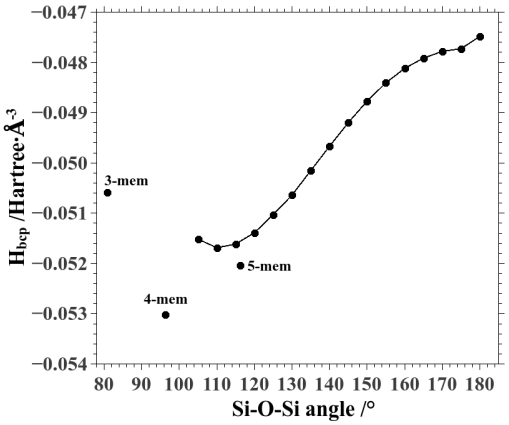


**Figure S3.** Total energy density of the disiloxane and cyclic siloxanes plotted against the Si – O – Si angle

## 6 Coordinates of the optimized structures

**Table S14.** Atomic coordinates (in Å) of the freely optimized $H_3SiOSiH_3$ molecule

| | x | y | z |
|---|---|---|---|
| O | 0.00000 | 0.0000 | 0.29177 |
| Si | 0.00000 | 1.59778 | -0.05113 |
| H | -1.20574 | 1.95087 | -0.83499 |
| H | 0.00000 | 2.35345 | 1.21875 |
| H | 1.20574 | 1.95087 | -0.83499 |
| Si | 0.00000 | -1.59778 | -0.05113 |
| H | 1.20574 | -1.95087 | -0.83499 |
| H | 0.00000 | -2.35345 | 1.21875 |
| H | -1.20574 | -1.95087 | -0.83499 |

**Table S15.** Atomic coordinates (in Å) of the freely optimized $H_3SiOSiH_3\cdots HOH$ complex

| | x | y | z |
|---|---|---|---|
| O | 0.13781 | 0.18219 | 0.00000 |
| Si | 0.13781 | 0.73073 | 1.55827 |
| H | -1.24429 | 1.03214 | 1.98718 |
| H | 0.71281 | -0.32742 | 2.41104 |
| H | 0.95990 | 1.95871 | 1.65031 |
| Si | 0.13781 | 0.73073 | -1.55827 |
| H | 0.95990 | 1.95871 | -1.65031 |
| H | 0.71281 | -0.32742 | -2.41104 |
| H | -1.24429 | 1.03214 | -1.98718 |
| H | -0.30697 | -1.86797 | 0.00000 |
| O | -0.69519 | -2.75228 | 0.00000 |
| H | 0.05042 | -3.35879 | 0.00000 |

**Table S16.** Atomic coordinates (in Å) of the freely optimized $H_3SiOSiH_3\cdots HOSiH_3$ complex

| | x | y | z |
|---|---|---|---|
| O | 0.24963 | -1.08361 | 0.00000 |
| Si | 0.35741 | -1.65426 | 1.55100 |
| H | 1.76351 | -1.98367 | 1.86883 |
| H | -0.13441 | -0.59380 | 2.44977 |
| H | -0.47428 | -2.87061 | 1.68847 |
| Si | 0.35741 | -1.65426 | -1.55100 |
| H | -0.47428 | -2.87061 | -1.68847 |
| H | -0.13441 | -0.59380 | -2.44977 |
| H | 1.76351 | -1.98367 | -1.86883 |
| H | 0.23549 | 0.92622 | 0.00000 |
| O | 0.35741 | 1.88364 | 0.00000 |
| Si | -0.95475 | 2.87767 | 0.00000 |
| H | -1.80608 | 2.67205 | 1.19859 |
| H | -0.43013 | 4.25760 | 0.00000 |
| H | -1.80608 | 2.67205 | -1.19859 |

**Table S17.** Atomic coordinates (in Å) of the freely optimized 3-membered cyclic siloxane molecule

| | x | y | z |
|---|---|---|---|
| O | 0.00000 | 0.00000 | 1.04343 |
| Si | 0.00000 | 1.10139 | -0.25120 |
| Si | 0.00000 | -1.10139 | -0.25120 |
| H | 1.21272 | 1.94304 | -0.32847 |
| H | -1.21272 | 1.94304 | -0.32847 |
| H | 1.21272 | -1.94304 | -0.32847 |
| H | -1.21272 | -1.94304 | -0.32847 |

**Table S18.** Atomic coordinates (in Å) of the freely optimized 3-membered cyclic siloxane···HOH complex

| | x | y | z |
|---|---|---|---|
| O | 0.21305 | 0.25515 | 0.00000 |
| Si | -0.06359 | -1.01820 | 1.10286 |
| Si | -0.06359 | -1.01820 | -1.10286 |
| H | 0.08596 | 2.18032 | 0.00000 |
| O | -0.06359 | 3.13899 | 0.00000 |
| H | 0.81281 | 3.53248 | 0.00000 |
| H | 1.11069 | -1.34304 | 1.93765 |
| H | -1.26765 | -0.83513 | 1.93700 |
| H | 1.11069 | -1.34304 | -1.93765 |
| H | -1.26765 | -0.83513 | -1.93700 |

**Table S19.** Atomic coordinates (in Å) of the freely optimized 4-membered cyclic siloxane molecule

| | x | y | z |
|---|---|---|---|
| O | -0.00006 | -1.18849 | 0.00000 |
| Si | -0.00004 | -0.06662 | 1.25119 |
| Si | -0.00004 | -0.06662 | -1.25119 |
| C | -0.00004 | 1.35717 | 0.00000 |
| H | 1.20599 | -0.18652 | -2.10034 |
| H | -1.20548 | -0.18661 | -2.10116 |
| H | 1.20599 | -0.18652 | 2.10034 |
| H | -1.20548 | -0.18661 | 2.10116 |
| H | 0.88701 | 1.98760 | 0.00000 |
| H | -0.88607 | 1.98896 | 0.00000 |

**Table S20.** Atomic coordinates (in Å) of the freely optimized 4-membered cyclic siloxane···HOH complex

| | x | y | z |
|---|---|---|---|
| O | 0.08031 | 0.50240 | 0.00000 |
| Si | 0.08031 | -0.62579 | 1.25761 |
| Si | 0.08031 | -0.62579 | -1.25761 |
| H | -0.25951 | 2.41523 | 0.00000 |
| O | -0.50385 | 3.35380 | 0.00000 |
| C | 0.09337 | -2.04006 | 0.00000 |
| H | -1.13087 | -0.50659 | -2.09548 |
| H | 1.28619 | -0.49057 | -2.10240 |
| H | -1.13087 | -0.50659 | 2.09548 |
| H | 1.28619 | -0.49057 | 2.10240 |
| H | 0.32849 | 3.83351 | 0.00000 |
| H | -0.78668 | -2.67990 | 0.00000 |
| H | 0.98650 | -2.66167 | 0.00000 |

**Table S21.** Atomic coordinates (in Å) of the freely optimized 5-membered cyclic siloxane molecule

| | x | y | z |
|---|---|---|---|
| O | 0.00000 | 0.00000 | 1.26380 |
| Si | 0.00000 | 1.41232 | 0.38736 |
| Si | 0.00000 | -1.41232 | 0.38736 |
| C | 0.26501 | 0.73352 | -1.36213 |
| C | -0.26501 | -0.73352 | -1.36213 |
| H | 1.33751 | 0.74064 | -1.57213 |
| H | -0.20851 | 1.33448 | -2.13964 |
| H | 0.20851 | -1.33448 | -2.13964 |
| H | -1.33751 | -0.74064 | -1.57213 |
| H | 1.29719 | -2.11123 | 0.55197 |
| H | -1.08212 | -2.30757 | 0.85441 |
| H | 1.08212 | 2.30757 | 0.85441 |
| H | -1.29719 | 2.11123 | 0.55197 |

**Table S22.** Atomic coordinates (in Å) of the freely optimized 5-membered cyclic siloxane···HOH complex

| | x | y | z |
|---|---|---|---|
| O | 0.63693 | -0.01347 | -0.08400 |
| Si | -0.26669 | -1.42068 | -0.09285 |
| Si | -0.22563 | 1.41461 | 0.03190 |
| H | 2.62065 | -0.02340 | 0.03923 |
| O | 3.58081 | -0.01759 | 0.16544 |
| C | -1.98089 | -0.72304 | 0.30031 |
| C | -1.98823 | 0.76040 | -0.17955 |
| H | -2.12662 | -0.76463 | 1.38252 |
| H | -2.79456 | -1.29607 | -0.14607 |
| H | -2.73610 | 1.35223 | 0.34968 |
| H | -2.24641 | 0.80693 | -1.24039 |
| H | 0.01613 | 2.03747 | 1.35282 |
| H | 0.20744 | 2.34723 | -1.03101 |
| H | 0.25483 | -2.36315 | 0.91882 |
| H | -0.18250 | -2.05010 | -1.43144 |
| H | 3.95250 | 0.06280 | -0.71694 |

## References


1. H.-J. Werner, P. J. Knowles, G. Knizia, F. R. Manby, M. Schütz, *Wiley Interdiscip. Rev.-Comput. Mol. Sci.* **2012**, *2*(2), 242–253.
2. A. Karton, J. M. Martin, *J. Chem. Phys.* **2012**, *136*(12), 124114.
3. J. M. Martin, G. de Oliveira, *J. Chem. Phys.* **1999**, *111*(5), 1843–1856.
4. K. A. Peterson, D. Feller, D. A. Dixon, *Theor. Chem. Acc.* **2012**, *131*(1), 1079.
5. T. Helgaker, W. Klopper, D. P. Tew, *Mol. Phys.* **2008**, *106*(16-18), 2107–2143.
6. A. Karton, S. Daon, J. M. Martin, *Chem. Phys. Lett.* **2011**, *510*(4), 165–178.
7. K. A. Peterson, T. B. Adler, H.-J. Werner, *J. Chem. Phys.* **2008**, *128*(8), 084102.
8. J. Ten-no, S.; Noga, *WIREs Comput. Mol. Sci.* **2012**, *2*, 114.
9. G. Knizia, H.-J. Werner, *J. Chem. Phys.* **2008**, *128*(15), 154103.
10. G. Knizia, T. B. Adler, H.-J. Werner, *J. Chem. Phys.* **2009**, *130*(5), 054104.
11. T. H. Dunning Jr, *J. Chem. Phys.* **1989**, *90*(2), 1007–1023.
12. R. A. Kendall, T. H. Dunning Jr, R. J. Harrison, *J. Chem. Phys.* **1992**, *96*(9), 6796–6806.
13. T. H. Dunning Jr, K. A. Peterson, A. K. Wilson, *J. Chem. Phys.* **2001**, *114*(21), 9244–9253.
14. K. A. Peterson, T. H. Dunning Jr, *J. Chem. Phys.* **2002**, *117*(23), 10548–10560.
15. M. Douglas, N. M. Kroll, *Ann. Phys.* **1974**, *82*(1), 89–155.
16. B. A. Hess, *Phys. Rev. A* **1986**, *33*(6), 3742.
17. W. A. De Jong, R. J. Harrison, D. A. Dixon, *Ann. Phys.* **2001**, *114*(1), 48–53.
18. P. J. Stephens, F. J. Devlin, C. F. Chabalowski, M. J. Frisch, *J. Phys. Chem.* **1994**, *98*, 11623.
19. S. Grimme, S. Ehrlich, L. Goerigk, *J. Comput. Chem.* **2011**, *32*(7), 1456–1465.
20. M. Frisch, G. Trucks, H. Schlegel, G. Scuseria, M. Robb, J. Cheeseman, G. Scalmani, V. Barone, B. Mennucci, G. Petersson, et al., Gaussian 09, revision D. 01, **2009**.

# Investigating the resonance in nitric acid and the nitrate anion based on a modern bonding analysis

**Malte Fugel[A], Florian Kleemiß[A], Lorraine A. Malaspina[A], Rumpa Pal[A], Peter R. Spackman[B], Dylan Jayatilaka[B], and Simon Grabowsky[A,*]**

[A]University of Bremen, Department 2 - Biology/Chemistry, Institute of Inorganic Chemistry and Crystallography, Leobener Str. 3, 28359 Bremen, Germany.
[B]University of Western Australia, School of Molecular Sciences, 35 Stirling Highway, 6009 Perth, Australia.
[*]simon.grabowsky@uni-bremen.de

## 1 Additional crystallographic information

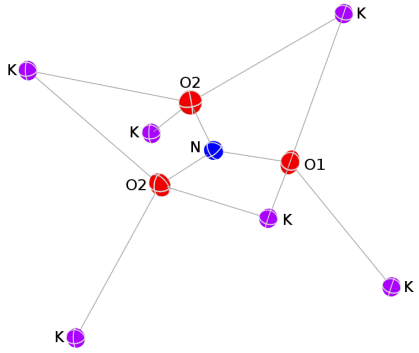


**Figure S1.** Geometry obtained from the multipole refinement (the corresponding bond lengths are listed in Table S1). The displacement parameters are visualized at 50% probability.

**Table S1.** N–O bond lengths and O–N–O angles of the $KNO_3$ crystal structure obtained from the refinements based on the IAM, MM and HAR

| | IAM | MM | HAR |
|---|---|---|---|
| r(N–O1) /Å | 1.2546(2) | 1.2551(3) | 1.2524(4) |
| r(N–O2) /Å | 1.2543(3) | 1.2523(8) | 1.2500(6) |
| $\theta$(O1–N–O2) /° | 120.03(2) | 120.12(2) | 120.07(2) |
| $\theta$(O2–N–O2) /° | 119.93(3) | 119.74(4) | 119.84(3) |

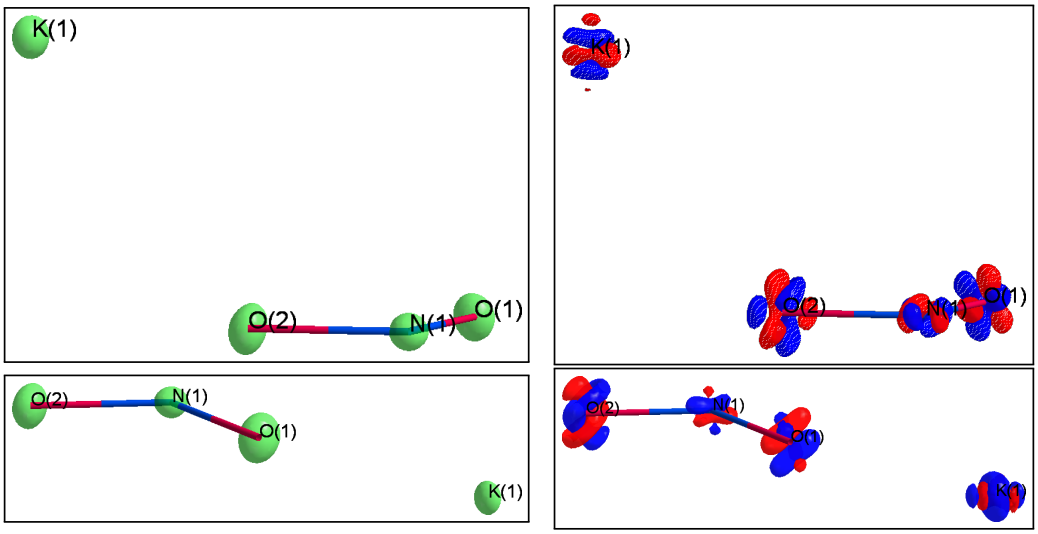


**Figure S2.** Plots of the probability density functiton (pdf): Total pdf including 2nd, 3rd and 4th order (left), and pdf including only 3rd order for N and O atoms, or 3rd and 4th order for K atoms (right) for the MM (top row) and HAR (bottom row). Different asymmetric units are shown for the MM and HAR.

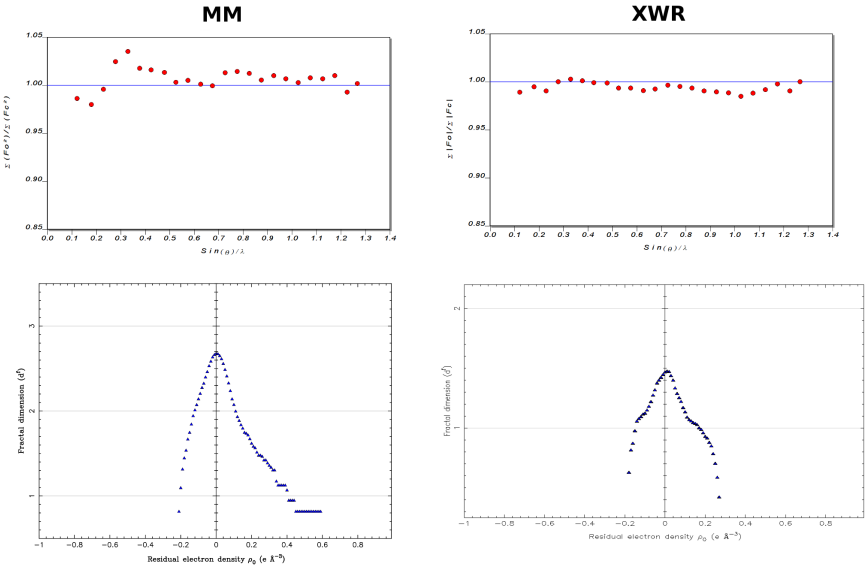


**Figure S3.** $F_o/F_c$ (top row) and fractal dimension plots (bottom row) of the MM and XWR of $KNO_3$

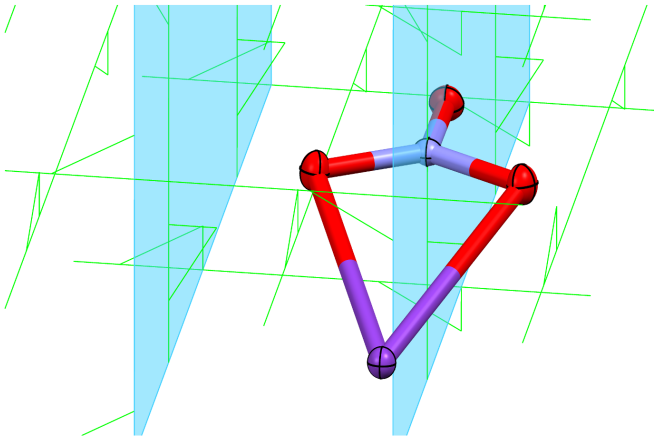

**Figure S4.** The $KNO_3$ formula unit and the crystallographic mirror plane (light blue) used to generate it from the asymmetric unit atoms. The light green lines correspond to 2-fold screw axes.

## 2 Atomic charges

**Table S2.** Bader charges (in e) for $NO_3^-$, $HNO_3$, $FNO_3$ and $KNO_3$ (from XWR and MM)

| | N | O1 | O2 | O3 | F/H/K |
|---|---|---|---|---|---|
| $NO_3^-$ | 0.846 | -0.615 | -0.615 | -0.615 | – |
| $HNO_3$ | 0.890 | -0.391 | -0.435 | -0.678 | 0.613 |
| $FNO_3$ | 0.919 | -0.373 | -0.358 | -0.037 | -0.149 |
| $KNO_3$ (MM) | 0.605 | -0.287 | -0.288 | – | 0.224 |
| $KNO_3$ (XWR) | 0.892 | -0.489 | -0.677 | – | 0.951 |

**Table S3.** NPA charges (in e) for $NO_3^-$, $HNO_3$, $FNO_3$ and $KNO_3$ (from XWR)

| | N | O1 | O2 | O3 | H/F/K |
|---|---|---|---|---|---|
| $NO_3^-$ | 0.687 | -0.562 | -0.562 | -0.562 | – |
| $HNO_3$ | 0.709 | -0.307 | -0.365 | -0.522 | 0.484 |
| $FNO_3$ | 0.699 | -0.281 | -0.263 | -0.046 | -0.109 |
| $KNO_3$ (XWR) | 0.675 | -0.431 | -0.612 | – | 0.979 |

## 3 Natural bond orbitals

**Table S4.** Delocalization energies from the second order perturbation theory (E2 energies; in kcal/mol) of the most significant interactions in $NO_3^-$, $HNO_3$ and $FNO_3$. The E2 energies correspond to the sum of the same type of interactions. The analysis is not applicable to the XWR of $KNO_3$.

| | | $NO_3^-$ | | | $HNO_3$ | | | $FNO_3$ | | |
|---|---|---|---|---|---|---|---|---|---|---|
| Donor | Acceptor | O1 | O2 | O3 | O1 | O2 | O3 | O1 | O2 | O3 |
| LP2(O) | BD*(N-O) | 33.4 | 33.4 | 33.4 | 57.7 | 54.0 | – | 74.4 | 66.4 | – |
| LP3(O) | LV(N) | 731.7 | 731.7 | 731.7 | 742.4 | 763.3 | 800.7 | 1069.4 | 975.8 | 338.5 |

**Table S5.** Population (N in e), polarization coefficients of N and O (c(N) and c(O), respectively) and the composition (%s and %p) of the N–O NBOs in $NO_3^-$, $HNO_3$, $FNO_3$ and $KNO_3$

| | | N | c(O) | %s(O) | %p(O) | c(N) | %s(N) | %p(N) |
|---|---|---|---|---|---|---|---|---|
| $NO_3^-$ | N-O1 | 1.9975 | 50.2 | 21.2 | 78.3 | 49.8 | 33.3 | 66.6 |
| | N-O2 | 1.9975 | 50.2 | 21.2 | 78.3 | 49.8 | 33.3 | 66.6 |
| | N-O3 | 1.9975 | 50.2 | 21.2 | 78.3 | 49.8 | 33.3 | 66.6 |
| $HNO_3$ | N-O1 | 1.9962 | 50.5 | 24.4 | 75.0 | 49.5 | 37.7 | 62.1 |
| | N-O2 | 1.9964 | 50.3 | 23.2 | 76.3 | 49.7 | 37.1 | 62.8 |
| | N-O3 | 1.9933 | 53.2 | 16.0 | 83.7 | 46.8 | 25.1 | 74.8 |
| $FNO_3$ | N-O1 | 1.9870 | 51.1 | 24.7 | 74.6 | 48.9 | 39.3 | 60.6 |
| | N-O2 | 1.9950 | 51.3 | 25.5 | 73.9 | 48.7 | 39.4 | 60.5 |
| | N-O3 | 1.9570 | 54.7 | 11.4 | 88.2 | 45.3 | 21.5 | 78.3 |
| $KNO_3$ (XCW) | N-O1 | 1.9964 | 49.0 | 20.4 | 79.1 | 51.0 | 34.0 | 65.84 |
| | N-O2 | 1.9976 | 50.5 | 21.6 | 77.9 | 49.5 | 32.9 | 66.9 |

## 4 Coordinates of geometry optimized structures

**Table S6.** Atomic coordinates of the optimized geometry of $NO_3^-$ (in Å)

| | x | y | z |
|---|---|---|---|
| N | 0.00000 | 0.000000 | -0.000159 |
| O1 | 0.00000 | 1.258092 | 0.000046 |
| O2 | 1.08954 | -0.629046 | 0.000046 |
| O3 | -1.08954 | -0.629046 | 0.000046 |

**Table S7.** Atomic coordinates of the optimized geometry of $HNO_3$ (in Å)

| x | y | z | |
|---|---|---|---|
| N | 0.152139 | 0.031663 | 0.000141 |
| O1 | 1.017828 | -0.788058 | -0.000059 |
| O2 | 0.216098 | 1.237747 | -0.000036 |
| O3 | -1.152162 | -0.511996 | -0.000003 |
| H | -1.719087 | 0.276816 | -0.000212 |

**Table S8.** Atomic coordinates of the optimized geometry of $HNO_3$ (in Å)

| | | | |
|---|---|---|---|
| N | 0.750672 | -0.106053 | -0.025906 |
| O1 | 1.766202 | -0.079431 | 0.602294 |
| O2 | 0.071812 | -0.961155 | -0.490280 |
| O3 | 0.296128 | 1.320257 | -0.233133 |
| F | -0.899559 | 1.276323 | -0.972875 |

CHEMISTRY
A European Journal

Supporting Information

# Revisiting a Historical Concept by Using Quantum Crystallography: Are Phosphate, Sulfate and Perchlorate Anions Hypervalent?

Malte Fugel,[a] Lorraine A. Malaspina,[a] Rumpa Pal,[a, d] Sajesh P. Thomas,[b, e] Ming W. Shi†,[b] Mark A. Spackman,[b] Kunihisa Sugimoto,[c] and Simon Grabowsky*[a]

chem_201806247_sm_miscellaneous_information.pdf

# Supporting Information – Revisiting a historic concept using quantum crystallography: Are the phosphate, sulfate and perchlorate anions hypervalent?

**Malte Fugel[a], Lorraine A. Malaspina[a], Rumpa Pal[b], Sajesh P. Thomas[c], Ming W. Shi[c], Mark A. Spackman[c], Kunihisa Sugimoto[d], and Simon Grabowsky[a,*]**

[a]University of Bremen, Department 2 - Chemistry/Biology, Institute of Inorganic Chemistry and Crystallography, Leobener Str. 3 and 7, 28359 Bremen, Germany
[b]University of Tsukuba, Division of Physics, Faculty of Pure and Applied Sciences, 1-1-1,Tennodai, Tsukuba, Ibaraki, 305-8571, Japan
[c]University of Western Australia, School of Molecular Sciences, 35 Stirling Highway, Perth WA 6009, Australia
[d]SPring-8 / JASRI, 1-1-1 Kouto, Sayo-cho, Sayo-gun, Hyogo 679-5198, Japan
[*]simon.grabowsky@uni-bremen.de

## 1 Crystallographic information and measurement details

Table S1 gives a selection of crystallographic information and measurement details of struvite ($MgNH_4PO_4$), lithium sulfate ($Li_2SO_4 \cdot H_2O$) and potassium perchlorate ($KClO_4$) measured at the home source (Bruker D8 Venture fitted with a micro-focus Mo$\kappa_\alpha$ radiation source and a Photon 100 detector) and at the synchrotron SPring-8 (beamline BL0B1 fitted with a curved image plate and open-flow He gas cooling system) in Hyogo, Japan. Only for the best data sets, an X-ray wavefunction refinement (XWR) was performed. For struvite, the synchrotron measurement yielded the highest quality data set, since the crystals did not scatter far at the home diffractometer set up. However, for $Li_2SO_4 \cdot H_2O$ and $KClO_4$ the home source gave superior data sets compared to the synchrotron measurements, because the sulfate crystal measured at SPring8 turned out to be twinned and the $KClO_4$ crystal underwent radiation damage, two problems which did not occur at the home measurement. Table 1 in the main text gives the refinement statistics after XWR. Crystallographic information files (CIFs) for the three XWRs have been deposited with the Inorganic Crystal Structure Database (ICSD) together with structure factor magnitudes under deposition numbers CSD-1861368–1861370. In addition, CIFs for the three inferior measurements after IAM refinement listed in Table S1 are available as supporting information with the journal.

**Table S1.** Crystallographic and measurement details from the synchrotron SPring-8 and the home source (Bruker D8 Venture) of struvite ($MgNH_4PO_4 \cdot 6H_2O$), $Li_2SO_4 \cdot H_2O$ and $KClO_4$

| | Phosphate | | Sulfate | | Perchlorate | |
|---|---|---|---|---|---|---|
| X-ray source | home | SPring-8 | home | SPring-8 | home | SPring-8 |
| Space group | $Pmn2_1$ | | $P2_1$ | | Pmna | |
| Crystal system | Orthorhombic | | Monoclinic | | Orthorhombic | |
| a /Å | 6.9495(3) | 6.9648(14) | 5.4535(2) | 5.4526(11) | 8.7504(2) | 8.7322(18) |
| b /Å | 6.1113(3) | 6.1122(12) | 4.8390(2) | 4.8346(10) | 5.60990(10) | 5.5999(11) |
| c /Å | 11.1895(4) | 11.198(2) | 8.1481(3) | 8.1430(16) | 7.1947(2) | 7.1833(14) |
| $\beta$ /° | 90 | | 107.196(1) | 107.20(3) | 90 | |
| Volume /Å$^3$ | 475.22(4) | 476.70(16) | 205.412(14) | 205.06(7) | 353.180(14) | 351.26(12) |
| Wavelength /Å | 0.71073 | 0.35463(5) | 0.71073 | 0.35463(5) | 0.71073 | 0.35463(5) |
| $T_{meas}$ /K | 100(1) | 20(1) | 100(1) | 20(1) | 100(1) | 20(1) |
| crystal size /mm$^3$ | 0.07x0.09x0.12 | 0.14x0.08x0.07 | 0.13x0.16x0.28 | 0.14x0.11x0.09 | 0.15x0.12x0.23 | 0.09x0.11x0.10 |
| $\sin(\theta)/\lambda$ /Å$^{-1}$ | 0.83 | 1.53 | 1.32 | 1.24 | 1.34 | 1.38 |
| $R_{int}$ | 0.0269 | 0.0338 | 0.0252 | 0.0394 | 0.0365 | 0.0353 |
| Redundancy | 12.6 | 22.4 | 7.6 | 11.6 | 13.4 | 5.6 |
| Compl. /% | 99.9 | 100 | 99.6 | 100 | 99.9 | 96.2 |
| $N_{meas}$ | 32323 | 106113 | 59047 | 75948 | 49960 | 22397 |
| $N_{uniq}$ | 2454 | 5912 | 7806 | 6558 | 3737 | 3974 |
| $N_{obs}$ ($F^2 > 2\sigma$) | 2418 | 5653 | 7721 | 6521 | 3570 | 3606 |
| CSD no. | N.A. | 1861370 | 1861369 | N.A. | 1861368 | N.A. |

**Table S2.** Refinement statistics of the best crystal structures after the independent atom model (IAM) and X-ray wavefunction refinement (XWR) of struvite ($MgNH_4PO_4 \cdot 6H_2O$), $Li_2SO_4 \cdot H_2O$ and $KClO_4$

| | Phosphate | Sulfate | Perchlorate |
|---|---|---|---|
| X-ray source | SPring-8 | home | home |
| | after IAM | | |
| R1 | 0.0189 | 0.0100 | 0.0192 |
| wR2 | 0.0509 | 0.0305 | 0.0566 |
| GooF | 1.04 | 1.12 | 1.14 |
| $\rho_{min/max}$ /eÅ$^{-3}$ | -0.53/0.90 | -0.58/0.33 | -0.77/0.87 |
| | after XWR | | |
| R1 | 0.0156 | 0.0070 | 0.0155 |
| wR2 | 0.0178 | 0.0146 | 0.0325 |
| GooF | 3.50 | 1.07 | 2.21 |
| $\rho_{min/max}$ /eÅ$^{-3}$ | -0.23/0.25 | -0.31/0.22 | -0.40/0.21 |

## 2 Residual density

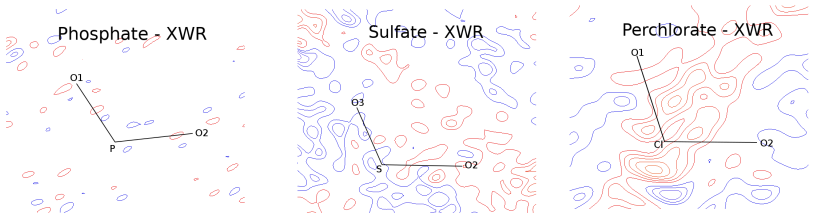


**Figure S1.** Residual density maps after XWR of the phosphate, sulfate and perchlorate anions plotted with XDGraph[1] (contour intervals = +/-0.05 e·Å$^{-3}$)

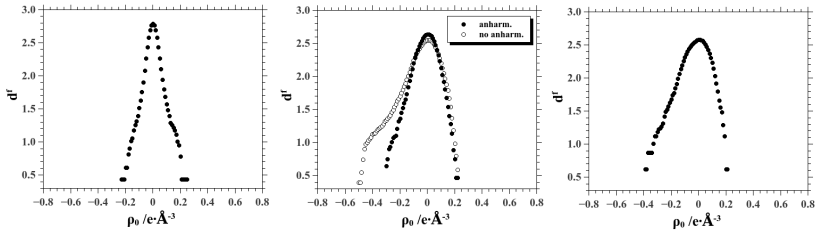


**Figure S2.** Meindl-Henn plots obtained from jnk2rda[2] of the unit cell residual density of struvite ($MgNH_4PO_4 \cdot 6H_2O$), $Li_2SO_4 \cdot H_2O$ and $KClO_4$ from XWR

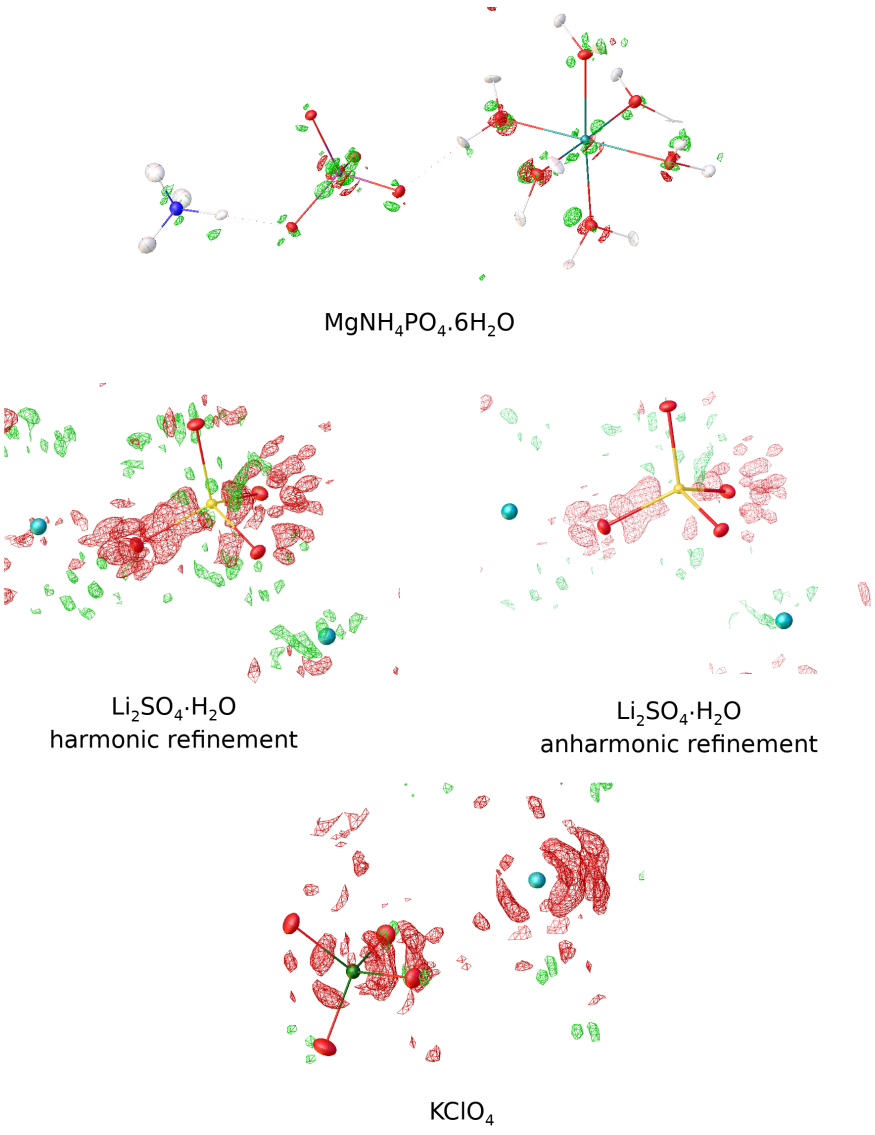


**Figure S3.** 3D residual density maps of $MgNH_4PO_4 \cdot 6H_2O$ (iso-value of 0.15 eÅ$^{-3}$), $Li_2SO_4 \cdot H_2O$ (iso-value of 0.15 eÅ$^{-3}$) and $KClO_4$ (iso-value of 0.20 eÅ$^{-3}$) plotted with Olex2[3]

## 3 DRK plots

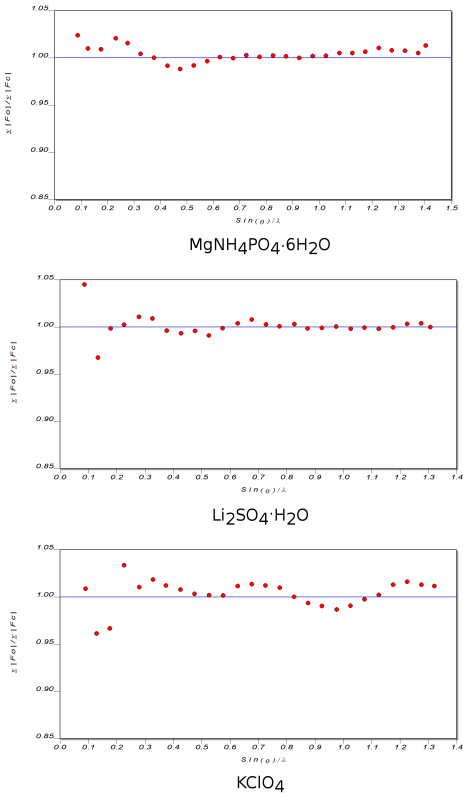


**Figure S4.** DRK plots of struvite, $Li_2SO_4 \cdot H_2O$ and $KClO_4$ obtained from and plotted with DRK-Plot implemented in WinGX[4]

## 4 Probability Density Function

To check whether the anharmonic refinement of the sulfur atom in $Li_2SO_4 \cdot H_2O$ is physically meaningful, probability density function (pdf) plots were generated (Fig. S5). A physically meaningful total pdf plot only contains positive regions. The plot in Figure S5 a) only contains small negative pdf regions, however, they are not significant and outside the core region of the sulfur atom.

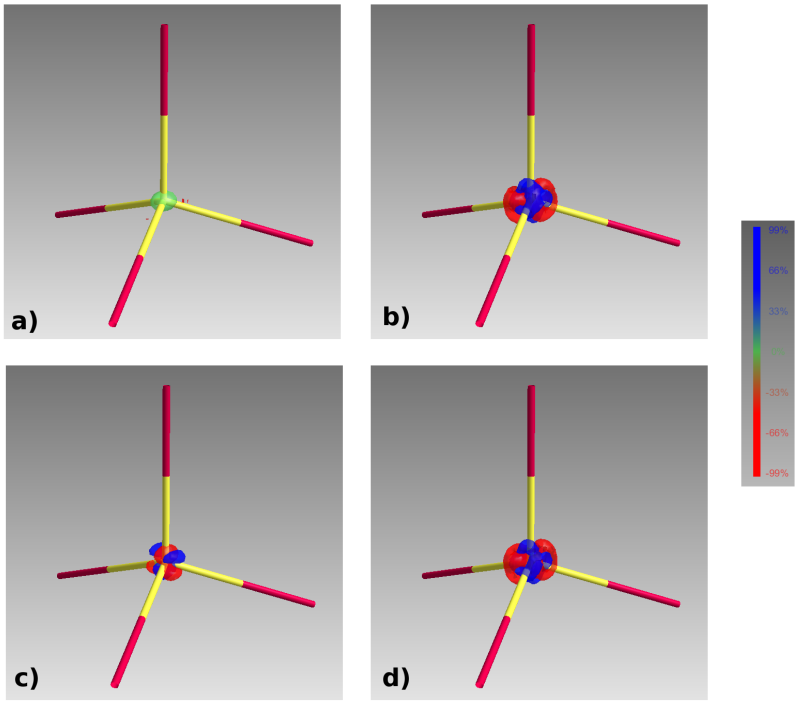


**Figure S5.** PDF plot of the sulfur atom of $Li_2SO_4 \cdot H_2O$ after HAR at 50% probability; a) 2nd, 3rd and 4th order, b) only 3rd and 4th order, c) only 3rd order, d) only 4th order (plotted with MolecoolQT)[5]

## 5 Intermolecular interactions

As mentioned in the main text, the $PO_4^{3-}$, $SO_4^{2-}$ and $ClO_4^-$ units are involved in a variety of intermolecular interactions in the respective crystal structures. Figure S6 depicts the closest contacts corresponding to either hydrogen bonds or ion-dipole complexes. All oxygen atoms of the $PO_4^{3-}$ unit in struvite are involved in a variety of strong hydrogen bonds. Oxygen atom O1 forms three hydrogen bonds to neighboring water molecules, while oxygen atoms O2 and O3 form two hydrogen bonds. One of the hydrogen bonds involving oxygen atom O3 is of N–H···O type, while the other ones are of O–H···O type. Figure S7 shows Hirshfeld surface fingerprint plots which reveal the interactions of the $PO_4^{3-}$, $SO_4^{2-}$ and $ClO_4^-$ units.[6] The sharp tip in the plot for $PO_4^{3-}$ is related to strong hydrogen bonding. The absence of a second tip indicates that there are no further significant interactions. For the $SO_4^{2-}$ unit in $Li_2SO_4 \cdot H_2O$, the Hirshfeld surface fingerprint plots shows two tips which can be related to the presence of ion-dipole interactions and hydrogen bonding. Figure S6 shows that each oxygen atom of the

$SO_4^{2-}$ unit has two interaction partners: Oxygen atoms O1, O2 and O3 interact with two neighboring lithium atoms, while oxygen atom O4 interacts with one lithium atom and forms one hydrogen bond. The only interaction involving the $ClO_4^-$ unit in $KClO_4$ is the ion-dipole interaction between K and O (compare with the single tip in the Hirshfeld fingerprint plot, Figure S7). With respect to the distances, the K – O interactions are significantly weaker than the Li – O or H···O interactions in the other two compounds.

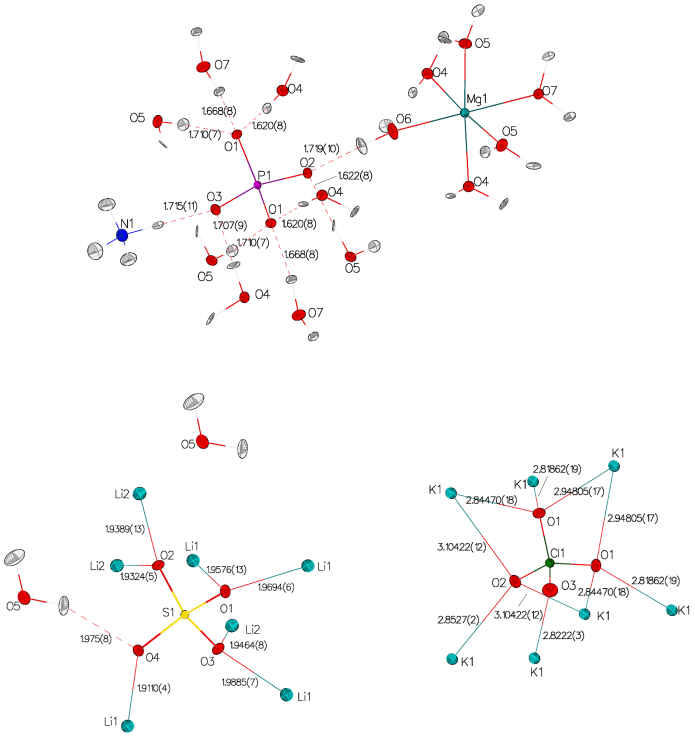


**Figure S6.** Ion-dipole interactions and hydrogen bonds involving the oxygen atoms of the $PO_4^{3-}$, $SO_4^{2-}$ and $ClO_4^-$ units plotted with Olex2[3]; the distances between the interacting atoms are given inside the figure (unit in Å)

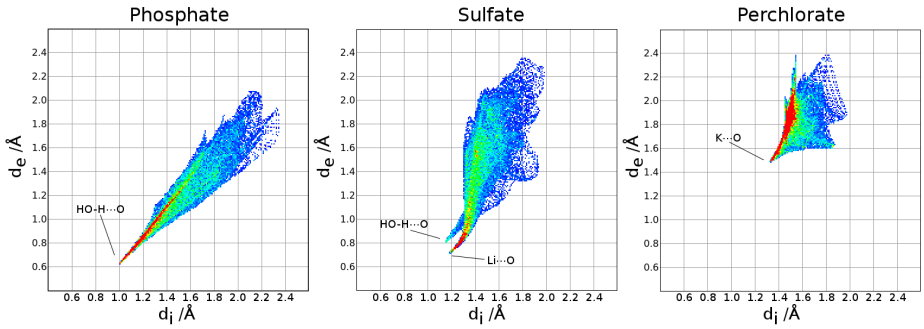


**Figure S7.** Hirshfeld fingerprint plots indicating the intermolecular interactions involving the $PO_4^{3-}$, $SO_4^{2-}$ and $ClO_4^-$ units (calculated and plotted with CrystalExplorer[7])

## 6 Periodic boundary calculations

**Table S3.** Comparison of the charges of X (in e) from isolated-molecule optimizations, periodic boundary calculations and XWR.

| | | P | S | Cl |
|---|---|---|---|---|
| charge of X | isolated | 3.73 | 3.91 | 2.46 |
| | periodic | 3.75 | 4.10 | 2.60 |
| | XWR | 4.07 | 4.48 | 3.60 |
| valency of X | isolated | 2.54 | 4.18 | 9.08 |
| | periodic | 2.50 | 3.80 | 8.80 |
| | XWR | 1.86 | 3.04 | 6.80 |

In the main text, it was found that the charges of the phosphorus, sulfur and chlorine atoms are more positive in XWR compared to the isolated molecule calculations. It was argued that this is caused by the crystal environment favoring a more ionic bonding situation. Consequently, the valency of the central atom is decreased as a consequence of the more ionic bonding situation. In order to validate the effect of the crystal environment, periodic boundary calculations using the Crystal14 software package (level of theory: B3LYP/pop-TZVP) were performed on the crystal geometries after HAR,[8] and a determination of the Bader charge was carried out with TOPOND.[9] Table S3 compares the periodic charges to the charges discussed in the paper. The periodic charges are, in fact, significantly more positive than those obtained from the gas phase optimization. However, they are less positive than the charges obtained from an XWR. It should be noted, though, that XWR and periodic charges refer to the same experimental geometry, whereas in the isolated state, the anions were optimized. The XWR charge of chlorine shows the highest deviation to the periodic charge.

## 7 Natural bond orbitals

**Table S4.** Compositions of the oxygen lone pair natural bond orbitals of $PO_4^{3-}$, $SO_4^{2-}$ and $ClO_4^-$ from theory and XWR

| | Theory | | XWR | | | | | | | |
|---|---|---|---|---|---|---|---|---|---|---|
| | | | O1 | | O2 | | O3 | | O4 | |
| | %s | %p | %s | %p | %s | %p | %s | %p | %s | %p |
| Phosphate | 66.72 | 33.26 | 63.51(22) | 36.42(24) | 59.31(94) | 40.62(94) | 60.96(170) | 38.94(172) | – | – |
| | 0.00 | 99.84 | 0.01(1) | 99.84(1) | 0.00(1) | 99.84(2) | 0.00(1) | 99.84(1) | – | – |
| | 0.00 | 99.84 | 0.06(4) | 99.76(4) | 6.24(94) | 93.59(94) | 4.84(128) | 94.96(122) | – | – |
| Sulfate | 75.11 | 24.87 | 71.92(10) | 28.03(10) | 70.33(20) | 29.63(18) | 72.55(18) | 27.39(18) | 72.02(26) | 27.95(26) |
| | 0.00 | 99.74 | 0.00(1) | 99.78(2) | 0.43(4) | 99.37(2) | 0.03(1) | 99.72(1) | 0.00(1) | 99.70(1) |
| | 0.00 | 99.75 | 0.14(4) | 99.48(6) | 0.01(1) | 99.74(2) | 0.01(1) | 99.62(1) | 0.01(1) | 99.67(2) |
| Perchlorate | 83.41 | 16.58 | 80.05(88) | 19.93(86) | 83.07(32) | 16.90(32) | 82.53(28) | 17.44(30) | – | – |
| | 0.00 | 99.69 | 0.00(1) | 99.60(1) | 0.01(2) | 99.57(4) | 0.08(1) | 99.44(4) | – | – |
| | 0.00 | 99.68 | 0.06(4) | 99.61(2) | 0.00(1) | 99.67(2) | 0.00(1) | 99.56(1) | – | – |

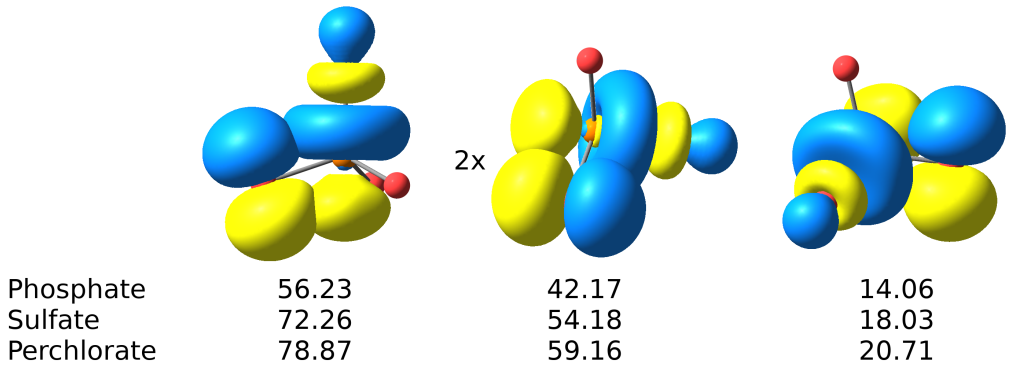


**Figure S8.** Interacting NBOs and the respective interaction energies (E2 in kJ·mol$^{-1}$) plotted with ChemCraft[10]

## 8 Electron localizability indicator (ELI-D)

The electron localizability indicator (ELI-D) yields basins which may be related to atomic shells, lone pairs and bonds. Localization domains associated with the ELI-D basins are revealed by plotting iso-surfaces of the ELI-D at appropriate iso-values. Figure S9 shows ELI-D iso-surfaces of the phosphate, sulfate and perchlorate anions of the theoretical calculations and the XWR. The topological analysis of the theoretically obtained ELI-D gives one X–O bond basin for each of the four X–O bonds and three oxygen lone pair basins for each of the four oxygen atoms. The localization domains of the oxygen lone pair basins are arranged circularly around the oxygen atoms, which is a common feature indicating the presence of three oxygen lone pairs.[12] Equivalent to the theoretical ELI-D, a corresponding analysis of the ELI-D obtained from the XWR gives one X–O bond basin for each of the four X–O bonds. However, the number of oxygen lone pair basins deviates between theory and XWR. It needs to be stated that the number of oxygen lone pair basins cannot be related to the number of lone pairs in a Lewis structure, but rather to the site symmetry of the corresponding atom.[12] Since the oxygen atoms of the isolated

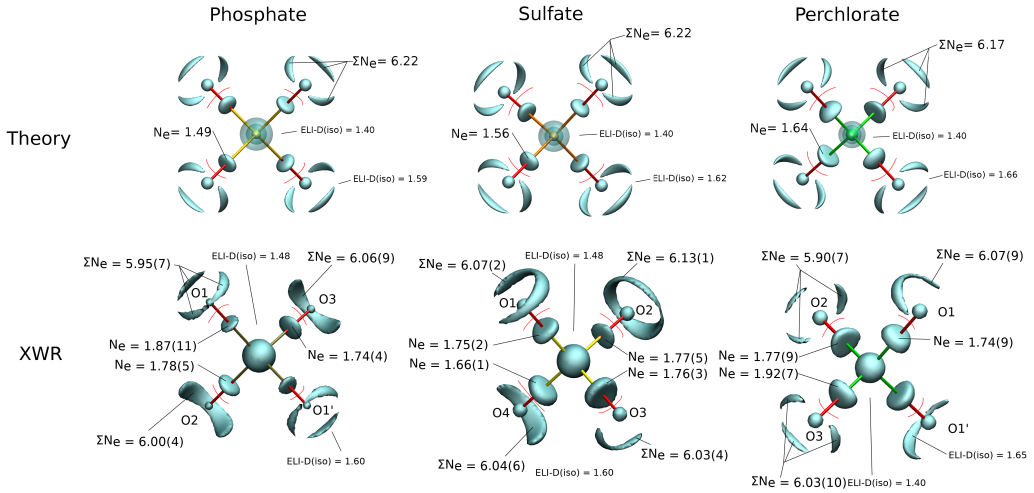


**Figure S9.** Iso-surfaces of the ELI-D showing localization domains of the X-O bonds, oxygen lone pairs and atomic shells (regions of different iso-values are separated by a red line); the electron populations of the X-O bonding basins and the oxygen lone pairs are given inside the figure; pictures generated with VMD.[11]

anions are located in a three-fold site symmetry, three oxygen lone pairs are dictated by symmetry. In the experimental systems, the counter cations and water molecules perturb the $T_d$ symmetry of the anions and, therefore, the three-fold site symmetry of the oxygen atoms. The localization domains of the oxygen lone pairs obtained from XWR are still arranged circularly around the oxygen atoms, but only in few cases three separated localization domains are obtained.

The electron populations of the oxygen lone pair and X−O bond basins are given inside Figure S9. The oxygen lone pair populations from theory slightly exceed a value of six in all anions. This is also the case for the populations from XWR, with the exception of O1 in the $PO_4^{3-}$ unit of struvite and O2 in the $ClO_4^-$ unit of $KClO_4$. The electron populations of lone pair basins are often somewhat larger than the anticipated values, because they absorb some of the electron density of neighboring bonds.[12] The oxygen lone pair populations of N ≈ 6, may be related to the presence of three oxygen lone pairs. As opposed to the populations of the oxygen lone pair NBOs, no conclusions concerning the presence of negative hyperconjugation may be drawn. The theoretical electron population of the X-O bond basins is lowest in the phosphate anion and highest in the perchlorate anion, however, it never exceeds a value of two. Consequently, all X−O bonds are "less" than single bonds and therefore indicate that the hypervalent Lewis structures **1a**, **2a** and **3a** are not significant. The X-O bond basin populations from XWR are also lower than two, but the populations in all anions are significantly larger and a clear trend is not discernible.

## 9 Coordinates of optimized structures

**Table S5.** Coordinates of $PO_4^{3-}$ (units in Å) at B3LYP/aug-cc-pVTZ

| No. | Type | x | y | z |
|---|---|---|---|---|
| 1 | P | -0.005405 | -0.513514 | 0.000000 |
| 2 | O | 0.525929 | 0.237887 | -1.301477 |
| 3 | O | -1.599382 | -0.513494 | 0.000000 |
| 4 | O | 0.52593 | 0.237888 | 1.301476 |
| 5 | O | 0.525902 | -2.016336 | 0.000000 |

**Table S6.** Coordinates of $PO_4^{3-}$ (units in Å) at CCSD/aug-cc-pVTZ

| No. | Type | x | y | z |
|---|---|---|---|---|
| 1 | P | -0.005405 | -0.513514 | 0.000000 |
| 2 | O | 0.523250 | 0.234098 | -1.294913 |
| 3 | O | -1.591344 | -0.513494 | 0.000000 |
| 4 | O | 0.523250 | 0.234099 | 1.294913 |
| 5 | O | 0.523222 | -2.008757 | 0.000000 |

**Table S7.** Coordinates of $SO_4^{2-}$ (units in Å) at B3LYP/aug-cc-pVTZ

| No. | Type | x | y | z |
|---|---|---|---|---|
| 1 | S | 0.621622 | 0.113513 | 0.000000 |
| 2 | O | 1.127110 | 0.828363 | 1.238167 |
| 3 | O | 1.127084 | -1.316205 | 0.000000 |
| 4 | O | -0.894817 | 0.113532 | 0.000000 |
| 5 | O | 1.127110 | 0.828363 | -1.238167 |

**Table S8.** Coordinates of $SO_4^{2-}$ (units in Å) at CCSD/aug-cc-pVTZ

| No. | Type | x | y | z |
|---|---|---|---|---|
| 1 | S | 0.000000 | 0.000000 | 0.000000 |
| 2 | O | 0.867966 | 0.867966 | 0.867966 |
| 3 | O | -0.867966 | -0.867966 | 0.867966 |
| 4 | O | -0.867966 | 0.867966 | -0.867966 |
| 5 | O | 0.867966 | -0.867966 | -0.867966 |

**Table S9.** Coordinates of $ClO_4^-$ (units in Å) at B3LYP/aug-cc-pVTZ

| No. | Type | x | y | z |
|---|---|---|---|---|
| 1 | Cl | 0.000000 | 0.000000 | 0.000000 |
| 2 | O | 0.854015 | 0.854015 | 0.854015 |
| 3 | O | -0.854015 | -0.854015 | 0.854015 |
| 4 | O | -0.854015 | 0.854015 | -0.854015 |
| 5 | O | 0.854015 | -0.854015 | -0.854015 |

**Table S10.** Coordinates of $ClO_4^-$ (units in Å) at CCSD/aug-cc-pVTZ

| No. | Type | x | y | z |
|---|---|---|---|---|
| 1 | Cl | 0.329730 | 0.070270 | 0.000000 |
| 2 | O | 0.816362 | 0.758454 | 1.191981 |
| 3 | O | 0.816337 | -1.306117 | 0.000000 |
| 4 | O | -1.130142 | 0.070288 | 0.000000 |
| 5 | O | 0.816362 | 0.758454 | -1.191981 |

## 10 Method and basis set dependencies

The geometry optimizations were performed at a B3LYP/aug-cc-pVTZ level of theory. The method was chosen because it accounts for electron correlation. The diffuse functions of the aug-cc-pVTZ basis set are required for anions such as $PO_4^{3-}$, $SO_4^{2-}$ and $ClO_4^-$. However, the XWR was performed at a different level of theory, namely RHF/def2-TZVP. As opposed to B3LYP, RHF does not account for electron correlation, however, the XWR retrieves this effect from experiment. So, ultimately, the XWR wavefunction does include electron correlation. The aug-cc-pVTZ and def2-TZVP basis sets are quite similar, however, a HAR does not converge using the former because of the diffuse functions. Of course, one may question whether the properties are greatly influenced by the choice of different methods. Therefore, we compare a selection of properties obtained from:

1. geometry optimization at a B3LYP/aug-cc-pVTZ level of theory (as found in the main paper)
2. XWR at a RHF/def2-TZVP level of theory (as found in the main paper)
3. single point calculation at the RHF/def2-TZVP level of theory on the formula unit of the three crystal structures
4. single point calculation at the B3LYP/def2-TZVP level of theory on the formula unit of the three crystal structures
5. single point calculation on the theoretical geometry at a B3LYP/def2-TZVP basis set

Point 3 serves as an indicator of the effect of the fitting to the RHF wavefunction, and point 4 reveals to what extent electron correlation is retrieved in comparison to the application of B3LYP. Point 5 reveals the basis set dependency of aug-cc-pVTZ versus def2-TZVP.

**Table S11.** NBO populations (unit in e) of sulfate obtained from different levels of theory

| | | $LP_{sp^{\lambda}}(O)$ | $LP_pO$ | | $\sigma^*$(X-O) |
|---|---|---|---|---|---|
| | | N(LP1) | N(LP2) | N(LP3) | N |
| O1 | opt. (B3LYP/aug-cc-pVTZ), theo. geom | 1.98 | 1.88 | 1.88 | 0.20 |
| | XWR (HF/def2-TZVP), exp. geom. | 1.98 | 1.91 | 1.88 | 0.17 |
| | s.p. (HF/def2-TZVP), exp. geom. | 1.98 | 1.89 | 1.88 | 0.15 |
| | s.p. (B3LYP/def2-TZVP), exp. geom. | 1.98 | 1.89 | 1.88 | 0.20 |
| | s.p. (B3LYP/def2-TZVP), theo. geom. | 1.99 | 1.87 | 1.87 | 0.20 |
| O2 | opt. (B3LYP/aug-cc-pVTZ), theo. geom | 1.98 | 1.88 | 1.88 | 0.20 |
| | XWR (HF/def2-TZVP), exp. geom. | 1.98 | 1.91 | 1.90 | 0.18 |
| | s.p. (HF/def2-TZVP), exp. geom. | 1.97 | 1.91 | 1.90 | 0.17 |
| | s.p. (B3LYP/def2-TZVP), exp. geom. | 1.97 | 1.91 | 1.90 | 0.22 |
| | s.p. (B3LYP/def2-TZVP), theo. geom. | 1.99 | 1.87 | 1.87 | 0.20 |
| O3 | opt. (B3LYP/aug-cc-pVTZ), theo. geom | 1.98 | 1.88 | 1.88 | 0.20 |
| | XWR (HF/def2-TZVP), exp. geom. | 1.98 | 1.89 | 1.88 | 0.16 |
| | s.p. (HF/def2-TZVP), exp. geom. | 1.98 | 1.88 | 1.88 | 0.15 |
| | s.p. (B3LYP/def2-TZVP), exp. geom. | 1.98 | 1.88 | 1.87 | 0.19 |
| | s.p. (B3LYP/def2-TZVP), theo. geom. | 1.99 | 1.87 | 1.87 | 0.20 |
| O4 | opt. (B3LYP/aug-cc-pVTZ), theo. geom | 1.98 | 1.88 | 1.88 | 0.20 |
| | XWR (HF/def2-TZVP), exp. geom. | 1.98 | 1.88 | 1.87 | 0.18 |
| | s.p. (HF/def2-TZVP), exp. geom. | 1.98 | 1.92 | 1.91 | 0.18 |
| | s.p. (B3LYP/def2-TZVP), exp. geom. | 1.98 | 1.91 | 1.91 | 0.22 |
| | s.p. (B3LYP/def2-TZVP), theo. geom. | 1.99 | 1.87 | 1.87 | 0.20 |

**Table S12.** Comparison of NRT weights (in %) of the $S^{2+}O_4{}^{4-}$ Lewis structure of sulfate from different levels of theory

| | |
|---|---|
| opt. (B3LYP/aug-cc-pVTZ), theo. geom | 57.1 |
| XWR (HF/def2-TZVP), exp. geom. | 62.0 |
| s.p. (HF/def2-TZVP), exp. geom. | 63.9 |
| s.p. (B3LYP/def2-TZVP), exp. geom. | 53.8 |
| s.p. (B3LYP/def2-TZVP), theo. geom. | 56.3 |

Generally, it shows that the results from XWR (RHF/def2-TZVP) and the single point calculation on the experimental geometry at the B3LYP/def2-TZVP level of theory are very close to each other. On the other hand, the (RHF/def2-TZVP) XWR and a single point calculation at a RHF/def2-TZVP level of theory show larger discrepancies. This shows that electron correlation plays a large role and the XWR can retrieve this effect from experiment, while also incorporating other effects. A comparison between the optimized geometry at the B3LYP/aug-cc-pVTZ level of theory and the single point calculation at the same geometry at the B3LYP/def2-TZVP level of theory shows that the basis set only has a minor influence on the properties. The largest deviations are obtained for the Laplacian of the electron density and the total energy density at the bond critical points, however, they do not change any of the obtained conclusions.

**Table S13.** QTAIM properties ($\rho_{bcp}$ in eÅ$^{-3}$, $\nabla^2\rho_{bcp}$ in eÅ$^{-5}$ and $H_{bcp}$ in Hartree) of sulfate obtained from different levels of theory

| | | $\rho_{bcp}$ | $\nabla^2\rho_{bcp}$ | $H_{bcp}$ |
|---|---|---|---|---|
| S – O1 | opt. (B3LYP/aug-cc-pVTZ), theo. geom | 1.87 | 7.2 | -0.38 |
| | XWR (HF/def2-TZVP), exp. geom. | 1.99 | 16.8 | -0.36 |
| | s.p. (HF/def2-TZVP), exp. geom. | 2.02 | 16.6 | -0.37 |
| | s.p. (B3LYP/def2-TZVP), exp. geom. | 1.99 | 12.3 | -0.36 |
| | s.p. (B3LYP/def2-TZVP), theo. geom. | 1.86 | 5.4 | -0.34 |
| S – O2 | opt. (B3LYP/aug-cc-pVTZ), theo. geom | 1.87 | 7.2 | -0.38 |
| | XWR (HF/def2-TZVP), exp. geom. | 1.99 | 17.1 | -0.36 |
| | s.p. (HF/def2-TZVP), exp. geom. | 1.97 | 17.9 | -0.35 |
| | s.p. (B3LYP/def2-TZVP), exp. geom. | 1.95 | 13.3 | -0.35 |
| | s.p. (B3LYP/def2-TZVP), theo. geom. | 1.86 | 5.4 | -0.34 |
| S – O3 | opt. (B3LYP/aug-cc-pVTZ), theo. geom | 1.87 | 7.2 | -0.38 |
| | XWR (HF/def2-TZVP), exp. geom. | 2.00 | 16.7 | -0.36 |
| | s.p. (HF/def2-TZVP), exp. geom. | 2.04 | 15.7 | -0.38 |
| | s.p. (B3LYP/def2-TZVP), exp. geom. | 2.00 | 11.7 | -0.37 |
| | s.p. (B3LYP/def2-TZVP), theo. geom. | 1.86 | 5.4 | -0.34 |
| S – O4 | opt. (B3LYP/aug-cc-pVTZ), theo. geom | 1.87 | 7.2 | -0.38 |
| | XWR (HF/def2-TZVP), exp. geom. | 1.92 | 28.6 | -0.31 |
| | s.p. (HF/def2-TZVP), exp. geom. | 1.98 | 22.5 | -0.34 |
| | s.p. (B3LYP/def2-TZVP), exp. geom. | 1.96 | 17.8 | -0.34 |
| | s.p. (B3LYP/def2-TZVP), theo. geom. | 1.86 | 5.4 | -0.34 |

## References


1. A. Volkov, P. Macchi, L. Farrugia, C. Gatti, P. Mallinson, T. Richter and T. Koritsanszky, *University at Buffalo, State University of New York, NY, USA*, 2006.
2. K. Meindl and J. Henn, *Acta Cryst. A*, 2008, **64**, 404–418.
3. O. V. Dolomanov, L. J. Bourhis, R. J. Gildea, J. A. Howard and H. Puschmann, *J.Appl. Cryst.*, 2009, **42**, 339–341.
4. L. J. Farrugia, *J. Appl. Cryst.*, 1999, **32**, 837–838.
5. C. B. Hübschle and B. Dittrich, *J. Appl. Cryst.*, 2011, **44**, 238–240.
6. J. J. McKinnon, D. Jayatilaka and M. A. Spackman, *Chem. Commun.*, 2007, 3814–3816.
7. M. J. Turner, J. J. McKinnon, S. K. Wolff, D. J. Grimwood, P. R. Spackman, D. Jayatilaka and M. A. Spackman, *CrystalExplorer17*, 2017, http://hirshfeldsurface.net.
8. R. Dovesi, R. Orlando, A. Erba, C. M. Zicovich-Wilson, B. Civalleri, S. Casassa, L. Maschio, M. Ferrabone, M. De La Pierre, P. D'Arco *et al.*, *International Journal of Quantum Chemistry*, 2014, **114**, 1287–1317.
9. C. Gatti and S. M. Casassa, 2013.
10. *Chemcraft*, http://www.chemcraftprog.com.
11. W. Humphrey, A. Dalke and K. Schulten, *J. Mol. Graphics*, 1996, **14**, 33–38.
12. M. Fugel, J. Beckmann, D. Jayatilaka, G. V. Gibbs and S. Grabowsky, *Chem. Eur. J.*, 2018, **24**, 6248–6261.

# Supporting Information – The difference between $S_N2$ reactions revealed by a complementary bonding analysis

**Malte Fugel**[a], **Anneke Dittmer**[a,b], **and Simon Grabowsky**[*a]

[a]Universität Bremen, Department 2: Biology / Chemistry, Leobener Str. 3, 28359 Bremen.
[b]*current address:* Max-Planck-Institut für Kohlenforschung, Kaiser-Wilhelm-Platz 1, 45470 Mülheim an der Ruhr, Germany.
[*]simon.grabowsky@uni-bremen.de

## 1 Potential energy surface

**Table S1.** Relative energies (in kJ·mol$^{-1}$) along the reaction coordinate of the silicon system ($ClSiH_3 + Cl^-$) calculated at the B3LYP/aug-cc-pVTZ level of theory with dispersion correction (GD3BJ).

| r(Si−Cl$_{leave}$) /Å | ΔE /kJ·mol$^{-1}$ |
|---|---|
| 2.37 | -104.3 |
| 2.45 | -103.8 |
| 2.55 | -101.3 |
| 2.65 | -97.7 |
| 2.75 | -93.4 |
| 2.85 | -89.0 |
| 2.95 | -84.4 |
| 3.05 | -79.7 |
| 3.15 | -75.0 |
| 3.25 | -70.5 |
| 3.35 | -66.1 |
| 3.45 | -61.8 |
| 3.55 | -57.8 |
| 3.65 | -53.9 |
| 3.75 | -50.3 |
| 3.85 | -46.9 |
| 3.95 | -43.7 |
| 4.10 | -39.3 |
| 4.25 | -35.5 |
| 4.40 | -32.0 |
| 4.60 | -28.2 |
| 4.80 | -24.9 |

**Table S2.** Relative energies (in kJ·mol$^{-1}$) along the reaction coordinate of the silicon system ($ClCH_3 + Cl^-$) calculated at the B3LYP/aug-cc-pVTZ level of theory with dispersion correction (GD3BJ).

| r(C−Cl$_{leave}$) /Å | ΔE /kJ·mol$^{-1}$ |
|---|---|
| 2.35 | -12.0 |
| 2.40 | -12.5 |
| 2.46 | -15.5 |
| 2.56 | -22.7 |
| 2.66 | -29.9 |
| 2.76 | -36.0 |
| 2.86 | -40.3 |
| 2.96 | -43.0 |
| 3.06 | -44.3 |
| 3.13 | -44.7 |
| 3.16 | -44.7 |
| 3.26 | -44.3 |
| 3.36 | -43.3 |
| 3.46 | -42.0 |
| 3.56 | -40.5 |
| 3.66 | -38.8 |
| 3.76 | -37.1 |
| 3.86 | -35.4 |
| 3.96 | -33.7 |
| 4.06 | -32.0 |
| 4.16 | -30.4 |
| 4.26 | -28.9 |
| 4.36 | -27.5 |

## 2 Geometry

**Table S3.** Coordinates at the transition state of the carbon system.

| Atom no. | Element | x /Å | y /Å | z /Å |
|---|---|---|---|---|
| 1 | Cl | -0.000069 | 0.000000 | 0.000000 |
| 2 | H | 0.534204 | 0.925415 | 0.000000 |
| 3 | H | 0.534204 | -0.925415 | 0.000000 |
| 4 | H | -1.068634 | 0.000000 | 0.000000 |
| 5 | Cl | 0.000146 | 0.000000 | -2.352452 |
| 6 | Cl | 0.000146 | 0.000000 | 2.352452 |

**Table S4.** Coordinates at the reaction complex of the carbon system.

| Atom no. | Element | x /Å | y /Å | z /Å |
|---|---|---|---|---|
| 1 | Cl | -0.000471 | 0.000000 | 0.676046 |
| 2 | H | 0.513350 | 0.890329 | 0.344815 |
| 3 | H | 0.513350 | -0.890329 | 0.344815 |
| 4 | H | -1.029010 | 0.000000 | 0.346603 |
| 5 | Cl | 0.001503 | 0.000000 | -2.452048 |
| 6 | Cl | 0.001279 | 0.000000 | 2.528075 |

**Table S5.** Coordinates at the transition complex of the silicon system.

| Atom no. | Element | x /Å | y /Å | z /Å |
|---|---|---|---|---|
| 1 | Si | -0.000284 | 0.000000 | 0.000000 |
| 2 | H | 0.735889 | 1.275589 | 0.000000 |
| 3 | H | 0.735889 | -1.275589 | 0.000000 |
| 4 | H | -1.473171 | 0.000000 | 0.000000 |
| 5 | Cl | 0.000839 | 0.000000 | -2.372625 |
| 6 | Cl | 0.000839 | 0.000000 | 2.372625 |

**Table S6.** The C – Cl distances along the reaction coordinate.

| fixed $r(C-Cl_{leave})$ /Å | optimized $r(C-Cl_{in})$ /Å |
|---|---|
| 2.35 | 2.352 |
| 2.40 | 2.219 |
| 2.46 | 2.112 |
| 2.56 | 2.002 |
| 2.66 | 1.945 |
| 2.76 | 1.911 |
| 2.86 | 1.887 |
| 2.96 | 1.871 |
| 3.06 | 1.859 |
| 3.13 | 1.852 |
| 3.16 | 1.850 |
| 3.26 | 1.843 |
| 3.36 | 1.837 |
| 3.46 | 1.834 |
| 3.56 | 1.831 |
| 3.66 | 1.828 |
| 3.76 | 1.826 |
| 3.86 | 1.824 |
| 3.96 | 1.823 |
| 4.06 | 1.821 |
| 4.16 | 1.820 |
| 4.26 | 1.819 |
| 4.36 | 1.818 |

**Table S7.** The Si – Cl distances along the reaction coordinate.

| fixed $r(Si-Cl_{leave})$ /Å | optimized $r(Si-Cl_{in})$ /Å |
|---|---|
| 2.37 | 2.373 |
| 2.45 | 2.338 |
| 2.55 | 2.303 |
| 2.65 | 2.273 |
| 2.75 | 2.247 |
| 2.85 | 2.226 |
| 2.95 | 2.208 |
| 3.05 | 2.195 |
| 3.15 | 2.183 |
| 3.25 | 2.173 |
| 3.35 | 2.165 |
| 3.45 | 2.158 |
| 3.55 | 2.151 |
| 3.65 | 2.146 |
| 3.75 | 2.141 |
| 3.85 | 2.137 |
| 3.95 | 2.134 |
| 4.10 | 2.129 |
| 4.25 | 2.125 |
| 4.40 | 2.121 |
| 4.60 | 2.118 |
| 4.80 | 2.114 |

## 3 Quantum Theory of Atoms in Molecules

**Table S8.** Properties at the $C-Cl_{leave}$ and $C-Cl_{in}$ bond critical points (bcp) of the carbon system along the reaction coordinate: The electron density $\rho_{bcp}$ (in eÅ$^{-3}$) and the total energy density $H_{bcp}$ (in a.u.).

| | $C-Cl_{leave}$ | | $C-Cl_{in}$ | |
|---|---|---|---|---|
| r /Å | $\rho_{bcp}$ | $H_{bcp}$ | $\rho_{bcp}$ | $H_{bcp}$ |
| 2.35 | 0.352 | -0.00828 | 0.352 | -0.00828 |
| 2.40 | 0.309 | -0.00558 | 0.466 | -0.01631 |
| 2.46 | 0.271 | -0.00350 | 0.588 | -0.02746 |
| 2.56 | 0.219 | -0.00121 | 0.746 | -0.04618 |
| 2.66 | 0.180 | 0.00007 | 0.848 | -0.06056 |
| 2.76 | 0.148 | 0.00083 | 0.914 | -0.07084 |
| 2.86 | 0.123 | 0.00127 | 0.965 | -0.07922 |
| 2.96 | 0.102 | 0.00150 | 1.002 | -0.08554 |
| 3.06 | 0.085 | 0.00158 | 1.030 | -0.09042 |
| 3.13 | 0.075 | 0.00158 | 1.045 | -0.09309 |
| 3.16 | 0.070 | 0.00156 | 1.052 | -0.09414 |
| 3.26 | 0.059 | 0.00148 | 1.068 | -0.09707 |
| 3.36 | 0.049 | 0.00135 | 1.082 | -0.09939 |
| 3.46 | 0.041 | 0.00121 | 1.091 | -0.10090 |
| 3.56 | 0.034 | 0.00106 | 1.100 | -0.10235 |
| 3.66 | 0.029 | 0.00091 | 1.107 | -0.10352 |
| 3.76 | 0.024 | 0.00078 | 1.113 | -0.10448 |
| 3.86 | 0.020 | 0.00066 | 1.118 | -0.10529 |
| 3.96 | 0.017 | 0.00056 | 1.122 | -0.10597 |
| 4.06 | 0.015 | 0.00047 | 1.126 | -0.10656 |
| 4.16 | 0.012 | 0.00040 | 1.130 | -0.10708 |
| 4.26 | 0.010 | 0.00034 | 1.133 | -0.10754 |
| 4.36 | 0.009 | 0.00028 | 1.134 | -0.10749 |

**Table S9.** Properties at the $Si-Cl_{leave}$ and $Si-Cl_{in}$ bond critical points (bcp) of the siliicon system along the reaction coordinate: The electron density $\rho_{bcp}$ (in eÅ$^{-3}$) and the total energy density $H_{bcp}$ (in a.u.).

| | $Si-Cl_{leave}$ | | $Si-Cl_{in}$ | |
|---|---|---|---|---|
| r /Å | $\rho_{bcp}$ | $H_{bcp}$ | $\rho_{bcp}$ | $H_{bcp}$ |
| 2.37 | 0.369 | -0.02574 | 0.369 | -0.02574 |
| 2.45 | 0.325 | -0.02099 | 0.392 | -0.02803 |
| 2.55 | 0.275 | -0.01483 | 0.418 | -0.03051 |
| 2.65 | 0.232 | -0.00976 | 0.441 | -0.03261 |
| 2.75 | 0.195 | -0.00618 | 0.461 | -0.03438 |
| 2.85 | 0.164 | -0.00379 | 0.479 | -0.03596 |
| 2.95 | 0.137 | -0.00221 | 0.496 | -0.03743 |
| 3.05 | 0.115 | -0.00118 | 0.508 | -0.03855 |
| 3.15 | 0.097 | -0.00051 | 0.519 | -0.03958 |
| 3.25 | 0.081 | -0.00009 | 0.530 | -0.04052 |
| 3.35 | 0.068 | 0.00019 | 0.538 | -0.04127 |
| 3.45 | 0.058 | 0.00035 | 0.545 | -0.04195 |
| 3.55 | 0.048 | 0.00043 | 0.552 | -0.04251 |
| 3.65 | 0.041 | 0.00047 | 0.558 | -0.04302 |
| 3.75 | 0.034 | 0.00047 | 0.562 | -0.04345 |
| 3.85 | 0.029 | 0.00046 | 0.566 | -0.04381 |
| 3.95 | 0.025 | 0.00043 | 0.570 | -0.04417 |
| 4.10 | 0.019 | 0.00038 | 0.576 | -0.04465 |
| 4.25 | 0.015 | 0.00033 | 0.580 | -0.04511 |
| 4.40 | 0.012 | 0.00028 | 0.585 | -0.04553 |
| 4.60 | 0.008 | 0.00022 | 0.589 | -0.04599 |
| 4.80 | 0.006 | 0.00017 | 0.594 | -0.04646 |

## 4 Charges

**Table S10.** Bader and NPA charges ($q_{Bader}$ and $q_{NPA}$ in e) of Si, $Cl_{leave}$ and $Cl_{in}$ in the silicon system.

| | Bader | | | NPA | | |
|---|---|---|---|---|---|---|
| r /Å | q(Si) | q($Cl_{leave}$) | q($Cl_{in}$) | q(Si) | q($Cl_{leave}$) | q($Cl_{in}$) |
| 2.37 | 2.717 | -0.839 | -0.839 | 0.891 | -0.660 | -0.660 |
| 2.45 | 2.710 | -0.837 | -0.837 | 0.896 | -0.691 | -0.640 |
| 2.55 | 2.705 | -0.838 | -0.835 | 0.903 | -0.728 | -0.617 |
| 2.65 | 2.706 | -0.844 | -0.833 | 0.910 | -0.763 | -0.597 |
| 2.75 | 2.710 | -0.854 | -0.830 | 0.916 | -0.794 | -0.580 |
| 2.85 | 2.716 | -0.865 | -0.828 | 0.921 | -0.822 | -0.565 |
| 2.95 | 2.722 | -0.877 | -0.826 | 0.925 | -0.847 | -0.551 |
| 3.05 | 2.727 | -0.888 | -0.823 | 0.930 | -0.868 | -0.540 |
| 3.15 | 2.732 | -0.898 | -0.820 | 0.934 | -0.887 | -0.530 |
| 3.25 | 2.736 | -0.908 | -0.818 | 0.935 | -0.903 | -0.522 |
| 3.35 | 2.740 | -0.917 | -0.816 | 0.938 | -0.918 | -0.514 |
| 3.45 | 2.742 | -0.926 | -0.814 | 0.940 | -0.930 | -0.507 |
| 3.55 | 2.744 | -0.933 | -0.812 | 0.942 | -0.940 | -0.501 |
| 3.65 | 2.746 | -0.940 | -0.810 | 0.944 | -0.949 | -0.496 |
| 3.75 | 2.748 | -0.947 | -0.808 | 0.945 | -0.957 | -0.491 |
| 3.85 | 2.749 | -0.952 | -0.806 | 0.946 | -0.963 | -0.487 |
| 3.95 | 2.751 | -0.958 | -0.805 | 0.947 | -0.969 | -0.483 |
| 4.10 | 2.752 | -0.964 | -0.803 | 0.947 | -0.976 | -0.477 |
| 4.25 | 2.754 | -0.970 | -0.801 | 0.947 | -0.981 | -0.473 |
| 4.40 | 2.755 | -0.975 | -0.799 | 0.947 | -0.985 | -0.468 |
| 4.60 | 2.756 | -0.980 | -0.797 | 0.946 | -0.990 | -0.463 |
| 4.80 | 2.757 | -0.984 | -0.795 | 0.944 | -0.993 | -0.458 |

**Table S11.** Bader and NPA charges ($q_{Bader}$ and $q_{NPA}$ in e) of C, $Cl_{leave}$ and $Cl_{in}$ in the carbon system.

| | Bader | | | NPA | | |
|---|---|---|---|---|---|---|
| r /Å | q(Si) | q($Cl_{leave}$) | q($Cl_{in}$) | q(Si) | q($Cl_{leave}$) | q($Cl_{in}$) |
| 2.35 | 0.121 | -0.698 | -0.698 | -0.342 | -0.624 | -0.624 |
| 2.40 | 0.128 | -0.753 | -0.638 | -0.366 | -0.694 | -0.533 |
| 2.46 | 0.134 | -0.798 | -0.582 | -0.395 | -0.756 | -0.451 |
| 2.56 | 0.135 | -0.848 | -0.516 | -0.432 | -0.829 | -0.357 |
| 2.66 | 0.134 | -0.877 | -0.476 | -0.454 | -0.873 | -0.302 |
| 2.76 | 0.132 | -0.896 | -0.449 | -0.467 | -0.902 | -0.268 |
| 2.86 | 0.130 | -0.911 | -0.429 | -0.476 | -0.924 | -0.242 |
| 2.96 | 0.129 | -0.922 | -0.414 | -0.482 | -0.940 | -0.224 |
| 3.06 | 0.128 | -0.931 | -0.402 | -0.486 | -0.952 | -0.210 |
| 3.13 | 0.128 | -0.937 | -0.395 | -0.488 | -0.958 | -0.202 |
| 3.16 | 0.128 | -0.939 | -0.392 | -0.488 | -0.961 | -0.198 |
| 3.26 | 0.128 | -0.946 | -0.383 | -0.490 | -0.968 | -0.189 |
| 3.36 | 0.129 | -0.952 | -0.376 | -0.491 | -0.974 | -0.182 |
| 3.46 | 0.130 | -0.957 | -0.370 | -0.491 | -0.979 | -0.176 |
| 3.56 | 0.131 | -0.962 | -0.365 | -0.492 | -0.983 | -0.171 |
| 3.66 | 0.131 | -0.966 | -0.360 | -0.492 | -0.986 | -0.166 |
| 3.76 | 0.132 | -0.970 | -0.356 | -0.493 | -0.988 | -0.162 |
| 3.86 | 0.133 | -0.973 | -0.352 | -0.494 | -0.990 | -0.159 |
| 3.96 | 0.133 | -0.976 | -0.348 | -0.495 | -0.992 | -0.155 |
| 4.06 | 0.134 | -0.979 | -0.345 | -0.496 | -0.993 | -0.152 |
| 4.16 | 0.133 | -0.981 | -0.342 | -0.496 | -0.994 | -0.149 |
| 4.26 | 0.134 | -0.983 | -0.339 | -0.497 | -0.995 | -0.147 |
| 4.36 | 0.134 | -0.985 | -0.337 | -0.498 | -0.996 | -0.145 |

## 5 Natural bond orbital analysis

**Table S12.** Populations of the lone valency at silicon (N(LV(Si))) and the chlorine lone pair populations (N(LP($Cl_{leave}$)) and N(LP($Cl_{in}$)) in e).

| r /Å | N(LV(Si)) | N(LP($Cl_{leave}$)) | N(LP($Cl_{in}$)) |
|---|---|---|---|
| 2.37 | 0.501 | 1.684 | 1.684 |
| 2.45 | 0.497 | 1.709 | 1.668 |
| 2.55 | 0.492 | 1.741 | 1.650 |
| 2.65 | 0.485 | 1.772 | 1.635 |
| 2.75 | 0.479 | 1.800 | 1.622 |
| 2.85 | 0.472 | 1.827 | 1.611 |
| 2.95 | 0.466 | 1.850 | 1.601 |
| 3.05 | 0.459 | 1.871 | 1.593 |
| 3.15 | 0.454 | 1.889 | 1.586 |
| 3.25 | 0.449 | 1.905 | 1.580 |
| 3.35 | 0.445 | 1.919 | 1.574 |
| 3.45 | 0.441 | 1.930 | 1.569 |
| 3.55 | 0.438 | 1.941 | 1.564 |
| 3.65 | 0.435 | 1.949 | 1.560 |
| 3.75 | 0.434 | 1.957 | 1.556 |
| 3.85 | 0.432 | 1.963 | 1.553 |
| 3.95 | 0.431 | 1.969 | 1.550 |
| 4.10 | 0.431 | 1.976 | 1.546 |
| 4.25 | 0.430 | 1.981 | 1.542 |
| 4.40 | 0.431 | 1.985 | 1.538 |
| 4.60 | 0.432 | 1.990 | 1.535 |
| 4.80 | 0.434 | 1.993 | 1.531 |

**Table S13.** Populations of the lone valency at silicon (N(LV(C))) and the chlorine lone pair populations (N(LP($Cl_{leave}$)) and N(LP($Cl_{in}$)) in e).

| r /Å | N(LV(C)) | N(LP($Cl_{leave}$)) | N(LP($Cl_{in}$)) |
|---|---|---|---|
| 2.35 | 0.724 | 1.626 | 1.626 |
| 2.40 | 0.739 | 1.695 | 1.537 |
| 2.46 | 0.754 | 1.757 | 1.458 |
| 2.56 | 0.771 | 1.831 | 1.369 |
| 2.66 | 0.779 | 1.875 | 1.319 |
| 2.76 | 0.784 | 1.905 | 1.287 |
| 2.86 | 0.788 | 1.926 | 1.264 |
| 2.96 | 0.791 | 1.942 | 1.248 |
| 3.06 | 0.794 | 1.953 | 1.235 |
| 3.13 | 0.795 | 1.960 | 1.228 |
| 3.26 | 0.798 | 1.970 | 1.217 |
| 3.36 | 0.800 | 1.975 | 1.210 |
| 3.46 | 0.801 | 1.980 | 1.205 |
| 3.56 | 0.803 | 1.983 | 1.200 |
| 3.66 | 0.805 | 1.986 | 1.196 |
| 3.76 | 0.807 | 1.989 | 1.192 |
| 3.86 | 0.809 | 1.991 | 1.189 |
| 3.96 | 0.810 | 1.992 | 1.186 |
| 4.06 | 0.812 | 1.994 | 1.183 |
| 4.16 | 0.814 | 1.995 | 1.180 |
| 4.26 | 0.816 | 1.996 | 1.178 |
| 4.36 | 0.817 | 1.996 | 1.176 |

## 6 Valence bond calculations

**Table S14.** Weights of the valence bond structures representing the silicon system.

| r /Å | $Cl^-_{in}$ $SiH_3-Cl_{leave}$ | $Cl_{in}-SiH_3$ $Cl^-_{leave}$ | $Cl^-_{in}$ $SiH_3^+$ $Cl^-_{leave}$ |
|---|---|---|---|
| 2.37 | 0.279 | 0.279 | 0.443 |
| 2.45 | 0.303 | 0.250 | 0.447 |
| 2.55 | 0.331 | 0.218 | 0.451 |
| 2.65 | 0.357 | 0.192 | 0.451 |
| 2.75 | 0.380 | 0.168 | 0.451 |
| 2.85 | 0.402 | 0.147 | 0.451 |
| 2.95 | 0.420 | 0.131 | 0.450 |
| 3.05 | 0.435 | 0.117 | 0.448 |
| 3.15 | 0.448 | 0.105 | 0.447 |
| 3.25 | 0.459 | 0.095 | 0.447 |
| 3.35 | 0.468 | 0.085 | 0.447 |
| 3.45 | 0.476 | 0.076 | 0.447 |
| 3.55 | 0.483 | 0.068 | 0.449 |
| 3.65 | 0.489 | 0.061 | 0.450 |
| 3.75 | 0.495 | 0.054 | 0.451 |
| 3.85 | 0.500 | 0.047 | 0.453 |
| 3.95 | 0.508 | 0.042 | 0.450 |
| 4.10 | 0.514 | 0.033 | 0.453 |
| 4.25 | 0.520 | 0.026 | 0.455 |
| 4.40 | 0.525 | 0.020 | 0.456 |
| 4.60 | 0.530 | 0.013 | 0.457 |
| 4.80 | 0.535 | 0.008 | 0.457 |

**Table S15.** Weights of the valence bond structures representing the carbon system.

| r /Å | $Cl^-_{in}$ $CH_3-Cl_{leave}$ | $Cl_{in}-CH_3$ $Cl^-_{leave}$ | $Cl^-_{in}$ $CH_3^+$ $Cl^-_{leave}$ |
|---|---|---|---|
| 2.35 | 0.274 | 0.274 | 0.452 |
| 2.40 | 0.194 | 0.357 | 0.449 |
| 2.46 | 0.145 | 0.416 | 0.439 |
| 2.56 | 0.088 | 0.495 | 0.418 |
| 2.66 | 0.064 | 0.534 | 0.402 |
| 2.76 | 0.051 | 0.558 | 0.391 |
| 2.86 | 0.042 | 0.574 | 0.384 |
| 2.96 | 0.036 | 0.585 | 0.379 |
| 3.06 | 0.031 | 0.594 | 0.375 |
| 3.13 | 0.028 | 0.599 | 0.373 |
| 3.16 | 0.027 | 0.601 | 0.372 |
| 3.26 | 0.023 | 0.606 | 0.371 |
| 3.36 | 0.020 | 0.611 | 0.369 |
| 3.46 | 0.017 | 0.616 | 0.367 |
| 3.56 | 0.015 | 0.619 | 0.366 |

# Supporting Information – The role of hydrogen bonding in gas-phase $S_N2$ reactions at silicon

**Malte Fugel[a], Anneke Dittmer[a,b], Florian Kleemiss[a], and Simon Grabowsky[*a]**

[a]Universität Bremen, Fachbereich 2 – Biologie / Chemie, Leobener Str. 3, 28359 Bremen, Germany.
[b]*current address:* Max-Planck-Institut für Kohlenforschung, Kaiser-Wilhelm-Platz 1, 45470 Mülheim an der Ruhr, Germany.
[*]simon.grabowsky@uni-bremen.de

## 1 Potential energy surface (PES) scans

**Table S1.** Dissociation energies from the PES scan of $ClSiH_3Cl$.

| r /Å | $\Delta E$ /kJ·mol$^{-1}$ |
|---|---|
| 2.37 | -104.3 |
| 2.45 | -103.8 |
| 2.55 | -101.3 |
| 2.65 | -97.7 |
| 2.75 | -93.4 |
| 2.85 | -89.0 |
| 2.95 | -84.4 |
| 3.05 | -79.7 |
| 3.15 | -75.0 |
| 3.25 | -70.5 |
| 3.35 | -66.1 |
| 3.45 | -61.8 |
| 3.55 | -57.8 |
| 3.65 | -53.9 |
| 3.75 | -50.3 |
| 3.85 | -46.9 |
| 3.95 | -43.7 |
| 4.10 | -39.3 |
| 4.25 | -35.5 |
| 4.40 | -32.0 |
| 4.60 | -28.2 |
| 4.80 | -24.9 |

**Table S2.** Dissociation energies from the PES scan of $ClSiMe_3Cl$.

| r /Å | $\Delta E$ /kJ·mol$^{-1}$ |
|---|---|
| 2.46 | -64.39 |
| 2.55 | -64.35 |
| 2.60 | -64.18 |
| 2.65 | -63.92 |
| 2.86 | -63.35 |
| 2.90 | -63.39 |
| 3.00 | -63.79 |
| 3.10 | -64.41 |
| 3.20 | -65.28 |
| 3.30 | -65.96 |
| 3.40 | -66.64 |
| 3.50 | -67.10 |
| 3.55 | -67.11 |
| 3.60 | -67.05 |
| 3.70 | -66.58 |
| 3.80 | -65.63 |
| 3.95 | -63.39 |
| 4.10 | -60.34 |
| 4.25 | -56.77 |
| 4.40 | -53.06 |
| 4.60 | -47.84 |
| 4.80 | -42.81 |

**Table S3.** Dissociation energies from the PES scan of $ClSi(OMe)_3Cl$.

| r /Å | $\Delta E$ /kJ·mol$^{-1}$ |
|---|---|
| 2.39 | -33.0 |
| 2.50 | -35.9 |
| 2.60 | -38.5 |
| 2.70 | -40.5 |
| 2.80 | -42.9 |
| 2.90 | -45.3 |
| 3.00 | -47.6 |
| 3.10 | -50.0 |
| 3.25 | -53.5 |
| 3.40 | -56.4 |
| 3.55 | -58.8 |
| 3.75 | -61.3 |
| 3.95 | -63.0 |
| 4.15 | -64.0 |
| 4.35 | -64.2 |
| 4.45 | -63.5 |
| 4.60 | -61.9 |
| 4.80 | -59.4 |

**Table S4.** Dissociation energies from the PES scan of $FSiH_3F$.

| r /Å | $\Delta E$ /kJ·mol$^{-1}$ |
|---|---|
| 1.76 | -211.5 |
| 1.80 | -211.0 |
| 1.85 | -208.3 |
| 1.90 | -203.9 |
| 1.95 | -198.4 |
| 2.05 | -185.4 |
| 2.15 | -171.6 |
| 2.25 | -157.3 |
| 2.35 | -143.8 |
| 2.45 | -131.1 |
| 2.55 | -119.6 |
| 2.65 | -109.1 |
| 2.75 | -99.6 |
| 2.85 | -91.0 |
| 2.95 | -83.2 |
| 3.05 | -76.2 |
| 3.15 | -69.9 |
| 3.25 | -64.1 |
| 3.35 | -58.9 |
| 3.45 | -54.3 |
| 3.55 | -50.0 |
| 3.65 | -46.2 |

**Table S5.** Dissociation energies from the PES scan of $FSiMe_3F$.

| r /Å | $\Delta E$ /kJ·mol$^{-1}$ |
|---|---|
| 1.78 | -167.7 |
| 1.85 | -165.7 |
| 1.90 | -161.6 |
| 1.95 | -158.9 |
| 2.05 | -149.1 |
| 2.15 | -138.7 |
| 2.25 | -128.2 |
| 2.35 | -119.9 |
| 2.45 | -111.5 |
| 2.55 | -106.5 |
| 2.65 | -101.8 |
| 2.75 | -98.5 |
| 2.85 | -96.0 |
| 2.95 | -93.8 |
| 3.05 | -91.5 |
| 3.15 | -89.2 |
| 3.35 | -83.8 |
| 3.45 | -80.6 |
| 3.55 | -77.8 |
| 3.65 | -75.4 |

**Table S6.** Dissociation energies from the PES scan of $FSi(OMe)_3F$.

| r /Å | $\Delta E$ /kJ·mol$^{-1}$ |
|---|---|
| 1.72 | -201.6 |
| 1.75 | -201.1 |
| 1.76 | -200.7 |
| 1.85 | -192.7 |
| 1.90 | -187.6 |
| 1.95 | -182.6 |
| 2.01 | -174.5 |
| 2.05 | -170.5 |
| 2.11 | -161.7 |
| 2.21 | -150.0 |
| 2.31 | -139.2 |
| 2.41 | -130.3 |
| 2.55 | -124.1 |
| 2.65 | -121.3 |
| 2.75 | -119.8 |
| 2.85 | -119.2 |
| 2.95 | -119.0 |
| 3.05 | -119.1 |
| 3.15 | -119.2 |
| 3.25 | -119.7 |
| 3.35 | -120.0 |
| 3.45 | -120.0 |
| 3.55 | -119.7 |
| 3.65 | -119.5 |

## 2 Energy decomposition analysis (EDA)

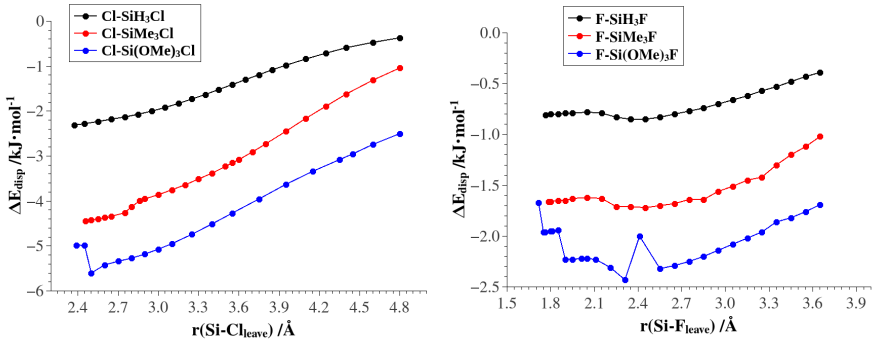


**Figure S1.** The dispersion interaction energy from the EDA of the chlorine (left) and fluorine (right) systems plotted against the $Si-X_{leave}$ distance.

**Table S7.** Energy contributions (in kJ·mol$^{-1}$) from the *energy decomposition analysis (EDA)* of Cl – $SiH_3$ – Cl.

| r /Å | $\Delta E_{orb}$ | $\Delta E_{elect}$ | $\Delta E_{Pauli}$ | $\Delta E_{disp}$ | $\Delta E_{int}$ | % of $\Delta E_{orb}$ |
|---|---|---|---|---|---|---|
| 2.37 | -60.80 | -77.55 | 90.75 | -2.31 | -49.91 | 43.2 |
| 2.45 | -51.81 | -67.38 | 75.50 | -2.28 | -45.97 | 42.7 |
| 2.55 | -42.15 | -56.40 | 59.59 | -2.23 | -41.19 | 41.8 |
| 2.65 | -34.34 | -47.41 | 47.06 | -2.18 | -36.87 | 40.9 |
| 2.75 | -28.09 | -40.03 | 37.16 | -2.13 | -33.09 | 40.0 |
| 2.85 | -23.07 | -33.93 | 29.35 | -2.07 | -29.72 | 39.1 |
| 2.95 | -19.06 | -28.87 | 23.17 | -2.00 | -26.76 | 38.2 |
| 3.05 | -15.89 | -24.78 | 18.25 | -1.92 | -24.34 | 37.3 |
| 3.15 | -13.35 | -21.38 | 14.36 | -1.83 | -22.20 | 36.5 |
| 3.25 | -11.30 | -18.58 | 11.29 | -1.73 | -20.32 | 35.7 |
| 3.35 | -9.64 | -16.25 | 8.89 | -1.63 | -18.63 | 35.0 |
| 3.45 | -8.28 | -14.34 | 7.00 | -1.52 | -17.14 | 34.3 |
| 3.55 | -7.17 | -12.74 | 5.51 | -1.41 | -15.81 | 33.6 |
| 3.65 | -6.24 | -11.41 | 4.35 | -1.30 | -14.60 | 32.9 |
| 3.75 | -5.47 | -10.29 | 3.44 | -1.19 | -13.51 | 32.3 |
| 3.85 | -4.82 | -9.35 | 2.73 | -1.08 | -12.52 | 31.6 |
| 3.95 | -4.27 | -8.53 | 2.18 | -0.98 | -11.60 | 31.0 |
| 4.10 | -3.60 | -7.52 | 1.56 | -0.84 | -10.40 | 30.1 |
| 4.25 | -3.06 | -6.71 | 1.14 | -0.71 | -9.34 | 29.2 |
| 4.40 | -2.62 | -6.03 | 0.84 | -0.59 | -8.40 | 28.4 |
| 4.60 | -2.15 | -5.23 | 0.57 | -0.47 | -7.28 | 27.4 |
| 4.80 | -1.79 | -4.73 | 0.40 | -0.37 | -6.49 | 26.0 |

**Table S8.** Energy contributions (in kJ·mol$^{-1}$) from the *energy decomposition analysis (EDA)* of Cl – $SiMe_3$ – Cl.

| r /Å | $\Delta E_{orb}$ | $\Delta E_{elect}$ | $\Delta E_{Pauli}$ | $\Delta E_{disp}$ | $\Delta E_{int}$ | % of $\Delta E_{orb}$ |
|---|---|---|---|---|---|---|
| 2.46 | -50.02 | -76.08 | 84.56 | -4.44 | -45.98 | 38.3 |
| 2.50 | -45.72 | -70.86 | 77.81 | -4.42 | -43.19 | 37.8 |
| 2.55 | -41.41 | -65.55 | 70.92 | -4.40 | -40.44 | 37.2 |
| 2.60 | -37.57 | -60.74 | 64.72 | -4.37 | -37.96 | 36.6 |
| 2.65 | -34.14 | -56.39 | 59.18 | -4.34 | -35.69 | 36.0 |
| 2.75 | -28.37 | -48.89 | 49.79 | -4.26 | -31.73 | 34.8 |
| 2.80 | -25.95 | -45.96 | 46.39 | -4.13 | -29.65 | 34.1 |
| 2.86 | -23.46 | -42.90 | 42.96 | -3.99 | -27.39 | 33.3 |
| 2.90 | -22.05 | -40.94 | 40.64 | -3.95 | -26.30 | 32.9 |
| 3.00 | -19.01 | -36.55 | 35.45 | -3.86 | -23.97 | 32.0 |
| 3.10 | -16.70 | -32.86 | 31.16 | -3.75 | -22.15 | 31.3 |
| 3.20 | -14.95 | -29.78 | 27.63 | -3.64 | -20.74 | 30.9 |
| 3.30 | -13.62 | -27.13 | 24.55 | -3.51 | -19.71 | 30.8 |
| 3.40 | -12.57 | -24.80 | 21.77 | -3.38 | -18.98 | 30.8 |
| 3.50 | -11.71 | -22.71 | 19.20 | -3.23 | -18.45 | 31.1 |
| 3.55 | -11.31 | -21.66 | 17.92 | -3.15 | -18.20 | 31.3 |
| 3.60 | -10.92 | -20.72 | 16.71 | -3.08 | -18.01 | 31.5 |
| 3.70 | -10.16 | -18.85 | 14.33 | -2.91 | -17.59 | 31.8 |
| 3.80 | -9.43 | -17.13 | 12.11 | -2.73 | -17.18 | 32.2 |
| 3.95 | -8.35 | -14.80 | 9.16 | -2.45 | -16.44 | 32.6 |
| 4.10 | -7.34 | -12.81 | 6.74 | -2.16 | -15.57 | 32.9 |
| 4.25 | -6.42 | -11.14 | 4.87 | -1.89 | -14.58 | 33.0 |
| 4.40 | -5.61 | -9.79 | 3.48 | -1.62 | -13.54 | 33.0 |
| 4.60 | -4.71 | -8.37 | 2.22 | -1.31 | -12.17 | 32.7 |
| 4.80 | -3.97 | -7.29 | 1.44 | -1.04 | -10.86 | 32.3 |

**Table S9.** Energy contributions (in kJ·mol$^{-1}$) from the *energy decomposition analysis (EDA)* of Cl – $Si(OMe)_3$ – Cl.

| r /Å | $\Delta E_{orb}$ | $\Delta E_{elect}$ | $\Delta E_{Pauli}$ | $\Delta E_{disp}$ | $\Delta E_{int}$ | % of $\Delta E_{orb}$ |
|---|---|---|---|---|---|---|
| 2.39 | -57.71 | -89.55 | 100.25 | -4.98 | -51.99 | 37.9 |
| 2.45 | -51.11 | -82.01 | 91.28 | -4.99 | -46.83 | 37.0 |
| 2.50 | -44.87 | -84.64 | 90.71 | -5.60 | -44.40 | 33.2 |
| 2.60 | -37.57 | -73.69 | 77.33 | -5.42 | -39.35 | 32.2 |
| 2.70 | -31.95 | -65.13 | 67.39 | -5.34 | -35.03 | 31.2 |
| 2.80 | -27.60 | -58.02 | 59.30 | -5.27 | -31.59 | 30.4 |
| 2.90 | -24.32 | -52.01 | 52.66 | -5.18 | -28.85 | 29.8 |
| 3.00 | -21.95 | -47.19 | 47.33 | -5.07 | -26.88 | 29.6 |
| 3.10 | -20.22 | -43.21 | 42.90 | -4.95 | -25.48 | 29.6 |
| 3.25 | -18.48 | -38.56 | 37.64 | -4.74 | -24.14 | 29.9 |
| 3.40 | -17.42 | -35.32 | 33.77 | -4.51 | -23.48 | 30.4 |
| 3.55 | -16.79 | -33.10 | 30.95 | -4.27 | -23.21 | 31.0 |
| 3.75 | -16.28 | -31.09 | 28.19 | -3.95 | -23.13 | 31.7 |
| 3.95 | -15.84 | -29.63 | 25.90 | -3.63 | -23.20 | 32.3 |
| 4.15 | -15.28 | -28.29 | 23.72 | -3.34 | -23.19 | 32.6 |
| 4.35 | -14.52 | -26.45 | 20.97 | -3.08 | -23.08 | 33.0 |
| 4.45 | -13.91 | -25.82 | 19.72 | -2.95 | -22.96 | 32.6 |
| 4.60 | -12.91 | -23.96 | 16.85 | -2.74 | -22.76 | 32.6 |
| 4.80 | -11.14 | -21.44 | 13.08 | -2.50 | -22.00 | 31.8 |

**Table S10.** Energy contributions (in kJ·mol$^{-1}$) from the *energy decomposition analysis (EDA)* of F – $SiH_3$ – F.

| r /Å | $\Delta E_{orb}$ | $\Delta E_{elect}$ | $\Delta E_{Pauli}$ | $\Delta E_{disp}$ | $\Delta E_{int}$ | % of $\Delta E_{orb}$ |
|---|---|---|---|---|---|---|
| 1.76 | -96.79 | -138.92 | 158.88 | -0.81 | -77.64 | 40.9 |
| 1.80 | -90.25 | -129.23 | 144.36 | -0.80 | -75.92 | 41.0 |
| 1.85 | -82.08 | -117.36 | 126.98 | -0.80 | -73.26 | 41.0 |
| 1.90 | -74.55 | -106.65 | 111.74 | -0.79 | -70.25 | 41.0 |
| 1.95 | -67.63 | -97.02 | 98.35 | -0.79 | -67.09 | 41.0 |
| 2.05 | -54.64 | -81.03 | 76.81 | -0.78 | -59.64 | 40.0 |
| 2.15 | -45.59 | -67.02 | 59.15 | -0.79 | -54.25 | 40.2 |
| 2.25 | -37.42 | -56.05 | 45.93 | -0.83 | -48.37 | 39.7 |
| 2.35 | -30.79 | -47.11 | 35.68 | -0.85 | -43.07 | 39.1 |
| 2.45 | -25.43 | -39.81 | 27.72 | -0.85 | -38.37 | 38.5 |
| 2.55 | -21.12 | -33.84 | 21.55 | -0.83 | -34.24 | 37.9 |
| 2.65 | -17.64 | -28.95 | 16.75 | -0.80 | -30.64 | 37.2 |
| 2.75 | -14.83 | -24.94 | 13.04 | -0.77 | -27.50 | 36.6 |
| 2.85 | -12.55 | -21.64 | 10.15 | -0.74 | -24.78 | 35.9 |
| 2.95 | -10.69 | -18.92 | 7.92 | -0.70 | -22.39 | 35.3 |
| 3.05 | -9.17 | -16.66 | 6.20 | -0.66 | -20.29 | 34.6 |
| 3.15 | -7.91 | -14.78 | 4.86 | -0.62 | -18.45 | 33.9 |
| 3.25 | -6.94 | -13.21 | 3.83 | -0.57 | -16.89 | 33.5 |
| 3.35 | -6.07 | -11.89 | 3.03 | -0.53 | -15.46 | 32.8 |
| 3.45 | -5.33 | -10.76 | 2.40 | -0.48 | -14.17 | 32.2 |
| 3.55 | -4.71 | -9.80 | 1.92 | -0.43 | -13.02 | 31.5 |
| 3.65 | -4.17 | -8.97 | 1.54 | -0.39 | -11.99 | 30.8 |

**Table S11.** Energy contributions (in kJ·mol$^{-1}$) from the *energy decomposition analysis (EDA)* of F – $SiMe_3$ – F.

| r /Å | $\Delta E_{orb}$ | $\Delta E_{elect}$ | $\Delta E_{Pauli}$ | $\Delta E_{disp}$ | $\Delta E_{int}$ | % of $\Delta E_{orb}$ |
|---|---|---|---|---|---|---|
| 1.79 | -92.54 | -140.04 | 162.95 | -1.66 | -71.29 | 39.5 |
| 1.80 | -89.99 | -136.01 | 157.19 | -1.66 | -70.47 | 39.5 |
| 1.85 | -82.17 | -123.74 | 139.61 | -1.65 | -67.95 | 39.6 |
| 1.90 | -74.82 | -112.53 | 124.96 | -1.65 | -64.04 | 39.6 |
| 1.95 | -68.51 | -102.81 | 110.75 | -1.63 | -62.20 | 39.6 |
| 2.05 | -57.03 | -85.92 | 88.56 | -1.62 | -56.01 | 39.4 |
| 2.15 | -47.61 | -72.28 | 71.39 | -1.63 | -50.13 | 39.2 |
| 2.25 | -39.97 | -61.26 | 58.14 | -1.71 | -44.80 | 38.8 |
| 2.35 | -34.04 | -53.92 | 50.50 | -1.71 | -39.17 | 38.0 |
| 2.45 | -29.30 | -46.96 | 42.58 | -1.72 | -35.40 | 37.6 |
| 2.55 | -25.88 | -42.10 | 37.81 | -1.70 | -31.87 | 37.1 |
| 2.65 | -23.30 | -38.05 | 33.73 | -1.68 | -29.30 | 37.0 |
| 2.75 | -21.44 | -34.80 | 30.55 | -1.64 | -27.33 | 37.0 |
| 2.85 | -21.77 | -34.48 | 32.02 | -1.64 | -25.87 | 37.6 |
| 2.95 | -19.02 | -29.78 | 25.34 | -1.56 | -25.02 | 37.8 |
| 3.05 | -18.06 | -27.49 | 22.75 | -1.51 | -24.31 | 38.4 |
| 3.15 | -17.03 | -25.23 | 20.01 | -1.45 | -23.70 | 39.0 |
| 3.25 | -17.74 | -24.91 | 20.42 | -1.42 | -23.65 | 40.3 |
| 3.35 | -14.81 | -20.90 | 14.79 | -1.30 | -22.22 | 40.0 |
| 3.45 | -15.55 | -21.02 | 16.22 | -1.20 | -21.55 | 41.2 |
| 3.55 | -15.40 | -20.13 | 15.75 | -1.12 | -20.90 | 42.0 |
| 3.65 | -16.22 | -20.35 | 17.80 | -1.02 | -19.79 | 43.1 |

**Table S12.** Energy contributions (in kJ·mol$^{-1}$) from the *energy decomposition analysis (EDA)* of F – $Si(OMe)_3$ – F.

| r /Å | $\Delta E_{orb}$ | $\Delta E_{elect}$ | $\Delta E_{Pauli}$ | $\Delta E_{disp}$ | $\Delta E_{int}$ | % of $\Delta E_{orb}$ |
|---|---|---|---|---|---|---|
| 1.72 | -107.38 | -168.04 | 175.30 | -1.67 | -101.79 | 38.8 |
| 1.75 | -98.72 | -165.93 | 170.59 | -1.96 | -96.02 | 37.0 |
| 1.76 | -97.08 | -163.08 | 166.79 | -1.96 | -95.33 | 37.0 |
| 1.80 | -90.85 | -152.30 | 152.66 | -1.95 | -92.44 | 37.1 |
| 1.81 | -89.34 | -149.73 | 149.35 | -1.95 | -91.67 | 37.1 |
| 1.85 | -83.54 | -139.97 | 137.01 | -1.94 | -88.44 | 37.1 |
| 1.90 | -76.74 | -140.90 | 135.81 | -2.23 | -84.06 | 34.9 |
| 1.95 | -71.46 | -132.12 | 125.02 | -2.23 | -80.79 | 34.7 |
| 2.01 | -64.22 | -120.19 | 110.83 | -2.22 | -75.80 | 34.4 |
| 2.05 | -60.67 | -114.36 | 104.09 | -2.22 | -73.16 | 34.2 |
| 2.11 | -54.76 | -104.67 | 93.21 | -2.23 | -68.45 | 33.9 |
| 2.21 | -47.30 | -92.34 | 80.01 | -2.31 | -61.94 | 33.3 |
| 2.31 | -41.15 | -81.95 | 69.47 | -2.43 | -56.06 | 32.8 |
| 2.41 | -38.58 | -76.28 | 65.31 | -2.00 | -51.55 | 33.0 |
| 2.55 | -37.01 | -69.78 | 62.63 | -2.32 | -46.48 | 33.9 |
| 2.65 | -35.48 | -65.47 | 59.56 | -2.29 | -43.68 | 34.4 |
| 2.75 | -34.55 | -62.17 | 57.19 | -2.25 | -41.78 | 34.9 |
| 2.85 | -33.85 | -59.44 | 55.28 | -2.20 | -40.21 | 35.4 |
| 2.95 | -33.41 | -57.24 | 53.75 | -2.14 | -39.04 | 36.0 |
| 3.05 | -33.10 | -55.47 | 52.41 | -2.08 | -38.24 | 36.5 |
| 3.15 | -32.96 | -54.22 | 51.40 | -2.02 | -37.80 | 37.0 |
| 3.25 | -32.63 | -52.75 | 50.00 | -1.96 | -37.34 | 37.4 |
| 3.35 | -32.30 | -51.45 | 48.63 | -1.86 | -36.98 | 37.7 |
| 3.45 | -31.84 | -50.11 | 47.05 | -1.82 | -36.72 | 38.0 |
| 3.55 | -31.22 | -48.67 | 45.18 | -1.76 | -36.47 | 38.2 |
| 3.65 | -30.34 | -46.99 | 42.83 | -1.69 | -36.19 | 38.4 |

## 3 Quantum Theory of Atoms in Molecules

**Table S13.** QTAIM properties of $ClSiH_3Cl$ ($\rho$ in eÅ$^{-3}$).

| r /Å | $\rho_{bcp}$(Si−Cl) |
|---|---|
| 2.37 | 0.369 |
| 2.45 | 0.325 |
| 2.55 | 0.275 |
| 2.65 | 0.232 |
| 2.75 | 0.195 |
| 2.85 | 0.164 |
| 2.95 | 0.137 |
| 3.05 | 0.115 |
| 3.15 | 0.096 |
| 3.25 | 0.081 |
| 3.35 | 0.068 |
| 3.45 | 0.057 |
| 3.55 | 0.049 |
| 3.65 | 0.041 |
| 3.75 | 0.034 |
| 3.85 | 0.029 |
| 3.95 | 0.024 |
| 4.1 | 0.019 |
| 4.25 | 0.015 |
| 4.4 | 0.011 |
| 4.6 | 0.008 |
| 4.8 | 0.006 |

**Table S14.** QTAIM properties of $ClSiMe_3Cl$ ($\rho$ in eÅ$^{-3}$).

| r | $\rho_{bcp}$(Si−Cl) | $\sum\rho_{bcp}$(Cl−H) | $\sum$DI(Cl−H) |
|---|---|---|---|
| 2.45 | 0.327 | – | 0.180 |
| 2.50 | 0.302 | – | 0.195 |
| 2.55 | 0.277 | – | 0.198 |
| 2.60 | 0.255 | – | 0.200 |
| 2.65 | 0.233 | – | 0.202 |
| 2.75 | 0.196 | – | 0.206 |
| 2.86 | 0.159 | – | 0.220 |
| 2.90 | 0.148 | – | 0.223 |
| 3.00 | 0.123 | – | 0.229 |
| 3.10 | 0.103 | 0.253 | 0.234 |
| 3.20 | 0.086 | 0.248 | 0.239 |
| 3.30 | 0.072 | 0.240 | 0.242 |
| 3.40 | 0.060 | 0.233 | 0.243 |
| 3.50 | 0.051 | 0.223 | 0.241 |
| 3.55 | – | 0.221 | 0.238 |
| 3.60 | – | 0.208 | 0.236 |
| 3.70 | – | 0.194 | 0.227 |
| 3.80 | – | 0.177 | 0.216 |
| 3.95 | – | 0.150 | 0.197 |
| 4.10 | – | 0.124 | 0.175 |
| 4.25 | – | 0.102 | 0.153 |
| 4.40 | – | 0.082 | 0.132 |
| 4.60 | – | 0.059 | 0.107 |
| 4.80 | – | 0.045 | 0.086 |

**Table S15.** QTAIM properties of $ClSi(OMe)_3Cl$ ($\rho$ in eÅ$^{-3}$).

| r | $\rho_{bcp}$(Si−Cl) | $\sum\rho_{bcp}$(Cl−H) | $\sum$DI(Cl−H) |
|---|---|---|---|
| 2.35 | 0.372 | – | 0.095 |
| 2.45 | 0.338 | – | 0.103 |
| 2.50 | 0.306 | 0.177 | 0.226 |
| 2.60 | 0.257 | 0.291 | 0.245 |
| 2.70 | 0.215 | 0.303 | 0.259 |
| 2.90 | 0.149 | 0.316 | 0.279 |
| 3.00 | 0.125 | 0.322 | 0.289 |
| 3.10 | 0.104 | 0.326 | 0.297 |
| 3.25 | 0.080 | 0.330 | 0.307 |
| 3.40 | 0.062 | 0.333 | 0.316 |
| 3.55 | 0.048 | 0.335 | 0.325 |
| 3.75 | 0.034 | 0.335 | 0.333 |
| 3.95 | – | 0.330 | 0.338 |
| 4.15 | – | 0.320 | 0.335 |
| 4.35 | – | 0.300 | 0.324 |
| 4.45 | – | 0.287 | 0.314 |
| 4.60 | – | 0.260 | 0.292 |
| 4.80 | – | 0.219 | 0.257 |

**Table S16.** QTAIM properties of $FSiH_3F$ ($\rho$ in eÅ$^{-3}$).

| r /Å | $\rho_{bcp}$(Si−F) |
|---|---|
| 1.76 | 0.619 |
| 1.80 | 0.570 |
| 1.85 | 0.512 |
| 1.90 | 0.463 |
| 1.95 | 0.420 |
| 2.05 | 0.349 |
| 2.15 | 0.294 |
| 2.25 | 0.248 |
| 2.35 | 0.210 |
| 2.45 | 0.177 |
| 2.55 | 0.149 |
| 2.65 | 0.125 |
| 2.75 | 0.105 |
| 2.85 | 0.088 |
| 2.95 | 0.074 |
| 3.05 | 0.062 |
| 3.15 | 0.052 |
| 3.25 | 0.043 |
| 3.35 | 0.036 |
| 3.45 | 0.030 |
| 3.55 | 0.026 |
| 3.65 | 0.021 |

**Table S17.** QTAIM properties of $FSiMe_3F$ ($\rho$ in eÅ$^{-3}$).

| r | $\rho_{bcp}$(Si−F) | $\sum\rho_{bcp}$(F−H) | $\sum$DI(F−H) |
|---|---|---|---|
| 1.78 | 0.589 | – | 0.149 |
| 1.80 | 0.569 | – | 0.136 |
| 1.85 | 0.512 | – | 0.138 |
| 1.90 | 0.462 | – | 0.143 |
| 1.95 | 0.420 | – | 0.143 |
| 2.05 | 0.349 | – | 0.149 |
| 2.15 | 0.294 | – | 0.153 |
| 2.25 | 0.248 | – | 0.158 |
| 2.35 | 0.209 | – | 0.182 |
| 2.45 | 0.175 | – | 0.189 |
| 2.55 | 0.147 | – | 0.204 |
| 2.65 | 0.123 | 0.310 | 0.216 |
| 2.75 | 0.103 | 0.310 | 0.227 |
| 2.85 | 0.086 | 0.310 | 0.235 |
| 2.95 | 0.073 | 0.308 | 0.241 |
| 3.05 | – | 0.300 | 0.243 |
| 3.15 | – | 0.285 | 0.239 |
| 3.35 | – | 0.244 | 0.219 |
| 3.45 | – | 0.233 | 0.216 |
| 3.55 | – | 0.238 | 0.217 |
| 3.65 | – | 0.240 | 0.203 |

**Table S18.** QTAIM properties of $FSi(OMe)_3F$ ($\rho$ in eÅ$^{-3}$).

| r | $\rho_{bcp}$(Si−F) | $\sum\rho_{bcp}$(F−H) | $\sum$DI(F−H) |
|---|---|---|---|
| 1.72 | 0.749 | – | 0.104 |
| 1.75 | 0.651 | – | 0.106 |
| 1.76 | 0.637 | – | 0.107 |
| 1.80 | 0.576 | – | 0.111 |
| 1.81 | 0.571 | – | 0.111 |
| 1.85 | 0.515 | – | 0.162 |
| 1.90 | 0.466 | – | 0.168 |
| 1.95 | 0.428 | – | 0.173 |
| 2.01 | 0.379 | – | 0.181 |
| 2.11 | 0.318 | – | 0.193 |
| 2.21 | 0.270 | – | 0.205 |
| 2.31 | 0.228 | 0.312 | 0.216 |
| 2.41 | 0.188 | 0.401 | 0.263 |
| 2.55 | 0.146 | 0.525 | 0.319 |
| 2.65 | 0.123 | 0.545 | 0.334 |
| 2.75 | 0.103 | 0.569 | 0.347 |
| 2.85 | 0.086 | 0.578 | 0.358 |
| 2.95 | 0.072 | 0.590 | 0.368 |
| 3.05 | 0.061 | 0.599 | 0.377 |
| 3.15 | 0.051 | 0.606 | 0.384 |
| 3.25 | 0.043 | 0.607 | 0.388 |
| 3.35 | 0.036 | 0.604 | 0.391 |
| 3.45 | – | 0.598 | 0.391 |
| 3.55 | – | 0.588 | 0.388 |
| 3.65 | – | 0.569 | 0.382 |

## 4 Atomic coordinates

**Table S19.** Coordinates of $ClSiH_3Cl$ at the TC.

| Atom No. | Element | x /Å | y /Å | z /Å |
|---|---|---|---|---|
| 1 | Si | -0.000284 | 0.000000 | 0.000000 |
| 2 | H | 0.735889 | 1.275589 | 0.000000 |
| 3 | H | 0.735889 | -1.275589 | 0.000000 |
| 4 | H | -1.473171 | 0.000000 | 0.000000 |
| 5 | Cl | 0.000839 | 0.000000 | -2.372625 |
| 6 | Cl | 0.000839 | 0.000000 | 2.372625 |

**Table S20.** Coordinates of $ClSiMe_3Cl$ at the TC.

| Atom No. | Element | x /Å | y /Å | z /Å |
|---|---|---|---|---|
| 1 | Si | 0.226996 | 0.344767 | 0.005823 |
| 2 | C | 2.113550 | 0.312043 | 0.087568 |
| 3 | C | -0.681575 | 1.999754 | -0.041316 |
| 4 | C | -0.749923 | -1.269391 | -0.077905 |
| 5 | H | -0.135438 | -2.031684 | -0.557712 |
| 6 | H | -1.625212 | -1.119825 | -0.710507 |
| 7 | H | -1.056489 | -1.606649 | 0.908509 |
| 8 | H | 2.505867 | 1.176483 | -0.448956 |
| 9 | H | 2.472164 | 0.318437 | 1.113374 |
| 10 | H | 2.476853 | -0.576559 | -0.429196 |
| 11 | H | -1.665222 | 1.877350 | 0.413313 |
| 12 | H | -0.787619 | 2.370532 | -1.057329 |
| 13 | H | -0.136072 | 2.722145 | 0.566014 |
| 14 | Cl | 0.057615 | 0.394468 | 2.452715 |
| 15 | Cl | 0.396025 | 0.289177 | -2.443116 |

**Table S21.** Coordinates of $ClSiMe_3Cl$ at the TS.

| Atom No. | Element | x /Å | y /Å | z /Å |
|---|---|---|---|---|
| 1 | Si | 0.200249 | -0.000494 | 0.002879 |
| 2 | C | 0.017575 | -1.524170 | -1.082652 |
| 3 | C | 0.016779 | 1.708676 | -0.757816 |
| 4 | C | 0.022707 | -0.190469 | 1.864499 |
| 5 | H | 0.546473 | -1.093189 | 2.183379 |
| 6 | H | -1.023342 | -0.245048 | 2.149003 |
| 7 | H | 0.499569 | 0.658568 | 2.357324 |
| 8 | H | 0.470951 | -1.326515 | -2.055560 |
| 9 | H | 0.563017 | -2.352573 | -0.627537 |
| 10 | H | -1.028249 | -1.785998 | -1.207442 |
| 11 | H | 0.575859 | 2.427660 | -0.156837 |
| 12 | H | -1.028239 | 1.996031 | -0.814415 |
| 13 | H | 0.455479 | 1.703103 | -1.757174 |
| 14 | Cl | 2.474481 | 0.002137 | -0.009042 |
| 15 | Cl | -2.661384 | 0.001431 | -0.005972 |

**Table S22.** Coordinates of $ClSiMe_3Cl$ at the RC.

| Atom No. | Element | x /Å | y /Å | z /Å |
|---|---|---|---|---|
| 1 | Si | 0.00020 | 0.00000 | 0.55111 |
| 2 | C | 1.80802 | 0.00000 | 0.08728 |
| 3 | C | -0.90535 | 1.56564 | 0.08963 |
| 4 | C | -0.90535 | -1.56564 | 0.08963 |
| 5 | H | -0.93286 | -1.61043 | -1.00064 |
| 6 | H | -1.92222 | -1.55683 | 0.48475 |
| 7 | H | -0.38919 | -2.44308 | 0.48191 |
| 8 | H | 1.85786 | 0.00000 | -1.00318 |
| 9 | H | 2.30975 | -0.88549 | 0.48018 |
| 10 | H | 2.30975 | 0.88549 | 0.48018 |
| 11 | H | -0.93286 | 1.61043 | -1.00064 |
| 12 | H | -0.38919 | 2.44308 | 0.48191 |
| 13 | H | -1.92222 | 1.55683 | 0.48475 |
| 14 | Cl | 0.00166 | 0.00000 | 2.72256 |
| 15 | Cl | 0.01203 | 0.00000 | -3.00035 |

**Table S23.** Coordinates of $ClSi(OMe)_3Cl$ at the TS.

| Atom No. | Element | x /Å | y /Å | z /Å |
|---|---|---|---|---|
| 1 | Si | 3.088904 | -0.034731 | -0.142551 |
| 2 | O | 3.449914 | 1.571710 | 0.021900 |
| 3 | O | 3.273220 | -0.682546 | -1.645545 |
| 4 | O | 2.536483 | -0.912350 | 1.144254 |
| 5 | C | 2.576746 | -0.401329 | -2.839188 |
| 6 | C | 2.999895 | 2.375163 | 1.086556 |
| 7 | C | 3.107827 | -2.011497 | 1.815969 |
| 8 | H | 3.287485 | 3.407147 | 0.874114 |
| 9 | H | 3.465680 | 2.074178 | 2.031521 |
| 10 | H | 1.913595 | 2.322206 | 1.191400 |
| 11 | H | 3.496912 | -2.757042 | 1.120327 |
| 12 | H | 2.316617 | -2.464229 | 2.419340 |
| 13 | H | 3.929139 | -1.702885 | 2.464394 |
| 14 | H | 2.462382 | 0.672387 | -2.998105 |
| 15 | H | 1.581041 | -0.846157 | -2.833797 |
| 16 | H | 3.163000 | -0.823761 | -3.659235 |
| 17 | Cl | 0.794436 | 0.522147 | -0.516248 |
| 18 | Cl | 5.329954 | -0.595766 | 0.288066 |

**Table S24.** Coordinates of $ClSi(OMe)_3Cl$ at the RC.

| Atom No. | Element | x /Å | y /Å | z /Å |
|---|---|---|---|---|
| 1 | Si | 1.932102 | -0.001994 | 0.001654 |
| 2 | O | 2.352555 | 1.570125 | 0.030062 |
| 3 | O | 2.362518 | -0.761229 | -1.372321 |
| 4 | O | 2.363443 | -0.808492 | 1.347984 |
| 5 | C | 3.438862 | -0.367668 | -2.237537 |
| 6 | C | 3.422377 | 2.131095 | 0.806542 |
| 7 | C | 3.430644 | -1.764679 | 1.439765 |
| 8 | H | 3.484157 | 3.186568 | 0.542980 |
| 9 | H | 4.370744 | 1.634835 | 0.589981 |
| 10 | H | 3.197970 | 2.041172 | 1.871422 |
| 11 | H | 3.206309 | -2.636151 | 0.821151 |
| 12 | H | 3.489164 | -2.073560 | 2.483065 |
| 13 | H | 4.380315 | -1.327326 | 1.124548 |
| 14 | H | 4.383397 | -0.309292 | -1.692547 |
| 15 | H | 3.218482 | 0.600999 | -2.690941 |
| 16 | H | 3.505674 | -1.121401 | -3.021583 |
| 17 | Cl | -0.159441 | -0.011170 | -0.000072 |
| 18 | Cl | 6.200686 | 0.007952 | 0.015905 |

**Table S25.** Coordinates of $FSiH_3F$ at the TC.

| Atom No. | Element | x /Å | y /Å | z /Å |
|---|---|---|---|---|
| 1 | Si | 0.000000 | 0.000173 | 0.000000 |
| 2 | H | 0.037976 | 0.751464 | 1.301661 |
| 3 | H | 0.037976 | 0.751464 | -1.301661 |
| 4 | H | -0.075774 | -1.501196 | 0.000000 |
| 5 | F | -1.760504 | 0.088693 | 0.000000 |
| 6 | F | 1.760484 | -0.089155 | 0.000000 |

**Table S26.** Coordinates of $FSiMe_3F$ at the TC.

| Atom No. | Element | x /Å | y /Å | z /Å |
|---|---|---|---|---|
| 1 | Si | 0.227642 | 0.344972 | 0.003871 |
| 2 | C | 2.139570 | 0.312458 | 0.097055 |
| 3 | C | -0.694771 | 2.021607 | -0.046000 |
| 4 | C | -0.763262 | -1.291033 | -0.080697 |
| 5 | H | -0.159923 | -2.059973 | -0.570847 |
| 6 | H | -1.649158 | -1.147607 | -0.705413 |
| 7 | H | -1.072047 | -1.650513 | 0.900915 |
| 8 | H | 2.546271 | 1.158324 | -0.463757 |
| 9 | H | 2.514101 | 0.346855 | 1.120119 |
| 10 | H | 2.513999 | -0.591650 | -0.390901 |
| 11 | H | -1.674551 | 1.913323 | 0.427459 |
| 12 | H | -0.827957 | 2.400468 | -1.059310 |
| 13 | H | -0.145177 | 2.759792 | 0.544385 |
| 14 | F | 0.105995 | 0.366665 | 1.780652 |
| 15 | F | 0.350787 | 0.317360 | -1.776251 |

**Table S27.** Coordinates of $FSi(OMe)_3F$ at the TC.

| Atom No. | Element | x /Å | y /Å | z /Å |
|---|---|---|---|---|
| 1 | Si | 3.219459 | -0.083793 | 0.002890 |
| 2 | O | 3.748608 | 1.405995 | 0.622312 |
| 3 | O | 3.400823 | -0.461928 | -1.642509 |
| 4 | O | 2.520248 | -1.223110 | 1.049795 |
| 5 | C | 2.410098 | -0.322032 | -2.621297 |
| 6 | C | 2.940820 | 2.528880 | 0.836171 |
| 7 | C | 3.231778 | -2.206121 | 1.749535 |
| 8 | H | 3.556606 | 3.306032 | 1.303841 |
| 9 | H | 2.093690 | 2.315870 | 1.497111 |
| 10 | H | 2.528288 | 2.933294 | -0.095248 |
| 11 | H | 3.762016 | -2.893473 | 1.081245 |
| 12 | H | 2.515325 | -2.786100 | 2.343013 |
| 13 | H | 3.976753 | -1.778676 | 2.429471 |
| 14 | H | 2.114754 | 0.722288 | -2.774132 |
| 15 | H | 1.499923 | -0.881316 | -2.379006 |
| 16 | H | 2.810138 | -0.706766 | -3.566719 |
| 17 | F | 1.638933 | 0.530574 | -0.260961 |
| 18 | F | 4.784000 | -0.680527 | 0.254816 |

# Supporting Information – Complementary bonding analysis of the N – Si interaction in pentacoordinated silicon compounds using quantum crystallography

**Malte Fugel[a], Maksym V. Ponomarenko[b], Maxie F. Hesse[a], Lorraine A. Malaspina[a], Florian Kleemiss[a], Kunihisa Sugimoto[c], Alessandro Genoni[d], Gerd-Volker Röschenthaler[b], and Simon Grabowsky[a*]**

[a]University of Bremen, Department 2: Biology/Chemistry, Institute of Inorganic Chemistry and Crystallography, Leobener Str. 3, 28359 Bremen, Germany.
[b]Jacobs University, Life Sciences & Chemistry, Campus Ring 1, 28759 Bremen, Germany.
[c]JASRI / Diffraction & Scattering Division, 1-1-1 Kouto, Sayo-cho, Sayo-gun, Hyogo 679-5198, Japan.
[d]Université de Lorraine, CNRS, Laboratoire LPCT, 1 Boulevard Arago, F-57078 Metz, France.

## 1 Characterization of the compounds

**8-(chloro(methyl)(phenyl)silyl)-N,N-dimethylnaphthalen-1-amine, 3**

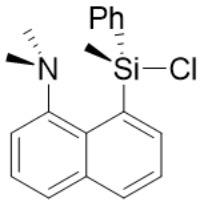


White crystals; melting point = 149 - 150°C; 1H NMR (401 MHz, $CDCl_3$) $\delta$ 8.73 (dd, J = 7.0, 1.1 Hz, 1H), 7.97 (dd, J = 8.1, 1.0 Hz, 1H), 7.76 (d, J = 8.1 Hz, 1H), 7.69 (dd, J = 8.1, 7.0 Hz, 1H), 7.46 (t, J = 7.8 Hz, 1H), 7.37 (m, 2H), 7.40-7.33 (m, 3H), 7.22 (dd, J = 7.4, 0.8 Hz, 1H), 2.57 (s, 3H, $NMe_2$), 1.69 (s, 3H, $NMe_2$), 1.08 (s, 3H, SiMe); 13C NMR (101 MHz, $CDCl_3$) $\delta$ 150.9, 140.1, 139.6, 134.7, 134.0, 131.3, 130.5, 129.0, 128.2, 128.0, 126.7, 126.2, 126.0, 116.5, 48.3 ($NMe_2$), 47.9 ($NMe_2$), 3.2 (SiMe); 29Si1H NMR (80 MHz, $CDCl_3$) $\delta$ -14.4; HRMS (EI) calculated for $C_{19}H_{20}ClNSi$ $[M]^+$: 325.10481, found: 325.10531.

**8-(fluoro(methyl)(phenyl)silyl)-N,N-dimethylnaphthalen-1-amine, 1**

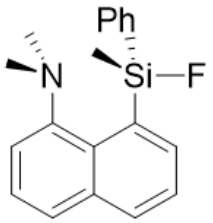


White crystals; mp = 84 - 85°C; $^1$H NMR (401 MHz, $CDCl_3$) $\delta$ 8.34 (dd, J = 6.8, 0.7 Hz, 1H), 7.96 (d, J = 8.1 Hz, 1H), 7.72 (d, J = 8.1 Hz, 1H), 7.64 (dd, J = 7.7, 7.3 Hz, 1H), 7.48-7.38 (m, 3H), 7.34-7.22 (m, 4H), 2.54 (s, 3H, $NMe_2$), 1.67 (s, 3H,

$NMe_2$), 0.77 (d, 3JHF = 8.4 Hz, 3H, SiMe); $^{13}C$ NMR (101 MHz, $CDCl_3$) $\delta$ 151.9, 138.2 (d, 2JCF = 23.0 Hz), 137.3 (d, 3JCF = 9.0 Hz), 135.1 (d, JCF = 2.6 Hz), 134.3 (d, JCF = 1.4 Hz), 132.4 (d, JCF = 1.0 Hz), 130.4 (d, JCF = 0.9 Hz), 129.6 (d, 2JCF = 18.3 Hz), 129.2 (d, JCF = 1.1 Hz), 127.8, 126.5, 126.2, 125.9, 117.2, 48.3 ($NMe_2$), 47.8 ($NMe_2$), -2.1 (d, 2JCF = 22.8 Hz, SiMe); $^{19}F$ NMR (377 MHz, $CDCl_3$) $\delta$ -134.5 (bs); 29SiH NMR (80 MHz, $CDCl_3$) $\delta$ -11.7 (d, 1JSiF = 264.4 Hz); HRMS (EI) calculated for $C_{19}H_{20}FNSi$ $[M]^+$: 309.13490, found: 309.13389.

**1-(8-(methoxy(methyl)(phenyl)silyl)naphthalen-1-yl)-N,N-dimethylmethanamine, 4**

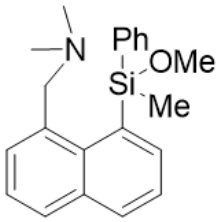


Yellow oil; $^1H$ NMR (400 MHz, $CDCl_3$) $\delta$ 8.18 (dd, J = 6.9, 1.3 Hz, 1H), 7.95 (dd, J = 8.1, 1.3 Hz, 1H), 7.77 (dd, J = 10.3, 7.7 Hz, 2H), 7.57–7.44 (m, 4H), 7.41–7.29 (m, 3H), 3.76 (d-AB, J = 14.0 Hz, 1H, $CH_2$), 3.72 (d-AB, J = 14.0 Hz, 1H, $CH_2$), 3.40 (d, J = 3.4 Hz, 3H, SiOMe), 1.88 (s, 6H, $NMe_2$), 0.80 (s, 3H, SiMe); $^{29}Si\{H\}$ NMR (80 MHz, $CD_2Cl_2$) $\delta$ -2.50.

**1-(8-(fluoro(methyl)(phenyl)silyl)naphthalen-1-yl)-N,N-dimethylmethanamine, 2**

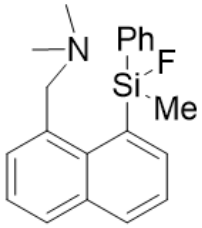


White crystals; mp = 79-80°C; $^1H$ NMR (400 MHz, $CDCl_3$) $\delta$ 8.41 (d, J = 7.1 Hz, 1H), 7.98 (dd, J = 8.1, 1.3 Hz, 1H), 7.83 (d, J = 7.9 Hz, 1H), 7.58 (dd, J = 7.7, 7.5 Hz, 1H), 7.55-7.50 (m, 2H), 7.45-7.26 (m, 5H), 3.86 (d-AB, 2J = 14.6 Hz, 1H, $CH_2$), 3.82 (d-AB, 2J = 14.6 Hz, 1H, $CH_2$), 1.85 (s, 6H, $NMe_2$), 0.84 (d, 3JHF = 9.5 Hz, 3H, SiMe); $^{13}C$ NMR (101 MHz, $CDCl_3$) $\delta$ 139.0 (d, J = 12.0 Hz), 135.7, 134.4, 133.9, 132.6, 132.0, 129.7, 128.9, 127.7, 127.7, 125.2, 124.9, 64.8 ($CH_2$), 45.5 ($NMe_2$), -0.5 (d, J = 28.3 Hz, SiMe); $^{19}F$ NMR (377 MHz, $CDCl_3$) $\delta$ -112.5 (bs); $^{29}Si\{H\}$ NMR (80 MHz, $CDCl_3$) $\delta$ -26.5 (d, J = 262.7 Hz); HRMS (EI) calculated for $C_{20}H_{22}FNSi$ $[M]^+$: 323.15001, found: 323.14977.

**1-(8-(fluoro(methyl)(phenyl)silyl)naphthalen-1-yl)-N,N-dimethyl ammonium tetrafluoroborate, 5**

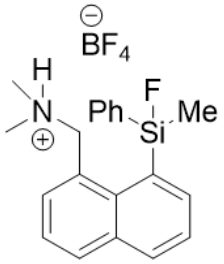


White crystals; mp = 119-120°C; $^1H$ NMR (401 MHz, $CD_2Cl_2$) $\delta$ 11.23 (bs, 1H, NH), 8.16 (ddd, J = 9.6, 7.6, 1.4 Hz, 2H), 8.09 (dd, J = 8.1, 1.4 Hz, 1H), 7.79 (dd, J = 7.2, 1.4 Hz, 1H), 7.71-7.62 (m, 2H), 7.57-7.48 (m, 3H), 7.43 (tm, J = 7.3 Hz, 2H),

4.81 (dd-ABX, J = 13.7, 6.3 Hz, 1H, $CH_2$), 4.41 (ddd-ABX, J = 13.7, 6.1, 1.5 Hz, 1H, $CH_2$), 2.44 (d, J = 4.6 Hz, 3H, $NMe_2$), 2.43 (d, J = 4.7 Hz, 3H, $NMe_2$), 0.88 (d, 3JHF = 7.9 Hz, 3H, SiMe); $^{13}$C NMR (101 MHz, $CD_2Cl_2$) $\delta$ 140.1 (d, J = 5.0 Hz), 136.5, 135.6, 135.4 (d, J = 16.2 Hz), 134.5, 134.0 (d, J = 1.7 Hz), 133.7, 132.3, 132.0, 129.4, 128.3 (d, J = 15.4 Hz), 126.9, 126.9, 125.8, 60.9 (d, J = 8.6 Hz, $CH_2$), 43.6 ($NMe_2$), 43.1 (d, J = 2.5 Hz, $NMe_2$), 0.7 (d, J = 17.7 Hz, SiMe); $^{19}$F NMR (377 MHz, $CD_2Cl_2$) $\delta$ -151.63 (4F, $BF_4$), -153.15 (q, 3JFH = 7.8 Hz, 1F, SiF); $^{29}$Si{H} NMR (80 MHz, $CD_2Cl_2$) $\delta$ 12.1 (d, J = 282.5 Hz); HR ESI-TOF MS (Positive mode) calculated for $C_{20}H_{23}FNSi$: 324.1584, found: 324.1581.

## 2 Crystallographic details

### 2.1 Fractal dimension plots

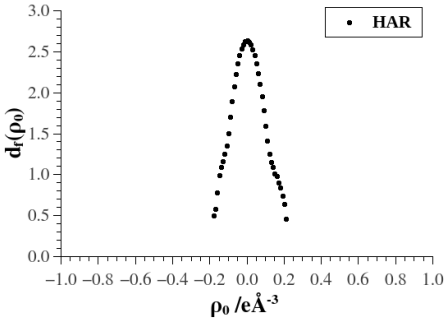


**Figure S1.** Fractal dimension plot of the HAR of the non-bridged compound (**1**) from the home measurement.

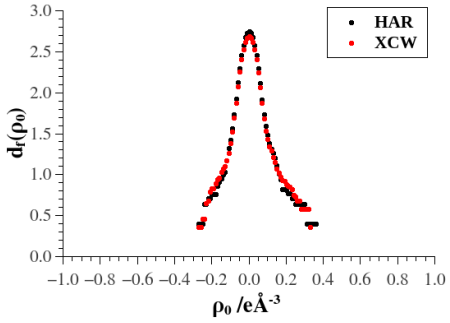


**Figure S2.** Fractal dimension plot of the HAR and XCW of the non-bridged compound (**1**) from the synchrotron measurement.

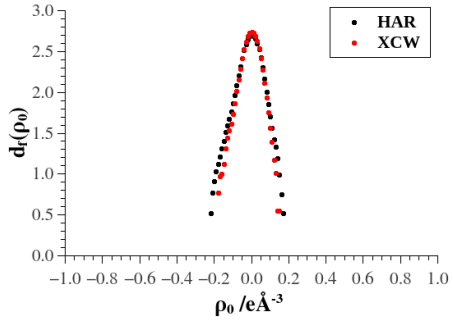


**Figure S3.** Fractal dimension plot of the HAR and XCW of the bridged compound (**2**) from the home measurement.

### 2.2 Residual and deformation density plots

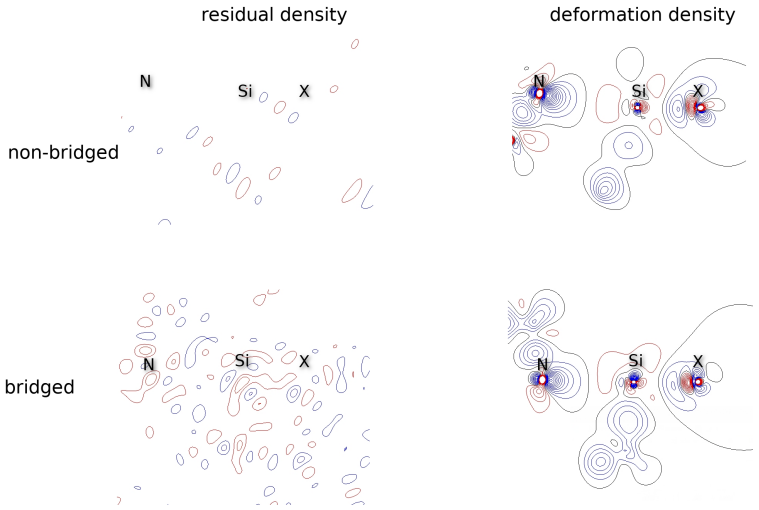


**Figure S4.** Residual and deformation density contour plots of the N–Si–X plane of the non-bridged and bridged compounds after XWR. Blue and red lines refer to positive and negative contour lines, respectively. The line separation is 0.05 e·Å$^{-3}$ in the residual density maps and 0.1 e·Å$^{-3}$ for the deformation density maps.

## 3 Coordinates of the optimized structures

**Table S1.** Coordinates of the isolated molecule optimization of the non-bridged compound (**1**).

| | | x /Å | y /Å | z /Å |
|---|---|---|---|---|
| 1 | Si | 10.098775 | 3.595633 | 2.791147 |
| 2 | F | 10.382040 | 3.108906 | 4.329202 |
| 3 | N | 9.843913 | 4.672309 | 0.269702 |
| 4 | C | 13.322215 | 6.031645 | 3.664503 |
| 5 | C | 9.468911 | 1.146900 | 1.478516 |
| 6 | C | 11.764999 | 5.410620 | -1.083508 |
| 7 | C | 11.430271 | 4.911171 | 2.603378 |
| 8 | C | 11.739902 | 1.864554 | 1.216049 |
| 9 | C | 12.001469 | 0.754852 | 0.421709 |
| 10 | C | 11.194904 | 5.128783 | 0.134470 |
| 11 | C | 11.910231 | 5.369093 | 1.339748 |
| 12 | C | 10.991728 | -0.162008 | 0.151714 |
| 13 | C | 13.040285 | 6.003840 | -1.159896 |
| 14 | C | 13.837777 | 6.389592 | 2.448968 |
| 15 | C | 12.144927 | 5.260049 | 3.733571 |
| 16 | C | 9.723840 | 0.033597 | 0.686797 |
| 17 | C | 10.467405 | 2.086851 | 1.752638 |
| 18 | C | 13.707850 | 6.350435 | -0.016584 |
| 19 | C | 13.161886 | 6.049986 | 1.253802 |
| 20 | C | 8.939270 | 5.824334 | 0.382049 |
| 21 | C | 9.387928 | 3.752732 | -0.767525 |
| 22 | C | 8.276695 | 4.006657 | 2.898081 |
| 23 | H | 7.736076 | 3.810486 | 1.974439 |
| 24 | H | 8.438927 | 3.316034 | -0.455730 |
| 25 | H | 12.535724 | 2.572614 | 1.409513 |
| 26 | H | 9.230652 | 4.248504 | -1.734586 |
| 27 | H | 8.934569 | -0.680163 | 0.486041 |
| 28 | H | 14.774804 | 6.929157 | 2.382111 |
| 29 | H | 8.472422 | 1.285064 | 1.881522 |
| 30 | H | 14.668180 | 6.848513 | -0.066889 |
| 31 | H | 11.221150 | 5.209166 | -1.996001 |
| 32 | H | 11.821529 | 4.894700 | 4.698564 |
| 33 | H | 9.244142 | 6.452804 | 1.216601 |
| 34 | H | 7.923248 | 5.476355 | 0.557788 |
| 35 | H | 8.120134 | 5.051435 | 3.169467 |
| 36 | H | 13.840940 | 6.295996 | 4.577194 |
| 37 | H | 13.470046 | 6.216655 | -2.130160 |
| 38 | H | 11.192705 | -1.025802 | -0.469269 |
| 39 | H | 12.992679 | 0.606131 | 0.011952 |
| 40 | H | 10.109292 | 2.949206 | -0.889333 |
| 41 | H | 8.950695 | 6.429367 | -0.534028 |
| 42 | H | 7.838583 | 3.393660 | 3.687947 |

**Table S2.** Coordinates of the isolated molecule optimization of the bridged compound (**2**).

| | | x /Å | y /Å | z /Å |
|---|---|---|---|---|
| 1 | Si | 4.967131 | 7.457496 | 2.479674 |
| 2 | F | 6.272435 | 6.725492 | 1.782263 |
| 3 | N | 2.864939 | 8.652628 | 3.558314 |
| 4 | C | 5.405173 | 10.347988 | 3.347530 |
| 5 | C | 6.443882 | 9.435931 | 1.359713 |
| 6 | C | 5.590902 | 9.248023 | 2.435851 |
| 7 | C | 4.462311 | 10.385792 | 4.424787 |
| 8 | C | 5.014795 | 6.580475 | 4.130734 |
| 9 | C | 6.204155 | 11.530096 | 3.155440 |
| 10 | C | 4.389564 | 4.711718 | 5.552013 |
| 11 | C | 4.281624 | 5.412014 | 4.355890 |
| 12 | C | 5.885080 | 7.010134 | 5.138367 |
| 13 | C | 5.996628 | 6.317093 | 6.337345 |
| 14 | C | 7.161800 | 10.622439 | 1.137053 |
| 15 | C | 3.456614 | 9.305473 | 4.725057 |
| 16 | C | 5.244030 | 5.167342 | 6.548850 |
| 17 | C | 7.067208 | 11.637852 | 2.041714 |
| 18 | C | 4.416979 | 11.477916 | 5.264135 |
| 19 | C | 6.131715 | 12.613104 | 4.061131 |
| 20 | C | 5.265473 | 12.584397 | 5.115258 |
| 21 | C | 2.261905 | 9.614964 | 2.636277 |
| 22 | C | 1.848481 | 7.711681 | 4.021418 |
| 23 | C | 3.693275 | 6.907843 | 1.220158 |
| 24 | H | 6.605536 | 8.619707 | 0.669895 |
| 25 | H | 3.810270 | 3.809628 | 5.704627 |
| 26 | H | 2.661129 | 9.756551 | 5.336552 |
| 27 | H | 3.017137 | 10.290019 | 2.243507 |
| 28 | H | 6.480752 | 7.902813 | 4.987936 |
| 29 | H | 3.613049 | 5.039040 | 3.588919 |
| 30 | H | 5.329445 | 4.625022 | 7.481883 |
| 31 | H | 7.642497 | 12.547876 | 1.922053 |
| 32 | H | 1.481157 | 10.211326 | 3.130225 |
| 33 | H | 3.683738 | 11.486564 | 6.061438 |
| 34 | H | 2.289885 | 7.005005 | 4.719821 |
| 35 | H | 3.910632 | 8.523351 | 5.333515 |
| 36 | H | 6.672433 | 6.671929 | 7.105339 |
| 37 | H | 3.927646 | 5.883106 | 0.925752 |
| 38 | H | 6.769569 | 13.471218 | 3.888675 |
| 39 | H | 1.809266 | 9.080067 | 1.802764 |
| 40 | H | 7.808066 | 10.705738 | 0.272831 |
| 41 | H | 1.434559 | 7.158045 | 3.180009 |
| 42 | H | 1.023417 | 8.235008 | 4.526577 |
| 43 | H | 5.202943 | 13.412753 | 5.808599 |
| 44 | H | 2.656106 | 6.948561 | 1.534875 |
| 45 | H | 3.798619 | 7.527182 | 0.326163 |

**Table S3.** Coordinates of the non-bridged compound (**1**) with an implicit water solvation.

| | | x /Å | y /Å | z /Å |
|---|---|---|---|---|
| 1 | F | 5.529848 | 9.535195 | 1.294919 |
| 2 | Si | 4.388115 | 8.905336 | 2.318801 |
| 3 | N | 2.681655 | 7.598786 | 3.914336 |
| 4 | C | 4.330569 | 11.733271 | 5.362906 |
| 5 | C | 6.40902 | 4.705543 | 2.767303 |
| 6 | C | 5.140816 | 4.292448 | 4.850786 |
| 7 | C | 6.677606 | 5.504613 | 1.687979 |
| 8 | C | 3.560752 | 6.545539 | 4.329395 |
| 9 | C | 2.099277 | 8.384354 | 5.002227 |
| 10 | C | 5.203114 | 11.20916 | 6.31079 |
| 11 | C | 4.640222 | 6.248102 | 3.454455 |
| 12 | C | 4.728646 | 9.825265 | 3.910181 |
| 13 | C | 4.098793 | 11.046015 | 4.176517 |
| 14 | C | 3.350356 | 5.790811 | 5.458036 |
| 15 | C | 5.84638 | 10.001145 | 6.061053 |
| 16 | C | 5.400108 | 5.064354 | 3.692527 |
| 17 | C | 4.161713 | 4.670298 | 5.73107 |
| 18 | C | 5.996708 | 6.729049 | 1.525916 |
| 19 | C | 5.6114 | 9.320493 | 4.871678 |
| 20 | C | 1.620798 | 7.041937 | 3.055629 |
| 21 | C | 4.992225 | 7.126282 | 2.387817 |
| 22 | C | 2.840235 | 9.451992 | 1.426844 |
| 23 | H | 7.446496 | 5.223976 | 0.979524 |
| 24 | H | 5.73613 | 3.406394 | 5.032616 |
| 25 | H | 5.380714 | 11.738574 | 7.238233 |
| 26 | H | 3.977919 | 4.089627 | 6.625646 |
| 27 | H | 2.537166 | 6.028707 | 6.129268 |
| 28 | H | 6.303996 | 7.38752 | 0.725025 |
| 29 | H | 2.88483 | 8.716492 | 5.675603 |
| 30 | H | 1.349502 | 7.822296 | 5.570767 |
| 31 | H | 3.827555 | 12.673673 | 5.55027 |
| 32 | H | 1.613132 | 9.261945 | 4.577332 |
| 33 | H | 6.969166 | 3.793457 | 2.933442 |
| 34 | H | 6.527724 | 9.588198 | 6.794367 |
| 35 | H | 0.979066 | 7.845236 | 2.701697 |
| 36 | H | 1.008231 | 6.319797 | 3.607943 |
| 37 | H | 3.405909 | 11.465227 | 3.456617 |
| 38 | H | 2.013613 | 9.671323 | 2.098911 |
| 39 | H | 2.064901 | 6.541093 | 2.197757 |
| 40 | H | 6.113074 | 8.376543 | 4.698705 |
| 41 | H | 3.072677 | 10.35974 | 0.866791 |
| 42 | H | 2.508064 | 8.697552 | 0.712649 |

**Table S4.** Coordinates of the bridged compound (**2**) with implicit water solvation.

| | | x /Å | y /Å | z /Å |
|---|---|---|---|---|
| 1 | Si | 4.811973 | 7.522685 | 2.536691 |
| 2 | F | 6.140688 | 6.737808 | 1.845386 |
| 3 | N | 2.91668 | 8.644157 | 3.527252 |
| 4 | C | 5.392283 | 10.372182 | 3.362829 |
| 5 | C | 6.406056 | 9.435932 | 1.377415 |
| 6 | C | 5.548157 | 9.269856 | 2.451994 |
| 7 | C | 4.450379 | 10.412839 | 4.437131 |
| 8 | C | 4.949989 | 6.600658 | 4.168105 |
| 9 | C | 6.210384 | 11.539979 | 3.174816 |
| 10 | C | 4.457743 | 4.666853 | 5.557779 |
| 11 | C | 4.271222 | 5.397936 | 4.388941 |
| 12 | C | 5.844451 | 7.034114 | 5.153745 |
| 13 | C | 6.035203 | 6.31037 | 6.325457 |
| 14 | C | 7.153395 | 10.607041 | 1.159586 |
| 15 | C | 3.444979 | 9.328911 | 4.716408 |
| 16 | C | 5.338044 | 5.124468 | 6.532172 |
| 17 | C | 7.078875 | 11.62818 | 2.062578 |
| 18 | C | 4.410936 | 11.500413 | 5.281924 |
| 19 | C | 6.146632 | 12.621845 | 4.083874 |
| 20 | C | 5.273418 | 12.598499 | 5.134724 |
| 21 | C | 2.308714 | 9.608524 | 2.595902 |
| 22 | C | 1.881207 | 7.70058 | 3.97354 |
| 23 | C | 3.626081 | 6.92024 | 1.213004 |
| 24 | H | 6.539844 | 8.621134 | 0.680224 |
| 25 | H | 3.916299 | 3.741112 | 5.707375 |
| 26 | H | 2.612494 | 9.774686 | 5.273944 |
| 27 | H | 3.065176 | 10.272462 | 2.188942 |
| 28 | H | 6.397216 | 7.955295 | 5.009919 |
| 29 | H | 3.580938 | 5.021272 | 3.643586 |
| 30 | H | 5.483056 | 4.559256 | 7.443973 |
| 31 | H | 7.673084 | 12.525494 | 1.940239 |
| 32 | H | 1.544934 | 10.207614 | 3.104205 |
| 33 | H | 3.676472 | 11.513983 | 6.077892 |
| 34 | H | 2.295065 | 7.024415 | 4.715829 |
| 35 | H | 3.878849 | 8.564864 | 5.36056 |
| 36 | H | 6.727566 | 6.67054 | 7.076108 |
| 37 | H | 3.70451 | 5.832219 | 1.156478 |
| 38 | H | 6.7943 | 13.473848 | 3.91839 |
| 39 | H | 1.837688 | 9.073085 | 1.775826 |
| 40 | H | 7.801662 | 10.677891 | 0.295623 |
| 41 | H | 1.516382 | 7.118135 | 3.130758 |
| 42 | H | 1.036443 | 8.239108 | 4.418181 |
| 43 | H | 5.21733 | 13.426278 | 5.829264 |
| 44 | H | 2.578769 | 7.180132 | 1.317002 |
| 45 | H | 3.978381 | 7.311504 | 0.255356 |

# Appendix: From structure correlations to bonding correlations

## Synthesis and characterization of the Pentacoordinated Silicon compounds

This section gives a report about the synthetic procedure and characterization of the compounds based on $^{13}C$, $^{1}H$, $^{19}F$ and $^{29}Si$ NMR and high resolution mass spectra. The following text was written by Dr. Maksym Ponomarenko and slightly modified by me.

All reagents from commercial suppliers were used without purification. $^{1}H$ NMR spectra were recorded on 400 or 401 MHz instruments. $^{13}C$, $^{19}F$, and $^{29}Si$ NMR spectra were recorded on 100 or 101 MHz, 376 or 377 MHz, and 80 MHz instruments, respectively. Chemical shifts are reported relative to TMS, $CHCl_3$ ($\delta$ = 7.26 ppm, $^{1}H$ NMR), $CDCl_3$ ($\delta$ = 77.16 ppm, $^{13}C$ NMR), and $CCl_3F$ ($^{19}F$ NMR) as internal standards. All non-aqueous reactions were carried out in an inert atmosphere of dry argon or nitrogen. All solvents used in reactions, as well as for crystallization, were preliminarily dried. High resolution mass spectra (EI) were obtained on a double-focusing mass spectrometer at 70 eV. High resolution electronspray-ionization time-of-flight mass spectra (EI-TOF MS) were obtained on a Bruker Daltonics micro time-of-flight (microTOF) mass spectrometer using the positive ESI mode.

### 8-(chloro(methyl)(phenyl)silyl)-N,N-dimethylnaphthalen-1-amine, 1 (*chloro*), *known*

12.52 mL (1 equiv) of n-BuLi (2.5 M, in n-hexane) was added at 0°C to a solution of N,N-dimethylnaphthalen-1-amine (5.36 g, 31.3 mmol) in 35 mL of diethyl ether. The mixture was stirred for 48 h at room temperature. The formed precipitate of the lithiated product **12** was filtered off, and washed with pentane (2 x 20 mL) under argon; then it was dried for 30 min in oil-pump vacuum at room temperature. The solid product was transferred into a 100 mL Schlenk flask, and then 40mL of diethyl ether was added. The mixture was cooled to -60°C,

and 4.46 g (23.33 mmol, 1.3 equiv) of $PhSiMeCl_2$ was added through a syringe. The cooling bath was removed after 30 min, and the mixture was stirred for 24 h at room temperature. The formed precipitate was filtered off under argon, and washed with diethyl ether (2 x 5 mL).

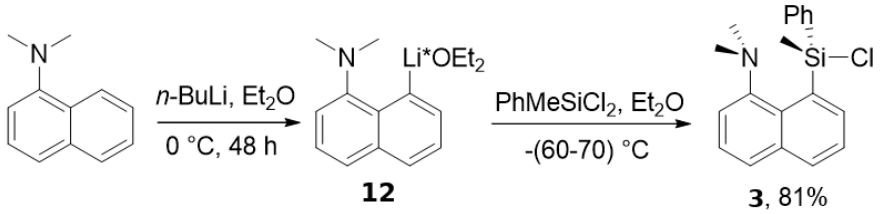


**Figure A1:** Reaction scheme for the synthesis of the chloro compound (**3**).

Diethyl ether was evaporated, and the rest was recrystallized from a saturated hot diethyl ether solution (under argon) giving 1.2 g (20%) of the clean product **3**. The white precipitate, which was collected after first filtration of the reaction mixture, was mixed with 20 mL of $CH_2Cl_2$, and the mixture was filtered to remove LiCl. The solvent was evaporated giving 3.6 g (61% yield) of **3**. Colorless good quality single crystals of **3** were grown from hot saturated diethyl ether solution under inert atmosphere.

Colourless crystals; melting point = 149 - 150°C; $^1$H NMR (401 MHz, $CDCl_3$) $\delta$ 8.73 (dd, J = 7.0, 1.1 Hz, 1H), 7.97 (dd, J = 8.1, 1.0 Hz, 1H), 7.76 (d, J = 8.1 Hz, 1H), 7.69 (dd, J = 8.1, 7.0 Hz, 1H), 7.46 (t, J = 7.8 Hz, 1H), 7.37 (m, 2H), 7.40–7.33 (m, 3H), 7.22 (dd, J = 7.4, 0.8 Hz, 1H), 2.57 (s, 3H, $NMe_2$), 1.69 (s, 3H, $NMe_2$), 1.08 (s, 3H, SiMe); $^{13}$C NMR (101 MHz, $CDCl_3$) $\delta$ 150.9, 140.1, 139.6, 134.7, 134.0, 131.3, 130.5, 129.0, 128.2, 128.0, 126.7, 126.2, 126.0, 116.5, 48.3 ($NMe_2$), 47.9 ($NMe_2$), 3.2 (SiMe); $^{29}$Si{1H} NMR (80 MHz, $CDCl_3$) $\delta$ -14.4; HRMS (EI) calculated for $C_{19}H_{20}ClNSi$ $[M]^+$: 325.10481, found: 325.10531.

## 8-(hydroxy(methyl)(phenyl)silyl)naphthalen-1-yl-N,N-dimethyl ammonium chloride (13)

All attempts to hydrolyze the chloro compound **3** to the corresponding silanol failed likely due to its transformation to the siloxane. However, when the white precipitate of the **2**/LiCl mixture (1 g), collected after first filtration of the reaction mixture obtained in the previous step, was exposed to air 2 weeks in a fritted filter funnel, its appearance did not change. This is in contrast to pure **3** that becomes dark oil upon storage in an open flask. After 2 weeks the **3**/LiCl mixture was mixed with 10 mL of acetone and filtered. The collected filtrate was evaporated, and the solid residue was recrystallized twice from a saturated acetonitrile solution at -30°C giving 0.53 g of **13**.

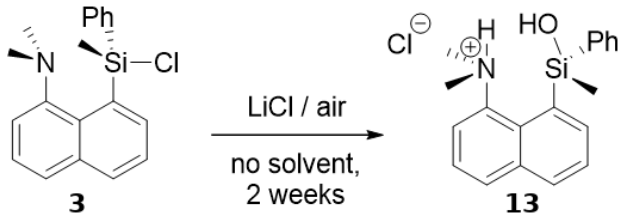


**Figure A2:** Reaction scheme for the synthesis of **13**

Colorless good quality single crystals of 2-OH-HCl were grown from $CH_3CN$ at -30°C.

Colourless crystals; mp = 115 - 116°C; $^1$H NMR (400 MHz, $CDCl_3$) $\delta$ 9.08 (bs, 2H, OH, NH), 8.02 (t, J = 6.9 Hz, 2H), 7.94 (d, J = 7.5 Hz, 1H), 7.64 (d, J = 9.1 Hz, 1H), 7.60 (d, J = 7.7 Hz, 1H), 7.50 (d, J = 6.8 Hz, 2H), 7.31 (m, 1H), 7.26 (tm, J = 7.1 Hz, 2H), 3.49 (s, 3H, NMe2), 3.12 (s, 3H, NMe2), 0.95 (s, 3H, SiMe); $^{13}$C NMR (101 MHz, $CDCl_3$) $\delta$ 140.8, 138.8, 136.4, 136.0, 134.2, 133.1, 132.6, 130.8, 130.4, 129.3, 128.2, 126.0, 125.8, 120.7, 48.3 ($NMe_2$), 48.2 ($NMe_2$), 1.6 (SiMe); 29Si{$^1$H} NMR (79 MHz, $CDCl_3$) $\delta$ -0.98; HR ESI-TOF MS (Positive mode) calculated for $C_{19}H_{22}NOSi$: 308.1465, found: 308.1471.

## 8-(dimethyl(phenyl)silyl)-N,N-dimethylnaphthalen-1-amine, 3 (*methyl*), *unknown*

0.5838 g (2.32 mmol) of lithiated N,N-dimethylnaphthalen-1-amine **12** was diluted with 20 mL of THF in a 50 mL Schlenk flask. The solution was cooled down to -60°C, and 0.396 g (2.32 mmol) of $PhSiMe_2Cl$ was added through a syringe. The cooling bath was removed after 15 minutes, and the mixture was stirred for 24 h at room temperature. THF was evaporated, the mixture was diluted with 70 mL of n-hexane, and the resulting mixture was washed with water (2 x 5 mL). After drying of the organic layer over sodium sulfate and evaporating the solvent, the raw product was purified by column chromatography on $SiO_2$ eluting with n-hexane, giving **10** (0.48 g, 68%). The same reaction carried out in diethyl ether for 24 h leads to the formation

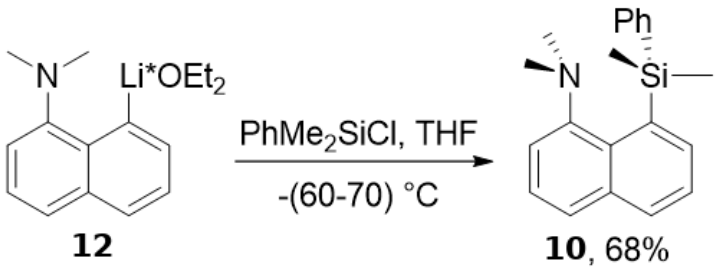


**Figure A3:** Reaction scheme for the synthesis of the methyl compound (**10**).

of the product **10** only as an admixture; the starting materials were almost fully recovered. Colorless good quality single crystals of **10** were grown from a $CH_3CN/Et_2O$ (90/10 v/v) mixture at -30°C under inert atmosphere. **10** is stable for a long time in inert atmosphere, but it becomes yellow after two to three weeks of storage at ambient conditions.

Colourless crystals; mp = 72-73°C; $^1$H NMR (400 MHz, $CDCl_3$) $\delta$ 7.94 (dd, J = 6.8, 1.3 Hz, 1H), 7.86 (dd, J = 8.1, 1.0 Hz, 1H), 7.64 (dd, J = 8.1, 0.9 Hz, 1H), 7.52–7.44 (m, 3H), 7.41 (dd, J = 7.9, 7.5 Hz, 1H), 7.31–7.26 (m, 3H), 7.20 (dd, J = 7.4, 1.1 Hz, 1H), 2.08 (s, 6H, NMe2), 0.52 (s, 6H, SiMe2); $^{13}$C NMR (101 MHz, $CDCl_3$) $\delta$ 153.4, 142.3, 137.2, 135.0, 134.7, 133.6, 132.7, 130.0, 127.8, 127.5, 125.8, 125.4, 125.3, 116.9, 47.1, 1.4; $^{29}$Si NMR (80 MHz, $CDCl_3$) $\delta$ -11.4 (m, 3JSiH = 12.0 Hz); HRMS (EI) calculated for $C_{20}H_{23}NSi$ $[M]^+$: 325.15998, found: 305.16014.

## 8-(fluoro(methyl)(phenyl)silyl)-N,N-dimethylnaphthalen-1-amine, 4 (*fluoro*), *known*

0.55 g (1.69 mmol) of **3** was added to a mixture of dried CsF (2.56 g, 16.9 mmol) in 20 mL of monoglyme. The mixture was refluxed for 12 h, and cooled to ambient temperature. 20 mL of $CH_2Cl_2$ was added, and then the reaction mixture was filtered under inert atmosphere. The solvents were removed in oil-pump vacuum. The residue was recrystallized from an n-hexane/$CH_2Cl_2$ mixture giving 0.318 g (61%) of the fluorinated product **5**. Colorless

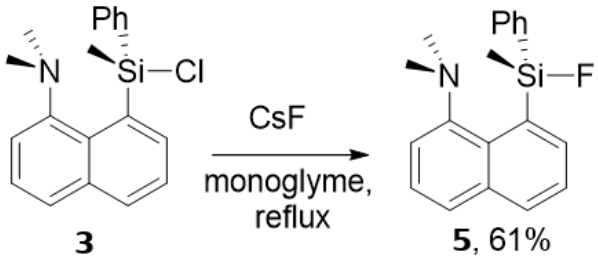


**Figure A4:** Reaction scheme for the synthesis of the fluoro compound (**5**).

good quality single crystals of **5** were grown by slow evaporation technique (air) from an n-hexane/$CH_2Cl_2$ ( 80/20 v/v) mixture. The fluorinated product **5** becomes darker after two to three weeks of storage at ambient conditions. However, **5** is stable for a long time under inert atmosphere.

Colourless crystals; mp = 84 - 85°C; $^1$H NMR (401 MHz, $CDCl_3$) $\delta$ 8.34 (dd, J = 6.8, 0.7 Hz, 1H), 7.96 (d, J = 8.1 Hz, 1H), 7.72 (d, J = 8.1 Hz, 1H), 7.64 (dd, J = 7.7, 7.3 Hz, 1H), 7.48–7.38 (m, 3H), 7.34–7.22 (m, 4H), 2.54 (s, 3H, $NMe_2$), 1.67 (s, 3H, $NMe_2$), 0.77 (d, 3JHF = 8.4 Hz, 3H, SiMe); $^{13}$C NMR (101 MHz, $CDCl_3$) $\delta$ 151.9, 138.2 (d, 2JCF = 23.0 Hz), 137.3

(d, 3JCF = 9.0 Hz), 135.1 (d, JCF = 2.6 Hz), 134.3 (d, JCF = 1.4 Hz), 132.4 (d, JCF = 1.0 Hz), 130.4 (d, JCF = 0.9 Hz), 129.6 (d, 2JCF = 18.3 Hz), 129.2 (d, JCF = 1.1 Hz), 127.8, 126.5, 126.2, 125.9, 117.2, 48.3 ($NMe_2$), 47.8 ($NMe_2$), -2.1 (d, 2JCF = 22.8 Hz, SiMe); $^{19}$F NMR (377 MHz, $CDCl_3$) $\delta$ -134.5 (bs); 29SiH NMR (80 MHz, $CDCl_3$) $\delta$ -11.7 (d, 1JSiF = 264.4 Hz); HRMS (EI) calculated for $C_{19}H_{20}FNSi$ $[M]^+$: 309.13490, found: 309.13389.

## 8-(methoxy(methyl)(phenyl)silyl)-N,N-dimethylnaphthalen-1-amine, 8 (*methoxy*), *known*

A mixture of 0.60 g (1.84 mmol) of **3** in 5 mL of diethyl ether was cooled to 0°C. 0.745 g (7.36 mmol) of triethylamine and 0.119 g (3.71 mmol) of methanol were added sequentially to the mixture. The cooling bath was removed after 1 hour, and the mixture was stirred for 12 h at room temperature. Then 50 mL of n-hexane was added, and the mixture was washed with water (3 x 5 mL). After drying of the organic layer over sodium sulfate and evaporating the solvent 0.49 g (82%) of the product **8** was obtained. **8** was additionally dried for 12 h in oil pump vacuo at room temperature and stored under argon. Colorless good quality single crystals of **8** were grown by slow evaporation technique from pentane under inert atmosphere using $\lambda$-shaped glassware closed with a Teflon tap. All attempts to grow crystals of **8** in an opened flask failed due to hydrolytic instability of the product exposed to air.

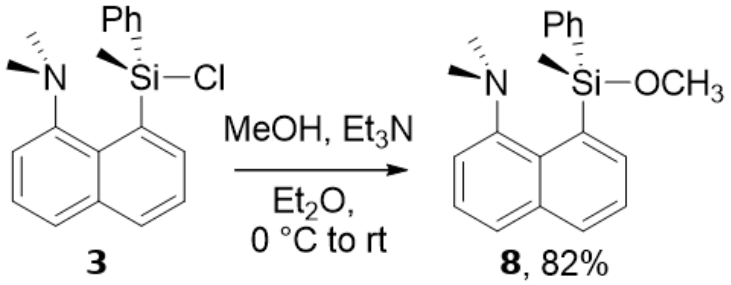


**Figure A5:** Reaction scheme for the synthesis of the methoxy compound (**8**).

Colourless crystals; mp = 65-67°C; $^1$H NMR (400 MHz, $CDCl_3$) $\delta$ 8.29 (dd, J = 6.9, 1.3 Hz, 1H), 7.90 (dd, J = 8.1, 1.3 Hz, 1H), 7.67 (dd, J = 8.1, 1.1 Hz, 1H), 7.59 (dd, J = 8.1, 6.9 Hz, 1H), 7.43–7.37 (m, 3H), 7.30–7.23 (m, 3H), 7.17 (dd, J = 7.4, 1.2 Hz, 1H), 3.27 (s, 3H, OMe), 2.45 (s, 3H, $NMe_2$), 1.56 (s, 3H, $NMe_2$), 0.67 (s, 3H, SiMe); $^{13}$C NMR (101 MHz, $CDCl_3$) $\delta$ 152.9, 138.3, 137.3, 135.4, 134.8, 132.8, 130.6, 130.1, 128.6, 127.6, 126.0, 125.8, 125.8, 117.1, 50.9 (s, OMe), 47.5 (s, $NMe_2$), 47.3 (s, $NMe_2$), -3.3 (s, SiMe); $^{29}$Si{H} NMR (80 MHz, $CDCl_3$) $\delta$ -11.0; HRMS (EI) calculated for $C_{20}H_{23}NOSi$ $[M]^+$: 321.15489, found: 321.15426.

## 8,8'-(methyl(phenyl)silanediyl)bis(N,N-dimethylnaphthalen-1-amine), 11 (*aryl*), *known*

0.57 g (2.27 mmol) of lithiated N,N-dimethylnaphthalen-1-amine **12** was diluted with 15 mL of THF in a 50 mL Schlenk flask. The solution was cooled down to -70°C, and 0.217 g (1.14 mmol) of $PhSiMeCl_2$ was added to the mixture. The cooling bath was removed after 15 min, and the mixture was stirred for 48 h at room temperature. THF was evaporated, 70 mL of n-hexane was added to the mixture, and the resulting suspension was washed with water (3 x 5 mL). After drying of the organic layer over sodium sulfate and evaporating the solvent, the mixture was separated by column chromatography on $SiO_2$ eluting with an n-hexane/$CH_2Cl_2$ (1/1) mixture. 0.25 g (48% yield) of the product **11** and 0.13 g of N,N-dimethylnaphthalen-1-amine were isolated after the column.

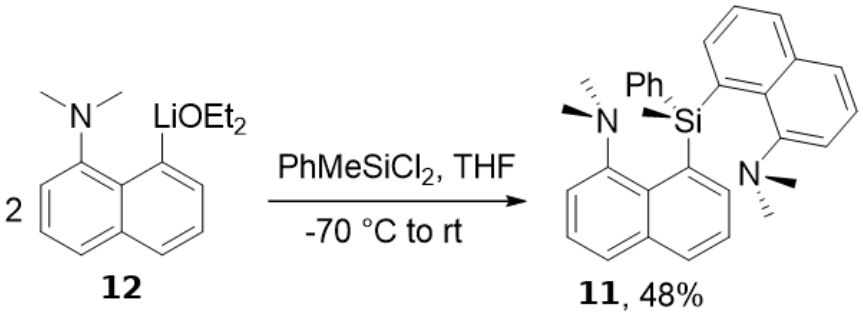


**Figure A6:** Reaction scheme for the synthesis of the aryl compound (**11**)

Colorless good quality single crystals of **11** were grown by slow evaporation technique (air) from pentane.

Colourless crystals; mp = 81-82°C; $^1$H NMR (400 MHz, $CDCl_3$) $\delta$ 7.93–7.50 (m, 6H), 7.48–6.98 (m, 11H), 2.65 (bs, 3H), 2.26 (bs, 3H), 1.63 (s, 3H), 0.97 (s, 6H); $^{13}$C NMR (101 MHz, $CDCl_3$) $\delta$ 153.7 (bs), 143.8, 138.2 (bs), 137.0 (bs), 135.6 (bs), 135.2 (bs), 133.2 (bs), 128.8 (bs), 127.5, 127.1, 125.7 (bs), 125.2, 124.8, 117.4 (bs), 116.2 (bs), 50.4 (bs, $NMe_2$), 48.2 (bs, $NMe_2$), 47.3 (bs, $NMe_2$), 45.0 (bs, $NMe_2$), 2.4 (bs, SiMe); $^{29}$Si{H} NMR (80 MHz, $CDCl_3$) $\delta$ -12.3 (bs); HRMS (EI) calculated for $C_{31}H_{32}N_2Si$ $[M]^+$: 460.23348, found: 460.23387.

## 8-(ethynyl(methyl)(phenyl)silyl)-N,N-dimethylnaphthalen-1-amine, 6 (*ethynyl*), *unknown*

A solution of **3** (2.2 g, 6.75 mmol) in 20 mL of THF was cooled to -78°C. A solution of HCCMgBr in THF (0.5M, 13.5 mL, 6.75 mmol) was slowly added to the stirred reaction mixture through a syringe. The resulting mixture was stirred for 12 h, while the temperature was allowed to

increase slowly to room temperature. THF was removed in oil pump vacuo. A mixture of $CH_2Cl_2$ (10 mL) and n-hexane (30 mL) was added to the resulting viscous oil. The formed precipitate was filtered off under argon, and the solvents were removed in oil pump vacuo. Then 40 mL of n-hexane was added to the concentrated mother liquor, the mixture was heated for a while at reflux upon stirring, and the turbid solution was frittered through Celite under argon. The solvent was removed, and the residue was recrystallized twice from hot n-hexane giving **6** (1.13 g, 53%).

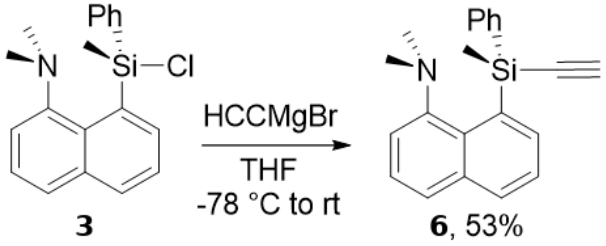


**Figure A7:** Reaction scheme for the synthesis of the ethylyn compound (**6**).

Colorless good quality single crystals of **6** were grown from a hot saturated n-hexane solution under inert atmosphere. **7** is stable for a long time only in inert atmosphere.

Colourless crystals; mp = 84-85°C; $^1$H NMR (401 MHz, $CDCl_3$) $\delta$ 8.55 (d, J = 6.9 Hz, 1H), 7.92 (dd, J = 8.1, 1.1 Hz, 1H), 7.68 (d, J = 8.1 Hz, 1H), 7.58 (dd, J = 8.1, 6.9 Hz, 1H), 7.50-7.45 (m, 2H), 7.42 (t, J = 7.7 Hz, 1H), 7.32–7.26 (m, 3H), 7.23 (dd, J = 7.7, 6.8 Hz, 1H), 2.61 (s, 1H, CCH), 2.37 (s, 3H, $NMe_2$), 1.79 (s, 3H, $NMe_2$), 0.77 (s, 3H, SiMe); $^{13}$C NMR (101 MHz, $CDCl_3$) $\delta$ 152.5, 139.4, 138.7, 134.7, 134.6, 132.7, 130.7, 128.8, 128.5, 127.8, 125.9, 125.9, 125.8, 117.2, 94.5 (CCH), 93.5 (CCH), 48.0 ($NMe_2$), 47.1 ($NMe_2$), 0.3 (SiMe); $^{29}$Si{H} NMR (80 MHz, $CDCl_3$) $\delta$ -32.41 (s); HRMS (EI) calculated for $C_{21}H_{21}NSi$ $[M]^+$: 315.14378, found: 315.14402.

## N,N-dimethyl-8-(methyl(phenyl)silyl)naphthalen-1-amine, 9 (*hydro*), *known*

$LiAlH_4$ (powder, 0.16 g, 4.21 mmol) was added in portions to a stirred mixture of **3** (0.68 g, 2.09 mmol) in 50 mL of diethyl ether at 0°C. The reaction mixture was stirred for 2 h at 0°C, and for additional 10 h at room temperature. The solvent was removed in oil pump vacuo, and 20 mL of pentane was added to the mixture. All solids were filtered off and washed with pentane (2 x 10 mL) under argon. Pentane was evaporated giving **9** (0.58 g, 95% yield) as oil that crystallizes on standing. The product **9** decomposes after two to three weeks of storage at ambient conditions. However, it is stable for a long time under inert atmosphere.

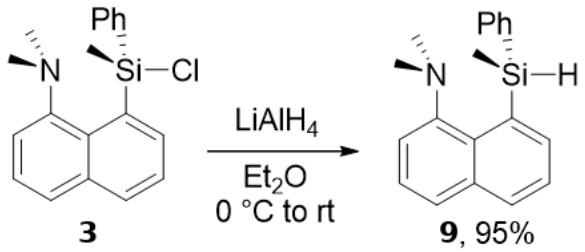


**Figure A8:** Reaction scheme for the synthesis of the hydro compound (**9**).

Colourless crystals; mp = 43-44°C; $^{1}$H NMR (400 MHz, $CDCl_3$) $\delta$ 7.87 (dd, J = 8.1, 1.2 Hz, 1H), 7.69 (dd, J = 8.1, 1.1 Hz, 1H), 7.61 (dd, J = 6.8, 1.3 Hz, 1H), 7.49-7.38 (m, 4H), 7.37-7.27 (m, 4H), 5.23 (q, 3J = 3.4 Hz, 1H, SiH), 2.62 (s, 3H, $NMe_2$), 2.29 (s, 3H, $NMe_2$), 0.52 (d, 3J = 3.4 Hz, 3H, SiMe); $^{13}$C NMR (101 MHz, $CDCl_3$) $\delta$ 152.5, 141.1, 137.5, 134.7, 134.7, 134.4, 131.3, 130.3, 128.3, 127.7, 125.9, 125.8, 125.8, 117.9, 47.7 ($NMe_2$), 46.7 ($NMe_2$), -1.17 (SiMe); $^{29}$Si NMR (80 MHz, $CDCl_3$) $\delta$ -23.1 (qm, 1JSiH = 220.8 Hz); HRMS (EI) calculated for $C_{19}H_{21}NSi$ $[M]^+$: 291.14378, found: 291.14458.

## (8-(dimethylamino)naphthalen-1-yl)(methyl)(phenyl)silyl-4-chlorobenzoate, 4 (*chlorobenzoate*), *unknown*

4-chlorobenzoic acid (0.192 g, 1.23 mmol) was added to a stirred mixture of **3** (0.40 g, 1.23 mmol) and triethyamine (0.496 g, 4.90 mmol) in 35 mL of diethyl ether at 0°C. The resulting mixture was stirred at room temperature for 12 h. All white solids were filtered off under argon, and washed with pentane. Pentane, diethyl ether and triethyamine were evaporated in oil pump vacuo. The residue (ca. 0.52 g) was washed with hot n-hexane (3 x 25 mL). The solvent was evaporated from the combined fractions, and the raw product was additionally recrystallized from hot n-hexane giving 0.20g of **4** (37%). Colorless good quality single crystals of **4** were grown from a hot saturated pentane solution under inert atmosphere. **4** hydrolyzes when exposed to air.

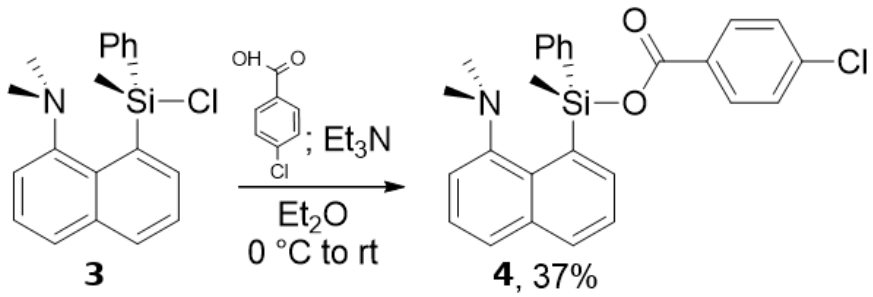


**Figure A9:** Reaction scheme for the synthesis of the p-Chlorobenzoate compound (**4**).

Colourless crystals; mp = 124-125°C; $^1$H NMR (401 MHz, $CDCl_3$) $\delta$ 8.42 (dd, J = 6.9, 1.2 Hz, 1H), 8.02–7.93 (m, 3H), 7.73 (dd, J = 8.2, 0.9 Hz, 1H), 7.65 (dd, J = 8.2, 6.9 Hz, 1H), 7.56–7.50 (m, 2H), 7.45 (dd, J = 8.0, 7.5 Hz, 1H), 7.40–7.35 (m, 2H), 7.31–7.21 (m, 4H), 2.58 (s, 3H, $NMe_2$), 1.59 (s, 3H, $NMe_2$), 0.96 (s, 3H, SiMe); 13C NMR (101 MHz, $CDCl_3$) $\delta$ 166.1 (C=O), 151.7, 138.8, 137.2, 135.1, 134.4, 132.8, 131.6, 130.5, 129.0, 128.6, 128.6, 127.6, 126.4, 126.2, 126.0, 116.9, 48.6 ($NMe_2$), 47.3 ($NMe_2$), -1.5 (SiMe); $^{29}$Si{H} NMR (80 MHz, $CDCl_3$) $\delta$ -17.4; HRMS (EI) calculated for $C_{26}H_{24}ClNO_2Si$ $[M]^+$: 445.12722, found: 445.12722.

## (8-(dimethylamino)naphthalen-1-yl)(methyl)(phenyl)silylium tetrakis-(pentafluorophenyl)borate, 1 (*silyl cation*), *unknown*

$[Ph_3C][B(C_6F_5)_4]$ was prepared by a slightly modified procedure than the one described in the literature [Ihara, E.; Young, V. G.; Jordan, R. F. J. Am. Chem. Soc. 1998, 120, 8277-8278]. A solution of $C_6F_5Br$ (15 g, 4 equiv) in n-hexane (250 ml) was cooled to -78°C. n-BuLi (24 mL, 2.5 M solution in hexane, 4 equiv) was added dropwise and the reaction mixture was stirred for 1.5 h at -78°C. $BCl_3$ (15 mL, 1.0 M solution in heptane, 1 equiv) was added over 15 min. The resulting viscous suspension was stirred and warmed to 10°C gradually over 15 h. 6.27 g (1.5 equiv) of $Ph_3CCl$ was added to the reaction mixture. The reaction occurred immediately and a yellow powder formed. The mixture was stirred for additional 3 h at room temperature, and filtered through a glass filter frit. The solid was washed with hexane (5 x 50 mL) and dried under vacuum for 1 h. The yellow solid was taken up with $CH_2Cl_2$ (150 mL) and filtered to remove LiCl. The filtrate was concentrated to ca. 70 mL and pentane (150 mL) was added. Phase separation occurred, the resulting mixture was stirred until the oily lower layer gradually solidified. The supernatant was removed by a cannula and the remaining powder was dried in oil pump vacuo giving a brownish-yellow powder of $[Ph_3C][B(C_6F_5)_4]$ (12.7 g, 92%).

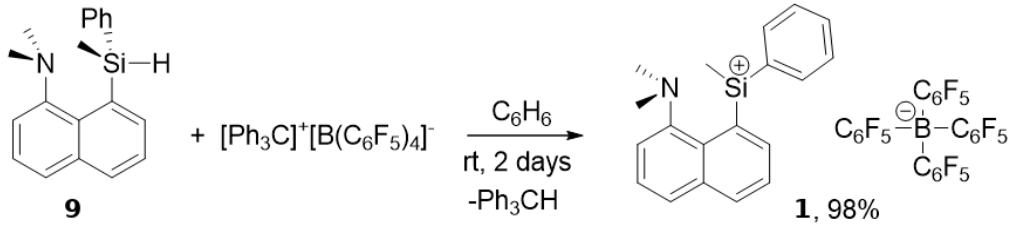


**Figure A10:** Reaction scheme for the synthesis of the silyl cation (**1**).

Two layers of a mixture of $[Ph_3C][B(C_6F_5)_4]$ (0.20 g, 0.217 mmol) and the silane **9** (0.07 g, 0.240 mmol) in dry benzene (2 mL) was stirred for 2 days at room temperature in a 25 mL Schlenk flask. The dark lower layer becomes colourless in a few minutes of vigorous stirring.

After 2 days the stirring was stopped, and then the upper layer was removed by a syringe. The bottom layer left was washed twice with benzene. 1 mL of benzene was added into the flask, and the suspension was stirred ca. 1 min. Then the stirring was stopped, and the upper layer was removed. The rest of the solvent was removed in oil pump vacuo giving 0.20 g (98%) of white solid **1**. Colorless good quality single crystals of **1** were grown by diffusion of n-hexane (3 mL) into a 0.1 g sample diluted in 0.8 mL of $CH_2Cl_2$ at room temperature. n-Hexane was carefully layered on top of the solution of **1** in $CH_2Cl_2$. All manipulations (weighting, washing, crystallization, etc.) were carried out in inert atmosphere of argon.

Colourless crystals; mp = 62-63°C; $^1$H NMR (401 MHz, $CD_2Cl_2$) $\delta$ 8.31 (dd, J = 8.4, 0.9 Hz, 1H), 8.16 (dd, J = 8.3, 0.7 Hz, 1H), 8.14 (dd, J = 6.8, 1.0 Hz, 1H), 7.93 (dd, J = 8.3, 6.8 Hz, 1H), 7.79 (dd, J = 8.2, 7.8 Hz, 1H), 7.75–7.68 (m, 2H), 7.58–7.53 (m, 4H), 3.41 (s, 3H, $NMe_2$), 2.96 (s, 4H, $NMe_2$), 1.29 (s, 3H, SiMe); 13C NMR (101 MHz, $CD_2Cl_2$) *delta* cation: 145.6, 136.1, 135.1, 135.1, 133.3, 133.3, 132.3, 130.3, 130.3, 130.1, 128.3, 125.2, 121.4, 117.1, 53.4 ($NMe_2$), 51.8 ($NMe_2$), -3.78 (SiMe), anion: 150.0 (bm), 147.6 (bm), 140.0 (bm), 138.1 (bm), 137.6 (bm), 135.7 (bm); 19F NMR (376 MHz, $CD_2Cl_2$) $\delta$ -132.7 (m, 8F), -163.2 (td, J = 20.5, 6.6 Hz, 4F), -167.1 (m, 8F); $^{11}$B NMR (128 MHz, $CD_2Cl_2$) $\delta$ -17.4 (s); $^{29}$Si{H} NMR (80 MHz, $CD_2Cl_2$) $\delta$ 42.6; HR ESI-TOF MS (Positive mode) calculated for $C_{19}H_{20}NSi$: 290.1360, found: 290.1365.

## 1-(8-(methoxy(methyl)(phenyl)silyl)naphthalen-1-yl)-N,N-dimethylmethanamine, 16, *unknown*

The amine **13** was prepared according to the literature [Gay, R. L.; Hauser, C. R. J. Am. Chem. Soc. 1967, 89, 2297–2303]. 3.1 mL (1 equiv) of n-BuLi (2.5 M, in n-hexane) was added at 0°C to a solution of **14** (1.44 g, 7.77 mmol) in 25 mL of diethyl ether. The mixture was stirred for 24 h at room temperature. The mixture was cooled to 0°C, and left to stay without stirring for a few hours. The dark red supernatant was removed using a syringe, and the solid lithiated amine **15** was dissolved in 50 mL of fresh diethyl ether. The mixture was cooled to -50°C, and 1.98 g (10.86 mmol, 1.4 equiv) of $PhSiMe(OMe)_2$ was added dropwise through a syringe. The cooling bath was removed after 30 min, and the mixture was stirred for 24 h at room temperature. The solvent was evaporated, and the residue was kept for 4 h in oil pump vacuo at 200°C giving 2.24 g (86%) of raw **16**. The product **16** was used in the next step without additional purification.

Yellow oil; $^1$H NMR (400 MHz, $CDCl_3$) $\delta$ 8.18 (dd, J = 6.9, 1.3 Hz, 1H), 7.95 (dd, J = 8.1, 1.3 Hz, 1H), 7.77 (dd, J = 10.3, 7.7 Hz, 2H), 7.57–7.44 (m, 4H), 7.41–7.29 (m, 3H), 3.76 (d-AB, J = 14.0 Hz, 1H, $CH_2$), 3.72 (d-AB, J = 14.0 Hz, 1H, $CH_2$), 3.40 (d, J = 3.4 Hz, 3H,

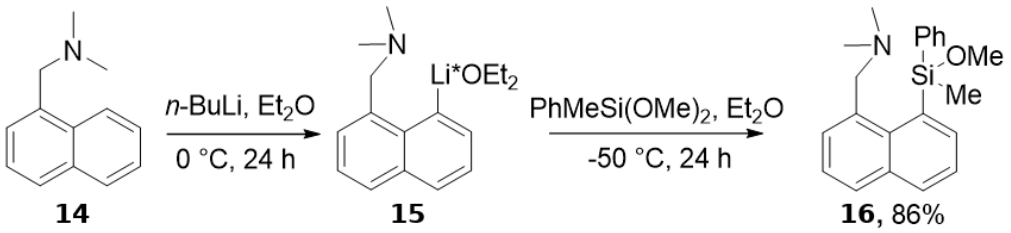


**Figure A11:** Reaction scheme for the synthesis of 1-(8-(methoxy(methyl)(phenyl)silyl)naphthalen-1-yl)-N,N-dimethylmethanamine (**16**).

SiOMe), 1.88 (s, 6H, $NMe_2$), 0.80 (s, 3H, SiMe); $^{29}Si\{H\}$ NMR (80 MHz, $CD_2Cl_2$) $\delta$ -2.50.

## 1-(8-(fluoro(methyl)(phenyl)silyl)naphthalen-1-yl)-N,N-dimethylmethanamine, 2 (*fluoro, bridged*), *unknown*, and 1-(8-(fluoro(methyl)-(phenyl)silyl)naphthalen-1-yl)-N,N-dimethyl ammonium tetrafluoroborate, 17, *unknown*

0.91 g (2.71 mmol) of **15** was diluted in 15 mL of n-hexane. The solution was cooled with an ice bath, and $BF_3$-etherate (0.19 g, 1.34 mmol) was added. The mixture was intensively stirred for 2 h at room temperature. The n-hexane phase was removed into another 50 mL Schlenk flask by a syringe. The solid residue was washed with hot n-hexane (3 x 5mL). All n-hexane fractions were combined in the Schlenk flask containing the n-hexane phase collected from the reaction mixture. The solvent was removed in oil pump vacuo. The white solid obtained was recrystallized three times from a hot saturated solution in n-hexane in inert atmosphere giving 0.40 g (48%) of **2** . The formed crystals were used in the structural study.

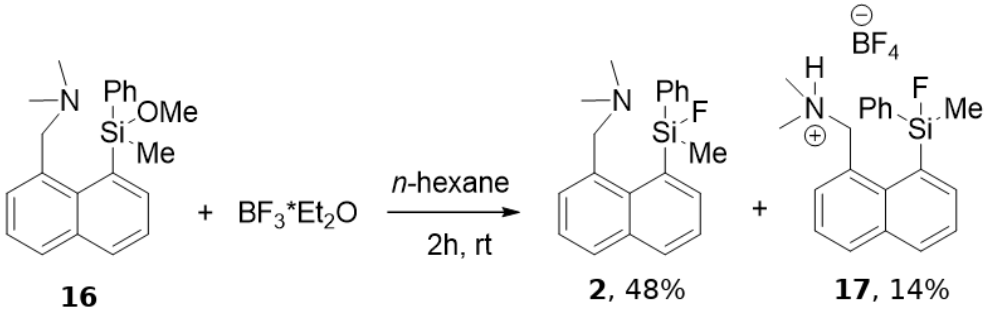


**Figure A12:** Reaction scheme for the synthesis of the bridged fluoro (**2**) compound and 1-(8-(fluoro(methyl)(phenyl)silyl)naphthalen-1-yl)-N,N-dimethyl ammonium tetrafluoroborat (**17**).

The slightly yellow residue left in the reaction flask after washing with n-hexane was dissolved in a small amount of $CH_2Cl_2$ (ca. 2 mL). 10 mL of n-hexane was carefully layered on top of the $CH_2Cl_2$ solution. During the solvents diffusion at room temperature white crystals of **17**

were formed. The solvents were removed using a syringe, and the product 17 was recrystallized twice in the same manner from a fresh $CH_2Cl_2$/n-hexane mixture giving 0.156 g (14%) of **17**. The formed crystals were used in the structural study.

**2**: Colourless crystals; mp = 79-80°C; $^1$H NMR (400 MHz, $CDCl_3$) $\delta$ 8.41 (d, J = 7.1 Hz, 1H), 7.98 (dd, J = 8.1, 1.3 Hz, 1H), 7.83 (d, J = 7.9 Hz, 1H), 7.58 (dd, J = 7.7, 7.5 Hz, 1H), 7.55–7.50 (m, 2H), 7.45–7.26 (m, 5H), 3.86 (d-AB, 2J = 14.6 Hz, 1H, $CH_2$), 3.82 (d-AB, 2J = 14.6 Hz, 1H, $CH_2$), 1.85 (s, 6H, $NMe_2$), 0.84 (d, 3JHF = 9.5 Hz, 3H, SiMe); $^{13}$C NMR (101 MHz, $CDCl_3$) $\delta$ 139.0 (d, J = 12.0 Hz), 135.7, 134.4, 133.9, 132.6, 132.0, 129.7, 128.9, 127.7, 127.7, 125.2, 124.9, 64.8 ($CH_2$), 45.5 ($NMe_2$), -0.5 (d, J = 28.3 Hz, SiMe); $^{19}$F NMR (377 MHz, $CDCl_3$) $\delta$ -112.5 (bs); $^{29}$Si{H} NMR (80 MHz, $CDCl_3$) $\delta$ -26.5 (d, J = 262.7 Hz); HRMS (EI) calculated for $C_{20}H_{22}FNSi$ $[M]^+$: 323.15001, found: 323.14977.

**17**: Colourless crystals; mp = 119-120°C; $^1$H NMR (401 MHz, $CD_2Cl_2$) $\delta$ 11.23 (bs, 1H, NH), 8.16 (ddd, J = 9.6, 7.6, 1.4 Hz, 2H), 8.09 (dd, J = 8.1, 1.4 Hz, 1H), 7.79 (dd, J = 7.2, 1.4 Hz, 1H), 7.71–7.62 (m, 2H), 7.57–7.48 (m, 3H), 7.43 (tm, J = 7.3 Hz, 2H), 4.81 (dd-ABX, J = 13.7, 6.3 Hz, 1H, $CH_2$), 4.41 (ddd-ABX, J = 13.7, 6.1, 1.5 Hz, 1H, $CH_2$), 2.44 (d, J = 4.6 Hz, 3H, $NMe_2$), 2.43 (d, J = 4.7 Hz, 3H, $NMe_2$), 0.88 (d, 3JHF = 7.9 Hz, 3H, SiMe); $^{13}$C NMR (101 MHz, $CD_2Cl_2$) $\delta$ 140.1 (d, J = 5.0 Hz), 136.5, 135.6, 135.4 (d, J = 16.2 Hz), 134.5, 134.0 (d, J = 1.7 Hz), 133.7, 132.3, 132.0, 129.4, 128.3 (d, J = 15.4 Hz), 126.9, 126.9, 125.8, 60.9 (d, J = 8.6 Hz, $CH_2$), 43.6 ($NMe_2$), 43.1 (d, J = 2.5 Hz, $NMe_2$), 0.7 (d, J = 17.7 Hz, SiMe); $^{19}$F NMR (377 MHz, $CD_2Cl_2$) $\delta$ -151.63 (4F, $BF_4$), -153.15 (q, 3JFH = 7.8 Hz, 1F, SiF); $^{29}$Si{H} NMR (80 MHz, $CD_2Cl_2$) $\delta$ 12.1 (d, J = 282.5 Hz); HR ESI-TOF MS (Positive mode) calculated for $C_{20}H_{23}FNSi$: 324.1584, found: 324.1581.

# Residual density maps of the crystal structures

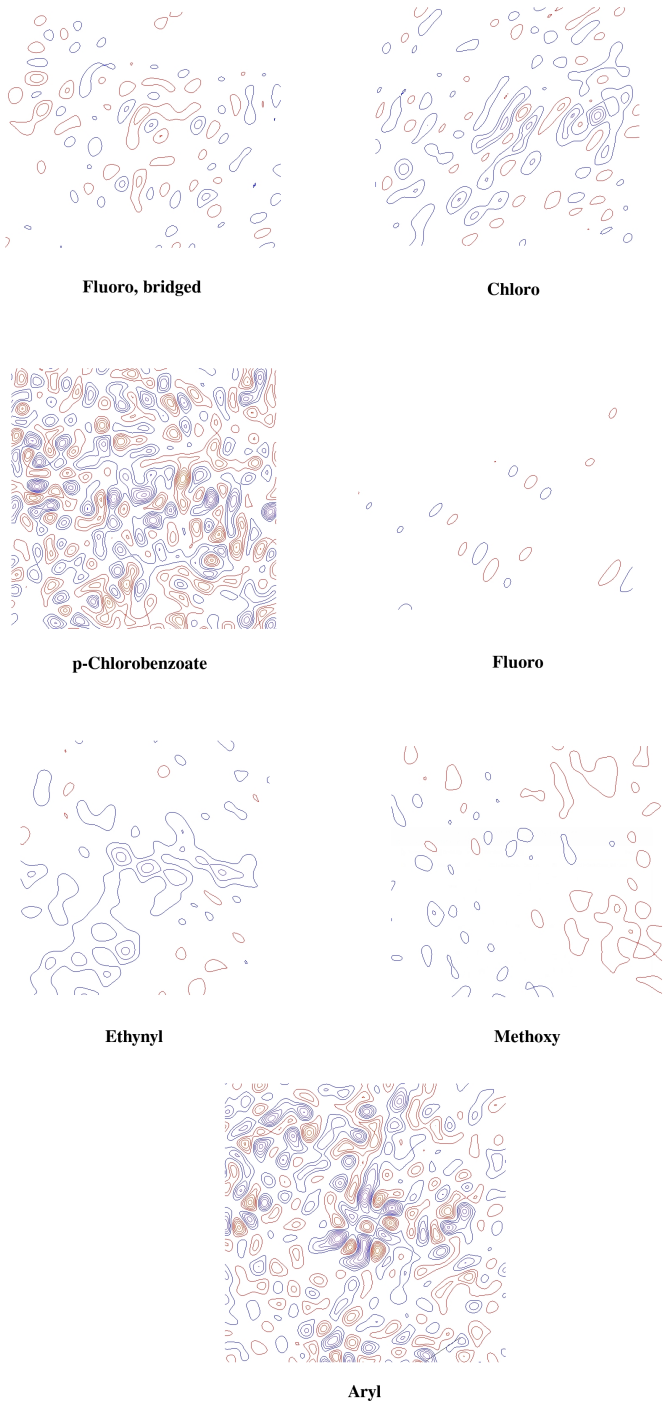


**Figure A13:** Residual density contour plots of the of the N−Si−X plane of the pentacoordinated silicon compounds after XWR. Blue and red lines refer to positive and negative contour lines, respectively. The separation between two lines is 0.05 e·Å$^{-3}$.

# Deformation density maps of the crystal structures

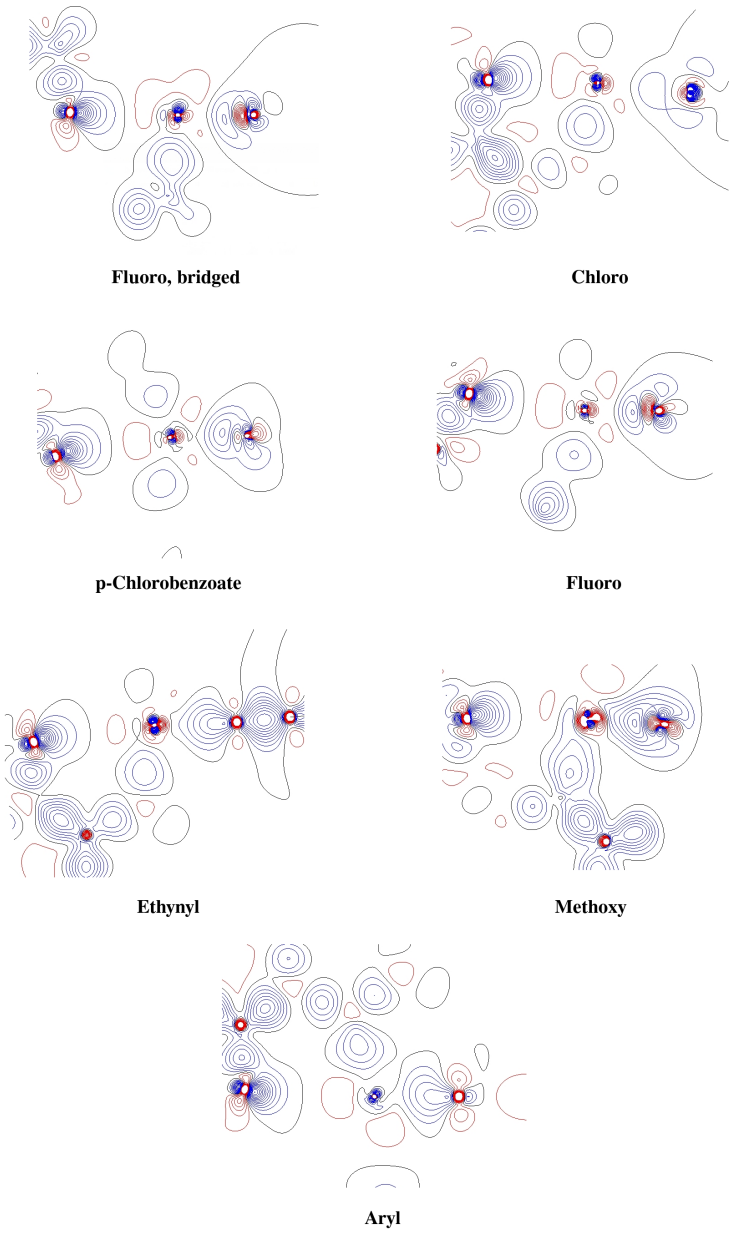


**Figure A14:** Deformation density contour plots of the N−Si−X plane of the pentacoordinated silicon compounds after XWR. Blue and red lines refer to positive and negative contour lines, respectively. The separation between two lines is 0.1 e·Å$^{-3}$.

# Coordinates of the optimized geometries

All optimizations (except for the Crystal14 optimization) were peformed at the B3LYP/def2-TZVP level of theory using Grimme's dispersion correction (GD3BJ).

**Table A1:** Coordinates of the isolated molecule optimization of the ethynyl compound.

| | | x /Å | y /Å | z /Å |
|---|---|---|---|---|
| 1 | Si | 9.666193 | 8.417338 | 8.595707 |
| 2 | N | 11.634214 | 6.642624 | 7.589396 |
| 3 | C | 11.209968 | 8.522538 | 6.105518 |
| 4 | C | 9.989353 | 8.838792 | 6.782024 |
| 5 | C | 11.154565 | 8.824650 | 9.658300 |
| 6 | C | 10.631472 | 10.121050 | 4.340382 |
| 7 | C | 9.120102 | 9.718114 | 6.164876 |
| 8 | C | 12.118906 | 7.537685 | 6.588547 |
| 9 | C | 11.570304 | 9.237615 | 4.922210 |
| 10 | C | 11.310451 | 8.234653 | 10.916037 |
| 11 | C | 13.373411 | 7.418583 | 6.038106 |
| 12 | C | 12.142959 | 9.713105 | 9.224312 |
| 13 | C | 8.384881 | 9.665449 | 9.100523 |
| 14 | C | 12.859082 | 9.066484 | 4.363540 |
| 15 | C | 13.756182 | 8.207086 | 4.936589 |
| 16 | C | 13.401201 | 9.378869 | 11.251203 |
| 17 | C | 12.420479 | 8.505489 | 11.706800 |
| 18 | C | 9.413263 | 10.323282 | 4.927072 |
| 19 | C | 13.257335 | 9.985579 | 10.008562 |
| 20 | C | 8.852662 | 6.800079 | 9.093616 |
| 21 | C | 12.629834 | 6.151151 | 8.532330 |
| 22 | C | 7.555436 | 10.448445 | 9.496373 |
| 23 | C | 10.901913 | 5.534289 | 6.966013 |
| 24 | H | 10.560091 | 7.546094 | 11.286074 |
| 25 | H | 8.692126 | 10.993124 | 4.476321 |
| 26 | H | 12.521367 | 8.034611 | 12.676808 |
| 27 | H | 14.014652 | 10.670904 | 9.648859 |
| 28 | H | 10.900412 | 10.638010 | 3.427142 |
| 29 | H | 9.574058 | 6.026268 | 9.345642 |
| 30 | H | 8.204107 | 9.997733 | 6.666932 |
| 31 | H | 13.124484 | 9.636573 | 3.481873 |
| 32 | H | 13.199319 | 6.985608 | 8.933666 |
| 33 | H | 10.473315 | 4.898393 | 7.738470 |
| 34 | H | 11.562810 | 4.922849 | 6.336436 |
| 35 | H | 14.749120 | 8.094072 | 4.520870 |
| 36 | H | 10.095989 | 5.924115 | 6.347270 |
| 37 | H | 14.269730 | 9.588869 | 11.862494 |
| 38 | H | 12.116439 | 5.659245 | 9.358843 |
| 39 | H | 14.065362 | 6.684123 | 6.425688 |
| 40 | H | 12.050989 | 10.190052 | 8.256857 |
| 41 | H | 6.831075 | 11.144598 | 9.845094 |
| 42 | H | 8.209979 | 6.426168 | 8.295101 |
| 43 | H | 8.219960 | 6.980461 | 9.963667 |
| 44 | H | 13.320541 | 5.423204 | 8.084452 |

**Table A2:** Coordinates of the isolated molecule optimization of the methyl compound.

| | | x /Å | y /Å | z /Å |
|---|---|---|---|---|
| 1 | Si | 13.633145 | 3.355449 | 8.999494 |
| 2 | N | 16.057306 | 4.308165 | 7.654731 |
| 3 | C | 15.077818 | 1.421556 | 5.520610 |
| 4 | C | 15.454023 | 3.506554 | 11.195627 |
| 5 | C | 12.655341 | 1.935429 | 6.791874 |
| 6 | C | 17.167693 | 1.899487 | 11.721173 |
| 7 | C | 15.003206 | 2.407107 | 6.553754 |
| 8 | C | 13.891092 | 0.787504 | 5.084345 |
| 9 | C | 16.777270 | 1.141197 | 10.623255 |
| 10 | C | 15.052492 | 2.765419 | 10.079457 |
| 11 | C | 12.693886 | 1.074769 | 5.677494 |
| 12 | C | 16.331655 | 1.079046 | 4.960959 |
| 13 | C | 17.473462 | 1.701065 | 5.385116 |
| 14 | C | 16.498658 | 3.083396 | 12.008971 |
| 15 | C | 13.376203 | 5.213770 | 9.156689 |
| 16 | C | 15.729476 | 1.569771 | 9.816854 |
| 17 | C | 15.617336 | 5.444401 | 6.841463 |
| 18 | C | 17.397379 | 2.755818 | 6.313549 |
| 19 | C | 13.774628 | 2.594280 | 7.266648 |
| 20 | C | 16.191429 | 3.138350 | 6.854949 |
| 21 | C | 12.076418 | 2.608760 | 9.772539 |
| 22 | C | 17.205423 | 4.654273 | 8.477510 |
| 23 | H | 14.953087 | 4.438153 | 11.432599 |
| 24 | H | 11.713236 | 2.038074 | 7.312517 |
| 25 | H | 17.985443 | 1.569098 | 12.349086 |
| 26 | H | 13.952544 | 0.067787 | 4.277006 |
| 27 | H | 17.291328 | 0.216368 | 10.392623 |
| 28 | H | 11.783183 | 0.599339 | 5.335910 |
| 29 | H | 16.369263 | 0.309168 | 4.200244 |
| 30 | H | 18.435089 | 1.422433 | 4.973623 |
| 31 | H | 16.793219 | 3.678278 | 12.864787 |
| 32 | H | 14.307438 | 5.762871 | 9.275496 |
| 33 | H | 12.749808 | 5.417872 | 10.027787 |
| 34 | H | 12.857037 | 5.611671 | 8.282960 |
| 35 | H | 15.447925 | 0.969179 | 8.961018 |
| 36 | H | 14.695903 | 5.193236 | 6.320036 |
| 37 | H | 16.376302 | 5.723342 | 6.096470 |
| 38 | H | 15.430343 | 6.303774 | 7.483326 |
| 39 | H | 18.297026 | 3.298585 | 6.566906 |
| 40 | H | 12.041044 | 2.904690 | 10.824079 |
| 41 | H | 12.077818 | 1.518217 | 9.736605 |
| 42 | H | 11.156421 | 2.966642 | 9.303657 |
| 43 | H | 16.904703 | 5.419291 | 9.194137 |
| 44 | H | 18.049041 | 5.052968 | 7.895441 |
| 45 | H | 17.536225 | 3.780443 | 9.033684 |

**Table A3:** Coordinates of the isolated molecule optimization of the aryl compound.

| | | x /Å | y /Å | z /Å |
|---|---|---|---|---|
| 1 | Si | 0.188076 | 0.757182 | 0.561602 |
| 2 | N | 3.054643 | -0.204691 | 0.603185 |
| 3 | N | -1.592071 | -1.477441 | 1.392761 |
| 4 | C | -2.763519 | 0.349529 | 0.265955 |
| 5 | C | -5.028900 | -0.084885 | -0.608391 |
| 6 | C | -4.004186 | 0.828092 | -0.264071 |
| 7 | C | 2.175905 | -3.957482 | -1.074783 |
| 8 | C | 1.173669 | 2.612916 | -1.384616 |
| 9 | C | -1.908189 | 2.596956 | 0.190692 |
| 10 | C | 0.332069 | -2.931506 | -2.342026 |
| 11 | C | -4.187418 | 2.217603 | -0.456314 |
| 12 | C | 2.671378 | -1.509650 | 0.196382 |
| 13 | C | -2.686746 | -1.039036 | 0.588912 |
| 14 | C | 1.847345 | 3.734832 | -1.848031 |
| 15 | C | 1.502722 | -1.631620 | -0.621037 |
| 16 | C | 0.499731 | -0.613044 | -0.721119 |
| 17 | C | 3.438698 | -2.620494 | 0.472454 |
| 18 | C | -1.655258 | 1.253290 | 0.399206 |
| 19 | C | -0.447977 | -0.748607 | -1.718922 |
| 20 | C | -3.691963 | -1.900059 | 0.212938 |
| 21 | C | -3.173208 | 3.090557 | -0.185100 |
| 22 | C | 1.717691 | 3.199454 | 0.865378 |
| 23 | C | -4.856842 | -1.428176 | -0.417970 |
| 24 | C | 2.394422 | 4.328097 | 0.412932 |
| 25 | C | -1.115112 | -2.828717 | 1.132982 |
| 26 | C | 2.465460 | 4.596765 | -0.948037 |
| 27 | C | 1.342065 | -2.848387 | -1.355355 |
| 28 | C | 3.163752 | -3.860757 | -0.134302 |
| 29 | C | 0.677232 | 0.427715 | 2.344173 |
| 30 | C | 3.876242 | -0.116112 | 1.796899 |
| 31 | C | -1.911077 | -1.304695 | 2.812221 |
| 32 | C | 3.674942 | 0.538467 | -0.499525 |
| 33 | C | -0.508972 | -1.875705 | -2.560188 |
| 34 | C | 1.100571 | 2.311931 | -0.019953 |
| 35 | H | 1.676111 | 3.013952 | 1.931333 |
| 36 | H | -5.946832 | 0.301611 | -1.033963 |
| 37 | H | -1.269462 | -1.927395 | -3.328767 |
| 38 | H | 1.893647 | 3.937360 | -2.910996 |
| 39 | H | 0.705536 | 1.949698 | -2.102160 |
| 40 | H | 4.305852 | -2.531983 | 1.111225 |
| 41 | H | -3.608637 | -2.952659 | 0.445028 |
| 42 | H | -5.143012 | 2.569782 | -0.825844 |
| 43 | H | 2.995016 | 5.470961 | -1.305083 |
| 44 | H | -3.313292 | 4.156087 | -0.316711 |
| 45 | H | -2.734042 | -1.966506 | 3.119430 |
| 46 | H | -1.779519 | -3.603694 | 1.542633 |
| 47 | H | 2.866267 | 4.996165 | 1.123071 |
| 48 | H | -1.011887 | -2.984671 | 0.063708 |
| 49 | H | 3.036715 | 0.509090 | -1.376951 |
| 50 | H | 4.906431 | -0.468761 | 1.638999 |
| 51 | H | -1.098537 | 3.308445 | 0.268218 |
| 52 | H | -5.632357 | -2.127948 | -0.702009 |
| 53 | H | 2.009985 | -4.882747 | -1.612566 |
| 54 | H | 3.785164 | -4.715968 | 0.098858 |
| 55 | H | -2.207312 | -0.275649 | 3.005001 |
| 56 | H | 0.239348 | -3.845297 | -2.916381 |
| 57 | H | -1.216920 | 0.002610 | -1.830651 |
| 58 | H | -1.035211 | -1.536596 | 3.416414 |
| 59 | H | 4.654160 | 0.109895 | -0.758973 |
| 60 | H | 3.930876 | 0.929277 | 2.103757 |
| 61 | H | 1.574114 | 0.980261 | 2.610427 |
| 62 | H | 0.878080 | -0.629168 | 2.509625 |
| 63 | H | 3.806417 | 1.578253 | -0.206590 |
| 64 | H | -0.134258 | -2.952725 | 1.593760 |
| 65 | H | 3.430551 | -0.693285 | 2.604685 |
| 66 | H | -0.121219 | 0.732349 | 3.019123 |

**Table A4:** Coordinates of the isolated molecule optimization of the silyl cation.

| | | x /Å | y /Å | z /Å |
|---|---|---|---|---|
| 1 | Si | 8.868735 | 18.256955 | 1.118764 |
| 2 | N | 10.690018 | 18.422825 | 1.820702 |
| 3 | C | 10.426642 | 20.198116 | 0.180325 |
| 4 | C | 9.218491 | 19.536656 | -0.160240 |
| 5 | C | 8.477599 | 20.011531 | -1.218396 |
| 6 | C | 8.919740 | 21.135797 | -1.948106 |
| 7 | C | 7.738620 | 18.835702 | 2.451587 |
| 8 | C | 10.075651 | 21.794719 | -1.604875 |
| 9 | C | 7.533769 | 20.208867 | 2.649832 |
| 10 | C | 10.868153 | 21.349548 | -0.520915 |
| 11 | C | 11.195102 | 19.699994 | 1.251294 |
| 12 | C | 6.079407 | 19.748025 | 4.509482 |
| 13 | C | 6.712838 | 20.661096 | 3.672969 |
| 14 | C | 7.086861 | 17.929937 | 3.299537 |
| 15 | C | 12.062341 | 21.976246 | -0.091727 |
| 16 | C | 6.263152 | 18.382507 | 4.320756 |
| 17 | C | 12.770710 | 21.478192 | 0.972774 |
| 18 | C | 12.345435 | 20.316071 | 1.656379 |
| 19 | C | 8.595993 | 16.496407 | 0.612240 |
| 20 | C | 11.550758 | 17.301141 | 1.311378 |
| 21 | C | 10.713514 | 18.413430 | 3.316382 |
| 22 | H | 6.560269 | 21.722732 | 3.814669 |
| 23 | H | 12.412205 | 22.858098 | -0.612604 |
| 24 | H | 7.542966 | 19.541396 | -1.496948 |
| 25 | H | 7.575799 | 16.417165 | 0.227588 |
| 26 | H | 8.011470 | 20.927944 | 1.995747 |
| 27 | H | 5.435968 | 20.100774 | 5.304622 |
| 28 | H | 7.213269 | 16.862899 | 3.162646 |
| 29 | H | 8.328024 | 21.490101 | -2.781313 |
| 30 | H | 10.391660 | 22.666921 | -2.162620 |
| 31 | H | 5.761471 | 17.673511 | 4.965700 |
| 32 | H | 10.165221 | 19.271539 | 3.689664 |
| 33 | H | 11.531476 | 17.302592 | 0.224983 |
| 34 | H | 12.940986 | 19.935506 | 2.474431 |
| 35 | H | 11.742729 | 18.442795 | 3.666374 |
| 36 | H | 10.241676 | 17.499342 | 3.669786 |
| 37 | H | 11.174009 | 16.354997 | 1.691368 |
| 38 | H | 12.571150 | 17.456763 | 1.654042 |
| 39 | H | 13.678394 | 21.968584 | 1.295988 |
| 40 | H | 9.272996 | 16.178237 | -0.179277 |
| 41 | H | 8.678014 | 15.798069 | 1.446534 |

**Table A5:** Coordinates of the isolated molecule optimization of the chlorine compound.

| | | x /Å | y /Å | z /Å |
|---|---|---|---|---|
| 1 | Cl | 5.871290 | 9.821960 | 0.999301 |
| 2 | Si | 4.424169 | 8.928566 | 2.293766 |
| 3 | N | 2.668107 | 7.606212 | 3.915114 |
| 4 | C | 4.299304 | 11.673152 | 5.399202 |
| 5 | C | 6.372029 | 4.690369 | 2.761386 |
| 6 | C | 5.177528 | 4.362403 | 4.897137 |
| 7 | C | 6.604959 | 5.443236 | 1.643654 |
| 8 | C | 3.577513 | 6.587501 | 4.343215 |
| 9 | C | 2.063774 | 8.395599 | 4.983050 |
| 10 | C | 5.144108 | 11.123604 | 6.356742 |
| 11 | C | 4.642497 | 6.276571 | 3.454055 |
| 12 | C | 4.739075 | 9.805130 | 3.912023 |
| 13 | C | 4.102333 | 11.018243 | 4.189962 |
| 14 | C | 3.400686 | 5.869434 | 5.501086 |
| 15 | C | 5.797668 | 9.925620 | 6.091445 |
| 16 | C | 5.401356 | 5.094338 | 3.706745 |
| 17 | C | 4.225719 | 4.766101 | 5.793600 |
| 18 | C | 5.943881 | 6.675209 | 1.469876 |
| 19 | C | 5.598794 | 9.276361 | 4.879079 |
| 20 | C | 1.634825 | 7.016631 | 3.050992 |
| 21 | C | 4.983665 | 7.125361 | 2.354343 |
| 22 | C | 2.849345 | 9.470350 | 1.436386 |
| 23 | H | 7.340167 | 5.127406 | 0.914694 |
| 24 | H | 5.779287 | 3.482721 | 5.088913 |
| 25 | H | 5.297234 | 11.629400 | 7.301600 |
| 26 | H | 4.070933 | 4.215683 | 6.712496 |
| 27 | H | 2.600322 | 6.124924 | 6.181238 |
| 28 | H | 6.242156 | 7.304476 | 0.644023 |
| 29 | H | 2.837054 | 8.757693 | 5.655105 |
| 30 | H | 1.318713 | 7.829839 | 5.557474 |
| 31 | H | 3.794545 | 12.610962 | 5.594839 |
| 32 | H | 1.562223 | 9.256950 | 4.541560 |
| 33 | H | 6.928179 | 3.778546 | 2.942230 |
| 34 | H | 6.463007 | 9.495994 | 6.829772 |
| 35 | H | 0.979802 | 7.800395 | 2.676150 |
| 36 | H | 1.028537 | 6.285681 | 3.601252 |
| 37 | H | 3.439080 | 11.460641 | 3.456187 |
| 38 | H | 2.018841 | 9.591305 | 2.128288 |
| 39 | H | 2.102381 | 6.515547 | 2.205801 |
| 40 | H | 6.113197 | 8.342943 | 4.690686 |
| 41 | H | 3.030690 | 10.423385 | 0.940308 |
| 42 | H | 2.559248 | 8.750919 | 0.669550 |

**Table A6:** Coordinates of the isolated molecule optimization of the fluorine compound.

| | | x /Å | y /Å | z /Å |
|---|---|---|---|---|
| 1 | Si | 10.098775 | 3.595633 | 2.791147 |
| 2 | F | 10.382040 | 3.108906 | 4.329202 |
| 3 | N | 9.843913 | 4.672309 | 0.269702 |
| 4 | C | 13.322215 | 6.031645 | 3.664503 |
| 5 | C | 9.468911 | 1.146900 | 1.478516 |
| 6 | C | 11.764999 | 5.410620 | -1.083508 |
| 7 | C | 11.430271 | 4.911171 | 2.603378 |
| 8 | C | 11.739902 | 1.864554 | 1.216049 |
| 9 | C | 12.001469 | 0.754852 | 0.421709 |
| 10 | C | 11.194904 | 5.128783 | 0.134470 |
| 11 | C | 11.910231 | 5.369093 | 1.339748 |
| 12 | C | 10.991728 | -0.162008 | 0.151714 |
| 13 | C | 13.040285 | 6.003840 | -1.159896 |
| 14 | C | 13.837777 | 6.389592 | 2.448968 |
| 15 | C | 12.144927 | 5.260049 | 3.733571 |
| 16 | C | 9.723840 | 0.033597 | 0.686797 |
| 17 | C | 10.467405 | 2.086851 | 1.752638 |
| 18 | C | 13.707850 | 6.350435 | -0.016584 |
| 19 | C | 13.161886 | 6.049986 | 1.253802 |
| 20 | C | 8.939270 | 5.824334 | 0.382049 |
| 21 | C | 9.387928 | 3.752732 | -0.767525 |
| 22 | C | 8.276695 | 4.006657 | 2.898081 |
| 23 | H | 7.736076 | 3.810486 | 1.974439 |
| 24 | H | 8.438927 | 3.316034 | -0.455730 |
| 25 | H | 12.535724 | 2.572614 | 1.409513 |
| 26 | H | 9.230652 | 4.248504 | -1.734586 |
| 27 | H | 8.934569 | -0.680163 | 0.486041 |
| 28 | H | 14.774804 | 6.929157 | 2.382111 |
| 29 | H | 8.472422 | 1.285064 | 1.881522 |
| 30 | H | 14.668180 | 6.848513 | -0.066889 |
| 31 | H | 11.221150 | 5.209166 | -1.996001 |
| 32 | H | 11.821529 | 4.894700 | 4.698564 |
| 33 | H | 9.244142 | 6.452804 | 1.216601 |
| 34 | H | 7.923248 | 5.476355 | 0.557788 |
| 35 | H | 8.120134 | 5.051435 | 3.169467 |
| 36 | H | 13.840940 | 6.295996 | 4.577194 |
| 37 | H | 13.470046 | 6.216655 | -2.130160 |
| 38 | H | 11.192705 | -1.025802 | -0.469269 |
| 39 | H | 12.992679 | 0.606131 | 0.011952 |
| 40 | H | 10.109292 | 2.949206 | -0.889333 |
| 41 | H | 8.950695 | 6.429367 | -0.534028 |
| 42 | H | 7.838583 | 3.393660 | 3.687947 |

**Table A7:** Coordinates of the isolated molecule optimization of the bridged fluorine compound.

| | | x /Å | y /Å | z /Å |
|---|---|---|---|---|
| 1 | Si | 4.967131 | 7.457496 | 2.479674 |
| 2 | F | 6.272435 | 6.725492 | 1.782263 |
| 3 | N | 2.864939 | 8.652628 | 3.558314 |
| 4 | C | 5.405173 | 10.347988 | 3.347530 |
| 5 | C | 6.443882 | 9.435931 | 1.359713 |
| 6 | C | 5.590902 | 9.248023 | 2.435851 |
| 7 | C | 4.462311 | 10.385792 | 4.424787 |
| 8 | C | 5.014795 | 6.580475 | 4.130734 |
| 9 | C | 6.204155 | 11.530096 | 3.155440 |
| 10 | C | 4.389564 | 4.711718 | 5.552013 |
| 11 | C | 4.281624 | 5.412014 | 4.355890 |
| 12 | C | 5.885080 | 7.010134 | 5.138367 |
| 13 | C | 5.996628 | 6.317093 | 6.337345 |
| 14 | C | 7.161800 | 10.622439 | 1.137053 |
| 15 | C | 3.456614 | 9.305473 | 4.725057 |
| 16 | C | 5.244030 | 5.167342 | 6.548850 |
| 17 | C | 7.067208 | 11.637852 | 2.041714 |
| 18 | C | 4.416979 | 11.477916 | 5.264135 |
| 19 | C | 6.131715 | 12.613104 | 4.061131 |
| 20 | C | 5.265473 | 12.584397 | 5.115258 |
| 21 | C | 2.261905 | 9.614964 | 2.636277 |
| 22 | C | 1.848481 | 7.711681 | 4.021418 |
| 23 | C | 3.693275 | 6.907843 | 1.220158 |
| 24 | H | 6.605536 | 8.619707 | 0.669895 |
| 25 | H | 3.810270 | 3.809628 | 5.704627 |
| 26 | H | 2.661129 | 9.756551 | 5.336552 |
| 27 | H | 3.017137 | 10.290019 | 2.243507 |
| 28 | H | 6.480752 | 7.902813 | 4.987936 |
| 29 | H | 3.613049 | 5.039040 | 3.588919 |
| 30 | H | 5.329445 | 4.625022 | 7.481883 |
| 31 | H | 7.642497 | 12.547876 | 1.922053 |
| 32 | H | 1.481157 | 10.211326 | 3.130225 |
| 33 | H | 3.683738 | 11.486564 | 6.061438 |
| 34 | H | 2.289885 | 7.005005 | 4.719821 |
| 35 | H | 3.910632 | 8.523351 | 5.333515 |
| 36 | H | 6.672433 | 6.671929 | 7.105339 |
| 37 | H | 3.927646 | 5.883106 | 0.925752 |
| 38 | H | 6.769569 | 13.471218 | 3.888675 |
| 39 | H | 1.809266 | 9.080067 | 1.802764 |
| 40 | H | 7.808066 | 10.705738 | 0.272831 |
| 41 | H | 1.434559 | 7.158045 | 3.180009 |
| 42 | H | 1.023417 | 8.235008 | 4.526577 |
| 43 | H | 5.202943 | 13.412753 | 5.808599 |
| 44 | H | 2.656106 | 6.948561 | 1.534875 |
| 45 | H | 3.798619 | 7.527182 | 0.326163 |

**Table A8:** Coordinates of the isolated molecule optimization of the hydro compound.

| | | x /Å | y /Å | z /Å |
|---|---|---|---|---|
| 1 | H | 5.567122 | 9.446513 | 1.295951 |
| 2 | Si | 4.507583 | 8.952136 | 2.226848 |
| 3 | N | 2.657680 | 7.597191 | 3.959776 |
| 4 | C | 4.268972 | 11.683212 | 5.360570 |
| 5 | C | 6.377099 | 4.694451 | 2.746333 |
| 6 | C | 5.168138 | 4.328404 | 4.862355 |
| 7 | C | 6.636330 | 5.470637 | 1.650867 |
| 8 | C | 3.568964 | 6.569918 | 4.346727 |
| 9 | C | 2.081131 | 8.376692 | 5.045779 |
| 10 | C | 5.109337 | 11.144066 | 6.327469 |
| 11 | C | 4.633779 | 6.268887 | 3.448135 |
| 12 | C | 4.770118 | 9.836091 | 3.861128 |
| 13 | C | 4.104362 | 11.033219 | 4.143113 |
| 14 | C | 3.400749 | 5.832518 | 5.495456 |
| 15 | C | 5.788575 | 9.959934 | 6.063407 |
| 16 | C | 5.393197 | 5.082155 | 3.686223 |
| 17 | C | 4.220282 | 4.720944 | 5.767652 |
| 18 | C | 5.973738 | 6.704185 | 1.494401 |
| 19 | C | 5.622035 | 9.317852 | 4.842302 |
| 20 | C | 1.618728 | 7.055029 | 3.079271 |
| 21 | C | 4.989078 | 7.131944 | 2.364996 |
| 22 | C | 2.909259 | 9.497434 | 1.400153 |
| 23 | H | 7.387371 | 5.170149 | 0.931378 |
| 24 | H | 5.767706 | 3.443701 | 5.037508 |
| 25 | H | 5.236085 | 11.644098 | 7.279346 |
| 26 | H | 4.064977 | 4.155747 | 6.677646 |
| 27 | H | 2.604640 | 6.080909 | 6.183277 |
| 28 | H | 6.285595 | 7.356015 | 0.687833 |
| 29 | H | 2.870968 | 8.725298 | 5.706833 |
| 30 | H | 1.339170 | 7.816554 | 5.632469 |
| 31 | H | 3.739651 | 12.607576 | 5.556233 |
| 32 | H | 1.581604 | 9.248915 | 4.622987 |
| 33 | H | 6.927209 | 3.777215 | 2.918613 |
| 34 | H | 6.446856 | 9.534531 | 6.810700 |
| 35 | H | 0.984315 | 7.863418 | 2.719922 |
| 36 | H | 0.988405 | 6.323409 | 3.604197 |
| 37 | H | 3.435915 | 11.464796 | 3.407379 |
| 38 | H | 2.090409 | 9.635827 | 2.103085 |
| 39 | H | 2.078099 | 6.565259 | 2.222831 |
| 40 | H | 6.152135 | 8.391772 | 4.658872 |
| 41 | H | 3.087861 | 10.448361 | 0.893580 |
| 42 | H | 2.592999 | 8.780400 | 0.640722 |

**Table A9:** Coordinates of the isolated molecule optimization of the methoxy compound.

| | | x /Å | y /Å | z /Å |
|---|---|---|---|---|
| 1 | Si | 8.465207 | 4.012352 | 8.819658 |
| 2 | O | 9.936366 | 3.644789 | 9.525708 |
| 3 | N | 5.851404 | 4.509830 | 7.804978 |
| 4 | C | 5.882976 | 2.784814 | 9.517080 |
| 5 | C | 6.887909 | 1.819971 | 11.947213 |
| 6 | C | 7.975510 | 1.916426 | 6.911178 |
| 7 | C | 5.265234 | 3.330054 | 8.354767 |
| 8 | C | 9.060379 | 3.864579 | 6.040103 |
| 9 | C | 7.189312 | 3.180804 | 9.939251 |
| 10 | C | 5.169585 | 1.787565 | 10.249018 |
| 11 | C | 5.694920 | 1.337508 | 11.482987 |
| 12 | C | 3.473211 | 1.713311 | 8.529582 |
| 13 | C | 4.110043 | 2.774529 | 7.857161 |
| 14 | C | 7.646065 | 2.703421 | 11.153212 |
| 15 | C | 9.099299 | 3.285826 | 4.777166 |
| 16 | C | 8.011226 | 1.330034 | 5.651446 |
| 17 | C | 10.556397 | 2.376040 | 9.478264 |
| 18 | C | 8.489080 | 3.198911 | 7.129646 |
| 19 | C | 5.716936 | 4.671197 | 6.363887 |
| 20 | C | 3.966898 | 1.259073 | 9.722146 |
| 21 | C | 5.370260 | 5.699157 | 8.516377 |
| 22 | C | 8.569393 | 2.016055 | 4.578792 |
| 23 | C | 8.570516 | 5.878956 | 8.755154 |
| 24 | H | 5.136418 | 0.601980 | 12.049327 |
| 25 | H | 3.657860 | 3.177942 | 6.961946 |
| 26 | H | 3.451665 | 0.483055 | 10.274595 |
| 27 | H | 2.564765 | 1.292705 | 8.117910 |
| 28 | H | 7.280222 | 1.484694 | 12.899017 |
| 29 | H | 7.600830 | 0.338426 | 5.506304 |
| 30 | H | 11.501823 | 2.437136 | 10.019484 |
| 31 | H | 8.636016 | 2.982830 | 11.488908 |
| 32 | H | 8.594878 | 1.562692 | 3.595954 |
| 33 | H | 9.476253 | 4.856615 | 6.173535 |
| 34 | H | 7.526310 | 1.370429 | 7.731107 |
| 35 | H | 6.023600 | 3.757790 | 5.860527 |
| 36 | H | 4.693489 | 4.927630 | 6.056151 |
| 37 | H | 6.375258 | 5.477791 | 6.039772 |
| 38 | H | 9.541594 | 3.824495 | 3.948229 |
| 39 | H | 9.624593 | 6.159828 | 8.743672 |
| 40 | H | 8.092004 | 6.297509 | 7.871564 |
| 41 | H | 10.760739 | 2.072075 | 8.447392 |
| 42 | H | 5.895322 | 6.579825 | 8.150771 |
| 43 | H | 5.560508 | 5.596126 | 9.582731 |
| 44 | H | 4.291740 | 5.845944 | 8.365668 |
| 45 | H | 9.938471 | 1.601856 | 9.946102 |
| 46 | H | 8.115488 | 6.335414 | 9.634905 |

**Table A10:** Coordinates of the isolated molecule optimization of the hydroxy compound.

| | | x /Å | y /Å | z /Å |
|---|---|---|---|---|
| 1 | Si | 8.467448 | 4.019566 | 8.823161 |
| 2 | O | 9.947802 | 3.687810 | 9.542797 |
| 3 | N | 5.856130 | 4.515363 | 7.810803 |
| 4 | C | 5.883926 | 2.784321 | 9.519755 |
| 5 | C | 6.910415 | 1.766345 | 11.920978 |
| 6 | C | 7.994186 | 1.909360 | 6.930972 |
| 7 | C | 5.261061 | 3.341777 | 8.366180 |
| 8 | C | 9.074879 | 3.852768 | 6.042644 |
| 9 | C | 7.198649 | 3.162832 | 9.934154 |
| 10 | C | 5.168372 | 1.784843 | 10.247596 |
| 11 | C | 5.703962 | 1.309112 | 11.467453 |
| 12 | C | 3.449096 | 1.747818 | 8.549795 |
| 13 | C | 4.093101 | 2.804785 | 7.878304 |
| 14 | C | 7.667228 | 2.655317 | 11.131769 |
| 15 | C | 9.113744 | 3.262946 | 4.785191 |
| 16 | C | 8.030248 | 1.311974 | 5.676116 |
| 17 | C | 8.506536 | 3.194586 | 7.138768 |
| 18 | C | 5.730830 | 4.665058 | 6.367285 |
| 19 | C | 3.952802 | 1.276373 | 9.731314 |
| 20 | C | 5.372218 | 5.709967 | 8.510989 |
| 21 | C | 8.586486 | 1.990082 | 4.597756 |
| 22 | C | 8.552442 | 5.887022 | 8.752345 |
| 23 | H | 5.142334 | 0.573559 | 12.030665 |
| 24 | H | 3.637583 | 3.219960 | 6.990154 |
| 25 | H | 3.435840 | 0.501078 | 10.283162 |
| 26 | H | 2.530225 | 1.342733 | 8.145841 |
| 27 | H | 7.312115 | 1.410738 | 12.861428 |
| 28 | H | 7.619768 | 0.319235 | 5.539392 |
| 29 | H | 8.664124 | 2.919233 | 11.459816 |
| 30 | H | 8.611463 | 1.529156 | 3.618426 |
| 31 | H | 9.488063 | 4.846946 | 6.167290 |
| 32 | H | 7.543405 | 1.370265 | 7.754781 |
| 33 | H | 6.036754 | 3.745880 | 5.874126 |
| 34 | H | 4.710665 | 4.923025 | 6.050426 |
| 35 | H | 6.394855 | 5.465468 | 6.039560 |
| 36 | H | 9.553839 | 3.795277 | 3.951011 |
| 37 | H | 9.603063 | 6.180418 | 8.764188 |
| 38 | H | 8.089086 | 6.297206 | 7.857090 |
| 39 | H | 5.897701 | 6.588502 | 8.141076 |
| 40 | H | 5.560488 | 5.614622 | 9.578486 |
| 41 | H | 4.293885 | 5.854429 | 8.357247 |
| 42 | H | 8.071700 | 6.340264 | 9.619992 |
| 43 | H | 10.243821 | 2.774975 | 9.501363 |

**Table A11:** Coordinates of the isolated molecule optimization of the p-chlorobenzoate compound.

| | | x /Å | y /Å | z /Å |
|---|---|---|---|---|
| 1 | Cl | -7.610201 | -0.300953 | -0.365830 |
| 2 | Si | 0.696796 | 0.455459 | 0.564420 |
| 3 | O | -1.013889 | 0.279024 | 0.371683 |
| 4 | O | -1.298049 | -1.626911 | 1.523297 |
| 5 | N | 3.438109 | 0.654533 | 0.565862 |
| 6 | C | 0.833265 | -2.853871 | -1.929200 |
| 7 | C | 0.479927 | -1.635997 | -1.316462 |
| 8 | C | 4.074518 | 1.216068 | 1.751267 |
| 9 | C | 2.051456 | -3.421270 | -1.673217 |
| 10 | C | 1.044564 | 3.298850 | 0.702707 |
| 11 | C | -3.201462 | -0.581730 | 0.552178 |
| 12 | C | 3.000203 | -2.750541 | -0.866936 |
| 13 | C | -3.699181 | 0.498129 | -0.176416 |
| 14 | C | 4.252300 | -3.331632 | -0.555174 |
| 15 | C | -5.430793 | -1.494001 | 0.716120 |
| 16 | C | 1.138010 | 4.580484 | 0.170882 |
| 17 | C | -5.053474 | 0.589392 | -0.460806 |
| 18 | C | 1.006999 | 0.291270 | 2.398358 |
| 19 | C | 0.778353 | 3.685453 | -2.030625 |
| 20 | C | -4.076388 | -1.573503 | 0.994758 |
| 21 | C | 0.685465 | 2.409017 | -1.491344 |
| 22 | C | -5.907467 | -0.409537 | -0.011356 |
| 23 | C | -1.752568 | -0.710349 | 0.874136 |
| 24 | C | 5.161522 | -2.653861 | 0.210619 |
| 25 | C | 2.677022 | -1.459133 | -0.353450 |
| 26 | C | 4.894518 | -1.334972 | 0.628150 |
| 27 | C | 1.009839 | 4.775839 | -1.199001 |
| 28 | C | 3.696243 | -0.733587 | 0.324826 |
| 29 | C | 1.358384 | -0.936051 | -0.513843 |
| 30 | C | 3.800192 | 1.445756 | -0.621457 |
| 31 | C | 0.825998 | 2.189425 | -0.117395 |
| 32 | H | 3.874093 | 0.587875 | 2.615806 |
| 33 | H | 0.113815 | -3.363181 | -2.557396 |
| 34 | H | -0.528929 | -1.271530 | -1.453377 |
| 35 | H | 1.145053 | 3.168333 | 1.773280 |
| 36 | H | 3.659495 | 2.208420 | 1.929298 |
| 37 | H | 4.474195 | -4.323914 | -0.927746 |
| 38 | H | 0.514715 | 1.567420 | -2.152870 |
| 39 | H | 2.307552 | -4.391270 | -2.081720 |
| 40 | H | 1.562841 | 1.136453 | 2.799900 |
| 41 | H | 1.309755 | 5.426041 | 0.825229 |
| 42 | H | 0.673006 | 3.831066 | -3.098444 |
| 43 | H | 0.059068 | 0.213938 | 2.929335 |
| 44 | H | 5.161129 | 1.325460 | 1.637558 |
| 45 | H | 5.661284 | -0.784374 | 1.155135 |
| 46 | H | 1.085993 | 5.772005 | -1.615829 |
| 47 | H | -5.447686 | 1.423690 | -1.023214 |
| 48 | H | -3.019248 | 1.266112 | -0.515422 |
| 49 | H | 6.110998 | -3.108096 | 0.462617 |
| 50 | H | 1.569430 | -0.619134 | 2.606088 |
| 51 | H | 4.881995 | 1.401225 | -0.802774 |
| 52 | H | -6.114793 | -2.258789 | 1.055219 |
| 53 | H | 3.282288 | 1.058619 | -1.494775 |
| 54 | H | 3.502323 | 2.481220 | -0.472392 |
| 55 | H | -3.676028 | -2.404349 | 1.558914 |

**Table A12:** Coordinates of the chlorine compound with cluster charges (r = 16 Å).

| | | x /Å | y /Å | z /Å |
|---|---|---|---|---|
| 1 | Cl | 5.810299 | 9.852272 | 1.050706 |
| 2 | Si | 4.363370 | 8.897586 | 2.355149 |
| 3 | N | 2.662329 | 7.584295 | 3.904663 |
| 4 | C | 4.372791 | 11.739474 | 5.381325 |
| 5 | C | 6.418659 | 4.707006 | 2.810020 |
| 6 | C | 5.146822 | 4.308307 | 4.891576 |
| 7 | C | 6.677100 | 5.484956 | 1.713373 |
| 8 | C | 3.550350 | 6.540210 | 4.333232 |
| 9 | C | 2.073365 | 8.374045 | 4.984011 |
| 10 | C | 5.225596 | 11.199847 | 6.338030 |
| 11 | C | 4.643074 | 6.253196 | 3.473440 |
| 12 | C | 4.710988 | 9.805214 | 3.952034 |
| 13 | C | 4.120800 | 11.047851 | 4.202533 |
| 14 | C | 3.323861 | 5.781486 | 5.455442 |
| 15 | C | 5.823554 | 9.966499 | 6.103793 |
| 16 | C | 5.407491 | 5.074702 | 3.729116 |
| 17 | C | 4.145562 | 4.675502 | 5.751045 |
| 18 | C | 5.995707 | 6.706507 | 1.534972 |
| 19 | C | 5.569720 | 9.279383 | 4.921866 |
| 20 | C | 1.605460 | 7.011462 | 3.050864 |
| 21 | C | 4.999515 | 7.123309 | 2.395910 |
| 22 | C | 2.796449 | 9.427738 | 1.477523 |
| 23 | H | 7.437251 | 5.203429 | 0.995589 |
| 24 | H | 5.759199 | 3.437163 | 5.094770 |
| 25 | H | 5.423769 | 11.745620 | 7.251562 |
| 26 | H | 3.955493 | 4.096676 | 6.645471 |
| 27 | H | 2.488100 | 6.005326 | 6.104180 |
| 28 | H | 6.305140 | 7.342266 | 0.718481 |
| 29 | H | 2.853750 | 8.712464 | 5.659901 |
| 30 | H | 1.320680 | 7.812378 | 5.551700 |
| 31 | H | 3.908411 | 12.700862 | 5.562033 |
| 32 | H | 1.586781 | 9.249727 | 4.554303 |
| 33 | H | 6.982295 | 3.800410 | 2.994933 |
| 34 | H | 6.489195 | 9.538983 | 6.843733 |
| 35 | H | 0.955770 | 7.805074 | 2.688824 |
| 36 | H | 1.003168 | 6.285523 | 3.610238 |
| 37 | H | 3.453225 | 11.483728 | 3.468230 |
| 38 | H | 1.995553 | 9.670388 | 2.173597 |
| 39 | H | 2.049906 | 6.508778 | 2.194678 |
| 40 | H | 6.039414 | 8.317769 | 4.757993 |
| 41 | H | 3.002448 | 10.309087 | 0.872136 |
| 42 | H | 2.431315 | 8.641479 | 0.815852 |

**Table A13:** Coordinates of the ethynyl compound with cluster charges (r = 16 Å).

| | | x /Å | y /Å | z /Å |
|---|---|---|---|---|
| 1 | Si | 9.663365 | 8.402895 | 8.595174 |
| 2 | N | 11.627285 | 6.641605 | 7.589571 |
| 3 | C | 11.208269 | 8.525019 | 6.112648 |
| 4 | C | 9.980201 | 8.827677 | 6.781061 |
| 5 | C | 11.153526 | 8.816116 | 9.654489 |
| 6 | C | 10.628126 | 10.122900 | 4.346945 |
| 7 | C | 9.103357 | 9.693337 | 6.155364 |
| 8 | C | 12.118476 | 7.542246 | 6.598914 |
| 9 | C | 11.572616 | 9.250313 | 4.937081 |
| 10 | C | 11.323377 | 8.218116 | 10.907247 |
| 11 | C | 13.380284 | 7.438200 | 6.061317 |
| 12 | C | 12.135480 | 9.710326 | 9.217144 |
| 13 | C | 8.391379 | 9.667479 | 9.103840 |
| 14 | C | 12.870049 | 9.095882 | 4.392241 |
| 15 | C | 13.767968 | 8.239698 | 4.970148 |
| 16 | C | 13.413415 | 9.370976 | 11.230900 |
| 17 | C | 12.440858 | 8.488664 | 11.688118 |
| 18 | C | 9.398929 | 10.301971 | 4.919464 |
| 19 | C | 13.255976 | 9.984674 | 9.992685 |
| 20 | C | 8.848243 | 6.789726 | 9.095724 |
| 21 | C | 12.618126 | 6.135880 | 8.530729 |
| 22 | C | 7.566716 | 10.459037 | 9.494513 |
| 23 | C | 10.887245 | 5.540883 | 6.958917 |
| 24 | H | 10.582912 | 7.519933 | 11.279435 |
| 25 | H | 8.670367 | 10.953856 | 4.454480 |
| 26 | H | 12.557139 | 8.003365 | 12.649293 |
| 27 | H | 14.007510 | 10.672892 | 9.625985 |
| 28 | H | 10.898755 | 10.649062 | 3.439470 |
| 29 | H | 9.576096 | 6.032931 | 9.380845 |
| 30 | H | 8.176696 | 9.955200 | 6.647574 |
| 31 | H | 13.139051 | 9.672878 | 3.516153 |
| 32 | H | 13.188404 | 6.964298 | 8.943760 |
| 33 | H | 10.447878 | 4.909619 | 7.728833 |
| 34 | H | 11.545583 | 4.924150 | 6.332782 |
| 35 | H | 14.766225 | 8.137640 | 4.564146 |
| 36 | H | 10.086760 | 5.937781 | 6.338449 |
| 37 | H | 14.285469 | 9.578076 | 11.838446 |
| 38 | H | 12.100487 | 5.635556 | 9.349215 |
| 39 | H | 14.074783 | 6.705960 | 6.448758 |
| 40 | H | 12.036872 | 10.186609 | 8.249896 |
| 41 | H | 6.848033 | 11.164511 | 9.838281 |
| 42 | H | 8.237335 | 6.388743 | 8.285354 |
| 43 | H | 8.191833 | 6.973202 | 9.947292 |
| 44 | H | 13.306957 | 5.409465 | 8.079124 |

**Table A14:** Coordinates of the optimization of the chlorine compound with implicit water solvation.

| | | x /Å | y /Å | z /Å |
|---|---|---|---|---|
| 1 | Cl | 5.792072 | 9.837885 | 1.057645 |
| 2 | Si | 4.305916 | 8.875724 | 2.376524 |
| 3 | N | 2.685439 | 7.603213 | 3.865031 |
| 4 | C | 4.357153 | 11.702990 | 5.411514 |
| 5 | C | 6.402656 | 4.702190 | 2.789294 |
| 6 | C | 5.163517 | 4.346482 | 4.906607 |
| 7 | C | 6.637201 | 5.467991 | 1.677821 |
| 8 | C | 3.568717 | 6.569928 | 4.330308 |
| 9 | C | 2.053039 | 8.393640 | 4.925913 |
| 10 | C | 5.247736 | 11.172059 | 6.338907 |
| 11 | C | 4.645601 | 6.256858 | 3.462741 |
| 12 | C | 4.704298 | 9.791548 | 3.954714 |
| 13 | C | 4.091269 | 11.017771 | 4.231701 |
| 14 | C | 3.361137 | 5.848053 | 5.479062 |
| 15 | C | 5.875281 | 9.959218 | 6.074364 |
| 16 | C | 5.411668 | 5.084035 | 3.723571 |
| 17 | C | 4.184970 | 4.743047 | 5.779844 |
| 18 | C | 5.953671 | 6.687989 | 1.494431 |
| 19 | C | 5.606497 | 9.278559 | 4.892100 |
| 20 | C | 1.649490 | 6.992391 | 3.003421 |
| 21 | C | 4.975670 | 7.113020 | 2.370505 |
| 22 | C | 2.782176 | 9.466351 | 1.465238 |
| 23 | H | 7.386831 | 5.166724 | 0.957488 |
| 24 | H | 5.763215 | 3.468474 | 5.111379 |
| 25 | H | 5.452980 | 11.701280 | 7.260631 |
| 26 | H | 4.009170 | 4.186400 | 6.690970 |
| 27 | H | 2.546462 | 6.096209 | 6.144424 |
| 28 | H | 6.242754 | 7.319776 | 0.667425 |
| 29 | H | 2.809392 | 8.747164 | 5.620428 |
| 30 | H | 1.298185 | 7.819258 | 5.472052 |
| 31 | H | 3.867407 | 12.648186 | 5.609138 |
| 32 | H | 1.562495 | 9.255276 | 4.475537 |
| 33 | H | 6.971882 | 3.798638 | 2.969537 |
| 34 | H | 6.572349 | 9.541947 | 6.790135 |
| 35 | H | 0.981152 | 7.764810 | 2.633115 |
| 36 | H | 1.063236 | 6.260153 | 3.567543 |
| 37 | H | 3.389143 | 11.444552 | 3.525526 |
| 38 | H | 1.926881 | 9.604983 | 2.122870 |
| 39 | H | 2.119809 | 6.493687 | 2.158878 |
| 40 | H | 6.100447 | 8.333473 | 4.705714 |
| 41 | H | 3.004095 | 10.418583 | 0.985889 |
| 42 | H | 2.505163 | 8.756848 | 0.684393 |

**Table A15:** Coordinates of the optimization of the chlorine compound with acetonitrile solvation.

| | | x /Å | y /Å | z /Å |
|---|---|---|---|---|
| 1 | Cl | 5.794762 | 9.836861 | 1.053817 |
| 2 | Si | 4.311433 | 8.878389 | 2.372329 |
| 3 | N | 2.684295 | 7.603295 | 3.867056 |
| 4 | C | 4.355190 | 11.701383 | 5.411265 |
| 5 | C | 6.401204 | 4.701682 | 2.788528 |
| 6 | C | 5.163992 | 4.347572 | 4.906698 |
| 7 | C | 6.635782 | 5.466742 | 1.676694 |
| 8 | C | 3.568812 | 6.570895 | 4.330929 |
| 9 | C | 2.052903 | 8.393814 | 4.927921 |
| 10 | C | 5.243797 | 11.169355 | 6.339880 |
| 11 | C | 4.645237 | 6.257847 | 3.462485 |
| 12 | C | 4.706337 | 9.792254 | 3.952445 |
| 13 | C | 4.092266 | 11.017818 | 4.229871 |
| 14 | C | 3.362664 | 5.849412 | 5.480274 |
| 15 | C | 5.872490 | 9.957237 | 6.074884 |
| 16 | C | 5.411036 | 5.084677 | 3.723187 |
| 17 | C | 4.186610 | 4.744579 | 5.780927 |
| 18 | C | 5.953258 | 6.687263 | 1.493537 |
| 19 | C | 5.606759 | 9.278305 | 4.890985 |
| 20 | C | 1.648786 | 6.993146 | 3.005221 |
| 21 | C | 4.975890 | 7.113525 | 2.369781 |
| 22 | C | 2.784837 | 9.466795 | 1.464165 |
| 23 | H | 7.384878 | 5.164771 | 0.956096 |
| 24 | H | 5.763857 | 3.469568 | 5.111055 |
| 25 | H | 5.446833 | 11.697307 | 7.262830 |
| 26 | H | 4.011783 | 4.188377 | 6.692525 |
| 27 | H | 2.548594 | 6.097995 | 6.146239 |
| 28 | H | 6.242906 | 7.318836 | 0.666566 |
| 29 | H | 2.809909 | 8.748298 | 5.621285 |
| 30 | H | 1.298619 | 7.819867 | 5.475599 |
| 31 | H | 3.864839 | 12.646233 | 5.609075 |
| 32 | H | 1.561581 | 9.255089 | 4.477549 |
| 33 | H | 6.969863 | 3.797801 | 2.968980 |
| 34 | H | 6.568235 | 9.539229 | 6.791515 |
| 35 | H | 0.981071 | 7.765907 | 2.634329 |
| 36 | H | 1.061529 | 6.260993 | 3.568691 |
| 37 | H | 3.391790 | 11.445473 | 3.522583 |
| 38 | H | 1.930741 | 9.604479 | 2.123542 |
| 39 | H | 2.119234 | 6.494214 | 2.160860 |
| 40 | H | 6.101646 | 8.333822 | 4.704146 |
| 41 | H | 3.004861 | 10.419205 | 0.984194 |
| 42 | H | 2.507111 | 8.757052 | 0.683788 |

**Table A16:** Coordinates of the optimization of the ethynyl compound with implicit water solvation.

| | | x /Å | y /Å | z /Å |
|---|---|---|---|---|
| 1 | Si | 9.666193 | 8.417338 | 8.595707 |
| 2 | N | 11.634214 | 6.642624 | 7.589396 |
| 3 | C | 11.209968 | 8.522538 | 6.105518 |
| 4 | C | 9.989353 | 8.838792 | 6.782024 |
| 5 | C | 11.154565 | 8.824650 | 9.658300 |
| 6 | C | 10.631472 | 10.121050 | 4.340382 |
| 7 | C | 9.120102 | 9.718114 | 6.164876 |
| 8 | C | 12.118906 | 7.537685 | 6.588547 |
| 9 | C | 11.570304 | 9.237615 | 4.922210 |
| 10 | C | 11.310451 | 8.234653 | 10.916037 |
| 11 | C | 13.373411 | 7.418583 | 6.038106 |
| 12 | C | 12.142959 | 9.713105 | 9.224312 |
| 13 | C | 8.384881 | 9.665449 | 9.100523 |
| 14 | C | 12.859082 | 9.066484 | 4.363540 |
| 15 | C | 13.756182 | 8.207086 | 4.936589 |
| 16 | C | 13.401201 | 9.378869 | 11.251203 |
| 17 | C | 12.420479 | 8.505489 | 11.706800 |
| 18 | C | 9.413263 | 10.323282 | 4.927072 |
| 19 | C | 13.257335 | 9.985579 | 10.008562 |
| 20 | C | 8.852662 | 6.800079 | 9.093616 |
| 21 | C | 12.629834 | 6.151151 | 8.532330 |
| 22 | C | 7.555436 | 10.448445 | 9.496373 |
| 23 | C | 10.901913 | 5.534289 | 6.966013 |
| 24 | H | 10.560091 | 7.546094 | 11.286074 |
| 25 | H | 8.692126 | 10.993124 | 4.476321 |
| 26 | H | 12.521367 | 8.034611 | 12.676808 |
| 27 | H | 14.014652 | 10.670904 | 9.648859 |
| 28 | H | 10.900412 | 10.638010 | 3.427142 |
| 29 | H | 9.574058 | 6.026268 | 9.345642 |
| 30 | H | 8.204107 | 9.997733 | 6.666932 |
| 31 | H | 13.124484 | 9.636573 | 3.481873 |
| 32 | H | 13.199319 | 6.985608 | 8.933666 |
| 33 | H | 10.473315 | 4.898393 | 7.738470 |
| 34 | H | 11.562810 | 4.922849 | 6.336436 |
| 35 | H | 14.749120 | 8.094072 | 4.520870 |
| 36 | H | 10.095989 | 5.924115 | 6.347270 |
| 37 | H | 14.269730 | 9.588869 | 11.862494 |
| 38 | H | 12.116439 | 5.659245 | 9.358843 |
| 39 | H | 14.065362 | 6.684123 | 6.425688 |
| 40 | H | 12.050989 | 10.190052 | 8.256857 |
| 41 | H | 6.831075 | 11.144598 | 9.845094 |
| 42 | H | 8.209979 | 6.426168 | 8.295101 |
| 43 | H | 8.219960 | 6.980461 | 9.963667 |
| 44 | H | 13.320541 | 5.423204 | 8.084452 |

**Table A17:** Coordinates of the optimization of the ethynyl compound with implicit acetonitrile solvation.

| | | x /Å | y /Å | z /Å |
|---|---|---|---|---|
| 1 | Si | 9.666193 | 8.417338 | 8.595707 |
| 2 | N | 11.634214 | 6.642624 | 7.589396 |
| 3 | C | 11.209968 | 8.522538 | 6.105518 |
| 4 | C | 9.989353 | 8.838792 | 6.782024 |
| 5 | C | 11.154565 | 8.824650 | 9.658300 |
| 6 | C | 10.631472 | 10.121050 | 4.340382 |
| 7 | C | 9.120102 | 9.718114 | 6.164876 |
| 8 | C | 12.118906 | 7.537685 | 6.588547 |
| 9 | C | 11.570304 | 9.237615 | 4.922210 |
| 10 | C | 11.310451 | 8.234653 | 10.916037 |
| 11 | C | 13.373411 | 7.418583 | 6.038106 |
| 12 | C | 12.142959 | 9.713105 | 9.224312 |
| 13 | C | 8.384881 | 9.665449 | 9.100523 |
| 14 | C | 12.859082 | 9.066484 | 4.363540 |
| 15 | C | 13.756182 | 8.207086 | 4.936589 |
| 16 | C | 13.401201 | 9.378869 | 11.251203 |
| 17 | C | 12.420479 | 8.505489 | 11.706800 |
| 18 | C | 9.413263 | 10.323282 | 4.927072 |
| 19 | C | 13.257335 | 9.985579 | 10.008562 |
| 20 | C | 8.852662 | 6.800079 | 9.093616 |
| 21 | C | 12.629834 | 6.151151 | 8.532330 |
| 22 | C | 7.555436 | 10.448445 | 9.496373 |
| 23 | C | 10.901913 | 5.534289 | 6.966013 |
| 24 | H | 10.560091 | 7.546094 | 11.286074 |
| 25 | H | 8.692126 | 10.993124 | 4.476321 |
| 26 | H | 12.521367 | 8.034611 | 12.676808 |
| 27 | H | 14.014652 | 10.670904 | 9.648859 |
| 28 | H | 10.900412 | 10.638010 | 3.427142 |
| 29 | H | 9.574058 | 6.026268 | 9.345642 |
| 30 | H | 8.204107 | 9.997733 | 6.666932 |
| 31 | H | 13.124484 | 9.636573 | 3.481873 |
| 32 | H | 13.199319 | 6.985608 | 8.933666 |
| 33 | H | 10.473315 | 4.898393 | 7.738470 |
| 34 | H | 11.562810 | 4.922849 | 6.336436 |
| 35 | H | 14.749120 | 8.094072 | 4.520870 |
| 36 | H | 10.095989 | 5.924115 | 6.347270 |
| 37 | H | 14.269730 | 9.588869 | 11.862494 |
| 38 | H | 12.116439 | 5.659245 | 9.358843 |
| 39 | H | 14.065362 | 6.684123 | 6.425688 |
| 40 | H | 12.050989 | 10.190052 | 8.256857 |
| 41 | H | 6.831075 | 11.144598 | 9.845094 |
| 42 | H | 8.209979 | 6.426168 | 8.295101 |
| 43 | H | 8.219960 | 6.980461 | 9.963667 |
| 44 | H | 13.320541 | 5.423204 | 8.084452 |

**Table A18:** Coordinates of the Crystal14 optimization of the chloro compound (level of theory: B3LYP/pob-TZVP).

| | x /Å | y /Å | z /Å |
|---|---|---|---|
| Cl | -1.205110 | -6.542081 | 1.162700 |
| Cl | 1.205110 | 1.620420 | 5.674300 |
| Cl | 1.205110 | 6.542081 | -1.162700 |
| Cl | -1.205110 | -1.620420 | -5.674300 |
| Si | -2.523776 | -7.453179 | 2.423443 |
| Si | 2.523776 | 0.709321 | 4.413557 |
| Si | 2.523776 | 7.453179 | -2.423443 |
| Si | -2.523776 | -0.709321 | -4.413557 |
| N | 3.270477 | 7.659690 | 3.930044 |
| N | -3.270477 | -0.502810 | 2.906956 |
| N | -3.270477 | -7.659690 | -3.930044 |
| N | 3.270477 | 0.502810 | -2.906956 |
| C | -2.341538 | -4.694091 | 5.449089 |
| C | 2.341538 | 3.468410 | 1.387911 |
| C | 2.341538 | 4.694091 | -5.449089 |
| C | -2.341538 | -3.468410 | -1.387911 |
| C | -0.601834 | 4.653278 | 2.738902 |
| C | 0.601834 | -3.509222 | 4.098098 |
| C | 0.601834 | -4.653278 | -2.738902 |
| C | -0.601834 | 3.509222 | -4.098098 |
| C | -1.490011 | 4.350286 | 4.888455 |
| C | 1.490011 | -3.812214 | 1.948545 |
| C | 1.490011 | -4.350286 | -4.888455 |
| C | -1.490011 | 3.812214 | -1.948545 |
| C | -0.488422 | 5.427410 | 1.651136 |
| C | 0.488422 | -2.735091 | 5.185865 |
| C | 0.488422 | -5.427410 | -1.651136 |
| C | -0.488422 | 2.735091 | -5.185865 |
| C | -3.038531 | 6.616686 | 4.380466 |
| C | 3.038531 | -1.545814 | 2.456534 |
| C | 3.038531 | -6.616686 | -4.380466 |
| C | -3.038531 | 1.545814 | -2.456534 |
| C | 2.799298 | -7.902606 | 5.006872 |
| C | -2.799298 | 0.259894 | 1.830128 |
| C | -2.799298 | 7.902606 | -5.006872 |
| C | 2.799298 | -0.259894 | -1.830128 |
| C | -1.366643 | -5.192493 | 6.405585 |
| C | 1.366643 | 2.970007 | 0.431415 |
| C | 1.366643 | 5.192493 | -6.405585 |
| C | -1.366643 | -2.970007 | -0.431415 |
| C | -2.116662 | 6.275983 | 3.495348 |
| C | 2.116662 | -1.886517 | 3.341652 |
| C | 2.116662 | -6.275983 | -3.495348 |
| C | -2.116662 | 1.886517 | -3.341652 |
| C | -2.008661 | -6.526898 | 3.985971 |
| C | 2.008661 | 1.635602 | 2.851029 |
| C | 2.008661 | 6.526898 | -3.985971 |
| C | -2.008661 | -1.635602 | -2.851029 |
| C | -2.653421 | -5.351498 | 4.247008 |
| C | 2.653421 | 2.811002 | 2.589992 |
| C | 2.653421 | 5.351498 | -4.247008 |
| C | -2.653421 | -2.811002 | -2.589992 |
| C | -3.103678 | 5.904753 | 5.521835 |
| C | 3.103678 | -2.257748 | 1.315165 |
| C | 3.103678 | -5.904753 | -5.521835 |
| C | -3.103678 | 2.257748 | -1.315165 |
| C | -0.689057 | -6.338018 | 6.147967 |
| C | 0.689057 | 1.824482 | 0.689033 |
| C | 0.689057 | 6.338018 | -6.147967 |
| C | -0.689057 | -1.824482 | -0.689033 |
| C | -1.396583 | 5.078055 | 3.711534 |
| C | 1.396583 | -3.084446 | 3.125466 |
| C | 1.396583 | -5.078055 | -3.711534 |
| C | -1.396583 | 3.084446 | -3.125466 |
| C | -2.291975 | 4.781919 | 5.792717 |
| C | 2.291975 | -3.380581 | 1.044283 |
| C | 2.291975 | -4.781919 | -5.792717 |
| C | -2.291975 | 3.380581 | -1.044283 |
| C | -1.084195 | 6.683292 | 1.529710 |
| C | 1.084195 | -1.479208 | 5.307290 |
| C | 1.084195 | -6.683292 | -1.529710 |
| C | -1.084195 | 1.479208 | -5.307290 |
| C | -1.013637 | -6.999834 | 4.947663 |
| C | 1.013637 | 1.162667 | 1.889337 |
| C | 1.013637 | 6.999834 | -4.947663 |
| C | -1.013637 | -1.162667 | -1.889337 |
| C | 2.110530 | 7.059420 | 3.119997 |
| C | -2.110530 | -1.103080 | 3.717003 |
| C | -2.110530 | -7.059420 | -3.119997 |
| C | 2.110530 | 1.103080 | -3.717003 |
| C | -1.899722 | 7.132882 | 2.427819 |
| C | 1.899722 | -1.029618 | 4.409181 |
| C | 1.899722 | -7.132882 | -2.427819 |
| C | -1.899722 | 1.029618 | -4.409181 |
| C | 3.083838 | -6.959348 | 1.477612 |
| C | -3.083838 | 1.203153 | 5.359388 |
| C | -3.083838 | 6.959348 | -1.477612 |
| C | 3.083838 | -1.203153 | -5.359388 |
| H | 0.005050 | 5.160333 | 0.973589 |
| H | -0.005050 | -3.002168 | 5.863411 |
| H | -0.005050 | -5.160333 | -0.973589 |
| H | 0.005050 | 3.002168 | -5.863411 |
| H | -0.988387 | 3.565380 | 5.052543 |
| H | 0.988387 | -4.597120 | 1.784457 |
| H | 0.988387 | -3.565380 | -5.052543 |
| H | -0.988387 | 4.597120 | -1.784457 |
| H | -1.129791 | -4.779960 | -6.447291 |
| H | 1.129791 | 3.382540 | -0.389709 |
| H | 1.129791 | 4.779960 | 6.447291 |
| H | -1.129791 | -3.382540 | 0.389709 |
| H | -2.289161 | 4.265723 | 6.552581 |
| H | 2.289161 | -3.896778 | 0.284419 |
| H | 2.289161 | -4.265723 | -6.552581 |
| H | -2.289161 | 3.896778 | -0.284419 |
| H | 3.506247 | 6.134935 | 6.091767 |
| H | -3.506247 | -2.027565 | 0.745233 |
| H | -3.506247 | -6.134935 | -6.091767 |
| H | 3.506247 | 2.027565 | -0.745233 |
| H | -0.893155 | 7.245035 | 0.778051 |
| H | 0.893155 | -0.917465 | 6.058949 |
| H | 0.893155 | -7.245035 | -0.778051 |
| H | -0.893155 | 0.917465 | -6.058949 |
| H | 3.545205 | -7.599288 | 5.622749 |
| H | -3.545205 | 0.563213 | 1.214251 |
| H | -3.545205 | 7.599288 | -5.622749 |
| H | 3.545205 | -0.563213 | -1.214251 |
| H | 2.207637 | 7.894770 | 5.501050 |
| H | -2.207637 | -0.267730 | 1.335950 |
| H | -2.207637 | -7.894770 | -5.501050 |
| H | 2.207637 | 0.267730 | -1.335950 |
| H | -2.847563 | -3.921265 | 5.613177 |
| H | 2.847563 | 4.241235 | 1.223823 |
| H | 2.847563 | 3.921265 | -5.613177 |
| H | -2.847563 | -4.241235 | -1.223823 |
| H | 2.264632 | -7.112803 | 4.586260 |
| H | -2.264632 | 1.049698 | 2.250740 |
| H | -2.264632 | 7.112803 | -4.586260 |
| H | 2.264632 | -1.049698 | -2.250740 |
| H | -0.149340 | 3.870658 | 2.842825 |
| H | 0.149340 | -4.291843 | 3.994175 |
| H | 0.149340 | -3.870658 | -2.842825 |
| H | -0.149340 | 4.291843 | -3.994175 |
| H | 0.014429 | -6.667130 | 6.801448 |
| H | -0.014429 | 1.495370 | 0.035552 |
| H | -0.014429 | 6.667130 | -6.801448 |
| H | 0.014429 | -1.495370 | -0.035552 |
| H | 1.502059 | 7.698870 | 2.820946 |
| H | -1.502059 | -0.463630 | 4.016054 |
| H | -1.502059 | -7.698870 | -2.820946 |
| H | 1.502059 | 0.463630 | -4.016054 |
| H | 1.727873 | 6.417358 | 3.627712 |
| H | -1.727873 | -1.745143 | 3.209288 |
| H | -1.727873 | -6.417358 | -3.627712 |
| H | 1.727873 | 1.745143 | -3.209288 |
| H | -3.322999 | -4.995450 | 3.619508 |
| H | 3.322999 | 3.167050 | 3.217492 |
| H | 3.322999 | 4.995450 | -3.619508 |
| H | -3.322999 | -3.167050 | -3.217492 |
| H | 2.400264 | -6.704678 | 2.008711 |
| H | -2.400264 | 1.457823 | 4.828289 |
| H | -2.400264 | 6.704678 | -2.008711 |
| H | 2.400264 | -1.457823 | -4.828289 |
| H | 2.375735 | 6.632848 | 2.351928 |
| H | -2.375735 | -1.529653 | 4.485072 |
| H | -2.375735 | -6.632848 | -2.351928 |
| H | 2.375735 | 1.529653 | -4.485072 |
| H | -0.538923 | -7.783760 | 4.773593 |
| H | 0.538923 | 0.378740 | 2.063407 |
| H | 0.538923 | 7.783760 | -4.773593 |
| H | -0.538923 | -0.378740 | -2.063407 |
| H | 3.198188 | -6.162688 | 0.883340 |
| H | -3.198188 | 1.999813 | 5.953660 |
| H | -3.198188 | 6.162688 | -0.883340 |
| H | 3.198188 | -1.999813 | -5.953660 |
| H | 2.771089 | -7.671118 | 0.887443 |
| H | -2.771089 | 0.491383 | 5.949557 |
| H | -2.771089 | 7.671118 | -0.887443 |
| H | 2.771089 | -0.491383 | -5.949557 |

# Tabulated values of the *structure* and *bonding correlations*

**Table A19:** The N−Si and N−C distances (in Å) obtained from theory and the crystal refinements (HAR or IAM).

| | Theory | | Crystal | |
|---|---|---|---|---|
| | r(N-Si) | r(N-C) | r(N-Si) | r(N-C) |
| Aryl, 1 | 2.975 | 1.427 | 2.955 | 1.447 |
| Aryl, 2 | 3.024 | 1.412 | 2.895 | 1.439 |
| Methyl | 2.931 | 1.423 | 2.865 | 1.433 |
| | – | – | 2.854 | 1.431 |
| Ethynyl | 2.835 | 1.428 | 2.771 | 1.432 |
| Methoxy | 2.848 | 1.427 | 2.800 | 1.435 |
| p-Chlorobenz. | 2.749 | 1.432 | 2.645 | 1.437 |
| Fluoro | 2.754 | 1.432 | 2.656 | 1.443 |
| | – | – | 2.708 | 1.446 |
| Chloro | 2.732 | 1.431 | 2.508 | 1.417 |
| Silyl cation | 1.959 | 1.487 | 1.936 | 1.489 |
| | – | – | 1.940 | 1.498 |
| Hydro | 2.874 | 1.427 | – | – |
| Hydroxy | 2.844 | 1.428 | – | – |

**Table A20:** The N−Si distance (in Å) and the average R−Si−X angle ($< \alpha >$ in °).

| | Theory | | Crystal | |
|---|---|---|---|---|
| | r(N-Si) | $< \alpha >$ | r(N-Si) | $< \alpha >$ |
| Aryl, 1 | 2.975 | 104.1 | 2.951 | 103.9 |
| Aryl, 2 | 3.024 | 105.6 | 2.889 | 105.3 |
| Methyl | 2.931 | 105.1 | 2.862 | 104.8 |
| | – | – | 2.850 | 104.3 |
| Ethynyl | 2.835 | 103.2 | 2.771 | 103.1 |
| Methoxy | 2.848 | 103.6 | 2.805 | 103.1 |
| p-Chlorobenz. | 2.749 | 101.5 | 2.642 | 100.4 |
| Fluoro | 2.754 | 101.7 | 2.665 | 100.1 |
| | – | – | 2.711 | 99.6 |
| Chloro | 2.732 | 101.6 | 2.548 | 99.4 |
| Fluoro, bridged | 2.648 | 98.0 | 2.450 | 95.6 |
| Hydro | 2.874 | 103.6 | – | – |
| OH | 2.844 | 103.6 | – | – |

**Table A21:** The N−Si distance (in Å) and $\sum \Delta\alpha$ (in °, for definition see Equation 15.1).

| | Theory | | Crystal | |
|---|---|---|---|---|
| | r(N-Si) | $\sum \Delta\alpha$ | r(N-Si) | $\sum \Delta\alpha$ |
| Aryl, 1 | 2.975 | -3.84 | 2.955 | -6.78 |
| Aryl, 2 | 3.024 | -2.96 | 2.895 | -5.30 |
| Methyl | 2.931 | -2.26 | 2.865 | -2.09 |
| | – | – | 2.854 | -2.25 |
| Ethynyl | 2.835 | -0.42 | 2.771 | 1.36 |
| Methoxy | 2.848 | -1.24 | 2.800 | -1.37 |
| p-Chlorobenzoate | 2.749 | 1.45 | 2.645 | 0.43 |
| Fluoro | 2.754 | -0.05 | 2.656 | 0.03 |
| | – | – | 2.708 | -1.76 |
| Chloro | 2.732 | 2.24 | 2.508 | 5.49 |
| Silyl cation | 1.959 | 17.24 | 1.936 | 16.63 |
| | – | – | 1.940 | 16.95 |
| Hydro | 2.874 | -2.31 | – | – |
| Hydroxy | 2.844 | -1.53 | – | – |

**Table A22:** The N−Si distance (in Å) and the difference between r(Si−C1) and r(N−C9) (in Å).

| | Theory | | Crystal | |
|---|---|---|---|---|
| | r(N-Si) | $r$(Si−C1) $-r$(N−C9) | r(N-Si) | $r$(Si−C1) $-r$(N−C9) |
| Aryl, 1 | 2.975 | 0.4762 | 2.955 | 0.478 |
| Aryl, 2 | 3.024 | 0.4837 | 2.895 | 0.474 |
| Methyl | 2.931 | 0.4745 | 2.865 | 0.464 |
| | – | – | 2.854 | 0.469 |
| Ethynyl | 2.835 | 0.4623 | 2.771 | 0.458 |
| Methoxy | 2.848 | 0.4627 | 2.800 | 0.451 |
| p-Chlorobenzoate | 2.749 | 0.4483 | 2.645 | 0.448 |
| Fluoro | 2.754 | 0.4487 | 2.656 | 0.441 |
| | – | – | 2.708 | 0.435 |
| Chloro | 2.732 | 0.4579 | 2.508 | 0.430 |
| Silyl cation | 1.959 | 0.3560 | 1.936 | 0.357 |
| | – | – | 1.940 | 0.344 |
| Hydro | 2.874 | 0.4612 | – | – |
| Hydroxy | 2.844 | 0.4634 | – | – |

**Table A23:** The N−Si distance (in Å) and the N−Si NLMO/NPA bond order.

| | Theory | | XWR | |
|---|---|---|---|---|
| | r(N-Si) | B.O. | r(N-Si) | B.O. |
| Aryl, 1 | 2.975 | 0.0189 | 2.9581 | 0.0209 |
| Aryl, 2 | 3.024 | 0.0144 | 2.8978 | 0.0228 |
| Methyl | 2.931 | 0.0185 | – | – |
| Ethynyl | 2.835 | 0.0226 | 2.7729 | 0.0316 |
| Methoxy | 2.848 | 0.0250 | 2.8020 | 0.0309 |
| p-Chlorobenzoate | 2.749 | 0.0434 | 2.6450 | 0.0506 |
| Fluoro | 2.754 | 0.0380 | 2.6593 | 0.0438 |
| | – | – | 2.7103 | 0.0426 |
| Fluoro, bridged | 2.648 | 0.0502 | 2.4530 | 0.0922 |
| Chloro | 2.732 | 0.0401 | 2.5080 | 0.0686 |
| Silyl cation | 1.959 | 0.2690 | – | – |
| Hydro | 2.874 | 0.0202 | – | – |
| Hydroxy | 2.844 | 0.0274 | – | – |

**Table A24:** The N−Si distance (in Å) and the N−Si delocalization index.

| | Theory | | XWR | |
|---|---|---|---|---|
| | r(N-Si) | DI | r(N-Si) | DI |
| Aryl, 1 | 2.975 | 0.0268 | 2.958 | 0.0260 |
| Aryl, 2 | 3.024 | 0.0209 | 2.898 | 0.0274 |
| Methyl | 2.931 | 0.0300 | – | – |
| Ethynyl | 2.835 | 0.0429 | 2.773 | 0.0532 |
| Methoxy | 2.848 | 0.0394 | 2.802 | 0.0530 |
| p-Chlorobenzoate | 2.749 | 0.0577 | 2.645 | 0.0596 |
| Fluoro | 2.754 | 0.0557 | 2.659 | 0.0508 |
| x | – | – | 2.710 | 0.0582 |
| Fluoro, bridged | 2.648 | 0.0817 | 2.453 | 0.1137 |
| Chloro | 2.732 | 0.0607 | 2.508 | 0.0773 |
| Silyl cation | 1.959 | 0.3014 | – | – |
| Hydro | 2.874 | 0.0376 | – | – |
| Hydroxy | 2.844 | 0.0402 | – | – |

**Table A25:** The N−Si distance (in Å) and the N−C9 NLMO/NPA bond order.

| | Theory | | XWR | |
|---|---|---|---|---|
| | r(N-Si) | B.O. | r(N-Si) | B.O. |
| Aryl, 1 | 2.975 | 0.8274 | 2.958 | 0.8232 |
| Aryl, 2 | 3.024 | 0.8398 | 2.898 | 0.8014 |
| Methyl | 2.931 | 0.8332 | – | – |
| Ethynyl | 2.835 | 0.8302 | 2.773 | 0.8153 |
| Methoxy | 2.848 | 0.8306 | 2.802 | 0.8201 |
| p-Chlorobenzoate | 2.749 | 0.8245 | 2.645 | 0.8053 |
| Fluoro | 2.754 | 0.8233 | 2.659 | 0.8066 |
| | – | – | 2.710 | 0.7772 |
| Chloro | 2.732 | 0.8226 | 2.508 | 0.7951 |
| Silyl cation | 1.959 | 0.7399 | – | – |
| Hydro | 2.874 | 0.8267 | – | – |
| Hydroxy | 2.844 | 0.8284 | – | – |

**Table A26:** The N−Si distance (in Å) and the N−C9 delocalization index.

| | Theory | | XWR | |
|---|---|---|---|---|
| | r(N-Si) | DI | r(N-Si) | DI |
| Aryl, 1 | 2.976 | 0.9871 | 2.958 | 0.9573 |
| Aryl, 2 | 3.024 | 1.0047 | 2.898 | 0.9319 |
| Methyl | 2.931 | 0.9924 | – | – |
| Ethynyl | 2.835 | 0.9859 | 2.773 | 0.9539 |
| Methoxy | 2.848 | 0.9861 | 2.802 | 0.9479 |
| p-Chlorobenzoate | 2.749 | 0.9818 | 2.645 | 0.9440 |
| Fluoro | 2.754 | 0.9780 | 2.659 | 0.9570 |
| | – | – | 2.710 | 0.9237 |
| Chloro | 2.732 | 0.9786 | 2.508 | 0.9506 |
| Silyl cation | 1.959 | 0.9062 | – | – |
| Hydro | 2.874 | 0.9874 | – | – |
| Hydroxy | 2.844 | 0.9855 | – | – |

**Table A27:** The N−Si distance (in Å) and the Si−X NLMO/NPA bond order.

| | Theory | | XWR | |
|---|---|---|---|---|
| | r(N-Si) | B.O. | r(N-Si) | B.O. |
| Aryl, 1 | 2.975 | 0.5040 | 2.958 | 0.4577 |
| Aryl, 2 | 3.023 | 0.5206 | 2.898 | 0.5151 |
| Methyl | 2.931 | 0.5477 | – | – |
| Ethynyl | 2.835 | 0.5554 | 2.773 | 0.5198 |
| Methoxy | 2.848 | 0.3303 | 2.802 | 0.3242 |
| p-Chlorobenzoate | 2.749 | 0.2754 | 2.645 | 0.2692 |
| Fluoro | 2.754 | 0.2919 | 2.659 | 0.2601 |
| | – | – | 2.710 | 0.2723 |
| Fluoro, bridged | 2.648 | 0.2775 | 2.453 | 0.2554 |
| Chloro | 2.732 | 0.4866 | 2.508 | 0.4399 |
| Hydro | 2.874 | 0.7535 | – | – |
| Hydroxy | 2.844 | 0.3504 | – | – |

**Table A28:** The N−Si distance (in Å) and the Si−X delocalization index.

| | Theory | | XWR | |
|---|---|---|---|---|
| | r(N-Si) | DI | r(N-Si) | DI |
| Aryl, 1 | 2.975 | 0.4341 | 2.958 | 0.3731 |
| Aryl, 2 | 3.024 | 0.4368 | 2.898 | 0.3859 |
| Methyl | 2.931 | 0.4515 | – | – |
| Ethynyl | 2.835 | 0.3913 | 2.773 | 0.3810 |
| Methoxy | 2.848 | 0.3737 | 2.802 | 0.4197 |
| p-Chlorobenzoate | 2.749 | 0.3213 | 2.645 | 0.2778 |
| Fluoro | 2.754 | 0.3373 | 2.659 | 0.2548 |
| | – | – | 2.710 | 0.2534 |
| Fluoro, bridged | 2.648 | 0.3235 | 2.453 | 0.2586 |
| Chloro | 2.732 | 0.3934 | 2.508 | 0.3075 |
| Hydro | 2.874 | 0.4598 | – | – |
| Hydroxy | 2.844 | 0.3808 | – | – |

**Table A29:** The N−Si distance (in Å) and the hybridization coefficient of the nitrogen lone pair from an NBO analysis.

| | Theory | | XWR | |
|---|---|---|---|---|
| | r(N-Si) | $\lambda$ | r(N-Si) | $\lambda$ |
| Aryl, 1 | 2.975 | 5.77 | 2.958 | 4.53 |
| Aryl, 2 | 3.024 | 6.25 | 2.898 | 5.46 |
| Methyl | 2.931 | 6.12 | – | – |
| Ethynyl | 2.835 | 5.74 | 2.773 | 5.27 |
| Methoxy | 2.848 | 5.77 | 2.802 | 4.74 |
| p-Chlorobenzoate | 2.749 | 5.34 | 2.645 | 4.82 |
| Fluoro | 2.754 | 5.40 | 2.659 | 4.59 |
| | – | – | 2.710 | 5.55 |
| Fluoro, bridged | 2.648 | 4.22 | 2.453 | 4.15 |
| Chloro | 2.732 | 5.46 | 2.508 | 5.13 |
| Silyl cation | 1.959 | 3.40 | – | – |
| Hydro | 2.874 | 5.91 | – | – |
| Hydroxy | 2.844 | 5.72 | – | – |

**Table A30:** The N−Si distance (in Å) and the N−Si bond ionicity from an NBO analysis.

| | Theory | | XWR | |
|---|---|---|---|---|
| | r(N-Si) | $i$ | r(N-Si) | $i$ |
| Aryl, 1 | 2.975 | 0.971 | 2.958 | 0.970 |
| Aryl, 2 | 3.024 | 0.988 | 2.898 | 0.964 |
| Methyl | 2.931 | 0.971 | – | – |
| Ethynyl | 2.835 | 0.959 | 2.773 | 0.949 |
| Methoxy | 2.848 | 0.964 | 2.802 | 0.962 |
| p-Chlorobenzoate | 2.749 | 0.948 | 2.645 | 0.933 |
| Fluoro | 2.754 | 0.952 | 2.659 | 0.941 |
| | – | – | 2.710 | 0.944 |
| Fluoro, bridged | 2.648 | 0.932 | 2.453 | 0.887 |
| Chloro | 2.732 | 0.937 | 2.508 | 0.898 |
| Silyl cation | 1.959 | 0.725 | – | – |
| Hydro | 2.874 | 0.959 | – | – |
| Hydroxy | 2.844 | 0.964 | – | – |

**Table A31:** The N−Si distance (in Å) and the electron population of the Si−X antibond (in e) from an NBO analysis.

| | Theory | | XWR | |
|---|---|---|---|---|
| | r(N-Si) | $N$ | r(N-Si) | $N$ |
| Aryl, 1 | 2.975 | 0.0592 | 2.958 | 0.0583 |
| Aryl, 2 | 3.024 | 0.0602 | 2.898 | 0.0639 |
| Methyl | 2.931 | 0.0424 | – | – |
| Ethynyl | 2.835 | 0.0499 | 2.773 | 0.0565 |
| Methoxy | 2.848 | 0.0624 | 2.802 | 0.0579 |
| p-Chlorobenzoate | 2.749 | 0.0831 | 2.645 | 0.0844 |
| Fluoro | 2.754 | 0.0634 | 2.659 | 0.0661 |
| | | | 2.710 | 0.0629 |
| Fluoro, bridged | 2.648 | 0.0900 | 2.453 | 0.0936 |
| Chloro | 2.732 | 0.0785 | 2.508 | 0.0949 |
| Hydro | 2.874 | 0.0421 | – | – |
| Hydroxy | 2.844 | 0.0545 | – | – |

**Table A32:** The N−Si distance (in Å) and the weight of the $N^+-SiX^-$ resonance structure obtained from an NRT analysis.

| | Theory | | XWR | |
|---|---|---|---|---|
| | r(N-Si) | $w_{NRT}$ | r(N-Si) | $w_{NRT}$ |
| Aryl, 1 | 2.975 | 2.69 | 2.958 | 2.41 |
| Aryl, 2 | 3.024 | 3.31 | 2.898 | 1.71 |
| Methyl | 2.931 | 2.96 | – | – |
| Ethynyl | 2.835 | 3.11 | 2.773 | 2.88 |
| Methoxy | 2.848 | 3.48 | 2.802 | 2.66 |
| p-Chlorobenzoate | 2.749 | 4.08 | 2.645 | 3.84 |
| Fluoro | 2.754 | 3.64 | 2.659 | 3.20 |
| x | – | – | 2.710 | 3.04 |
| Fluoro, bridged | 2.648 | 4.09 | 2.453 | 4.89 |
| Chloro | 2.732 | 3.96 | 2.508 | 4.44 |
| Hydro | 2.874 | 2.83 | – | – |
| Hydroxy | 2.844 | 3.32 | – | – |

**Table A33:** The N−Si distance (in Å) and the electron density at the N−Si bond critical point (in e·Å$^{-3}$) from QTAIM.

| | Theory | | XWR | |
|---|---|---|---|---|
| | r(N-Si) | $\rho_{bcp}$ | r(N-Si) | $\rho_{bcp}$ |
| Methyl | 2.931 | 0.106 | – | – |
| Ethynyl | 2.835 | 0.123 | 2.773 | 0.142 |
| Methoxy | 2.848 | 0.119 | 2.802 | 0.125 |
| p-Chlorobenzoate | 2.749 | 0.142 | 2.645 | 0.164 |
| Fluoro | 2.754 | 0.140 | 2.659 | 0.156 |
| | | | 2.7103 | 0.149 |
| Fluoro, bridged | 2.648 | 0.168 | 2.453 | 0.240 |
| Chloro | 2.732 | 0.146 | 2.508 | 0.206 |
| Silyl cation | 1.959 | 0.590 | – | – |
| Hydro | 2.874 | 0.117 | – | – |
| Hydroxy | 2.844 | 0.120 | – | – |

**Table A34:** The N−Si distance (in Å) and the total energy density at the N−Si bond critical point (in Hartree/Å$^{-3}$) from QTAIM.

| | Theory | | XWR | |
|---|---|---|---|---|
| | r(N-Si) | $H_{bcp}$ | r(N-Si) | $H_{bcp}$ |
| Methyl | 2.931 | 0.0005 | – | – |
| Ethynyl | 2.835 | -0.0005 | 2.773 | -0.0025 |
| Methoxy | 2.848 | -0.0002 | 2.802 | -0.0006 |
| p-Chlorobenzoate | 2.749 | -0.0015 | 2.645 | -0.0041 |
| Fluoro | 2.754 | -0.0014 | 2.659 | -0.0034 |
| | | | 2.710 | -0.001948 |
| Fluoro, bridged | 2.648 | -0.0038 | 2.453 | -0.0114 |
| Chloro | 2.732 | -0.0019 | 2.508 | -0.0077 |
| Silyl cation | 1.959 | -0.0413 | – | – |
| Hydro | 2.874 | 0 | – | – |
| Hydroxy | 2.844 | -0.0002 | – | – |

**Table A35:** The N−Si distance (in Å) and the total energy density at the Si−X bond critical point (in Hartree/Å$^{-3}$) from QTAIM.

| | Theory | | XWR | |
|---|---|---|---|---|
| | r(N-Si) | $H_{bcp}$ | r(N-Si) | $H_{bcp}$ |
| Aryl, 1 | 2.975 | -0.0711 | 2.958 | -0.0610 |
| Aryl, 2 | 3.024 | -0.0681 | 2.898 | -0.0626 |
| Methyl | 2.931 | -0.0731 | – | – |
| Ethynyl | 2.835 | -0.0594 | 2.773 | -0.0706 |
| Methoxy | 2.848 | -0.0489 | 2.802 | -0.1209 |
| p-Chlorobenzoate | 2.749 | -0.0399 | 2.645 | -0.0387 |
| Fluoro | 2.754 | -0.0376 | 2.659 | -0.0189 |
| | | | 2.710 | -0.0263 |
| Fluoro, bridged | 2.648 | -0.0365 | 2.453 | -0.0275 |
| N_Si-Cl | 2.732 | -0.0432 | 2.508 | -0.0411 |
| Hydro | 2.874 | -0.0747 | – | – |
| Hydroxy | 2.844 | -0.0490 | – | – |

**Table A36:** The N−Si distance (in Å) and the angle defined by the nitrogen atom, the attractor of the nitrogen lone pair or N−Si bond basin and the silicon atom (in °) from the ELI analysis.

| | Theory | | XWR | |
|---|---|---|---|---|
| | r(N-Si) | $H_{bcp}$ | r(N-Si) | $H_{bcp}$ |
| Aryl, 1 | 2.975 | 162.9 | 2.958 | 162.5 |
| Aryl, 2 | 3.024 | 158.3 | 2.898 | 161.2 |
| Methyl | 2.931 | 162.3 | – | – |
| Ethynyl | 2.835 | 164.0 | 2.773 | 167.7 |
| Methoxy | 2.848 | 164.2 | 2.802 | 164.6 |
| p-Chlorobenzoate | 2.749 | 164.6 | 2.645 | 164.1 |
| Fluoro | 2.754 | 166.4 | 2.659 | 165.6 |
| x | | | 2.710 | 174.4 |
| Fluoro, bridged | 2.648 | 171.2 | 2.453 | 176.1 |
| Chloro | 2.732 | 165.8 | 2.509 | 169.6 |
| Silyl cation | 1.959 | 174.9 | – | – |
| Hydro | 2.874 | 164.0 | – | – |
| Hydroxy | 2.844 | 164.7 | – | – |

**Table A37:** The N−Si distance (in Å) and the ratio between the electron population and the volume of the nitrogen lone par or N−Si bond basin (in e·bohr$^{-3}$) from the ELI analysis.

| | Theory | | XWR | |
|---|---|---|---|---|
| | r(N-Si) | $H_{bcp}$ | r(N-Si) | $H_{bcp}$ |
| Aryl, 1 | 2.975 | 0.0617 | 2.958 | 0.0586 |
| Aryl, 2 | 3.024 | 0.0610 | 2.898 | 0.0607 |
| Methyl | 2.931 | 0.0631 | – | – |
| Ethynyl | 2.835 | 0.0643 | 2.773 | 0.0657 |
| Methoxy | 2.848 | 0.0638 | 2.802 | 0.0637 |
| p-Chlorobenzoate | 2.749 | 0.0638 | 2.645 | 0.0657 |
| Fluoro | 2.754 | 0.0649 | 2.659 | 0.0661 |
| x | | | 2.710 | 0.0610 |
| Fluoro, bridged | 2.648 | 0.0658 | 2.453 | 0.0678 |
| Chloro | 2.732 | 0.0660 | 2.509 | 0.0715 |
| Silyl cation | 1.959 | 0.0761 | – | – |
| Hydro | 2.874 | 0.0634 | – | – |
| Hydroxy | 2.844 | 0.0638 | – | – |

**Table A38:** N – C9 distances (in Å) obtained from the PES scan.

| r(N-Si) | Chloro | p-Chlorobenzoate | Fluoro | Ethynyl | Hydroxy | Methoxy | Hydro | Methyl |
|---|---|---|---|---|---|---|---|---|
| 1.9 | 1.477 | 1.479 | 1.478 | 1.476 | 1.477 | 1.478 | 1.478 | 1.476 |
| 2.0 | 1.468 | 1.470 | 1.470 | 1.468 | 1.469 | 1.469 | 1.469 | 1.467 |
| 2.1 | 1.461 | 1.463 | 1.462 | 1.460 | 1.461 | 1.462 | 1.461 | 1.459 |
| 2.2 | 1.454 | 1.456 | 1.456 | 1.453 | 1.455 | 1.455 | 1.454 | 1.452 |
| 2.3 | 1.448 | 1.450 | 1.450 | 1.447 | 1.449 | 1.449 | 1.448 | 1.446 |
| 2.4 | 1.443 | 1.445 | 1.445 | 1.442 | 1.444 | 1.444 | 1.443 | 1.441 |
| 2.5 | 1.439 | 1.441 | 1.441 | 1.438 | 1.439 | 1.440 | 1.439 | 1.437 |
| 2.6 | 1.435 | 1.437 | 1.437 | 1.434 | 1.435 | 1.436 | 1.434 | 1.433 |
| 2.7 | 1.432 | 1.434 | 1.434 | 1.431 | 1.432 | 1.432 | 1.432 | 1.430 |
| 2.8 | 1.429 | 1.431 | 1.431 | 1.428 | 1.430 | 1.429 | 1.429 | 1.427 |
| 2.9 | 1.427 | 1.428 | 1.429 | 1.426 | 1.427 | 1.426 | 1.426 | 1.424 |
| 3.0 | 1.425 | 1.425 | 1.427 | 1.423 | 1.424 | 1.423 | 1.424 | 1.422 |
| 3.1 | 1.422 | 1.423 | 1.425 | 1.421 | 1.422 | 1.421 | 1.422 | 1.420 |

**Table A39:** N – C distances (in Å) obtained from the PES scan.

| r(N-Si) | Fluoro, bridged | Chloro | p-Chlorobenzoate | Fluoro | Ethynyl | Hydroxy | Methoxy | Hydro | Methyl |
|---|---|---|---|---|---|---|---|---|---|
| 1.9 | 88.2 | 89.5 | 90.1 | 90.7 | 90.8 | 91.6 | 91.5 | 90.8 | 91.9 |
| 2.0 | 89.5 | 91.0 | 91.6 | 92.0 | 92.2 | 92.8 | 92.8 | 92.1 | 93.2 |
| 2.1 | 90.8 | 92.7 | 93.0 | 93.4 | 93.7 | 94.2 | 94.2 | 93.5 | 94.6 |
| 2.2 | 92.2 | 94.3 | 94.5 | 94.8 | 95.1 | 95.6 | 95.6 | 95.0 | 96.0 |
| 2.3 | 93.5 | 95.8 | 95.9 | 96.1 | 96.5 | 97.0 | 97.0 | 96.4 | 97.5 |
| 2.4 | 94.8 | 97.2 | 97.2 | 97.5 | 97.9 | 98.4 | 98.4 | 97.9 | 98.9 |
| 2.5 | 96.2 | 98.6 | 98.5 | 98.8 | 99.3 | 99.7 | 99.7 | 99.2 | 100.3 |
| 2.6 | 97.4 | 100.0 | 99.8 | 99.9 | 100.5 | 100.9 | 100.9 | 100.6 | 102.2 |
| 2.7 | 98.5 | 101.2 | 101.0 | 101.1 | 101.7 | 102.1 | 102.1 | 101.7 | 103.4 |
| 2.8 | 99.6 | 102.4 | 102.0 | 102.2 | 102.8 | 103.1 | 103.1 | 102.7 | 103.8 |
| 2.9 | 100.5 | 103.3 | 102.9 | 103.1 | 103.8 | 104.1 | 104.1 | 103.8 | 104.8 |
| 3.0 | 101.3 | 104.2 | 103.7 | 103.9 | 104.7 | 104.9 | 104.9 | 104.7 | 105.7 |
| 3.1 | 102.0 | 104.9 | 104.4 | 104.6 | 105.5 | 105.6 | 105.5 | 105.5 | 106.5 |

**Table A40:** $\sum \Delta\alpha$ (in °, for definition see Equation 15.1) obtained from the PES scan.

| r(N-Si) | Chloro | p-Chlorobenzoate | Fluoro | Ethynyl | Hydroxy | Methoxy | Hydro | Methyl |
|---|---|---|---|---|---|---|---|---|
| 1.9 | 19.9 | 20.3 | 18.5 | 19.1 | 18.8 | 19.2 | 18.2 | 19.6 |
| 2.0 | 17.8 | 18.0 | 16.3 | 17.1 | 16.6 | 17.0 | 15.9 | 17.3 |
| 2.1 | 15.6 | 15.7 | 14.0 | 14.9 | 14.3 | 14.7 | 13.8 | 15.1 |
| 2.2 | 13.4 | 13.5 | 11.8 | 12.8 | 12.1 | 12.5 | 11.7 | 12.9 |
| 2.3 | 11.2 | 11.3 | 9.7 | 10.7 | 9.9 | 10.8 | 9.5 | 10.7 |
| 2.4 | 9.1 | 9.0 | 7.6 | 8.5 | 7.8 | 8.1 | 7.5 | 8.5 |
| 2.5 | 7.0 | 6.7 | 5.4 | 6.4 | 5.8 | 5.9 | 5.2 | 6.4 |
| 2.6 | 4.9 | 4.6 | 3.2 | 4.3 | 3.6 | 3.7 | 3.2 | 4.4 |
| 2.7 | 2.8 | 2.5 | 1.1 | 2.3 | 1.4 | 1.7 | 1.2 | 2.3 |
| 2.8 | 0.9 | 0.4 | -1.0 | 0.2 | -0.7 | -0.4 | -0.8 | 0.2 |
| 2.9 | -1.1 | -1.7 | -3.0 | -1.6 | -2.5 | -2.3 | -2.8 | -1.7 |
| 3.0 | -2.9 | -3.6 | -4.9 | -3.5 | -4.4 | -4.1 | -4.7 | -3.5 |
| 3.1 | -4.6 |  | -6.7 | -5.3 | -6.2 | -5.9 | -6.5 | -5.2 |

**Table A41:** The difference between r(Si−C1) and r(N−C9) (in Å) obtained from the PES scan.

| r(N-Si) | Chloro | p-Chlorobenzoate | Fluoro | Ethynyl | Hydroxy | Methoxy | Hydro | Methyl |
|---|---|---|---|---|---|---|---|---|
| 1.9 | 0.429 | 0.421 | 0.431 | 0.443 | 0.445 | 0.441 | 0.440 | 0.461 |
| 2.0 | 0.434 | 0.425 | 0.432 | 0.444 | 0.445 | 0.442 | 0.441 | 0.460 |
| 2.1 | 0.438 | 0.428 | 0.435 | 0.445 | 0.447 | 0.443 | 0.442 | 0.459 |
| 2.2 | 0.442 | 0.432 | 0.435 | 0.447 | 0.447 | 0.445 | 0.443 | 0.459 |
| 2.3 | 0.445 | 0.435 | 0.438 | 0.449 | 0.448 | 0.447 | 0.446 | 0.460 |
| 2.4 | 0.448 | 0.438 | 0.440 | 0.451 | 0.450 | 0.448 | 0.447 | 0.461 |
| 2.5 | 0.451 | 0.440 | 0.442 | 0.453 | 0.453 | 0.450 | 0.449 | 0.462 |
| 2.6 | 0.454 | 0.443 | 0.445 | 0.456 | 0.456 | 0.453 | 0.453 | 0.464 |
| 2.7 | 0.457 | 0.446 | 0.447 | 0.458 | 0.459 | 0.457 | 0.454 | 0.466 |
| 2.8 | 0.460 | 0.450 | 0.450 | 0.462 | 0.461 | 0.461 | 0.458 | 0.469 |
| 2.9 | 0.463 | 0.455 | 0.453 | 0.465 | 0.465 | 0.465 | 0.462 | 0.473 |
| 3.0 | 0.467 | 0.460 | 0.457 | 0.469 | 0.470 | 0.470 | 0.466 | 0.477 |
| 3.1 | 0.471 | 0.465 | 0.461 | 0.474 | 0.475 | 0.474 | 0.471 | 0.481 |

**Table A42:** The N−Si NLMO/NPA bond order obtained from the PES scans.

| r(N−Si) | Fluoro, bridged | Chloro | p-Chlorobenzoate | Fluoro | Ethynyl | Hydroxy | Methoxy | Hydro | Methyl |
|---|---|---|---|---|---|---|---|---|---|
| 1.9 | 0.1875 | 0.173 | 0.186 | 0.189 | 0.171 | 0.183 | 0.180 | 0.160 | 0.169 |
| 2.0 | 0.1625 | 0.162 | 0.169 | 0.166 | 0.152 | 0.160 | 0.156 | 0.138 | 0.150 |
| 2.1 | 0.1458 | 0.140 | 0.145 | 0.143 | 0.130 | 0.137 | 0.134 | 0.119 | 0.127 |
| 2.2 | 0.1242 | 0.119 | 0.123 | 0.120 | 0.109 | 0.117 | 0.114 | 0.099 | 0.107 |
| 2.3 | 0.1051 | 0.101 | 0.104 | 0.101 | 0.087 | 0.095 | 0.091 | 0.081 | 0.083 |
| 2.4 | 0.0872 | 0.084 | 0.086 | 0.080 | 0.070 | 0.074 | 0.074 | 0.062 | 0.067 |
| 2.5 | 0.0713 | 0.067 | 0.070 | 0.064 | 0.052 | 0.059 | 0.060 | 0.049 | 0.053 |
| 2.6 | 0.0525 | 0.054 | 0.057 | 0.051 | 0.041 | 0.047 | 0.048 | 0.038 | 0.042 |
| 2.7 | 0.0466 | 0.043 | 0.048 | 0.043 | 0.032 | 0.037 | 0.037 | 0.028 | 0.032 |
| 2.8 | 0.0365 | 0.032 | 0.037 | 0.034 | 0.025 | 0.030 | 0.028 | 0.024 | 0.025 |
| 2.9 | 0.0283 | 0.025 | 0.030 | 0.028 | 0.021 | 0.025 | 0.021 | 0.019 | 0.019 |
| 3.0 | 0.0223 | 0.020 | 0.025 | 0.023 | 0.015 | 0.020 | 0.016 | 0.015 | 0.017 |
| 3.1 | 0.0167 | 0.017 | 0.020 | 0.018 | 0.012 | 0.017 | 0.013 | 0.012 | 0.013 |

**Table A43:** The N−Si delocalization index obtained from the PES scans.

| | Fluoro, bridged | Chloro | p-Chlorobenzoate | Fluoro | Ethynyl | Hydroxy | Methoxy | Hydro | Methyl |
|---|---|---|---|---|---|---|---|---|---|
| 1.9 | 0.249 | 0.249 | 0.242 | 0.239 | 0.237 | 0.235 | 0.234 | 0.237 | 0.233 |
| 2.0 | 0.224 | 0.223 | 0.217 | 0.214 | 0.212 | 0.209 | 0.209 | 0.211 | 0.206 |
| 2.1 | 0.201 | 0.199 | 0.193 | 0.191 | 0.187 | 0.185 | 0.185 | 0.187 | 0.181 |
| 2.2 | 0.179 | 0.175 | 0.170 | 0.168 | 0.165 | 0.162 | 0.161 | 0.164 | 0.158 |
| 2.3 | 0.157 | 0.152 | 0.147 | 0.145 | 0.142 | 0.139 | 0.138 | 0.142 | 0.136 |
| 2.4 | 0.134 | 0.129 | 0.125 | 0.123 | 0.120 | 0.117 | 0.115 | 0.118 | 0.112 |
| 2.5 | 0.112 | 0.105 | 0.103 | 0.101 | 0.098 | 0.095 | 0.094 | 0.097 | 0.091 |
| 2.6 | 0.090 | 0.084 | 0.083 | 0.081 | 0.078 | 0.075 | 0.075 | 0.077 | 0.072 |
| 2.7 | 0.072 | 0.066 | 0.065 | 0.064 | 0.061 | 0.059 | 0.058 | 0.060 | 0.056 |
| 2.8 | 0.056 | 0.051 | 0.050 | 0.050 | 0.047 | 0.046 | 0.045 | 0.046 | 0.043 |
| 2.9 | 0.043 | 0.038 | 0.039 | 0.038 | 0.036 | 0.035 | 0.034 | 0.037 | 0.033 |
| 3.0 | 0.033 | 0.029 | 0.029 | 0.029 | 0.028 | 0.026 | 0.026 | 0.027 | 0.025 |
| 3.1 | 0.025 | 0.022 | 0.019 | 0.022 | 0.020 | 0.020 | 0.020 | 0.021 | 0.019 |

**Table A44:** The C−N NLMO/NPA bond order obtained from the PES scans.

| | Chloro | p-Chlorobenzoate | Fluoro | Ethynyl | Hydroxy | Methoxy | Hydro | Methyl |
|---|---|---|---|---|---|---|---|---|
| 1.9 | 0.747 | 0.753 | 0.751 | 0.752 | 0.752 | 0.751 | 0.750 | 0.753 |
| 2.0 | 0.761 | 0.768 | 0.764 | 0.764 | 0.766 | 0.764 | 0.766 | 0.767 |
| 2.1 | 0.775 | 0.779 | 0.777 | 0.778 | 0.779 | 0.778 | 0.779 | 0.780 |
| 2.2 | 0.786 | 0.790 | 0.789 | 0.789 | 0.790 | 0.789 | 0.791 | 0.792 |
| 2.3 | 0.796 | 0.800 | 0.798 | 0.799 | 0.800 | 0.799 | 0.801 | 0.802 |
| 2.4 | 0.805 | 0.808 | 0.806 | 0.807 | 0.808 | 0.807 | 0.810 | 0.810 |
| 2.5 | 0.811 | 0.814 | 0.812 | 0.813 | 0.814 | 0.813 | 0.815 | 0.816 |
| 2.6 | 0.817 | 0.820 | 0.817 | 0.819 | 0.819 | 0.819 | 0.821 | 0.822 |
| 2.7 | 0.821 | 0.822 | 0.822 | 0.823 | 0.824 | 0.823 | 0.825 | 0.826 |
| 2.8 | 0.827 | 0.827 | 0.825 | 0.829 | 0.827 | 0.829 | 0.825 | 0.829 |
| 2.9 | 0.830 | 0.830 | 0.825 | 0.832 | 0.826 | 0.832 | 0.827 | 0.832 |
| 3.0 | 0.833 | 0.834 | 0.827 | 0.835 | 0.830 | 0.836 | 0.830 | 0.831 |
| 3.1 | 0.837 | 0.837 | 0.830 | 0.838 | 0.833 | 0.838 | 0.833 | 0.833 |

**Table A45:** The N−C delocalization index obtained from the PES scans.

| | Chloro | p-Chlorobenzoate | Fluoro | Ethynyl | Hydroxy | Methoxy | Hydro | Methyl |
|---|---|---|---|---|---|---|---|---|
| 1.9 | 0.920 | 0.923 | 0.922 | 0.924 | 0.924 | 0.925 | 0.924 | 0.926 |
| 2.0 | 0.930 | 0.932 | 0.931 | 0.934 | 0.934 | 0.934 | 0.934 | 0.936 |
| 2.1 | 0.939 | 0.941 | 0.940 | 0.942 | 0.943 | 0.942 | 0.943 | 0.945 |
| 2.2 | 0.947 | 0.949 | 0.948 | 0.950 | 0.951 | 0.951 | 0.951 | 0.953 |
| 2.3 | 0.954 | 0.956 | 0.955 | 0.958 | 0.958 | 0.958 | 0.959 | 0.961 |
| 2.4 | 0.961 | 0.963 | 0.961 | 0.964 | 0.964 | 0.964 | 0.966 | 0.968 |
| 2.5 | 0.967 | 0.969 | 0.967 | 0.970 | 0.970 | 0.970 | 0.971 | 0.973 |
| 2.6 | 0.972 | 0.975 | 0.972 | 0.976 | 0.975 | 0.975 | 0.977 | 0.979 |
| 2.7 | 0.977 | 0.979 | 0.976 | 0.980 | 0.979 | 0.980 | 0.981 | 0.983 |
| 2.8 | 0.982 | 0.984 | 0.980 | 0.984 | 0.983 | 0.984 | 0.984 | 0.987 |
| 2.9 | 0.986 | 0.988 | 0.984 | 0.989 | 0.987 | 0.989 | 0.988 | 0.991 |
| 3.0 | 0.990 | 0.994 | 0.987 | 0.993 | 0.991 | 0.993 | 0.992 | 0.995 |
| 3.1 | 0.995 | 0.998 | 0.991 | 0.998 | 0.996 | 0.997 | 0.996 | 0.998 |

**Table A46:** The Si−X NLMO/NPA bond order obtained from the PES scans.

| r(N-Si) | Fluoro, bridged | Chloro | p-Chlorobenzoate | Fluoro | Ethynyl | Hydroxy | Methoxy | Hydro | Methyl |
|---|---|---|---|---|---|---|---|---|---|
| 2.4 | 0.266 | 0.446 | 0.259 | 0.278 | 0.537 | 0.328 | 0.302 | 0.716 | 0.505 |
| 2.5 | 0.271 | 0.459 | 0.264 | 0.282 | 0.542 | 0.333 | 0.307 | 0.725 | 0.514 |
| 2.6 | 0.275 | 0.472 | 0.269 | 0.286 | 0.548 | 0.339 | 0.312 | 0.734 | 0.522 |
| 2.7 | 0.280 | 0.483 | 0.273 | 0.290 | 0.552 | 0.343 | 0.317 | 0.742 | 0.531 |
| 2.8 | 0.284 | 0.493 | 0.278 | 0.294 | 0.554 | 0.348 | 0.328 | 0.749 | 0.538 |
| 2.9 | 0.288 | 0.502 | 0.282 | 0.297 | 0.558 | 0.353 | 0.333 | 0.755 | 0.546 |
| 3.0 | 0.292 | 0.510 | 0.287 | 0.301 | 0.566 | 0.357 | 0.337 | 0.761 | 0.552 |
| 3.1 | 0.295 | 0.517 | 0.289 | 0.304 | 0.569 | 0.361 | 0.342 | 0.766 | 0.558 |

**Table A47:** The Si−X delocalization index obtained from the PES scans.

| r(N-Si) | Fluoro, bridged | Chloro | p-Chlorobenzoate | Fluoro | Ethynyl | Hydroxy | Methoxy | Hydro | Methyl |
|---|---|---|---|---|---|---|---|---|---|
| 2.4 | 0.308 | 0.358 | 0.294 | 0.317 | 0.359 | 0.353 | 0.345 | 0.423 | 0.412 |
| 2.5 | 0.315 | 0.369 | 0.303 | 0.324 | 0.367 | 0.360 | 0.353 | 0.431 | 0.421 |
| 2.6 | 0.321 | 0.381 | 0.310 | 0.329 | 0.376 | 0.367 | 0.360 | 0.441 | 0.429 |
| 2.7 | 0.326 | 0.391 | 0.318 | 0.335 | 0.383 | 0.372 | 0.366 | 0.449 | 0.437 |
| 2.8 | 0.331 | 0.400 | 0.323 | 0.340 | 0.389 | 0.378 | 0.372 | 0.456 | 0.444 |
| 2.9 | 0.334 | 0.406 | 0.329 | 0.345 | 0.395 | 0.383 | 0.377 | 0.463 | 0.450 |
| 3.0 | 0.338 | 0.412 | 0.334 | 0.348 | 0.400 | 0.387 | 0.381 | 0.468 | 0.456 |
| 3.1 | 0.341 | 0.417 | 0.337 | 0.351 | 0.404 | 0.391 | 0.385 | 0.473 | 0.460 |

**Table A48:** The hybridization of the nitrogen lone pair from NBO obtained from the PES scans.

| r(N-Si) | Fluoro, bridged | Chloro | p-Chlorobenzoate | Fluoro | Ethynyl | Hydroxy | Methoxy | Hydro | Methyl |
|---|---|---|---|---|---|---|---|---|---|
| 1.9 | 3.216 | 3.737 | 3.584 | 3.475 | 3.505 | 3.420 | 3.455 | 3.433 | 3.416 |
| 2.0 | 3.281 | 3.836 | 3.658 | 3.566 | 3.611 | 3.515 | 3.560 | 3.526 | 3.515 |
| 2.1 | 3.374 | 3.945 | 3.761 | 3.692 | 3.736 | 3.637 | 3.687 | 3.651 | 3.623 |
| 2.2 | 3.496 | 4.083 | 3.901 | 3.847 | 3.889 | 3.773 | 3.842 | 3.805 | 3.777 |
| 2.3 | 3.631 | 4.254 | 4.073 | 4.058 | 4.076 | 3.972 | 4.025 | 3.992 | 3.979 |
| 2.4 | 3.775 | 4.463 | 4.268 | 4.270 | 4.304 | 4.196 | 4.229 | 4.224 | 4.183 |
| 2.5 | 3.940 | 4.716 | 4.508 | 4.532 | 4.569 | 4.457 | 4.468 | 4.492 | 4.427 |
| 2.6 | 4.129 | 5.007 | 4.804 | 4.842 | 4.859 | 4.757 | 4.764 | 4.764 | 4.721 |
| 2.7 | 4.336 | 5.337 | 5.154 | 5.192 | 5.196 | 5.094 | 5.121 | 5.124 | 5.057 |
| 2.8 | 4.537 | 5.725 | 5.537 | 5.597 | 5.592 | 5.510 | 5.544 | 5.561 | 5.455 |
| 2.9 | 4.733 | 6.163 | 5.994 | 6.073 | 6.048 | 6.013 | 6.037 | 6.027 | 5.944 |
| 3.0 | 4.913 | 6.675 | 6.548 | 6.605 | 6.576 | 6.593 | 6.576 | 6.542 | 6.519 |
| 3.1 | 5.002 | 7.279 | 7.233 | 7.192 | 7.231 | 7.198 | 7.204 | 7.164 | 7.143 |

**Table A49:** The N−Si bond ionicity obtained from the PES scans.

| r(N-Si) | Fluoro, bridged | Chloro | p-Chlorobenzoate | Fluoro | Ethynyl | Hydroxy | Methoxy | Hydro | Methyl |
|---|---|---|---|---|---|---|---|---|---|
| 1.9 | 0.796 | 0.788 | 0.792 | 0.792 | 0.777 | 0.793 | 0.802 | 0.758 | 0.789 |
| 2.0 | 0.809 | 0.799 | 0.807 | 0.808 | 0.793 | 0.809 | 0.817 | 0.775 | 0.804 |
| 2.1 | 0.827 | 0.816 | 0.826 | 0.829 | 0.815 | 0.831 | 0.837 | 0.797 | 0.824 |
| 2.2 | 0.848 | 0.836 | 0.848 | 0.852 | 0.839 | 0.854 | 0.859 | 0.823 | 0.848 |
| 2.3 | 0.869 | 0.857 | 0.871 | 0.875 | 0.864 | 0.877 | 0.881 | 0.849 | 0.872 |
| 2.4 | 0.890 | 0.878 | 0.892 | 0.896 | 0.887 | 0.899 | 0.902 | 0.875 | 0.894 |
| 2.5 | 0.909 | 0.899 | 0.911 | 0.916 | 0.908 | 0.919 | 0.920 | 0.898 | 0.914 |
| 2.6 | 0.925 | 0.917 | 0.927 | 0.932 | 0.927 | 0.935 | 0.936 | 0.919 | 0.932 |
| 2.7 | 0.940 | 0.933 | 0.942 | 0.946 | 0.942 | 0.949 | 0.949 | 0.936 | 0.946 |
| 2.8 | 0.952 | 0.946 | 0.954 | 0.957 | 0.955 | 0.960 | 0.960 | 0.950 | 0.958 |
| 2.9 | 0.963 | 0.958 | 0.963 | 0.967 | 0.965 | 0.969 | 0.969 | 0.961 | 0.968 |
| 3.0 | 0.971 | 0.967 | 0.972 | 0.975 | 0.973 | 0.977 | 0.976 | 0.970 | 0.976 |
| 3.1 | 0.978 | 0.975 | 0.978 | 0.981 | 0.980 | 0.982 | 0.982 | 0.977 | 0.982 |

**Table A50:** The Si−X antibond population obtained from the PES scans.

| r(N-Si) | Fluoro, bridged | Chloro | p-Chlorobenzoate | Fluoro | Ethynyl | Hydroxy | Methoxy | Hydro | Methyl |
|---|---|---|---|---|---|---|---|---|---|
| 1.9 | 0.133 | 0.161 | 0.260 | 0.134 | 0.118 | 0.128 | 0.132 | 0.113 | 0.114 |
| 2.0 | 0.125 | 0.150 | 0.148 | 0.124 | 0.109 | 0.118 | 0.123 | 0.103 | 0.105 |
| 2.1 | 0.116 | 0.138 | 0.135 | 0.114 | 0.099 | 0.108 | 0.113 | 0.093 | 0.095 |
| 2.2 | 0.106 | 0.126 | 0.124 | 0.103 | 0.089 | 0.098 | 0.103 | 0.083 | 0.086 |
| 2.3 | 0.098 | 0.114 | 0.114 | 0.094 | 0.080 | 0.088 | 0.095 | 0.074 | 0.077 |
| 2.4 | 0.090 | 0.104 | 0.105 | 0.085 | 0.072 | 0.080 | 0.087 | 0.066 | 0.069 |
| 2.5 | 0.083 | 0.095 | 0.098 | 0.078 | 0.065 | 0.072 | 0.080 | 0.059 | 0.062 |
| 2.6 | 0.077 | 0.087 | 0.091 | 0.071 | 0.060 | 0.066 | 0.074 | 0.053 | 0.056 |
| 2.7 | 0.072 | 0.080 | 0.085 | 0.066 | 0.055 | 0.061 | 0.069 | 0.048 | 0.051 |
| 2.8 | 0.068 | 0.075 | 0.081 | 0.061 | 0.051 | 0.056 | 0.064 | 0.044 | 0.047 |
| 2.9 | 0.064 | 0.070 | 0.077 | 0.058 | 0.048 | 0.053 | 0.061 | 0.041 | 0.043 |
| 3.0 | 0.060 | 0.066 | 0.073 | 0.055 | 0.046 | 0.050 | 0.058 | 0.039 | 0.041 |
| 3.1 | 0.057 | 0.063 | 0.069 | 0.052 | 0.044 | 0.048 | 0.056 | 0.037 | 0.039 |

**Table A51:** NRT weights of the $N^+-SiX^-$ resonance structure (in %) obtained from the PES scans.

| r(N-Si) | Fluoro, bridged | Chloro | Fluoro | Ethynyl | Hydroxy | Methoxy | Hydro | Methyl |
|---|---|---|---|---|---|---|---|---|
| 2.4 | 5.14 | 5.30 | 4.99 | 4.21 | 4.73 | 4.82 | 3.78 | 4.11 |
| 2.5 | 4.67 | 4.82 | 4.52 | 3.85 | 4.28 | 4.40 | 3.45 | 3.75 |
| 2.6 | 4.27 | 4.40 | 4.12 | 3.55 | 3.91 | 4.06 | 3.21 | 3.47 |
| 2.7 | 3.92 | 4.05 | 3.79 | 3.33 | 3.62 | 3.78 | 3.02 | 3.25 |
| 2.8 | 3.61 | 3.78 | 3.53 | 3.16 | 3.39 | 3.57 | 2.90 | 3.09 |
| 2.9 | 3.36 | 3.57 | 3.33 | 3.04 | 3.23 | 3.41 | 2.81 | 2.98 |
| 3.0 | 3.14 | 3.42 | 3.18 | 2.97 | 3.12 | 3.29 | 2.76 | 2.92 |
| 3.1 | 2.95 | 3.33 | 3.10 | 2.94 | 3.05 | 3.23 | 2.75 | 2.89 |

**Table A52:** The electron density at the N−Si bond critical point (in e·Å$^{-3}$) obtained from the PES scans.

| r(N-Si) | Fluoro, bridged | Chloro | p-Chlorobenzoate | Fluoro | Ethynyl | Hydroxy | Methoxy | Hydro | Methyl |
|---|---|---|---|---|---|---|---|---|---|
| 1.9 | 0.610 | 0.613 | 0.610 | 0.606 | 0.608 | 0.604 | 0.604 | 0.605 | 0.604 |
| 2.0 | 0.506 | 0.509 | 0.506 | 0.503 | 0.505 | 0.500 | 0.500 | 0.502 | 0.501 |
| 2.1 | 0.423 | 0.426 | 0.424 | 0.421 | 0.423 | 0.419 | 0.418 | 0.421 | 0.420 |
| 2.2 | 0.358 | 0.360 | 0.358 | 0.356 | 0.358 | 0.353 | 0.353 | 0.357 | 0.355 |
| 2.3 | 0.303 | 0.306 | 0.304 | 0.302 | 0.305 | 0.300 | 0.300 | 0.304 | 0.303 |
| 2.4 | 0.257 | 0.260 | 0.258 | 0.256 | 0.259 | 0.255 | 0.254 | 0.258 | 0.257 |
| 2.5 | 0.217 | 0.219 | 0.218 | 0.217 | 0.219 | 0.215 | 0.215 | 0.219 | 0.218 |
| 2.6 | 0.182 | 0.184 | 0.183 | 0.183 | 0.184 | 0.182 | 0.182 | 0.185 | 0.184 |
| 2.7 | 0.153 | 0.155 | 0.154 | 0.154 | 0.155 | 0.153 | 0.153 | 0.156 | 0.155 |
| 2.8 | 0.128 | 0.130 | 0.130 | 0.130 | 0.130 | 0.130 | 0.130 | 0.132 | 0.131 |
| 2.9 | 0.107 | 0.110 | 0.109 | 0.110 | 0.110 | 0.110 | 0.111 | 0.113 | 0.111 |
| 3.0 | 0.090 | – | – | – | – | – | – | – | – |
| 3.1 | 0.076 | – | – | – | – | – | – | – | – |

**Table A53:** The total energy density at the N−Si bond critical point (in Hartree/Å$^{-3}$) obtained from the PES scans.

| r(N-Si) | Fluoro, bridged | Chloro | p-Chlorobenzoate | Fluoro | Ethynyl | Hydroxy | Methoxy | Hydro | Methyl |
|---|---|---|---|---|---|---|---|---|---|
| 1.9 | -0.0369 | -0.0374 | -0.0370 | -0.0363 | -0.0368 | -0.0359 | -0.0359 | -0.0361 | -0.0360 |
| 2.0 | -0.0312 | -0.0317 | -0.0313 | -0.0307 | -0.0312 | -0.0304 | -0.0303 | -0.0307 | -0.0306 |
| 2.1 | -0.0264 | -0.0268 | -0.0264 | -0.0260 | -0.0266 | -0.0257 | -0.0257 | -0.0262 | -0.0260 |
| 2.2 | -0.0221 | -0.0224 | -0.0221 | -0.0217 | -0.0223 | -0.0215 | -0.0215 | -0.0220 | -0.0219 |
| 2.3 | -0.0177 | -0.0177 | -0.0176 | -0.0173 | -0.0176 | -0.0169 | -0.0169 | -0.0173 | -0.0172 |
| 2.4 | -0.0128 | -0.0126 | -0.0125 | -0.0122 | -0.0124 | -0.0119 | -0.0119 | -0.0119 | -0.0119 |
| 2.5 | -0.0083 | -0.0080 | -0.0080 | -0.0070 | -0.0078 | -0.0074 | -0.0074 | -0.0074 | -0.0074 |
| 2.6 | -0.0050 | -0.0047 | -0.0046 | -0.0045 | -0.0045 | -0.0042 | -0.0042 | -0.0042 | -0.0042 |
| 2.7 | -0.0027 | -0.0024 | -0.0024 | -0.0023 | -0.0023 | -0.0021 | -0.0021 | -0.0021 | -0.0021 |
| 2.8 | -0.0012 | -0.0010 | -0.0009 | -0.0008 | -0.0008 | -0.0007 | -0.0006 | -0.0007 | -0.0007 |
| 2.9 | -0.0003 | 0.0000 | 0.0001 | 0.0002 | 0.0001 | 0.0003 | 0.0004 | 0.0002 | 0.0002 |
| 3.0 | 0.0003 | – | – | – | – | – | – | – | – |
| 3.1 | 0.0006 | – | – | – | – | – | – | – | – |

**Table A54:** The total energy density at the Si−X bond critical point (in Hartree/Å$^{-3}$) obtained from the PES scans.

| r(N-Si) | Fluoro, bridged | Chloro | p-Chlorobenzoate | Fluoro | Ethynyl | Hydroxy | Methoxy | Hydro | Methyl |
|---|---|---|---|---|---|---|---|---|---|
| 2.4 | -0.0351 | -0.0387 | -0.0362 | -0.0357 | -0.0548 | -0.0468 | -0.0459 | -0.0707 | -0.0688 |
| 2.5 | -0.0357 | -0.0402 | -0.0373 | -0.0363 | -0.0560 | -0.0474 | -0.0467 | -0.0716 | -0.0698 |
| 2.6 | -0.0362 | -0.0416 | -0.0384 | -0.0368 | -0.0571 | -0.0479 | -0.0474 | -0.0726 | -0.0707 |
| 2.7 | -0.0367 | -0.0429 | -0.0394 | -0.0373 | -0.0582 | -0.0484 | -0.0481 | -0.0734 | -0.0715 |
| 2.8 | -0.0371 | -0.0439 | -0.0403 | -0.0377 | -0.0591 | -0.0488 | -0.0486 | -0.0742 | -0.0723 |
| 2.9 | -0.0375 | -0.0449 | -0.0411 | -0.0381 | -0.0599 | -0.0492 | -0.0491 | -0.0748 | -0.0729 |
| 3.0 | -0.0378 | -0.0456 | -0.0416 | -0.0384 | -0.0606 | -0.0496 | -0.0495 | -0.0754 | -0.0735 |
| 3.1 | -0.0381 | -0.0463 | -0.0421 | -0.0387 | -0.0612 | -0.0498 | -0.0498 | -0.0759 | -0.0740 |

**Table A55:** The angle defined by the nitrogen atom, the attractor of the nitrogen lone pair or N−Si bond basin and the silicon atom (in °) obtained from the PES scans.

| r(N-Si) | Fluoro, bridged | Chloro | Fluoro | Ethynyl | Hydroxy | Methoxy | Hydro | Methyl |
|---|---|---|---|---|---|---|---|---|
| 1.9 | 177.3 | 175.6 | 173.5 | 175.1 | 173.1 | 173.1 | 177.3 | 174.8 |
| 2.0 | 177.5 | 178.5 | 177.4 | 179.3 | 178.2 | 178.2 | 175.3 | 178.7 |
| 2.1 | 177.6 | 177.0 | 174.3 | 175.1 | 173.5 | 173.5 | 173.6 | 175.7 |
| 2.2 | 177.2 | 173.5 | 171.9 | 175.4 | 174.2 | 174.2 | 172.8 | 175.7 |
| 2.3 | 174.8 | 175.5 | 171.8 | 170.1 | 173.1 | 173.1 | 172.1 | 170.0 |
| 2.4 | 172.9 | 171.3 | 171.0 | 171.1 | 171.4 | 171.4 | 169.9 | 172.3 |
| 2.5 | 176.6 | 170.7 | 170.8 | 165.9 | 170.0 | 170.0 | 171.8 | 167.3 |
| 2.6 | 172.3 | 168.4 | 168.9 | 167.0 | 164.8 | 164.8 | 169.2 | 169.0 |
| 2.7 | 169.4 | 166.3 | 166.9 | 164.6 | 165.9 | 165.9 | 168.3 | 166.2 |
| 2.8 | 170.5 | 164.9 | 168.3 | 161.6 | 165.1 | 165.1 | 167.7 | 165.9 |
| 2.9 | 164.9 | 161.5 | 163.9 | 162.5 | 164.7 | 164.7 | 164.8 | 161.0 |
| 3.0 | 163.8 | 162.7 | 162.6 | 161.4 | 163.2 | 163.2 | 163.2 | 162.1 |
| 3.1 | 158.6 | 159.7 | 161.7 | 159.5 | 158.6 | 158.6 | 161.0 | 157.3 |

**Table A56:** The ratio between the electron population and the volume of the nitrogen lone pair or N−Si bond basin (in e·bohr$^{-3}$) obtained from the PES scans.

| r(N-Si) | Fluoro,bridged | Chloro | Fluoro | Ethynyl | Hydroxy | Methoxy | Hydro | Methyl |
|---|---|---|---|---|---|---|---|---|
| 1.9 | 0.0969 | 0.0960 | 0.0969 | 0.0978 | 0.0962 | 0.0942 | 0.0933 | 0.0956 |
| 2.0 | 0.0908 | 0.0902 | 0.0908 | 0.0917 | 0.0903 | 0.0885 | 0.0874 | 0.0895 |
| 2.1 | 0.0855 | 0.0852 | 0.0855 | 0.0865 | 0.0853 | 0.0836 | 0.0822 | 0.0844 |
| 2.2 | 0.0812 | 0.0810 | 0.0812 | 0.0825 | 0.0813 | 0.0795 | 0.0781 | 0.0799 |
| 2.3 | 0.0778 | 0.0774 | 0.0778 | 0.0789 | 0.0777 | 0.0762 | 0.0744 | 0.0765 |
| 2.4 | 0.0748 | 0.0746 | 0.0748 | 0.0760 | 0.0746 | 0.0734 | 0.0715 | 0.0734 |
| 2.5 | 0.0719 | 0.0719 | 0.0719 | 0.0733 | 0.0719 | 0.0708 | 0.0690 | 0.0708 |
| 2.6 | 0.0696 | 0.0696 | 0.0696 | 0.0708 | 0.0697 | 0.0686 | 0.0666 | 0.0684 |
| 2.7 | 0.0673 | 0.0673 | 0.0673 | 0.0684 | 0.0675 | 0.0666 | 0.0645 | 0.0660 |
| 2.8 | 0.0649 | 0.0650 | 0.0649 | 0.0660 | 0.0651 | 0.0644 | 0.0626 | 0.0637 |
| 2.9 | 0.0626 | 0.0626 | 0.0626 | 0.0637 | 0.0628 | 0.0622 | 0.0606 | 0.0616 |
| 3.0 | 0.0606 | 0.0604 | 0.0606 | 0.0615 | 0.0606 | 0.0600 | 0.0583 | 0.0596 |
| 3.1 | 0.0583 | 0.0583 | 0.0583 | 0.0592 | 0.0582 | 0.0577 | 0.0561 | 0.0572 |

# List of publications

All publications, which are marked by ⋆ are included in this thesis.


1. M. Fugel, V. C. Weiss, "A corresponding-states analysis of the liquid-vapor equilibrium properties of common water models", *J. Chem. Phys.* **2017**, *146*(6)

2. E. Hupf, M. Olaru, C. I. Rat, M. Fugel, C. B. Hübschle, E. Lork, S. Grabowsky, S. Mebs, J. Beckmann, "Mapping the Trajectory of Nucleophilic Substitution at Silicon Using a peri-Substituted Acenaphthyl Scaffold", *Chem. Eur. J* **2017**, *23*(44), 10568–10579.

3. M. Fugel, D. Jayatilaka, E. Hupf, J. Overgaard, V. R. Hathwar, P. Macchi, M. J. Turner, J. A. K. Howard, O. V. Dolomanov, H. Puschmann, B. B. Iversen, H.-B. Bürgi, S. Grabowsky, "Probing the accuracy and precision of Hirshfeld atom refinement with HARt interfaced with Olex2", *IUCrJ* **2018**, *5*(1), 32-44.

4. M. Fugel, J. Beckmann, D. Jayatilaka, G. V. Gibbs, S. Grabowsky, "A variety of Bond Analysis Methods, One Answer? An Investigation of the Element-Oxygen Bond of Hydroxides $H_nXOH$" *Chem. Eur. J* **2018**, *24*(23), 6248-6261. ⋆

5. M. Fugel, F. Kleemiss, L. A. Malaspina, R. Pal, P. R. Spackman, D. Jayatilaka, S. Grabowsky "Investigating the resonance in nitric acid and the nitrate anion based on a modern bonding analysis", *Austr. J. Chem.* **2018**, *71*(4), 227-237. ⋆

6. M. Fugel, M. F. Hesse, R. Pal, J. Beckmann, D. Jayatilaka, M. J. Turner, A. Karton, P. Bultinck, G. S. Chandler, S. Grabowsky, "Covalency and Ionicity Do Not Oppose Each Other—Relationship Between Si−O Bond Character and Basicity of Siloxanes" *Chem. Eur. J.* **2018**, *24*(57), 15275–15286. ⋆

7. M. Fugel, L. A. Malaspina, R. Pal, S. P. Thomas, M. W. Shi, M. A. Spackman, K. Sugimoto, S. Grabowsky, "Revisiting a historic concept using quantum crystallography: Are phosphate, sulfate and perchlorate anions hypervalent?" *Chem. Eur. J.* **2019**, *25*(26), 6523–6532. ⋆

8. J. Köhling, V. Kozel, V. Jovanov, R. Pajkert, S. N. Tverdomed, O. Gridenco, M. Fugel, S. Grabowsky, G.-V. Röschenthaler, V. Wagner, "Synthesis and Characterization of Oxazaborinin Phosphonate for Blue OLED Emitter Applications" *ChemPhysChem* **2019**, *20*(5), 665-671.

# Acknowledgments

An erster Stelle möchte ich mich ganz herzlich bei meinem Doktorvater **Prof. Dr. Simon Grabowsky** bedanken, der es mir ermöglicht hat dieses Promotionsprojekt in Angriff zu nehmen. Er hat mir stets viel Vertrauen entgegengebracht und mir viele Freiheiten eingeräumt. Außerdem stand er mir immer mit viel Rat und Tat zur Seite. Mit seiner wissenschaftlichen Arbeitsweise hat er mich stets inspiriert. Außerdem bedanke ich mich für die Möglichkeit während meiner Doktorarbeit zahlreiche internationale Konferenzen (z.B. in Indien und Kanada) zu besuchen und Messungen am Synchrotron SPring-8 in Japan durchzuführen. Es ist mir bewusst, dass diese Möglichkeiten einem Doktoranden für gewöhnlich nicht geboten werden. Ich hoffe sehr, dass unsere Zusammenarbeit an den noch offenen Projekten auch so erfolgreich weiterläuft nachdem ich die Arbeitsgruppe verlasse.

Vielen Dank an **Prof. Dr. Jens Beckmann**, dass er viele der Projekte mit seinen Ideen und Anmerkungen tatkräftig unterstützt hat. Sein ausgeprägter chemischer Sachverstand war stets eine große Hilfe für meine Arbeit. Ich möchte mich auch dafür bedanken, dass er die Begutachtung meiner Dissertation übernimmt.

Ich bedanke mich auch bei **Prof. Dr. Thomas Müller**, dass er sich dazu bereiterklärt hat, meine Dissertation zu begutachten.

**Dr. Maksym Ponomarenko** hat viel Arbeit in die Synthese und Kristallisation der pentakoordinierten Siliziumverbindungen aus Part V gesteckt. Durch sein synthetisches Geschick hat er diese Studie erst ermöglicht.

**Prof. Dr. Dylan Jayatilaka** – also known as the "Lord of Tonto" – helped me perform *Hirshfeld Atom Refinements* and *X-ray constrained wavefunction fittings*. I could talk to him about technical problems involving these programs. Furthermore, it was always nice to talk science with him.

**Florian Kleemiß** konnte mir mit seinem ausgeprägten Computerverstand unzählige Male bei

meinen Computerproblemen helfen. Ohne ihn hätte ich vermutlich meinen vermutlich Computer schon längst aus dem Fenster geworfen. Danke für die gute Zusammenarbeit mit dir, die wir beispielsweise bei unsere gemeinsame Messzeit in Japan unter Beweis stellen konnten.

**Lorraine Andrade Malaspina** was such a big help to me whenever I encountered crystallographic problems. I learned so about crystallography from you. Thanks for the many coffee breaks we had together and for always being there for me! Obrigado!

Thanks to my long-time office partner **Dr. Rumpa Pal**. I enjoyed sharing an office with you and we always had a great time together!

Vielen Dank an **Dr. Emanuel Hupf** für die schöne Zeit, die wir miteinander verbracht haben!

Das selbe lässt sich zu **Dr. Pim Puylaert** sagen. Danke, dass du mit deiner Art stets für gute Laune gesorgt hast! Dank je well!

Danke auch **Anneke Dittmer** für die Zusammenarbeit an den Projekten des zweiten Teils "Transformation of chemical bonds".

Mit **Erna Wieduwilt** habe ich mir lange ein Büro geteilt. Wir hatten immer eine gute Zeit zusammen, für die ich mich bedanken möchte.

Danke auch an alle weiteren Studenten, mit denen ich mir ein Büro geteilt habe. Zu erwähnen sind hier vor allem **Justin Bergmann** und **Arta Safari**.

On countless conferences, which I could attend, I got into contact with many excellent researchers, with who I had many fruitful discussions concerning my work. In particular, I would like to thank **Prof. Dr. Alessandro Genoni**, **Prof. Dr. Dietmar Stalke** and **Dr. Miroslav Kohout**.

I would like to thank **Ming Wen Shi** and **Dr. Sajesh P. Thomas** for attending my first beamtime at SPring-8 with me. I could learn a lot from your experience. Also thanks to the beamline technician **Dr. Kunihisa Sugimoto**, who was alway a big help when problems occured.

Zuletzt möchte ich mich natürlich auch bei meiner Familie, meinen Freunden und meiner Freundin dafür bedanken, dass ihr mich stets moralisch unterstützt habt. Auf euch war immer

Verlass! Ganz besonders möchte ich jedoch bei meinem Vater **Hans Fugel** bedanken, ohne den ich nie so weit gekommen wäre und der immer hinter mich stand!

**Declaration on the contribution of the candidate to a multi-author article/manuscript which is included as a chapter in the submitted doctoral thesis**

**Chapter 5 "A variety of Bond Analysis Methods, One Answer?":**

**Contribution of the candidate in % of the total work load (up to 100% for each of the following categories):**

| | |
|---|---|
| Experimental concept and design: | ca. 50% |
| Experimental work and/or acquisition of (experimental) data: | ca. 100% |
| Data analysis and interpretation: | ca. 100% |
| Preparation of Figures and Tables: | ca. 100% |
| Drafting of the manuscript: | ca. 90% |

**Chapter 6 "Covalency and Ionicity Do Not Oppose Each Other":**

**Contribution of the candidate in % of the total work load (up to 100% for each of the following categories):**

| | |
|---|---|
| Experimental concept and design: | ca. 30% |
| Experimental work and/or acquisition of (experimental) data: | ca. 20% |
| Data analysis and interpretation: | ca. 80% |
| Preparation of Figures and Tables: | ca. 100% |
| Drafting of the manuscript: | ca. 70% |

**Chapter 7 "Investigating the Resonance in Nitrate Anion and Nitric Acid":**

**Contribution of the candidate in % of the total work load (up to 100% for each of the following categories):**

| | |
|---|---|
| Experimental concept and design: | ca. 50% |
| Experimental work and/or acquisition of (experimental) data: | ca. 20% |
| Data analysis and interpretation: | ca. 70% |
| Preparation of Figures and Tables: | ca. 85% |
| Drafting of the manuscript: | ca. 85% |

**Chapter 8 "Are Phosphate, Sulfate and Perchlorate Anions Hypervalent":**

**Contribution of the candidate in % of the total work load (up to 100% for each of the following categories):**

| | |
|---|---|
| Experimental concept and design: | ca. 50% |
| Experimental work and/or acquisition of (experimental) data: | ca. 80% |
| Data analysis and interpretation: | ca. 100% |
| Preparation of Figures and Tables: | ca. 100% |
| Drafting of the manuscript: | ca. 90% |

**Chapter 9 "The different nature of carbon and silicon in $S_N2$ reactions":**

**Contribution of the candidate in % of the total work load (up to 100% for each of the following categories):**

| | |
|---|---|
| Experimental concept and design: | ca. 50% |
| Experimental work and/or acquisition of (experimental) data: | ca. 100% |
| Data analysis and interpretation: | ca. 90% |
| Preparation of Figures and Tables: | ca. 100% |
| Drafting of the manuscript: | ca. 90% |

**Chapter 10 "The role of hydrogen bonding in gas-phase $S_N2$ reactions at silicon":**

**Contribution of the candidate in % of the total work load (up to 100% for each of the following categories):**

| | |
|---|---|
| Experimental concept and design: | ca. 50% |
| Experimental work and/or acquisition of (experimental) data: | ca. 100% |
| Data analysis and interpretation: | ca. 90% |
| Preparation of Figures and Tables: | ca. 100% |
| Drafting of the manuscript: | ca. 90% |

**Chapter 10 "The nature of the N-Si interaction":**

**Contribution of the candidate in % of the total work load (up to 100% for each of the following categories):**

| | |
|---|---|
| Experimental concept and design: | ca. 50% |
| Experimental work and/or acquisition of (experimental) data: | ca. 33% |
| Data analysis and interpretation: | ca. 80% |
| Preparation of Figures and Tables: | ca. 90% |
| Drafting of the manuscript: | ca. 80% |

Date:

Signatures:

Universität Bremen

Ort, Datum: _____

**Versicherung an Eides Statt**

Ich, Malte Fugel, Isarstraße 31, 28199 Bremen, 2613866 (Vorname, Name, Anschrift, Matr.-Nr.)

.

versichere an Eides Statt durch meine Unterschrift, dass ich die vorstehende Arbeit selbständig und ohne fremde Hilfe angefertigt und alle Stellen, die ich wörtlich dem Sinne nach aus Veröffentlichungen entnommen habe, als solche kenntlich gemacht habe, mich auch keiner anderen als der angegebenen Literatur oder sonstiger Hilfsmittel bedient habe.
Ich versichere an Eides Statt, dass ich die vorgenannten Angaben nach bestem Wissen und Gewissen gemacht habe und dass die Angaben der Wahrheit entsprechen und ich nichts verschwiegen habe.
Die Strafbarkeit einer falschen eidesstattlichen Versicherung ist mir bekannt, namentlich die Strafandrohung gemäß § 156 StGB bis zu drei Jahren Freiheitsstrafe oder Geldstrafe bei vorsätzlicher Begehung der Tat bzw. gemäß § 161 Abs. 1 StGB bis zu einem Jahr Freiheitsstrafe oder Geldstrafe bei fahrlässiger Begehung.

_____
Ort, Datum Unterschrift

Der Arbeit liegt eine CD-ROM mit einer elektronischen Version der Arbeit vor. Hiermit versichere ich, Malte Fugel, mit meiner Unterschrift, dass die darin enthaltene Version mit der abgegebenen abgedruckten Version identisch ist.

_____

Ort, Datum, Unterschrift

Außerdem enthält die CD-ROM *crystallographic information files (cifs)* zu den in der Arbeit enthaltenen Kristallstrukturen.